Abstract

Jet-Hadron Correlations Measured in Pb–Pb Collisions at $\sqrt{s_{\mathrm{NN}}} = 5.02$ TeV with ALICE

Raymond Ehlers III

2020

Quantum Chromodynamics (QCD) describes the interactions of quarks and gluons. Due to asymptotic freedom, sufficiently high energy density can cause matter to transition to a deconfined state of matter known as the Quark-Gluon Plasma. As partons propagate through this QCD medium, which can be formed in ultra-relativistic heavy-ion collisions, they lose energy and the resulting jets are known to be modified in a phenomena known as jet quenching.

This thesis investigates the potential path length dependence of jet quenching via the measurement of azimuthal jet-hadron correlations with respect to the event plane orientation in Pb–Pb collisions at $\sqrt{s_{\mathrm{NN}}} = 5.02$ TeV with the ALICE detector. A study of this type also helps constrain the large background underlying this measurement. The associated hadron yields and correlation widths associated with the trigger and recoil jets are compared as a function of event plane orientation. They are found to be predominately consistent between the different orientations within uncertainties, although there are suggestions of deviations at low associated particle transverse momentum. Indeed, theoretical predictions suggest that any deviations are expected to be small, which may be due to competing processes associated with jet quenching. I also discuss my contributions to ALICE Overwatch, a project to enable nearly real-time data quality monitoring and assurance using the capabilities of the High Level Trigger.

Jet-Hadron Correlations Measured in Pb–Pb Collisions at $\sqrt{s_{\mathrm{NN}}} = 5.02$ TeV with ALICE

A Dissertation
Presented to the Faculty of the Graduate School
of
Yale University
in Candidacy for the Degree of
Doctor of Philosophy

by
Raymond Ehlers III

Dissertation Director: Professor Helen Caines

May 2020

Contents

Acknowledgements

This thesis and all of the work contained within could not have been completed without the unwaivering support from my extraordinary colleagues, friends, and family. First and foremost, I want to thank my advisor Professor Helen Caines and my co-advisor Professor John Harris. Helen's exceptional insight into both physics and problem solving taught me a huge volume of physics, and also how best to approach seemingly intractable problems. Her endless knowledge, support, and advice through the ups and downs over the course of my Ph.D, especially during the writing process, was a critical contributor to my success. John's tireless advocacy, support, and insight have been invaluable to my development as a physicist and the research that I have conducted in the RHI Group. He always knows the right question to ask at the right time, probing to the key issue at hand, and has given me the confidence to express my physics understanding. Both of you are exemplary physicists, and I'm inspired by your advocacy for a diverse and equitable work environment. I will continue to aspire to emulate your example.

To Professor Keith Baker and Professor Thomas Appelquist, for serving on my thesis committee and for providing invaluable feedback through the course of my Ph.D.

To the Yale RHI Group, thanks to John and Helen for inviting me to join your group and for providing for an unparalleled set of opportunities and the environment to make the most of them. It's been an absolute joy to be a member of such a diverse and supportive group. I feel extremely fortunate to have had this opportunity to work with the brightest and kindest group of people that I have ever known. To Dr. James Mulligan and Dr. Salvatore Aiola, for your insights into physics, coding, and life, all of which have taught me so much and have had a hugely positive impact both professionally and personally. I'm honored to be your friend and colleague.

To my ALICE colleagues. It has been incredibly rewarding to have the opportunity to collaborate with such a diverse set of exceptionally talented and intelligent physicists. Although there are too many collaborators to enumerate, thanks to everyone who has had a positive impact on me, especially to Professor Christine Nattrass and Dr. Joel Mazer for your physics and technical insights, as well as your patience in addressing my endless questions, and to Professor Jacek Otwinowski and Barthélémy von Haller, for your support, advice, and encouragement on Overwatch, allowing me to learn and explore, and for the project to thrive.

To Professor Brian Cole of Columbia University, for his passion and insight about physics in general, as well as in our field, that inspired my interest in pursuing a Ph.D. in physics. Concepts and modes of thinking introduced in the first few days of class when I arrived on campus have had an indelible positive impact on my development as a physicist.

To my family. To my father, for teaching and showing me the right way to approach the world, shaping who am I and how I think about it. To my mother, for her support, kindness, and curiosity, always knowing when I needed that extra bit of encouragement. And to my sister, for showing me every day how to be an exceptional human being.

Finally, the writing itself could not have been possible without everyone's support, with special thanks to Dr. Laura Havener and Hannah Bossi for reading through countless drafts, and providing invaluable comments, advice, and support within our physics "club" through many days and nights.

Chapter 1

Introduction

1.1 Quantum Chromodynamics (QCD)

Quantum Chromodynamics (QCD) is a quantum field theory describing the interaction between quarks and gluons[1]. This non-abelean Yang-Mills theory is invariant under the SU(3) gauge group [1]. Interactions between spin-$\frac{1}{2}$ quarks are mediated by spin-1 gluons, which themselves carry QCD charge that is known as color charge[2]. Unlike Quantum Electrodynamics (QED) where the photon is electrically neutral, the self-interaction of the gluon causes a number of consequences which are discussed in further detail below. The QCD Lagrangian is given by:

$$\mathcal{L}_{\mathrm{QCD}} = -\frac{1}{4\pi g} G^{a}_{\mu\nu} G^{a\mu\nu} + \sum_{f=1}^{6} \bar{\psi}_f (i\gamma^{\mu} D_{\mu} - m_f)\psi_f \tag{1.1}$$

1. Quarks and gluons can be referred to together as partons.

2. There are three color charges which are referred to as red, green, and blue.

where g is the strong coupling, $G^a_{\mu\nu}$ is the gluon field strength tensor with gluon color index a running over the SU(3) gauge group, ψ_f is a quark field of flavor f, m_f is the quark mass of flavor f, $D_\mu = \partial_\mu - iA_\mu$ is the covariant derivative and A_μ is the gluon gauge field. In the standard model, f runs over six quark flavors: up, down, strange, charm, bottom, and top.

The gluon self-interactions lead to screening effects, which make interactions dependent on the energy scale. When calculated to one loop order using perturbative QCD (pQCD), the coupling goes as

$$\alpha_s(Q^2) = \frac{12\pi}{(11n_c - 2/3n_f)\log\left(Q^2/\Lambda^2_{\mathrm{QCD}}\right)} \tag{1.2}$$

where $\alpha_s = g/4\pi$, Q^2 is the momentum transfer in the system, n_c is the number of colors[3], n_f is the number of fermions in the theory[4], and $\Lambda_{\mathrm{QCD}} \approx 200$ MeV is the characteristic scale for QCD. As Q^2 increases[5], the coupling becomes weaker, asymptotically approaching 0 as $Q^2 \to \infty$. This behavior is known as asymptotic freedom. The evolution of α_s as a function of resolution scale $Q = \sqrt{Q^2}$ is shown in Fig. 1.1. The data clearly illustrates the decreasing coupling strength with increasing Q, and a particular model calculation based on pQCD is able to reproduce the behavior.

In the other direction, at sufficiently low Q^2, we move into the non-perturbative regime. In this regime, we cannot calculate the evolution of the coupling from first principles. However, data such as that shown in Fig. 1.1 show that the potential between pairs

3. This corresponds to the three color charges mentioned above.

4. This corresponds to the six quark flavors.

5. High Q^2 is equivalent to probing smaller distances.

of quarks and gluons increases as a function of separation. For sufficiently large separation, it becomes energetically favorable to produce new pairs of particles out of the vacuum. This phenomena, which is known as confinement, prevents the observation of free quarks in nature, and is why we only observe color charge neutral hadrons[6].

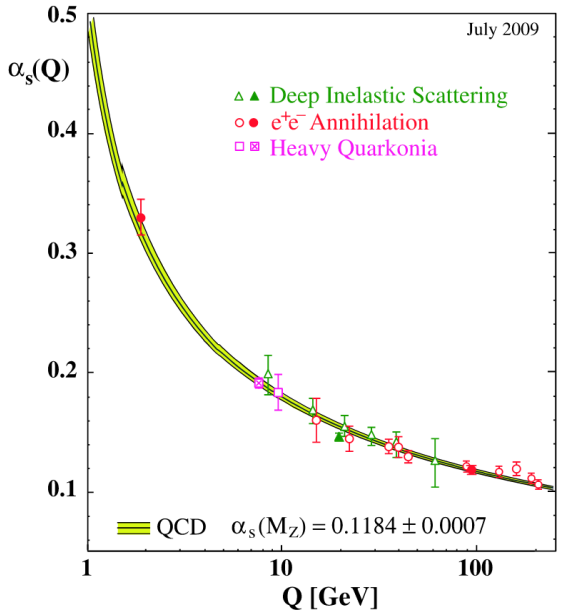

Figure 1.1: Measurements and predictions of α_s as a function of the energy scale Q. The data points are measurements while the curves are QCD predictions of the world average within a particular set of modeling assumptions. Figure is from [2].

1.2 Perturbative QCD and Jet Production

With a basic understanding of pQCD, we can consider the high momentum[7] scattering between two partons that are contained inside of hadrons. Due to the QCD factorization theorem [3], we are able to consider the perturbative and non-perturbative parts separately. The cross section for this interaction is given by

6. Hadrons are color neutral particles (meaning containing one of each color or color-anti-color pairs) formed out of combinations of quarks.

7. A high momentum transfer interaction is often described as a hard scattering, while a small momentum transfer interaction is often described as soft.

$$\sigma^{pp\to \mathrm{h/jet+X}} \propto \int \mathrm{d}x_1 \mathrm{d}x_2 f_a(x_1, Q^2) \otimes f_b(x_2, Q^2) \otimes \sigma^{a+b\to c+X} D_{a\to \mathrm{h/jet}}(z, Q^2) \qquad (1.3)$$

where x_i is the fraction of the parent hadron momentum carried by parton a, $f_a(x_1, Q^2)$ is the parton distribution function of parton a in a hadron as described below, and $\sigma^{a+b\to c+X}$ is the partonic scattering cross section.

Parton distribution functions (PDFs) describe the probability of finding a parton with x inside of a hadron when probing at scale Q. Since the probabilities depend on the internal dynamics within a hadron, they are inherently non-perturbative. However, despite this non-perturbative nature, as long as they are probed with a sufficiently large scale Q to be within the perturbative regime, then the distributions can be evolved to another perturbative scale, Q' using the DGLAP equations [4–6]. Experimentally, this means that if the PDFs are measured once, they can be evolved to other Q as necessary. PDFs as determined by a global fit to the available data by the NNPDF Collaboration is shown in Fig. 1.2. The probability of finding an up or down quark peaks near $x = 1/3$ as expected for valence quarks, while at low x gluons dominate.

As discussed above, due to confinement we do not observe outgoing partons. Instead, the outgoing partons fragment into collimated sprays of hadrons which are known as jets. This process is governed by the fragmentation function, $D_{a\to \mathrm{h/jet}}(z, Q^2)$, where z is the fraction of the parent parton momentum carried by the created hadron. Similar to the PDFs, the fragmentation functions are also non-perturbative, but can be evolved using the DGLAP evolution equations.

The scattering process described above can be simulated using Monte Carlo techniques. One of the most prevalent pp generators is PYTHIA [8,9], which samples the calculated

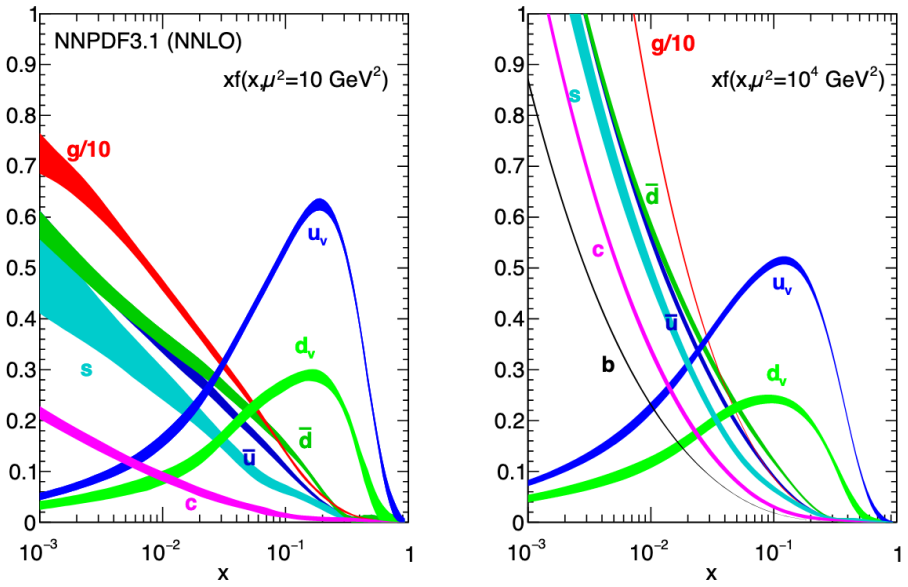

Figure 1.2: The NNPDF3.1 parton distribution functions at $Q^2 = 10$ and 10^4. The y-axis is $xf(x)$. Note that the gluon contribution is scaled down by a factor of 10. Figure from [7]

cross sections and measured parton distribution functions, and then fragments into hadrons using the Lund String model, which creates hadrons by breaking strings connecting partons which are closely linked in phase space. By simulating this process, full pp collisions can be generated to compare against data.

1.3 Quark-Gluon Plasma

As discussed above, partons are confined to hadrons at low Q^2 due to the strength of the coupling and gluon self-interaction, but as Q^2 increases, α_s decreases. Consequently, for sufficiently small values of α_s, we expect a transition from fully confined partons to partons becoming asymptotically free. During this phase transition, the relevant degrees of freedom for describing the system will transition from hadronic to partonic. This new state is known as the Quark-Gluon Plasma (QGP).

The QGP can be better understood from the perspective of the QCD phase diagram,

which is shown in Fig. 1.3. The phase diagram is plotted as a function of the baryon chemical potential, μ_B, and the temperature, T. The QGP is found at relatively large temperature T, but with a wide range of μ_B values. At the Large Hadron Collider, $\mu_B \approx 0$.

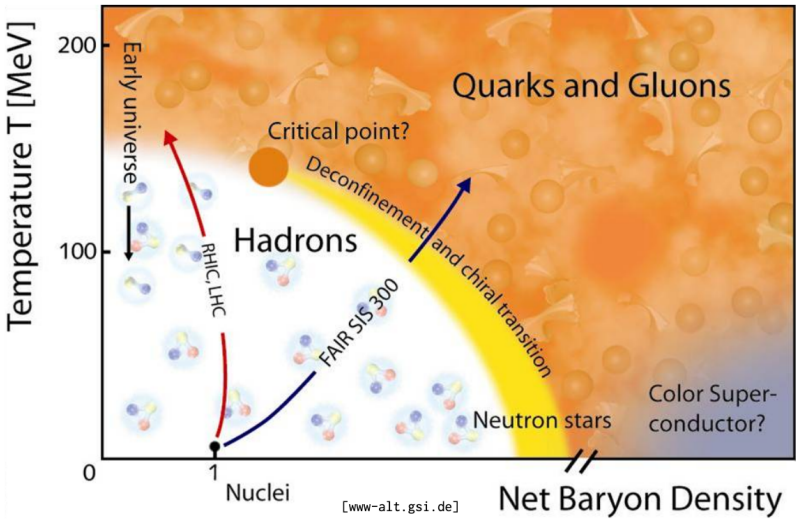

Figure 1.3: QCD phase diagram as a function of the net baryon density and the temperature, T. The net baryon density is correlated with the baryon chemical potential, μ_B. Collisions at RHIC and the LHC trace trajectories through the phase space. Note that this diagram is only schematic, as large sections of the phase space remain unexplored. Figure from [10].

The phase transition occurs in the non-perturbative regime, so it cannot be directly calculated. However, this doesn't preclude all calculation. In particular, there is a thriving field devoted to calculating QCD on a lattice. In this approach, thermodynamic quantities are calculated on a grid, and then the continuum limit is evaluated. The result of one calculation is shown in Fig. 1.4, with the yellow band representing the predicted range of the critical temperature where the transition occurs, T_c[8]. The energy density normalized by the temperature shown in the figure is proportional to the number of relativistic degrees of freedom, illustrating the transition from hadronic to partonic degrees of freedom mentioned above. Lattice also predicts that the phase

8. More recent results from Lattice QCD predict $T_c = 156.5 \pm 1.5$ MeV/k_B [11].

transition occurs as a crossover, meaning that the transition from hadronic matter to the QGP is continuous[9].

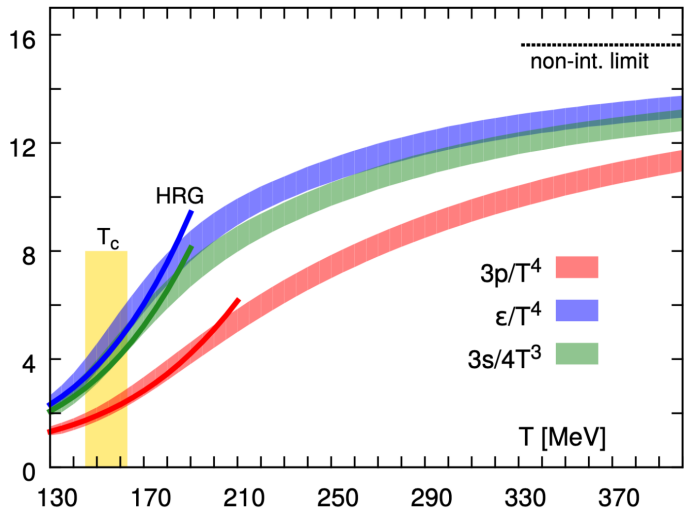

Figure 1.4: Pressure, energy density, and entropy density plotted as a function of T. The yellow band illustrates the predicted crossover region [12].

Measurements continue to show that the QGP properties are at the extreme of a variety of measured quantities, including the highest recorded temperature of $T \approx 240 - 300$ MeV/k_B [13,14], lowest shear viscosity [15–17], and most vortical [18] system ever measured. Studying the QGP provides a unique opportunity to study such extremes in the laboratory, thereby providing a wide variety of new constraints for theory.

1.4 Heavy Ion Collisions

In order to access this phase transition experimentally, we must provide sufficient energy density for the transition to occur. To create the necessary large energy densities, heavy ions are accelerated to ultra-relativistic velocities and collided together. Due to the energy carried by the accelerated ions and Lorentz contraction, when the nuclei

9. The Beam Energy Scan at RHIC is attempting to look for the critical point where the phase transition becomes a first order transition.

collide, the energy density in the collision is approximately $\epsilon \approx 1$ GeV/fm^3.

There are two key facilities where heavy ions are collided: The Relativistic Heavy Ion Collider (RHIC) at Brookhaven National Lab in Upton, NY, USA and at the Large Hadron Collider at The European Organization for Nuclear Research (CERN) in Geneva, Switzerland, which will be discussed further in Ch. 2.

A cartoon of the stages of a heavy ion collision is shown in Fig. 1.5. In the initial stage, the nuclei are highly Lorentz contracted and are often modeled via the Glauber model, as described below. Upon the initial collision, a hard scattering may occur between two of the incoming partons. From the uncertainty principle, this scattering occurs on a short time scale, far before the medium has formed. This provides the opportunity for it to probe the evolving medium as the struck parton propagates through it.

In a typical heavy ion collision, the hard scattering tends to occur alongside a large number of softer collisions. The participants in these inelastic soft collisions impart their energy into the collision region, providing sufficient energy density to form the Quark Gluon Plasma. During this period, the medium is far from equilibrium. After $\tau \approx 1.0$ fm/c, the system has sufficiently thermalized such that the evolution of the medium can be described using viscous hydrodynamics, typically in 3+1 dimensions[10] [19]. However, the exact mechanism for thermalization of the QGP remains unknown.

As the medium expands and evolves, the temperature drops, eventually undergoing a phase transition from the QGP to a hadron gas. During this transition, the partons in the medium are paired and grouped into hadrons in a process known as hadronization. After forming hadrons, they can still interact inelastically and change flavors until chemical freeze-out. In the next stage, the hadrons may interact elastically until

10. The dimensionality is stated this way because some Hydrodynamic predictions are only performed in 2 spatial dimensions plus time, or 2+1D.

kinetic freeze-out. After that, the particles free stream toward the detector.

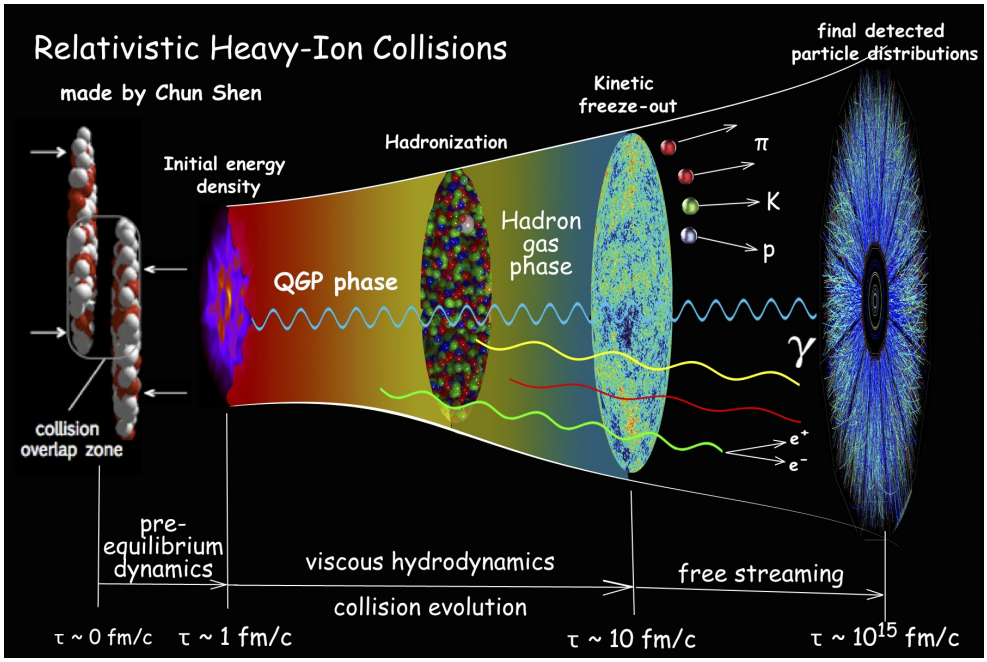

Figure 1.5: Cartoon of the stages of a heavy ion collision from the initial state to the detection of the created particles. Each stage is covered in the text. Figure from [20].

In heavy ion experiments, a cylindrical coordinate system is utilized, with the azimuthal angle φ, and polar angle, θ. For experimental convenience, the polar angle, which is defined with respect to the beam axis, is instead converted to the pseudorapidity, $\eta = -\log\tan\frac{\theta}{2}$, which is approximately equal to the rapidity when $p \gg m$, where p is the momentum and m is the mass. For the other two components in a four-vector, particles are usually characterized by their transverse momentum, p_{T}, and their mass, m.

1.4.1 Centrality

In each collision, the event properties can vary dramatically depending on the impact parameter, which is the vector between the centers of the two colliding nuclei. Experimentally, we don't have direct access to this impact parameter, but instead we can

use the multiplicity at forward rapidity as a proxy. This multiplicity can be related to the initial collision geometry via the Glauber model.

In the Glauber model, nuclear collisions are modeled under the assumption that an entire collision can simply be treated as a superposition of individual nucleon-nucleon interactions [21–23]. Under this model, the nucleon density is distributed according to the Woods-Saxon potential, and then an MC process is utilized to sample these distributions, providing the number of binary collisions in a particular event. By fitting this distribution to an experimentally measured multiplicity distribution, we can extract the relationship between impact parameter distribution (and corresponding geometry) and multiplicity.

This distribution, divided into percentiles, is termed the centrality. An example of this distribution for Pb–Pb collisions at $\sqrt{s_{\mathrm{NN}}} = 2.76$ TeV measured by ALICE is shown in Fig. 1.6. 0–10% corresponds to the most central collisions with the highest particle multiplicity and smallest impact parameter distribution. My thesis will focus on central collisions, as well as 30–50% semi-central collisions, where the overlap region is ellipsoidal shaped.

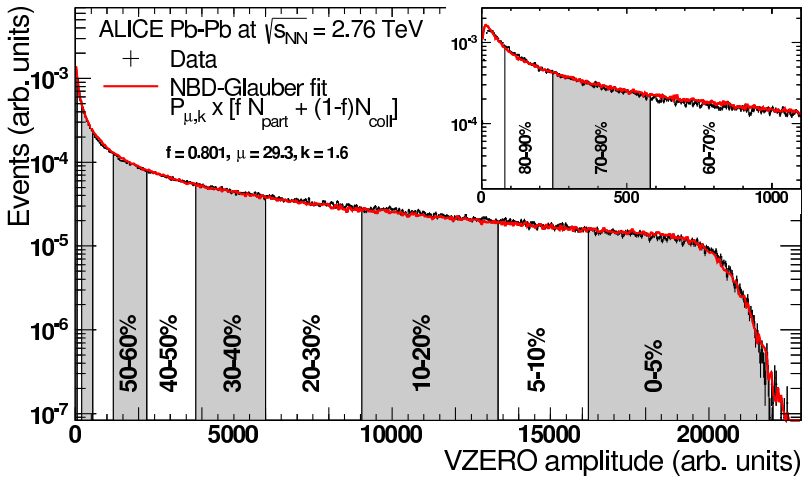

Figure 1.6: Multiplicity in the ALICE V0 detector located at forward rapidity, fit with the Glauber model, as shown in the red curve. The data are divided up in percentiles. Figure from [24].

1.4.2 Jets in Experiment

As described above, partons outgoing from a hard scattering fragment into a collimated spray of hadrons known as jets. Ideally, our experimentally found jets would fully encompass all of the final state hadrons from the fragmentation, but even in the case of pp collisions, the complexity of interactions between quarks and gluons inside of the protons, along with initial and final state radiation, preclude this direct connection. Consequently, jets measured by experiments only approximate the outgoing partons, and are only precisely defined by the jet algorithm that is used to find them.

For any jet finding algorithm, there is a characteristic parameter, R, which is known as the jet resolution parameter and roughly translates to the maximum distance a jet constituent can be from the jet centroid[11]. There are a broad variety of possible jet finding algorithms, but I will only focus on those predominately used at the LHC.

With the aid of modern computing power and computational techniques, it is possible to utilize sequential recombination algorithms which iteratively cluster particles to perform jet finding. These sequential recombination algorithms are desirable because they are inherently insensitive to the radiation of soft particles and splitting between collinear branches[12]. This class of algorithms is implemented via a set of metrics:

$$d_{ij} = \min(p_{T_i}^{2p}, p_{T_j}^{2p}) \frac{\Delta_{ij}^2}{R^2} \tag{1.4}$$

$$d_{iB} = p_{T_i}^{2p} \tag{1.5}$$

11. In the early years of jet finding, it was common to find jets using a cone. In that instance, R was the radius of the cone.

12. This set of properties is known as Infrared and Collinear (IRC) safety.

where p is the parameter governing the algorithm's behavior, $\Delta_{ij}^2 = (\eta_i - \eta_j)^2 + (\varphi_i - \varphi_j)^2$, B represents the beam line, and i and j index the particles in an event. The algorithm operates by iterating over all of the possible contributors[13] and identifying $\min(d_{ij}, d_{iB})$. If d_{ij} is the smallest value, particles i and j are added together and returned to the list of contributors. If d_{iB} is the smallest value, entry i is called a jet and it is removed from the list of contributors. This algorithm repeats until there are no contributors left [25]. This algorithm is implemented in the FastJet software package [26].

The behavior of the algorithm depends heavily on the parameter p. In the simplest case of $p = 0$, the metrics are weighted by the angular separation. This configuration is known as the Cambridge/Aachen algorithm and is often utilized in jet substructure measurements. For $p = 1$, the softest particles are clustered together first. This approach is called the k_T algorithm and it closely mirrors the QCD splittings. It is more sensitive to background particles, so it is often used for the characterization of the jet background, as explained below. Lastly, the anti-k_{T} algorithm corresponds to $p = -1$, which leads to the hardest particles being clustered together first [25]. In experimental jet finding, we want to be as insensitive to the background as possible, so starting with the hardest particles is preferred. Consequently, the anti-k_{T} algorithm is utilized for primary jet finding.

However, jet finding in heavy ion collisions doesn't have to deal with just the hard scattering. Bulk hadrons from the medium, whether radiated or from hadronization, create a major collection of background particles on which the jets sit[14]. Consequently, a portion of the measured $p_{\mathrm{T,jet}}$ is from the background and must be accounted for. This background contribution is characterized per unit area by the parameter ρ, which

13. On the first iteration, this is simply the list of particles in an event. However, as the algorithm iterates, this collection contains both particles, as well as particles combined together.

14. Even though this hydrodynamically flowing background is of interest to our field, it is just a background for jet finding, so I will sometimes refer to it as a "flow background".

is defined as:

$$\rho = median(p_{\mathrm{T,jet}}/A_{\mathrm{jet}}) \tag{1.6}$$

where the jets are found using the k_{T} algorithm, and A_{jet} is the area of the jet [27]. In order to avoid the influence of any possible hard scatterings, the leading and sub-leading jets are excluded from the calculation of the median. For ALICE, ρ is calculated using charged particle jets, and then the value is scaled up to account for the neutral contribution. In 0–10% central collisions at $\sqrt{s_{\mathrm{NN}}} = 5.02$ TeV, ALICE found that $R = 0.2$ inclusive full jets contain a mean background contribution of ≈ 27 GeV/c.

A common approach for correcting a jet spectra is as follows: First, the k_{T} algorithm is used to calculate the background and ρ is extracted for the current event. Next, the main jet finding is performed using the anti-k_{T} algorithm, and then the value of $\rho \times A$ is subtracted from $p_{\mathrm{T,jet}}$ on a jet-by-jet basis. Note that not only is the background contribution large, but it fluctuates event-by-event, and even within regions of a single event. Fully accounting for these fluctuations requires statistical unfolding. The approach for handling the background in this thesis is discussed in Sec. 3.2.4.

1.5 Experimental Evidence for the QGP

Evidence for the observation of the QGP consists of a wide variety of complementary measurements. The strength of this evidence has grown substantially with time since the initial discovery at RHIC was announced almost two decades ago, although small systems have complicated our understanding [28]. For my thesis, I will only focus on

two measurements.

1.5.1 Hydrodynamic flow

If we consider the case of a semi-central collision, ellipsoidal geometry in the plane transverse to the beam axis is expected to dominate the shape of the initial interaction region, which leads to a coordinate space anisotropy. When the particle multiplicity is measured as function of azimuthal angle, ϕ, the modulation is seen to have transfered into momentum space, and is usually characterized by

$$\frac{\mathrm{d}N}{\mathrm{d}\varphi} = \frac{N_0}{2\pi}(1 + \sum_n 2v_n \cos n(\varphi - \Psi)) \tag{1.7}$$

where N_0 is the number of measured particles, v_n are the magnitude of the n-th harmonic[15], and Ψ is the plane defined by the impact parameter and the beam axis, known as the reaction plane [29]. This momentum space anisotropy is understood to be caused by pressure gradients in the coordinate space anisotropy being translated into a momentum space anisotropy. A visualization of an idealized interaction is shown in Fig. 1.7, with the panel on the left showing the coordinate space anisotropy, and on the right showing the momentum space anisotropy.

Such a transfer is remarkable because it requires a strongly interacting fluid – a gaseous state is not sufficiently coupled. This coupling is characterized by the shear viscosity normalized by the entropy density, η/s. As shown in Fig. 1.8, predicting the v_n coefficients requires a small value of η/s, which should be interpreted as an

15. These coefficients are often referred to as flow or v_n coefficients. The $n = 2$ harmonic is known as elliptic flow and the $n = 3$ harmonic as triangular flow.

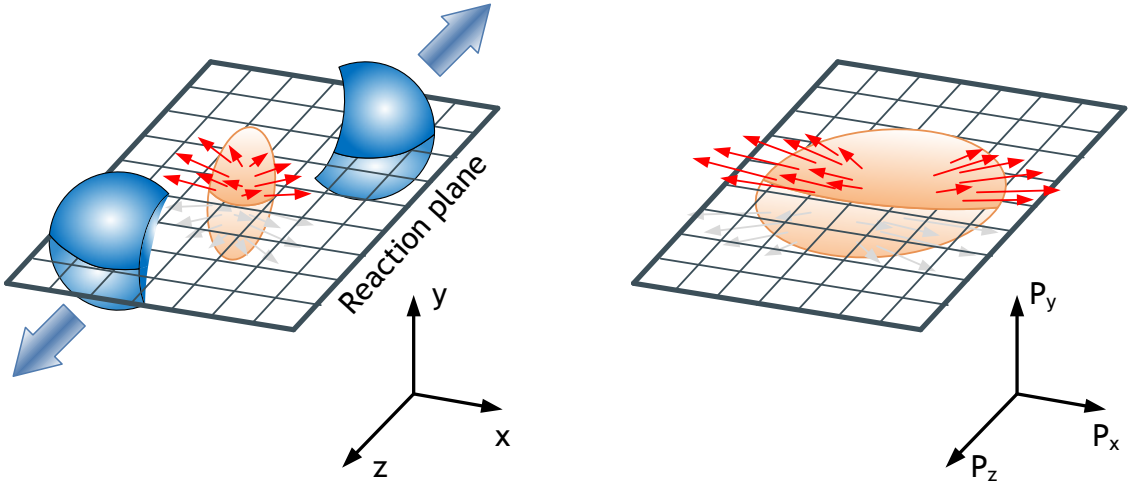

Figure 1.7: A cartoon of an idealized semi-central iteraction region. The left figure shows coordinate space, with the overlap region shown in orange, the spectators in blue, and the red arrows illustrate the pressure gradient. The right figure shows the interaction in momentum space, with red arrows illustrating the magnitude of the momentum. Figure from [30].

extremely viscous and strongly coupled system [17]. This value is near the lower limit of $1/4\pi$ predicted via AdS/CFT [15,16].

Although we considered the example of semi-central collisions due to the simplicity of the ellipsoidal collision geometry, this same phenomena applies to all collision centralities. However, the dominant collision geometry is not the entire story. Higher order n odd terms are possible due to fluctuations in the initial state, and higher order n even terms are produced due to initial state anisotropies or induced by lower order even harmonics. In the case of ultra-central collisions, as shown in Fig. 1.9, there is no dominant interaction region geometry, and instead higher order harmonics are seen to contribute heavily to the measured angular distributions.[16]

16. In this case, the distribution is derived from two particle correlations, which will be discussed more in Chapter 3.

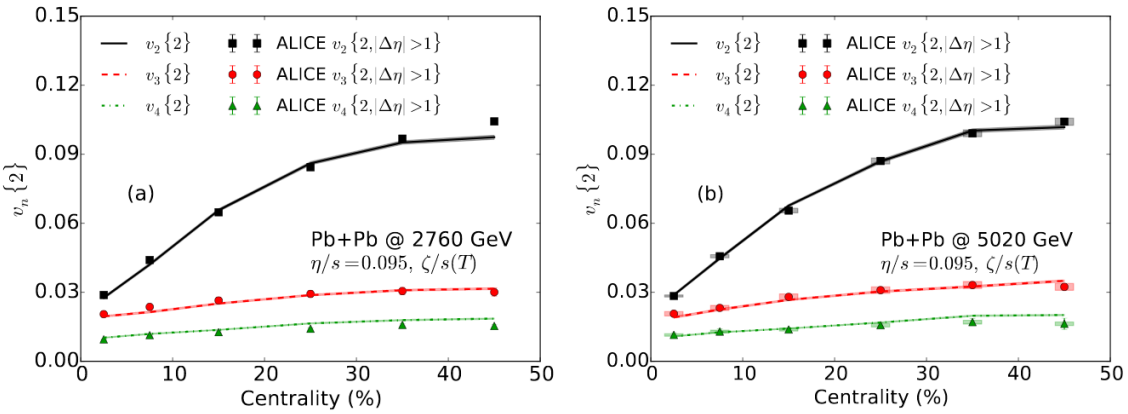

Figure 1.8: Predictions of v_n coefficients as a function of centrality using a particular set of models for the intial state, hydrodynamics, and hadronization. The predictions are compared to ALICE data measured at $\sqrt{s_{\rm NN}} = 2.76$ and 5.02 TeV. To predict the measured values, a value of $\eta/s = 0.095$ is required. The figure is from [17].

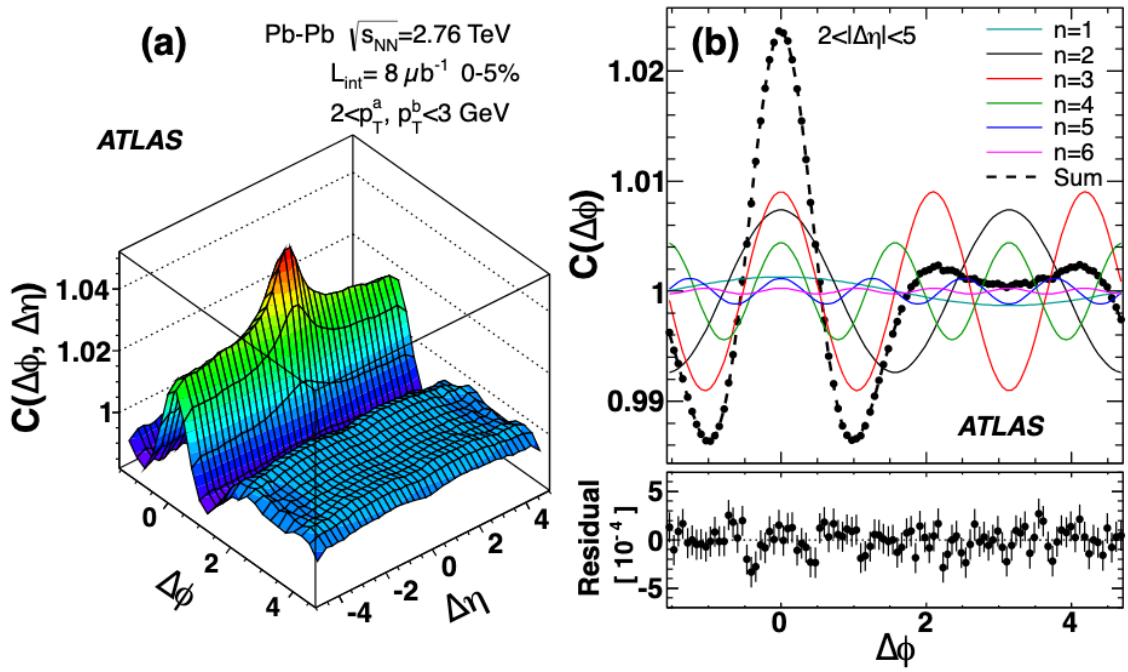

Figure 1.9: ATLAS ultra-central two particle angular correlation is shown on the left. A projection onto the $\Delta\varphi$ axis is shown on the right. The v_n components are apparent in both images.

1.5.2 Jet Quenching

As described below, when partons propagate through the medium, they are expected to interact and lose energy through a phenomena known as jet quenching. Experimentally, we expect to observe the impact of these jet-medium interactions as some sort of modification of the jet, but precisely how it appears depends on the particular observable. As described below, we generally expect that quenching will reduce the p_{T} and modify the internal jet structure. Crucially, such a measurement cannot be made solely on its own – it also requires a reference, which is usually the same measurement in pp collisions.

One of the first measurements of jet quenching was performed by measuring the yield of azimuthal two particle correlations. In this measurement, a high p_{T} hadron is selected, and then the angular distance $\Delta\varphi = \varphi_{\mathrm{trigger}} - \varphi_{\mathrm{assoc}}$ is calculated between the trigger and each associated hadron in an event[17]. Since we are interested in how each jet is modified, it is normalized by the number of triggers. These correlations are shown in Fig. 1.10, comparing 0–10% central Au–Au against the same measurement in pp and d-Au. All three measurements were performed at $\sqrt{s_{\mathrm{NN}}} = 200$ GeV. For all three systems, there is a clear peak around the high p_{T} trigger at $\Delta\varphi = 0$, while the corresponding recoil jet peak around $\Delta\varphi = \pi$ is clearly visible in pp and d-Au collisions, but is suppressed in Au–Au collisions [31–34]. This suppression is caused by quenching of the recoil jet as it propagates through the medium.

Jet quenching can also be seen through the nuclear modification factor, R_{AA}. The R_{AA} compares spectra measured in different collision systems by taking the ratio of the spectrum measured in Pb–Pb to the spectrum measured in pp. In order to make

17. My thesis analysis also utilizes these correlation techniques, and is discussed in more detail in Secs. 3.1 and 3.4.

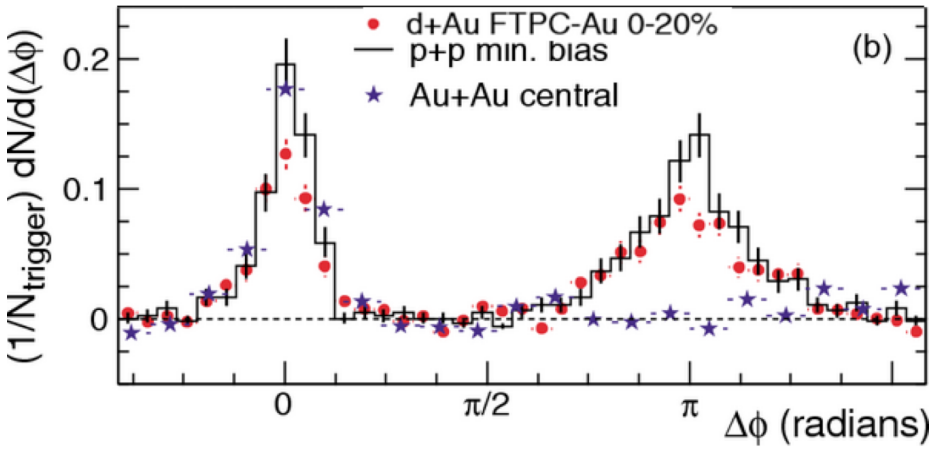

Figure 1.10: STAR two particle correlations measured in pp, d-Au, and Au–Au collisions. Despite similar peaks around the trigger particle, the recoil jet peak is suppressed in Au–Au compared to pp and d-Au. Figure from [32,34].

a comparison between comparable quantities, the pp spectrum is multiplied by the number of binary collisions in the Pb–Pb sample as determined in the Glauber model described above. This ratio can be constructed for a variety of spectra, including for hadrons, identified hadrons, or jets. Measurements of the R_{AA} for 0–10% central Pb–Pb collisions at $\sqrt{s_{\mathrm{NN}}} = 5.02$ TeV are shown in Fig. 1.11, with the left figure showing the ALICE jet R_{AA} [35], and the right showing the ATLAS jet R_{AA} [36]. Although there are some differences between the two measurements, significant suppression is clear over $40 < p_{\mathrm{T,jet}} < 1000$ GeV/c compared to pp collisions.

Beyond measuring suppression as a function of $p_{\mathrm{T,jet}}$, we can also investigate where the lost energy goes. To do so, we can analyze the angular distribution of the yield of particles relative to the jet axis. CMS measured this information as a function of the dijet axis. In the analysis, they measure the yield difference between the leading jet and sub-leading jet as a function of distance from the dijet axis, Δ, and as a function of associated hadron p_{T}. The measurement in Pb–Pb and pp collisions at $\sqrt{s_{\mathrm{NN}}} = 2.76$ TeV is shown in Fig. 1.12[18]. This carries a tremendous amount of information, but the

18. This analysis is sometimes referred to as measuring the missing p_{T}. Note that this is different than missing p_{T} or E_{T} measurements made in pp collisions.

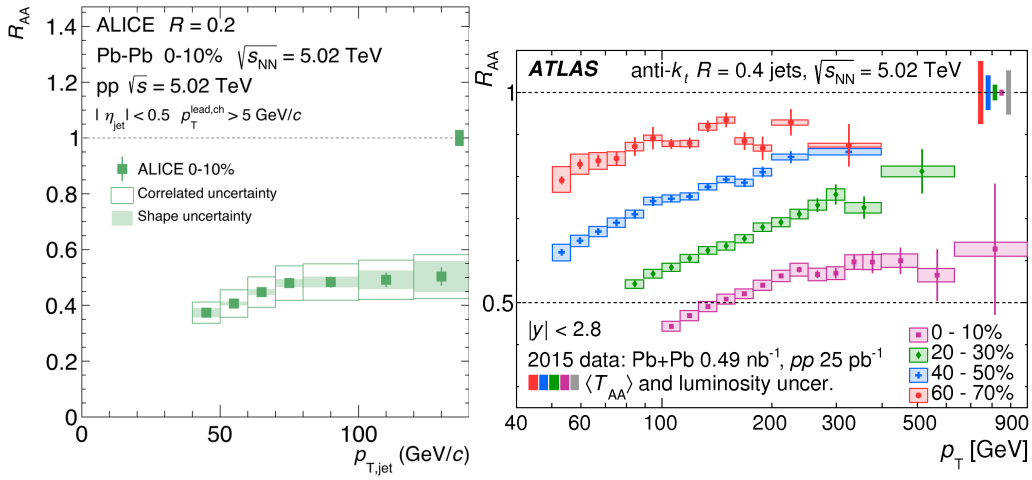

(a) ALICE Jet R_{AA} for $R = 0.2$ jets. (b) ATLAS Jet R_{AA} for $R = 0.4$ jets.

Figure 1.11: Jet R_{AA} measured in 0–10% central Pb–Pb collisions at $\sqrt{s_{\mathrm{NN}}} = 5.02$ TeV. There are some differences in the measurements, but both show significant jet suppression over a wide $p_{\mathrm{T,jet}}$ range. Figures from [35,36].

main figure of interest is in the comparison between central Pb–Pb - pp in the lower right panel. Here we see that there are more high p_{T} particles going in the direction of the leading jet in Pb–Pb compared to pp. For the subleading jet, we see that more lower p_{T} particles are distributed further away from the jet axis. This result shows that the sub-leading jet is quenched near the jet axis, and that energy is redistributed to softer particles further away from the jet axis [37]. Similar information can be also be extracted from the jet fragmentation functions, as measured by CMS [38] and ATLAS [39].

1.6 Jet Quenching Models

As partons propagate through the medium, they are expected to interact and lose energy via both elastic collisional energy loss with the medium constituents and radiative energy loss induced by the medium. Those two interactions are illustrated in Fig. 1.13. Radiative energy loss is expected to be the dominant mechanism [40].

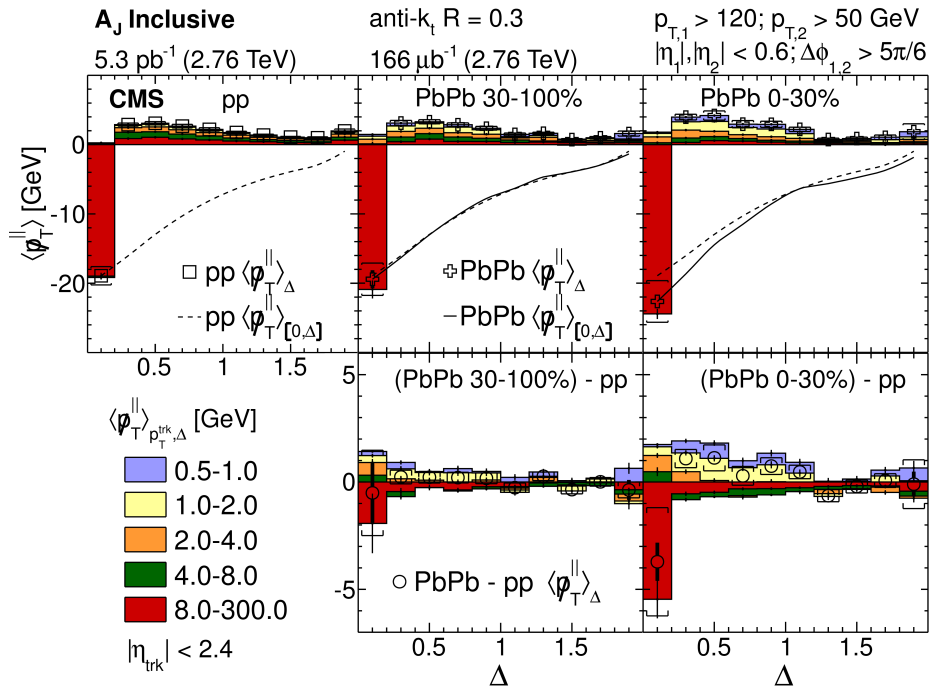

Figure 1.12: CMS particle yield relative to the dijet axis measured in Pb–Pb and pp collisions at $\sqrt{s_{\mathrm{NN}}} = 2.76$ TeV. The symbols show the sum of the momentum balance at a given distance from the dijet axis, Δ, while the colored boxes show the distribution of particles within the given Δ as a function of particle p_{T}. See the text for further details. Figure from [37].

Within this general framework, there are a variety of theoretical approaches to jet quenching. These models can be characterized by $\hat{q}$, which describes the average transverse momentum squared per unit path length, L, that is transfered by a jet traversing the medium. As described in Ch. 3, this thesis explores the path length dependence of energy loss, so we will characterize the models by their path length dependence.

There are a number of pQCD based models which make a variety of different assumptions about how to describe the interaction, but all share roughly the same goal of trying to calculate the rate of gluon emissions by the jet [40]. Note that these models assume that the effects of energy loss are largely manifest in modifications of fragmentation functions in the medium. For these models, collision energy loss is expected to be proportional to L, while radiative it is expected to be proportional to L^2. An alternative to this pQCD approach is available through AdS/CFT. This approach calculates energy loss as equivalent to drag of the jet propagating through a medium, with energy loss proportional to L^3.

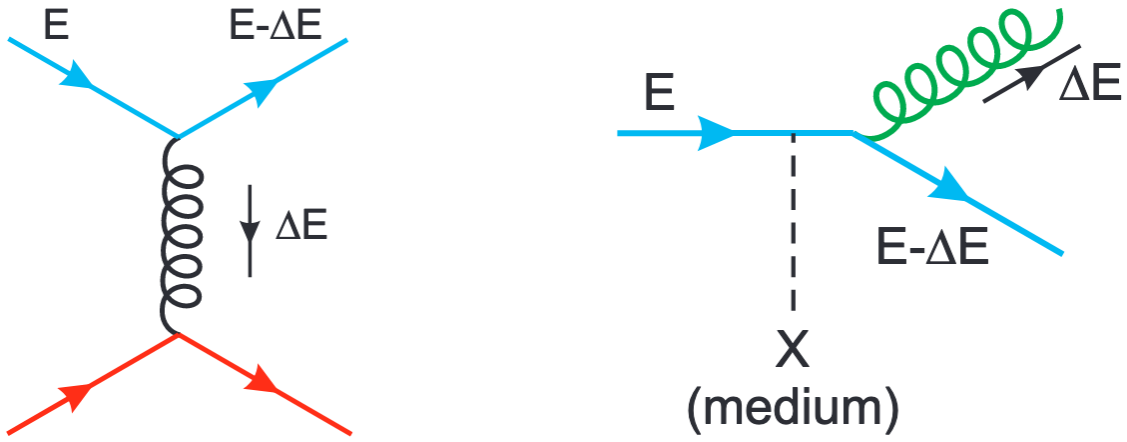

Figure 1.13: Base interactions for parton energy loss in the medium. The parton loses ΔE for its initial energy E due to collisional energy on the left, and radiation energy loss on the right. Figure from [40].

Due to the complexity of a single heavy ion collision as described in Sec. 1.4, it is not

yet feasible to simulate an entire collision. Instead, most models deal with one aspect of the collision in detail, and then use approximations for the rest of the collision[19]. Despite this limitation, these models can still provide insight into the physics of jet quenching. Of particular note is the JEWEL (Jet Evolution With Energy Loss) Monte Carlo [42,43]. JEWEL simulates the medium as a longitudinally expanding thermal spectrum, and utilizes PYTHIA for the hard scattering and hadronization. As the jet propagates through the medium, it samples the spectrum, performing $2 \rightarrow 2$ collisional elastic scatterings between the partons or the medium. This scattering includes a variety of initial and final state radiation terms to account for radiative energy loss. There are two primary output modes for JEWEL: one in which the recoiling partons from the medium are kept in the output, and one in which they are not. In the case of keeping the recoils, the energy lost by the propagating parton is redistributed in the event, but it also adds in the energy of the medium recoil. When the medium recoils are discarded, energy that is lost by the propagating parton is entirely removed from the event. Jet energy loss is expected to be bounded by these two modes. JEWEL has a number of tunable parameters, the most of important of which is the initial temperature. For Pb–Pb collisions at the LHC, this temperature is $\approx 500 MeV$.

1.7 Previous measurements

In Chapter 3, I will discuss my measurement of jet-hadron correlations with ALICE. However, there have also have been a number of previous jet-hadron correlation measurements at both RHIC and the LHC characterizing both the trigger and recoil jet. The first measurement of jet-hadron correlations was performed by the STAR

19. Efforts are under way within the JETSCAPE collaboration to develop a modular framework to simulate collisions, allowing one stage of the simulation to be replaced while all the others are kept the same, but the effort is still under development [41].

collaboration in 0–20% central Au–Au and pp collisions at $\sqrt{s_{\mathrm{NN}}} = 200$ GeV [44]. The measurement characterized the distribution of hadrons of the recoil jet, which they attempted to bias towards the longest possible path length. They compared measurements in Au–Au and pp at detector level by embedding the pp spectra into minimum bias Au–Au data[20]. The gaussian widths of the angular distribution of associated hadron of the recoil jet are shown in the upper panel of Fig. 1.14. These widths qualitatively suggest broadening at low $p_{\mathrm{T}}^{\mathrm{assoc}}$, but the uncertainties were too large for quantitative conclusions. The yield differences, $D_{\mathrm{AA}} \propto Y_{\mathrm{AA}} - Y_{\mathrm{pp}}$, measured between Au–Au and pp are shown in the lower panel of Fig. 1.14. At high $p_{\mathrm{T}}^{\mathrm{assoc}}$, the Au–Au yields are suppressed compared to pp, while at low $p_{\mathrm{T}}^{\mathrm{assoc}}$ they are enhanced. The sum of these yields over the $p_{\mathrm{T}}^{\mathrm{assoc}}$ range is consistent with zero, so the suppression at high $p_{\mathrm{T}}^{\mathrm{assoc}}$ is recovered at low $p_{\mathrm{T}}^{\mathrm{assoc}}$.

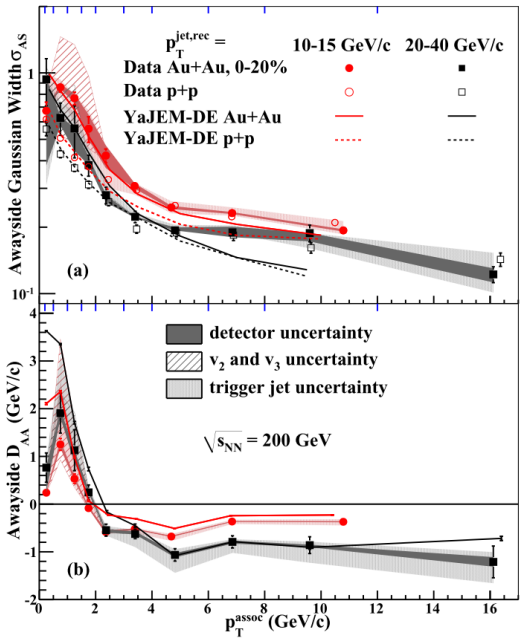

Figure 1.14: STAR jet-hadron measurement for Au–Au and pp collisions at $\sqrt{s_{\mathrm{NN}}} = 200$ GeV. The away-side gaussian widths are shown in the upper panel, while the away-side D_{AA} is shown in the lower panel.

20. Note that the STAR $p_{\mathrm{T,jet}}$ range overlaps with the jet-hadron measurement presented in this thesis. The jet spectra that contribute to the measurements are compared in Sec. 4.4.

CMS measured jet-hadron correlations at $\sqrt{s_{\mathrm{NN}}} = 2.76$ TeV in Pb–Pb collisions. They measured correlations around the trigger peak as a function of both azimuth and pseudorapidity[21]. Their azimuthal correlations as a function of centrality are shown in Fig. 1.15. For their selection of high $p_{\mathrm{T,jet}}$ and low $p_{\mathrm{T}}^{\mathrm{assoc}}$, they measured a larger yield for all centralities than in pp, with increasing yield towards more central collisions. This larger yield also corresponds to wider distributions as a function of φ compared to pp. They see similar trends as a function of pseudorapidity. We can understand these results as showing an increased yield at low $p_{\mathrm{T}}^{\mathrm{assoc}}$ and at wider angles from the jet axis when compared to pp, consistent with the other jet quenching measurements presented above.

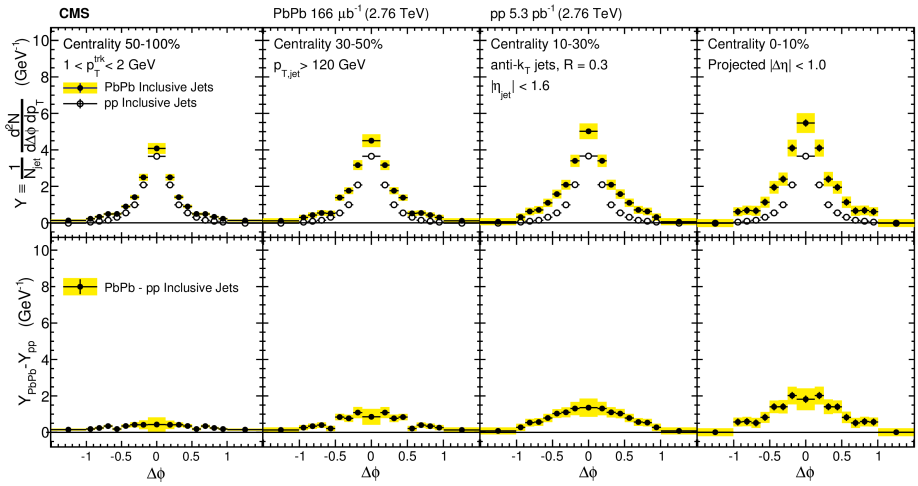

Figure 1.15: CMS azimuthal jet-hadron correlations measured in Pb–Pb and pp collisions at $\sqrt{s_{\mathrm{NN}}} = 2.76$ TeV. The difference in yield increases in more central collisions. Figure from [45].

From here, the rest of this thesis is organized as follows: An introduction to the Large Hadron Collider and the ALICE detector is described in Chapter 2, my analysis of jet-hadron correlations is described in Chapter 3, the results of this analysis are described, discussed, and compared in Chapter 4, the ALICE Overwatch project is described in App. A, and my contributions to analysis software packages and the

21. CMS refers to them as jet-track correlations.

ALICE Run 3 upgrade are described in Apps. B, and C.

Chapter 2

A Large Ion Collider Experiment at the Large Hadron Collider

2.1 The Large Hadron Collider (LHC)

The Large Hadron Collider (LHC) [46–49] is a circular hadron and ion collider located approximately 100 meters underground on the border between France and Switzerland at the European Organization for Nuclear Research (CERN). The LHC, with its 27 km circumference ring, is the largest collider in world, enabling the acceleration of proton beams to energies of 6.5 TeV, and Pb ion beams to 2.56 TeV per nucleon[1]. Built as the successor to the Large Electron-Positron Collider and utilizing the same tunnel, the primary motivations for building the LHC was to discover the Higgs Boson and investigate supersymmetry.

The LHC was constructed from 1998 to 2008 and began operating in 2009, providing

1. As of the end of Run 2, the maximum collision energy utilized for Pb–Pb collisions is 5.02 TeV to allow for direct comparison with p–Pb data taken at the same center-of-mass energy.

high quality proton and Pb beams to its four major experiments, A Large Ion Collider Experiment (ALICE) [50] which is discussed below, A Toroidal LHC Apparatus (ATLAS) [51], Compact Muon Solenoid (CMS) [52], and Large Hadron Collider beauty (LHCb) [53]. A schematic view of the LHC is shown in Fig. 2.1, highlighting the locations of the four major experiments. In 2012, the Higgs boson was discovered by ATLAS and CMS collaborations [54,55], fulfilling one of the primary goals within the first few years of operations. While the LHC spends most of each year colliding protons, approximately one month a year is devoted to the priorities of heavy ion physicists. These periods have included Pb–Pb, p–Pb, pp, and Xe–Xe collisions [56].

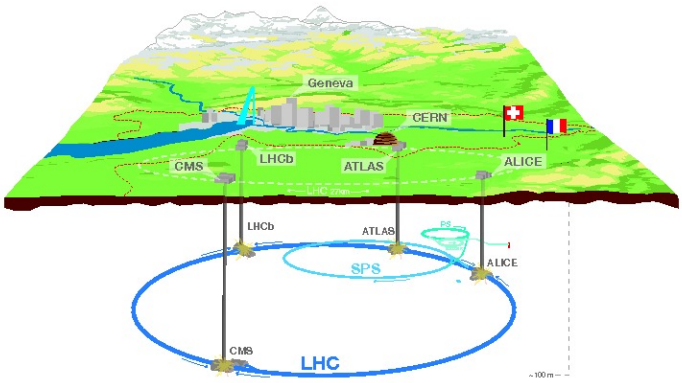

Figure 2.1: A schematic view of the LHC, showing its location relative to Geneva and the four major experiments. Figure from [57].

Providing a stable beam suitable for collisions is a complex operation. A schematic view of the LHC injector system is shown in Fig. 2.2. The procedure for proton beams is as follows: they are initially accelerated in LINC2, and then transfered and accelerated through the PS Booster (PSB), Proton Synchrotron (PS), Super Proton Synchrotron (SPS), and then injected into the LHC. For Pb beams, it's a similar approach with some variation in the beginning: the nuclei are partially stripped of their electrons, accelerated by LINAC3, and then moved to the Low Energy Ion Ring

(LEIR). For the LEIR, they are transfered into PS where the rest of the electrons are stripped away, and then they are accelerated by the SPS and finally by the LHC. The bunches of beams are carefully arranged to maximize the performance in terms of luminosity delivered and beam lifetime. Thanks to the excellent LHC operations, the experiments are able to focus their efforts on understanding the physics of their measurements.

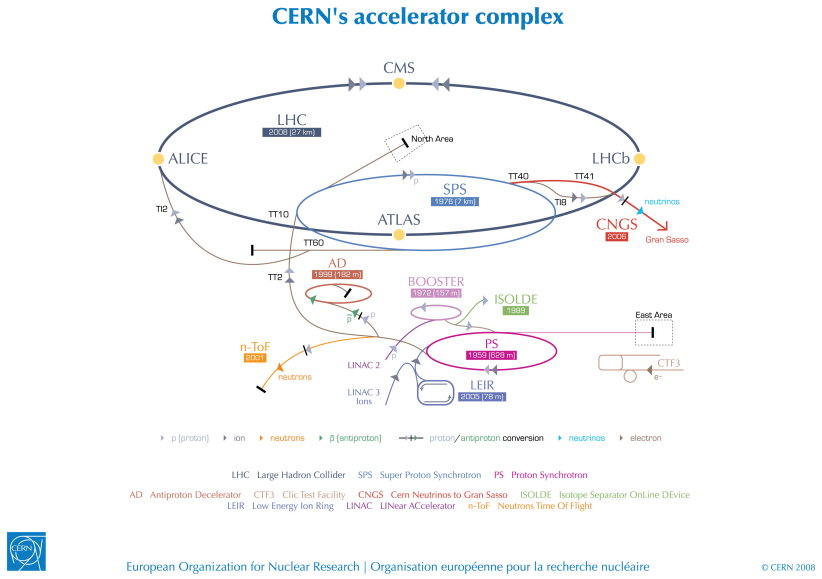

Figure 2.2: Schematic view of the LHC injector system. Injection begins with LINAC2 for protons and LINAC3 for Pb ions. Figure from [58].

2.2 A Large Ion Collider Experiment (ALICE)

A Large Ion Collider Experiment is the dedicated heavy-ion detector at the LHC[2]. Due to the broad range of measurements of interest in heavy ion collisions, ALICE needs to have good tracking resolution over a broad range of momenta, strong particle identification, and the ability to operate in an extremely high multiplicity environment. In order to meet these goals, ALICE has a range of sub-detectors, including precision

2. ATLAS, CMS, and LHCb also operate heavy ion programs in addition to their pp programs.

tracking and calorimetry in the central barrel at mid-rapidity which is described below, muon detectors at forward rapidity, and particle multiplicity detectors throughout the experiment. A schematic three dimensional view of the ALICE detector is shown in Fig. 2.3, with a label for each sub-detector. I will discuss the sub-detectors that are relevant for this thesis measurement in further detail below.

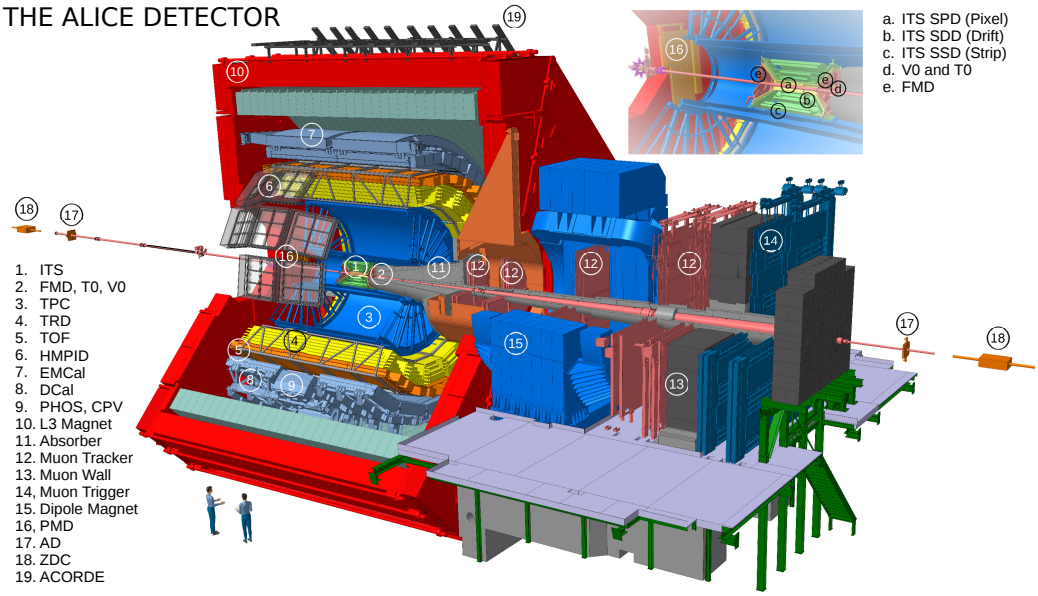

Figure 2.3: Three dimensional schematic view of the ALICE detector, with labels of each of the sub-detectors. The people in the bottom left are included for scale.

ALICE has collected data in pp collisions at $\sqrt{s_{\rm NN}}$ = 0.9, 2.76, 5.02, 7, 8, and 13 TeV, p–Pb collisions at $\sqrt{s_{\rm NN}}$ = 5.02 and 8.16 TeV, and Pb–Pb collisions at $\sqrt{s_{\rm NN}}$ = 2.76 and 5.02 TeV. Utilizing this variety of collected data as well as the broad capabilities of the sub-detectors has enabled the measurement of a diverse set of phenomena, which span the range from enhanced strangeness production in high-multiplicity pp, p–Pb and Pb–Pb [59], to precision measurement of the mass of ${}^3\bar{H}e$ [60], to the potential thermalization of charm quarks in the QGP via the measurement of low $p_{\rm T}$ J/ψ with $\mu^+\mu^-$ in the forward direction [61].

2.2.1 Central Barrel Tracking

Tracking of charged particles in ALICE is performed within what is termed the central barrel of the experiment, with the major sub-detectors positioned in concentric cylinders around the LHC beam pipe. Combined together, the central barrel tracking provides coverage over $|\eta| < 0.9$. Listed from radially inner-most to outer-most, the sub-detectors included in this grouping are:

- The Inner Tracking System (ITS), which consists of six layers of silicon detectors. The inner-most two layers are the Silicon Pixel Detector (SPD), the next two layers consist of the Silicon Drift Detector (SDD), followed by the Silicon Strip Detector (SSD) as the last two layers. The layers of the SPD are located only 3.9 cm and 7.6 cm from the beam. The SPD is of critical importance to the experiment, providing precision tracking with 50 μm x 425 μm pixels, secondary vertex information for charm and beauty identification, particle identification, and event activity estimation. The layers of the SDD are located 15.0 cm and 23.9 cm from the beam, and the layers of the SSD are located 38 and 43 cm from the beam.
- The Time Projection Chamber (TPC) gaseous ionizing detector. It is described in further detail below.
- The Time of Flight (TOF) detector, which utilizes Multigap Resistive Plate Chambers. Each chamber consists of a series of plates placed inside a gas volume within a large electric field. As charged particles traverse the chambers, they ionize the gas, which induces a signal that this is read out from the detector. TOF provides precise timing information, with a resolution of ~ 100 ps or better, enabling particle identification up to $p_{\mathrm{T}} \approx 4$ GeV/c.
- The Transition Radiation Detector (TRD), which utilizes a radiator and drift chamber to induce and measure transition radiation. Transition radiation occurs

when charged particles pass through an inhomogeneous medium such as the radiator. This induced radiation is then amplified via a drift chamber and the induced charge is read out. The TRD can be used to identify electrons.

Utilizing the information measured in each detector, tracks are reconstructed using a Kalman Filter [62] in three passes. The first pass seeds tracks starting at the outermost edge of the TPC and moves in towards the ITS. Tracks which are matched between the TPC and ITS are then used to construct a vertex. Using the vertex, tracks are then propagated outwards through the ITS and TPC to the TOF and TRD. The constraints from these other tracking detectors are then used to perform the third and final pass moving inward to further constrain the vertex. The tracking algorithm is described in greater detail in [63].

2.2.2 Time Projection Chamber

The ALICE Time Projection Chamber (TPC) [64] is the largest gaseous TPC in the world, spanning 510 cm long, with an inner radius of 90 cm and an outer radius of 250 cm. The volume is filled with a gas mixture of Ne-CO_2 (90%-10%)[3]. When charged particles traverse the active volume of the TPC, they ionize the gas. The volume is contained within a uniform electric field, which causes the resulting electrons to drift towards the endcaps. At the endcaps, the electrons are amplified, which induces charge on the readout pads. By recording the time when the electrons arrive, as well as knowledge of the electron drift velocity, we can reconstruct their position in three dimensional space. Generally, the tracking efficiency is $\approx 80 - 90\%$. Charged particles are tracked down to 150 MeV/c.

As charged particles traverse the TPC volume, they lose energy according to the

3. Ar-CO_2 was utilized in 2015 before reverting back to the Ne-CO_2 mixture.

Bethe-Bloch formula. By measuring $\mathrm{d}E/\mathrm{d}x$, known as the specific energy loss, as well as the particle momentum, the particle type can be identified. Depending on the momentum range, this identification may be performed on a track-by-track or statistical basis. The $\mathrm{d}E/\mathrm{d}x$ performance of the TPC is shown in Fig. 2.4, illustrating its PID capabilities over a broad momentum range.

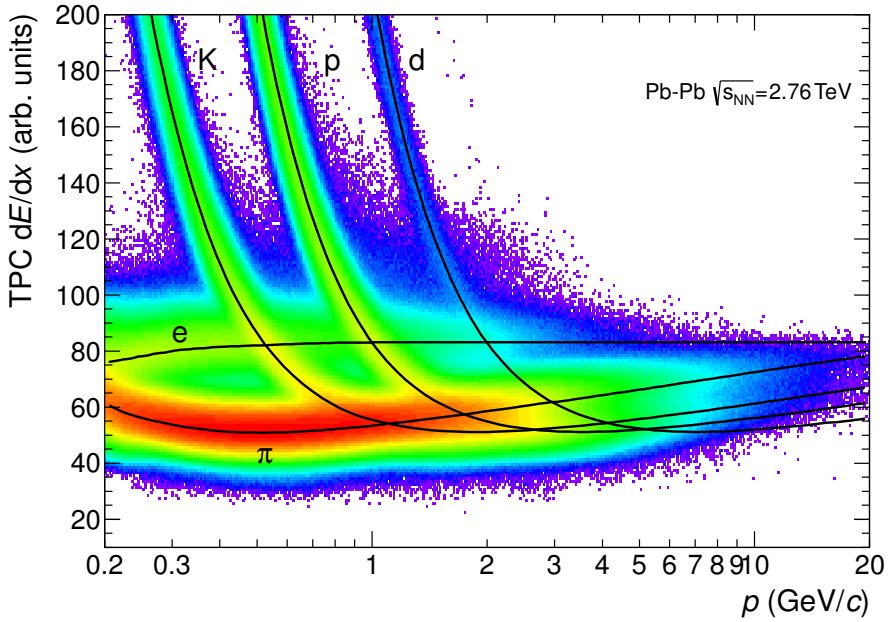

Figure 2.4: ALICE Time Projection Chamber $\mathrm{d}E/\mathrm{d}x$ as a function of momentum. The black curves show the expected mean energy loss for each identified particle. Figure from [63].

In order to increase the data taking rate in Run 3, substantial changes are in progress to the TPC, as described in App. Sec. C.

2.2.3 Electromagnetic Calorimeter

The ALICE Electromagnetic Calorimeter (EMCal) [65] measures photons, electrons, and neutral hadrons primarily via their decays to photons[4]. Although it was not

4. Primarily the π^0. The EMCal contains only one radiation length for particles which interact hadronically.

included in the original ALICE design, it has quickly become an integral part of the experiment. It utilizes a sampling calorimeter design and contains 12,288 towers[5] which consist of 77 alternating layers of Pb-scintillator and scintillator. During LHC Run 1 from 2009–2013, the EMCal covered $|\eta| < 0.7$, and $80 < \varphi < 180$ degrees, while during Run 2, it was slightly expanded to $80 < \varphi < 187$ degrees. Run 2 also saw the addition of the DCal (dijet calorimeter) opposite the EMCal in φ, spanning from $0.22 < |\eta| < 0.7$ within $260 < \varphi < 320$ degrees and from $|\eta| < 0.7$ within $320 < \varphi < 327$ degrees[6].

The EMCal provides the ability for ALICE to measure jets which including both the charged and the neutral components, where the charged component is provided by the central barrel tracking, and the neutral component by the EMCal. As discussed in Sec. B.3, this requires special attention to avoid double counting charged particles. However, this additional consideration is a worthwhile trade-off for measuring jets which are more directly comparable to theoretical predictions. By searching for a high energy deposition in a localized area, the EMCal is also able to provide a jet trigger for ALICE.

2.2.4 Forward Detectors

When determining event activity[7] from particle multiplicity for a particular measurement, it is important to measure in a region that is uncorrelated with the measurement. Usually, when making a measurement at mid-rapidity, this is achieved by going to

5. Also referred to as cells.

6. This complicated DCal geometry is necessary for it to fit around the Photon Spectrometer (PHOS), which occupies the region around $\eta \approx 0$.

7. This is a general term to describe how much activity occurred in one collision, usually based on particle multiplicity. Centrality in Pb–Pb collisions is a specific measure of event activity.

large $|\eta|$, referred to as the forward direction. In ALICE, event activity is often determined using the V0detector, which consists of two set of modules of segmented plastic scintillator, known as the V0-A and V0-C. The V0-A covers from $2.8 < \eta < 5.1$, while the V0-C covers from $-3.7 < \eta < -1.7$. The centrality distribution determined by the V0 detector in Pb–Pb collisions at $\sqrt{s_{\mathrm{NN}}} = 2.76$ TeV is shown in Fig. 1.6.

2.2.5 Trigger Selection

ALICE operates in both minimum bias and triggered mode. The minimum bias trigger is defined by accepting all collisions that have a minimal amount of event activity. The precise minimum bias definition depends on the data taking period.

In addition, a number of the sub-detectors can provide triggers for ALICE. As one example, the EMCal provides a jet trigger when the sum of energy in a group of cells is above a high energy threshold. These triggers are covered in detail in [63].

Chapter 3

Jet-Hadron Correlations

As introduced in Sec. 1.5.2, partons lose energy as they traverses the Quark-Gluon Plasma. As discussed, a variety of measurements have begun to constrain the properties of jet-medium interactions, indicating that these interaction modify the internal structure of the jet, and that some of the lost energy is radiated out via soft particles[1] at large angles relative to the jet axis. However, the exact mechanism and nature of these jet-medium interactions is still under investigation.

This dissertation approaches this question from the perspective of the path length dependence of jet energy loss. By taking advantage of different collision geometries and the corresponding differences in medium shape, we can study how the variations in the length of the medium that the jets traverses impact the measured jet energy loss. We characterize these path length differences as a function of the angle between a trigger jet and the event plane orientation, where the trigger and recoil jets are expected to traverse a shorter path length when aligned with the event plane orientation and a longer path when traversing in the perpendicular direction. The jet modification is

1. Particles which have large transverse momentum are sometimes described as hard, while those with low transverse momentum can be described as soft.

characterized via angular correlations that are measured as a function of the difference in azimuthal angle between the jet and the rest of the particles in the event. These angular correlations can then be used to characterize and compare the trigger and recoil jet peaks via a variety of observables with are discussed further below.

In this chapter, I describe the measurement of these jet-hadron correlations in 0–10% central and 30–50% semi-central Pb–Pb collisions at $\sqrt{s_{\mathrm{NN}}} = 5.02$ TeV. I also contributed significantly to the ALICE analysis of jet-hadron correlations measured in 30–50% semi-central Pb–Pb collisions at $\sqrt{s_{\mathrm{NN}}} = 2.76$ TeV. That analysis is described in detail in [66], and at the time of writing, this analysis is under ALICE collaboration review and will be submitted in the near future. Consequently, I will focus on the measurement at $\sqrt{s_{\mathrm{NN}}} = 5.02$ TeV, and only discuss a selection of the results of the $\sqrt{s_{\mathrm{NN}}} = 2.76$ TeV analysis.

This chapter is organized as follows: Sec. 3.1 introduces the jet-hadron observables, Sec. 3.2 describes the data and analysis selections utilized to measure the correlations, Sec. 3.3 characterizes the jets measured in this analysis, Sec. 3.4 describes the correlation methods utilized, Sec. 3.5 describes the method for removing the underlying flow background from the correlation, Sec. 3.6 describes the systematic uncertainties and error propagation. The results, theoretical and experimental comparisons, and discussion are presented in Chapter 4.

3.1 Observables

The basic measurements for this analysis are known as jet-hadron correlations. They are measured by recording the difference in azimuthal angle between a trigger jet and the rest of the charged particles in the collision. Those other particles[2] include the

2. These particles are often referred to as the associated hadrons or charged particles.

particles used to find the trigger jet, as well as those in the recoil jet. Since we want a measurement of the properties of a particular jet population aggregated over all of the available data, these correlations are normalized by the number of jet triggers. The correlations are defined as:

$$C(\Delta\varphi) = \frac{1}{N_{\text{trig}}} \frac{\mathrm{d}N}{\mathrm{d}\Delta\varphi} \tag{3.1}$$

where N is the number of associated particles measured in a $\Delta\varphi$ bin, N_{trig} is the number of trigger jets and $\Delta\varphi = \varphi_{\text{jet}} - \varphi_{\text{hadron}}$.

As explained above, these correlations are further measured as a function of the azimuthal angle between the jet and the event plane[3] as a proxy for the path length that the trigger and recoil jets traverse. The event plane bins utilized in this analysis are shown in Fig. 3.1. The three bins are known as the in-plane, mid-plane, and out-of-plane bins and are defined in detail in Sec. 3.5. The correlations are also measured as a function of the associated hadron transverse momentum, $p_{\text{T}}^{\text{assoc}}$.

This base correlation in Eq. 3.1 allows for the investigation of associated hadrons on the near-side ($\Delta\varphi \sim 0$), which correspond to the particles associated with the trigger jet, and on the away-side ($\Delta\varphi \sim \pi$), which correspond to those associated with the recoil jet. One way to characterize these peaks is via the per trigger associated hadron correlation yield, which is defined as

$$\mathrm{Y} = \int_a^b \int_c^d C(\Delta\varphi, \Delta\eta)\mathrm{d}\Delta\varphi\mathrm{d}\Delta\eta = \frac{1}{N_{\text{trig}}} \int_a^b \frac{\mathrm{d}(N_{\text{signal}} - N_{\text{b}})}{\mathrm{d}\Delta\varphi}\mathrm{d}\Delta\varphi \tag{3.2}$$

3. For the sake of brevity, I will refer to these different bins as event plane orientations.

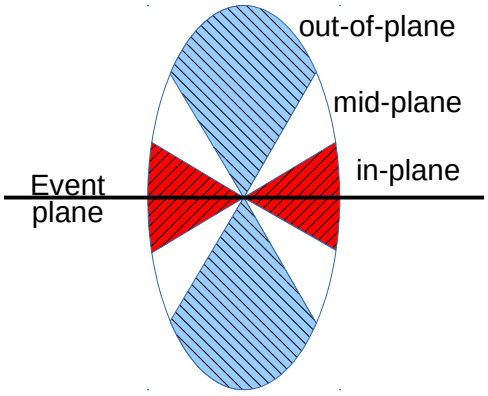

Figure 3.1: Event plane bins utilized for measuring jet-hadron correlations. See Sec. 3.5 for a detailed definition. Figure from [67]

where a, b, c, and d are integration limits in $\Delta\varphi$ and $\Delta\eta = \eta_{\text{jet}} - \eta_{\text{hadron}}$, respectively, $C(\Delta\varphi, \Delta\eta)$ is an intermediate two dimensional correlation discussed in Sec. 3.4, $N = N_{\text{signal}} - N_{\text{b}}$ where N_{signal} is the signal contribution to the correlation, and N_{b} is the background contribution to the correlation. On the near-side, the limits are symmetric around the trigger peak from $(-\pi/3, \pi/3)$, while on the away-side, the limits are symmetric around the recoil jet from $(2\pi/3, 4\pi/3)$[4]. The $\Delta\eta$ limits c and d range over the signal and background dominated regions, as defined in Sec. 3.5. The yields are measured as a function of event plane orientation, as well as a function of $p_{\text{T}}^{\text{assoc}}$.

To better quantify the difference yields between the different event plane orientations, we can also derive yield differences, D_{RP}, and yield ratios, $R_{a,b}$ from the measured yields. The yield difference is defined as

$$D_{\text{RP}} = \text{Y}^a - \text{Y}^b = (\text{Y}_s^a - \text{Y}_s^b) - (\text{Y}_s^a - \text{Y}_s^b) \tag{3.3}$$

4. The recoil jet will be back-to-back from the trigger jet in $\Delta\varphi$ due to momentum conservation.

where a and b are event plane orientations, Y_s^a is the yield of the signal for event plane orientation a, and Y_b^a is the yield of the background for event plane orientation a. The yield difference will be measured for $\mathrm{Y}^{\mathrm{out}} - \mathrm{Y}^{\mathrm{in}}$ and $\mathrm{Y}^{\mathrm{mid}} - \mathrm{Y}^{\mathrm{in}}$ for the near- and away-side. The yield ratio is defined as

$$R_{a,b} = \frac{\mathrm{Y}^a}{\mathrm{Y}^b} = \frac{\mathrm{Y}_s^a - \mathrm{Y}_b^a}{\mathrm{Y}_s^a - \mathrm{Y}_b^a} \tag{3.4}$$

where a and b are event plane orientations, Y_s^a is the yield of the signal for event plane orientation a, and Y_b^a is the yield of the background for event plane orientation a. The yield ratio is calculated for $\mathrm{Y}^{\mathrm{out}}/\mathrm{Y}^{\mathrm{in}}$ and $\mathrm{Y}^{\mathrm{mid}}/\mathrm{Y}^{\mathrm{in}}$ for both the near- and away-side.

In addition to the yields, the correlations can also be characterized by the near-side and away-side peaks widths. The peak widths are determined by fitting a Gaussian to peaks in the $\Delta\varphi$ correlations. The extended Gaussian fit function is defined as

$$\frac{\mathrm{d}N}{\mathrm{d}\Delta\varphi} = \frac{A}{\sqrt{2\pi\sigma^2}} * e^{-(\Delta\varphi-\mu)^2/2\sigma^2} \tag{3.5}$$

where A is the amplitude, μ is the mean, and σ is the width. When fitting to the near-side, we fix $\mu = 0$, while on the away-side, $\mu = \pi$. Although the peaks are known to not be exactly Gaussian [68], it provides a convenient standard method for comparison.

3.2 Data, Event, and Trigger Selections

These measurements are performed in Pb–Pb collisions at $\sqrt{s_{\mathrm{NN}}} = 5.02$ TeV that were collected by ALICE in November-December 2015. From the entire dataset, we require a variety of conditions to ensure that we are analyzing collisions which have similar properties and are within a regime where the ALICE detectors' measurement performance is well characterized.

3.2.1 Event selection

Events to be included in the analysis were selected according to standardized ALICE criteria for selecting events of sufficiently high quality for physics analysis[5]. In particular, these selections require sufficient event activity, avoiding contamination due to piling up collisions. The event must also be contained within enough of the ALICE fiducial acceptance for successful reconstruction with reasonable measurement performance. These selections include:

- Event cuts:
  - There must be at least one contributor to the primary vertex.
  - $|z_{\mathrm{vertex}}| < 10$ cm of the nominal interaction point of the ALICE detector.
  - The primary vertex determined via the SPD and via the other ALICE tracking detectors must:
    - be within 0.2 mm of each other.
    - be within 10σ of the SPD value, and 20σ of the tracking value, where σ is the spatial resolution for the SPD and tracking, respectively.
    - The maximum SPD resolution must be < 2.5 mm if only the z_{vertex} of

5. The event selection was performed by the `AliEventCuts` class.

the SPD is available.

- Pileup cuts are based on multi-detector correlations, which have different sensitivity to pileup events. These correlations are a standard ALICE approach which are tailored for each particular data taking period and include:
  - Correlating the number of tracks found in the ITS + TPC and those which can be matched to the TOF[6].
  - Correlating the number of tracks found in an event to those found only in the TPC.

The selection of events which passed each stage of the event selection is shown in Fig. 3.2. In order to analyze events with similar properties, we study collisions grouped by event activity as measured by particle multiplicity in the forward direction. We analyze 0–10% centrality collisions where parton energy loss is expected to be greatest. We also study 30–50% semi-central collisions where collision geometry, which can be related to particle multiplicity, is expected to emphasize an ellipsoidal shape. This is discussed in further detail in Sec. 4.4.1. From the entire dataset, we selected 4.54 million collisions in 0–10% central collisions, and 9.11 million events in 30–50% semi-central collisions. The data were collected with a minimum bias trigger, which accepts all collisions that pass minimal event activity requirements.

3.2.2 Track Selection

For a jet analysis, we require tracks to be reconstructed uniformly with good momentum resolution. Due an azimuthally non-uniform SPD detector response, if we require the same track selection over the entire acceptance, the tracking efficiency will necessarily be non-uniform. To achieve the uniformity requirement, ALICE includes two different

6. The precision timing in the TOF can be used to separate pileup events.

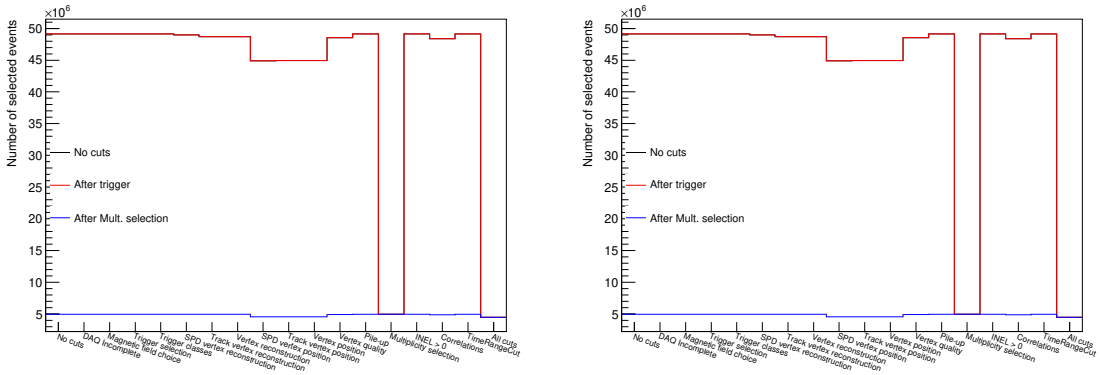

(a) Event selection for 0–10% central collisions

(b) Event selection for 30–50% semi-central collisions

Figure 3.2: Event selection from Pb–Pb collisions at $\sqrt{s_{\mathrm{NN}}} = 5.02$ TeV. Each bin is the number of events which pass the labeled event selection criteria. The black line (underneath the red line) shows no additional cuts beyond those labeled, while the red shows those selected after requiring the minimum bias trigger, and the blue after requiring the specified centrality selection. The red line is superimposed on top of the black line because only the minimum bias trigger was required.

classes of tracks termed hybrid tracks which provided the desired properties when combined together. The two classes are known as global tracks, where global tracks are required to have at least one hit in the SPD, and complementary tracks, which are not required to have an SPD hit, but are re-fit with the requirement that they pass through the primary vertex. The contributions of the two classes of tracks are shown in Fig. 3.3. In addition to those broad properties, the tracks are required to have at least 70 TPC space points associated with the track[7], $\chi^2/\mathrm{ndf} < 2$ within the TPC, and additional requirements on the matching between tracks in the ITS and TPC.

In addition to those broader requirements, the tracks are required to be within the central barrel acceptance of $|\eta| < 0.9$ with $p_{\mathrm{T}} > 150$ MeV/c. The same requirements are applied to tracks utilized for jet finding described below and for the charged hadrons which are correlated with the trigger jet.

7. A track traversing the entire TPC could have a maximum of 159 space points.

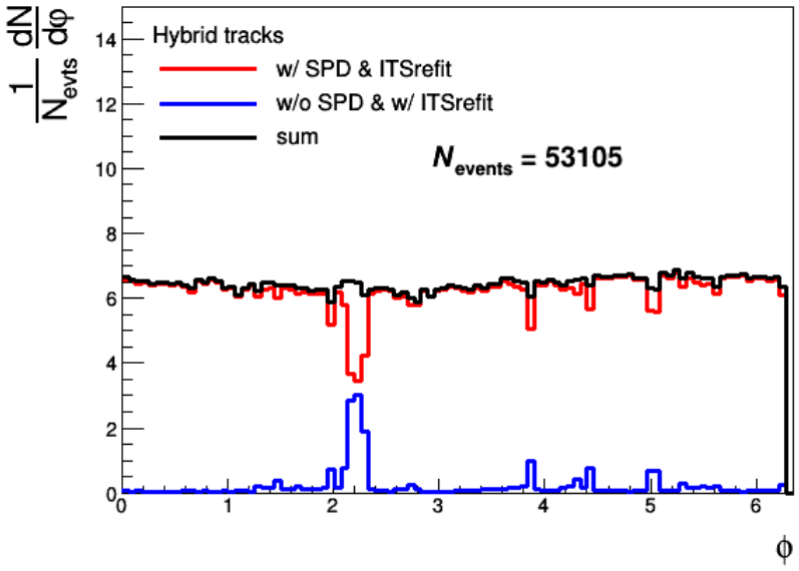

Figure 3.3: φ distribution of charged tracks in the dataset. The combination of the global and constrained tracks defined in the text provides a uniform track distribution in φ.

During tracking, a variety of effects such as missing tracks that travel along TPC sector boundaries, misreconstructed tracks, interactions with detector materials that cause the particles to move outside of the detector acceptance, or missing hits within a track can all contribute to an inefficiency for measuring single particles. This inefficiency will decrease the associated hadron yields, and therefore must be corrected for in the measured correlation. In order to measure this efficiency, HIJING[69,70] is used to simulate Pb–Pb collisions at $\sqrt{s_{\rm NN}} = 5.02$ TeV[8]. The efficiency is then measured as the ratio of particles measured at detector level to generator level particles within the detector acceptance. The tracking efficiency is measured as a function of $p_{\rm T}$ and η, and is shown for 0–10% central collisions in Fig. 3.4a and for 30–50% semi-central collisions in Fig. 3.4b. The efficiency is approximately 75–85% over a majority of the acceptance, with approximately constant values above $p_{\rm T} > 2-3$ GeV/c and $|\eta| \lesssim 0.8$. The efficiency decreases at low $p_{\rm T}$ and large $|\eta|$.

8. This particular HIJING dataset is known in ALICE as LHC16g1.

Due to the complexity of the shape of this efficiency in $p_{\mathrm{T}} - \eta$ space, the efficiency values, $\epsilon(p_{\mathrm{T}}, \eta)$ are parametrized according to a functional form with no physical significance beyond the ability to describe the measurement distribution fairly well. The parametrized tracking efficiency is decomposed into

$$\epsilon(p_{\mathrm{T}}, \eta) = \epsilon(p_{\mathrm{T}})\epsilon(\eta) \tag{3.6}$$

where $\epsilon(p_{\mathrm{T}})$ is parametrized as a piecewise function of the form

$$\epsilon(p_{\mathrm{T}}) = p_i + p_{i+1}p_{\mathrm{T}} + p_{i+2}{p_{\mathrm{T}}}^2 + p_{i+3}{p_{\mathrm{T}}}^3 + p_{i+4}{p_{\mathrm{T}}}^4 \tag{3.7}$$

where p_{T} is the charged hadron transverse momentum, p_0–p_4 are the parameters[9] for $p_{\mathrm{T}} \leq 3.5$ GeV/c, and p_5–p_9 are the parameters[10] for $p_{\mathrm{T}} > 3.5$ GeV/c. The parameter values are enumerated in Table 3.1[11]. $\epsilon(\eta)$ is parametrized as a piecewise function of the form

Table 3.1: p_{T} dependent tracking efficiency parameters utilized in Eq. 3.7.

Parameter	0–10%	30–50%
p_0	0.8350	0.8381
p_1	0.0621	0.0648
p_2	0.0986	0.1052
p_3	0.2000	0.1478
p_4	1.0124	1.0320

9. i.e. Index i starts at 0, corresponding to parameter p_0.

10. i.e. Index i starts at 5, corresponding to parameter p_5.

11. The parameterization is provided courtesy of Dr. Eliane Epple (LANL).

Parameter	0–10%	30–50%
p_5	0.7568	0.7628
p_6	0.0277	0.0263
p_7	-0.0034	-0.0032
p_8	1.506e-4	1.443e-4
p_9	2.3e-6	-2.3e-6

$$\epsilon(\eta) = 1/p_{12}(p_i e^{(-(\frac{p_{i+1}}{|s\eta+0.91|})^{p_{i+2}})} + p_{i+3}\eta + p_{i+4}\frac{1}{\sqrt{2\pi p_{i+5}}}e^{-(\frac{\eta+0.04}{2p_{i+5}})^2}) \tag{3.8}$$

where η is the pseudorapidity of the track, p_{12} is the normalization such that the function maximum is 1, the sign coefficient s is 1 and p_0–p_5 are parameters[12] for $\eta \leq -0.04$, and $s = -1$ and p_6 - p_{11} are parameters[13] for $\eta > -0.04$. The parameter values are enumerated in Table 3.2[14]. When measuring the correlations, each associated hadron is weighted by $1/\epsilon(p_{\mathrm{T}}, \eta)$ to correct for the detector efficiency.

Table 3.2: η dependent tracking efficiency parameters utilized in Eq. 3.8.

Parameter	0–10%	30–50%
p_0	1.0086	0.9076
p_1	0.0074	0.0065
p_2	0.2404	0.3216
p_3	-0.1230	-0.1130
p_4	-0.0107	-0.0107

12. i.e. Index i starts at 0, corresponding to parameter p_0.

13. i.e. Index i starts at 6, corresponding to parameter p_6.

14. The parameterization is provided courtesy of Dr. Eliane Epple (LANL).

Parameter	0–10%	30–50%
p_5	0.0427	0.0456
p_6	0.8579	0.8521
p_7	0.0088	0.0073
p_8	0.4697	0.4764
p_9	0.0772	0.0668
p_{10}	-0.0352	-0.0363
p_{11}	0.0645	0.0668
p_{12}	0.7716	0.7748

The residual for the tracking efficiency parametrization, $(\epsilon(p_{\mathrm{T}}, \eta)_{\mathrm{sim}} - \epsilon(p_{\mathrm{T}}, \eta))/\epsilon(p_{\mathrm{T}}, \eta)$ is shown in Fig. 3.5 for both 0–10% central and 30–50% semi-central collisions. In both centralities, the parametrization reproduces the simulation well over a majority of the phase-space.

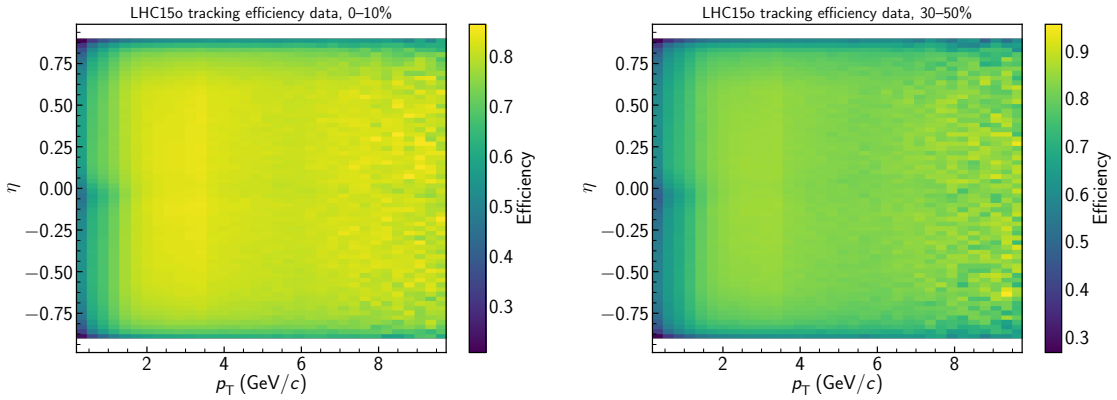

(a) Central collisions.

(b) Semi-central collisions.

Figure 3.4: Tracking efficiency measured in Pb–Pb collisions at $\sqrt{s_{\mathrm{NN}}} = 5.02$ TeV for central and semi-central collisions. The efficiency is measured as function of p_{T} and η since the largest variations are in these axes.

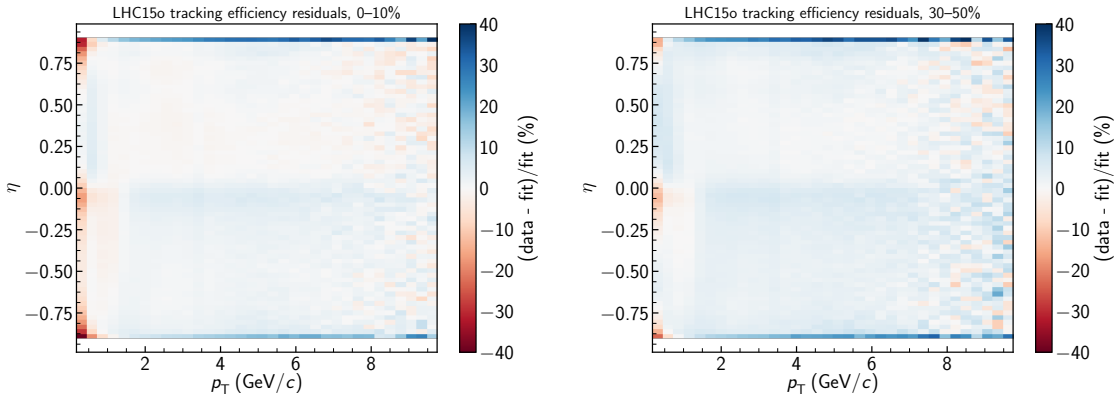

(a) Central collisions.

(b) Semi-central collisions.

Figure 3.5: Residuals for the tracking efficiency parametrized for Pb–Pb collisions at $\sqrt{s_{\mathrm{NN}}} = 5.02$ TeV for central and semi-central collisions. The tracking efficiency is reproduced well except at the edges of the acceptance where the efficiency changes rapidly. The mean efficiency residual is 1-3%.

3.2.3 EMCal Cells and Clusters

For the measurement of full jets in ALICE, the neutral component of the jet is measured using the EMCal. A broad collection of corrections are applied to the calorimeter data to make them suitable for use in this measurement. In summary, the individual cells are first corrected for various detector effects and quality requirements, then they are combined together into clusters using a clusterization algorithm, and finally the clusters are further calibrated and corrected for contamination from charged particles. All of these corrections are explained in further detail in Sec. B.3, so only the most relevant details are described here. For this analysis, the clusterization algorithm is seeded with cells with $E_{\mathrm{cell}} > 300$ MeV and all cells that contribute to a cluster are required to have $E_{\mathrm{cell}} > 100$ MeV. Most charged particles traverse the EMCal as minimum ionizing particles, which may leave a deposition in the EMCal. Since full jets, which are described below, are found in ALICE via the combination of charged tracks and EMCal clusters, it is important to remove the charged particle contributions to the measured clusters to avoid double counting the energy. This correction is performed

by what is termed the hadronic correction – tracks are propagated to the EMCal, matched to clusters, and then the track transverse momentum is subtracted from the cluster.

3.2.4 Jet Selection and Spectra

Jet finding is performed via FastJet v3.2.1 [26,71] using the anti-k_{T} algorithm [25,27]. As described in Sec. 1.4.2, the anti-k_{T} algorithm is characterized by a jet resolution parameter which loosely translates to the maximum distance a jet constituent can be from the jet centroid. It is generally preferred to select a larger resolution parameter to better encompass the fragmentation from the outgoing parton. However, large resolution parameters increase the probability of background contamination, and reduces the fiducial acceptance. To balance these competing concerns, a resolution parameter of $R = 0.2$ was selected for this analysis. Input to the jet finding consists of accepted charged tracks and EMCal clusters, with the energy of the cluster specified as the energy after the hadronic correction. The jets found using this combination of these particles and clusters are known as full jets[15]. Although the additional complication of full jet finding in ALICE can make analyses more difficult, it allows for more direct comparison with theoretical predictions. As part of this thesis work, I developed a number of tools to aid in full jet analyses, as described in Sec. B. Jet constituents are recombined using the p_{T} recombination scheme.

As mentioned in Sec. 1.4.2, the bulk hadrons create a large underlying background that is clustered into the jets that are found in an event. There are two main approaches to addressing this background:

- Perform jet finding with inclusive track and cluster selection, and then remove

15. As opposed to charged jets, which are found using only the charged particles.

the background contributions on a jet-by-jet basis, as described in Sec. 1.4.2.

- Restrict the constituents which contribute to the jet, such as imposing a minimum constituent p_{T}. This reduces the background, but in exchange it imposes a bias on the jet selection.

For this measurement, a constituent cut of 3 GeV is applied to the charged tracks and calorimeter clusters. Although this produces a highly biased selection of jets, it removes nearly all of the background. To characterize the precise background level, ρ can be measured with this constituent cut. This measurement was performed with the otherwise standard ALICE procedure of charged jet finding using the k_{T} algorithm for $R = 0.4$. The results are shown in Fig. 3.6, with the mean ρ for each centrality value shown in red points. The maximum mean ρ value for the most central jets is ≈ 14 GeV/c/rad^2, which for a $R = 0.2$ jet corresponds to a background contribution of ≈ 1.76 GeV/c, which is less than 10% of the minimum $p_{\mathrm{T,jet}}$. For semi-central collisions, the contribution is less than 0.94 GeV/c. These estimates are similar to those measured in $\sqrt{s_{\mathrm{NN}}} = 2.76$ TeV for similar constituent cuts [72]. This set of biases is also beneficial because it decouples the near-side jet finding from the near-side correlations below the constituent cut, allowing for a less biased measurement of the associated hadron yields at low $p_{\mathrm{T}}^{\mathrm{assoc}}$.

In addition to the selections above, the following selections are applied:

- The jet centroid is required to be within the fiducial volume of the EMCal.
- EMCal clusters which contribute to the jet are required to have arrived between $-50 < t_{\mathrm{cluster}} < 100$ ns, as determined by the time of the leading cell in the cluster.
- Each jet must contain a 5 GeV/c leading track bias. This requirement is imposed in alignment with other ALICE measurements to ensure that any combinatorial jets which pass the constituent cut are removed.

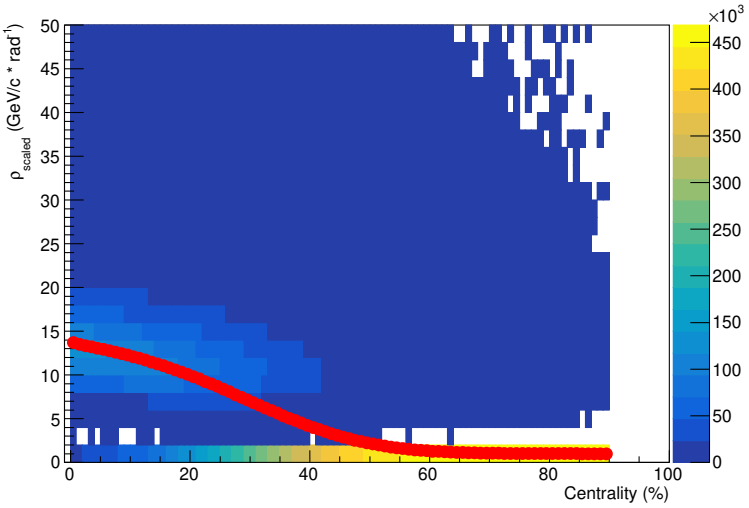

Figure 3.6: ρ background for jets measured with a 3 GeV constituent cut in Pb–Pb collisions at 5.02 TeV. Red points are the mean for each centrality value.

- The jet area, A_{jet} must be greater than $0.6 * \pi R^2$. This also reduces any potential contribution from combinatorial jets.
- The jet must not contain any tracks with $p_{\text{T}} > 100$ GeV/c due to unreliable tracking.

Jets found using the selections described above are shown in Fig. 3.7. The spectra are displayed as a function of the azimuthal angle between the jet and the event plane, as described below. The number of triggers in each event plane orientation is similar, with slightly more in-plane. The inclusive spectra is a sum of the three orientations.

3.2.5 Event Plane

The reaction plane is defined by the plane formed by the beam axis and the impact parameter. Due to asymmetries and fluctuations, the true plane depends on the harmonic used to calculate it. This true plane is known as the symmetry plane. The event plane is the experimentally determined symmetry plane, which also depends on

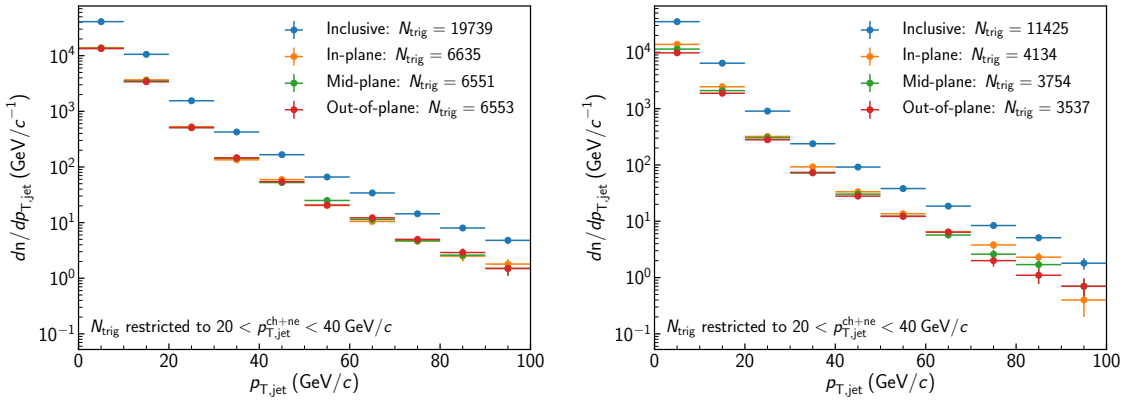

(a) Central collisions.

(b) Semi-central collisions.

Figure 3.7: Trigger jet spectra measured in 0–10% central and 30–50% semi-central Pb–Pb collisions at $\sqrt{s_{\rm NN}} = 5.02$ as a function of event plane orientation. The number of triggers is measured for the $20 < p_{\rm T,jet} < 40$ GeV/c.

the harmonic used to calculate it. The event plane is reconstructed according to:

$$\Psi_n = \tan^{-1}\left(\frac{\sum_i w_i \sin\left(n\varphi_i\right)}{\sum_i w_i \cos\left(n\varphi_i\right)}\right)/n$$

where n is the order of the event plane harmonic, i runs over all of the objects used in the event plane determination, and w_i is a weight on each entry [73]. In this measurement, jets are measured with respect to the second order event plane[16]. The V0-A and -C detectors were utilized to calculate this event plane, with the above sum running over the sectors, weighted by the amplitude in each sector. Since the event plane determination depends on particle multiplicity, we use a forward detector for event plane determination to minimize the auto correlation between the event plane and the jet. Additional corrections are then applied to account for gain equalization, detector alignment, and detector acceptance [74,75].

The determination of the event plane depends on properties of the detector used

16. For brevity, we will refer to the second order event plane as just "event plane".

to calculate it, with coarser detectors providing worse resolution. This lowered resolution has the effect of decreasing the measured flow coefficients[17]. As explained in Sec. 3.5, the reaction plane fit utilizes this resolution parameter to better describe the background. In order to calculate the resolution, we used the 3-sub event method [73]. In this method, the event plane is separately measured in three sub-detectors which do not overlap in acceptance. By comparing these values, we can extract the resolution $\Re_{n,2}$. The comparison is constructed via

$$\Re_n^a(\Psi_2) = \langle \cos\left(n[\Psi_{\rm EP}^a - \Psi_{\rm EP}]\right)\rangle = \sqrt{\frac{\langle \cos\left(n[\Psi_{\rm EP}^a - \Psi_{\rm EP}^b]\right)\rangle \langle \cos\left(n[\Psi_{\rm EP}^a - \Psi_{\rm EP}^c]\right)\rangle}{\langle \cos\left(n[\Psi_{\rm EP}^b - \Psi_{\rm EP}^c]\right)\rangle}}$$

where Ψ is the true measured event plane, and Ψ_a, Ψ_b, and Ψ_c correspond to the event planes measured in the different sub-detectors. The Ψ_2 denotes that this resolution is measured for the second harmonic event plane. [73]

3.3 Jet Energy Scale

In an ideal measurement, it is preferred to report a measurement which is corrected back to the "true" particle level from the measured detector level. This correction is usually performed by statistically unfolding for the detector effects and background fluctuations present in the measurement. However, unfolding this correlations measurement would require at least a two-dimensional unfolding, which is not feasible given the statistics. Consequently, these measurements are reported at the detector level. To put them in context, a detector response was determined for the jets selected in this analysis, as

17. Measured v_n coefficients are corrected for this effect by scaling by $1/\Re$.

explained in detail in Sec. 3.3.1. This response can then be used for folding detector effects onto theoretical predictions or other experimental measurements, as well as providing insight into the distribution of true jets that contribute to the correlations.

3.3.1 Detector Response and Embedding

To determine the effects of the ALICE detector on the measured jets, we must construct a response matrix mapping between a known probe and the measured jet, including all of the possible detector effects and background fluctuations. In order to construct the detector response, we take a known probe jet, embed the jet constituents into measured Pb–Pb data, reconstruct and analyze the combined event, and then determine the mapping between the probe and the measured jet. The probe jet is known as the particle level jet, while jets found in the combined event are termed hybrid jets.

The particle level jets are simulated in PYTHIA 8 with the Monash 2013 tune[18][9,76]. The generated particles are then propagated through a detailed model of the full ALICE detector using GEANT3 [77] to produce simulated particles at the detector level. The detector conditions and geometry were tuned to be the same as during the Pb–Pb data taking. Those detector level particles are then combined with the real Pb–Pb data. The embedding procedure is explained in further detail in Sec. B.4. The combined tracks and clusters can be used in a standard jet analysis to perform hybrid full jet finding, including applying all corrections to the EMCal data[19].

Due to differences in tracking between pp and Pb–Pb, a fraction of the tracks which are embedded can be rejected to simulate the application of this inefficiency. For

18. This production is known in ALICE as LHC16j5.

19. The difference in the energy scale between data and MC generated cells is accounted for by shifting the MC cells to the data energy scale before combining the data and MC cells together.

0–10%, 2% are randomly rejected, while for 30–50%, 1% are randomly rejected. This rejection factor is determined by integrating the ratio of central to peripheral tracking efficiency as determined in a HIJING simulation, where the peripheral events are known to have similar tracking efficiency as in pp.

The resulting hybrid jets are matched back to the particle level through a two step matching process:

1. Geometrical matching between hybrid jets, and the PYTHIA detector level jets. We additionally impose a further requirement that at least half of the p_{T} of the detector level jet must be contained within the hybrid jet. This requirement ensures that detector level jets are not matched to hybrid level jets to which they only contributed a small fraction of their momentum.

2. Geometrical matching between PYTHIA detector level and particle level jets.

In both cases, any match is required to be within a distance of $0.3 = 1.5 * R$. All hybrid level jets are required to pass the jet constituent cut. We elect to require that all detector and particle level jets also pass these cuts. All accepted and matched jets are filled into the response matrix, requiring that the hybrid level jet also passes the leading track bias. The resulting response matrices for 0–10% central and 30–50% semi-central collisions at $\sqrt{s_{\mathrm{NN}}} = 5.02$ TeV are shown in Fig. 3.8. The response matrices were produced using outlier removal, as described in Sec. B.4.1.

3.3.2 Particle Level Jet Spectra

Although the measurement will not be unfolded, we can characterize the distribution of particle level jets that contributed to the measured correlations. By weighting theoretical predictions by this distribution of particle level jets, a direct comparison

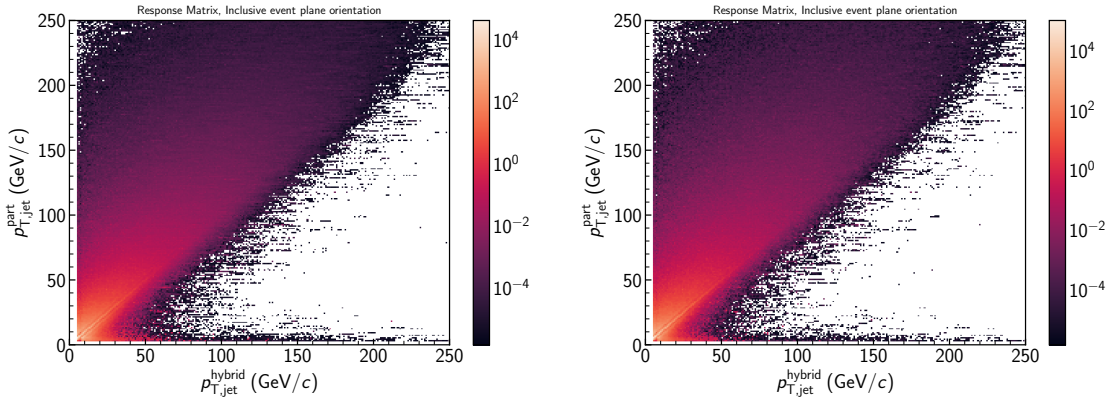

(a) Response matrix for hybrid and particle level jets for 0–10% central collisions at $\sqrt{s_{\mathrm{NN}}} = 5.02$ TeV.

(b) Response matrix for hybrid and particle level jets for 30–50% semi-central collisions at $\sqrt{s_{\mathrm{NN}}} = 5.02$ TeV.

Figure 3.8: Response matrices between hybrid and particle level jets for central and semi-central Pb–Pb collisions at $\sqrt{s_{\mathrm{NN}}} = 5.02$ TeV. The responses are unnormalized and inclusive in event plane orientations.

can be made to the measured correlations. In particular, this can be achieved by selecting all matches with hybrid jets within $20 < p_{\mathrm{T,jet}} < 40$ GeV/c and projecting onto the particle level jet axis. The result of this for procedure is shown in Fig. 3.9 for Pb–Pb collisions at $\sqrt{s_{\mathrm{NN}}} = 5.02$ TeV.

These spectra are shown as a function of event plane orientation, and all spectra are consistent within uncertainties. The distributions are sharply peaked in the $20 < p_{\mathrm{T,jet}}^{\mathrm{part}} < 25$ GeV/c bin, which corresponds to the peak of the $p_{\mathrm{T,jet}}^{\mathrm{hybrid}}$ distribution. These peaks reflect the steeply falling nature of the underlying jet spectrum, and the correspondence of the peaks indicate the strong correlation between the particle and hybrid level jets due to the jet constituent cuts. Background contributions to jets without a constituent cut are expected to depend on the event plane orientation because of the flow background. The agreement between the orientations reinforces that the constituent cuts are an effective measure for removing the background contributions, as indicated by the jet background described in Sec. 3.2.4.

For $p_{\mathrm{T,jet}}^{\mathrm{part}} < 20$ GeV/c, jets occur more frequently than would be expected from pp spectra. Since the background negligibly contributes to the measured jets, this region must correspond to probe jets which overlap with existing jets in the Pb–Pb data. Since this effect is a consequence of the embedding procedure rather than a physical process[20], we neglect this region when comparing the spectra, and normalize the spectra between $20 < p_{\mathrm{T,jet}} < 100$ GeV/c to focus on the physical processes of interest.

This agreement can be further quantified by taking the ratio of the spectra with respect to the inclusive orientation. The ratios are then fit with a first degree polynomial to allow for the possibility of a shape-dependent spectra, within $20 < p_{\mathrm{T,jet}} < 100$ GeV/c as described above. The ratios and fits are shown in Fig. 3.10. All fits are consistent with the inclusive orientation spectra within that range.

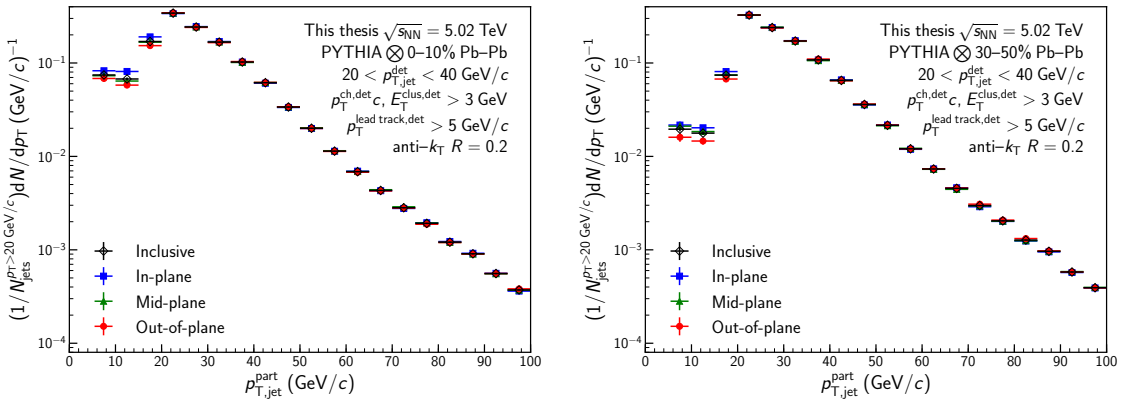

(a) Particle level spectra for 0–10% central collisions at $\sqrt{s_{\mathrm{NN}}} = 5.02$ TeV.

(b) Particle level spectra for 30–50% semi-central collisions at $\sqrt{s_{\mathrm{NN}}} = 5.02$ TeV.

Figure 3.9: Particle level spectra for central and semi-central Pb–Pb collisions at $\sqrt{s_{\mathrm{NN}}} = 5.02$ TeV. The spectra are shown as a function of event plane orientation, and are all consistent with the event plane inclusive spectra within uncertainties.

Although the above spectra provide the opportunity to fold particle level results, the constituent cuts provided a biased selection of jets which are less widely used in the jet community. To improve intuition, the particle level spectra produced above are

20. The rate of multiple dijets overlapping is much smaller than this effect.

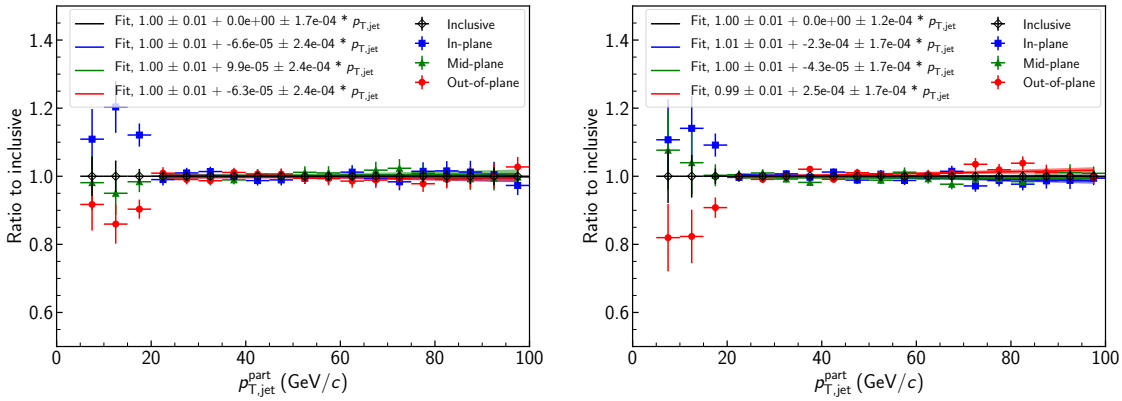

(a) Ratios of particle level spectra for 0–10% central collisions at $\sqrt{s_{\mathrm{NN}}} = 5.02$ TeV.

(b) Ratios of particle level spectra for 30–50% semi-central collisions at $\sqrt{s_{\mathrm{NN}}} = 5.02$ TeV.

Figure 3.10: Event plane selected particle spectra relative to the inclusive spectra for central and semi-central Pb–Pb collisions at $\sqrt{s_{\mathrm{NN}}} = 5.02$ TeV. The ratios are fit with a first degree polynomial and are all consistent within uncertainties.

compared to an alternative response matrix where the constituent p_{T} cut is removed from the PYTHIA particle and detector level. A leading track bias of 5 GeV/c remains to prevent the matching from being overwhelmed by the high multiplicity of low $p_{\mathrm{T,jet}}$ jets. The comparison of inclusive event plane orientation spectra are shown in Fig. 3.11. By including the full set of jet constituents, the jets are shifted towards higher $p_{\mathrm{T,jet}}^{\mathrm{part}}$ as expected. The shift is approximately 5 GeV/c.

3.4 Correlation Methods

After the jet and track selection is performed, we can proceed to measure the actual jet-hadron correlations. These angular correlations are measured as a function of $\Delta\varphi$ and $\Delta\eta$, where $\Delta\varphi = \varphi_{\mathrm{jet}} - \varphi_{\mathrm{hadron}}$, and $\Delta\eta = \eta_{\mathrm{jet}} - \eta_{\mathrm{hadron}}$. For each accepted jet, these angles are calculated between the jet and every accepted hadron to form the raw signal correlation, as defined in Sec. 3.4.1. Each accepted jet is also correlated with a collection of hadrons from other events to form a mixed event that describes

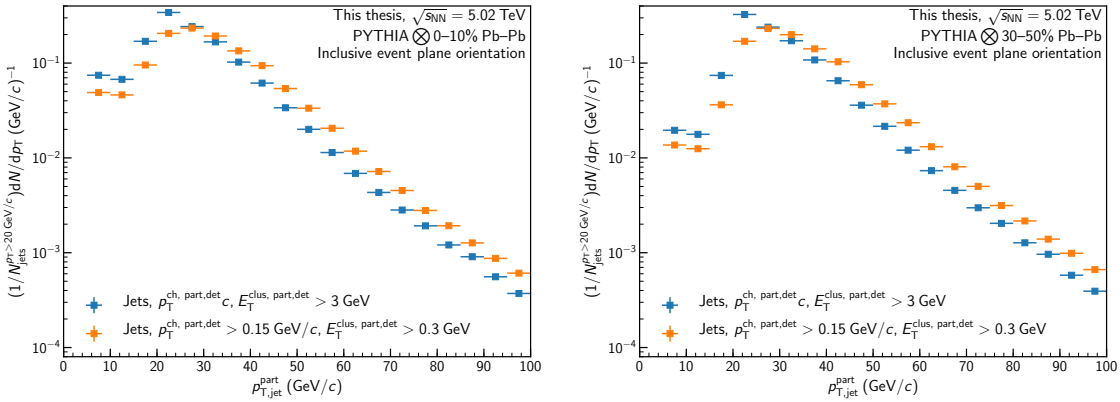

(a) Particle level spectra for 0–10% central collisions at $\sqrt{s_{\rm NN}} = 5.02$ TeV.

(b) Particle level spectra for 30–50% semi-central collisions at $\sqrt{s_{\rm NN}} = 5.02$ TeV.

Figure 3.11: Particle level spectra with and without constituent cuts on the particle or detector jets for central and semi-central Pb–Pb collisions at $\sqrt{s_{\rm NN}} = 5.02$ TeV. The additional constituents cause the $p_{\rm T,jet}$ to shift to higher values compared to jets which include the consistent cut.

detector and acceptance conditions, but does not contain any physical correlations. The mixed event procedure is described in Sec. 3.4.2.

The jet-hadron correlations are measured for $20 < p_{\rm T,jet} < 40$ GeV/c jets that pass the event selection described in Sec. 3.2.4, while the associated hadrons are measured in bins of $0.5 < p_{\rm T}^{\rm assoc} < 1.0$, $1.0 < p_{\rm T}^{\rm assoc} < 1.5$, $1.5 < p_{\rm T}^{\rm assoc} < 2.0$, $2.0 < p_{\rm T}^{\rm assoc} < 3.0$, $3.0 < p_{\rm T}^{\rm assoc} < 4.0$, $4.0 < p_{\rm T}^{\rm assoc} < 5.0$, $5.0 < p_{\rm T}^{\rm assoc} < 6.0$, and $6.0 < p_{\rm T}^{\rm assoc} < 10.0$ GeV/c. Since the correlations are measured over a wide range of $p_{\rm T}^{\rm assoc}$ values, I will discuss only a subset of values which are representative of the correlations as a whole. Since low $p_{\rm T}^{\rm assoc}$ values are treated differently than high $p_{\rm T}^{\rm assoc}$, we will discuss correlations for the $1.0 < p_{\rm T}^{\rm assoc} < 1.5$ GeV/c bin and the $4 < p_{\rm T}^{\rm assoc} < 5$ GeV/c bin. In both cases, the considered correlations are measured for $20 < p_{\rm T,jet} < 40$ GeV/c and are inclusive in event plane orientation.

3.4.1 Raw Correlation

The fully corrected correlation, $C(\Delta\varphi, \Delta\eta)$, is defined as

$$C(\Delta\varphi, \Delta\eta) = \frac{1}{N_{\text{trig}}} \frac{\mathrm{d}^2 N_{\text{assoc}}}{\mathrm{d}\Delta\varphi \mathrm{d}\Delta\eta} = \frac{1}{N_{\text{trig}}} \frac{\mathrm{d}^2}{\mathrm{d}\Delta\varphi \mathrm{d}\Delta\eta} \frac{N_{\text{meas}} - N_{\text{bkg}}}{\epsilon(p_{\text{T}}, \eta) a(\Delta\varphi, \Delta\eta)} \tag{3.9}$$

where N_{trig} is the number of trigger jets, N_{meas} is the raw number of same event jet-hadron pairs, N_{bkg} is the flow background contribution, $\epsilon(p_{\text{T}}, \eta)$ corresponds to the single hadron acceptance times tracking efficiency correction, and $a(\Delta\varphi, \Delta\eta)$ corresponds to the pair acceptance correction from the mixed events, which is described in further detail below in Sec. 3.4.2.

To obtain $C(\Delta\varphi, \Delta\eta)$, we first measure the same event jet-hadron correlations,

$$C_{\text{meas}}(\Delta\varphi, \Delta\eta) = \frac{\mathrm{d}^2}{\mathrm{d}\Delta\varphi \mathrm{d}\Delta\eta} \frac{N_{\text{assoc}}}{\epsilon(p_{\text{T}}, \eta)}. \tag{3.10}$$

where the $\Delta\varphi$ and $\Delta\eta$ angles are calculated and stored between each accepted jet and the associated hadrons in the event. The raw correlations still contain a large background component which must be removed after the acceptance correction is applied.

A raw correlation for $20 < p_{\text{T,jet}} < 40$ GeV/c and $1.0 < p_{\text{T}}^{\text{assoc}} < 1.5$ GeV/c is shown in Fig. 3.12. The trigger jet is clearly visible centered around $(\Delta\varphi, \Delta\eta) = (0, 0)$. The recoil jet is centered around $\Delta\varphi = \pi$, but due to x[21] mismatch between the incoming partons, the recoil jet signal extends over the entire acceptance in $\Delta\eta$. Beneath the trigger and recoil jet signals is a triangular shape as a function of $\Delta\eta$ that is caused

21. x is the momentum fraction carried by the parton, ${p_{\text{T}}}^{\text{parton}}/{p_{\text{T}}}^{\text{nucleon}}$

by the finite η acceptance of TPC and EMCal: for a large $\Delta\eta$ value, contributions can only come from a trigger jet and associated particle which are on the edges of the detector acceptance, so it will have fewer entries than for a trigger and associated particle in the center of the acceptance. When the trigger and associated are near the center of the acceptance, combinatorics dictate that there are more opportunities for pairs to contribute to the correlation. Since the trigger jet is required to be within the fiducial acceptance of the EMCal, the region $|\Delta\eta| < 0.9 - 0.5 = 0.4$ is fully efficient, which causes a plateau.

As $p_{\mathrm{T}}^{\mathrm{assoc}}$ increases, as in Fig. 3.13, the background decreases substantially, but so does the recoil jet contribution because the higher $p_{\mathrm{T}}^{\mathrm{assoc}}$ requires a harder and rarer fragmentation. Entries into the mixed event correlation are weighted by the single track efficiency correction $\epsilon(p_{\mathrm{T}}, \eta)$ described in Sec. 3.2.2.

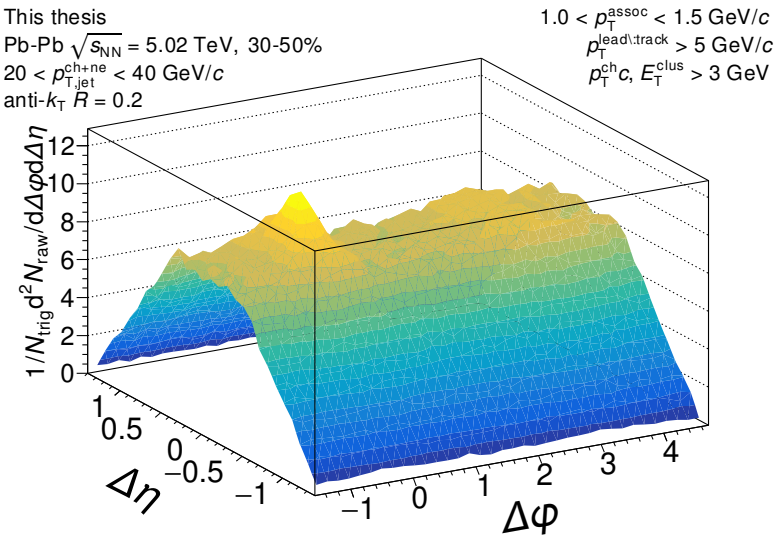

Figure 3.12: The measured correlation function with the efficiency correction $\epsilon(p_{\mathrm{T}}, \eta)$ applied, but before acceptance correction via the mixed events. The correlation is measured inclusive in event plane orientation for $20 < p_{\mathrm{T,jet}} < 40$ GeV/c jets with $1.0 < p_{\mathrm{T}}^{\mathrm{assoc}} < 1.5$ GeV/c in 30–50% semi-central Pb–Pb collisions at $\sqrt{s_{\mathrm{NN}}} = 5.02$ TeV.

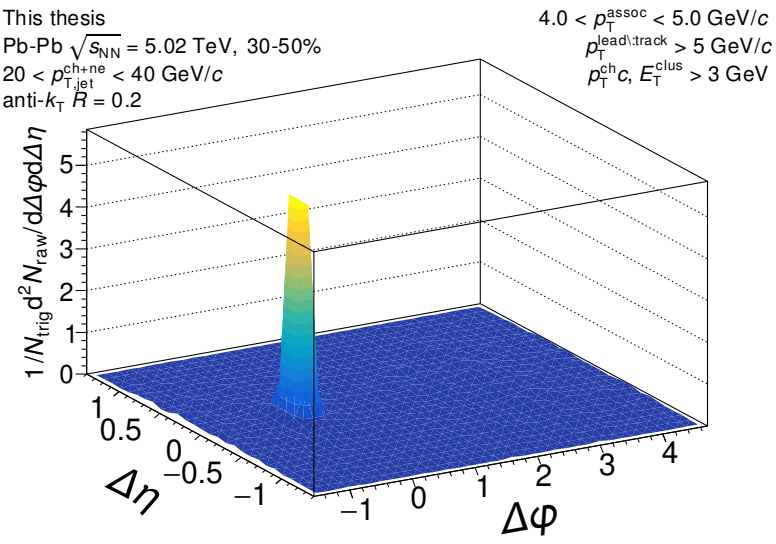

Figure 3.13: The measured correlation function with the efficiency correction $\epsilon(p_{\mathrm{T}}, \eta)$ applied, but before acceptance correction via the mixed events. The correlation is measured inclusive in event plane orientation for $20 < p_{\mathrm{T,jet}} < 40$ GeV/c jets with $4.0 < p_{\mathrm{T}}^{\mathrm{assoc}} < 5.0$ GeV/c in 30–50% semi-central Pb–Pb collisions at $\sqrt{s_{\mathrm{NN}}} = 5.02$ TeV.

3.4.2 Pair Acceptance Correction

As described above, the raw correlation function is modified due to the restricted detector acceptance in η for both trigger jet and associated particles, causing the characteristic triangular shape at large $\Delta\eta$, as well as the plateau at smaller $\Delta\eta$ where the triggers and associated particles are fully efficient. In addition to these finite acceptance effects, there are additional detector acceptance effects, such as the sector boundaries within the TPC.

Both of these effects can be corrected via a technique known as event mixing, where trigger jets are correlated with charged hadrons from events other than those which produced the trigger jet. In doing so, physical correlations between particles are removed, while the correlations reflecting the acceptance of the detector are preserved. The mixed events are defined as

$$a(\Delta\varphi, \Delta\eta) = a_0 \frac{\mathrm{d}^2 N_{\mathrm{pair}}^{\mathrm{mixed}}}{\mathrm{d}\Delta\varphi \mathrm{d}\Delta\eta}, \tag{3.11}$$

where $N_{\mathrm{pair}}^{\mathrm{mixed}}$ is the number of trigger jet-hadron pairs in the mixed events, and a_0 normalizes the correction to unity at maximum efficiency, as described in Sec. 3.4.2.1. Note that after applying the mixed event correction, the underlying flow background still remains and will be addressed in Sec. 3.5.

Event mixing is performed by constructing collections of tracks, known as pools. Since the mixed events are intended to account for pair acceptance effects within each correlation, it is important that the mixed events are composed of events that are similar to the same events used to measure the raw correlation. In particular, the pair acceptance can depend on the z_{veretx} position, and detector occupancy, which will correlate with event activity. Thus, the pools are constructed from events which share the same centrality range, and are within 2 cm of the z_{vertex}. In order to ensure there are sufficient statistics for a meaningful description of the detector conditions, at least 5000 tracks are required in a pool before mixing begins. A maximum of 50000 tracks are allowed in a pool before the oldest ones are removed from the queue, and then replaced by the newest tracks. In order to account for the track multiplicity in a given pool, each track that is used for event mixing is weighted by the number of tracks in that pool.

Mixed event correlations for our low and high $p_{\mathrm{T}}^{\mathrm{assoc}}$ bins are shown in Fig. 3.14. The correlations have already been normalized to unity at the region of maximum efficiency according to the procedure described below in Sec. 3.4.2.1. As expected, the shape of the correlations in $\Delta\eta$ mirrors those in the raw signal correlations, except for the jet peaks. Entries into the mixed event correlation are weighted by the single track efficiency correction $\epsilon(p_{\mathrm{T}}, \eta)$ described in Sec. 3.2.2.

As described in Sec. 3.5, having sufficient statistics at large $\Delta\eta$ is important for effectively describing the background contributions. However, the statistics at large $\Delta\eta$ tend to be limited due to the detector acceptance, and therefore are corrected substantially by the mixed events. If the mixed event does not have sufficient statistics in this region, it can cause the correction to be dominated by statistical fluctuations. Therefore, a number of techniques proposed in [66] are applied to increase the statistics and thereby reduce the fluctuations, including

- All mixed events with $p_{\mathrm{T}}^{\mathrm{assoc}} > 2$ GeV/c are combined together. Since tracks with $p_{\mathrm{T}}^{\mathrm{assoc}} > 2$ GeV/c are nearly straight, the detector acceptance doesn't vary much above this range.
- Mixed events for the three event plane orientations are combined together. Since the mixed events are dominated by the acceptance effects described above, combining the event plane orientations has a negligible effect.
- As noted above, the mixed event can vary as a function of z_{vertex}. The standard approach in a correlations analysis is to apply the mixed event correction to the raw signal correlation as a function of z_{vertex} and then to sum over the z_{vertex} bins to get corrected signal correlation. However, this technique can increase the statistical fluctuations due to highly weighted bins with poor statistics. Consequently, our nominal technique is to sum over z_{vertex} bins before apply the mixed event correction. This variations leads to the correlated scale systematic uncertainty that is discussed in Sec. 3.6.

3.4.2.1 Mixed Event Normalization

Since the mixed event measures the efficiency of accepting pairs of particles, the maximal value of the correlation should be normalized such that the most efficient point is unity. Normally, this would be $(0, 0)$ where the probability for detecting the

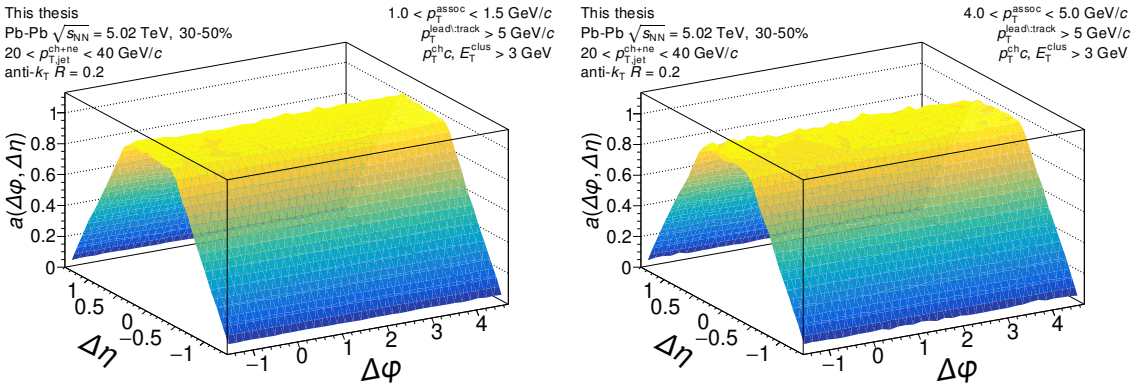

(a) The mixed event pair acceptance correction for $1.0 < p_{\mathrm{T}}^{\mathrm{assoc}} < 1.5$ GeV/c.

(b) The mixed event pair acceptance correction for $4.0 < p_{\mathrm{T}}^{\mathrm{assoc}} < 5.0$ GeV/c.

Figure 3.14: The mixed event pair acceptance correction with the efficiency correction $\epsilon(p_{\mathrm{T}}, \eta)$ applied. The correlations are measured inclusive in event plane orientation for $20 < p_{\mathrm{T,jet}} < 40$ GeV/c jets in 30–50% semi-central Pb–Pb collisions at $\sqrt{s_{\mathrm{NN}}} = 5.02$ TeV. They have already been normalized such that they are unity at maximum efficiency. Above 2 GeV/c, the mixed events are merged together to increase statistics, so it is the same for all for correlations within $2.0 < p_{\mathrm{T}}^{\mathrm{assoc}} < 10.0$ GeV/c.

pair particle should be highest. However, as shown in Fig. 3.15, there is a tracking inefficiency in front of the EMCal. Since triggers are restricted to be in this region, there is a corresponding inefficiency in detecting a second particle in that acceptance. Since the position of maximal efficiency depends on the mixed event correlation and is susceptible to statistical fluctuations, a procedure was developed to automatically determine the location of maximum efficiency.

First, in order to reduce the statistical fluctuations, we project the mixed event onto the $\Delta\varphi$ axis over the $\Delta\eta$ plateau region for $-0.3 < \Delta\eta < 0.3$. Next, we calculate our normalization over a wide range in $\Delta\varphi$ in order to reduce the sensitivity to the fluctuations. Our nominal method of a moving average is calculated with a window of π over the entire $\Delta\varphi$ range, and then we take the maximum value as the nominal normalization. A one dimensional fit over $\pi/2 < \Delta\varphi < 3\pi/2$ and a two dimensional fit over $-0.3 < \Delta\eta < 0.3$ and the same $\Delta\varphi$ range were also considered. The methods are compared in Fig. 3.16. The fits are more sensitive to structures in $\Delta\varphi$ and therefore

are considered only as possible systematic errors in Sec. 3.6. A variety of additional methods were considered for smoothing the data, such as gaussian smoothing, but were found to be inconsistent over the range of mixed events.

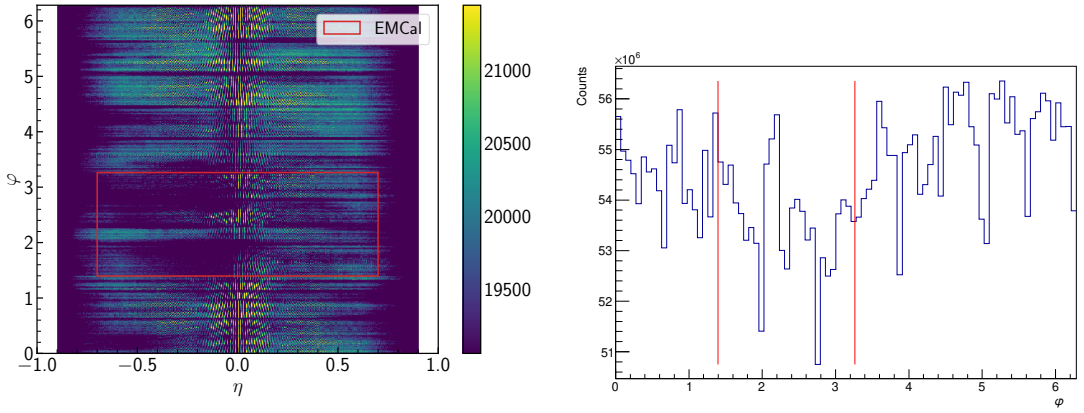

(a) Number of tracks measured as a function of (η, φ). The EMCal acceptance is shown by the red box.

(b) Number of tracks measured as a function of φ. The EMCal acceptance in φ is shown between the red lines.

Figure 3.15: Number of tracks which have $p_{\mathrm{T}} > 0.5$ GeV/c measured in (η, φ) for 30–50% semi-central Pb–Pb collisions at $\sqrt{s_{\mathrm{NN}}} = 5.02$. There is a relative inefficiency at $\eta < 0$ inside of the EMCal acceptance. The scale is truncated to emphasize this inefficiency.

3.4.3 Corrected Correlations

Once the pair acceptance correction has been determined, the signal correlation, $C(\Delta\varphi, \Delta\eta)$, can be measured by dividing the raw correlation, $C_{\mathrm{meas}}(\Delta\varphi, \Delta\eta)$, by the normalized mixed event, $a(\Delta\varphi, \Delta\eta)$. The corrected signal correlation for our low and high $p_{\mathrm{T}}^{\mathrm{assoc}}$ bins are shown in Fig. 3.17. In the low $p_{\mathrm{T}}^{\mathrm{assoc}}$ bin in Fig. 3.17a, there is a clear trigger jet around $(\Delta\varphi, \Delta\eta) = (0, 0)$, while there is a weak recoil jet signal around $\Delta\varphi \approx \pi$ and spread along $\Delta\eta$. There are clear statistical fluctuations in the background regions, especially at large $\Delta\eta$. In the high $p_{\mathrm{T}}^{\mathrm{assoc}}$ bin shown in Fig. 3.17b, a narrow trigger peak is clear, and there are limited background fluctuations, but the recoil jet signal is even weaker than for low $p_{\mathrm{T}}^{\mathrm{assoc}}$.

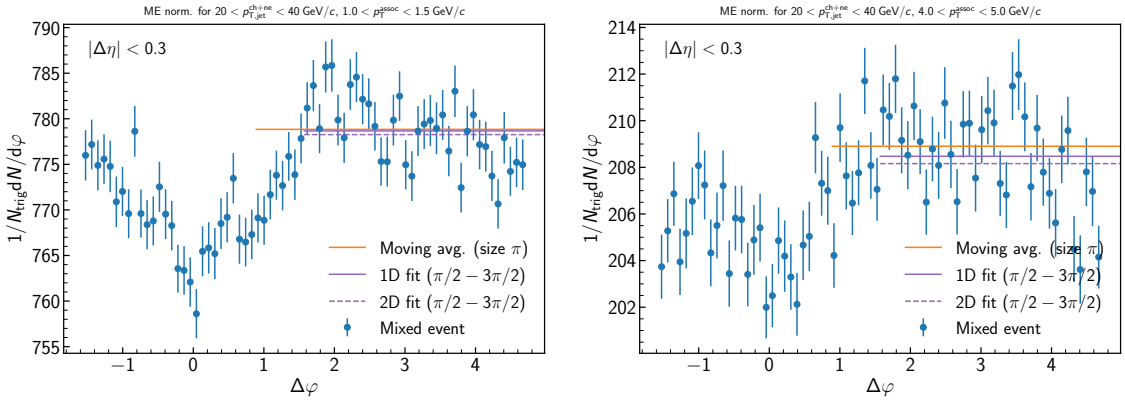

(a) Mixed event normalization for $1.0 < p_{\mathrm{T}}^{\mathrm{assoc}} < 1.5$ GeV/c.

(b) Mixed event normalization for $4.0 < p_{\mathrm{T}}^{\mathrm{assoc}} < 5.0$ GeV/c.

Figure 3.16: Determination of the normalization of the mixed event for the for inclusive event plane orientation in 30–50% semi-central Pb–Pb collisions at $\sqrt{s_{\mathrm{NN}}} = 5.02$ TeV. Here the mixed event is projected over the plateau range in $\Delta\eta$ onto to the $\Delta\varphi$ axis. The moving average is evaluated over the entire $\Delta\varphi$ range using a window of π, while the fit range is fixed from $\pi/2 < \Delta\varphi < 3\pi/2$. Since the mixed events are merged above 2 GeV/c, the normalization factor is also the same for all correlations within $2.0 < p_{\mathrm{T}}^{\mathrm{assoc}} < 10.0$ GeV/c. A variety of normalization methods were evaluated, with further details described in the text.

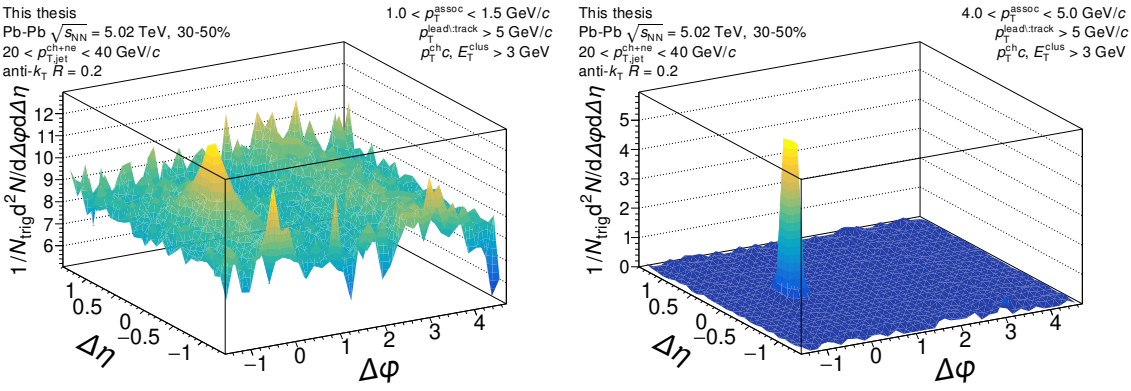

(a) The signal correlation for $1.0 < p_{\mathrm{T}}^{\mathrm{assoc}} < 1.5$.

(b) The signal correlation for $4.0 < p_{\mathrm{T}}^{\mathrm{assoc}} < 5.0$.

Figure 3.17: The signal correlation corrected by pair acceptance. The correlations are measured inclusive in event plane orientation for $20 < p_{\mathrm{T,jet}} < 40$ GeV/c jets in 30–50% semi-central Pb–Pb collisions at $\sqrt{s_{\mathrm{NN}}} = 5.02$ TeV.

Using the corrected correlations, we can project down to $\Delta\varphi$ or $\Delta\eta$ and extract the correlation properties. These projections will focus on the region $-\pi/2 < \Delta\varphi < \pi/2$, which is termed the near-side and contains the trigger jet, as well as on the region $\pi/2 < \Delta\varphi < 3\pi/2$, which is termed the away-side and contains the recoil jet signal. A low $p_{\mathrm{T}}^{\mathrm{assoc}}$ $\Delta\eta$ projection onto the near-side is shown in Fig. 3.18. A clear trigger jet signal is seen on top of a large background contribution, with apparent statistical fluctuations at large $|\Delta\eta| > 1.2$. Since there is no flow background in $\Delta\eta$, this background contribution can be removed by fitting to a constant value at large $\Delta\eta$ outside of contributions from the trigger peak. A low $p_{\mathrm{T}}^{\mathrm{assoc}}$ $\Delta\varphi$ projection is shown in Fig. 3.19, with clear near-side and away-side signals, modulated by a large background contribution. This background contribution will be addressed in the next section.

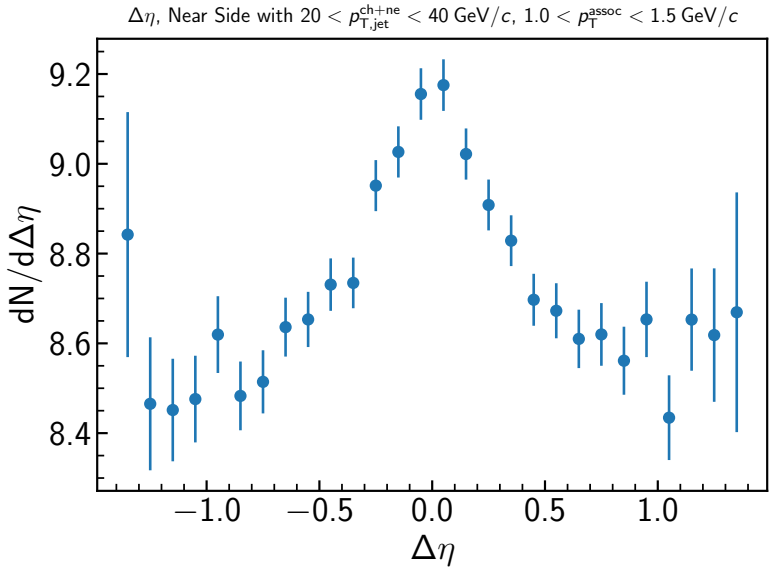

Figure 3.18: Projection of the near-side correlation onto $\Delta\eta$ for $1.0 < p_{\mathrm{T}}^{\mathrm{assoc}} < 1.5$ GeV/c. There is a clear trigger jet signal on top of a large background contribution. Statistical fluctuations are apparent at large $|\Delta\eta|$. Note that the y-axis scale does not go to zero. The correlations are measured inclusive in event plane orientation for $20 < p_{\mathrm{T,jet}} < 40$ GeV/c jets in 30–50% semi-central Pb–Pb collisions at $\sqrt{s_{\mathrm{NN}}} = 5.02$ TeV.

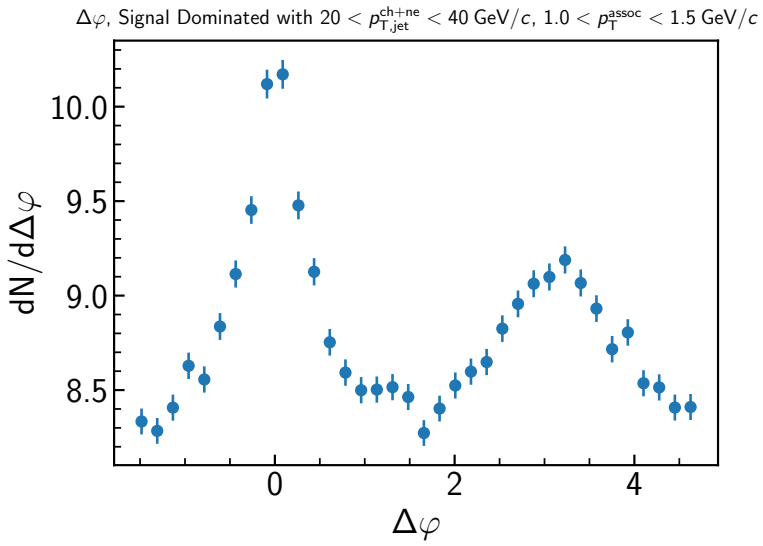

Figure 3.19: Projection of the signal correlation onto $\Delta\varphi$ for $1.0 < p_{\mathrm{T}}^{\mathrm{assoc}} < 1.5$ GeV/c. There are clear near-side and away-side signals, as well as a large background contribution. Note that the y-axis scale does not go to zero. The projection is limited to the signal dominated region, as described in Sec. 3.5. The correlations are measured inclusive in event plane orientation for $20 < p_{\mathrm{T,jet}} < 40$ GeV/c jets in 30–50% semi-central Pb–Pb collisions at $\sqrt{s_{\mathrm{NN}}} = 5.02$ TeV.

3.5 Reaction Plane Fit

In order to measure the jet-hadron correlation properties, we must characterize the underlying azimuthal anisotropic background. Typically, this flow background is decomposed into a Fourier series and described via its corresponding coefficients. However, this particular approach presents difficulties for measuring jet-hadron correlations. First, it would require independent measurements of both v_n^{assoc} and v_n^{jet} for harmonics up to $n = 4$. Although v_n^{assoc} measurements are widely available [78–83], v_n^{jet} has only been measured up to $n = 3$ for charged jets and $n = 2$ for full jets at $\sqrt{s_{\mathrm{NN}}} = 2.76$ TeV [84,85]. Given the biased jet selection utilized in this measurement, describing the background would likely require any independent measurements to use the same jet finding parameters. Second, given the differences in event properties that accompany a jet, such as event activity, it is possible that the v_n coefficients may vary

in the presence of the measured jet. Given these difficulties, a method to extract the correlation background directly from the measured correlations is required.

The Reaction Plane Fit (RPF) method is therefore selected to determine the background level and shape [67,86,87]. This technique takes advantage of the sensitivity of different event plane orientations to different v_n terms. To utilize this method, the correlations are measured as a function of the orientation of the trigger with respect to the event plane[22]. The correlations are then fit simultaneously in all event plane orientations, thereby constraining the v_n coefficients. This method then extracts a set of effective v_n coefficients which describe the background. The fit is defined as

$$\tilde{B} = \frac{N_t N_a c}{\pi^2}\left(1 + 2\sum_{k=1}^{\infty} \frac{v_{2k}^{\mathrm{trig}}}{2kc} \sin(2kc) \Re_{2k} C_{2k,0} \cos(2k\phi_s)\right), \tag{3.12}$$

$$\tilde{v}_n^{\mathrm{trig}} = \frac{v_n + \frac{\delta_{n,\mathrm{mult}\ 2}}{nc} \sin(nc) \Re_n C_{n,0} \cos(n\phi_s) + \sum_{k=1}^{\infty} (v_{2k+n}^{\mathrm{trig}} C_{|2k+n|,n} + v_{|2k-n|}^{\mathrm{trig}} C_{|2k-n|,n}) \frac{\sin(2kc)\cos(2k\phi_s)\Re_{2k}}{2kc}}{1 + 2\sum_{k=1}^{\infty} \frac{v_{2k}^{\mathrm{trig}}}{2kc} \sin(nc) \Re_{2k} C_{2k,0} \cos(2k\phi_s)}$$

$$C_{n,m} = \langle \cos(n\psi_n + m\psi_m - (n+m)\psi_2) \rangle$$

$\tilde{B}$ is the effective background level, N_t and N_a are the number of trigger and associated particles, c is the width of the event plane bin, ϕ_s is the center of the event plane bin, $\Re_{2,k}$ is the event plane resolution as described in Sec. 3.2.5, and Ψ_n is the event plane of harmonic n. The overall background, $B(\Delta\phi)$, is then defined as

$$B(\Delta\phi) = \tilde{B}\left(1 + 2\sum_{n=1}^{\infty} \tilde{v}_n^t \tilde{v}_n^a \cos(n\Delta\phi)\right) \tag{3.13}$$

22. Unless otherwise specified, when a result is mentioned regarding "each event plane orientation", this also includes the inclusive event plane orientation.

The general background expression in Eq. 3.12 simplifies for particular selections for event plane bins. For this analysis, the correlations were measured within three event plane bins defined with respect to the second order harmonic within the region ($-\pi$, π):

- From $-\pi/6$ to $\pi/6$ corresponding to $\phi_s = 0$ and $c = \pi/6$, known as in-plane.
- From $-\pi/3$ to $-\pi/6$ and $\pi/6$ to $\pi/3$ corresponding to $\phi_s = \pi/4$ and $c = \pi/12$[23], known as mid-plane.
- From $-\pi/2$ to $-\pi/3$ and $\pi/3$ to $\pi/2$ corresponding to $\phi_s = \pi/2$ and $c = \pi/6$, known as out-of-plane.

Since the trigger angle can be anywhere within the $[-\pi, \pi)$ range, triggers outside of the ranges defined above are reflected into the defined region. The regions are defined in Fig. 3.1. The number of event plane bins are dictated by the requirement of sufficient statistics in each event plane bin in order to measure the correlation, as well as sufficient event plane resolution as measured by ALICE. When Eq. 3.12 is evaluated for the three event plane bins defined, and only terms which are able to be reconstructed experimentally are included, the effective v_n^t can be expressed as

$$\tilde{v}_2^t = \frac{v_2^t + \frac{\cos(2\phi)\sin(2c)}{2c}\Re_2(\Psi_2) + v_4^t\frac{\cos(2\phi)\sin(2c)}{2c}\Re_2(\Psi_2) + v_2^t\frac{\cos(4\phi)\sin(4c)}{4c}\Re_4(\Psi_2) + v_4^t\frac{\cos(6\phi)\sin(6c)}{6c}\Re_6(\Psi_2)}{1 + 2v_2^t\frac{\cos(2\phi)\sin(2c)}{2c}\Re_2(\Psi_2) + 2v_4^t\frac{\cos(4\phi)\sin(4c)}{4c}\Re_4(\Psi_2)} \quad (3.14)$$

$$\tilde{v}_4^t = \frac{v_4^t + \frac{\cos(4\phi)\sin(4c)}{4c}\Re_4(\Psi_2) + v_2^t\frac{\cos(2\phi)\sin(2c)}{2c}\Re_2(\Psi_2) + v_2^t\frac{\cos(6\phi)\sin(6c)}{6c}\Re_6(\Psi_2)}{1 + 2v_2^t\frac{\cos(2\phi)\sin(2c)}{2c}\Re_2(\Psi_2) + 2v_4^t\frac{\cos(4\phi)\sin(4c)}{4c}\Re_4(\Psi_2)} \quad (3.15)$$

In order for this method to describe the background, we must select a region where

23. The bin width for the mid-plane bin is half of the other two bins because it corresponds to four regions when defined over the entire 2π range. The other two bins only contain two regions. This factor is compensated for when the fit is performed.

it dominates. As discussed in the previous section, the away-side jet signal extends over the entire measured $\Delta\eta$ range, so we must restrict the fit to the near-side. On the near-side, using the jet as the correlation trigger localizes the jet to small $\Delta\eta$. So as long as the width of the near-side peak is small enough, the large $\Delta\eta$ on the near-side should be dominated by background. Therefore, we select the near-side in $\Delta\varphi$, and $|\Delta\eta| > 0.8$. Due to statistical considerations[24], this region is limited to $0.8 < |\Delta\eta| < 1.2$. It is termed the background dominated region, while the region $|\Delta\eta| < 0.6$ without any restriction on $\Delta\varphi$ is termed the signal dominated region. The signal dominated region is highlighted in blue and the background dominated region is highlighted in orange in Fig. 3.20. When the regions are projected, they are normalized by their respective $\Delta\eta$ projection lengths[25] to ensure they have the same level background contribution.

The fit parameters extracted in the background dominated region are extrapolated from the near-side to the away-side, and then used to described the background in the signal dominated region. This procedure is visualized in Fig. 3.21, where the fit is performed using the fully solid orange, it's extrapolated to cover the semi-transparent orange points, and then it is used to describe the background in the blue signal dominated region.

Once the correlations are projected into the $\Delta\varphi$ signal and background dominated regions in the three event plane orientations, the RPF method can be applied simultaneously to the near-side of the background dominated regions, resulting in the fit shown in Fig. 3.22 for $1.0 < p_{\mathrm{T}}^{\mathrm{assoc}} < 1.5$. In the upper panels, the RPF is shown

24. Extending the region into larger $\Delta\eta$ does not improve the background determination. The mixed event in that region is dominated by a small number of measurements with large weights due to the ALICE acceptance. The errors on those points negate any benefit from the increase in statistics.

25. i.e. 1.2 for the signal dominated region, and 0.8 for the background dominated region.

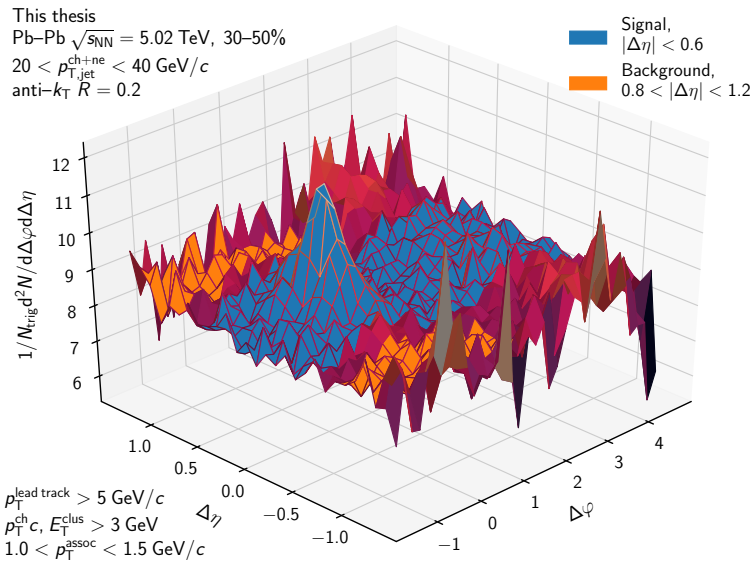

Figure 3.20: Highlights of the signal and background dominated regions in the corrected signal jet-hadron correlation measured in the inclusive event plane orientation for $1.0 < p_{\mathrm{T}}^{\mathrm{assoc}} < 1.5$ GeV/c in 30–50% semi-central Pb–Pb collisions.

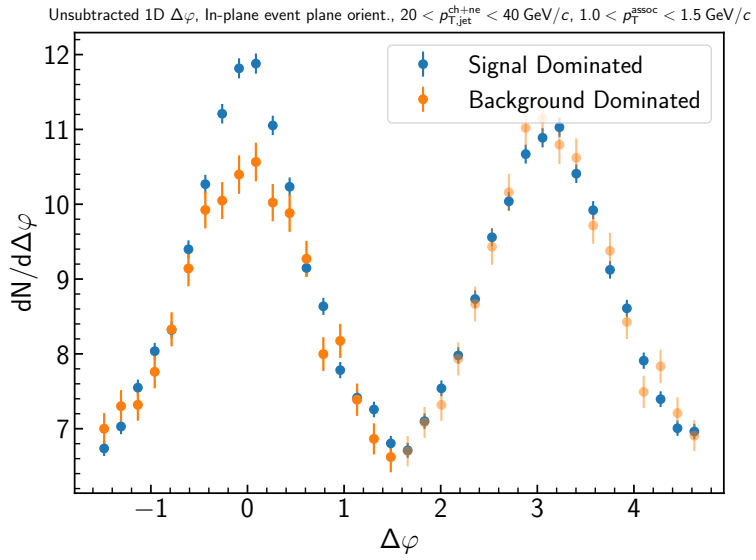

Figure 3.21: Comparison between the signal and background dominated regions for jet-hadron correlations measured in the in-plane event plane orientation for $1.0 < p_{\mathrm{T}}^{\mathrm{assoc}} < 1.5$ GeV/c in 30–50% semi-central collisions. The blue points are from the signal dominated region, while the orange points are from the background dominated region. The solid orange points are used for the RPF, and then the background is extrapolated to the semi-transparent orange points.

in the purple band, while the signal and background regions are shown in blue and orange points, respectively, for each event plane orientation, as well as inclusively. The width of the purple band represents the fit uncertainty, which is calculated via Eq. 3.16 and described below. The RP fit curve shown for the inclusive orientation is calculated using a Fourier series, plugging the effective v_n coefficients extracted in the fit. In each upper panel, both trigger and recoil jet signals are clearly visible above the background on the near- and away-sides, respectively. Due to the statistical uncertainties on the data, the background dominated region is sometimes larger than the signal dominated region, especially on the away-side where the recoil jet signal sits on top of the background. In the lower panels, the fit residual is calculated for the background dominated region in each event plane orientation, with the band again representing the uncertainty. Although the fit is restricted to the near-side, the residuals shown in the lower panels are evaluated over the entire $\Delta\varphi$ range. Consequently, the away-side jet signal, which extends to large $\Delta\eta$, can appear as an increase in the residual even if the fit describes the background well. This can be seen most clearly in the out-of-plane panel.

The RPF result for our high $p_{\mathrm{T}}^{\mathrm{assoc}}$ bin is shown in Fig. 3.23. In this case, the background contribution to the correlations is small compared to the size of the near-side jet peak. This leads to weaker constraints on the background parameters and therefore a more uncertain fit, as represented by the larger fractional errors.

The point-by-point errors on $\Delta\varphi$ from the fit, $\sigma(\Delta\varphi)$, are calculated according to the general error propagation expression,

$$\sigma(\Delta\varphi) = \sqrt{\sum_i \sum_j \frac{\partial f(\Delta\varphi, p_i)}{\partial p_i} \frac{\partial f(\Delta\varphi, p_j}{\partial p_j} \sigma_{i,j}} \tag{3.16}$$

where $\sigma_{i,j}$ is the covariance matrix from the fit, $f(p_i)$ is the fit function that depends

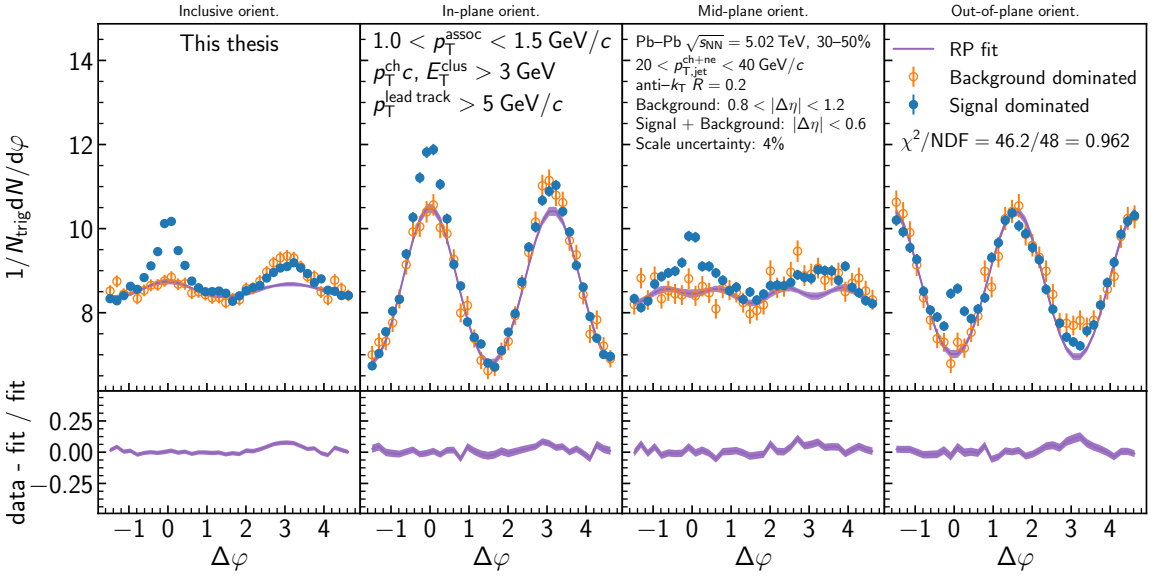

Figure 3.22: The Reaction Plane Fit of jet-hadron correlations measured for $20 < p_{\mathrm{T,jet}} < 40$ GeV/c and $1.0 < p_{\mathrm{T}}^{\mathrm{assoc}} < 1.5$ GeV/c in 30–50% semi-central collisions. The signal dominated data are shown in blue, the background dominated in orange, and the fit in purple. The upper panels show the signal and background dominated correlations measured in each event plane orientation. The lower panels show the fit residuals.

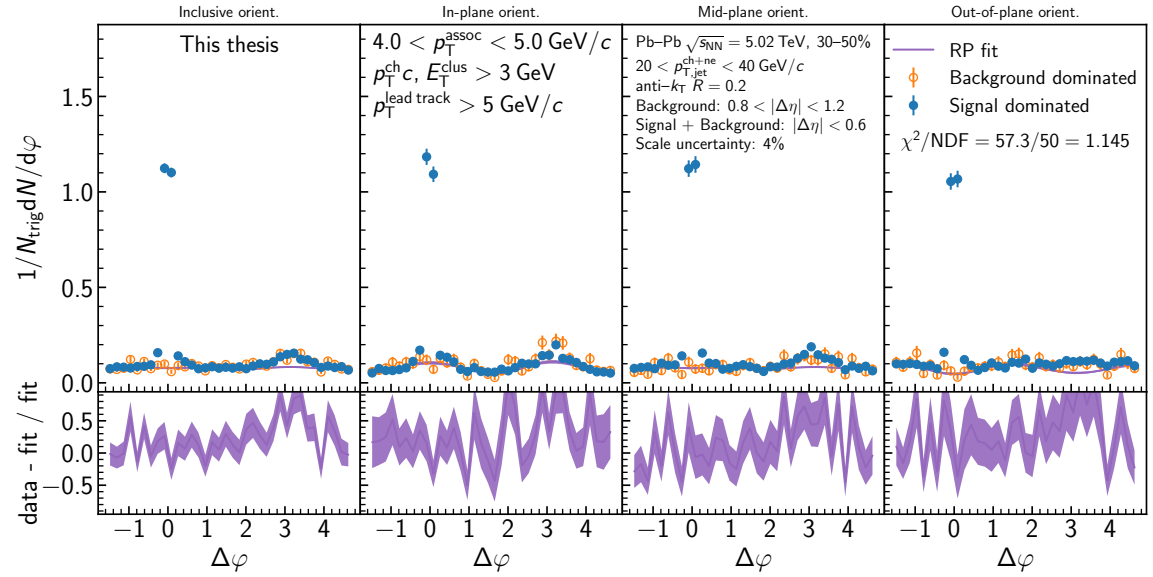

Figure 3.23: The Reaction Plane Fit of jet-hadron correlations measured for $20 < p_{\mathrm{T,jet}} < 40$ GeV/c and $4.0 < p_{\mathrm{T}}^{\mathrm{assoc}} < 5.0$ GeV/c in 30–50% semi-central collisions. The upper panels show the signal and background dominated correlations measured in each event plane orientation. The lower panels show the fit residuals.

on parameters p_i, and i and j range over the free parameters in the fit[26]. These errors are non-trivially correlated point-to-point.

3.5.1 Fit Quality and Convergence

Given the complexity of the Reaction Plane Fit, it is important to evaluate a variety of criteria for each $p_{\mathrm{T}}^{\mathrm{assoc}}$ bin to determine the quality of the fit. These factors include:

- The χ^2/ndf[27] must not be improbable, which would indicate that the fit cannot describe the shape of the data.
- To ensure that the Minuit parameter error estimation is valid, the value determined by the fit must be far away from the parameter limits.
- The effective parameters should approximately agree with the external measurements. This criteria is discussed further in Sec. 3.5.2.
- The Minos error calculation provided by Minuit must pass the valid criteria [88,89].
- The asymmetric errors calculated by Minos should approximately agree with the symmetric errors calculated by Hesse. Agreement between these calculations suggests that the fit function is well approximated by a hyperparabola at the minima, which in turn suggests that the minimization has found a valid minima [88–90].

In the ideal case, all of the criteria would be satisfied for all fits. However, in some cases, such as described below for central collisions, we must balance between minimizing the χ^2/ndf and agreement with external measurements. Once a fit satisfies at least most

26. This error propagation is implemented via numerical differentiation in `pachyderm.fit.calculate_function_errors(...)`.

27. Number of degrees of freedom.

of the above criteria, it is considered stable and is used to measure derived values.

Although the final measurements are reported per trigger, this normalization removes information about the relative distribution of particles between the different event plane orientations, which makes accurate determination of the parameters more difficult. As a consequence, the fit is performed *without* the number of triggers normalization, and then after the fit is evaluated, the fit results are scaled back down. Since the fit scaling is proportional to $\tilde{B}$, the per trigger scaling only scales that value.

In the default case, a binned χ^2 cost function is utilized to minimize the RPF. However, at large $p_{\mathrm{T}}^{\mathrm{assoc}}$, the background becomes so small that some $\Delta\varphi$ bins do not contain any counts. In this case, the χ^2 is not well defined, and we must use a binned log-likelihood cost function to perform the minimization. This cost function will perform the optimization, but the parameter constraints are weaker, leading to larger point-by-point fit errors. Function minimization and the implications are discussed in further detail in Sec. B.2.

As $p_{\mathrm{T}}^{\mathrm{assoc}}$ increases, the background contribution decreases, which decreases the necessary degrees of freedom needed to fit the background. As a consequence, at high $p_{\mathrm{T}}^{\mathrm{assoc}}$, the fit parameters are not well constrained, increasing the fit errors. To prevent this issue, each fit was performed with $\tilde{v_4}^a$ and $\tilde{v_4}^t$ free, and if the errors on the both parameters were much larger than the parameter values (i.e. $\sigma_{\tilde{v_4}^{a,t}} >> \tilde{v_4}^{a,t}$), the parameters were fixed to 0 and the fit was performed again. For 30–50% semi-central collisions, $\tilde{v_4}$ terms were fixed starting at $4.0 < p_{\mathrm{T}}^{\mathrm{assoc}} < 5.0$ GeV/c, while for 0–10% central, terms were fixed starting at $3.0 < p_{\mathrm{T}}^{\mathrm{assoc}} < 4.0$ GeV/c. Given the worse event plane resolution in central collisions, it is unsurprising that the terms needed to be fixed at a lower $p_{\mathrm{T}}^{\mathrm{assoc}}$.

3.5.2 Fit Parameters

As a consequence of the fit, we also extract a set of effective $\tilde{v_n}$ parameters independent from other measurements. These results will be shown in Sec. 4. $\tilde{v_2}$ and $\tilde{v_4}$ are expected to agree approximately with independent experimental measurements. However, precise agreement is not necessarily required due to differences in how the effective $\tilde{v_n}$ are calculated, differences in event selection, and event plane decorrelation between v_2 and higher order event planes, which will lead to an increased ${\tilde{v_n}}^a$ and decreased ${\tilde{v_n}}^{\text{jet}}$ [91]. Note that even if the effective parameters do not agree precisely with other measurements, the RPF method will still provide a valid description of the background. ${\tilde{v_3}}^a{\tilde{v_3}}^{\text{jet}}$ is expected to be approximately zero because v_3^{jet} doesn't correlate with the second event plane. $\tilde{v_1}$ is set to zero[28] because jets are not expected to have a preferred direction.

3.5.3 Signal Fit

The RPF method describes the underlying background by utilizing the background dominated region. The widths as defined in Sec. 3.1 are then extracted by subtracting the RPF background and fitting a Gaussian to the remaining peak. While these steps can be accomplished separately, there is additional background information in the signal dominated region if it can be accessed. Consequently, I investigated the possibility of modeling the peaks of the signal dominated region directly as Gaussians and simultaneously fitting the signal and background dominated regions in all three event plane orientations. Concretely, the function is defined as

28. The fits were also performed for a free v_1, where the values were found to be consistent with zero. However, the large parameter errors substantially increased the point-by-point errors on the fit, so v_1 is fixed to 0 in the nominal case.

$$\frac{\mathrm{d}N}{\mathrm{d}\Delta\varphi} = \sum_i \frac{A_i}{\sqrt{2\pi{\sigma_i^{\mathrm{NS}}}^2}} e^{-1/2(\frac{\Delta\varphi}{\sigma_i^{\mathrm{NS}}})^2} + \sum_i \frac{A_i}{\sqrt{2\pi{\sigma_i^{\mathrm{AS}}}^2}} e^{-1/2(\frac{\Delta\varphi-\pi}{\sigma_i^{\mathrm{AS}}})^2} + \tilde{B}\Big(1+2\sum_{n=1}^{\infty}\tilde{v}_n^t\tilde{v}_n^a\cos(n\Delta\phi)\Big) \tag{3.17}$$

where i ranges over all the three event plane orientations, and the last term represent the RPF background. By combining the signal and background extraction, we should fully account for the covariance between the two regions which is neglected in the background RPF. Although the near- and away-side peaks are known to not actually be Gaussian in shape, it provides a convenient standard for characterizing the peaks. Consequently, the absolute value of the χ^2/ndf is less critical than in the RPF background fits described above. However, we should expect for the effective parameters extracted in the two methods to be similar.

The Signal Reaction Plane Fit is shown in Fig. 3.24 for jet-hadron correlations measured in the $1.0 < p_{\mathrm{T}}^{\mathrm{assoc}} < 1.5$ GeV/c. For the three event plane orientations, Gaussians are successfully fit to the near- and away-side peaks. The inclusive orientation is not fit, but instead the background is described using the effective parameters.

To fully evaluate the performance of the fit, it is most instructive to compare the widths with those extracted in the background method[29]. The near-side and away-side widths are compared in Fig. 3.25, 3.26. The widths extracted from the two fit methods are compatible within uncertainties. Although this approach was an interesting avenue of investigation, in practice, the complexity of the fit lead to instabilities in minimizing the function and extracting the effective parameters, such that correlations for higher $p_{\mathrm{T}}^{\mathrm{assoc}}$ could not be fit. Consequently, the standard background RPF is utilized for the reported results.

29. The yields are extracted by subtracting the background yield, which is similar between the two fits. The widths are extracted directly from the fit, and therefore are a better comparisons.

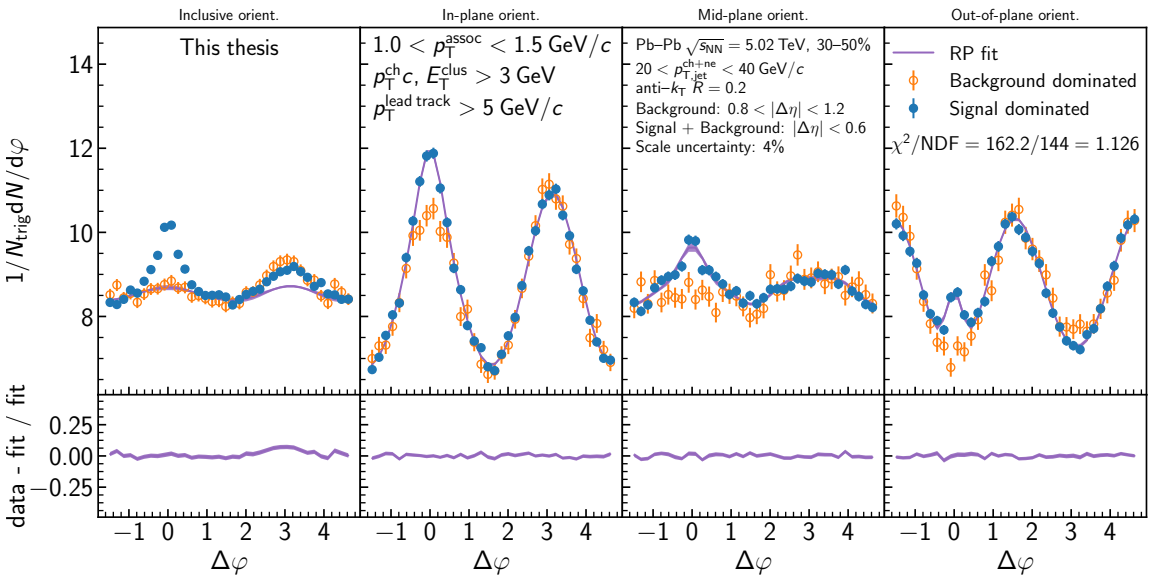

Figure 3.24: The Signal Reaction Plane Fit of jet-hadron correlations measured for $20 < p_{\mathrm{T,jet}} < 40$ GeV/c and $1.0 < p_{\mathrm{T}}^{\mathrm{assoc}} < 1.5$ GeV/c in 30–50% semi-central collisions. The signal dominated data is shown in blue, the background dominated in orange, and the fit in purple. The upper panels show the signal and background dominated correlations measured in each event plane orientation. The lower panels show the fit residuals for the signal region fits.

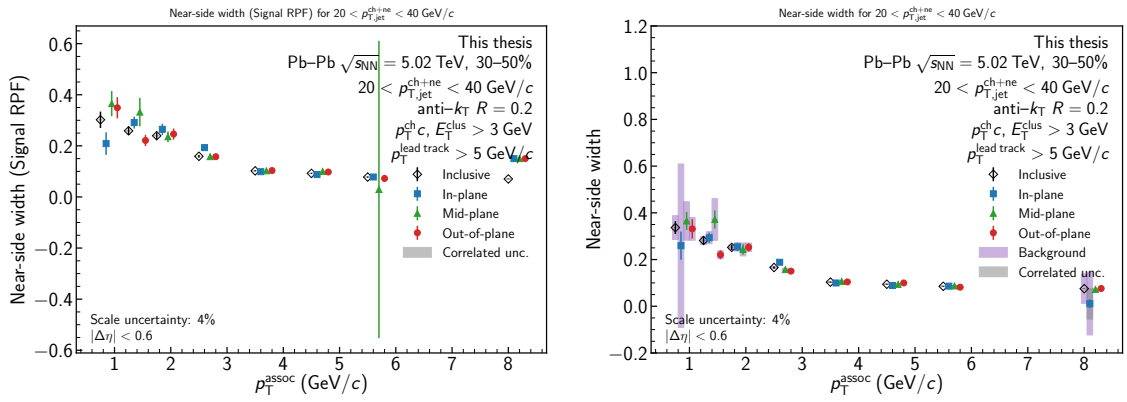

(a) Signal Reaction Plane Fit.

(b) Background Reaction Plane Fit.

Figure 3.25: Near-side correlation widths for the Signal and Background Reaction Plane Fits for 30–50% semi-central Pb–Pb collisions at $\sqrt{s_{\mathrm{NN}}} = 5.02$ TeV. The widths extracted from the Signal Fit are shown for $p_{\mathrm{T}}^{\mathrm{assoc}}$ where the fit converged, and the statistical uncertainties are omitted.

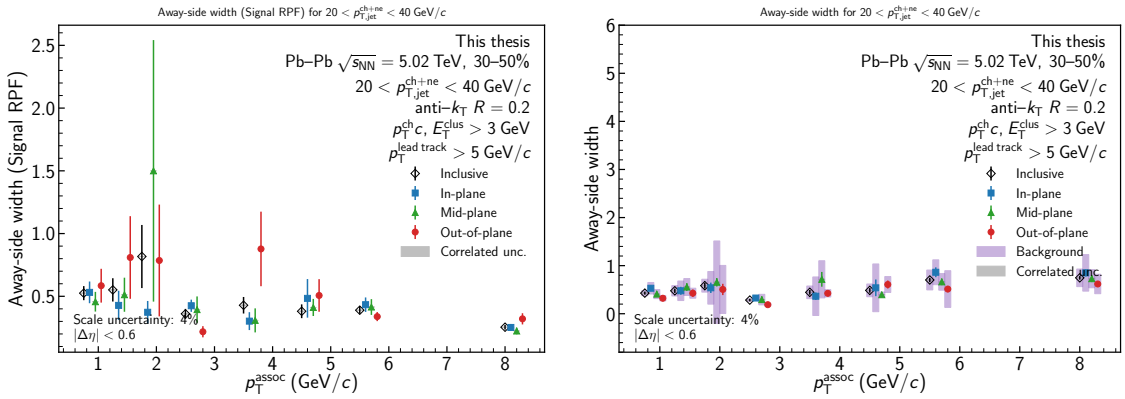

(a) Signal Reaction Plane Fit.

(b) Background Reaction Plane Fit.

Figure 3.26: Away-side correlation widths for the Signal and Background Reaction Plane Fits for 30–50% semi-central Pb–Pb collisions at $\sqrt{s_{\mathrm{NN}}} = 5.02$ TeV. The widths extracted from the Signal Fit are shown for $p_{\mathrm{T}}^{\mathrm{assoc}}$ where the fit converged, and the statistical uncertainties are omitted.

3.6 Statical and Systematic Uncertainties

3.6.1 Systematic Uncertainties

In this analysis, systematic uncertainties are divided into three major categories: the global scale uncertainty, the correlated scale uncertainty, and the background uncertainty.

The global scale uncertainty is dominated by the uncertainty on the tracking efficiency. By varying the hybrid track cuts, as well as the ITS-TPC matching efficiency, it was determined to be 4% [92]. Additional contributions were considered from the mixed event normalization procedure described in Sec. 3.4.2.1. However, extracted yields were modified by less than 0.2% for all $p_{\mathrm{T}}^{\mathrm{assoc}}$ bins, so when the uncertainties are combined in quadrature, the contribution is negligible. Consequently, the global scale uncertainty is kept at 4%. This uncertainty is correlated point-to-point.

For the correlated scale uncertainty, we return to the mixed event correction and

its relationship to the RPF. There is a correlation between the z_{vertex} position and the background level and shape at large $\Delta\eta$. Since the RPF method depends on the large $\Delta\eta$ background dominated region, it is sensitive to changes of the level in this region. As described in Sec. 3.4.2, our nominal method integrates over the z_{vertex} bins before applying the mixed event correction to the measured correlation. In order to account for possible scale variations that depend on z_{vertex}, this procedure is modified to perform the mixed event correction as a function of z_{vertex}[30]. We calculate the scale variation as

$$\alpha = \frac{s_{\text{nom}}}{s_{\text{var}}} = \frac{\frac{\int_{\text{sig}} C_{\text{nom}}}{\int_{\text{bkg}} C_{\text{nom}}}}{\frac{\int_{\text{sig}} C_{\text{var}}}{\int_{\text{bkg}} C_{\text{var}}}} \tag{3.18}$$

where $s = \frac{\int_{\text{sig}} C}{\int_{\text{bkg}} C}$ is the signal to background ratio for a corrected correlation, "nom" represents the nominal procedure and "var" represents the variation procedure. This scale uncertainty is then propagated to the RPF background by scaling the $\tilde{B}$ parameter from the RPF up and down by $|1 - \alpha|$. This uncertainty is correlated between event plane orientations.

There is also a background systematic uncertainty associated with the RPF. The uncertainties in the covariance matrix are propagated to point-to-point errors via Eq. 3.16 as explained in Sec. 3.5. These points are non-trivially correlated point-to-point, between event plane orientations, as well as between the near- and away-sides. An event plane resolution uncertainty could also be included here, but the statistical errors on those values are small and varying them by their errors was found to have a

30. i.e. For the nominal case, we sum and then apply the correction. For this systematic, we apply the correction and then sum.

negligible effect on the yields.

3.6.2 Error propagation

To measure the yield, we individually evaluate the signal and background yield integrals, Y_s and Y_b respectively, and then subtract them to measure the final yield. The statistical error of the signal yield is reported as the statistical error bar. Since the RPF background is non-trivially correlated point-to-point and between different event plane orientations, we report it as a separate error band.

To then construct the yield differences and ratios, we treat the statistical and background errors separately. The statistical errors are added in quadrature. We conservatively estimate the background uncertainty by also adding them in quadrature. The correlated scale uncertainty is fully correlated, and therefore it partially cancels for the yield differences, and it fully cancels for the yield ratios. The global scale uncertainty remains for the yield differences, but it also fully cancels for the yield ratios.

For the correlation widths, the background uncertainty is addressed by evaluating the varying each of the background parameters individually by their errors, reevaluating the background function and subtracting it from the signal, and repeating the width fit. The maximum variation from the nominal width is taken for each parameter. Those width parameter errors are then treated as uncorrelated and are added in quadrature. The correlated scale uncertainty is determined by scaling the background by the scale uncertainty and repeating the fit.

Chapter 4

Results

Using the background characterized by the Reaction Plane Fit, the associated hadron yields and correlation widths can be measured. Each observable shown below is presented as a function of event plane orientation, with in-plane shown in blue, mid-plane shown in green, out-of-plane shown in red, and the inclusive orientation in black. To reduce overlap between the points, they are offset in $p_{\mathrm{T}}^{\mathrm{assoc}}$. The black inclusive orientation points are always located at the center of the $p_{\mathrm{T}}^{\mathrm{assoc}}$ bin. The yield ratio is calculated for $\mathrm{Y}^{\mathrm{out}}/\mathrm{Y}^{\mathrm{in}}$ and $\mathrm{Y}^{\mathrm{mid}}/\mathrm{Y}^{\mathrm{in}}$ for both the near- and away-side. The yield difference is calculated for $\mathrm{Y}^{\mathrm{out}} - \mathrm{Y}^{\mathrm{in}}$ and $\mathrm{Y}^{\mathrm{mid}} - \mathrm{Y}^{\mathrm{in}}$ for the near- and away-side.

In this chapter, Sec. 4.1, 4.2, 4.3 presents the results, and Sec. 4.4 presents and compares to theoretical predictions and experimental results, and Sec. 4.5 discusses the results and predictions.

4.1 Jet-Hadron Correlations Measured in 30–50% Semi-Central Pb–Pb Collisions

As will be discussed in further detail in Sec. 4.4.1, the path length difference is expected to be larger for semi-central collisions, so we will consider these measurements first. The fit parameters extracted by the Reaction Plane Fit are shown in Fig. 4.1, 4.2, 4.3. These measurements approximately agree with all independent measurements for which there is comparable reference data, including v_2^a, v_2^{jet}, and v_4^a, although as discussed in Sec. 3.5.2, that is not necessarily required to be the case.

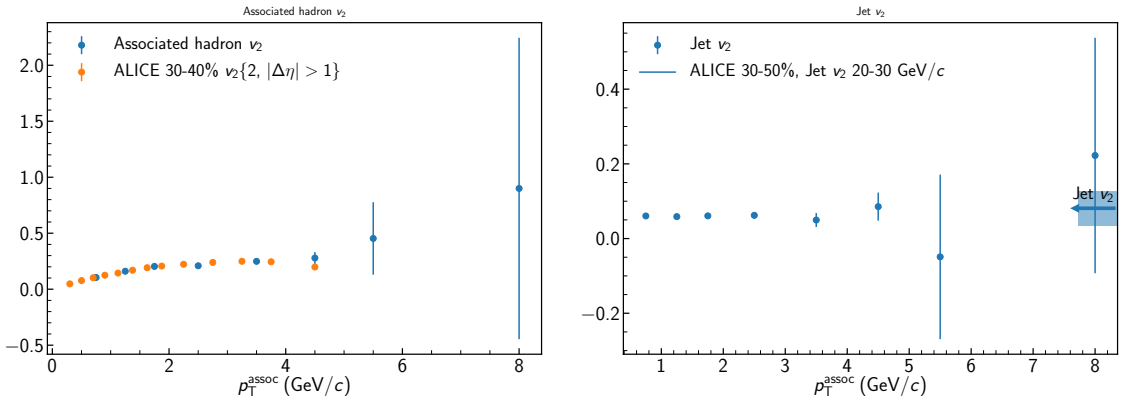

(a) $\tilde{v_2}^a$ (b) $\tilde{v_2}^{\text{jet}}$

Figure 4.1: $\tilde{v_2}^a$ and $\tilde{v_2}^{\text{jet}}$ extracted via the Reaction Plane Fit for 30–50% semi-central Pb–Pb collisions at $\sqrt{s_{\text{NN}}} = 5.02$ TeV. The values are compared to ALICE reference data [78,84].

The associated hadron yields for the near- and away-side are shown in Fig. 4.4. The statistical errors are displayed as colored bars, while background uncertainty is shown in purple boxes, and the correlated scale uncertainty in gray. The yields decrease with increasing $p_{\text{T}}^{\text{assoc}}$, as expected due to the steep falling charged particle p_{T} spectrum. On the near-side, the yields are compatible within uncertainties. On the away-side at low $p_{\text{T}}^{\text{assoc}}$, there are hints of a depletion of the out-of-plane yield compared to in-plane, while at mid $p_{\text{T}}^{\text{assoc}}$ this reverses, and at high $p_{\text{T}}^{\text{assoc}}$, they are compatible. The

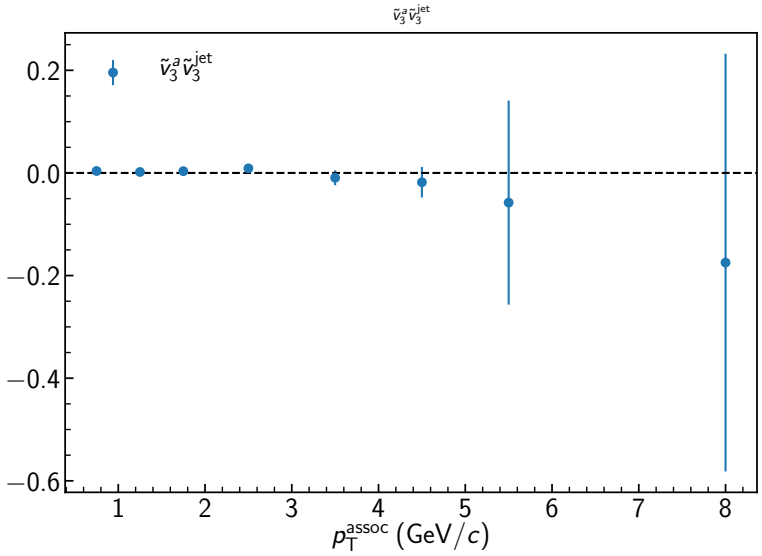

Figure 4.2: $\tilde{v_3}^a \tilde{v_3}^t$ extracted via the Reaction Plane Fit for 30–50% semi-central Pb–Pb collisions at $\sqrt{s_{\text{NN}}} = 5.02$ TeV. The values are expected to be approximately zero.

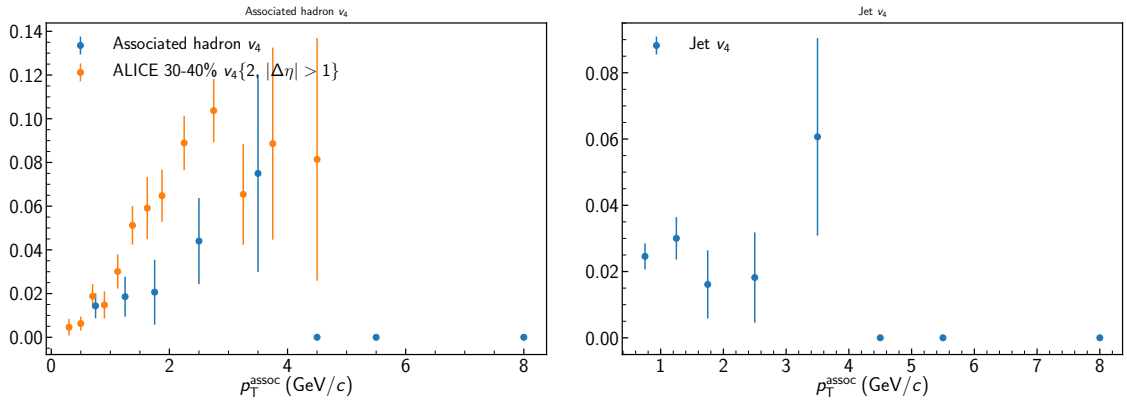

(a) $\tilde{v_4}^a$ (b) $\tilde{v_4}^{\text{jet}}$

Figure 4.3: $\tilde{v_4}^a$ and $\tilde{v_4}^{\text{jet}}$ extracted via the Reaction Plane Fit for 30–50% semi-central Pb–Pb collisions at $\sqrt{s_{\text{NN}}} = 5.02$ TeV. The values are compared to ALICE reference data [78,84].

mid-plane and inclusive orientations tend to be bounded by the other two orientations. Statistical fluctuations are clearly visible on both the near- and away-side.

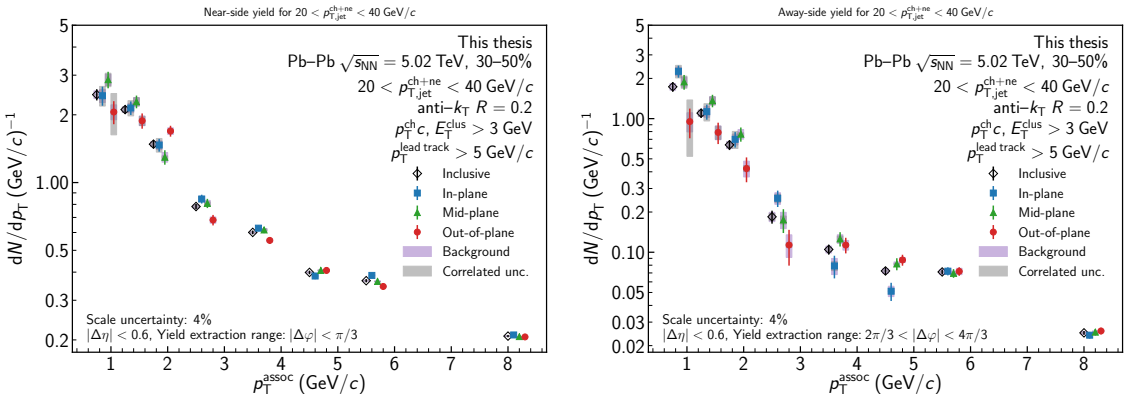

(a) Near-side associated hadron yield

(b) Away-side associated hadron yield

Figure 4.4: Near- and away-side associated hadron yields measured for jet-hadron correlations for $20 < p_{T,jet} < 40$ GeV/c and $0.5 < p_T^{assoc} < 10$ GeV/c as a function of event plane orientation in 30–50% semi-central Pb–Pb collisions at $\sqrt{s_{NN}} = 5.02$ TeV. The bars correspond to the statistical uncertainty, the purple boxes to the background uncertainty, and the gray boxes to the correlated scale uncertainty.

The yield differences, D_{RP}, as defined in Eq. 3.3, are shown in Fig. 4.5 for $Y^{out} - Y^{in}$ and in Fig. 4.6 for $Y^{mid} - Y^{in}$. On both the near- and away-sides of Fig. 4.5, the low p_T^{assoc} differences are depressed slightly below zero, but are still consistent with no difference within uncertainties. The uncertainties are smaller at high p_T^{assoc}, but the points are still consistent with no difference between the in-plane and out-of-plane yields. The $Y^{mid} - Y^{in}$ difference is also consistent with no difference over the entire $0.5 < p_T^{assoc} < 10$ GeV/c. $Y^{mid} - Y^{in}$ is consistent with zero across the entire range of p_T^{assoc} values.

Next, we consider the yield ratios defined in Eq. 3.4. The ratio cancels the correlated scale uncertainty, leaving only the background uncertainty represented by the purple boxes. The Y^{out}/Y^{in} is shown in Fig. 4.7. On the near-side, the ratios at low and high p_T^{assoc} are consistent with unity. For intermediate p_T^{assoc}, there is a hint of a suppressed

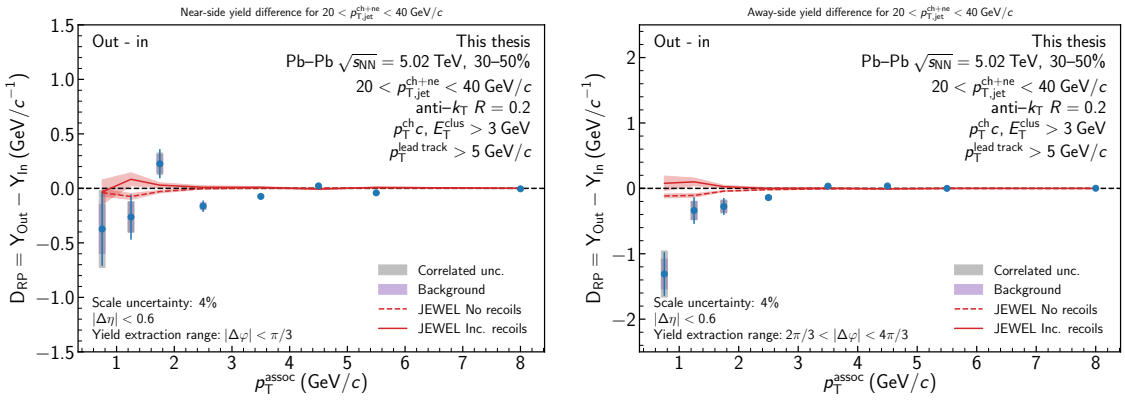

(a) Near-side yield difference (b) Away-side yield difference

Figure 4.5: Near-side and away-side associated hadron yield difference for $Y^{\text{out}} - Y^{\text{in}}$ for 30–50% semi-central Pb–Pb collisions at $\sqrt{s_{\text{NN}}} = 5.02$ TeV. The bars correspond to the statistical uncertainty, the purple boxes to the background uncertainty, and the gray boxes to the correlated scale uncertainty. JEWEL model predictions with and without recoils are shown in solid and dashed red curves, respectively, with the bands corresponding to the statistical uncertainties, and are discussed in Sec. 4.4.1.

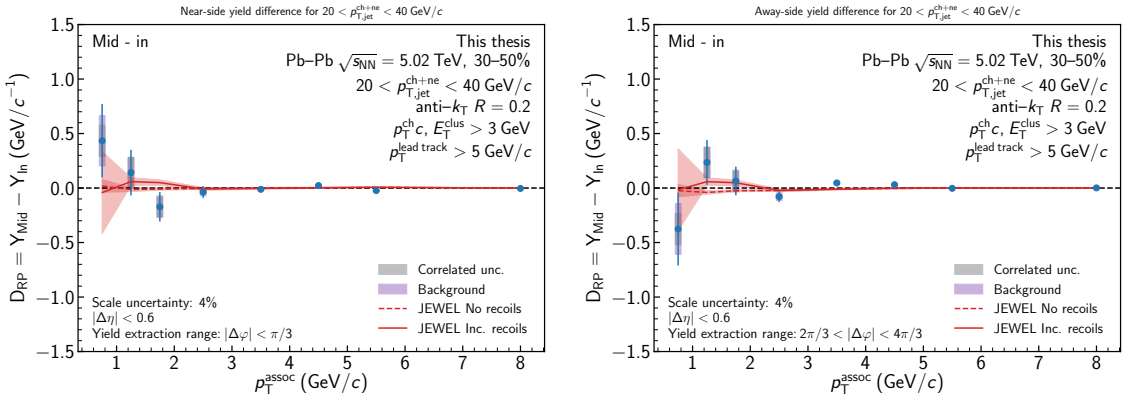

(a) Near-side yield difference (b) Away-side yield difference

Figure 4.6: Near-side and away-side associated hadron yield difference for $\mathrm{Y}^{\text{mid}} - \mathrm{Y}^{\text{in}}$ for 30–50% semi-central Pb–Pb collisions at $\sqrt{s_{\text{NN}}} = 5.02$ TeV. The bars correspond to the statistical uncertainty, the purple boxes to the background uncertainty, and the gray boxes to the correlated scale uncertainty. JEWEL model predictions with and without recoils are shown in solid and dashed red curves, respectively, with the bands corresponding to the statistical uncertainties, and are discussed in Sec. 4.4.1.

ratio, although it occurs near the constituent cut, which introduces an autocorrelation between the hadrons used to find the jet and the measured associated hadrons. In the away-side, lowest four $p_{\mathrm{T}}^{\mathrm{assoc}}$ values hint towards to a systematic depletion. At intermediate $p_{\mathrm{T}}^{\mathrm{assoc}}$, the ratios fluctuate upwards, but along with the high $p_{\mathrm{T}}^{\mathrm{assoc}}$ values, they are all consistent with unity. Fig. 4.8 displays $\mathrm{Y}^{\mathrm{mid}}/\mathrm{Y}^{\mathrm{in}}$. This plots shows similar trends to the other yield differences and ratios, with both the near- and away-side ratios consistent with unity.

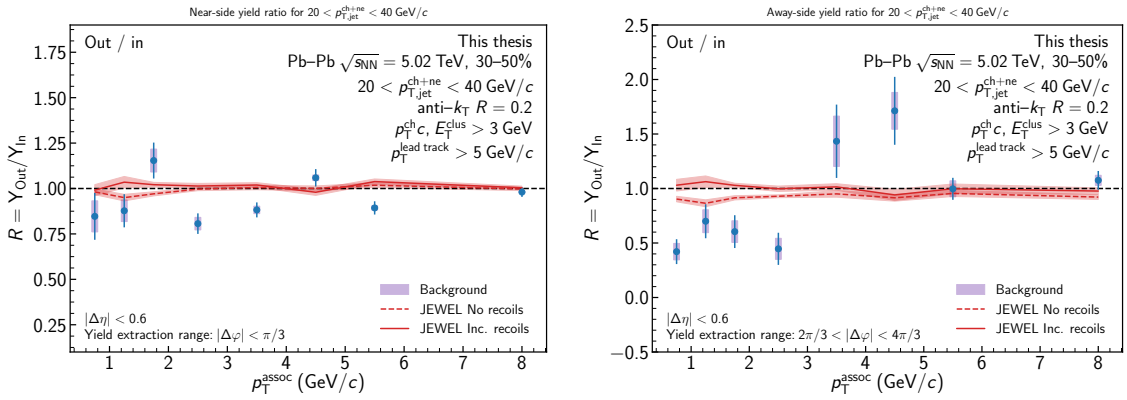

(a) Near-side yield ratio

(b) Away-side yield ratio

Figure 4.7: Near-side and away-side associated hadron yield ratio for $\mathrm{Y}^{\mathrm{out}}/\mathrm{Y}^{\mathrm{in}}$ for 30–50% semi-central Pb–Pb collisions at $\sqrt{s_{\mathrm{NN}}} = 5.02$ TeV. The bars correspond to the statistical uncertainty and the purple boxes to the background uncertainty. JEWEL model predictions with and without recoils are shown in solid and dashed red curves, respectively, with the bands corresponding to the statistical uncertainties, and are discussed in Sec. 4.4.1.

In addition to the correlation yields and derived observables, we also measured the Gaussian widths for each event plane orientation. The extracted correlation widths are displayed in Fig. 4.9. On both the near- and away-sides, the widths are consistent over the entire $p_{\mathrm{T}}^{\mathrm{assoc}}$ range. The large statistical error bars highlight the difficulty in measuring the peaks due to statistical fluctuations. These fluctuations persist even after subtracting the background.

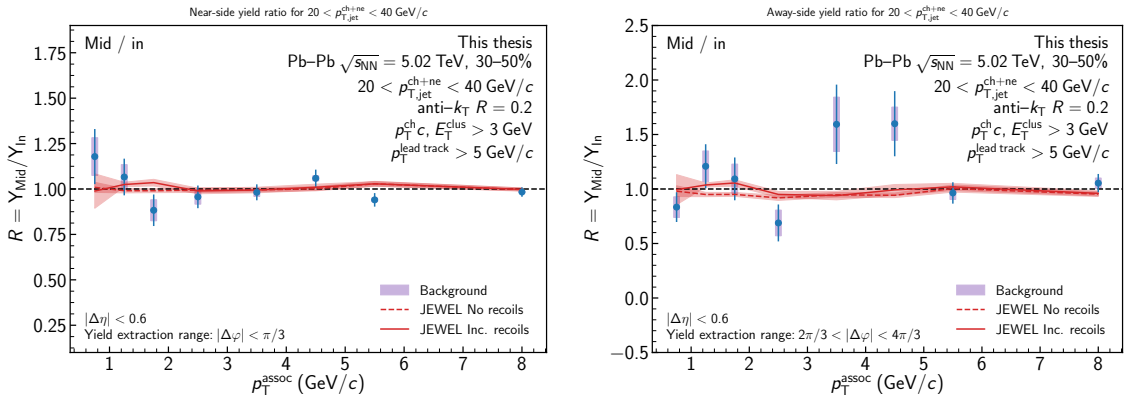

(a) Near-side yield ratio

(b) Away-side yield ratio

Figure 4.8: Near-side and away-side associated hadron yield ratio for Y^{mid}/Y^{in} for 30–50% semi-central Pb–Pb collisions at $\sqrt{s_{NN}} = 5.02$ TeV. The bars correspond to the statistical uncertainty and the purple boxes to the background uncertainty. JEWEL model predictions with and without recoils are shown in solid and dashed red curves, respectively, with the bands corresponding to the statistical uncertainties, and are discussed in Sec. 4.4.1.

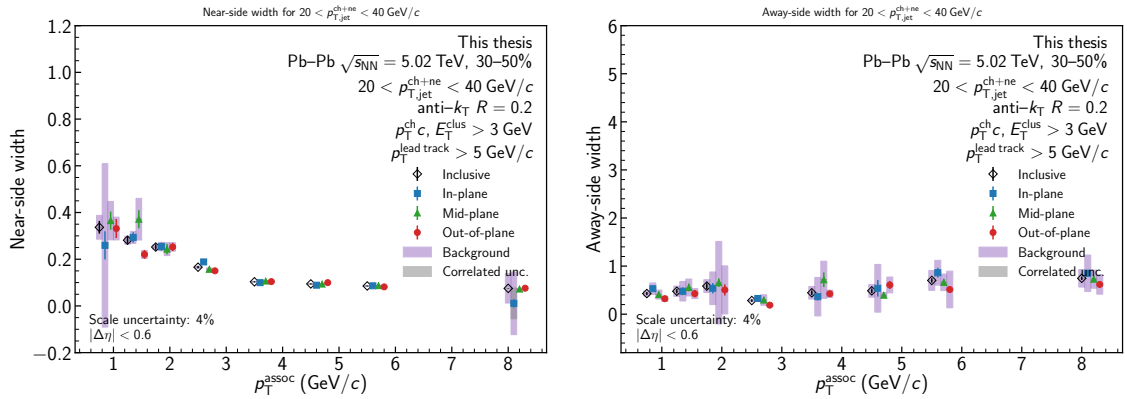

(a) Near-side correlation widths

(b) Away-side correlation widths

Figure 4.9: Near- and away-side correlation widths measured for jet-hadron correlations measured for $20 < p_{T,jet} < 40$ GeV/c and $0.5 < p_T^{assoc} < 10$ GeV/c as a function of event plane orientation in 30–50% semi-central Pb–Pb collisions at $\sqrt{s_{NN}} = 5.02$ TeV. The bars correspond to the statistical uncertainty, the purple boxes to the background uncertainty, and the gray boxes to the correlated scale uncertainty.

4.2 Jet-Hadron Correlations Measured in 0–10% Central Collisions Pb–Pb Collisions

The same observables were also measured for 0–10% central Pb–Pb collisions at $\sqrt{s_{\mathrm{NN}}} = 5.02$ TeV and are presented below. Due to strong fluctuations in the $0.5 < p_{\mathrm{T}}^{\mathrm{assoc}} < 1.0$ GeV/c, we were unable to satisfy the fit stability criteria described in Sec. 3.5. Consequently, this bin was dropped from the analysis.

The fit parameters extracted by the Reaction Plane Fit are shown in Fig. 4.10, 4.11, 4.12. For these fits, a smaller $\tilde{v_2}^{\mathrm{jet}}$ and a correspondingly larger $\tilde{v_2}^{a}$ are preferred by the minimization as compared to the reference data. However, as discussed in Sec. 3.5.2, agreement is not necessarily required or expected. With or without agreement, the RPF method will still describe the background effectively.

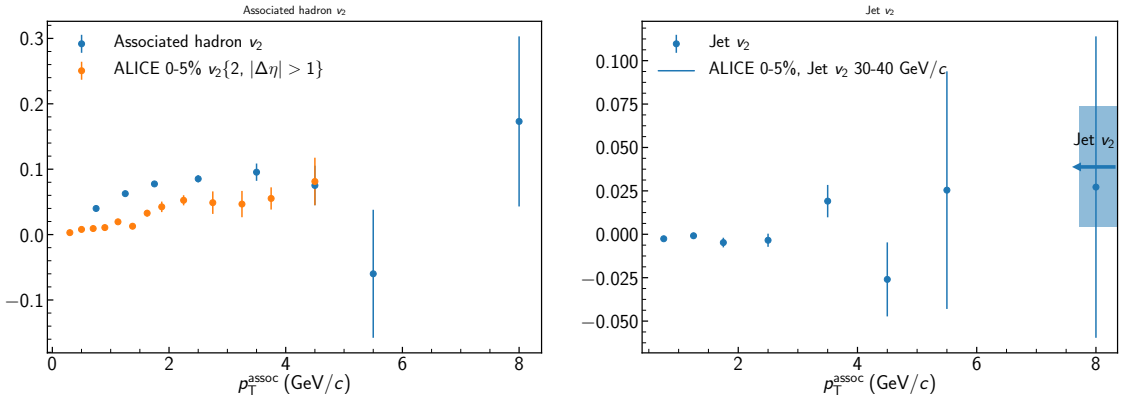

(a) $\tilde{v_2}^{a}$ (b) $v\tilde{n}C2^{\mathrm{jet}}$

Figure 4.10: $\tilde{v_2}^{a}$ and $\tilde{v_2}^{\mathrm{jet}}$ extracted via the Reaction Plane Fit for 0–10% central Pb–Pb collisions at $\sqrt{s_{\mathrm{NN}}} = 5.02$ TeV. The values are compared to ALICE reference data [78,84].

The associated hadron yields for the near- and away-side are shown in Fig. 4.13. Similar to the semi-central case, the general shape of the yields is consistent with expectations. On the near-side, the yields are compatible within uncertainties, with

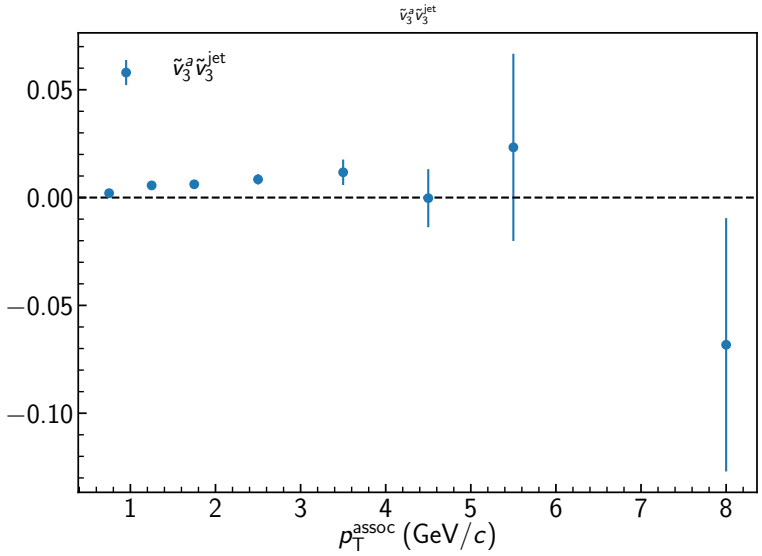

Figure 4.11: $\tilde{v_3}^a \tilde{v_3}^t$ extracted via the Reaction Plane Fit for 0–10% central Pb–Pb collisions at $\sqrt{s_{\text{NN}}} = 5.02$ TeV. The values are expected to be approximately zero.

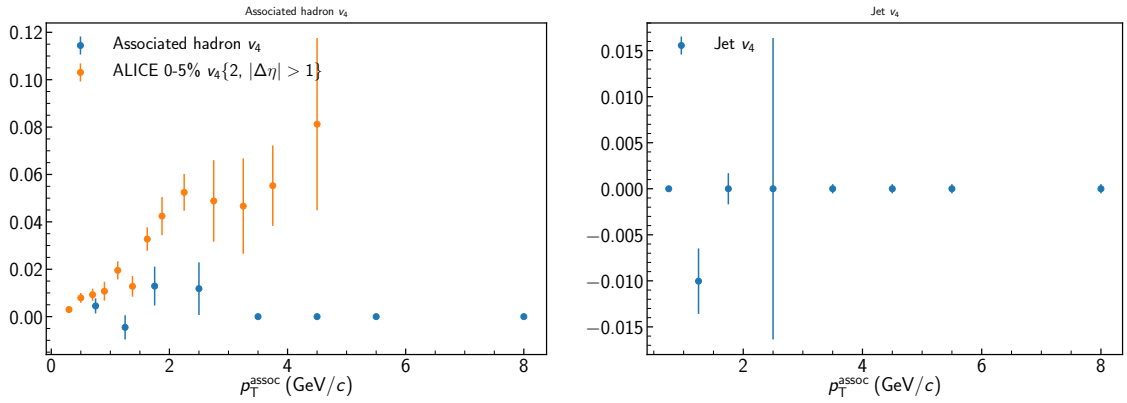

(a) $\tilde{v_4}^a$ (b) $\tilde{v_4}^{\text{jet}}$

Figure 4.12: $\tilde{v_4}^a$ and $\tilde{v_4}^{\text{jet}}$ extracted via the Reaction Plane Fit for 0–10% central Pb–Pb collisions at $\sqrt{s_{\text{NN}}} = 5.02$ TeV. The values are compared to ALICE reference data [78,84].

especially large error bars for the lowest two $p_{\mathrm{T}}^{\mathrm{assoc}}$. On the away-side, a similar trend is apparent. The especially large mid-plane errors are due to upward fluctuations in the background dominated region in that event plane orientation at low $p_{\mathrm{T}}^{\mathrm{assoc}}$. This causes the background yield to be overestimated.

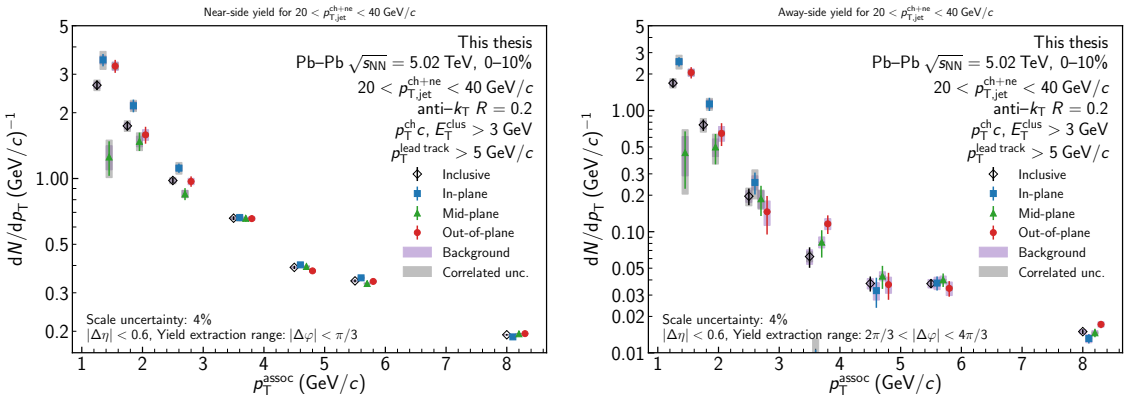

(a) Near-side associated hadron yield

(b) Away-side associated hadron yield

Figure 4.13: Near- and away-side associated hadron yields measured for jet-hadron correlations measured for $20 < p_{\mathrm{T,jet}} < 40$ GeV/c and $1.0 < p_{\mathrm{T}}^{\mathrm{assoc}} < 10$ GeV/c as a function of event plane orientation in 0–10% central Pb–Pb collisions at $\sqrt{s_{\mathrm{NN}}} = 5.02$ TeV. The bars correspond to the statistical uncertainty, the purple boxes to the background uncertainty, and the gray boxes to the correlated scale uncertainty.

The yield differences, D_{RP}, as defined in Eq. 3.3, are shown in Fig. 4.14 for $Y^{\mathrm{out}} - Y^{\mathrm{in}}$ and in Fig. 4.15 for $Y^{\mathrm{mid}} - Y^{\mathrm{in}}$. On both the near- and away-sides of Fig. 4.14, the low $p_{\mathrm{T}}^{\mathrm{assoc}}$ differences are depressed slightly below zero, but are still consistent with no event plane dependence within uncertainties. $\mathrm{Y}^{\mathrm{mid}} - \mathrm{Y}^{\mathrm{in}}$ is also consistent with no difference over the $1.5 < p_{\mathrm{T}}^{\mathrm{assoc}} < 10$ GeV/c. The lowest $p_{\mathrm{T}}^{\mathrm{assoc}}$ bin is heavily suppressed due to statistical fluctuations.

Next, we consider the yield ratios defined in Eq. 3.4. The $\mathrm{Y}^{\mathrm{out}}/\mathrm{Y}^{\mathrm{in}}$ is shown in Fig. 4.16. There is a small of a depletion at low $p_{\mathrm{T}}^{\mathrm{assoc}}$ on the near- and away-sides, with the rest of the points consistent with unity. The large uncertainty for the point in the $3.0 < p_{\mathrm{T}}^{\mathrm{assoc}} < 4.0$ GeV/c bin is due to a downward fluctuation in the away-side peak.

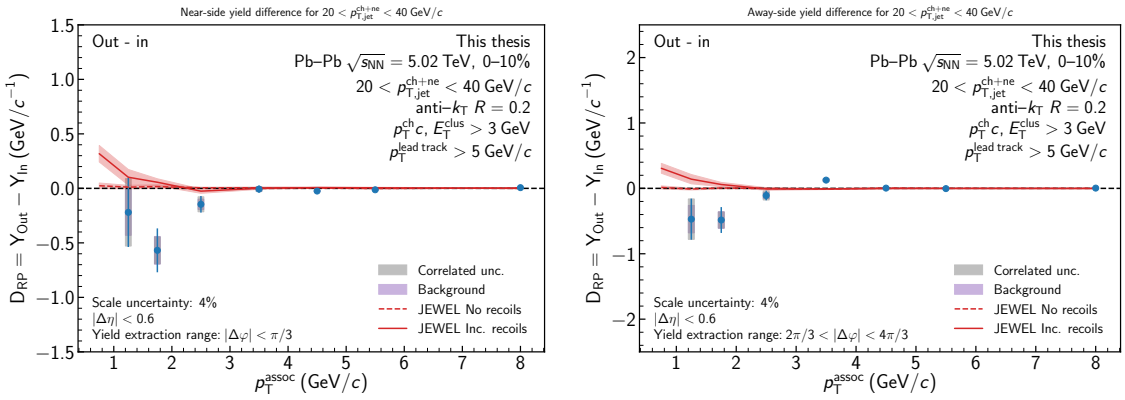

(a) Near-side yield difference

(b) Away-side yield difference

Figure 4.14: Near-side and away-side associated hadron yield difference for $Y^{\mathrm{out}} - Y^{\mathrm{in}}$ for 0–10% central Pb–Pb collisions at $\sqrt{s_{\mathrm{NN}}} = 5.02$ TeV. The bars correspond to the statistical uncertainty, the purple boxes to the background uncertainty, and the gray boxes to the correlated scale uncertainty. JEWEL model predictions with and without recoils are shown in solid and dashed red curves, respectively, with the bands corresponding to the statistical uncertainties, and are discussed in Sec. 4.4.1.

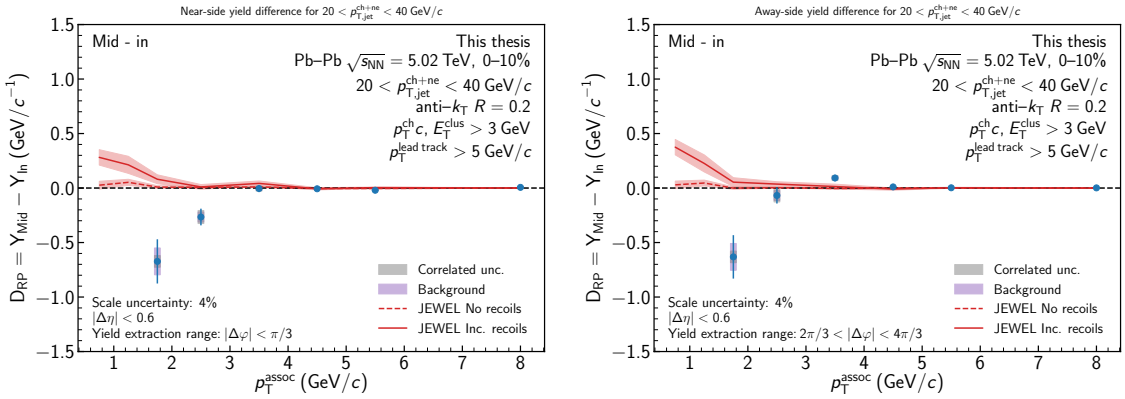

(a) Near-side yield difference

(b) Away-side yield difference

Figure 4.15: Near-side and away-side associated hadron yield difference for $\mathrm{Y}^{\mathrm{mid}} - \mathrm{Y}^{\mathrm{in}}$ for 0–10% central Pb–Pb collisions at $\sqrt{s_{\mathrm{NN}}} = 5.02$ TeV. The bars correspond to the statistical uncertainty, the purple boxes to the background uncertainty, and the gray boxes to the correlated scale uncertainty. JEWEL model predictions with and without recoils are shown in solid and dashed red curves, respectively, with the bands corresponding to the statistical uncertainties, and are discussed in Sec. 4.4.1.

Fig. 4.17 displays $\mathrm{Y}^{\mathrm{mid}}/\mathrm{Y}^{\mathrm{in}}$. There appears to be a hint of depletion at low $p_{\mathrm{T}}^{\mathrm{assoc}}$, but the lowest $p_{\mathrm{T}}^{\mathrm{assoc}}$ point appears to be heavily influenced by an upward background fluctuation distorting the fit.

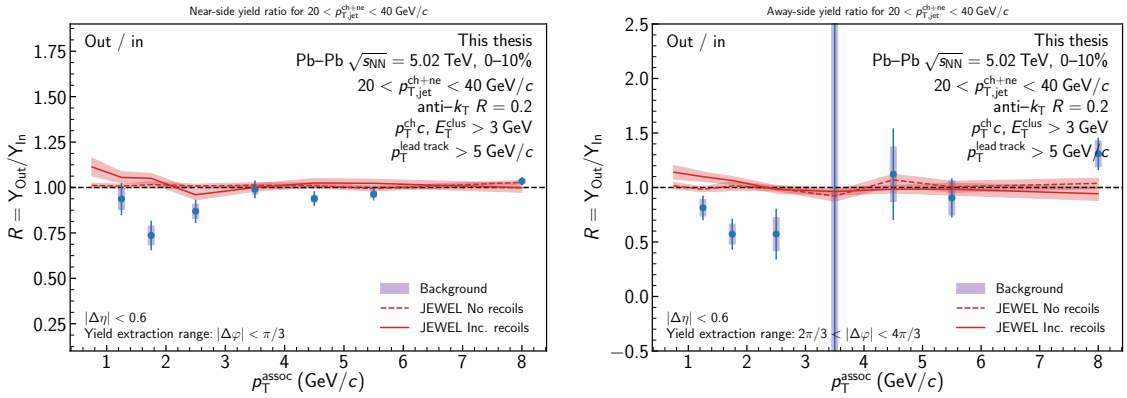

(a) Near-side yield ratio

(b) Away-side yield ratio

Figure 4.16: Near-side and away-side associated hadron yield ratio for $\mathrm{Y}^{\mathrm{out}}/\mathrm{Y}^{\mathrm{in}}$ for 0–10% central Pb–Pb collisions at $\sqrt{s_{\mathrm{NN}}} = 5.02$ TeV. The bars correspond to the statistical uncertainty and the purple boxes to the background uncertainty. JEWEL model predictions with and without recoils are shown in solid and dashed red curves, respectively, with the bands corresponding to the statistical uncertainties, and are discussed in Sec. 4.4.1.

In addition to the correlation yields and derived observables, we also measured the Gaussian widths for each event plane orientation. The extracted correlation widths are displayed in Fig. 4.18. On both the near- and away-sides, the widths are consistent over the entire $p_{\mathrm{T}}^{\mathrm{assoc}}$ range. The large statistical error bars highlight the difficulty in measuring the peaks due to statistical fluctuations. These fluctuations persist even after subtracting the background.

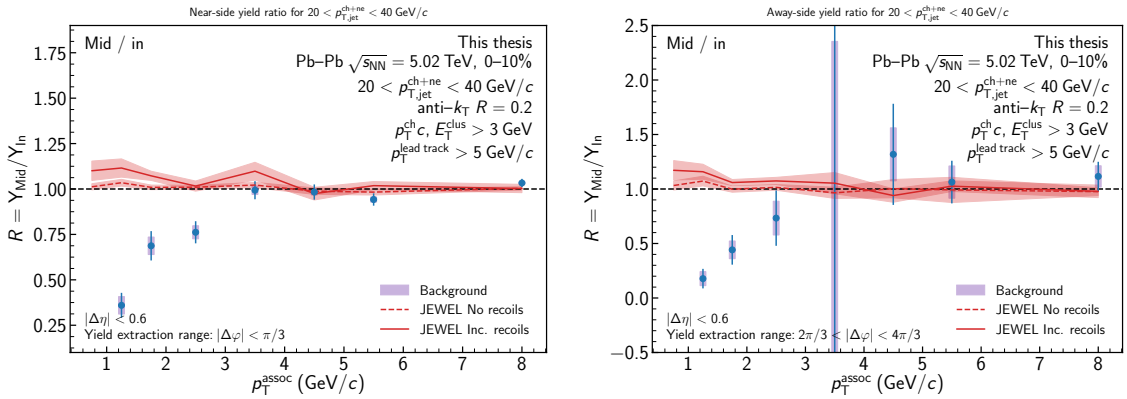

(a) Near-side yield ratio

(b) Away-side yield ratio

Figure 4.17: Near-side and away-side associated hadron yield ratio for Y^{mid}/Y^{in} for 0–10% central Pb–Pb collisions at $\sqrt{s_{NN}} = 5.02$ TeV. The bars correspond to the statistical uncertainty and the purple boxes to the background uncertainty. JEWEL model predictions with and without recoils are shown in solid and dashed red curves, respectively, with the bands corresponding to the statistical uncertainties, and are discussed in Sec. 4.4.1.

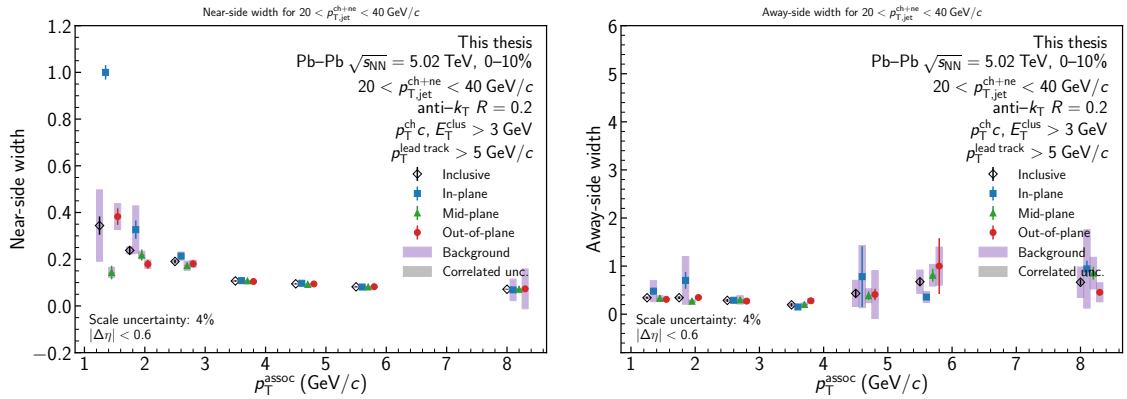

(a) Near-side correlation widths

(b) Away-side correlation widths

Figure 4.18: Near- and away-side correlation widths measured for jet-hadron correlations measured for $20 < p_{T,jet} < 40$ GeV/c and $1.0 < p_T^{assoc} < 10$ GeV/c as a function of event plane orientation in 0–10% central Pb–Pb collisions at $\sqrt{s_{NN}} = 5.02$ TeV. The bars correspond to the statistical uncertainty, the purple boxes to the background uncertainty, and the gray boxes to the correlated scale uncertainty.

4.3 Jet-Hadron Correlations Measured in 30–50% Semi-Central Pb–Pb Collisions at $\sqrt{s_{\mathrm{NN}}} = 2.76$ TeV

As mentioned at the beginning of this chapter, I also made contributions to the ALICE jet-hadron correlations measured in 30–50% semi-central Pb–Pb collisions at $\sqrt{s_{\mathrm{NN}}} = 2.76$ TeV. Both analyses share the same set of observables, although the dataset collected at $\sqrt{s_{\mathrm{NN}}} = 2.76$ TeV is smaller than the 5.02 TeV dataset by a factor of 5-10. Nearly all of the analysis parameters were shared between the two studies, with the exception that a 6 GeV cluster bias was applied to the 2.76 TeV analysis instead of a 5 GeV/c track bias.

The associated hadron yield differences are shown in Fig. 4.19. At low $p_{\mathrm{T}}^{\mathrm{assoc}}$, the differences fluctuate from high to low, all while staying consistent with zero. At high $p_{\mathrm{T}}^{\mathrm{assoc}}$, the background and the uncertainties decreases, but the points remain consistent with zero. The yield differences are consistent with those measured at 5.02 TeV.

The associated hadron yield ratios are displayed in Fig. 4.20. At low $p_{\mathrm{T}}^{\mathrm{assoc}}$, the ratios fluctuate around one, but remain consistent due to the large statistical uncertainties. The high $p_{\mathrm{T}}^{\mathrm{assoc}}$ ratios have smaller uncertainties, but are still consistent with unity.

The particle level spectra were also measured for the $\sqrt{s_{\mathrm{NN}}} = 2.76$ TeV analysis. The input was simulated with PYTHIA 6 [8], Tune A [93]. The particle and detector level jets were required to pass the jet constituent cuts. The particle level spectra derived from the response matrix are show in Fig. 4.21. Similar to the $\sqrt{s_{\mathrm{NN}}} = 5.02$ TeV data, the spectra are consistent within uncertainties. The larger uncertainties at small $p_{\mathrm{T,jet}}^{\mathrm{part}}$ are due to the relative scarcity of low $p_{\mathrm{T}}^{\mathrm{hard}}$ jets which overlap with Pb–Pb jets. The

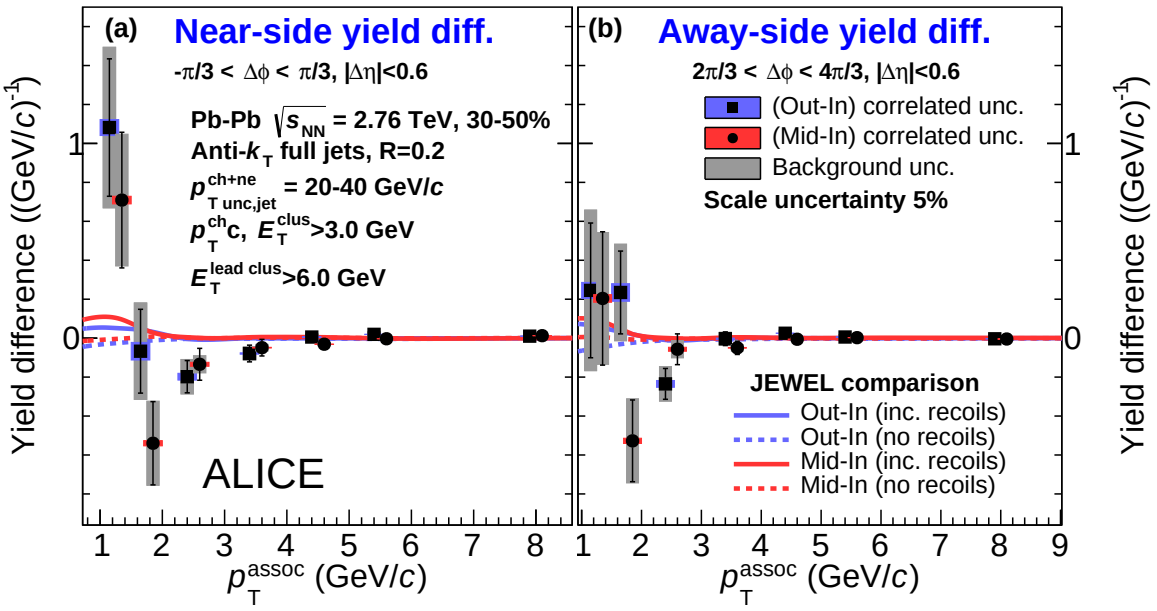

Figure 4.19: Near-side and away-side associated hadron yield difference for $Y^{out} - Y^{in}$ and $Y^{mid} - Y^{in}$ for 30–50% semi-central Pb–Pb collisions at $\sqrt{s_{NN}} = 2.76$ TeV. The bars correspond to the statistical uncertainty, the gray boxes to the background uncertainty, and the colored boxes correspond to the correlated scale uncertainty. JEWEL model predictions with and without recoils are shown in red and blues curves.

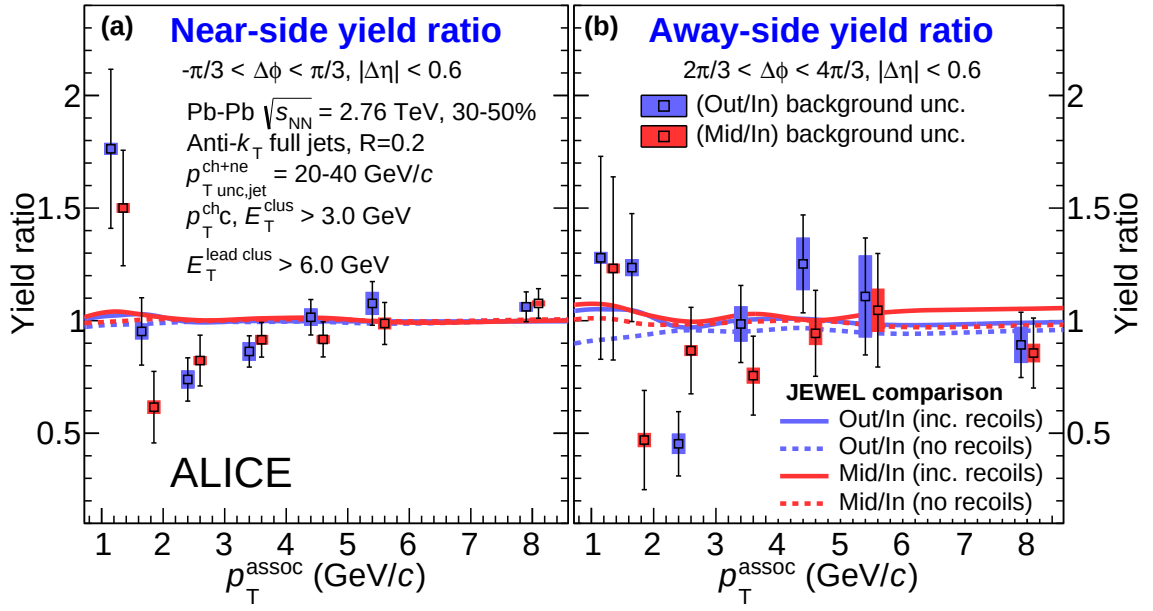

Figure 4.20: Near-side and away-side associated hadron yield ratio for Y^{out}/Y^{in} and Y^{mid}/Y^{in} for 30–50% semi-central Pb–Pb collisions at $\sqrt{s_{NN}} = 2.76$ TeV. The bars correspond to the statistical uncertainty and the gray boxes to the background uncertainty. JEWEL model predictions with and without recoils are shown in red and blue curves.

5.02 $p_{\mathrm{T}}^{\mathrm{hard}}$ data is more finely binned than in the 2.76 data, which leads to smaller uncertainties in this region.

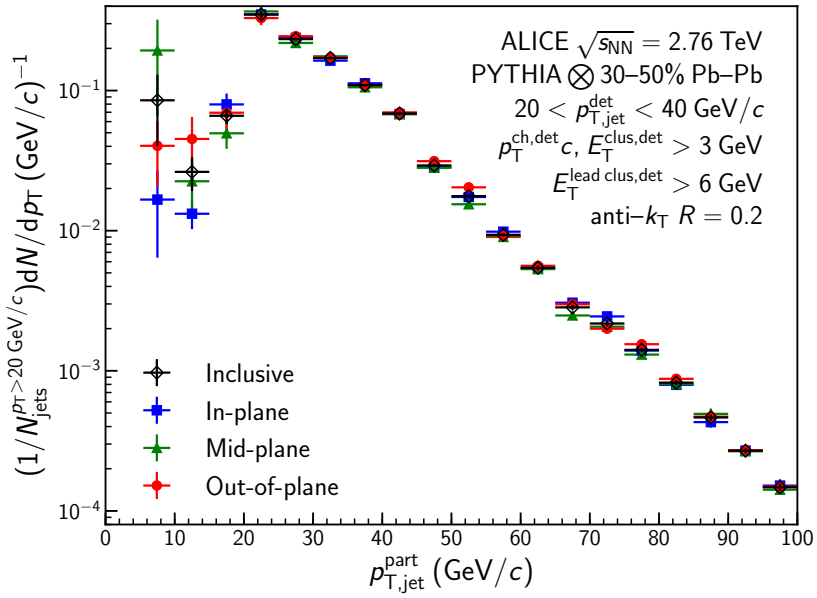

Figure 4.21: Particle level spectra for 30–50% semi-central collisions at $\sqrt{s_{\mathrm{NN}}} = 2.76$ TeV.

4.4 Comparisons

4.4.1 Theoretical Expectations

To put a measurement in proper context and to use the measurement to make physics conclusions, theoretical predictions are needed. In particular, toy models can be useful to predict qualitative effects and give a sense of the order of magnitude of an expected signal. More comprehensive models can provide quantitative predictions that can be compared to experimental measurements to further constrain physical effects. For this jet-hadron measurement, both qualitative and quantitative predictions have been created, and are explained in detail below.

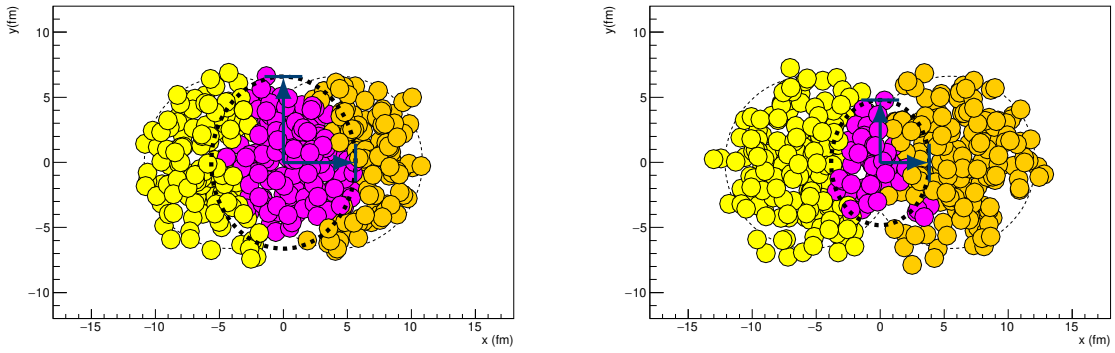

(a) $b = 8.5$ fm (b) $b = 11$ fm

Figure 4.22: Sample of Pb–Pb collisions via the Glauber MC for a selection of impact parameters. The two colliding nuclei are shown as dashed circles, with the participating nucleons in magenta and the spectator nucleons in yellow and orange, corresponding to spectators from nuclei A and B, respectively. The max x and y values for the illustrated collision are indicated by the blue perpendicular lines at the end of the arrows. The ellipse created using those maximum length parameters is shown in the black dotted curve.

A simple estimate of the difference in event plane dependent yield can be constructed via the Glauber Model [21–23], as described in Sec. 1.4.1. For each event, the model is used to determine the participant nucleons in each interacting nuclei. Example simulations for impact parameters of 8.5 and 11 fm (corresponding approximately to centrality of 30% and 50%, respectively) are shown in Fig. 4.22. The position of the participants are defined with respect to the reaction plane, with the x axis corresponding to the in-plane orientation, and the y axis corresponding to the out-of-plane orientation. Event-by-event fluctuations in the participant positions have a clear impact on the precise event shape. As the lowest order estimate of the maximum yield difference expected due to path length dependence, we assume a linear energy loss and an approximately elliptical collision region. The path length, which will be proportional to the yield, can be estimated event-by-event as the maximum position of the participants in the positive direction of each axis. The expected yield ratio can be then constructed event-by-event as $r = x_{\mathrm{max}}/y_{\mathrm{max}}$. Note that $1/r$ corresponds to

Y^{out}/Y^{in} yield because a shorter path length corresponds to less energy loss, which will be measured as a larger yield. Although the eccentricity can also be calculated event-by-event as described in [94,95], the eccentricity used in this field is typically defined using the RMS widths of the positions of the participants, and therefore is not directly related to the geometric eccentricity [94]. Thus, r is utilized to provide more direct access to the collision path lengths.

Table 4.1: Parameters used for generating collisions with the Glauber MC at $\sqrt{s_{\mathrm{NN}}} = 5.02$ TeV [95]. Note that the corresponding N_{coll} and N_{part} values agree with ALICE calculated values described in [96].

Center-of-momentum energy (TeV)	Cross section (mb)	Centrality (%)	Impact parameter (fm)
5.02	67.6 ± 0.6	0 – 10	0 – 4.92
5.02	67.6 ± 0.6	30 – 50	8.5 – 11

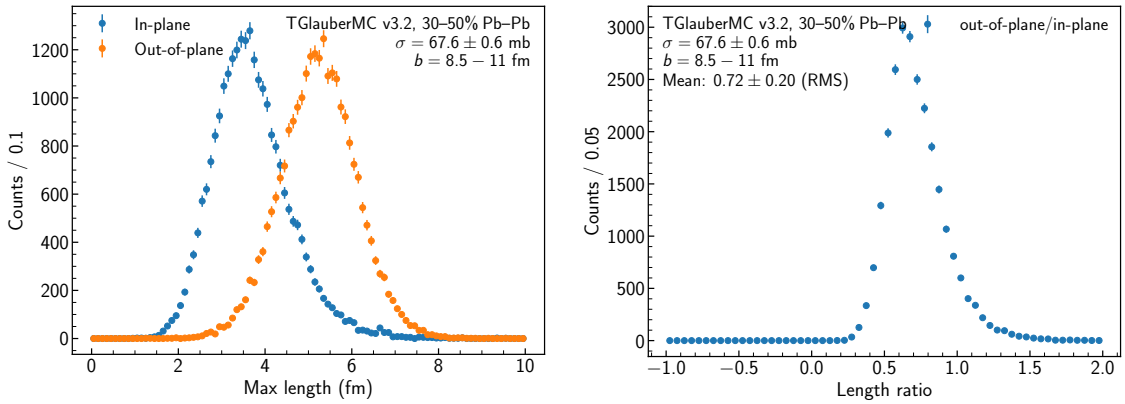

(a) The maximum participant location in-plane and out-of-plane measured with respect to the reaction plane in the MC Glauber toy model.

(b) The ratio of in-plane/out-of-plane maximum location, which corresponds to the out-of-plane/in-plane yield ratio.

Figure 4.23: Maximum participant location and length ratio for 30-50% Pb–Pb collisions at $\sqrt{s_{\mathrm{NN}}} = 5.02$ TeV.

The `TGlauberMC v3.2` [95] Monte Carlo was used to generate 250000 interactions of both central and semi-central Pb–Pb collisions at 5.02 TeV. The parameters used for

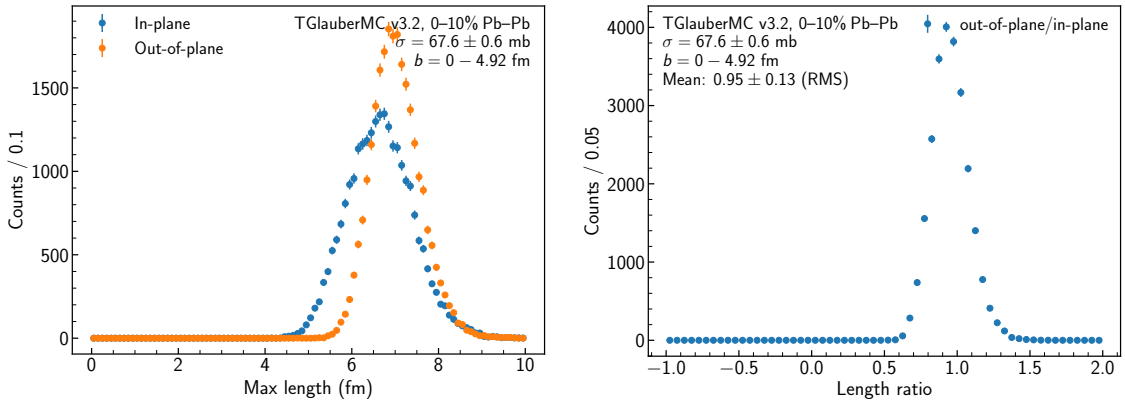

(a) The maximum participant location in-plane and out-of-plane measured with respect to the reaction plane in the MC Glauber toy model.

(b) The ratio of in-plane/out-of-plane maximum location, which corresponds to the out-of-plane/in-plane yield ratio.

Figure 4.24: Maximum participant location and length ratio for 0-10% Pb–Pb collisions at $\sqrt{s_{\mathrm{NN}}} = 5.02$ TeV.

the simulation are described in Table 4.1. Note that these parameters agree with ALICE estimates for N_{coll} and N_{part} described in [96]. The distribution of maximum in-plane and out-of-plane path lengths for 30-50% Pb–Pb collisions at $\sqrt{s_{\mathrm{NN}}} = 5.02$ TeV are show in Fig. 4.23a. The corresponding ratio r is illustrated in Fig. 4.23b. The mean and RMS of the ratio are extracted to be 0.72 and 0.20 respectively, as shown in Table 4.2. The corresponding length distributions and ratios for central collisions are shown in Fig. 4.24a and Fig. 4.24b, respectively, and the extracted ratio is listed in Table 4.2. As expected from geometrical arguments, central collisions are substantially less elliptical than semi-central collisions. Although this simple toy model neglects most of the relevant physics of energy loss in the quark gluon plasma, it allows for zeroth order estimation of the maximum expected yield ratio effect, which is $\sim 30\%$ in semi-central collisions, and $\sim 5\%$ in central collisions.

Table 4.2: Extracted path length ratio and RMS for central and semi-central collisions at $\sqrt{s_{\mathrm{NN}}} = 5.02$ TeV extracted from the Glauber toy model.

Centrality (%)	Path length ratio	Path length ratio RMS
0–10	0.95	0.13
30–50	0.72	0.20

The Glauber toy model approach corresponds to the collision geometry seen for low p_{T} particle production, and is related to the momentum-space anisotropy that produces low p_{T} v_n components. At high p_{T}, path length dependent energy loss can also generate a similar v_2 signal. Although it is anticipated that the corresponding difference in the yields should correlate with the path length determined by the collision geometry if path length dependent energy loss dominates, it is instructive to verify the consistency of these different measurements. In particular, this can be checked via the measurement of jet v_2. In this measurement, the azimuthal distribution of single inclusive jets is measured, and then the distribution is fit according to $\mathrm{d}N/\mathrm{d}\Delta\varphi \propto 1 + 2v_2 \cos 2\Delta\varphi$. These measurements have been performed by the ALICE collaboration for $R = 0.2$ charged jets [84], as well as by the ATLAS collaboration for $R = 0.2$ calorimeter jets [85]. The measurements were made for central and semi-central collisions as seen in Fig. 4.25. Despite the differences in a number of analysis details, the ALICE and ATLAS results are consistent with each other. The charged hadron v_2 cannot be directly compared, but qualitatively agrees. The ATLAS measurement shows statistically significant $v_2 > 0$ for all centrality bins from 5–60% for $p_{\mathrm{T,jet}} < 160$ GeV/c. In contrast, due to the large statistical and systematic uncertainties in the ALICE measurement, only the semi-central measurement was found to be significantly greater than 0. ALICE also showed that JEWEL is consistent with the jet v_2 in 30–50% semi-central collisions, but it appears to systematically underpredict the data in 0–5%

central collisions.

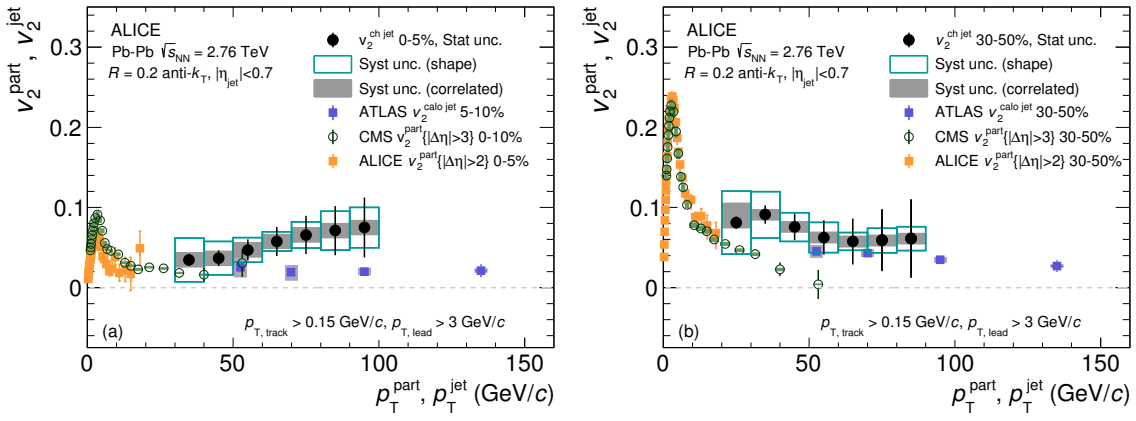

(a) Central collisions. (b) Semi-central collisions.

Figure 4.25: Jet and charged hadron v_2 measured in Pb–Pb collisions at $\sqrt{s_{\mathrm{NN}}} = 2.76$ TeV for central and semi-central collisions. All measurements are consistent within uncertainties.

In addition to the jet v_2 measurement, ATLAS also extracted a ratio, $f_{\mathrm{corr}}^2 = 1 - Y_{\mathrm{out}}/Y_{\mathrm{in}}$, which is extremely similar to the path length ratio described above. The measurement is illustrated in Fig. 4.26. For $45 < p_{\mathrm{T,jet}} < 60$ GeV/c, they found $f_{\mathrm{corr}}^2 \sim 10 - 20\%$, with the value linearly decreasing with centrality. Extracting the path length ratio with the ALICE data yields similar estimates.

Table 4.3: Mean path length for jets propagating through the medium in JEWEL with respect to the reaction plane orientation for Pb–Pb collisions at $\sqrt{s_{\mathrm{NN}}} = 2.76$ TeV. The path lengths are not expected to vary significantly at $\sqrt{s_{\mathrm{NN}}} = 5.02$ TeV. Data provided by [97].

Centrality (%)	In-plane (fm)	Mid-plane (fm)	Out-of-plane (fm)	In / out	Mid / out
0–10	6.1	6.2	6.4	0.95	0.97
30–50	3.5	3.8	4.5	0.78	0.85

For a more sophisticated estimate of the yield ratio, the path length dependence

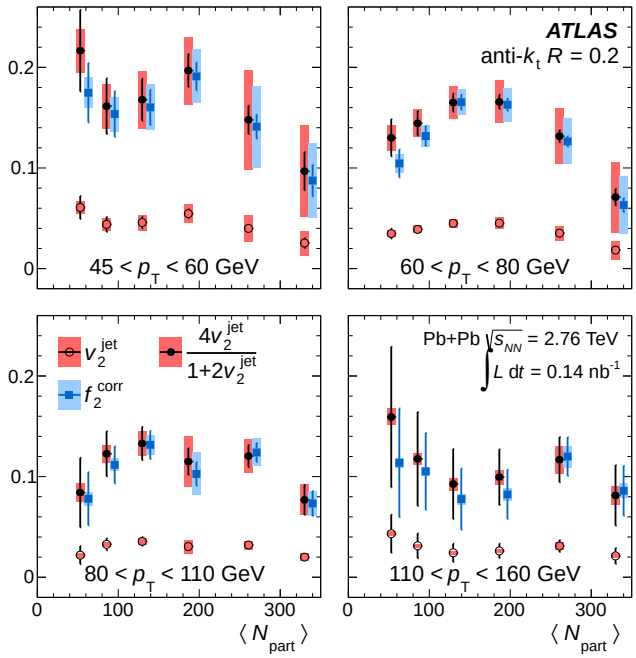

Figure 4.26: The ATLAS jet yield ratio, f_2^{corr}, and jet v_2 measured in Pb–Pb collisions at $\sqrt{s_{\mathrm{NN}}} = 2.76$ TeV as a function of $p_{\mathrm{T,jet}}$ and number of participants. $4v_2^{\mathrm{jet}}/(1+2v_2^{\mathrm{jet}})$ corresponds to the case where f_2^{corr} is described by a pure $\cos 2\Delta\varphi$ modulation. The full details of the measurement are described in [85].

within particular reaction plane orientations was measured in the JEWEL Monte Carlo generator[42], which is described in Sec. 1.6. The medium density and location of the hard scattering is sampled from a participant density derived from the Glauber model. The medium energy density and lifetime are then determined by the participant density and the initial temperature.

To generate events with JEWEL, a centrality range and initial temperature must be selected. A Glauber model is used to generate an impact parameter distribution for the given centrality range. This distribution is in approximate agreement with the ranges specified in Table 4.1. For Pb–Pb collisions at $\sqrt{s_{\mathrm{NN}}} = 5.02$ TeV, an initial temperature of 500 MeV/k_{B} was utilized. The hard scattering location is selected according to the participant density, and then the jet is propagated in a random direction with respect to the reaction plane. The average path lengths[1] and path

1. Provided courtesy of Dr. Kirill Lapidus (CERN)

length ratios are shown in Table 4.3 [97]. For semi-central collisions, the path length ratio of in-plane/out-of-plane indicates a possible signal of $\sim 20\%$ in the yield ratio, while for central collisions, an effect on the order of 5% is expected. These values are qualitatively consistent with the Glauber toy model and ATLAS jet v_2 estimates. Note that these deviations from unity in the yield ratio would be seen as a enhancement at low $p_{\mathrm{T}}^{\mathrm{assoc}}$, but the yield ratios shown in Sec. 4.1, 4.2 are predominately consistent with no deviation, with a few hints of depletion at low $p_{\mathrm{T}}^{\mathrm{assoc}}$, such as in Fig. 4.7.

In order to provide quantitative comparisons, a full set of JEWEL simulations for central and semi-central collisions was generated[2] [98]. The initial temperature was again set to 530 MeV/k_{B}. To measure jet-hadron correlations, the particle level $p_{\mathrm{T,jet}}$ is folded bin-by-bin with the response matrix described in Sec. 3.3.1, providing weights which are used to store the correlation in each $p_{\mathrm{T,jet}}^{\mathrm{det}}$ bin. Note that the error bands include statistical and systematic uncertainties added in quadrature.

4.4.2 Previous measurements

Due to the existing and upcoming jet-hadron measurements performed at STAR made at the same $p_{\mathrm{T,jet}}^{\mathrm{det}}$ range with approximately the same analysis selections, it is instructive to compare the corresponding particle level spectra. To compare to STAR, PYTHIA 6 using the Perugia 2012 tune [99] was used to produce a jet spectra for pp collisions at $\sqrt{s_{\mathrm{NN}}} = 200$ GeV.[3] Perugia 2012 was selected because it reproduces a variety of STAR measurements in pp collisions, and therefore is frequently used by STAR for comparisons to new measurements. Au–Au detector conditions are applied

2. Provided courtesy of Michael Oliver (Yale)

3. The spectra was produced using the `jet_hadron.event_gen.jet_analysis` module, and the response matrix and comparison was produced using the `jet_hadron.analysis.star_response_matrix` module.

to generated particles before jet finding by:

- Applying the single particle tracking efficiency from the Run 14 Au–Au data taking [100].
- Smearing the particle momentum according to $\sigma_{p_{\mathrm{T,jet}}}/p_{\mathrm{T,jet}} = (0.5 + 0.25 * p_{\mathrm{T,jet}})$. [100].

This new collection of particles approximates detector level particles. Jets are found using the anti-k_{T} algorithm with $R = 0.4$. The STAR "hard core jet" selection is applied, requiring that all jet constituents are greater than 2 GeV/c, as well as a leading track requirement of 4 GeV/c. In order to match the ALICE analysis, the particle level jet constituents are also required to be greater than 2 GeV/c. After the jets are found, they are matched geometrically with the requirement that they be within $0.6 = 1.5 * R$. An additional momentum fraction requirement is not necessary because there is no flow background like in the embedding. The matched jets are then used to construct a response matrix, and a particle level spectrum is extracted as described in Sec. 3.3.2.

The comparison between particle level spectra for STAR and ALICE at $\sqrt{s_{\mathrm{NN}}} = 2.76$ and 5.02 TeV is shown in Fig. 4.27. All plotted spectra are for the inclusive event plane orientation. The STAR spectrum peaks strongly at the lower end of the $p_{\mathrm{T,jet}}^{\mathrm{det}}$ range and decreases rapidly with $p_{\mathrm{T,jet}}^{\mathrm{part}}$. By $p_{\mathrm{T,jet}}^{\mathrm{part}} = 40$ GeV/c, the STAR spectrum is already an order of magnitude lower than the ALICE spectra. The ALICE 5.02 TeV data are slightly harder than the 2.76 data, as is expected due to the difference in $\sqrt{s_{\mathrm{NN}}}$. The ALICE spectra are higher than the STAR spectra at low $p_{\mathrm{T,jet}}$ due to overlapping jets that are present in the ALICE embedding, but not in the STAR detector effects.

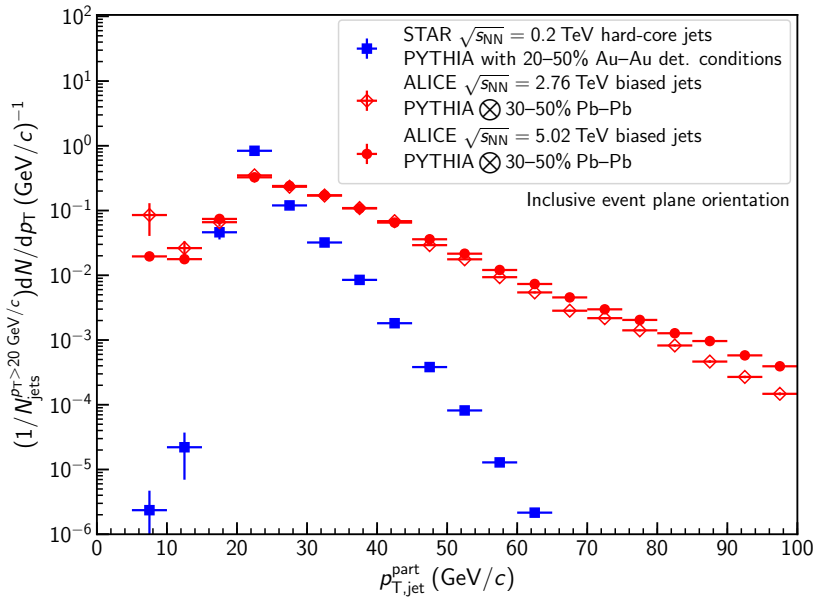

Figure 4.27: Particle level spectra measured in the STAR and ALICE jet-hadron measurements. Each spectrum represents a biased selection of jets as used in each measurement and as described in the text.

4.5 Discussion and Outlook

Broadly speaking, most $p_{\mathrm{T}}^{\mathrm{assoc}}$ bins for the correlation widths, yield differences, and yields ratios are consistent with no event plane dependence on both the near- and away-sides. Although this is partially a function of the statistical limitations of the measurement, the values also seem to favor a relatively small event plane dependence. The JEWEL predictions also support the conclusion that any event plane dependent effects are limited to $\approx 10\%$ or less. It should also be noted that the consistency with no event plane dependence is still compatible with a non-zero v_2^{jet}, as indicated by the non-zero $\tilde{v_2}^{\mathrm{jet}}$ values extracted in 30–50% semi-central collisions from the Reaction Plane Fit. The JEWEL predictions are also consistent with this picture, as they predict $v_2^{\mathrm{jet}} \approx 0.04$. The yield differences and ratios are consistent for the $\sqrt{s_{\mathrm{NN}}} = 5.02$ and 2.76 TeV measurements.

However, there are a few exceptions to this broad conclusion. At low $p_{\mathrm{T}}^{\mathrm{assoc}}$, there are a few hints of event plane dependence, especially for $p_{\mathrm{T}}^{\mathrm{assoc}} < 3$ GeV/c in the away-side $\mathrm{Y}^{\mathrm{out}}/\mathrm{Y}^{\mathrm{in}}$ measured in 30–50% semi-central collisions. $\mathrm{Y}^{\mathrm{mid}}/\mathrm{Y}^{\mathrm{in}}$ in 0–10% also hints at a depletion at low $p_{\mathrm{T}}^{\mathrm{assoc}}$, but upon close inspection of the correlation functions which are available in Sec. D, it appears that downward fluctuations in the mid-plane bin are suppressing this yield.

If these hints are indicative of event plane dependent energy loss, what does it suggest about path length dependent energy loss? The yield ratio may be influenced by a variety of physical effects. A simplified picture of jet energy loss as presented in the toy model would suggest that medium induced gluon emission would increase $\mathrm{Y}^{\mathrm{out}}/\mathrm{Y}^{\mathrm{in}}$ at low $p_{\mathrm{T}}^{\mathrm{assoc}}$ and then deplete it at high $p_{\mathrm{T}}^{\mathrm{assoc}}$ as hard jet constituents radiate softer gluons that are measured at low $p_{\mathrm{T}}^{\mathrm{assoc}}$. However, another possibility is that medium induced radiation equilibrates with the medium. In this case, radiation from the jet becomes so soft through interactions with the medium that it would becoming indistinguishable from it. In such a scenario, a depletion of $\mathrm{Y}^{\mathrm{out}}/\mathrm{Y}^{\mathrm{in}}$ at low $p_{\mathrm{T}}^{\mathrm{assoc}}$ would be expected. The competition between the soft gluon radiation and medium equilibration of the radiation may offset each other to appear as if there is no event plane dependence.

There are many promising approaches to attempt to disentangle any possible event plane dependence. The simplest step would be to increase the number of event plane bins used for the measurement, thereby providing a more differential measurement, and perhaps reveal some event plane dependence that is washed out of with the relatively broad bins. Although statistical fluctuations made the interpretation of these results more difficult, there may already be enough statistics for finer binning in the 2015 dataset. ALICE also collected more Pb–Pb data at $\sqrt{s_{\mathrm{NN}}} = 5.02$ TeV in 2018, dramatically increasing the number of the jets. Unfolding for the event plane

resolution is another possibility which may help if the event plane dependence is being washed out. However, the interaction between the unfolding and the Reaction Plane Fit requires further study. Additional studies of the signal RPF method may also facilitate its use, which may reduce the uncertainties on the yield differences and ratios.

Alternatively, it may be that fluctuations of the initial geometry within the centrality bins are dominating over any possible event plane dependence [101,102]. This possibility could be investigated via event shape engineering by selecting on low and high ellipticity events as determined by the q_n flow vector within a selected centrality range.

Appendix A

ALICE Overwatch

In addition to my dissertation analysis, I also focused on improving the quality assurance process within ALICE through the founding and completion of the ALICE Overwatch project, as I described in the proceedings published in [103] and largely reproduced below. In particular, given the high particle-multiplicity physics environment, large data rates, and complexity of the detectors, effective data-quality monitoring is an integral part of recording useful physics data. For the ALICE collaboration, this important task has been successfully addressed during LHC Run 1 and 2 by the data-quality monitoring (DQM) system known as AMORE [104].

Despite the success of AMORE, there were still remaining open questions related to data-quality monitoring within ALICE, particularly with regard to the increased data rates in LHC Run 3 and beyond due to the continuous readout of the ALICE apparatus. In order to address these questions, we leveraged the ALICE High Level Trigger (HLT) [105,106], which provided substantial additional processing power beyond that available in AMORE. There were two main questions that had to be investigated in order to determine the usefulness of an HLT-based online monitoring system. First, what

novel data-quality monitoring capabilities could be implemented during Run 2 by taking advantage of this additional processing power? Second, looking further forward, ALICE is planning major upgrades for Run 3, which include a substantial software project known as O^2 [107] – since the current HLT operates in a similar manner as O^2, what experiences related to operating a quality assurance (QA) system in such an environment could be developed while still in Run 2?

In an effort to address these questions, I co-founded the ALICE Overwatch project[1][108] in November 2015 to monitor and visualize the QA information provided by the ALICE HLT. The project handles all steps from receiving the initial data to displaying enhanced visualizations of processed data through a web application. To further enhance the utility of this project for different users, a plugin system allows for ALICE detectors to customize processing, trending, and visualizing the data.

In comparison to the existing DQM system, Overwatch provides complementary functionality, with a focus on providing information most useful to expert level users. By taking advantage of the preprocessed and time-stamped nature of the HLT data, Overwatch is able to provide certain unique capabilities within ALICE. In particular, the data received by Overwatch has already been highly preprocessed by the HLT, such that the data rate is substantially reduced compared to the raw ALICE data rate. Overwatch stores $\sim$ 350+ GB/year, with the volume increasing with each year of data taking. Given this manageable volume of data, Overwatch is able to store it persistently. The time-stamping of the data enables unique exploration of the evolution of data quality within a particular run, fill, or longer time period. Moreover, such time-series data could be useful for training machine learning models for automated QA monitoring.

1. **O**nline **V**isualization of **E**merging t**R**ends and **W**eb **A**ccessible de**T**ector **C**onditions using the **H**LT

A.1 Overwatch Architecture and Capabilities

The Overwatch architecture illustrating the workflow from data collected in ALICE to final visualization in the Overwatch web application is shown in Fig. A.1. The entire process starts when particles are detected and recorded by the ALICE apparatus. Every recorded event is sent to the HLT. Within the HLT, the data are reconstructed and compressed, and the output is stored, as well as provided for further processing and analysis. Of particular significance to Overwatch are the detector specific QA components which are distributed throughout the HLT and run in parallel to process the reconstructed data and extract information relevant for each detector. Each distributed component is provided a subset of the reconstructed data, and the output is sent to a group of centralized mergers per detector via the ZeroMQ (ZMQ) messaging library [109]. The QA component outputs are merged and are made available for further processing via ZMQ. The model for data flow from the QA components through the output of the data mergers is compatible with that of O^2.

The Overwatch receiver component is written in C++ [110] and makes requests for data to the HLT data mergers approximately every minute. However, the round-robin nature of how the data are distributed to the QA components means that the time resolution is on the order of a few minutes, with a strong dependence on the properties and processing rate of a particular component [105]. The messages provided via ZMQ consist of metadata, as well as collections of ROOT-based objects. `TH1`-derived histograms are the primary type of data received, although other more complicated objects, such as `TObjArray`, are also utilized. Each request contains cumulative data, such that the difference between the objects in the currently received message and the previous message corresponds to the data that was collected in the time between the requests. Objects are only reset at the beginning of each run, which typically last on the order of several hours. In 2015, the Electromagnetic Calorimeter (EMCal) implemented

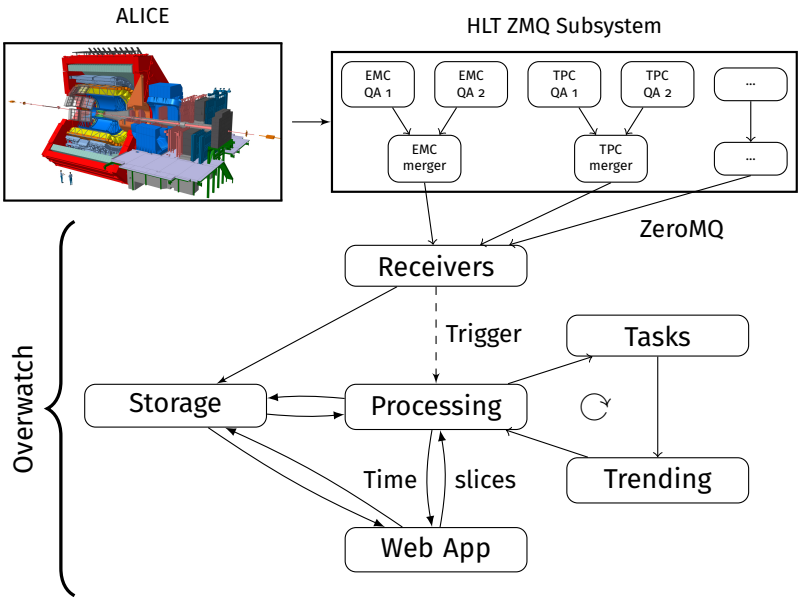

Figure A.1: The Overwatch architecture, illustrating the data flow from collection in the ALICE apparatus through visualization in the Overwatch web application. Data flows along the arrows in the diagram. The HLT ZMQ subsystem, which shows contributions from the ALICE EMC and TPC detectors, represents only a small portion of the High Level Trigger. The processing tasks and trending are performed for each input object (such as a histogram) within the received data, as represented by the circular arrow.

a QA component, while the Time Projection Chamber (TPC) added a QA component in 2016. The HLT itself also provides some QA information generated during the data reconstruction. As an example of the information provided by a detector, during the 2015 Pb–Pb data taking period, the EMCal QA component provided tower energy spectra, number of triggers vs. position, and median vs. maximum tower energy to characterize the event background, as well as a number of other histograms. All of these were provided as a function of different regions in the detector. It is worth noting that the data volume depends heavily on the data taking period and the detectors themselves, with some payloads as small as ~ 10 kB/request, while others are larger than 1 MB/request.

A number of processing actions are performed upon the newly received data. These actions are managed by the Overwatch processing module, which is written in Python [111], utilizes PyROOT [112,113], and is generally responsible for transforming the data into more easily comprehensible forms. The received data is organized and metadata related to the run and the available subsystems (detectors) are extracted. The histograms and other objects available for each subsystem are also classified and sorted into related groups for visualization purposes. Overwatch then enters into the main processing routine which adds additional context, extracts derived information, and stores enhanced visualizations (such as highlighting trigger regions within a detector to aid in identifying channels which fire too frequently). This step also has the capability to extract derived values as the data are processed for trending purposes. Afterwards, the trended information is processed in a similar manner to the originally received data. The output of the processing and trending includes metadata related to the runs and included subsystems, as well as JSON and image representations of the processed data.

This information is then made available through the web application, where the

data are organized and displayed in the main view according to run and subsystem. The web application back end is written in Python and is built with the Flask microframework [114]. The front end is built on top of Google's Polymer library [115] and JSRoot [116,117]. Within a selected run and subsystem, the data are displayed according to their previously classified groups, along with any information extracted from the displayed object. Predefined data exploration capabilities are provided for the displayed data, as will be illustrated in Sec. A.2. To further enable data exploration beyond the capabilities provided by Overwatch, the underlying unprocessed ROOT files are also made accessible to the user.

A typical example of the Overwatch web application interface is shown in Fig. A.2. The main object is a histogram which represents the number of triggers vs. position in the EMCal integrated over the length of an entire run. The white gaps which are surrounded by data are caused by disabled trigger channels. Overwatch enhances this visualization by superimposing a black grid which corresponds to trigger regions within the calorimeter. Such additional content improves the user experience by allowing identification of whether a particular trigger region is firing too frequently (ie. "hot") at a glance. Since this visualization of the data utilizes JSRoot, further investigation of each trigger is possible by zooming in. Additional EMCal histograms are available via the list on the left.

While there are some standard capabilities that will be used by all detectors and therefore can be implemented by the main Overwatch packages, each detector has a unique set of requirements. Consequently, Overwatch implements a plugin system to allow each detector to customize the processing, trending, and visualization of their data to meet their needs. This is implemented through the dynamic loading of detector specific Python modules. Each function call is then redirected to the module if the relevant step is implemented. This approach allows each detector to add any

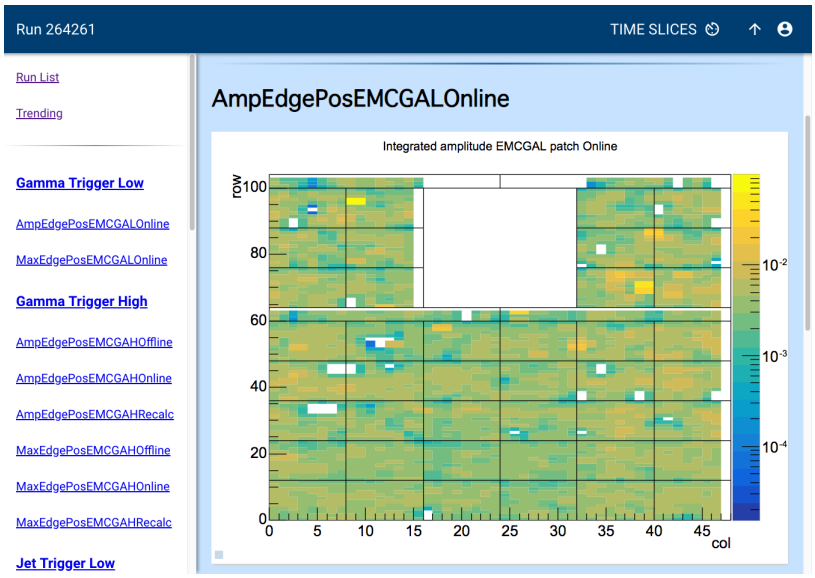

Figure A.2: Typical view of the Overwatch interface showing number of triggers vs. position for the ALICE Electromagnetic Calorimeter for a particular run. The black lines superimposed on the image display trigger regions within the calorimeter to aid in the identification of hot trigger regions. See the text for further details.

arbitrary functionality that is required. An example result of this system can be seen in Fig. A.2, where the black grid was superimposed on the displayed data via a detector plugin in the processing module.

A.2 Time slices and reprocessing

Beyond the basic functionality described above, the most important Overwatch features revolve around taking advantage of the time-stamped persistently stored data. To utilize the time-stamps, Overwatch allows the user to request that data within a user specified start and end time be reprocessed, thereby only using information within that time window. This is a major data exploration feature in Overwatch, enabling characterization of the time dependence of the data quality. This capability is known as time slices.

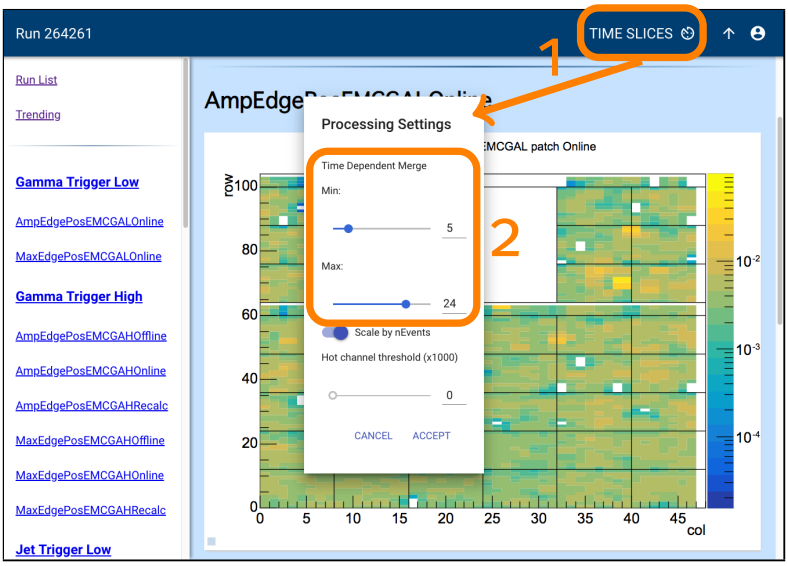

Figure A.3: The Overwatch time slices interface allows for the reprocessing of data within a specified time window. To perform a time slice, the user opens the time slice panel by clicking on the (1) highlighted "time slice" button. This opens a panel that is shown in the middle of the image. Within this panel, the user selects a time window within the (2) highlighted region. Five minutes from the start of the run to 24 minutes into the run is selected. Once submitted, the resulting histogram would be displayed in the same page.

Overwatch exposes this functionality directly to the user through the web application interface shown in Fig. A.3. To create a new time slice, the user selects the highlighted "time slices" button, which opens a new panel. This panel allows the user to specify the minimum and maximum times of their time slice, as shown in the second highlighted region. After processing the data within the specified time window, the results are then displayed in the same page. These results are stored and cached based on the input parameters to allow for immediate results and an improved user experience if the time slice has already been processed.

To illustrate the value of this approach, consider the case of a histogram which measures the occurrence of large amplitude hits in a detector vs. their position. Even if the histogram indicates that a channel had some large amplitude entries, the user doesn't necessarily know the cause. However, if they have some external information, such as

the knowledge that the electronics initialization at the start of run can cause large amplitude spikes that have no impact on the data quality of the run, time slices allow the user to directly check whether these large amplitude entries are problematic. The user would simply deselect the first few minutes of the run, and if the large amplitude counts disappear, then the data quality for that run is still good.

The time slice reprocessing is performed by the exact same code as the standard Overwatch processing, including all detector plugins – it just utilizes different input data corresponding to the selected time window. This procedure can then be generalized further to allow the user to specify any exposed set of processing parameters. Such an approach adds a new dimension to the data exploration capabilities provided by Overwatch, enabling the extraction of custom information, as well as the selection of different areas of the parameter space which might be otherwise inaccessible behind other data.

As an example, consider again a histogram which measures the occurrence of large amplitude hits in a detector vs. their position. If there has been a particularly noisy run, the user can extract all channels (bins) whose entries are above a user specified threshold in order to take further actions. Fig. A.4 illustrates just such a histogram from the EMCal and demonstrates how these reprocessing capabilities can be used. The user first selects the reprocessing and time slices button, which is labeled with "time slices" and is highlighted in the first selection. This opens a panel to direct the reprocessing. The user can select their desired threshold for maximum number of counts, as shown in the second highlighted selection. Once submitted, the data will be reprocessed, and the identifiers of the hot channels are displayed in a list inside of the third highlight, alongside the original histogram. With this information, a detector expert can take the appropriate actions to address the identified channels. As with all other parts of Overwatch, these capabilities are extensible, such that new reprocessing

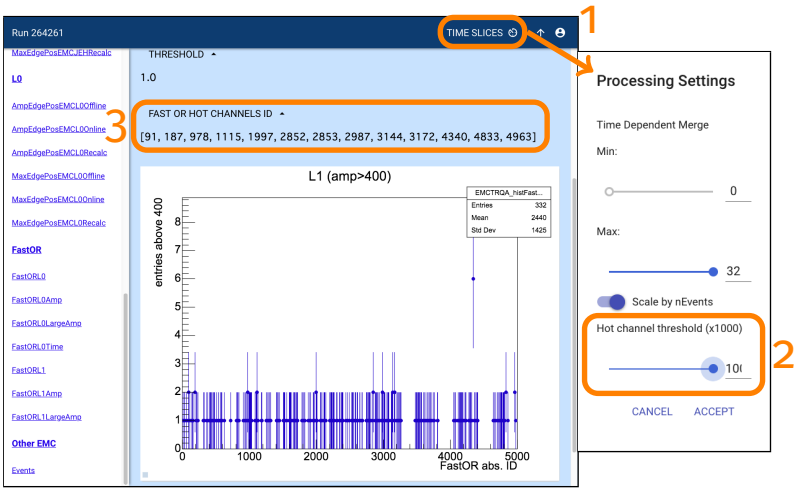

Figure A.4: Overwatch allows the reprocessing of histograms with different parameters. An EMCal histogram is shown which measures large amplitude hits vs. channel identifier. To perform the reprocessing, the user opens the reprocessing panel (1) by clicking on the highlighted "time slices" button. This opens a panel that is shown on the right. In this example, the user selects a threshold (which is multiplied by a trivial scaling factor for display purposes) in (2), which specifies the maximum counts threshold for the reprocessing. The text (3) displays the channels found above this threshold, with the reprocessed histogram displayed below. Note that in this example the reprocessed histogram is identical to the original histogram, but in general this need not be the case.

options can be added by any detector subsystems. Options which are not relevant for the currently displayed histogram will be disabled. Note that it is also acceptable to specify a time slice window along with other reprocessing options.

A.3 Contributions For Run 3

While most of the Overwatch infrastructure was shut down at the end of 2018 with the completion of LHC Run 2, it still provided substantial contributions before the run was completed. As noted in Sec. A.1, the data model for the HLT QA data is compatible with that of O^2. Furthermore, the Overwatch architecture to handle and process data closely matches the design of the ALICE Quality Control (QC) project for data-quality monitoring in O^2. Although Overwatch processes much less data than will be handled during Run 3, the strong similarities demonstrate that Overwatch can inform future developments. Consequently, in addition to maintaining the project's existing capabilities, Overwatch is being utilized to develop experiences and prototypes necessary for O^2 in Run 3 while still in Run 2. The focus of these efforts is on the trending and alarms subsystems in Overwatch. The existing systems have fairly basic capabilities, so new developments are ongoing which attempt to satisfy the requirements of both Run 2 and Run 3. The practical knowledge, and perhaps the code itself, will help inform the development of the corresponding systems within the QC project.

Post Run 2, Overwatch has continued to provide valuable experience by taking advantage of the persistently stored data. This data can be replayed as if it was just received from the HLT. For any QC related developments, prototypes can be quickly implemented through the Overwatch plugin system, allowing testing of new ideas with real data. The time-stamped nature of the data can also be useful as time-series data

for training machine learning models. Such capabilities ensure that Overwatch will continue to make contributions beyond the end of Run 2.

Appendix B

Analysis Software

A broad variety of software was written in python [111] and C++ [110] to organize, analyze and plot the body of work described in this dissertation. The software frameworks and packages utilized, as well as their mode of operation, are described below.

B.1 Analysis tasks and trains

The main analysis was conducted using a set of classes stored in AliPhysics. All of the tasks are built using the EMCal-jet analysis framework. The main classes are:

- `AliAnalysisTaskEmcalJetHCorrelations`: Performs the main correlation analyses, measuring the correlations, mixed events, and number of triggers.
- `AliAnalysisTaskEmcalJetHPerformance`: Performs quality assurance, event plane resolution measurements, and other general tasks.
- `AliAnalysisTaskEmcalJetHUtils`: Utilities and shared functionality between the two analysis tasks.

The tasks also utilize the EMCal Corrections[1] which are described in more detail in Sec. B.3 and the EMCal Embedding Frameworks[2] which is described in more detail in Sec. B.4. I am one of the main authors of the Corrections Framework, and the main author of the Embedding Framework.

The tasks were run on the ALICE LEGO train analysis system on the `Jets_EMC_PbPb` train. The analyses described in this dissertation were extracted from the following train numbers:

- 0–10% central and 30–50% semi-central Pb–Pb collisions at $\sqrt{s_{\mathrm{NN}}} = 5.02$ TeV
  - Correlations: 4837
  - Event plane resolution: 4731
  - Assessment of systematic uncertainties: 4837
  - Response matrix with one train pt $p_{\mathrm{T}}^{\mathrm{hard}}$ bin: 4738-4754, 4761-4764
- 30–50% semi-central Pb–Pb collisions at $\sqrt{s_{\mathrm{NN}}} = 2.76$ TeV
  - Response matrix with one train pt $p_{\mathrm{T}}^{\mathrm{hard}}$ bin: 4477-4486

The output of these analysis tasks were post processed via a separate set of packages which I developed:

- The main post processing code is contained in the `alice-jet-hadron`[3] python package. It includes analysis and plotting code for the correlations and the response matrix analyses, as well as a number of toy models, and an event generation framework.

- The Reaction Plane Fit described in Sec. 3.5 is implemented via the

1. The task is defined in AliPhysics in `PWG/EMCAL/EMCALtasks/AliEmcalCorrectionTask`.

2. The task is defined in AliPhysics in `PWG/EMCAL/EMCALbase/AliAnalysisTaskEmcalEmbeddingHelper`.

3. https://github.com/raymondEhlers/alice-jet-hadron

`reaction_plane_fit`[4] [118] python package. This package allows others to easily utilize and implement extensions to the fit.

- Both on these rely on the base package of heavy ion analysis tools which is known as `pachyderm`[5]. It provides a one-dimensional histogram package, a fit framework based on Minuit, and outliers removal as described in Sec. B.4.1, amongst many other utilities. `Pachyderm` utilizes a number of packages, including [90,113,119–122]

B.2 Fitting and Minimization

Fitting is performed via the minimization of a cost function, which provides a measure of goodness-of-fit of the fit function to the data. In order to construct a well defined[6] cost function, the cost is constructed as a likelihood ratio utilizing the saturation model. Normalizing by the likelihood function where the fit exactly describes the data[7] [123,124] ensures a bound. This analysis utilized both χ^2 and log likelihood cost functions. The cost functions require modifications when working with binned data, such as data stored in a histogram, to ensure that the constraints of the binned data do not distort the minimization [123–125].

With these considerations in mind, we can define the χ^2 cost function,

4. https://github.com/raymondEhlers/reactionPlaneFit

5. https://github.com/raymondEhlers/pachyderm/

6. i.e. a bounded cost function

7. This corresponds to when the model is saturated.

$$\chi^2 \sim \sum_i (\frac{y_i - f(x_i, \vec{p})}{\sigma_i})^2 \tag{B.1}$$

where (x_i, y_i) are the i pairs of binned input data, σ_i is the error on y_i, and $f(x_i, \vec{p})$ is the fit function with parameters $\vec{p}$ integrated over the entire bin width represented by each x_i.

In the case of datasets which may contain empty bins, dividing by $\sigma_i = 0$ in the χ^2 is problematic. In that case, we determine the fit parameters by finding the maximum likelihood of an alternative cost function, which is in turn equivalent to minimizing a log likelihood cost function. In particular, we can construct a log likelihood ratio which builds in the assumption that the number of counts in each bin follow Poisson statistics. This likelihood, L is defined as

$$L \sim -\sum_i s_i (y_i \log \frac{f(x_i, \vec{p})}{y_i} + (y_i - f(x_i, \vec{p}))) \tag{B.2}$$

where s_i is a overall scale factor which is equal to $y_i/\sigma i$ when performing a weighted likelihood fit or one otherwise, and $f(x_i, \vec{p})$ is still the fit function with parameters $\vec{p}$ integrated over the entire bin width represented by each x_i [125]. In practice, this cost function tends to constrain the fit parameters more weakly than the χ^2, but it converges over a broader range of input data.

Regardless of the cost function, the actual minimization procedure is performed using Minuit2 via the iminuit python package [88,90]. These cost functions, as well as a fitting framework are implemented in the `pachyderm.fit` package.

B.3 ALICE EMCal Corrections Framework

EMCal corrections are performed in ALICE via the EMCal Corrections Framework [126]. This modular frameworks provides a set of corrections and tools to be applied to cells and clusters. The framework is controlled via a YAML configuration file[8]. The user's configuration file is only required to specify the options which need to be modified for a particular analysis, improving the user experience and reducing the probability of misconfiguration.

The framework provides components for cell and cluster level corrections. The corrections for cells are as follows:

- **Energy calibration**: Iterative calibration of the cell energy based on the location of the π_0 peak.
- **Bad channel removal**: Removes channels which are large deviations away from the mean energy spectrum.
- **Time calibration**: Calibrates the differences in timing between different supermodules.
- **Energy shift**: Utilized in embedding to shift the MC to the same energy scale as the data or vice-versa. This allows the use of the same non-linearity correction on the clusters.

The corrections for clusters include:

- **Clusterization**: Combines cells into aggregate objects via a clustering algorithm. In this analysis, the `v2` venison of clusterizer is utilized. This algorithm utilizes seed cells above a specified energy threshold. It then searches through neighboring cells, clustering them together if they are above the minimum energy threshold

8. The framework and configuration options are extensively documented in [126].

until it reaches a local energy minima.

- **Exotic cluster removal**: Remove clusters where all of the energy is centered in a single cell, as measured by the expression $f_{\text{cross}} = 1 - \frac{E_{\text{cross}}}{E_{\text{cell}}}$.
- **Detector non-linearity**: Corrects for the non-linear response of the detector as a function of the cluster energy. It provides a correction for both a non-linearity shape, as well as an energy shift.
- **Cluster-track matching**: Extrapolates and matches tracks found by the ALICE tracking system to the clusters found in the EMCal. Is often used to apply an isolation requirement, or in conjunction withe hadronic correction described below.
- **Hadronic correction**: Charges hadrons will deposit energy into the EMCal as they traverse it. In order to account for this, the transverse momentum of matched tracks are removed from the cluster. This prevents double counting when performing jet finding for full jets which use both the charged particles and EMCal clusters.

B.4 ALICE Embedding and the EMCal Embedding Framework

Embedding is performed in ALICE via the EMCal Embedding Framework [127]. This framework provides the ability to generically embed one dataset into another[9]. For each event processed, two events are made available:

1. The external event, corresponding to the data that will be embedded.
2. The internal event, corresponding to the data into which we will embed.

9. The framework is extensively documented in [127].

The internal event should contain the larger of the two events in order to improve performance and minimize stress on the ALICE computing grid.

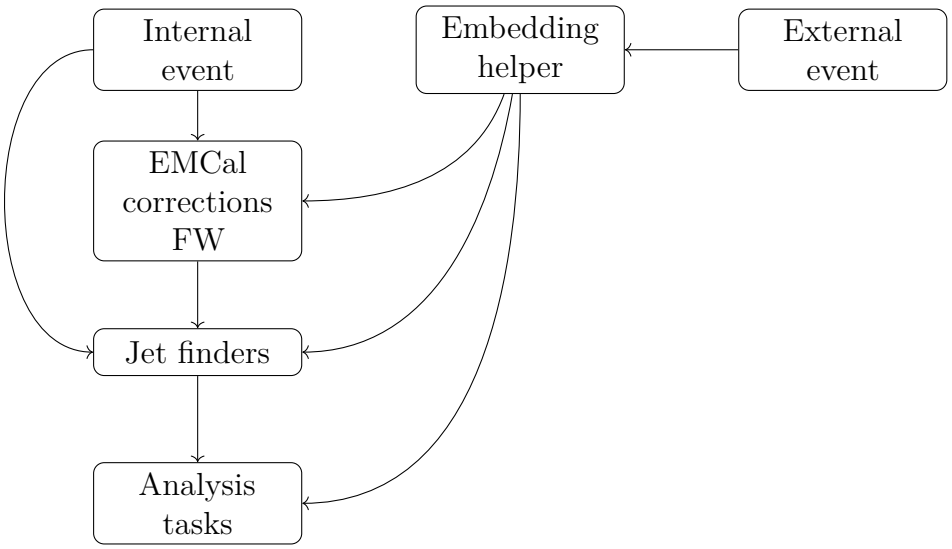

Figure B.1: Architecture of the EMCal embedding framework. This architecture is described in full detail in the text.

The architecture of the embedding framework is illustrated in Fig. B.1. The embedding helper is a singleton class which is responsible for managing managing access to the external event. During design and development, I took great care to ensure that the helper would always provide the external event in such a way that optimized performance. The task provides a variety of options, including control of event randomization, filtering of external files, and internal event selection for improved performance. It is always the first step executed in the analysis chain.

Due to the precise spatial resolution of the central barrel tracking, it is unlikely that tracks from the external and internal events will overlap. This allows for the embedding to be performed at measurement level without having to repeat all of the computationally expensive reconstruction and tracking, and dramatically reduces the complexity for accessing the charged particles from each event. The charged particles from the external event can be made by simply appending them to the internal event array. Additional bookkeeping is performed in the framework to ensure that each

particle is uniquely identified and can be traced back to its parent event.

Due to the coarser EMCal cell size, we must explicitly account for occupancy effects. As an initial reprocessing step, all cell level corrections for the EMCal are performed separately for the internal and external events. Due to the difference in the energy scale between data and MC generated cells, the MC cells are shifted to the data energy scale before combining the data and MC cells together. The cells are then combined by taking advantage of the recursive search of the EMCal Clusterizer v2, which looks for cells which neighbor the seed cell. If there are two cells that are in the same position, the leading cell will be added to the cluster first, and then after moving to the next cell, the subleading cell will be found as a neighbor and added into the cluster[10]. The clusters found by the clusterization then encompass the cells from both the internal and the external events.

B.4.1 Outliers Removal

In order to generate sufficient MC statistics at high $p_{\mathrm{T,jet}}$, a common technique is to restrict the phase space of the outgoing hard partons to a particular range. Although this is not a precise correlation with $p_{\mathrm{T,jet}}$ due to the impact of other processes in the event, such as hadronization, underlying event activity, and the jet clustering algorithm, $p_{\mathrm{T}}^{\mathrm{hard}}$[11], selection provides provides a proxy for $p_{\mathrm{T,jet}}$ [8]. Jets generated according to this approach are then reweighed by $\sigma/n_{\mathrm{trials}}$, where n_{trials} is the number of trials necessary to receive a hard scattering in the selected phase space.

As a consequence of this technique, jets from small $p_{\mathrm{T}}^{\mathrm{hard}}$ are weighed up by a large

10. This clusterization approach is fine as long as relatively hard jets are used when embedding, such as when embedding a ${p_{\mathrm{T}}}^{\mathrm{hard}}$ distribution. If the data and MC cells are approximately the same intermediate energy, then this assumption may lead the cell seed to move from the expected location.

11. Also know as $\hat{p}_{\mathrm{T}}$ in PYTHIA 8.

factor. This can be problematic when, for example, the expected counts in a bin are less than one, but fluctuates upward to one count. This fluctuation is then weighed highly, which causes the fluctuation to appear as an outlier in the measured jet spectra. These outliers can be addressed via two methods:

1. Requiring that jets produced in a particular are not too large compared to $p_{\mathrm{T}}^{\mathrm{hard}}$.
2. Truncating bins that are expected to have few entries before reweighing for a particular $p_{\mathrm{T}}^{\mathrm{hard}}$ bin.

For method 1, events are rejected if there are jets such that $4p_{\mathrm{T}}^{\mathrm{jet,pythia}} > p_{\mathrm{T}}^{\mathrm{hard}}$, where $p_{\mathrm{T}}^{\mathrm{jet,pythia}}$ are simplified jets found at the PYTHIA particle level. This accounts for jets which are produced far outside the $p_{\mathrm{T}}^{\mathrm{hard}}$ bin, such as those produced via initial state radiation.

For method 2, a moving average of 5 bins is calculated over the entire range of the particle level jet spectrum of a measured histogram before reweighing. Once the moving average drops below one, all bins at larger $p_{\mathrm{T,jet}}^{\mathrm{part}}$ are removed. Removal can only begin after the moving average initially becomes larger than one. Since this technique is only supposed to remove outliers and therefore not change the distribution significantly, the procedure is not allowed to modify the median or the mean of the particle level spectrum by more than 1%.[12]

12. This procedure is implemented in the `pachyderm.remove_outliers` module.

Appendix C

ALICE Run 3 Upgrades

During LHC runs 1 and 2, ALICE has successfully measured a wide variety of phenomena related to the quark-gluon plasma. Looking towards to the future, some of our main physics goals include measurements of the properties of heavy flavor quarks in the QGP, low p_{T} quarkonia, low mass di-electrons, and precision jet energy loss studies [128].

In order to accomplish these goals, ALICE must modify its approach to data collection. In particular, these measurements require the tracking and PID capabilities of ALICE, but with much higher statistics data samples than are possible in the current detector configuration. Consequently, ALICE is moving towards a continuous data readout that will increase the data rate by ≈ 100. One part of this effort is on the software side through the ALICE O^2 project as mentioned in Sec. A. However, it also requires substantial modifications to many of the ALICE sub-detectors, including the TPC.

For runs 1 and 2, the TPC utilized multi-wire proportional chambers (MWPCs) to perform gas amplification. During this amplification, a substantial number of ions are produced which flow back into the TPC drift volume. To prevent the drifting ions

from distorting the electric field in the TPC, the ions are collected using a gating grid. However, this gating grid imposes an inherent dead time of ≈ 300 μs[1]. For Run 3, the gas amplification will instead be performed using a stack of 4 Gas Electron Multipliers [129], which when operated in the proper configuration, produce substantially back flowing ions as compared to MWPCs. Although the stack of GEMs were the nominal option for this upgrade, and at the time of writing, are currently being installed, the Relativistic Heavy Ion group at Yale participated in a research and development effort to investigate alternative solutions.

This alternative design consisted of 2 GEMs stacked in front, with a MicroMegas (MMG) [130] behind it. This 2-GEM + MMG design utilized the two components in a complementary configuration. The GEMs act as a pre-amplifier, providing minimal gas amplification, but help spread ionization electrons, thereby reducing the MMG spark rate. They also served to suppress ion back flow. The MMG then provides most of the gas amplification. In combining these different gain elements, there is a large phase space of possible configurations to explore. I helped characterize the performance, with a particular focus on the how the performance varies as a function of gas mixture. The results of these investigations are reported in [131].

To further validate this proposed design, I also participated in a test beam at the CERN Proton Synchrotron (PS) to directly compare the performance of the nominal 4 GEM stack with the 2-GEM + MMG design. Although the 2-GEM + MMG design showed promise, more time was needed for the design to fully mature. These efforts are described in [132].

1. Which is dictated by the ion drift velocity.

Appendix D

Additional Correlations

For this thesis, low and high $p_{\mathrm{T}}^{\mathrm{assoc}}$ bins were used to illustrate the correlation methods. However, the yields, yield differences, yield ratios, and widths are reported over the entire $p_{\mathrm{T}}^{\mathrm{assoc}}$ range. In order to better understand some of these results, it is at times instructive to look at the correlation functions themselves, especially when considering whether particular values were caused by statistical fluctuations. Consequently, the jet-hadron $\Delta\varphi$ correlations functions, Reaction Plane Fit correlation and covariance matrices, and subtracted $\Delta\varphi$ correlation functions are shown below. They are presented for $20 < p_{\mathrm{T,jet}} < 40$ GeV/c and $0.5 < p_{\mathrm{T}}^{\mathrm{assoc}} < 10$ GeV/c in 30-50% semi-central collisions at $\sqrt{s_{\mathrm{NN}}} = 5.02$ TeV and for $20 < p_{\mathrm{T,jet}} < 40$ GeV/c and $1.0 < p_{\mathrm{T}}^{\mathrm{assoc}} < 10$ GeV/c in 0-10% central collisions at $\sqrt{s_{\mathrm{NN}}} = 5.02$ TeV.

D.1 30–50% Semi-Central Pb–Pb Collisions

D.1.1 $20 < p_{\mathrm{T,jet}}^{\mathrm{ch+ne}} < 40\,\mathrm{GeV}/c$, $0.5 < p_{\mathrm{T}}^{\mathrm{assoc}} < 1.0\,\mathrm{GeV}/c$, Inclusive orientation

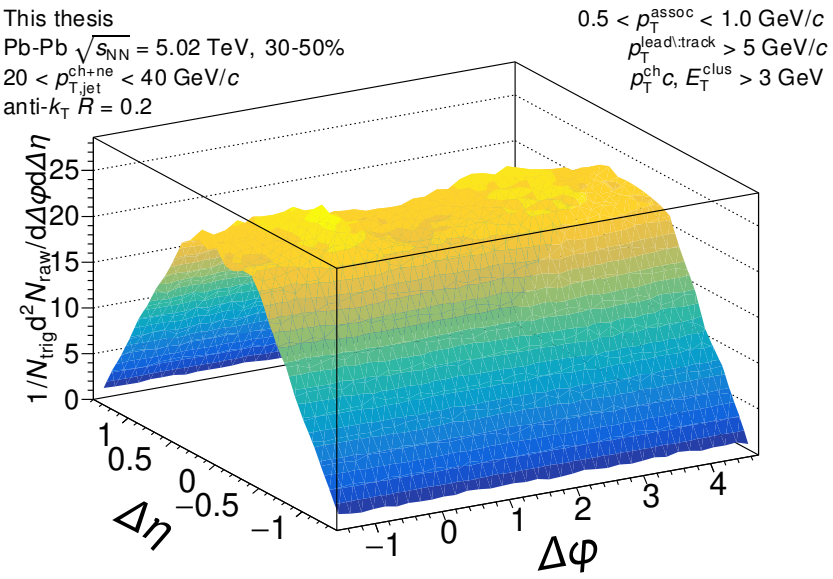

Figure D.1: The measured correlation function with the the efficiency correction $\epsilon(p_{\mathrm{T}}, \eta)$ applied, but before acceptance correction via the mixed events. The correlation is measured for inclusive orientation for $20 < p_{\mathrm{T,jet}}^{\mathrm{ch+ne}} < 40\,\mathrm{GeV}/c$ jets with $0.5 < p_{\mathrm{T}}^{\mathrm{assoc}} < 1.0\,\mathrm{GeV}/c$ in 30–50% Pb–Pb collisions at $\sqrt{s_{\mathrm{NN}}} = 5.02\,\mathrm{TeV}$.

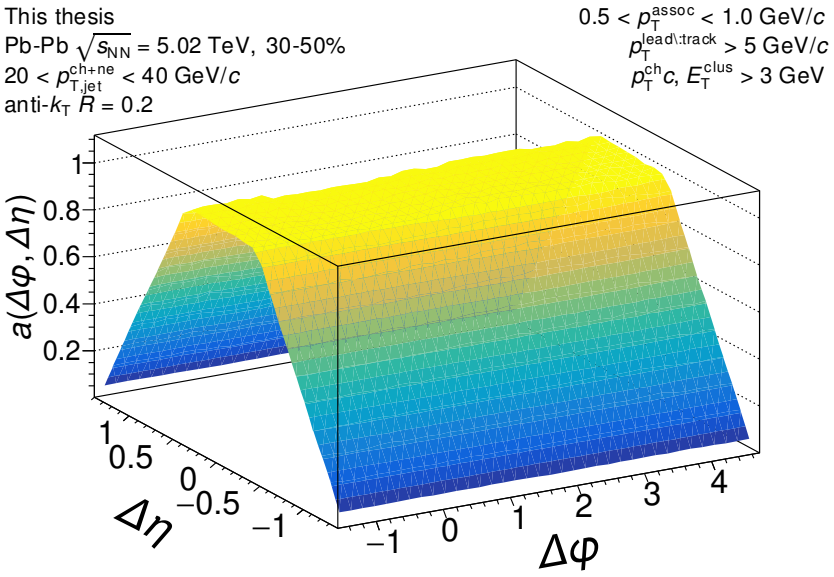

Figure D.2: The mixed event pair acceptance correction with the efficiency correction $\epsilon(p_{\mathrm{T}}, \eta)$ applied. The correlations are measured for inclusive orientation for $20 < p_{\mathrm{T,jet}}^{\mathrm{ch+ne}} < 40\,\mathrm{GeV}/c$ jets with $0.5 < p_{\mathrm{T}}^{\mathrm{assoc}} < 1.0\,\mathrm{GeV}/c$ in 30–50% Pb–Pb collisions at $\sqrt{s_{\mathrm{NN}}} = 5.02\,\mathrm{TeV}$. They have already been normalized such that it they are unity at maximum efficiency. Above 2 GeV/c, the mixed events are merged together to increase statistics, so it is the same for all for correlations within $2.0 \leq p_{\mathrm{T}}^{\mathrm{assoc}} < 10$ GeV/c.

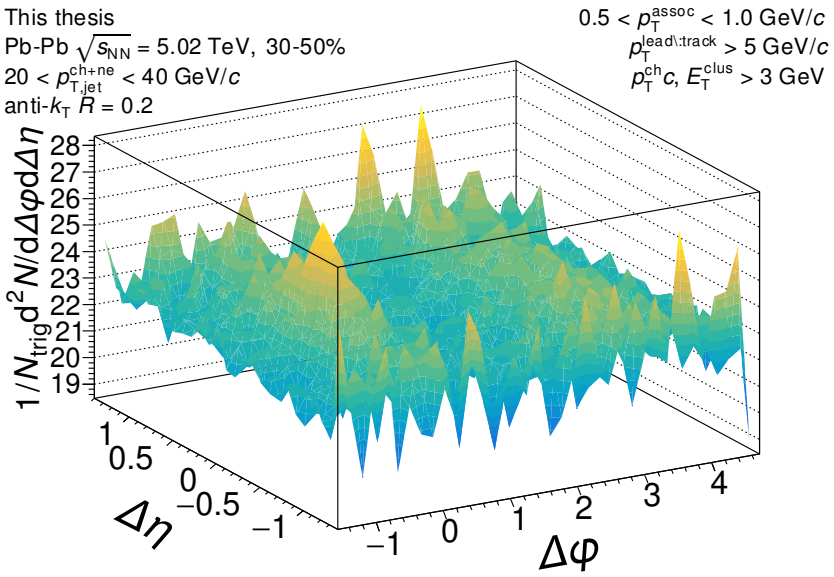

Figure D.3: The signal correlation corrected by pair acceptance. The correlations are measured for inclusive orientation for $20 < p_{\mathrm{T,jet}}^{\mathrm{ch+ne}} < 40\,\mathrm{GeV}/c$ jets with $0.5 < p_{\mathrm{T}}^{\mathrm{assoc}} < 1.0\,\mathrm{GeV}/c$ in 30–50% Pb–Pb collisions at $\sqrt{s_{\mathrm{NN}}} = 5.02\,\mathrm{TeV}$.

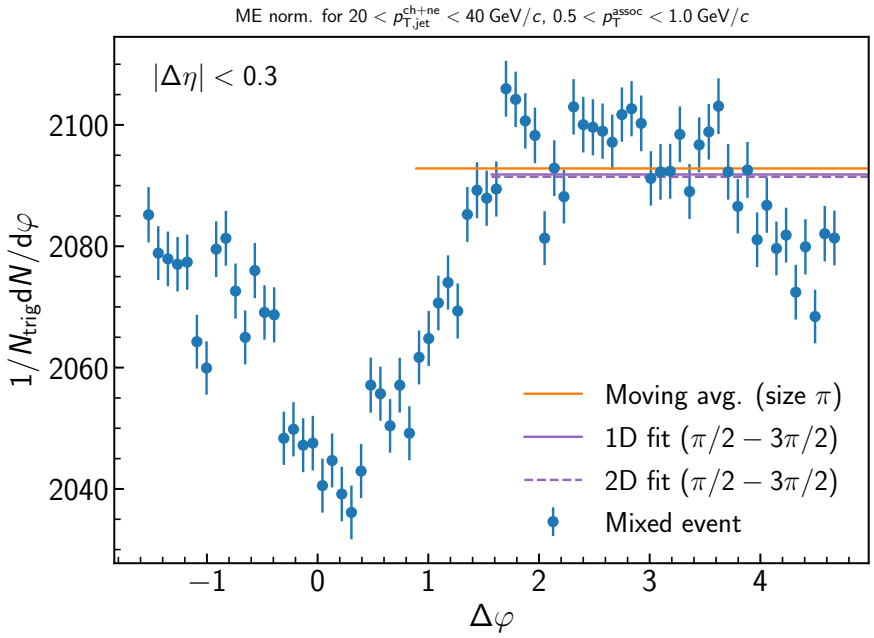

Figure D.4: Determination of the normalization of the mixed event for the inclusive event plane orientation in 30–50% Pb–Pb collisions at $\sqrt{s_{\mathrm{NN}}} = 5.02$ TeV. Here the mixed event is projected over the plateau range in $\Delta\eta$ onto to the $\Delta\varphi$ axis. The moving average is evaluated over the entire $\Delta\varphi$ range using a window of π, while the fit range is fixed from $\pi/2 < \Delta\varphi < 3\pi/2$. Since the mixed events are merged above 2 GeV/c, the normalization factor is also the same for all correlations within $0.5 < p_{\mathrm{T}}^{\mathrm{assoc}} < 1.0$ GeV/c. A variety of normalization methods were evaluated, with further details described in the text.

D.1.2 $20 < p_{\mathrm{T,jet}}^{\mathrm{ch+ne}} < 40\,\mathrm{GeV}/c$, $1.0 < p_{\mathrm{T}}^{\mathrm{assoc}} < 1.5\,\mathrm{GeV}/c$, Inclusive orientation

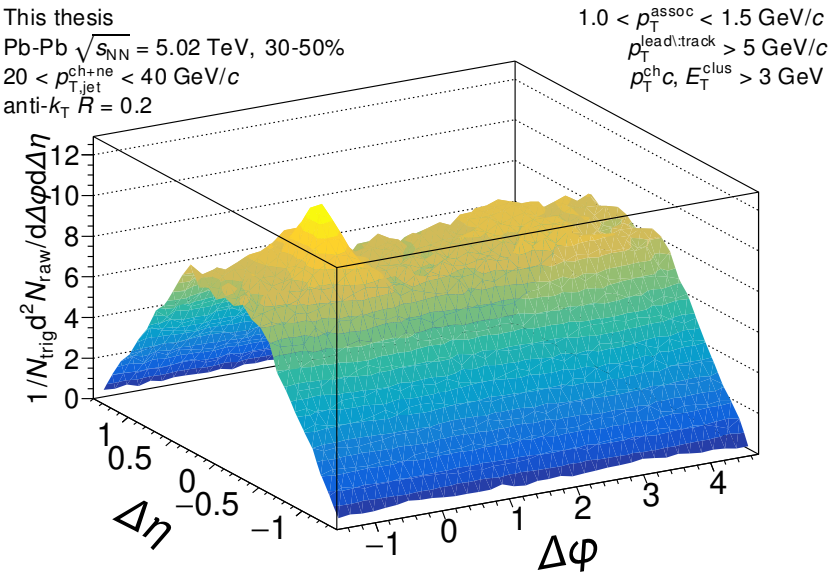

Figure D.5: The measured correlation function with the the efficiency correction $\epsilon(p_{\mathrm{T}}, \eta)$ applied, but before acceptance correction via the mixed events. The correlation is measured for inclusive orientation for $20 < p_{\mathrm{T,jet}}^{\mathrm{ch+ne}} < 40\,\mathrm{GeV}/c$ jets with $1.0 < p_{\mathrm{T}}^{\mathrm{assoc}} < 1.5\,\mathrm{GeV}/c$ in 30–50% Pb–Pb collisions at $\sqrt{s_{\mathrm{NN}}} = 5.02\,\mathrm{TeV}$.

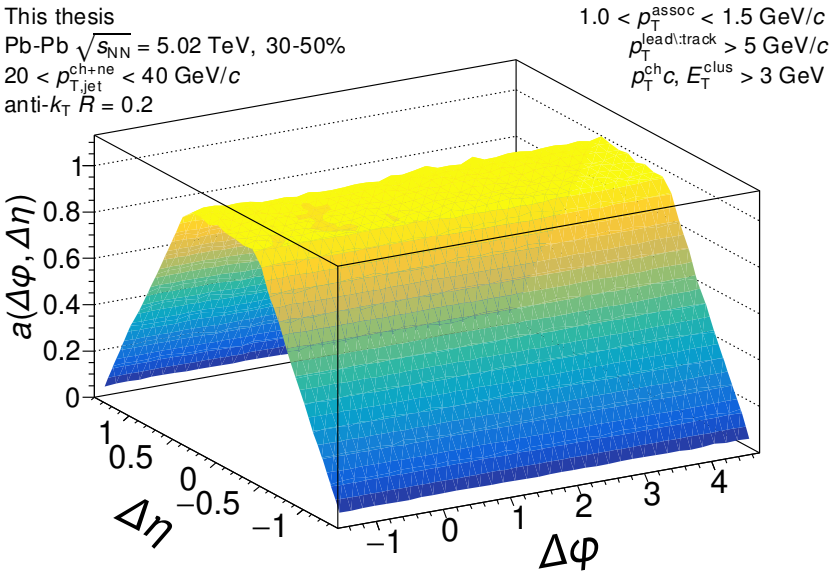

Figure D.6: The mixed event pair acceptance correction with the efficiency correction $\epsilon(p_{\mathrm{T}}, \eta)$ applied. The correlations are measured for inclusive orientation for $20 < p_{\mathrm{T,jet}}^{\mathrm{ch+ne}} < 40$ GeV/c jets with $1.0 < p_{\mathrm{T}}^{\mathrm{assoc}} < 1.5$ GeV/c in 30–50% Pb–Pb collisions at $\sqrt{s_{\mathrm{NN}}} = 5.02$ TeV. They have already been normalized such that it they are unity at maximum efficiency. Above 2 GeV/c, the mixed events are merged together to increase statistics, so it is the same for all for correlations within $2.0 \leq p_{\mathrm{T}}^{\mathrm{assoc}} < 10$ GeV/c.

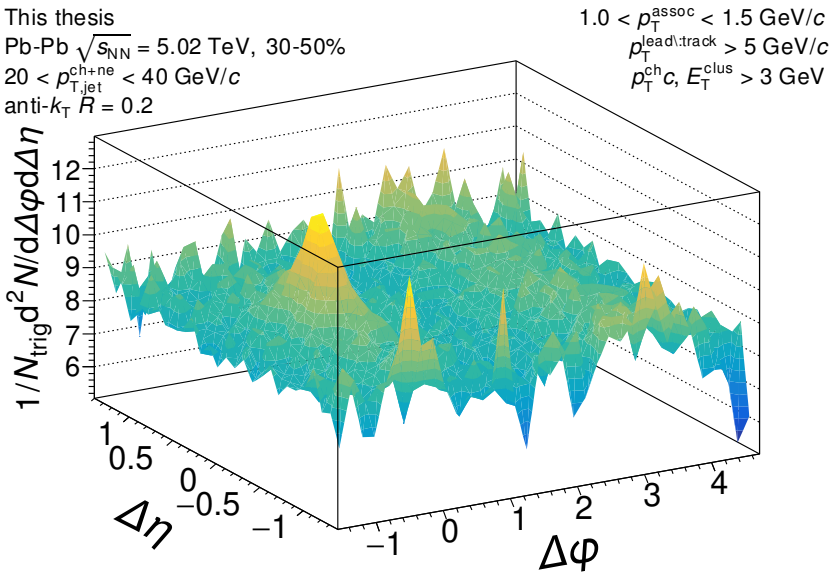

Figure D.7: The signal correlation corrected by pair acceptance. The correlations are measured for inclusive orientation for $20 < p_{\mathrm{T,jet}}^{\mathrm{ch+ne}} < 40$ GeV/c jets with $1.0 < p_{\mathrm{T}}^{\mathrm{assoc}} < 1.5$ GeV/c in 30–50% Pb–Pb collisions at $\sqrt{s_{\mathrm{NN}}} = 5.02$ TeV.

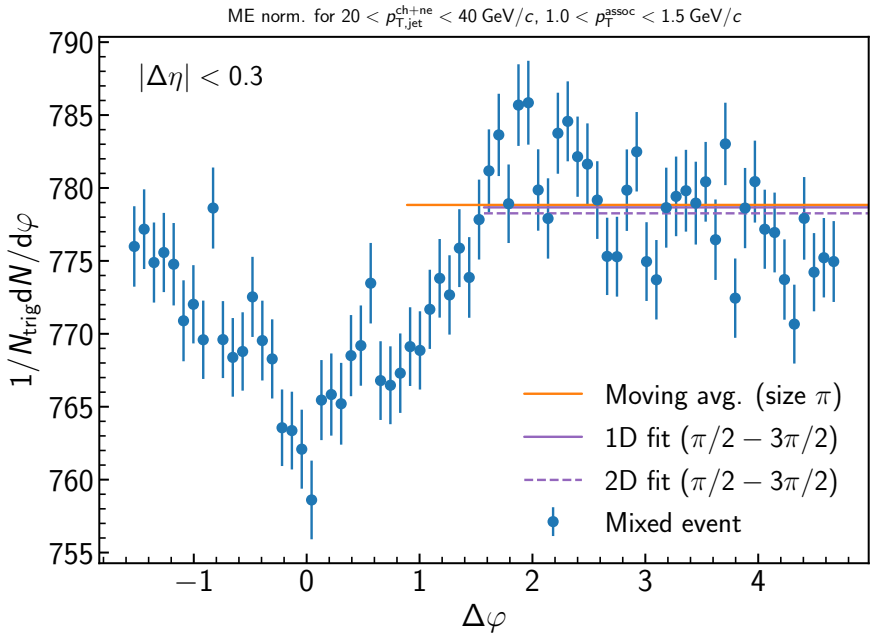

Figure D.8: Determination of the normalization of the mixed event for the inclusive event plane orientation in 30–50% Pb–Pb collisions at $\sqrt{s_{\mathrm{NN}}} = 5.02$ TeV. Here the mixed event is projected over the plateau range in $\Delta\eta$ onto to the $\Delta\varphi$ axis. The moving average is evaluated over the entire $\Delta\varphi$ range using a window of π, while the fit range is fixed from $\pi/2 < \Delta\varphi < 3\pi/2$. Since the mixed events are merged above 2 GeV/c, the normalization factor is also the same for all correlations within $1.0 < p_{\mathrm{T}}^{\mathrm{assoc}} < 1.5$ GeV/c. A variety of normalization methods were evaluated, with further details described in the text.

D.1.3 $20 < p_{\mathrm{T,jet}}^{\mathrm{ch+ne}} < 40\,\mathrm{GeV}/c$, $1.5 < p_{\mathrm{T}}^{\mathrm{assoc}} < 2.0\,\mathrm{GeV}/c$, Inclusive orientation

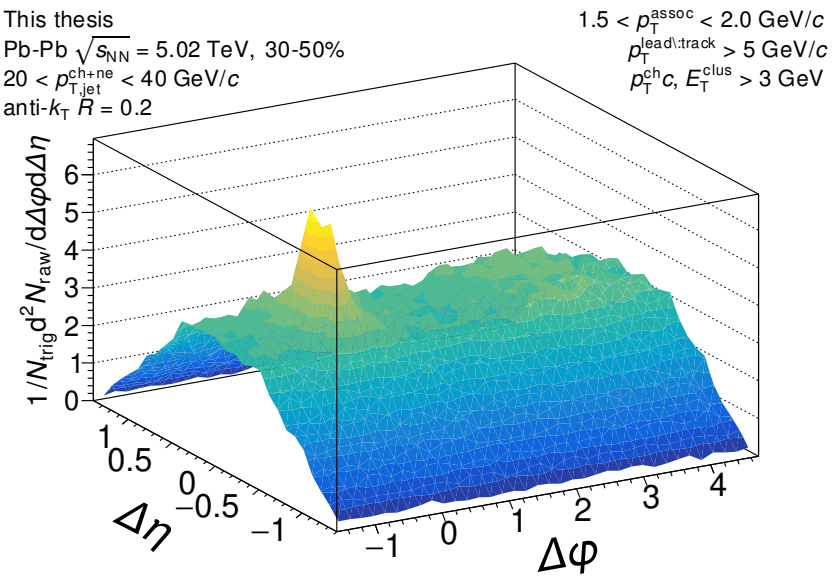

Figure D.9: The measured correlation function with the the efficiency correction $\epsilon(p_{\mathrm{T}}, \eta)$ applied, but before acceptance correction via the mixed events. The correlation is measured for inclusive orientation for $20 < p_{\mathrm{T,jet}}^{\mathrm{ch+ne}} < 40\,\mathrm{GeV}/c$ jets with $1.5 < p_{\mathrm{T}}^{\mathrm{assoc}} < 2.0\,\mathrm{GeV}/c$ in 30–50% Pb–Pb collisions at $\sqrt{s_{\mathrm{NN}}} = 5.02\,\mathrm{TeV}$.

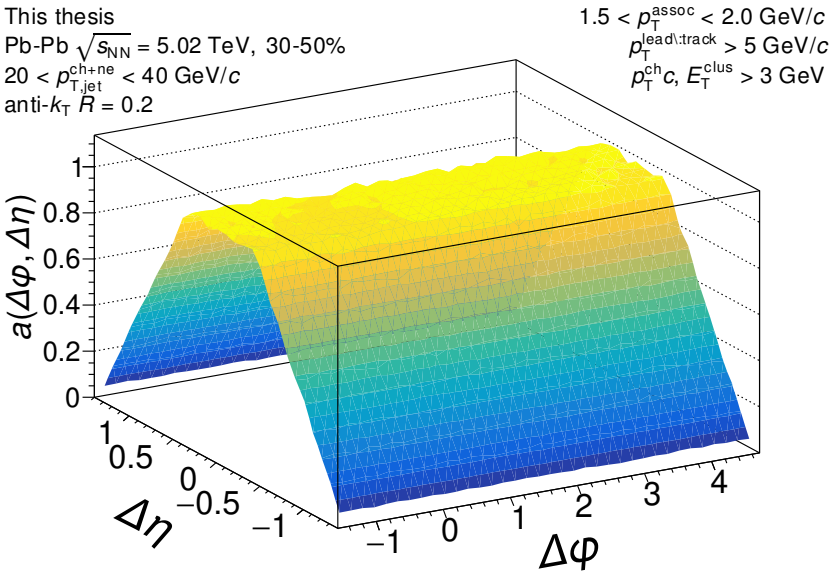

Figure D.10: The mixed event pair acceptance correction with the efficiency correction $\epsilon(p_{\mathrm{T}}, \eta)$ applied. The correlations are measured for inclusive orientation for $20 < p_{\mathrm{T,jet}}^{\mathrm{ch+ne}} < 40$ GeV/c jets with $1.5 < p_{\mathrm{T}}^{\mathrm{assoc}} < 2.0$ GeV/c in 30–50% Pb–Pb collisions at $\sqrt{s_{\mathrm{NN}}} = 5.02$ TeV. They have already been normalized such that it they are unity at maximum efficiency. Above 2 GeV/c, the mixed events are merged together to increase statistics, so it is the same for all for correlations within $2.0 \leq p_{\mathrm{T}}^{\mathrm{assoc}} < 10$ GeV/c.

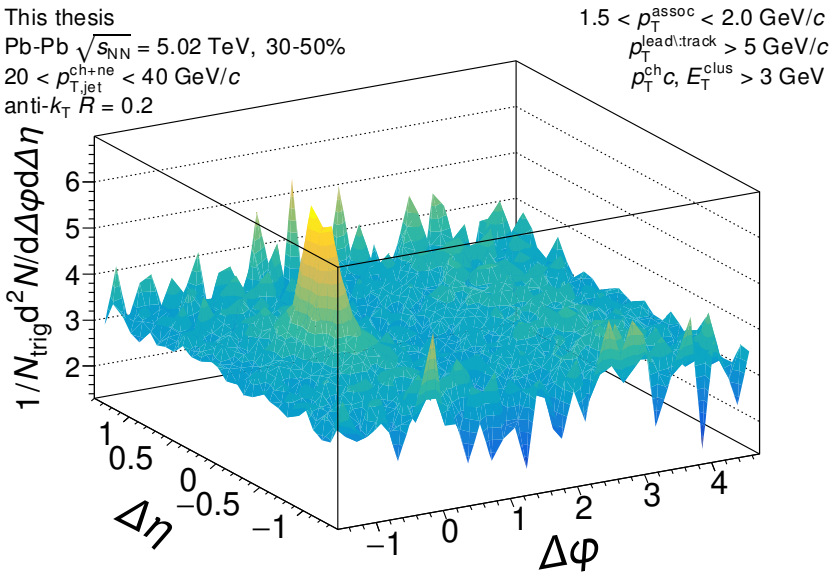

Figure D.11: The signal correlation corrected by pair acceptance. The correlations are measured for inclusive orientation for $20 < p_{\mathrm{T,jet}}^{\mathrm{ch+ne}} < 40$ GeV/c jets with $1.5 < p_{\mathrm{T}}^{\mathrm{assoc}} < 2.0$ GeV/c in 30–50% Pb–Pb collisions at $\sqrt{s_{\mathrm{NN}}} = 5.02$ TeV.

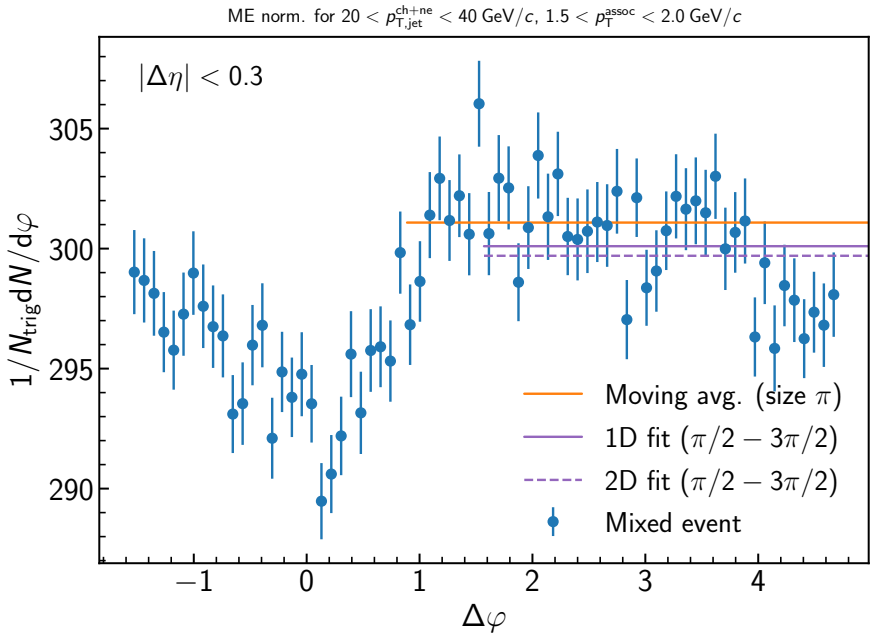

Figure D.12: Determination of the normalization of the mixed event for the inclusive event plane orientation in 30–50% Pb–Pb collisions at $\sqrt{s_{\mathrm{NN}}} = 5.02$ TeV. Here the mixed event is projected over the plateau range in $\Delta\eta$ onto to the $\Delta\varphi$ axis. The moving average is evaluated over the entire $\Delta\varphi$ range using a window of π, while the fit range is fixed from $\pi/2 < \Delta\varphi < 3\pi/2$. Since the mixed events are merged above 2 GeV/c, the normalization factor is also the same for all correlations within $1.5 < p_{\mathrm{T}}^{\mathrm{assoc}} < 2.0$ GeV/c. A variety of normalization methods were evaluated, with further details described in the text.

D.1.4 $20 < p_{\mathrm{T,jet}}^{\mathrm{ch+ne}} < 40\,\mathrm{GeV}/c$, $2.0 < p_{\mathrm{T}}^{\mathrm{assoc}} < 3.0\,\mathrm{GeV}/c$, Inclusive orientation

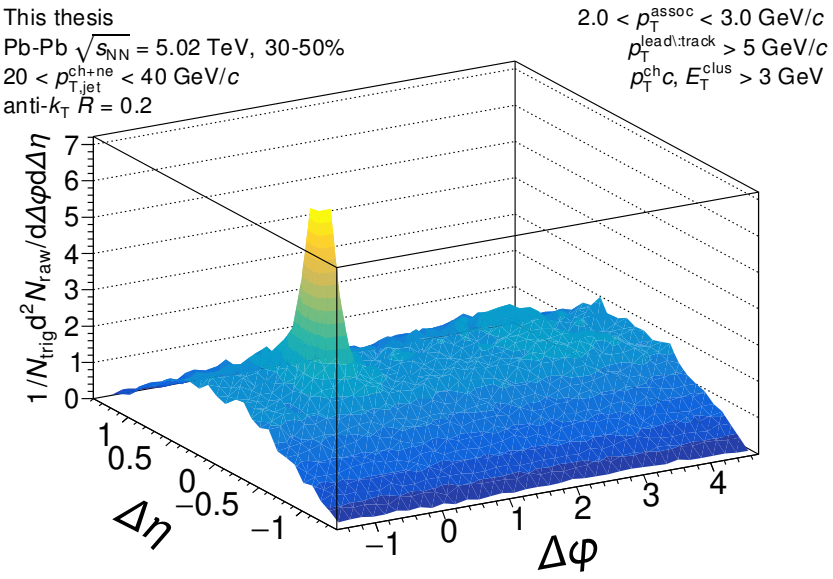

Figure D.13: The measured correlation function with the the efficiency correction $\epsilon(p_{\mathrm{T}}, \eta)$ applied, but before acceptance correction via the mixed events. The correlation is measured for inclusive orientation for $20 < p_{\mathrm{T,jet}}^{\mathrm{ch+ne}} < 40\mathrm{GeV}/c$ jets with $2.0 < p_{\mathrm{T}}^{\mathrm{assoc}} < 3.0\,\mathrm{GeV}/c$ in 30–50% Pb–Pb collisions at $\sqrt{s_{\mathrm{NN}}} = 5.02\,\mathrm{TeV}$.

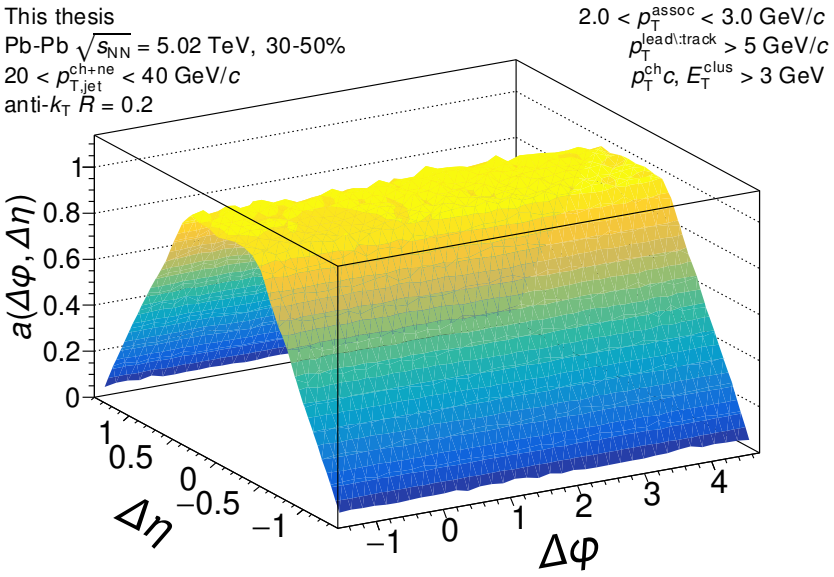

Figure D.14: The mixed event pair acceptance correction with the efficiency correction $\epsilon(p_{\mathrm{T}}, \eta)$ applied. The correlations are measured for inclusive orientation for $20 < p_{\mathrm{T,jet}}^{\mathrm{ch+ne}} < 40$ GeV/c jets with $2.0 < p_{\mathrm{T}}^{\mathrm{assoc}} < 3.0$ GeV/c in 30–50% Pb–Pb collisions at $\sqrt{s_{\mathrm{NN}}} = 5.02$ TeV. They have already been normalized such that it they are unity at maximum efficiency. Above 2 GeV/c, the mixed events are merged together to increase statistics, so it is the same for all for correlations within $2.0 \leq p_{\mathrm{T}}^{\mathrm{assoc}} < 10$ GeV/c.

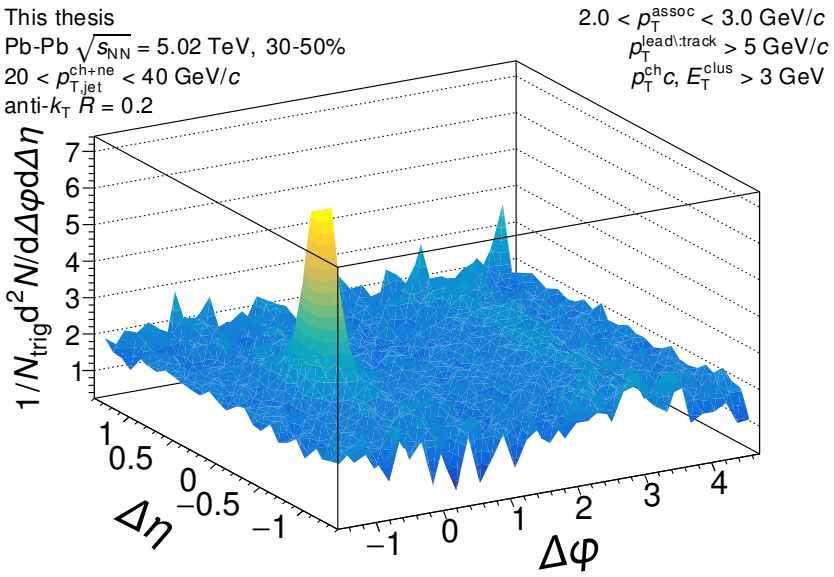

Figure D.15: The signal correlation corrected by pair acceptance. The correlations are measured for inclusive orientation for $20 < p_{\mathrm{T,jet}}^{\mathrm{ch+ne}} < 40$ GeV/c jets with $2.0 < p_{\mathrm{T}}^{\mathrm{assoc}} < 3.0$ GeV/c in 30–50% Pb–Pb collisions at $\sqrt{s_{\mathrm{NN}}} = 5.02$ TeV.

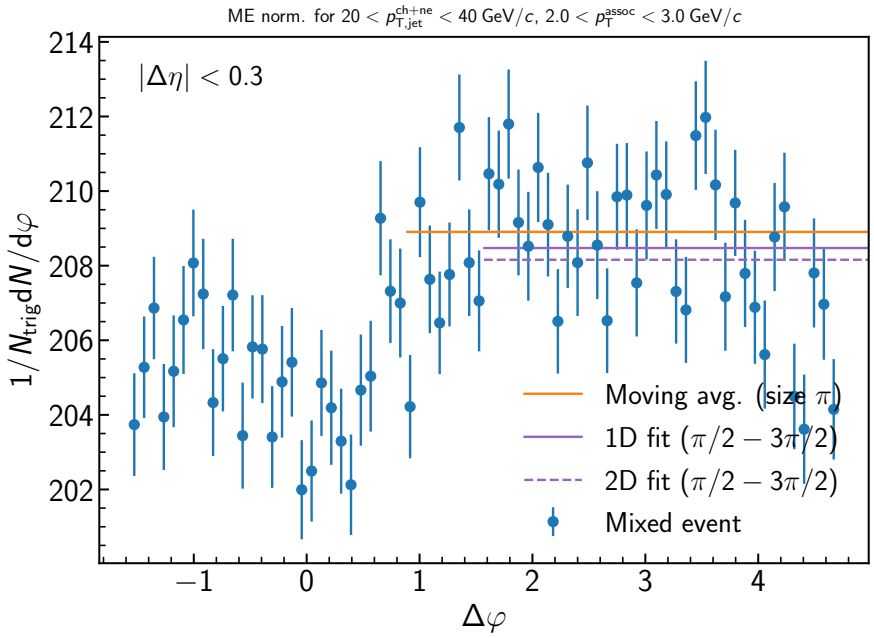

Figure D.16: Determination of the normalization of the mixed event for the inclusive event plane orientation in 30–50% Pb–Pb collisions at $\sqrt{s_{\mathrm{NN}}} = 5.02$ TeV. Here the mixed event is projected over the plateau range in $\Delta\eta$ onto to the $\Delta\varphi$ axis. The moving average is evaluated over the entire $\Delta\varphi$ range using a window of π, while the fit range is fixed from $\pi/2 < \Delta\varphi < 3\pi/2$. Since the mixed events are merged above 2 GeV/c, the normalization factor is also the same for all correlations within $2.0 < p_{\mathrm{T}}^{\mathrm{assoc}} < 3.0$ GeV/c. A variety of normalization methods were evaluated, with further details described in the text.

D.1.5 $20 < p_{\mathrm{T,jet}}^{\mathrm{ch+ne}} < 40\,\mathrm{GeV}/c$, $3.0 < p_{\mathrm{T}}^{\mathrm{assoc}} < 4.0\,\mathrm{GeV}/c$, Inclusive orientation

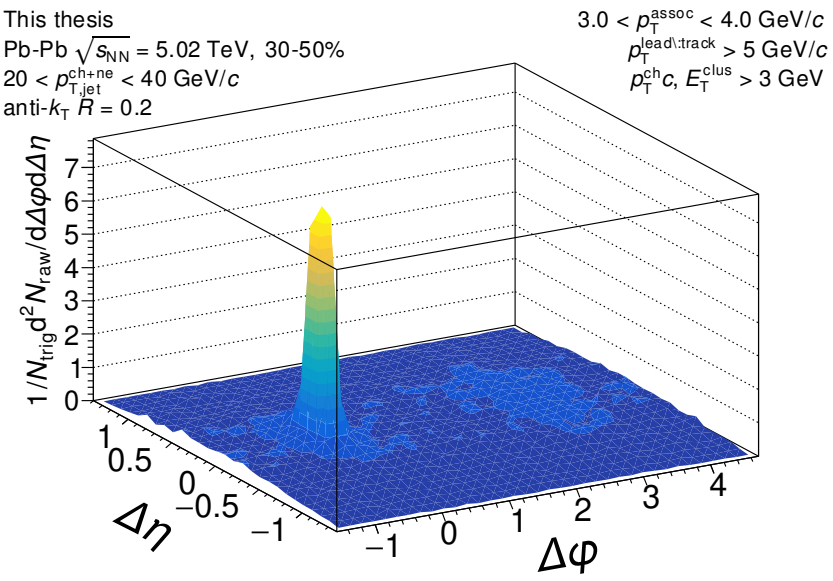

Figure D.17: The measured correlation function with the the efficiency correction $\epsilon(p_{\mathrm{T}}, \eta)$ applied, but before acceptance correction via the mixed events. The correlation is measured for inclusive orientation for $20 < p_{\mathrm{T,jet}}^{\mathrm{ch+ne}} < 40\mathrm{GeV}/c$ jets with $3.0 < p_{\mathrm{T}}^{\mathrm{assoc}} < 4.0\,\mathrm{GeV}/c$ in 30–50% Pb–Pb collisions at $\sqrt{s_{\mathrm{NN}}} = 5.02\,\mathrm{TeV}$.

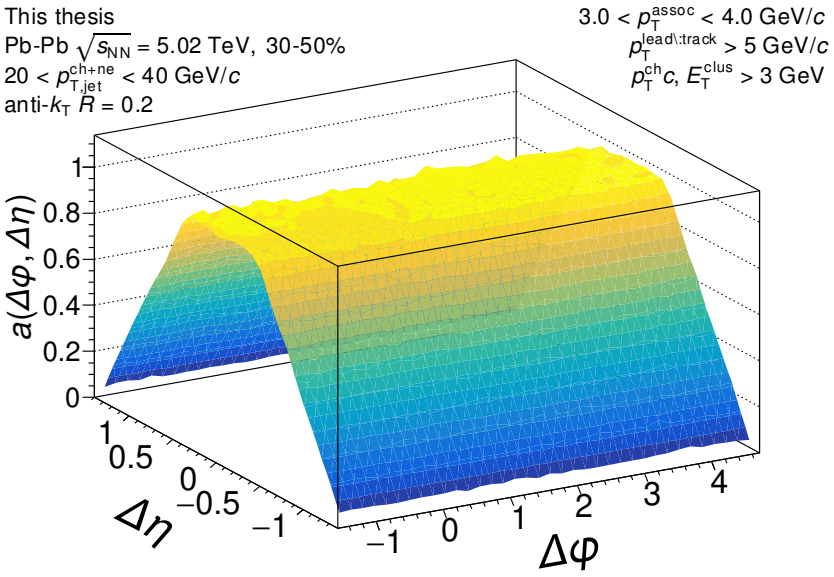

Figure D.18: The mixed event pair acceptance correction with the efficiency correction $\epsilon(p_{\mathrm{T}}, \eta)$ applied. The correlations are measured for inclusive orientation for $20 < p_{\mathrm{T,jet}}^{\mathrm{ch+ne}} < 40\,\mathrm{GeV}/c$ jets with $3.0 < p_{\mathrm{T}}^{\mathrm{assoc}} < 4.0\,\mathrm{GeV}/c$ in 30–50% Pb–Pb collisions at $\sqrt{s_{\mathrm{NN}}} = 5.02\,\mathrm{TeV}$. They have already been normalized such that it they are unity at maximum efficiency. Above 2 GeV/c, the mixed events are merged together to increase statistics, so it is the same for all for correlations within $2.0 \leq p_{\mathrm{T}}^{\mathrm{assoc}} < 10$ GeV/c.

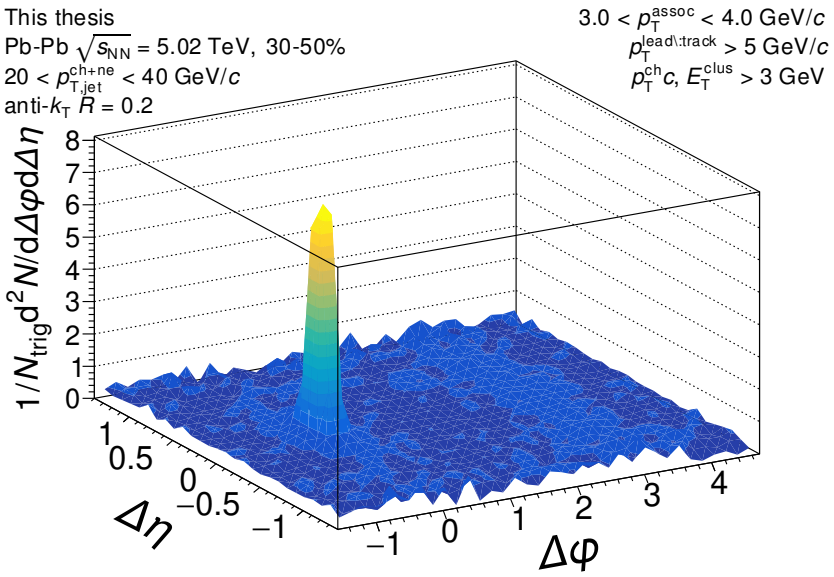

Figure D.19: The signal correlation corrected by pair acceptance. The correlations are measured for inclusive orientation for $20 < p_{\mathrm{T,jet}}^{\mathrm{ch+ne}} < 40\,\mathrm{GeV}/c$ jets with $3.0 < p_{\mathrm{T}}^{\mathrm{assoc}} < 4.0\,\mathrm{GeV}/c$ in 30–50% Pb–Pb collisions at $\sqrt{s_{\mathrm{NN}}} = 5.02\,\mathrm{TeV}$.

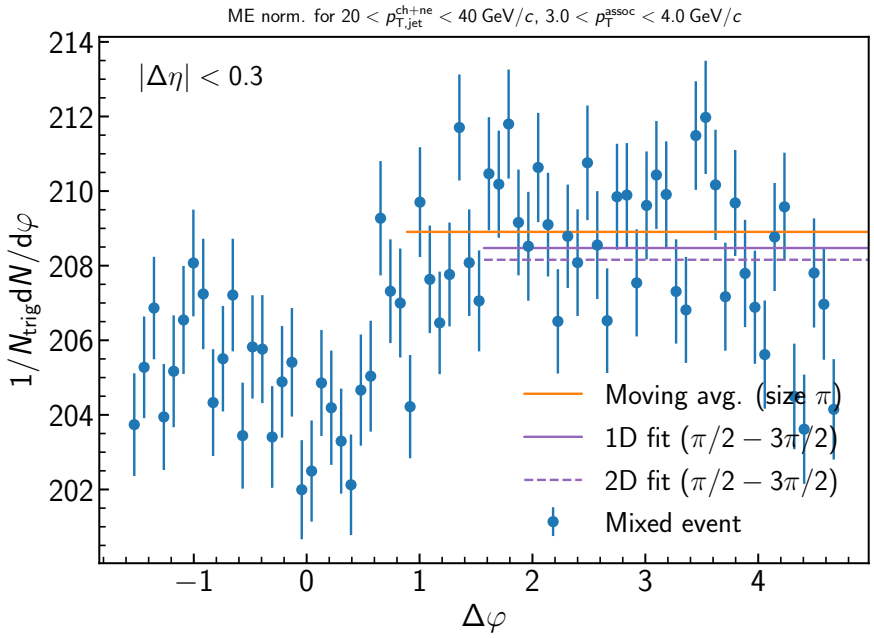

Figure D.20: Determination of the normalization of the mixed event for the inclusive event plane orientation in 30–50% Pb–Pb collisions at $\sqrt{s_{\mathrm{NN}}} = 5.02$ TeV. Here the mixed event is projected over the plateau range in $\Delta\eta$ onto to the $\Delta\varphi$ axis. The moving average is evaluated over the entire $\Delta\varphi$ range using a window of π, while the fit range is fixed from $\pi/2 < \Delta\varphi < 3\pi/2$. Since the mixed events are merged above 2 GeV/c, the normalization factor is also the same for all correlations within $3.0 < p_{\mathrm{T}}^{\mathrm{assoc}} < 4.0$ GeV/c. A variety of normalization methods were evaluated, with further details described in the text.

D.1.6 $20 < p_{\mathrm{T,jet}}^{\mathrm{ch+ne}} < 40\,\mathrm{GeV}/c$, $4.0 < p_{\mathrm{T}}^{\mathrm{assoc}} < 5.0\,\mathrm{GeV}/c$, Inclusive orientation

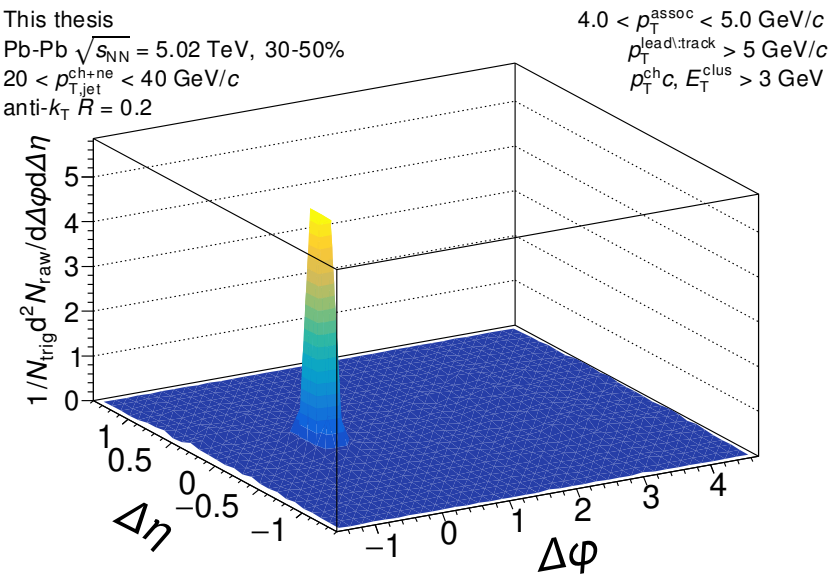

Figure D.21: The measured correlation function with the the efficiency correction $\epsilon(p_{\mathrm{T}}, \eta)$ applied, but before acceptance correction via the mixed events. The correlation is measured for inclusive orientation for $20 < p_{\mathrm{T,jet}}^{\mathrm{ch+ne}} < 40\mathrm{GeV}/c$ jets with $4.0 < p_{\mathrm{T}}^{\mathrm{assoc}} < 5.0\,\mathrm{GeV}/c$ in 30–50% Pb–Pb collisions at $\sqrt{s_{\mathrm{NN}}} = 5.02\,\mathrm{TeV}$.

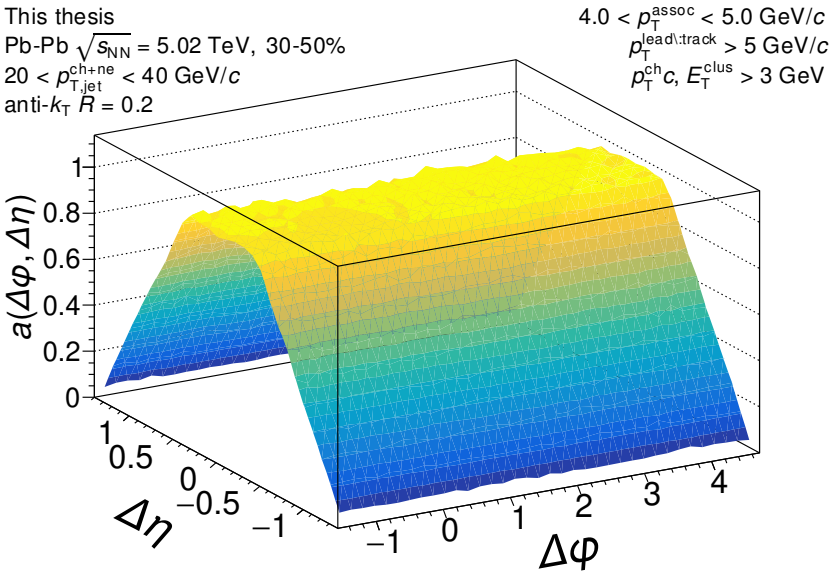

Figure D.22: The mixed event pair acceptance correction with the efficiency correction $\epsilon(p_{\mathrm{T}}, \eta)$ applied. The correlations are measured for inclusive orientation for $20 < p_{\mathrm{T,jet}}^{\mathrm{ch+ne}} < 40\,\mathrm{GeV}/c$ jets with $4.0 < p_{\mathrm{T}}^{\mathrm{assoc}} < 5.0\,\mathrm{GeV}/c$ in 30–50% Pb–Pb collisions at $\sqrt{s_{\mathrm{NN}}} = 5.02\,\mathrm{TeV}$. They have already been normalized such that it they are unity at maximum efficiency. Above 2 GeV/c, the mixed events are merged together to increase statistics, so it is the same for all for correlations within $2.0 \leq p_{\mathrm{T}}^{\mathrm{assoc}} < 10$ GeV/c.

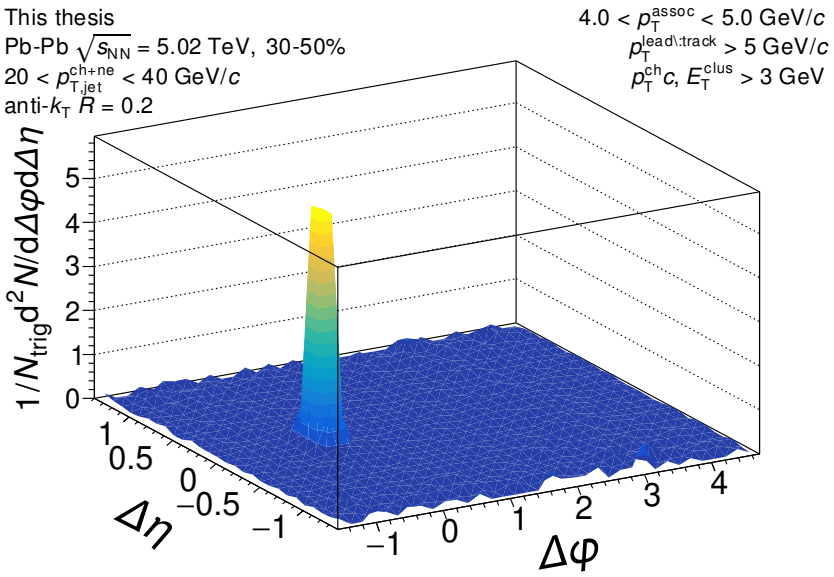

Figure D.23: The signal correlation corrected by pair acceptance. The correlations are measured for inclusive orientation for $20 < p_{\mathrm{T,jet}}^{\mathrm{ch+ne}} < 40\,\mathrm{GeV}/c$ jets with $4.0 < p_{\mathrm{T}}^{\mathrm{assoc}} < 5.0\,\mathrm{GeV}/c$ in 30–50% Pb–Pb collisions at $\sqrt{s_{\mathrm{NN}}} = 5.02\,\mathrm{TeV}$.

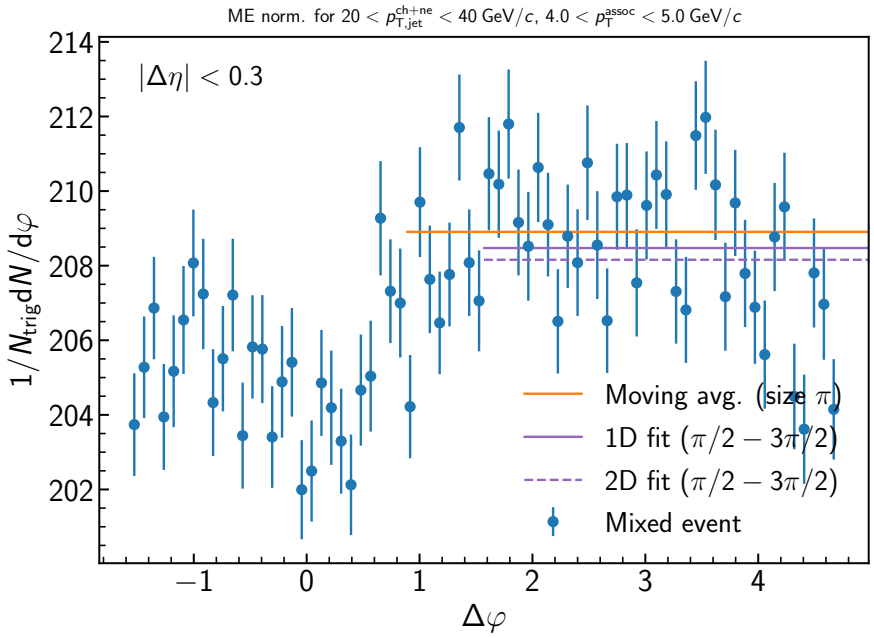

Figure D.24: Determination of the normalization of the mixed event for the inclusive event plane orientation in 30–50% Pb–Pb collisions at $\sqrt{s_{\mathrm{NN}}} = 5.02$ TeV. Here the mixed event is projected over the plateau range in $\Delta\eta$ onto to the $\Delta\varphi$ axis. The moving average is evaluated over the entire $\Delta\varphi$ range using a window of π, while the fit range is fixed from $\pi/2 < \Delta\varphi < 3\pi/2$. Since the mixed events are merged above 2 GeV/c, the normalization factor is also the same for all correlations within $4.0 < p_{\mathrm{T}}^{\mathrm{assoc}} < 5.0$ GeV/c. A variety of normalization methods were evaluated, with further details described in the text.

D.1.7 $20 < p_{\mathrm{T,jet}}^{\mathrm{ch+ne}} < 40\,\mathrm{GeV}/c$, $5.0 < p_{\mathrm{T}}^{\mathrm{assoc}} < 6.0\,\mathrm{GeV}/c$, Inclusive orientation

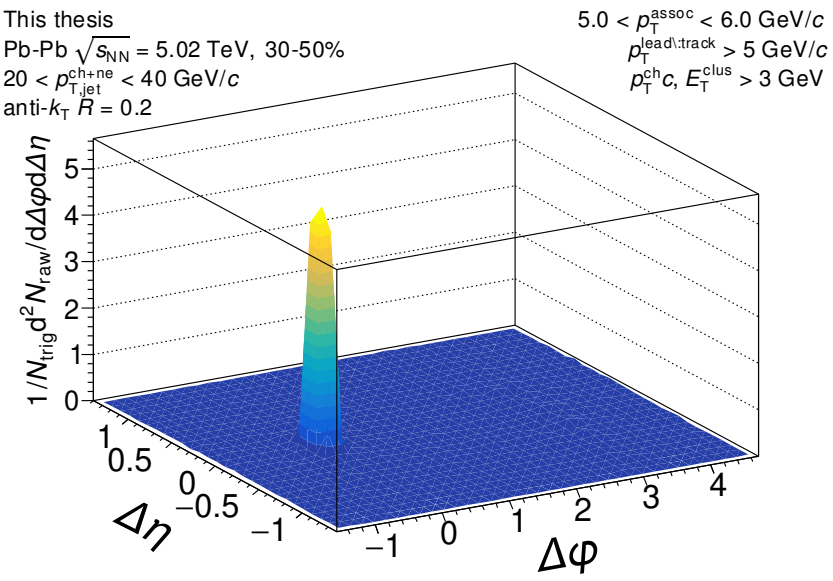

Figure D.25: The measured correlation function with the the efficiency correction $\epsilon(p_{\mathrm{T}}, \eta)$ applied, but before acceptance correction via the mixed events. The correlation is measured for inclusive orientation for $20 < p_{\mathrm{T,jet}}^{\mathrm{ch+ne}} < 40\mathrm{GeV}/c$ jets with $5.0 < p_{\mathrm{T}}^{\mathrm{assoc}} < 6.0\,\mathrm{GeV}/c$ in 30–50% Pb–Pb collisions at $\sqrt{s_{\mathrm{NN}}} = 5.02\,\mathrm{TeV}$.

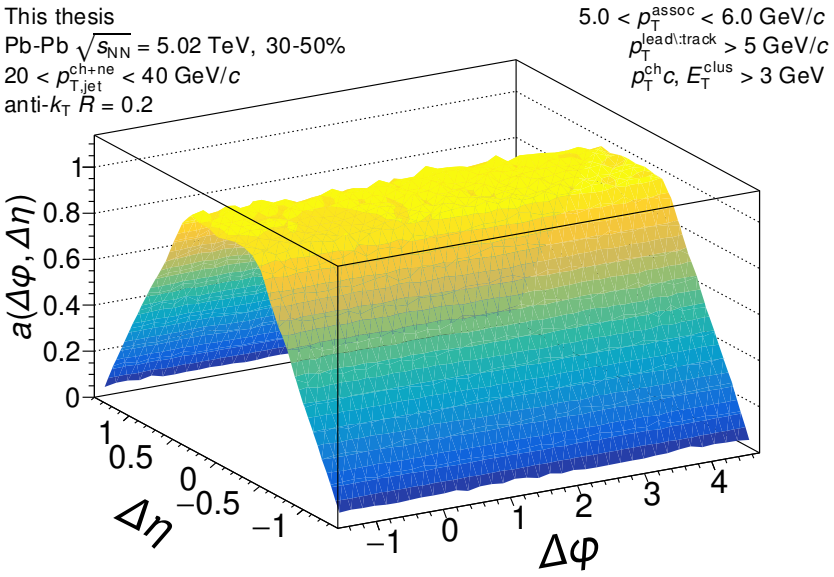

Figure D.26: The mixed event pair acceptance correction with the efficiency correction $\epsilon(p_{\mathrm{T}}, \eta)$ applied. The correlations are measured for inclusive orientation for $20 < p_{\mathrm{T,jet}}^{\mathrm{ch+ne}} < 40\,\mathrm{GeV}/c$ jets with $5.0 < p_{\mathrm{T}}^{\mathrm{assoc}} < 6.0\,\mathrm{GeV}/c$ in 30–50% Pb–Pb collisions at $\sqrt{s_{\mathrm{NN}}} = 5.02\,\mathrm{TeV}$. They have already been normalized such that it they are unity at maximum efficiency. Above 2 GeV/c, the mixed events are merged together to increase statistics, so it is the same for all for correlations within $2.0 \leq p_{\mathrm{T}}^{\mathrm{assoc}} < 10$ GeV/c.

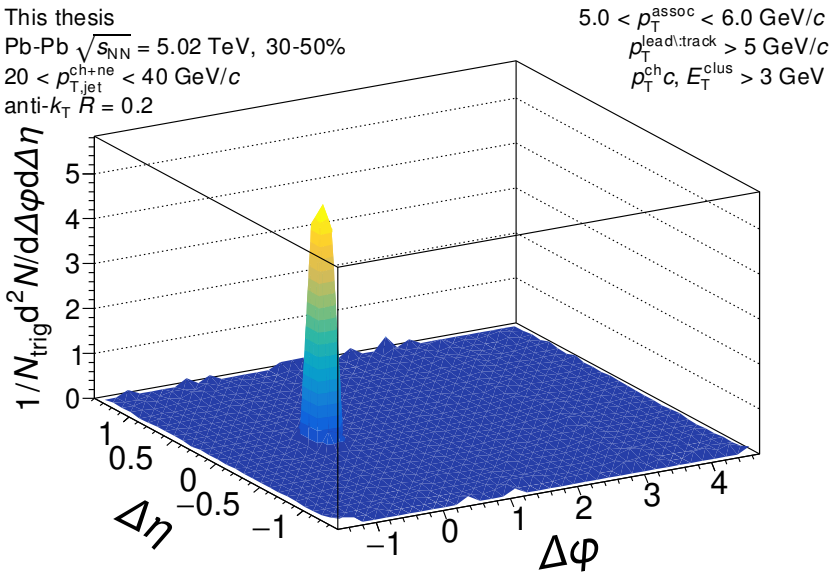

Figure D.27: The signal correlation corrected by pair acceptance. The correlations are measured for inclusive orientation for $20 < p_{\mathrm{T,jet}}^{\mathrm{ch+ne}} < 40\,\mathrm{GeV}/c$ jets with $5.0 < p_{\mathrm{T}}^{\mathrm{assoc}} < 6.0\,\mathrm{GeV}/c$ in 30–50% Pb–Pb collisions at $\sqrt{s_{\mathrm{NN}}} = 5.02\,\mathrm{TeV}$.

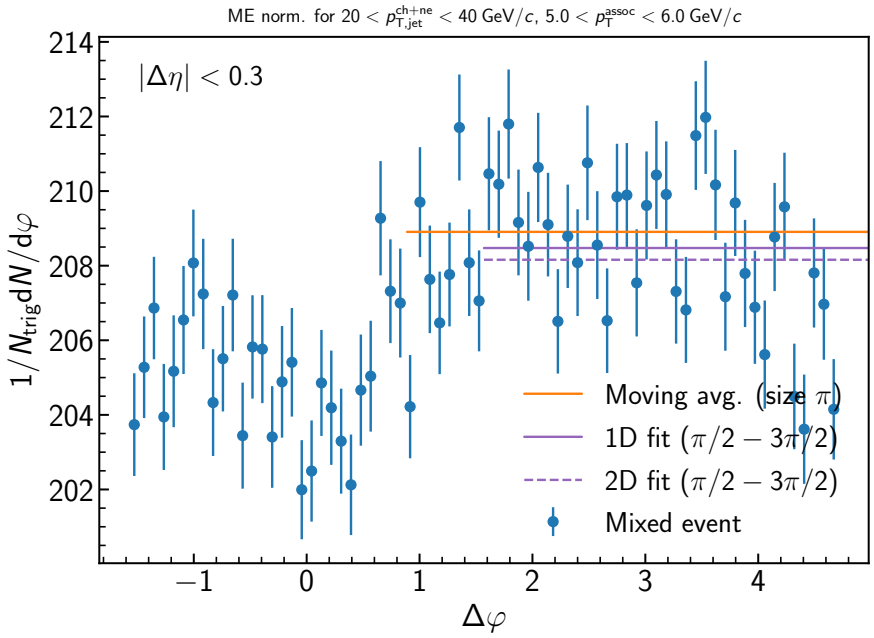

Figure D.28: Determination of the normalization of the mixed event for the inclusive event plane orientation in 30–50% Pb–Pb collisions at $\sqrt{s_{\mathrm{NN}}} = 5.02$ TeV. Here the mixed event is projected over the plateau range in $\Delta\eta$ onto to the $\Delta\varphi$ axis. The moving average is evaluated over the entire $\Delta\varphi$ range using a window of π, while the fit range is fixed from $\pi/2 < \Delta\varphi < 3\pi/2$. Since the mixed events are merged above 2 GeV/c, the normalization factor is also the same for all correlations within $5.0 < p_{\mathrm{T}}^{\mathrm{assoc}} < 6.0$ GeV/c. A variety of normalization methods were evaluated, with further details described in the text.

D.1.8 $20 < p_{\mathrm{T,jet}}^{\mathrm{ch+ne}} < 40\mathrm{GeV}/c$, $6.0 < p_{\mathrm{T}}^{\mathrm{assoc}} < 10.0\mathrm{GeV}/c$, Inclusive orientation

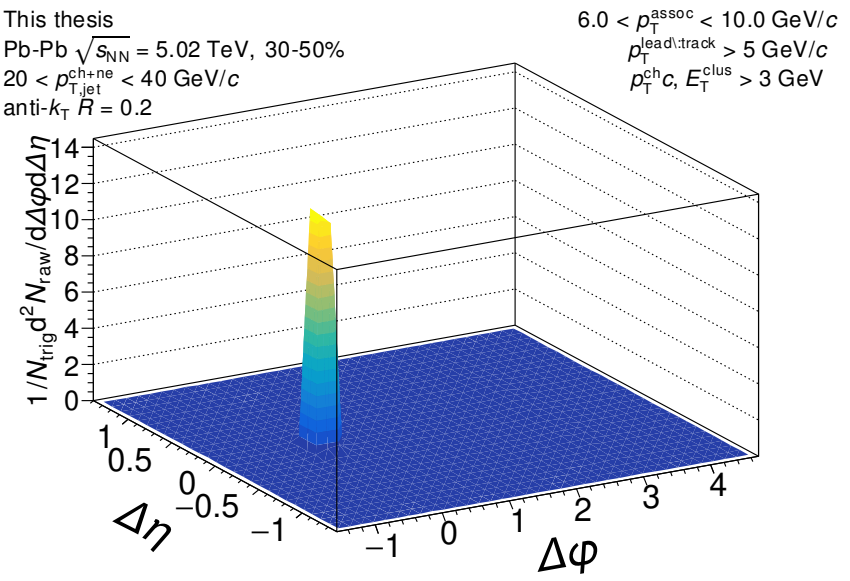

Figure D.29: The measured correlation function with the the efficiency correction $\epsilon(p_{\mathrm{T}}, \eta)$ applied, but before acceptance correction via the mixed events. The correlation is measured for inclusive orientation for $20 < p_{\mathrm{T,jet}}^{\mathrm{ch+ne}} < 40\mathrm{GeV}/c$ jets with $6.0 < p_{\mathrm{T}}^{\mathrm{assoc}} < 10.0\,\mathrm{GeV}/c$ in 30–50% Pb–Pb collisions at $\sqrt{s_{\mathrm{NN}}} = 5.02\,\mathrm{TeV}$.

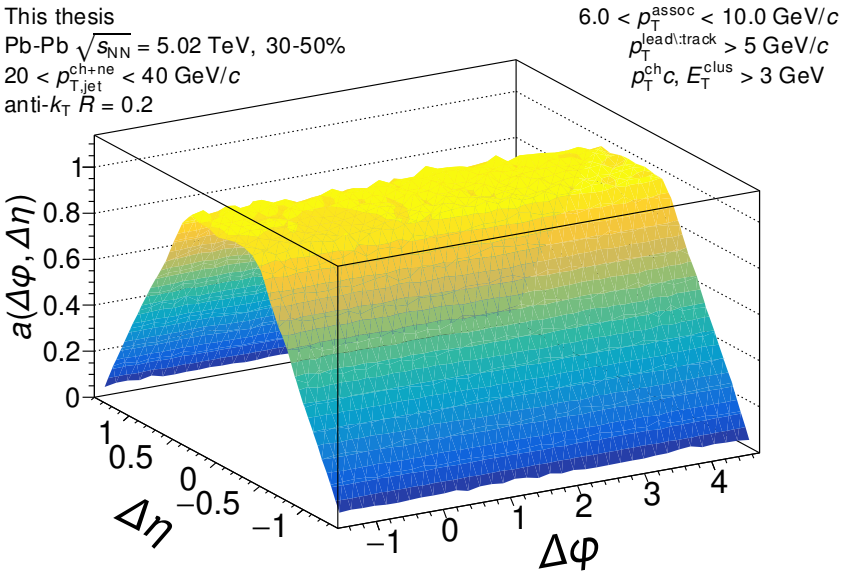

Figure D.30: The mixed event pair acceptance correction with the efficiency correction $\epsilon(p_T, \eta)$ applied. The correlations are measured for inclusive orientation for $20 < p_{T,jet}^{ch+ne} < 40$ GeV/c jets with $6.0 < p_T^{assoc} < 10.0$ GeV/c in 30–50% Pb–Pb collisions at $\sqrt{s_{NN}} = 5.02$ TeV. They have already been normalized such that it they are unity at maximum efficiency. Above 2 GeV/c, the mixed events are merged together to increase statistics, so it is the same for all for correlations within $2.0 \leq p_T^{assoc} < 10$ GeV/c.

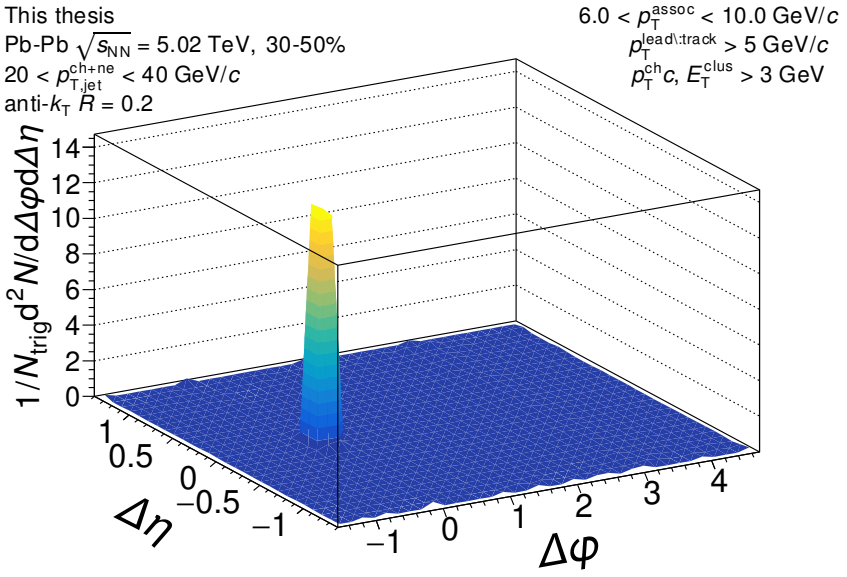

Figure D.31: The signal correlation corrected by pair acceptance. The correlations are measured for inclusive orientation for $20 < p_{T,jet}^{ch+ne} < 40$ GeV/c jets with $6.0 < p_T^{assoc} < 10.0$ GeV/c in 30–50% Pb–Pb collisions at $\sqrt{s_{NN}} = 5.02$ TeV.

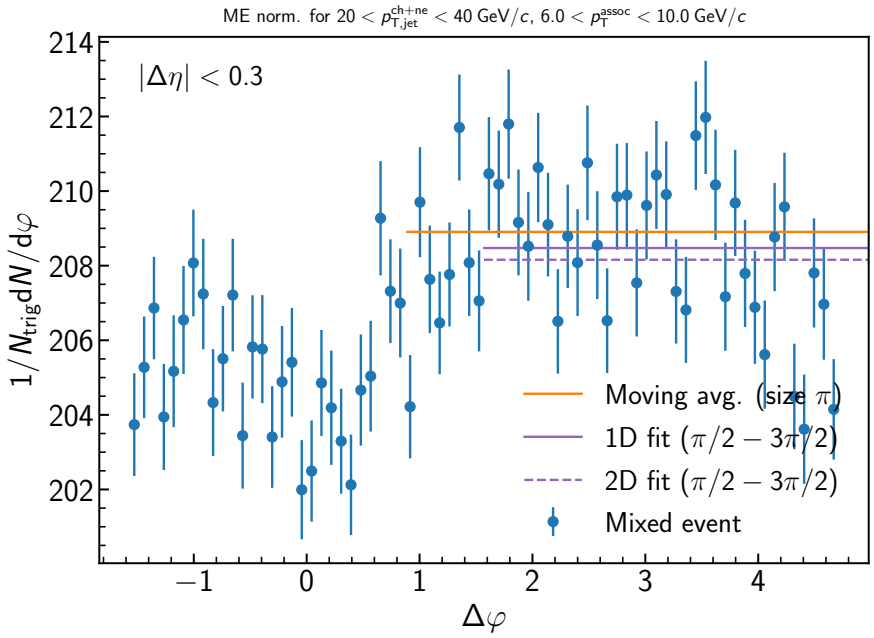

Figure D.32: Determination of the normalization of the mixed event for the inclusive event plane orientation in 30–50% Pb–Pb collisions at $\sqrt{s_{\mathrm{NN}}} = 5.02$ TeV. Here the mixed event is projected over the plateau range in $\Delta\eta$ onto to the $\Delta\varphi$ axis. The moving average is evaluated over the entire $\Delta\varphi$ range using a window of π, while the fit range is fixed from $\pi/2 < \Delta\varphi < 3\pi/2$. Since the mixed events are merged above 2 GeV/c, the normalization factor is also the same for all correlations within $6.0 < p_{\mathrm{T}}^{\mathrm{assoc}} < 10.0$ GeV/c. A variety of normalization methods were evaluated, with further details described in the text.

D.1.9 $20 < p_{\mathrm{T,jet}}^{\mathrm{ch+ne}} < 40\ \mathrm{GeV}/c$, $0.5 < p_{\mathrm{T}}^{\mathrm{assoc}} < 1.0\ \mathrm{GeV}/c$, In-plane orientation

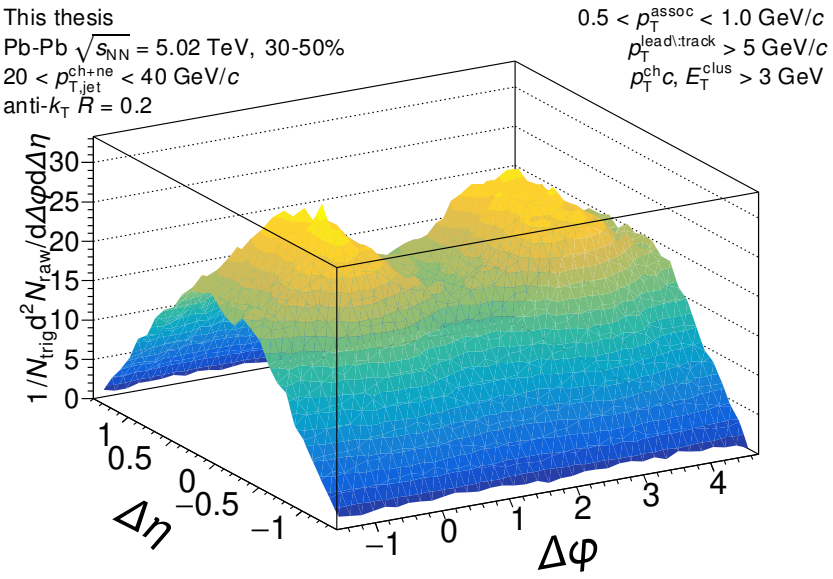

Figure D.33: The measured correlation function with the the efficiency correction $\epsilon(p_{\mathrm{T}}, \eta)$ applied, but before acceptance correction via the mixed events. The correlation is measured for in-plane orientation for $20 < p_{\mathrm{T,jet}}^{\mathrm{ch+ne}} < 40\,\mathrm{GeV}/c$ jets with $0.5 < p_{\mathrm{T}}^{\mathrm{assoc}} < 1.0\ \mathrm{GeV}/c$ in 30–50% Pb–Pb collisions at $\sqrt{s_{\mathrm{NN}}} = 5.02$ TeV.

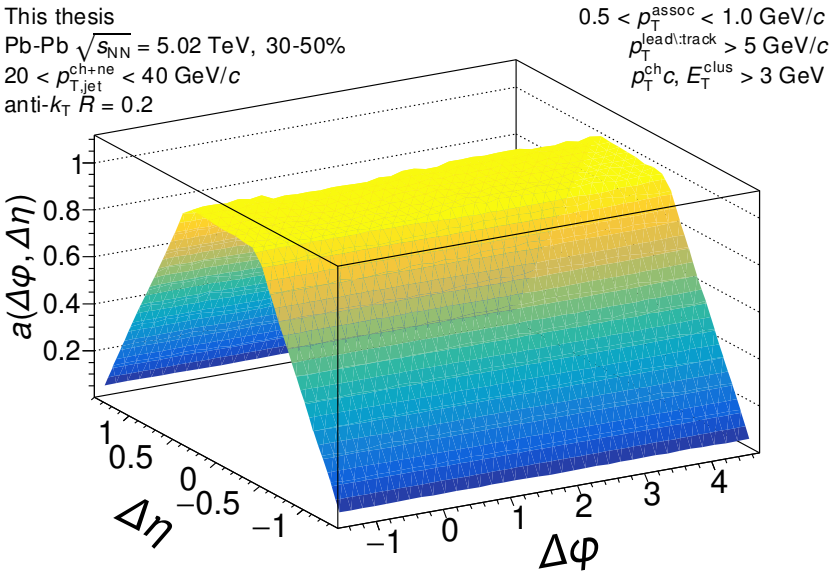

Figure D.34: The mixed event pair acceptance correction with the efficiency correction $\epsilon(p_{\mathrm{T}}, \eta)$ applied. The correlations are measured for in-plane orientation for $20 < p_{\mathrm{T,jet}}^{\mathrm{ch+ne}} < 40$ GeV/c jets with $0.5 < p_{\mathrm{T}}^{\mathrm{assoc}} < 1.0$ GeV/c in 30–50% Pb–Pb collisions at $\sqrt{s_{\mathrm{NN}}} = 5.02$ TeV. They have already been normalized such that it they are unity at maximum efficiency. Above 2 GeV/c, the mixed events are merged together to increase statistics, so it is the same for all for correlations within $2.0 \leq p_{\mathrm{T}}^{\mathrm{assoc}} < 10$ GeV/c.

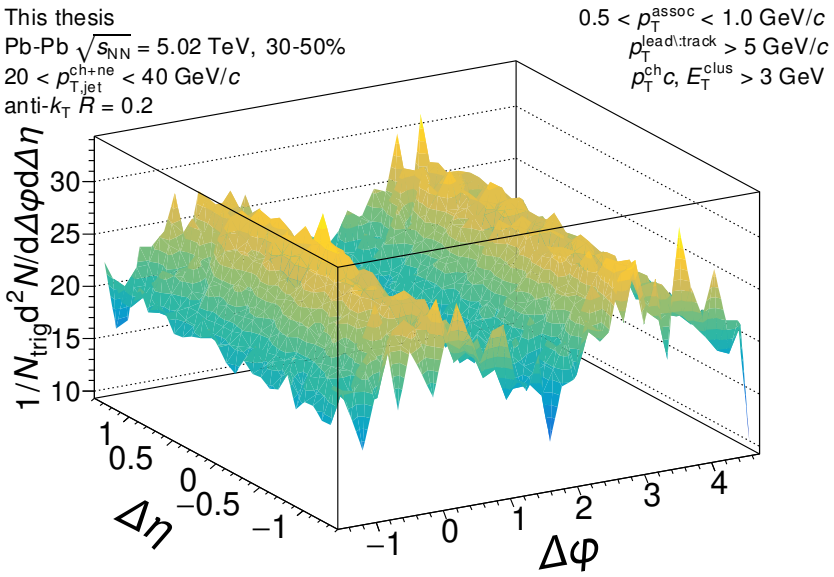

Figure D.35: The signal correlation corrected by pair acceptance. The correlations are measured for in-plane orientation for $20 < p_{\mathrm{T,jet}}^{\mathrm{ch+ne}} < 40$ GeV/c jets with $0.5 < p_{\mathrm{T}}^{\mathrm{assoc}} < 1.0$ GeV/c in 30–50% Pb–Pb collisions at $\sqrt{s_{\mathrm{NN}}} = 5.02$ TeV.

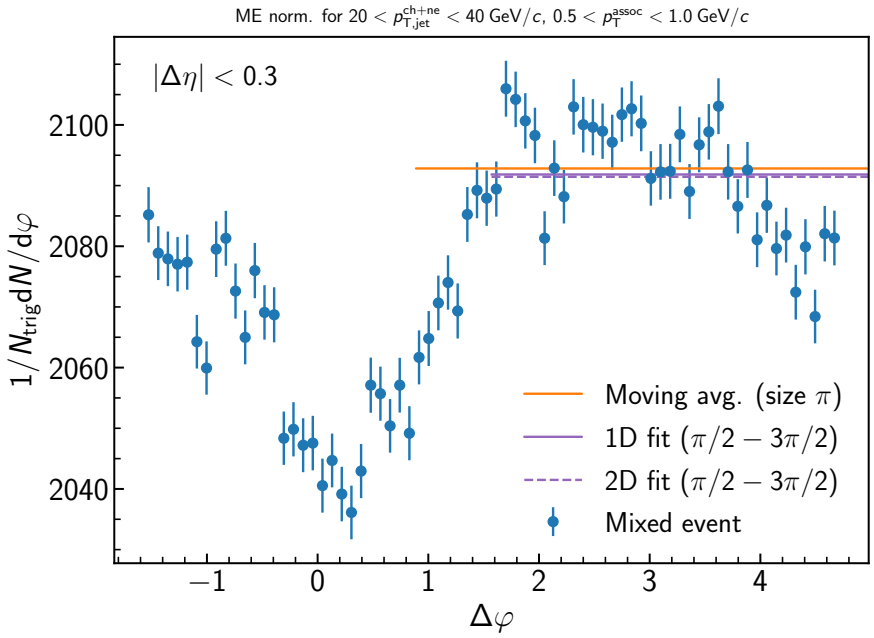

Figure D.36: Determination of the normalization of the mixed event for the inclusive event plane orientation in 30–50% Pb–Pb collisions at $\sqrt{s_{\mathrm{NN}}} = 5.02$ TeV. Here the mixed event is projected over the plateau range in $\Delta\eta$ onto to the $\Delta\varphi$ axis. The moving average is evaluated over the entire $\Delta\varphi$ range using a window of π, while the fit range is fixed from $\pi/2 < \Delta\varphi < 3\pi/2$. Since the mixed events are merged above 2 GeV/c, the normalization factor is also the same for all correlations within $0.5 < p_{\mathrm{T}}^{\mathrm{assoc}} < 1.0$ GeV/c. A variety of normalization methods were evaluated, with further details described in the text.

D.1.10 $20 < p_{\mathrm{T,jet}}^{\mathrm{ch+ne}} < 40\,\mathrm{GeV}/c$, $1.0 < p_{\mathrm{T}}^{\mathrm{assoc}} < 1.5\,\mathrm{GeV}/c$, In-plane orientation

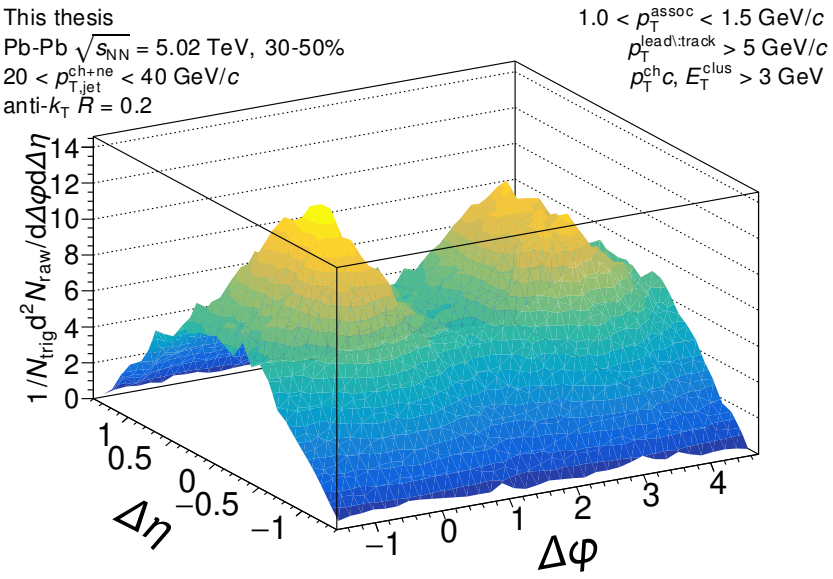

Figure D.37: The measured correlation function with the the efficiency correction $\epsilon(p_{\mathrm{T}}, \eta)$ applied, but before acceptance correction via the mixed events. The correlation is measured for in-plane orientation for $20 < p_{\mathrm{T,jet}}^{\mathrm{ch+ne}} < 40\,\mathrm{GeV}/c$ jets with $1.0 < p_{\mathrm{T}}^{\mathrm{assoc}} < 1.5\,\mathrm{GeV}/c$ in 30–50% Pb–Pb collisions at $\sqrt{s_{\mathrm{NN}}} = 5.02$ TeV.

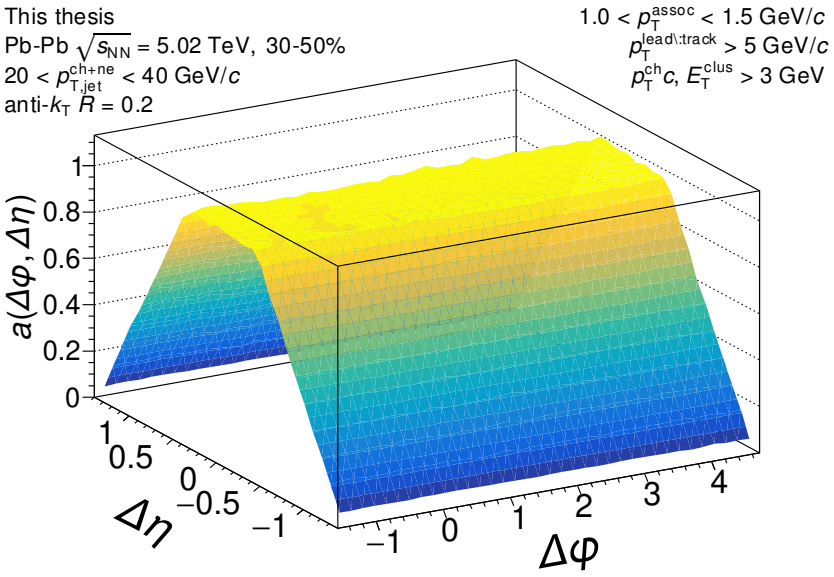

Figure D.38: The mixed event pair acceptance correction with the efficiency correction $\epsilon(p_{\mathrm{T}}, \eta)$ applied. The correlations are measured for in-plane orientation for $20 < p_{\mathrm{T,jet}}^{\mathrm{ch+ne}} < 40$ GeV/c jets with $1.0 < p_{\mathrm{T}}^{\mathrm{assoc}} < 1.5$ GeV/c in 30–50% Pb–Pb collisions at $\sqrt{s_{\mathrm{NN}}} = 5.02$ TeV. They have already been normalized such that it they are unity at maximum efficiency. Above 2 GeV/c, the mixed events are merged together to increase statistics, so it is the same for all for correlations within $2.0 \leq p_{\mathrm{T}}^{\mathrm{assoc}} < 10$ GeV/c.

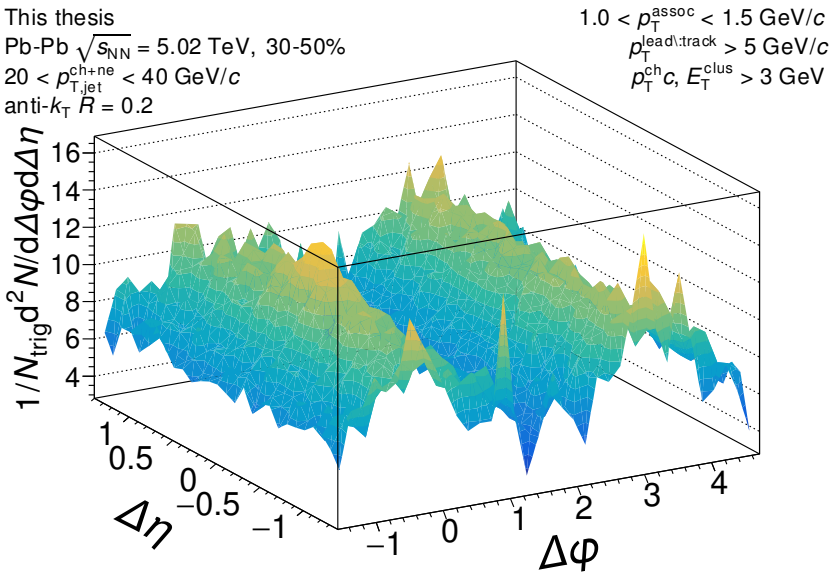

Figure D.39: The signal correlation corrected by pair acceptance. The correlations are measured for in-plane orientation for $20 < p_{\mathrm{T,jet}}^{\mathrm{ch+ne}} < 40$ GeV/c jets with $1.0 < p_{\mathrm{T}}^{\mathrm{assoc}} < 1.5$ GeV/c in 30–50% Pb–Pb collisions at $\sqrt{s_{\mathrm{NN}}} = 5.02$ TeV.

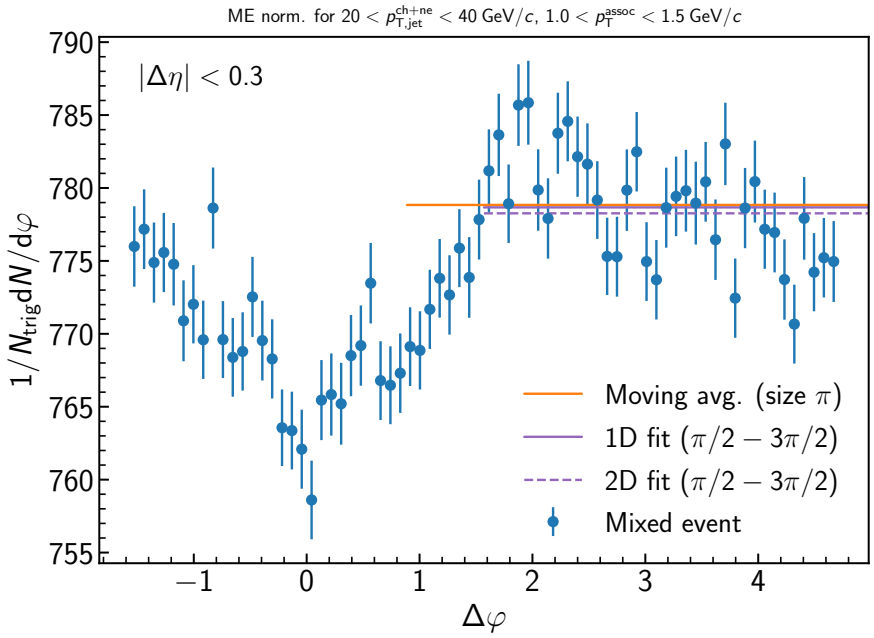

Figure D.40: Determination of the normalization of the mixed event for the inclusive event plane orientation in 30–50% Pb–Pb collisions at $\sqrt{s_{\mathrm{NN}}} = 5.02$ TeV. Here the mixed event is projected over the plateau range in $\Delta\eta$ onto to the $\Delta\varphi$ axis. The moving average is evaluated over the entire $\Delta\varphi$ range using a window of π, while the fit range is fixed from $\pi/2 < \Delta\varphi < 3\pi/2$. Since the mixed events are merged above 2 GeV/c, the normalization factor is also the same for all correlations within $1.0 < p_{\mathrm{T}}^{\mathrm{assoc}} < 1.5$ GeV/c. A variety of normalization methods were evaluated, with further details described in the text.

D.1.11 $20 < p_{\mathrm{T,jet}}^{\mathrm{ch+ne}} < 40\,\mathrm{GeV}/c$, $1.5 < p_{\mathrm{T}}^{\mathrm{assoc}} < 2.0\,\mathrm{GeV}/c$, In-plane orientation

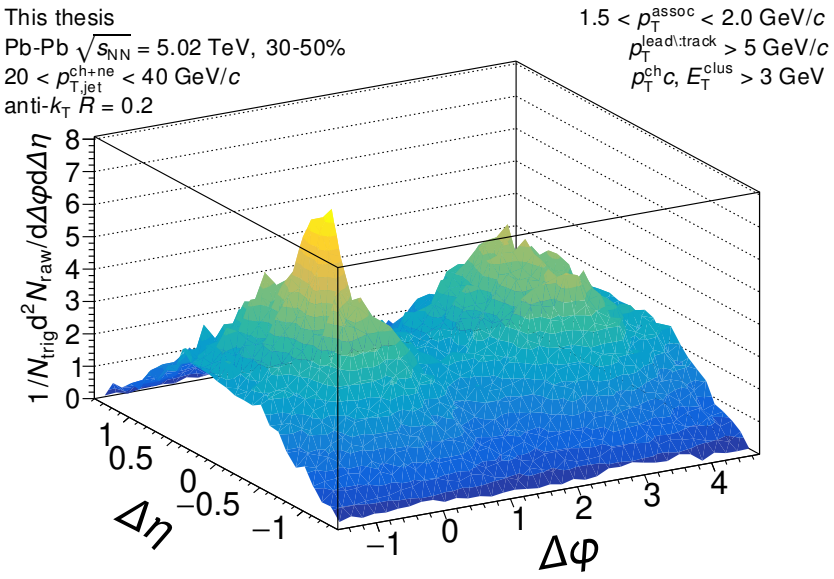

Figure D.41: The measured correlation function with the the efficiency correction $\epsilon(p_{\mathrm{T}}, \eta)$ applied, but before acceptance correction via the mixed events. The correlation is measured for in-plane orientation for $20 < p_{\mathrm{T,jet}}^{\mathrm{ch+ne}} < 40\,\mathrm{GeV}/c$ jets with $1.5 < p_{\mathrm{T}}^{\mathrm{assoc}} < 2.0\,\mathrm{GeV}/c$ in 30–50% Pb–Pb collisions at $\sqrt{s_{\mathrm{NN}}} = 5.02\,\mathrm{TeV}$.

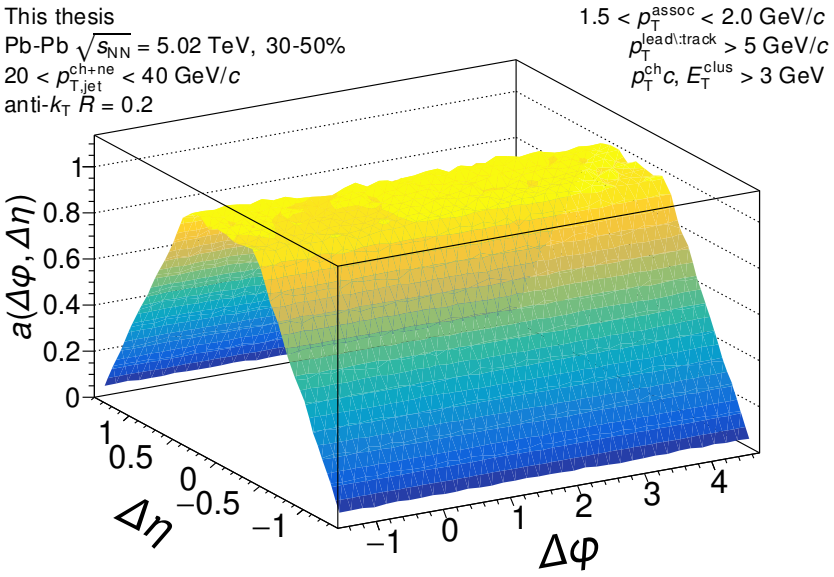

Figure D.42: The mixed event pair acceptance correction with the efficiency correction $\epsilon(p_{\mathrm{T}}, \eta)$ applied. The correlations are measured for in-plane orientation for $20 < p_{\mathrm{T,jet}}^{\mathrm{ch+ne}} < 40\,\mathrm{GeV}/c$ jets with $1.5 < p_{\mathrm{T}}^{\mathrm{assoc}} < 2.0\,\mathrm{GeV}/c$ in 30–50% Pb–Pb collisions at $\sqrt{s_{\mathrm{NN}}} = 5.02\,\mathrm{TeV}$. They have already been normalized such that it they are unity at maximum efficiency. Above 2 GeV/c, the mixed events are merged together to increase statistics, so it is the same for all for correlations within $2.0 \leq p_{\mathrm{T}}^{\mathrm{assoc}} < 10$ GeV/c.

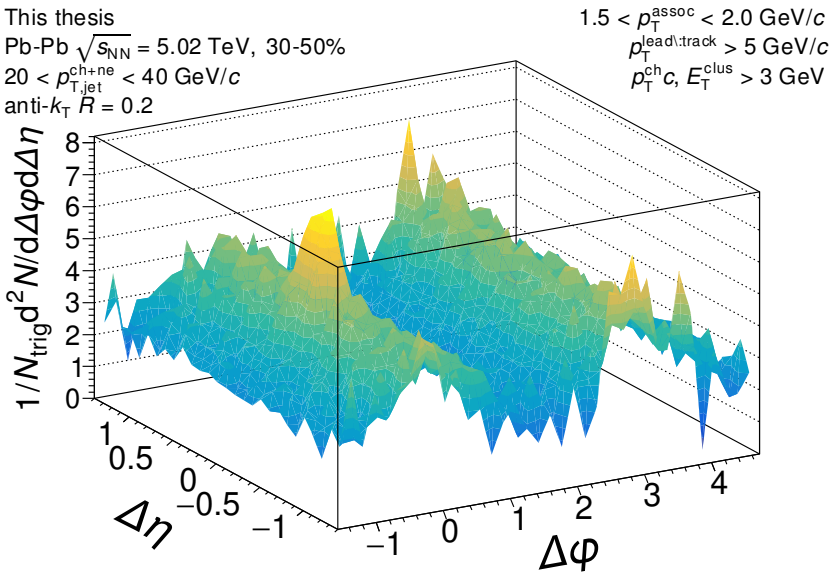

Figure D.43: The signal correlation corrected by pair acceptance. The correlations are measured for in-plane orientation for $20 < p_{\mathrm{T,jet}}^{\mathrm{ch+ne}} < 40\,\mathrm{GeV}/c$ jets with $1.5 < p_{\mathrm{T}}^{\mathrm{assoc}} < 2.0\,\mathrm{GeV}/c$ in 30–50% Pb–Pb collisions at $\sqrt{s_{\mathrm{NN}}} = 5.02\,\mathrm{TeV}$.

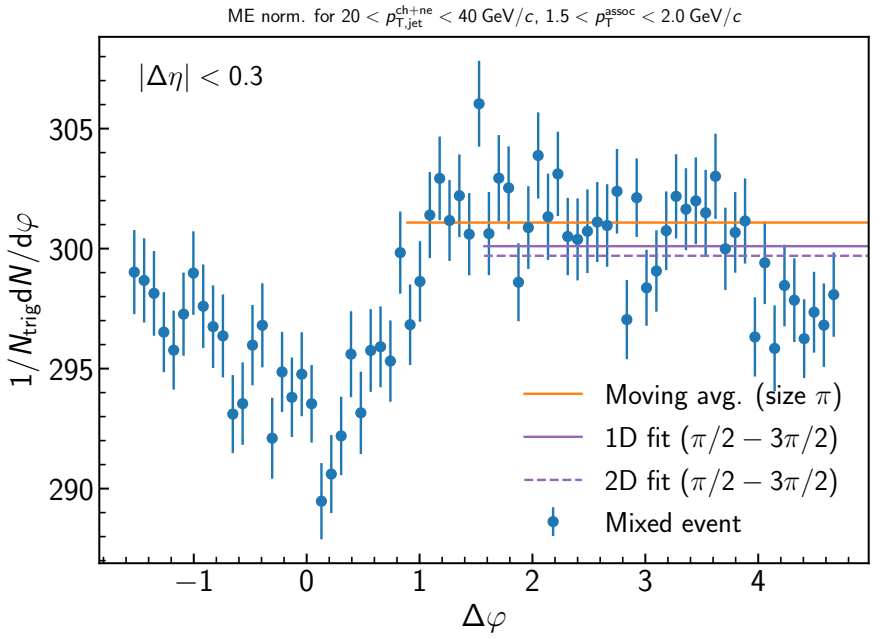

Figure D.44: Determination of the normalization of the mixed event for the inclusive event plane orientation in 30–50% Pb–Pb collisions at $\sqrt{s_{\mathrm{NN}}} = 5.02$ TeV. Here the mixed event is projected over the plateau range in $\Delta\eta$ onto to the $\Delta\varphi$ axis. The moving average is evaluated over the entire $\Delta\varphi$ range using a window of π, while the fit range is fixed from $\pi/2 < \Delta\varphi < 3\pi/2$. Since the mixed events are merged above 2 GeV/c, the normalization factor is also the same for all correlations within $1.5 < p_{\mathrm{T}}^{\mathrm{assoc}} < 2.0$ GeV/c. A variety of normalization methods were evaluated, with further details described in the text.

D.1.12 $20 < p_{\mathrm{T,jet}}^{\mathrm{ch+ne}} < 40\,\mathrm{GeV}/c$, $2.0 < p_{\mathrm{T}}^{\mathrm{assoc}} < 3.0\,\mathrm{GeV}/c$, In-plane orientation

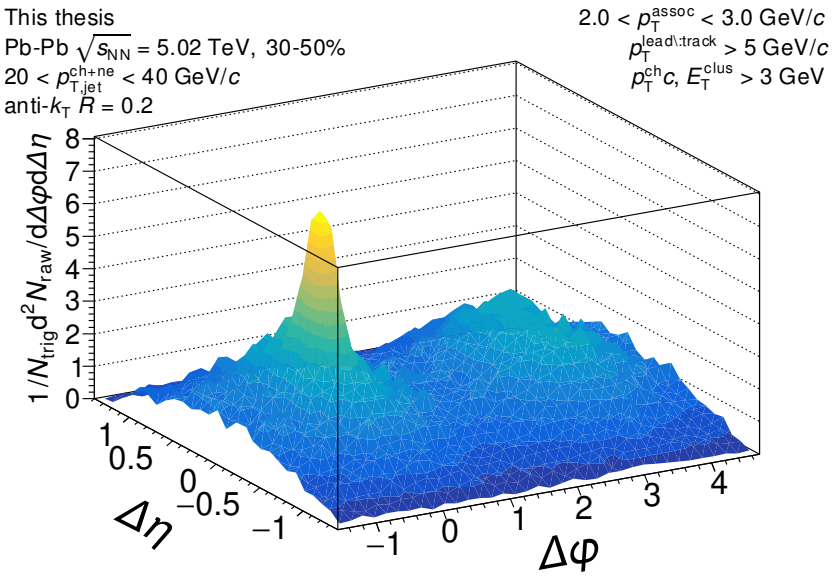

Figure D.45: The measured correlation function with the the efficiency correction $\epsilon(p_{\mathrm{T}}, \eta)$ applied, but before acceptance correction via the mixed events. The correlation is measured for in-plane orientation for $20 < p_{\mathrm{T,jet}}^{\mathrm{ch+ne}} < 40\,\mathrm{GeV}/c$ jets with $2.0 < p_{\mathrm{T}}^{\mathrm{assoc}} < 3.0\,\mathrm{GeV}/c$ in 30–50% Pb–Pb collisions at $\sqrt{s_{\mathrm{NN}}} = 5.02\,\mathrm{TeV}$.

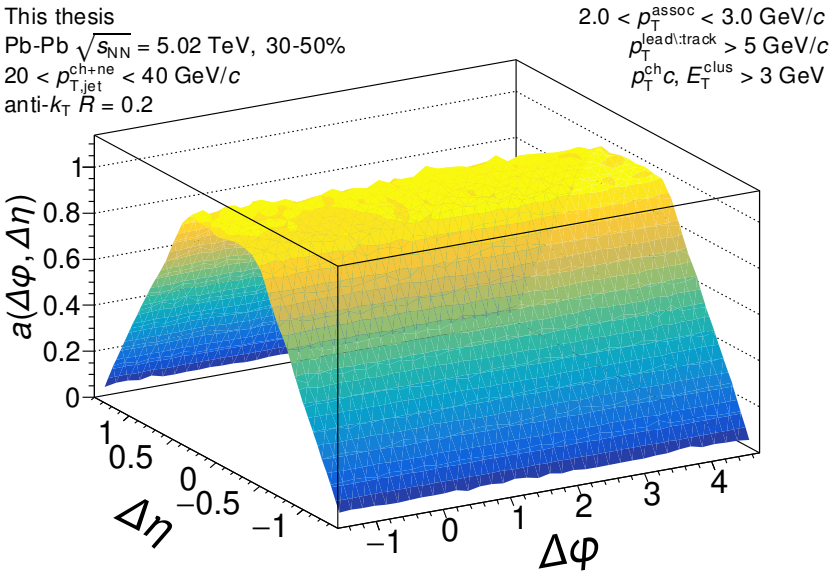

Figure D.46: The mixed event pair acceptance correction with the efficiency correction $\epsilon(p_{\mathrm{T}}, \eta)$ applied. The correlations are measured for in-plane orientation for $20 < p_{\mathrm{T,jet}}^{\mathrm{ch+ne}} < 40$ GeV/c jets with $2.0 < p_{\mathrm{T}}^{\mathrm{assoc}} < 3.0$ GeV/c in 30–50% Pb–Pb collisions at $\sqrt{s_{\mathrm{NN}}} = 5.02$ TeV. They have already been normalized such that it they are unity at maximum efficiency. Above 2 GeV/c, the mixed events are merged together to increase statistics, so it is the same for all for correlations within $2.0 \leq p_{\mathrm{T}}^{\mathrm{assoc}} < 10$ GeV/c.

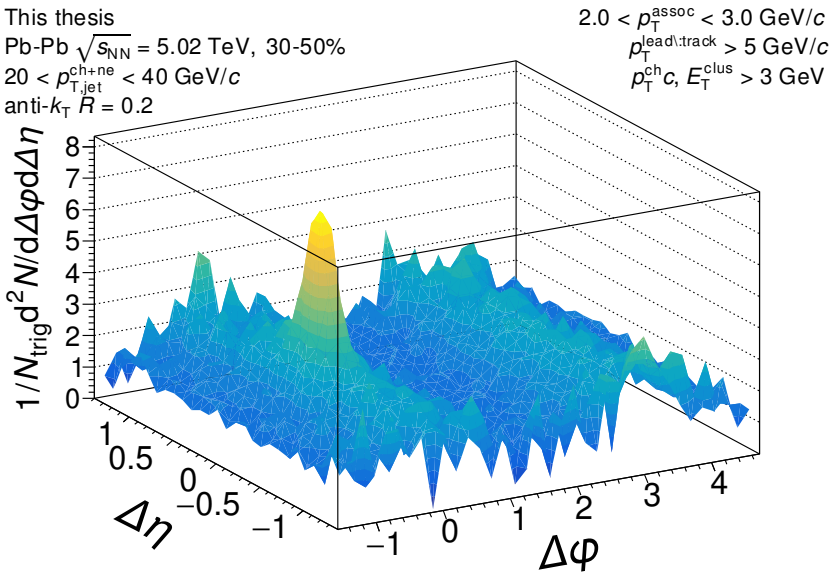

Figure D.47: The signal correlation corrected by pair acceptance. The correlations are measured for in-plane orientation for $20 < p_{\mathrm{T,jet}}^{\mathrm{ch+ne}} < 40$ GeV/c jets with $2.0 < p_{\mathrm{T}}^{\mathrm{assoc}} < 3.0$ GeV/c in 30–50% Pb–Pb collisions at $\sqrt{s_{\mathrm{NN}}} = 5.02$ TeV.

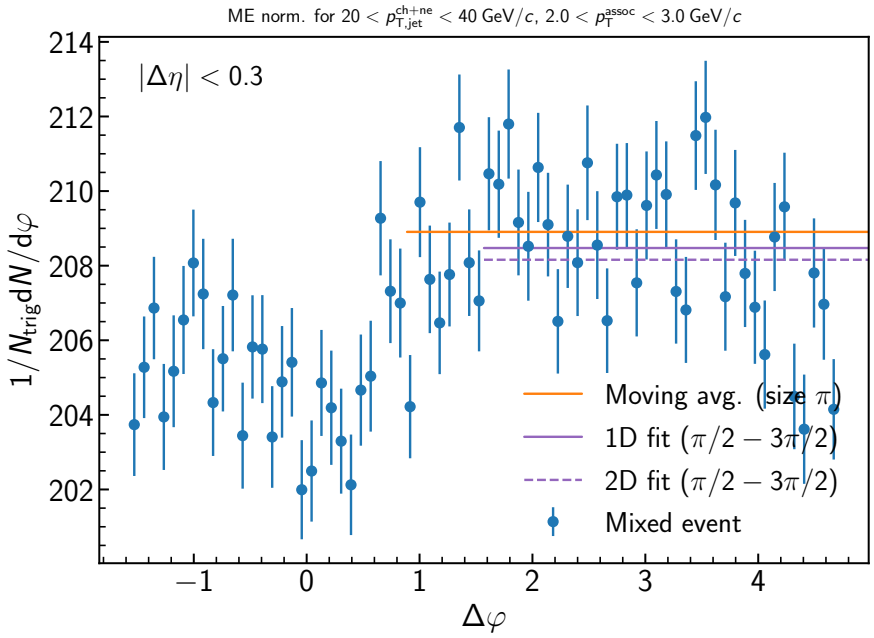

Figure D.48: Determination of the normalization of the mixed event for the inclusive event plane orientation in 30–50% Pb–Pb collisions at $\sqrt{s_{\mathrm{NN}}} = 5.02$ TeV. Here the mixed event is projected over the plateau range in $\Delta\eta$ onto to the $\Delta\varphi$ axis. The moving average is evaluated over the entire $\Delta\varphi$ range using a window of π, while the fit range is fixed from $\pi/2 < \Delta\varphi < 3\pi/2$. Since the mixed events are merged above 2 GeV/c, the normalization factor is also the same for all correlations within $2.0 < p_{\mathrm{T}}^{\mathrm{assoc}} < 3.0$ GeV/c. A variety of normalization methods were evaluated, with further details described in the text.

D.1.13 $20 < p_{\mathrm{T,jet}}^{\mathrm{ch+ne}} < 40\,\mathrm{GeV}/c$, $3.0 < p_{\mathrm{T}}^{\mathrm{assoc}} < 4.0\,\mathrm{GeV}/c$, In-plane orientation

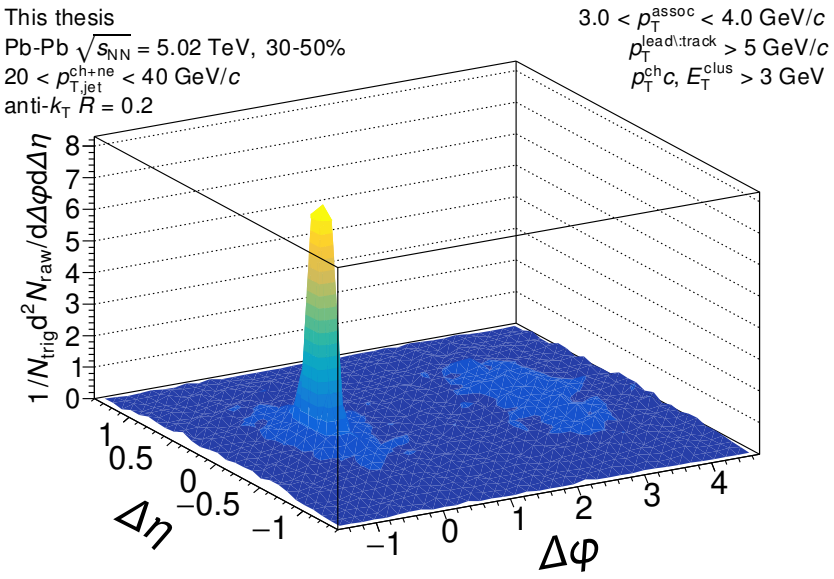

Figure D.49: The measured correlation function with the the efficiency correction $\epsilon(p_{\mathrm{T}}, \eta)$ applied, but before acceptance correction via the mixed events. The correlation is measured for in-plane orientation for $20 < p_{\mathrm{T,jet}}^{\mathrm{ch+ne}} < 40\,\mathrm{GeV}/c$ jets with $3.0 < p_{\mathrm{T}}^{\mathrm{assoc}} < 4.0\,\mathrm{GeV}/c$ in 30–50% Pb–Pb collisions at $\sqrt{s_{\mathrm{NN}}} = 5.02\,\mathrm{TeV}$.

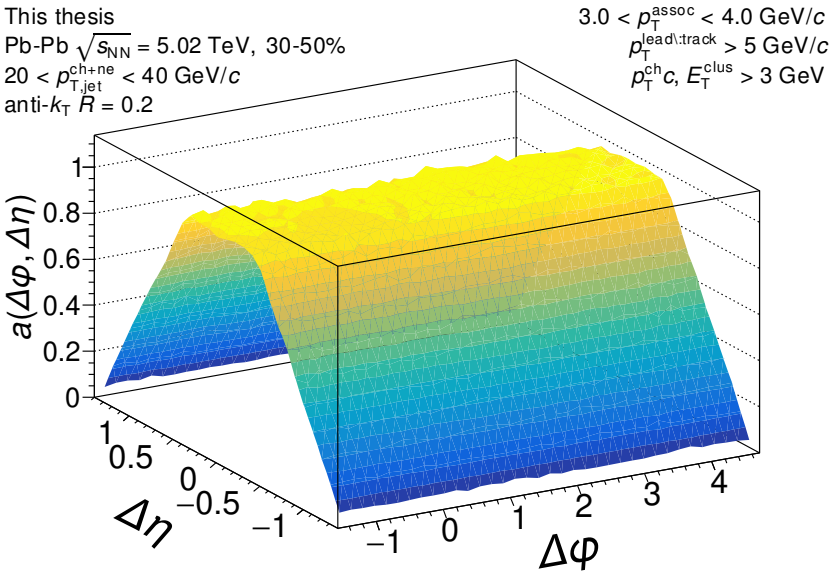

Figure D.50: The mixed event pair acceptance correction with the efficiency correction $\epsilon(p_{\mathrm{T}}, \eta)$ applied. The correlations are measured for in-plane orientation for $20 < p_{\mathrm{T,jet}}^{\mathrm{ch+ne}} < 40\,\mathrm{GeV}/c$ jets with $3.0 < p_{\mathrm{T}}^{\mathrm{assoc}} < 4.0\,\mathrm{GeV}/c$ in 30–50% Pb–Pb collisions at $\sqrt{s_{\mathrm{NN}}} = 5.02\,\mathrm{TeV}$. They have already been normalized such that it they are unity at maximum efficiency. Above 2 GeV/c, the mixed events are merged together to increase statistics, so it is the same for all for correlations within $2.0 \leq p_{\mathrm{T}}^{\mathrm{assoc}} < 10$ GeV/c.

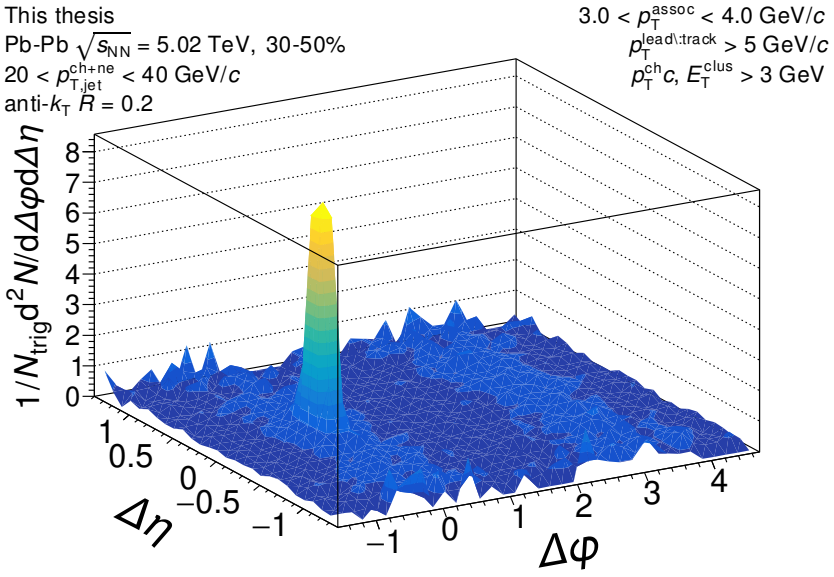

Figure D.51: The signal correlation corrected by pair acceptance. The correlations are measured for in-plane orientation for $20 < p_{\mathrm{T,jet}}^{\mathrm{ch+ne}} < 40\,\mathrm{GeV}/c$ jets with $3.0 < p_{\mathrm{T}}^{\mathrm{assoc}} < 4.0\,\mathrm{GeV}/c$ in 30–50% Pb–Pb collisions at $\sqrt{s_{\mathrm{NN}}} = 5.02\,\mathrm{TeV}$.

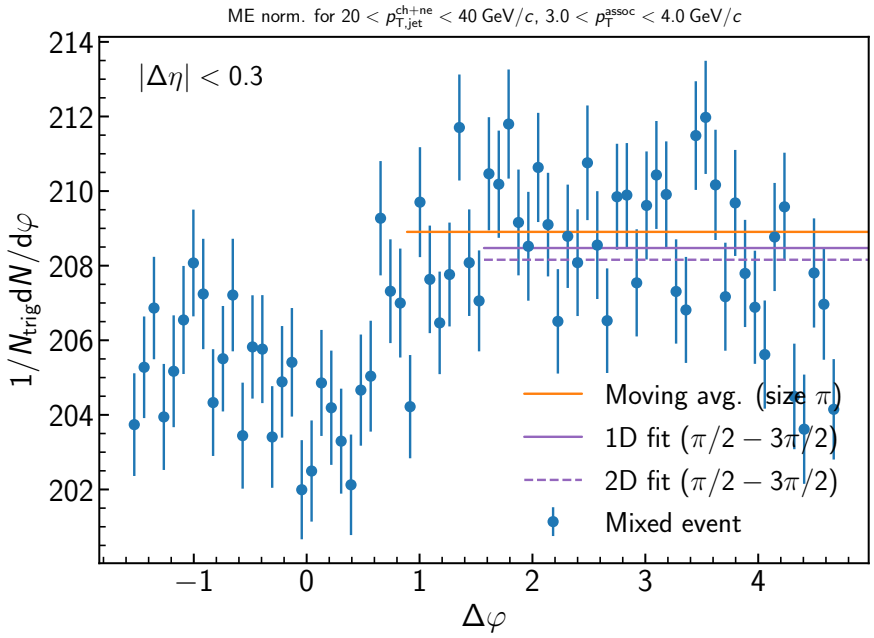

Figure D.52: Determination of the normalization of the mixed event for the inclusive event plane orientation in 30–50% Pb–Pb collisions at $\sqrt{s_{\mathrm{NN}}} = 5.02$ TeV. Here the mixed event is projected over the plateau range in $\Delta\eta$ onto to the $\Delta\varphi$ axis. The moving average is evaluated over the entire $\Delta\varphi$ range using a window of π, while the fit range is fixed from $\pi/2 < \Delta\varphi < 3\pi/2$. Since the mixed events are merged above 2 GeV/c, the normalization factor is also the same for all correlations within $3.0 < p_{\mathrm{T}}^{\mathrm{assoc}} < 4.0$ GeV/c. A variety of normalization methods were evaluated, with further details described in the text.

D.1.14 $20 < p_{\mathrm{T,jet}}^{\mathrm{ch+ne}} < 40\,\mathrm{GeV}/c$, $4.0 < p_{\mathrm{T}}^{\mathrm{assoc}} < 5.0\,\mathrm{GeV}/c$, In-plane orientation

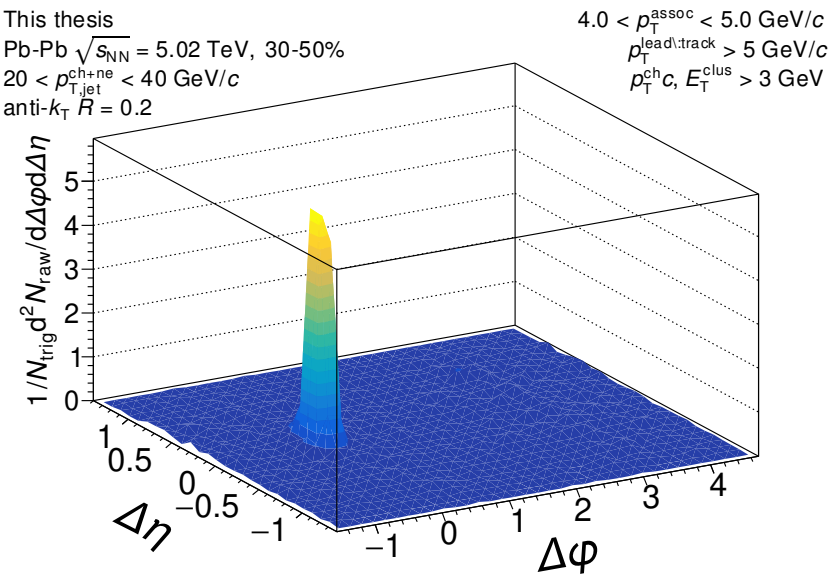

Figure D.53: The measured correlation function with the the efficiency correction $\epsilon(p_{\mathrm{T}}, \eta)$ applied, but before acceptance correction via the mixed events. The correlation is measured for in-plane orientation for $20 < p_{\mathrm{T,jet}}^{\mathrm{ch+ne}} < 40\,\mathrm{GeV}/c$ jets with $4.0 < p_{\mathrm{T}}^{\mathrm{assoc}} < 5.0\,\mathrm{GeV}/c$ in 30–50% Pb–Pb collisions at $\sqrt{s_{\mathrm{NN}}} = 5.02\,\mathrm{TeV}$.

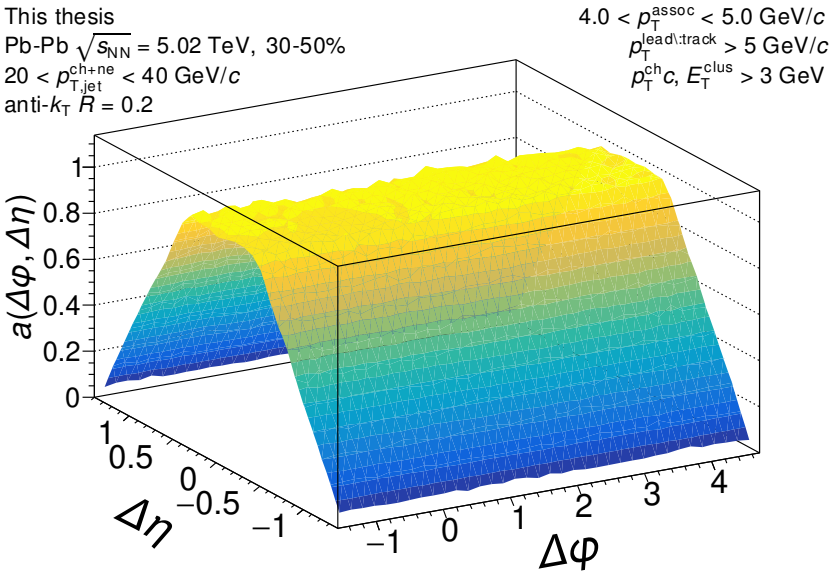

Figure D.54: The mixed event pair acceptance correction with the efficiency correction $\epsilon(p_{\mathrm{T}}, \eta)$ applied. The correlations are measured for in-plane orientation for $20 < p_{\mathrm{T,jet}}^{\mathrm{ch+ne}} < 40\,\mathrm{GeV}/c$ jets with $4.0 < p_{\mathrm{T}}^{\mathrm{assoc}} < 5.0\,\mathrm{GeV}/c$ in 30–50% Pb–Pb collisions at $\sqrt{s_{\mathrm{NN}}} = 5.02\,\mathrm{TeV}$. They have already been normalized such that it they are unity at maximum efficiency. Above 2 GeV/c, the mixed events are merged together to increase statistics, so it is the same for all for correlations within $2.0 \leq p_{\mathrm{T}}^{\mathrm{assoc}} < 10$ GeV/c.

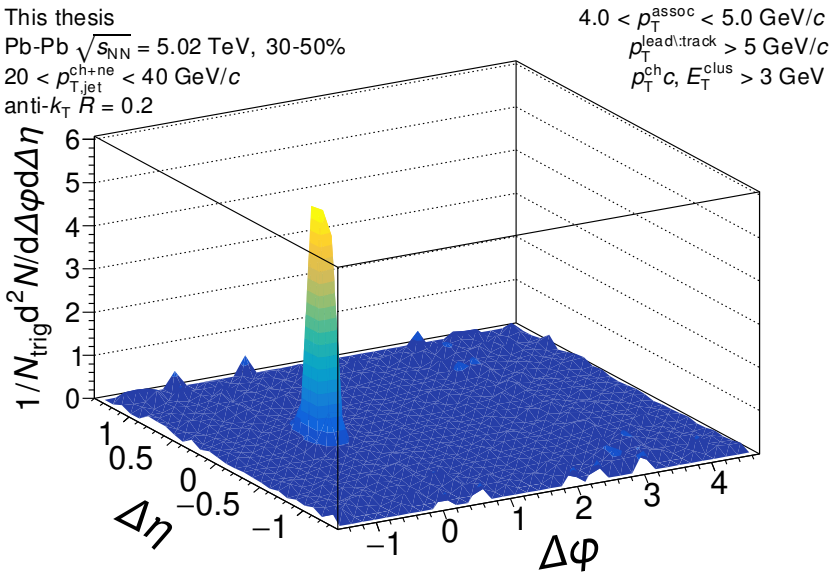

Figure D.55: The signal correlation corrected by pair acceptance. The correlations are measured for in-plane orientation for $20 < p_{\mathrm{T,jet}}^{\mathrm{ch+ne}} < 40\,\mathrm{GeV}/c$ jets with $4.0 < p_{\mathrm{T}}^{\mathrm{assoc}} < 5.0\,\mathrm{GeV}/c$ in 30–50% Pb–Pb collisions at $\sqrt{s_{\mathrm{NN}}} = 5.02\,\mathrm{TeV}$.

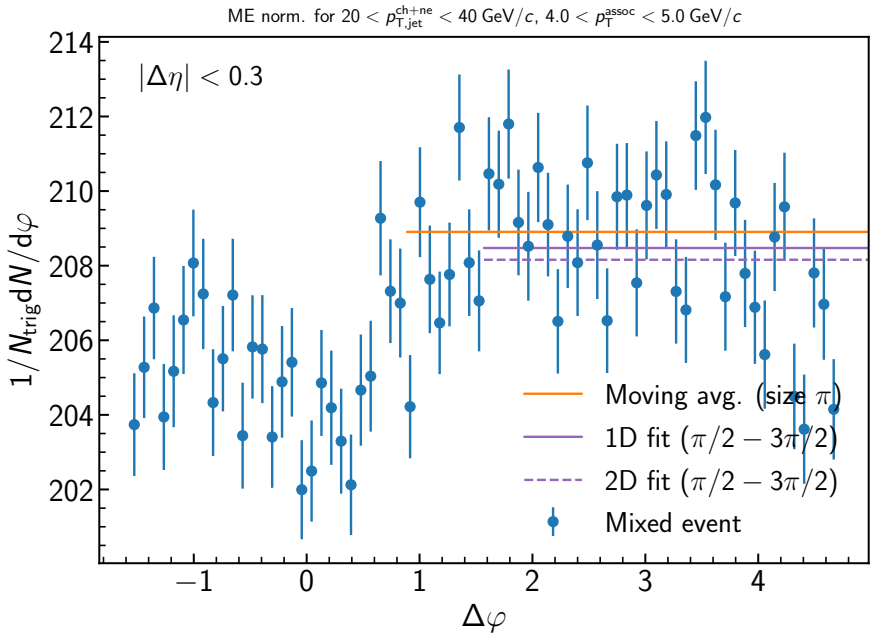

Figure D.56: Determination of the normalization of the mixed event for the inclusive event plane orientation in 30–50% Pb–Pb collisions at $\sqrt{s_{\mathrm{NN}}} = 5.02$ TeV. Here the mixed event is projected over the plateau range in $\Delta\eta$ onto to the $\Delta\varphi$ axis. The moving average is evaluated over the entire $\Delta\varphi$ range using a window of π, while the fit range is fixed from $\pi/2 < \Delta\varphi < 3\pi/2$. Since the mixed events are merged above 2 GeV/c, the normalization factor is also the same for all correlations within $4.0 < p_{\mathrm{T}}^{\mathrm{assoc}} < 5.0$ GeV/c. A variety of normalization methods were evaluated, with further details described in the text.

D.1.15 $20 < p_{\mathrm{T,jet}}^{\mathrm{ch+ne}} < 40\,\mathrm{GeV}/c$, $5.0 < p_{\mathrm{T}}^{\mathrm{assoc}} < 6.0\,\mathrm{GeV}/c$, In-plane orientation

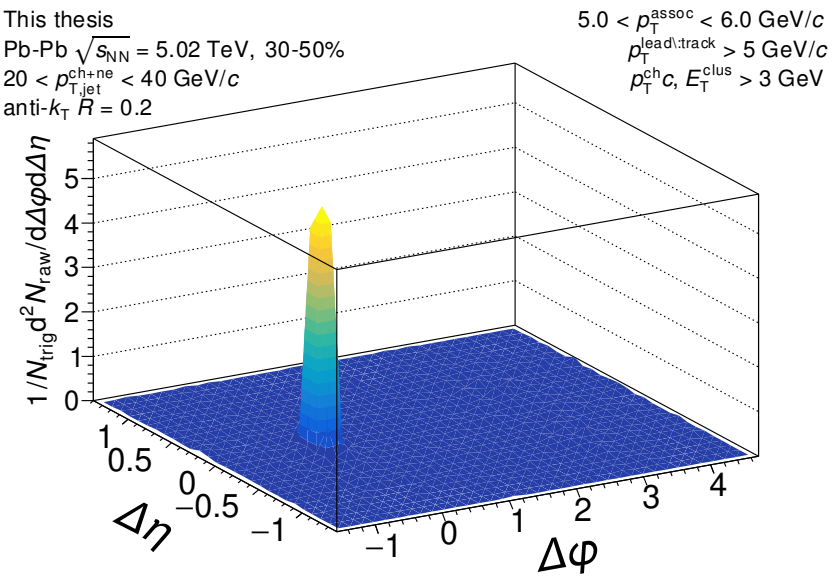

Figure D.57: The measured correlation function with the the efficiency correction $\epsilon(p_{\mathrm{T}}, \eta)$ applied, but before acceptance correction via the mixed events. The correlation is measured for in-plane orientation for $20 < p_{\mathrm{T,jet}}^{\mathrm{ch+ne}} < 40\,\mathrm{GeV}/c$ jets with $5.0 < p_{\mathrm{T}}^{\mathrm{assoc}} < 6.0\,\mathrm{GeV}/c$ in 30–50% Pb–Pb collisions at $\sqrt{s_{\mathrm{NN}}} = 5.02\,\mathrm{TeV}$.

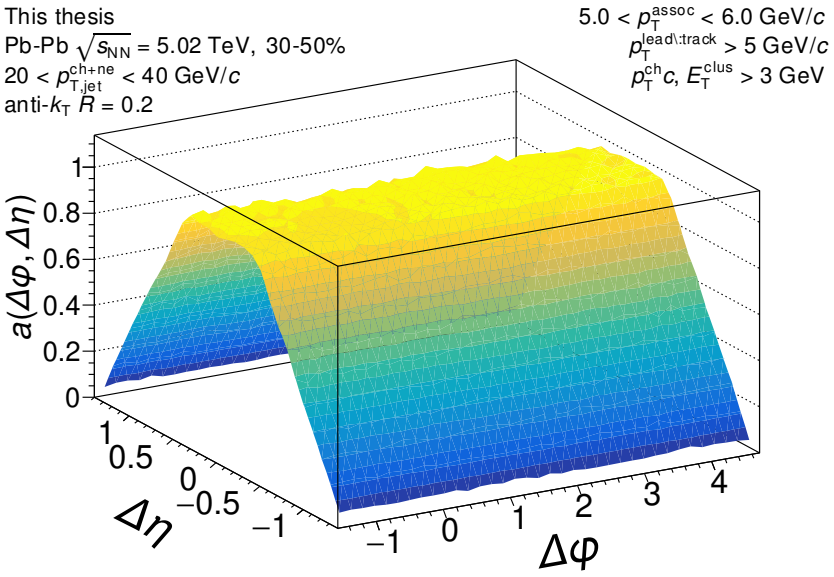

Figure D.58: The mixed event pair acceptance correction with the efficiency correction $\epsilon(p_{\mathrm{T}}, \eta)$ applied. The correlations are measured for in-plane orientation for $20 < p_{\mathrm{T,jet}}^{\mathrm{ch+ne}} < 40\,\mathrm{GeV}/c$ jets with $5.0 < p_{\mathrm{T}}^{\mathrm{assoc}} < 6.0\,\mathrm{GeV}/c$ in 30–50% Pb–Pb collisions at $\sqrt{s_{\mathrm{NN}}} = 5.02\,\mathrm{TeV}$. They have already been normalized such that it they are unity at maximum efficiency. Above 2 GeV/c, the mixed events are merged together to increase statistics, so it is the same for all for correlations within $2.0 \leq p_{\mathrm{T}}^{\mathrm{assoc}} < 10$ GeV/c.

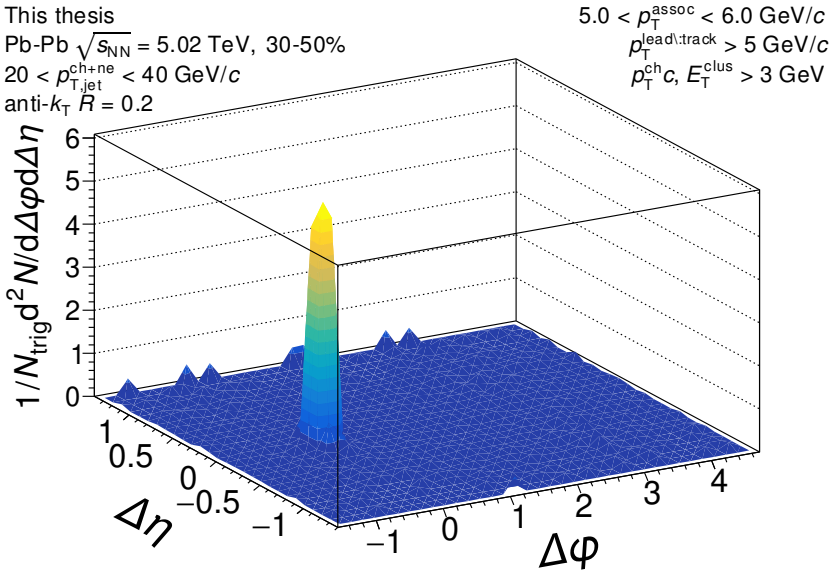

Figure D.59: The signal correlation corrected by pair acceptance. The correlations are measured for in-plane orientation for $20 < p_{\mathrm{T,jet}}^{\mathrm{ch+ne}} < 40\,\mathrm{GeV}/c$ jets with $5.0 < p_{\mathrm{T}}^{\mathrm{assoc}} < 6.0\,\mathrm{GeV}/c$ in 30–50% Pb–Pb collisions at $\sqrt{s_{\mathrm{NN}}} = 5.02\,\mathrm{TeV}$.

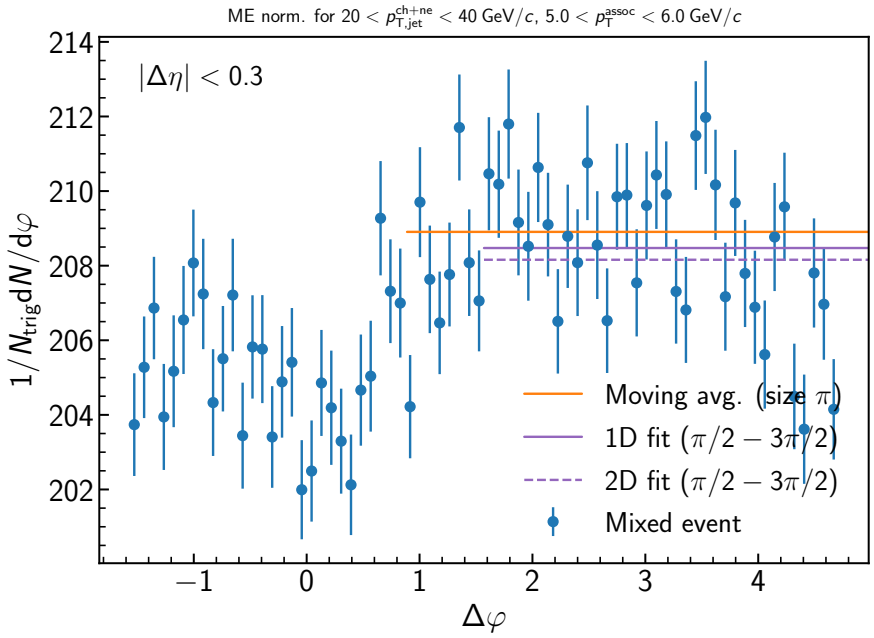

Figure D.60: Determination of the normalization of the mixed event for the inclusive event plane orientation in 30–50% Pb–Pb collisions at $\sqrt{s_{\mathrm{NN}}} = 5.02$ TeV. Here the mixed event is projected over the plateau range in $\Delta\eta$ onto to the $\Delta\varphi$ axis. The moving average is evaluated over the entire $\Delta\varphi$ range using a window of π, while the fit range is fixed from $\pi/2 < \Delta\varphi < 3\pi/2$. Since the mixed events are merged above 2 GeV/c, the normalization factor is also the same for all correlations within $5.0 < p_{\mathrm{T}}^{\mathrm{assoc}} < 6.0$ GeV/c. A variety of normalization methods were evaluated, with further details described in the text.

D.1.16 $20 < p_{\mathrm{T,jet}}^{\mathrm{ch+ne}} < 40$ GeV/c, $6.0 < p_{\mathrm{T}}^{\mathrm{assoc}} < 10.0$ GeV/c, In-plane orientation

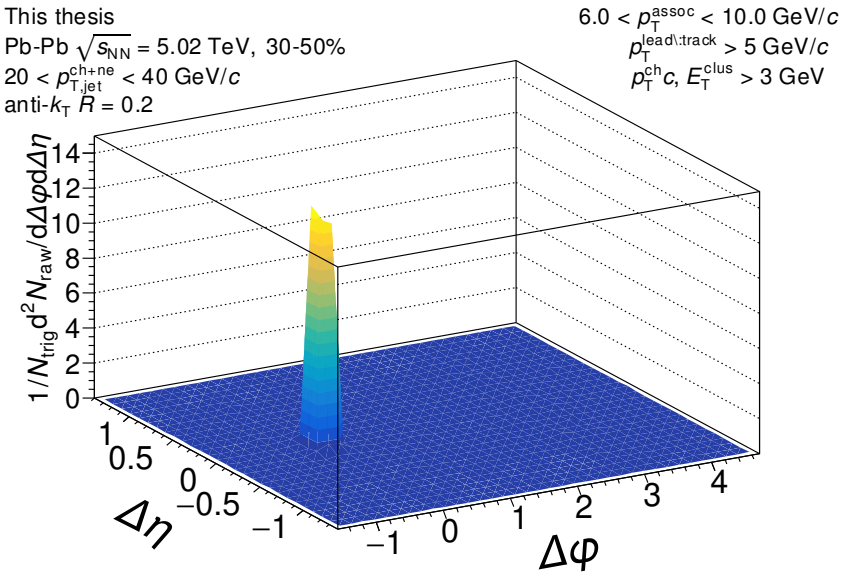

Figure D.61: The measured correlation function with the the efficiency correction $\epsilon(p_{\mathrm{T}}, \eta)$ applied, but before acceptance correction via the mixed events. The correlation is measured for in-plane orientation for $20 < p_{\mathrm{T,jet}}^{\mathrm{ch+ne}} < 40\,\mathrm{GeV}/c$ jets with $6.0 < p_{\mathrm{T}}^{\mathrm{assoc}} < 10.0\,\mathrm{GeV}/c$ in 30–50% Pb–Pb collisions at $\sqrt{s_{\mathrm{NN}}} = 5.02$ TeV.

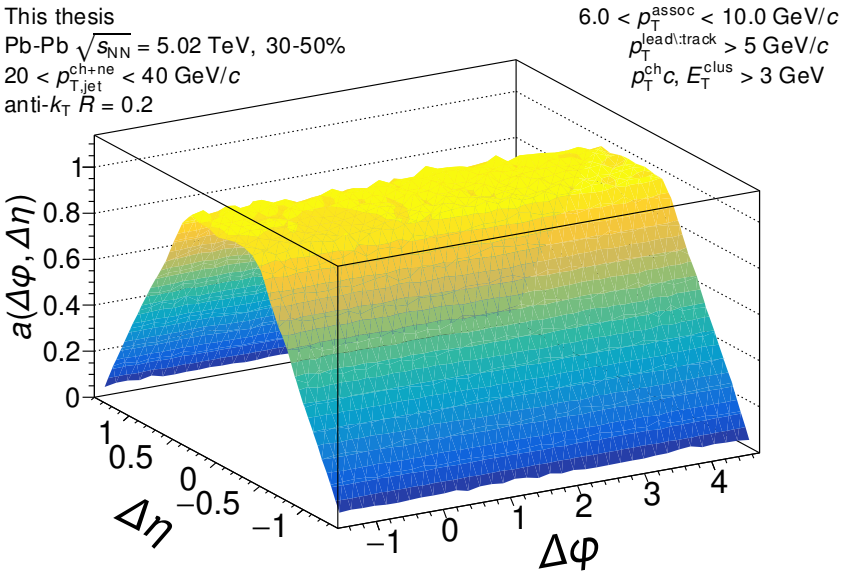

Figure D.62: The mixed event pair acceptance correction with the efficiency correction $\epsilon(p_{\mathrm{T}}, \eta)$ applied. The correlations are measured for in-plane orientation for $20 < p_{\mathrm{T,jet}}^{\mathrm{ch+ne}} < 40\,\mathrm{GeV}/c$ jets with $6.0 < p_{\mathrm{T}}^{\mathrm{assoc}} < 10.0\,\mathrm{GeV}/c$ in 30–50% Pb–Pb collisions at $\sqrt{s_{\mathrm{NN}}} = 5.02\,\mathrm{TeV}$. They have already been normalized such that it they are unity at maximum efficiency. Above 2 GeV/c, the mixed events are merged together to increase statistics, so it is the same for all for correlations within $2.0 \leq p_{\mathrm{T}}^{\mathrm{assoc}} < 10$ GeV/c.

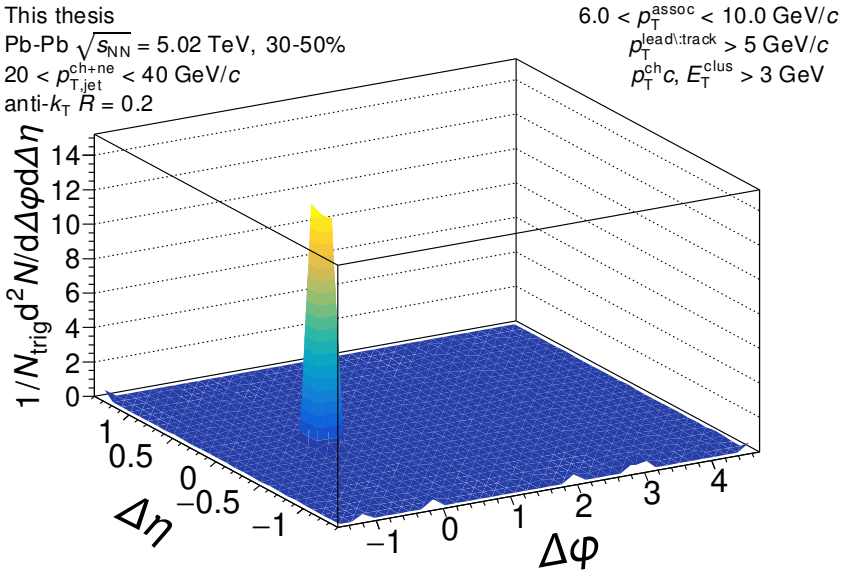

Figure D.63: The signal correlation corrected by pair acceptance. The correlations are measured for in-plane orientation for $20 < p_{\mathrm{T,jet}}^{\mathrm{ch+ne}} < 40\,\mathrm{GeV}/c$ jets with $6.0 < p_{\mathrm{T}}^{\mathrm{assoc}} < 10.0\,\mathrm{GeV}/c$ in 30–50% Pb–Pb collisions at $\sqrt{s_{\mathrm{NN}}} = 5.02\,\mathrm{TeV}$.

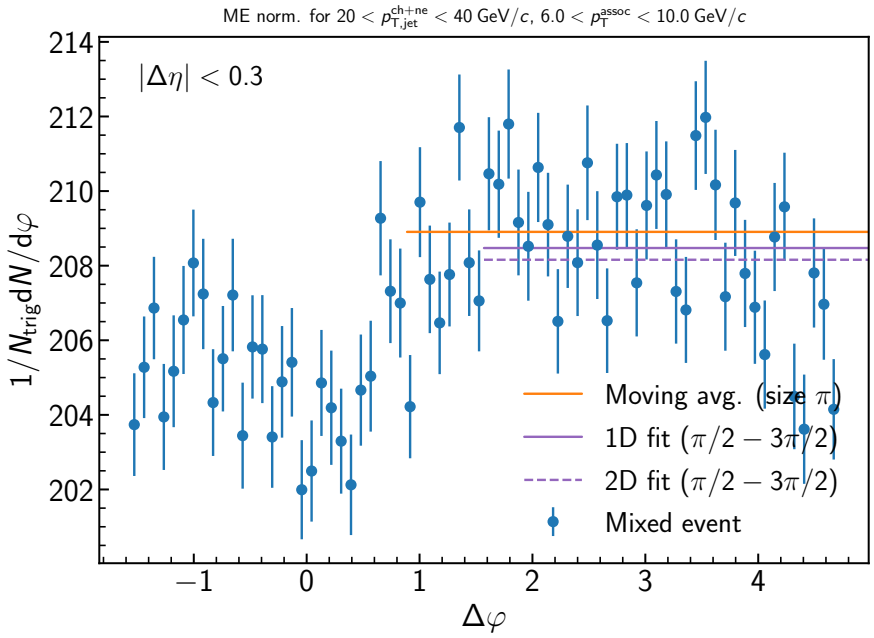

Figure D.64: Determination of the normalization of the mixed event for the inclusive event plane orientation in 30–50% Pb–Pb collisions at $\sqrt{s_{\mathrm{NN}}} = 5.02$ TeV. Here the mixed event is projected over the plateau range in $\Delta\eta$ onto to the $\Delta\varphi$ axis. The moving average is evaluated over the entire $\Delta\varphi$ range using a window of π, while the fit range is fixed from $\pi/2 < \Delta\varphi < 3\pi/2$. Since the mixed events are merged above 2 GeV/c, the normalization factor is also the same for all correlations within $6.0 < p_{\mathrm{T}}^{\mathrm{assoc}} < 10.0$ GeV/c. A variety of normalization methods were evaluated, with further details described in the text.

D.1.17 $20 < p_{\mathrm{T,jet}}^{\mathrm{ch+ne}} < 40$ GeV/c, $0.5 < p_{\mathrm{T}}^{\mathrm{assoc}} < 1.0$ GeV/c, Mid-plane orientation

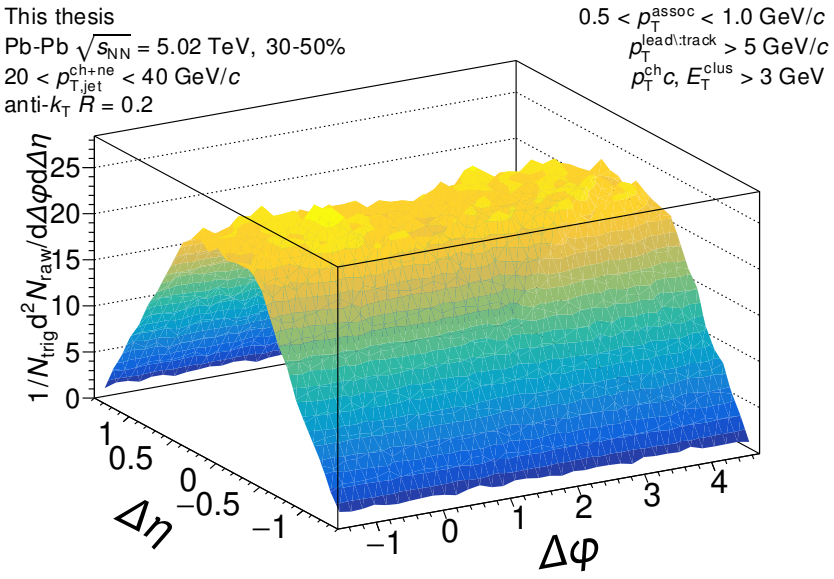

Figure D.65: The measured correlation function with the the efficiency correction $\epsilon(p_{\mathrm{T}}, \eta)$ applied, but before acceptance correction via the mixed events. The correlation is measured for mid-plane orientation for $20 < p_{\mathrm{T,jet}}^{\mathrm{ch+ne}} < 40$ GeV/c jets with $0.5 < p_{\mathrm{T}}^{\mathrm{assoc}} < 1.0$ GeV/c in 30–50% Pb–Pb collisions at $\sqrt{s_{\mathrm{NN}}} = 5.02$ TeV.

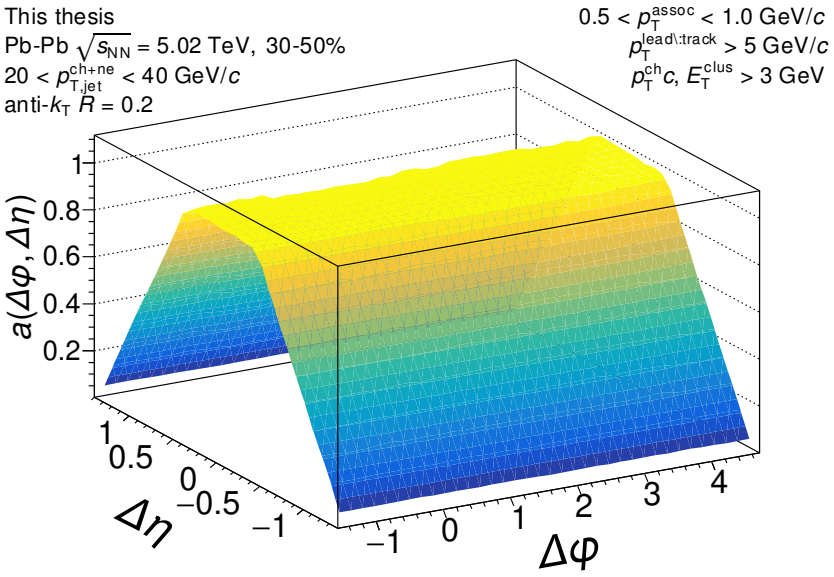

Figure D.66: The mixed event pair acceptance correction with the efficiency correction $\epsilon(p_{\mathrm{T}}, \eta)$ applied. The correlations are measured for mid-plane orientation for $20 < p_{\mathrm{T,jet}}^{\mathrm{ch+ne}} < 40$ GeV/c jets with $0.5 < p_{\mathrm{T}}^{\mathrm{assoc}} < 1.0$ GeV/c in 30–50% Pb–Pb collisions at $\sqrt{s_{\mathrm{NN}}} = 5.02$ TeV. They have already been normalized such that it they are unity at maximum efficiency. Above 2 GeV/c, the mixed events are merged together to increase statistics, so it is the same for all for correlations within $2.0 \leq p_{\mathrm{T}}^{\mathrm{assoc}} < 10$ GeV/c.

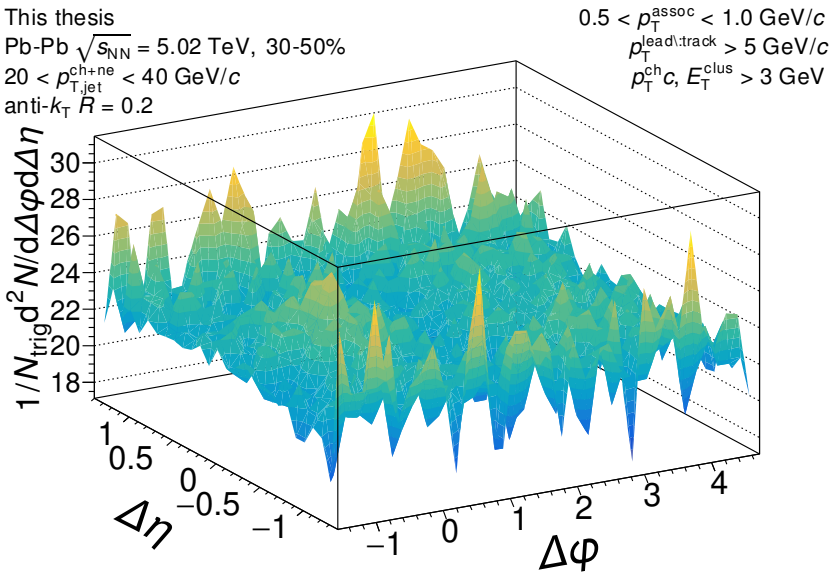

Figure D.67: The signal correlation corrected by pair acceptance. The correlations are measured for mid-plane orientation for $20 < p_{\mathrm{T,jet}}^{\mathrm{ch+ne}} < 40$ GeV/c jets with $0.5 < p_{\mathrm{T}}^{\mathrm{assoc}} < 1.0$ GeV/c in 30–50% Pb–Pb collisions at $\sqrt{s_{\mathrm{NN}}} = 5.02$ TeV.

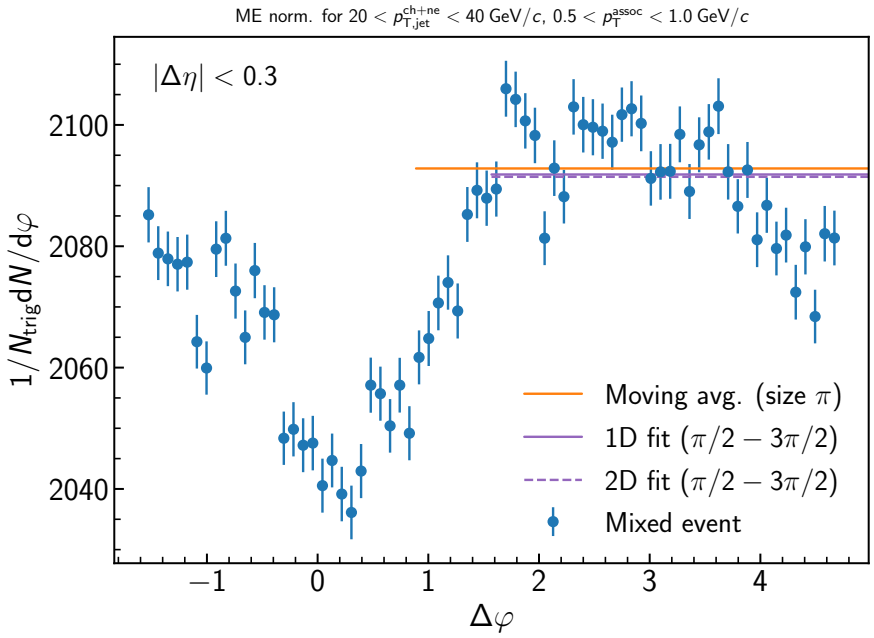

Figure D.68: Determination of the normalization of the mixed event for the inclusive event plane orientation in 30–50% Pb–Pb collisions at $\sqrt{s_{\mathrm{NN}}} = 5.02$ TeV. Here the mixed event is projected over the plateau range in $\Delta\eta$ onto to the $\Delta\varphi$ axis. The moving average is evaluated over the entire $\Delta\varphi$ range using a window of π, while the fit range is fixed from $\pi/2 < \Delta\varphi < 3\pi/2$. Since the mixed events are merged above 2 GeV/c, the normalization factor is also the same for all correlations within $0.5 < p_{\mathrm{T}}^{\mathrm{assoc}} < 1.0$ GeV/c. A variety of normalization methods were evaluated, with further details described in the text.

D.1.18 $20 < p_{\mathrm{T,jet}}^{\mathrm{ch+ne}} < 40\ \mathrm{GeV}/c$, $1.0 < p_{\mathrm{T}}^{\mathrm{assoc}} < 1.5\ \mathrm{GeV}/c$, Mid-plane orientation

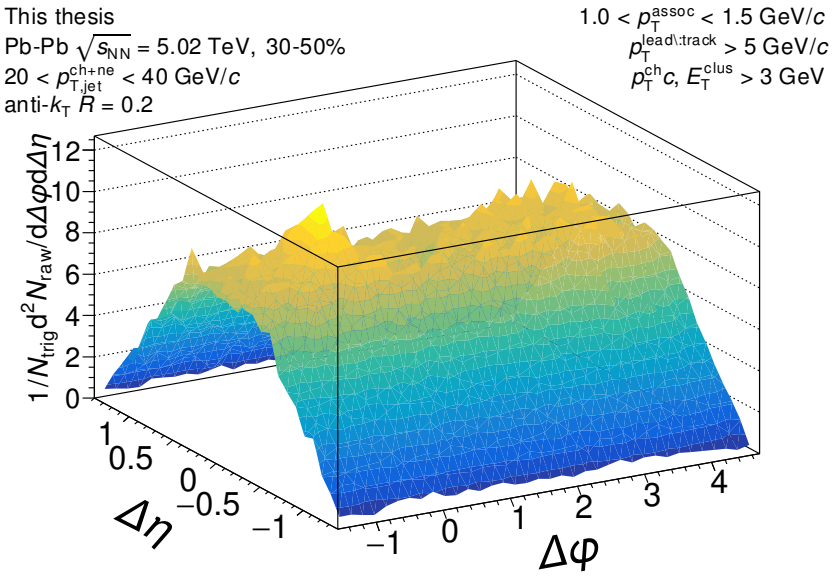

Figure D.69: The measured correlation function with the the efficiency correction $\epsilon(p_{\mathrm{T}}, \eta)$ applied, but before acceptance correction via the mixed events. The correlation is measured for mid-plane orientation for $20 < p_{\mathrm{T,jet}}^{\mathrm{ch+ne}} < 40\ \mathrm{GeV}/c$ jets with $1.0 < p_{\mathrm{T}}^{\mathrm{assoc}} < 1.5\ \mathrm{GeV}/c$ in 30–50% Pb–Pb collisions at $\sqrt{s_{\mathrm{NN}}} = 5.02$ TeV.

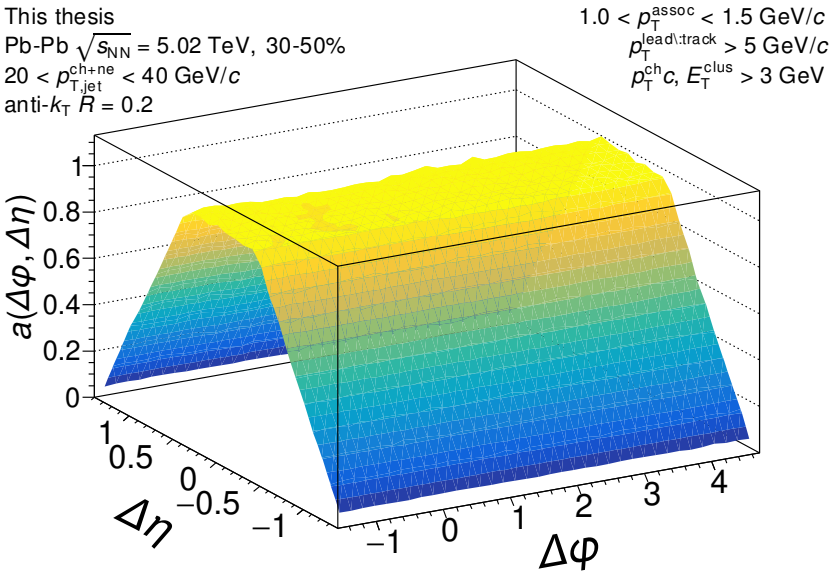

Figure D.70: The mixed event pair acceptance correction with the efficiency correction $\epsilon(p_{\mathrm{T}}, \eta)$ applied. The correlations are measured for mid-plane orientation for $20 < p_{\mathrm{T,jet}}^{\mathrm{ch+ne}} < 40$ GeV/c jets with $1.0 < p_{\mathrm{T}}^{\mathrm{assoc}} < 1.5$ GeV/c in 30–50% Pb–Pb collisions at $\sqrt{s_{\mathrm{NN}}} = 5.02$ TeV. They have already been normalized such that it they are unity at maximum efficiency. Above 2 GeV/c, the mixed events are merged together to increase statistics, so it is the same for all for correlations within $2.0 \leq p_{\mathrm{T}}^{\mathrm{assoc}} < 10$ GeV/c.

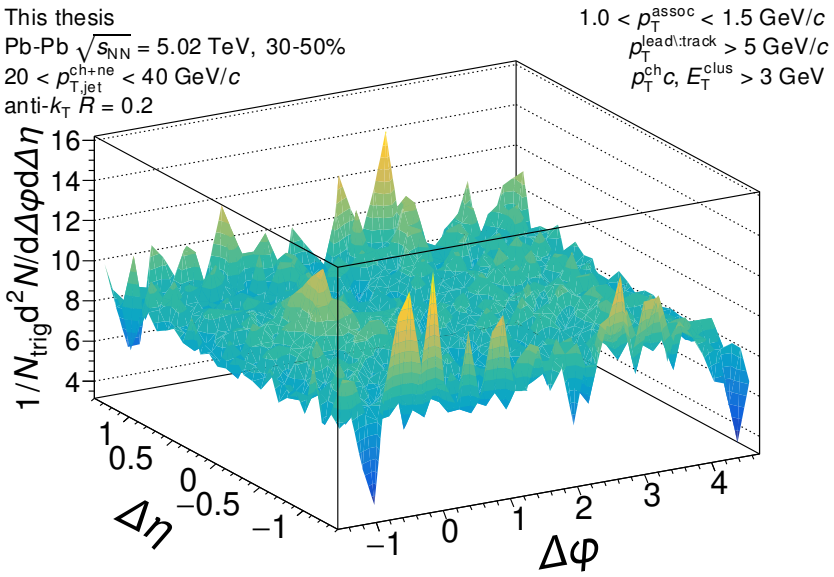

Figure D.71: The signal correlation corrected by pair acceptance. The correlations are measured for mid-plane orientation for $20 < p_{\mathrm{T,jet}}^{\mathrm{ch+ne}} < 40$ GeV/c jets with $1.0 < p_{\mathrm{T}}^{\mathrm{assoc}} < 1.5$ GeV/c in 30–50% Pb–Pb collisions at $\sqrt{s_{\mathrm{NN}}} = 5.02$ TeV.

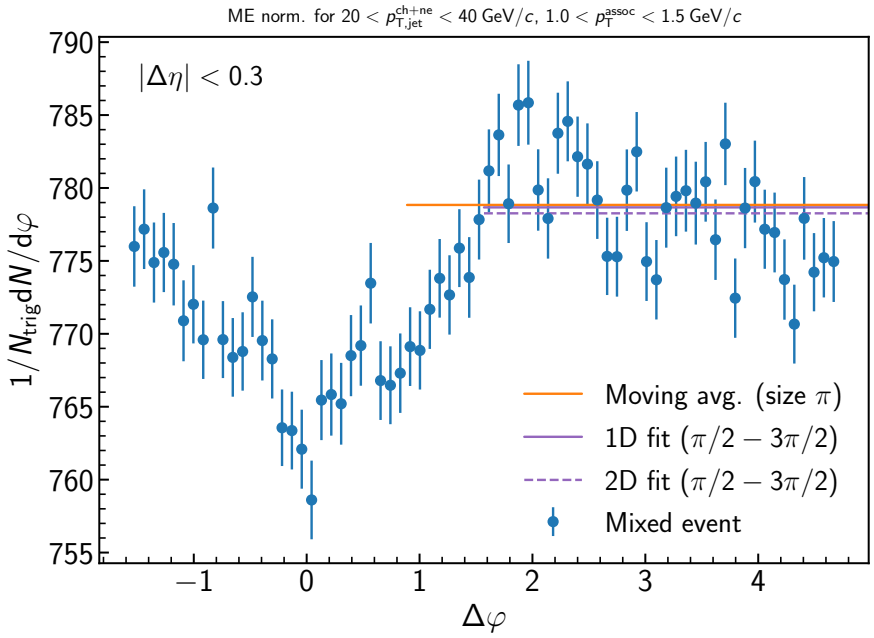

Figure D.72: Determination of the normalization of the mixed event for the inclusive event plane orientation in 30–50% Pb–Pb collisions at $\sqrt{s_{\mathrm{NN}}} = 5.02$ TeV. Here the mixed event is projected over the plateau range in $\Delta\eta$ onto to the $\Delta\varphi$ axis. The moving average is evaluated over the entire $\Delta\varphi$ range using a window of π, while the fit range is fixed from $\pi/2 < \Delta\varphi < 3\pi/2$. Since the mixed events are merged above 2 GeV/c, the normalization factor is also the same for all correlations within $1.0 < p_{\mathrm{T}}^{\mathrm{assoc}} < 1.5$ GeV/c. A variety of normalization methods were evaluated, with further details described in the text.

D.1.19 $20 < p_{\mathrm{T,jet}}^{\mathrm{ch+ne}} < 40$ GeV/c, $1.5 < p_{\mathrm{T}}^{\mathrm{assoc}} < 2.0$ GeV/c, Mid-plane orientation

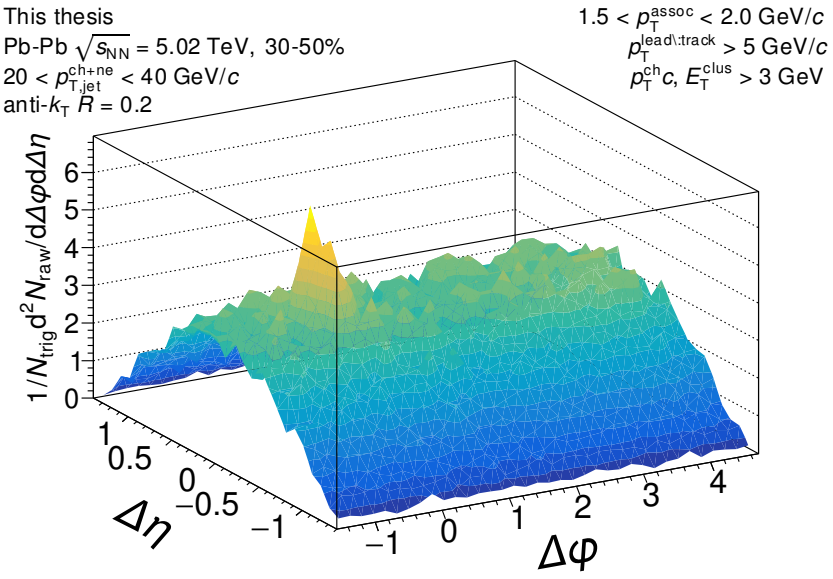

Figure D.73: The measured correlation function with the the efficiency correction $\epsilon(p_{\mathrm{T}}, \eta)$ applied, but before acceptance correction via the mixed events. The correlation is measured for mid-plane orientation for $20 < p_{\mathrm{T,jet}}^{\mathrm{ch+ne}} < 40$ GeV/c jets with $1.5 < p_{\mathrm{T}}^{\mathrm{assoc}} < 2.0$ GeV/c in 30–50% Pb–Pb collisions at $\sqrt{s_{\mathrm{NN}}} = 5.02$ TeV.

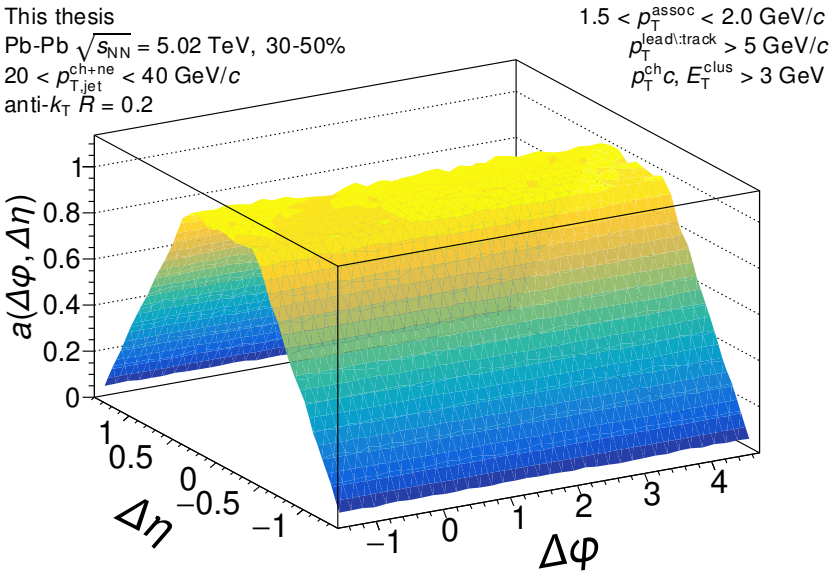

Figure D.74: The mixed event pair acceptance correction with the efficiency correction $\epsilon(p_T, \eta)$ applied. The correlations are measured for mid-plane orientation for $20 < p_{T,jet}^{ch+ne} < 40$ GeV/c jets with $1.5 < p_T^{assoc} < 2.0$ GeV/c in 30–50% Pb–Pb collisions at $\sqrt{s_{NN}} = 5.02$ TeV. They have already been normalized such that it they are unity at maximum efficiency. Above 2 GeV/c, the mixed events are merged together to increase statistics, so it is the same for all for correlations within $2.0 \leq p_T^{assoc} < 10$ GeV/c.

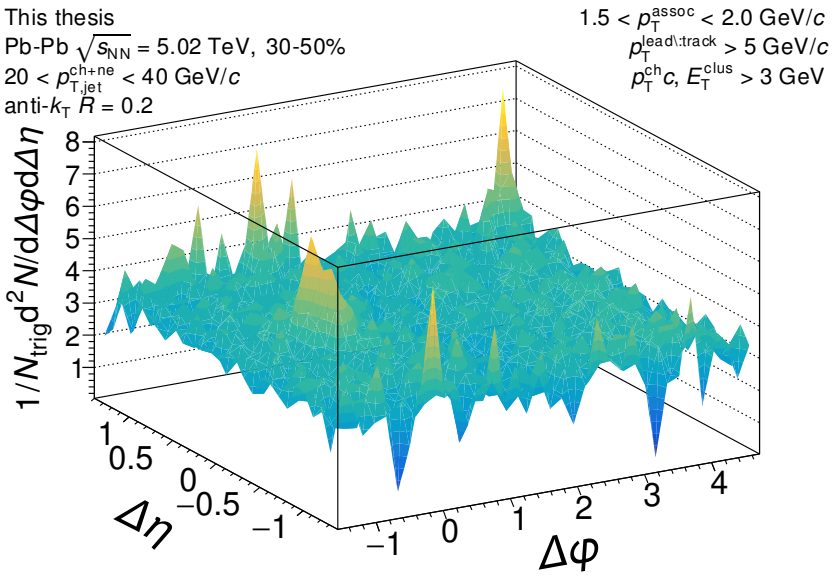

Figure D.75: The signal correlation corrected by pair acceptance. The correlations are measured for mid-plane orientation for $20 < p_{T,jet}^{ch+ne} < 40$ GeV/c jets with $1.5 < p_T^{assoc} < 2.0$ GeV/c in 30–50% Pb–Pb collisions at $\sqrt{s_{NN}} = 5.02$ TeV.

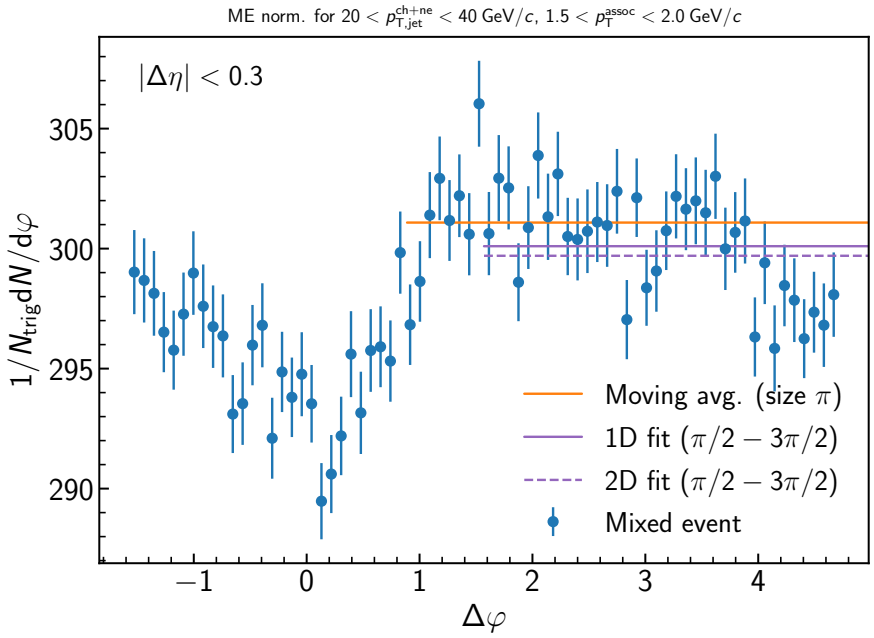

Figure D.76: Determination of the normalization of the mixed event for the inclusive event plane orientation in 30–50% Pb–Pb collisions at $\sqrt{s_{\mathrm{NN}}} = 5.02$ TeV. Here the mixed event is projected over the plateau range in $\Delta\eta$ onto to the $\Delta\varphi$ axis. The moving average is evaluated over the entire $\Delta\varphi$ range using a window of π, while the fit range is fixed from $\pi/2 < \Delta\varphi < 3\pi/2$. Since the mixed events are merged above 2 GeV/c, the normalization factor is also the same for all correlations within $1.5 < p_{\mathrm{T}}^{\mathrm{assoc}} < 2.0$ GeV/c. A variety of normalization methods were evaluated, with further details described in the text.

D.1.20 $20 < p_{\mathrm{T,jet}}^{\mathrm{ch+ne}} < 40$ GeV/c, $2.0 < p_{\mathrm{T}}^{\mathrm{assoc}} < 3.0$ GeV/c, Mid-plane orientation

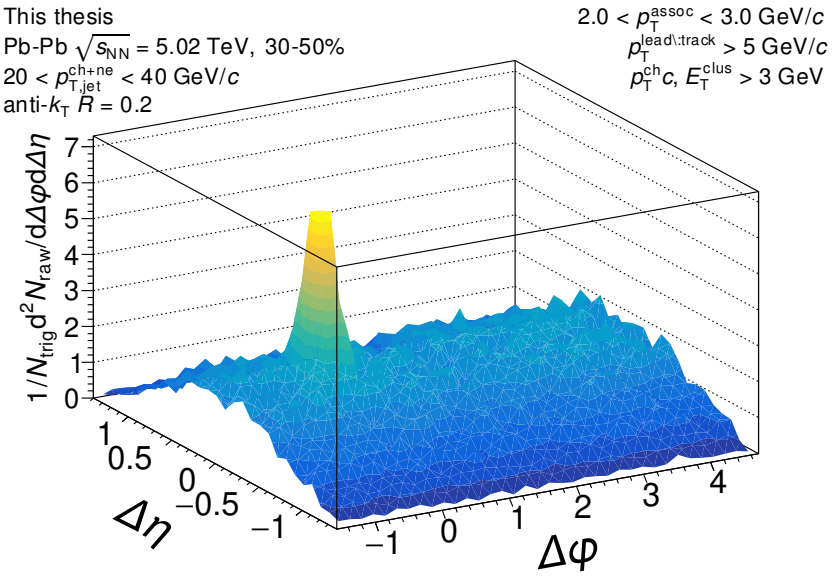

Figure D.77: The measured correlation function with the the efficiency correction $\epsilon(p_{\mathrm{T}}, \eta)$ applied, but before acceptance correction via the mixed events. The correlation is measured for mid-plane orientation for $20 < p_{\mathrm{T,jet}}^{\mathrm{ch+ne}} < 40$ GeV/c jets with $2.0 < p_{\mathrm{T}}^{\mathrm{assoc}} < 3.0$ GeV/c in 30–50% Pb–Pb collisions at $\sqrt{s_{\mathrm{NN}}} = 5.02$ TeV.

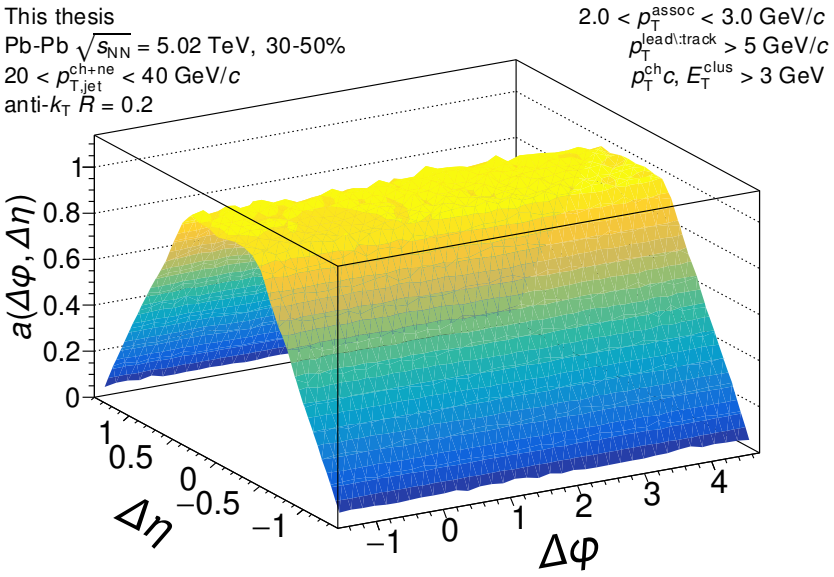

Figure D.78: The mixed event pair acceptance correction with the efficiency correction $\epsilon(p_{\mathrm{T}}, \eta)$ applied. The correlations are measured for mid-plane orientation for $20 < p_{\mathrm{T,jet}}^{\mathrm{ch+ne}} < 40$ GeV/c jets with $2.0 < p_{\mathrm{T}}^{\mathrm{assoc}} < 3.0$ GeV/c in 30–50% Pb–Pb collisions at $\sqrt{s_{\mathrm{NN}}} = 5.02$ TeV. They have already been normalized such that it they are unity at maximum efficiency. Above 2 GeV/c, the mixed events are merged together to increase statistics, so it is the same for all for correlations within $2.0 \leq p_{\mathrm{T}}^{\mathrm{assoc}} < 10$ GeV/c.

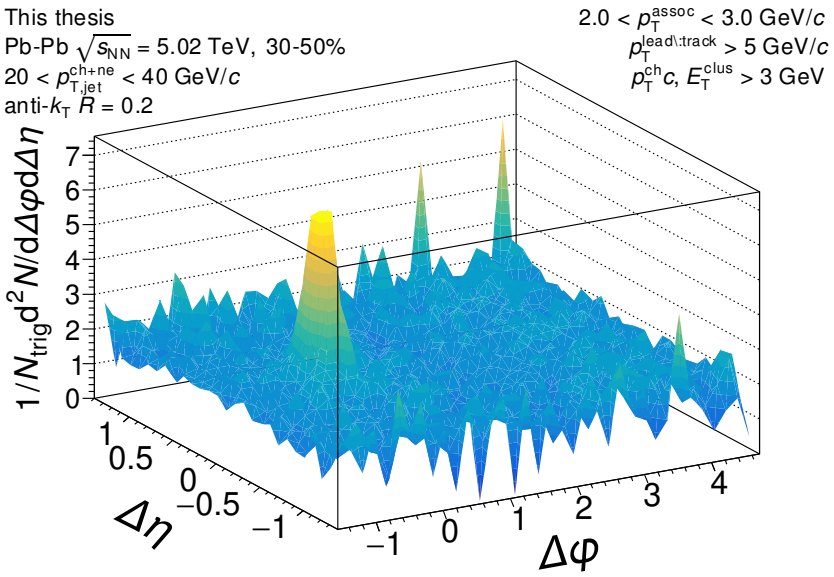

Figure D.79: The signal correlation corrected by pair acceptance. The correlations are measured for mid-plane orientation for $20 < p_{\mathrm{T,jet}}^{\mathrm{ch+ne}} < 40$ GeV/c jets with $2.0 < p_{\mathrm{T}}^{\mathrm{assoc}} < 3.0$ GeV/c in 30–50% Pb–Pb collisions at $\sqrt{s_{\mathrm{NN}}} = 5.02$ TeV.

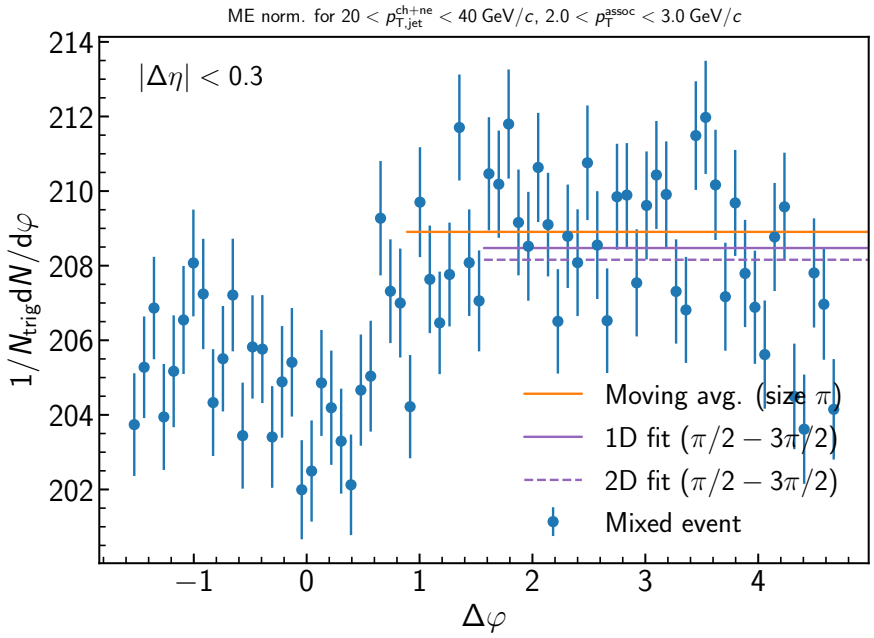

Figure D.80: Determination of the normalization of the mixed event for the inclusive event plane orientation in 30–50% Pb–Pb collisions at $\sqrt{s_{\mathrm{NN}}} = 5.02$ TeV. Here the mixed event is projected over the plateau range in $\Delta\eta$ onto to the $\Delta\varphi$ axis. The moving average is evaluated over the entire $\Delta\varphi$ range using a window of π, while the fit range is fixed from $\pi/2 < \Delta\varphi < 3\pi/2$. Since the mixed events are merged above 2 GeV/c, the normalization factor is also the same for all correlations within $2.0 < p_{\mathrm{T}}^{\mathrm{assoc}} < 3.0$ GeV/c. A variety of normalization methods were evaluated, with further details described in the text.

D.1.21 $20 < p_{\mathrm{T,jet}}^{\mathrm{ch+ne}} < 40$ GeV/c, $3.0 < p_{\mathrm{T}}^{\mathrm{assoc}} < 4.0$ GeV/c, Mid-plane orientation

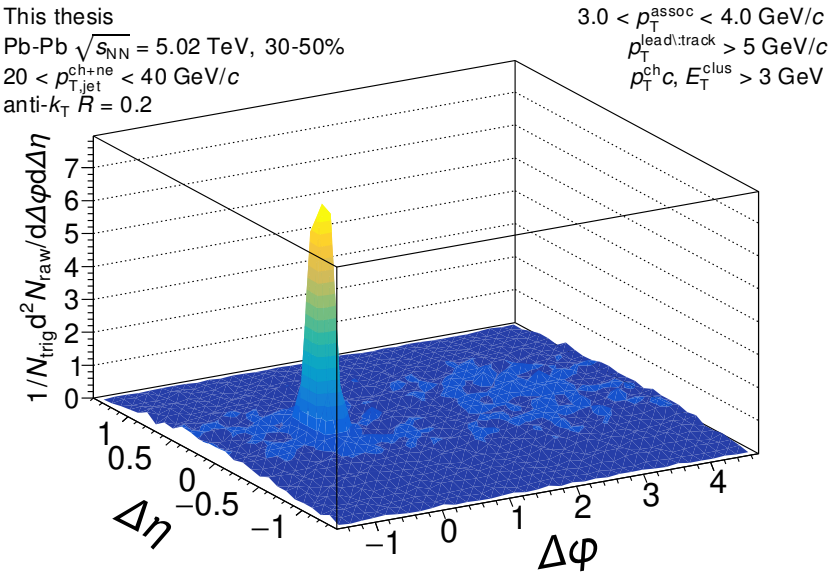

Figure D.81: The measured correlation function with the the efficiency correction $\epsilon(p_{\mathrm{T}}, \eta)$ applied, but before acceptance correction via the mixed events. The correlation is measured for mid-plane orientation for $20 < p_{\mathrm{T,jet}}^{\mathrm{ch+ne}} < 40$ GeV/c jets with $3.0 < p_{\mathrm{T}}^{\mathrm{assoc}} < 4.0$ GeV/c in 30–50% Pb–Pb collisions at $\sqrt{s_{\mathrm{NN}}} = 5.02$ TeV.

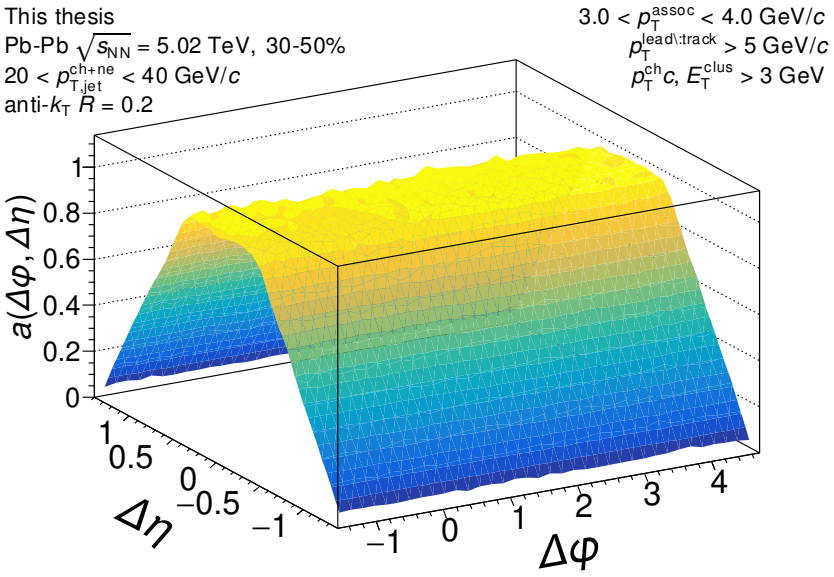

Figure D.82: The mixed event pair acceptance correction with the efficiency correction $\epsilon(p_T, \eta)$ applied. The correlations are measured for mid-plane orientation for $20 < p_{T,jet}^{ch+ne} < 40$ GeV/c jets with $3.0 < p_T^{assoc} < 4.0$ GeV/c in 30–50% Pb–Pb collisions at $\sqrt{s_{NN}} = 5.02$ TeV. They have already been normalized such that it they are unity at maximum efficiency. Above 2 GeV/c, the mixed events are merged together to increase statistics, so it is the same for all for correlations within $2.0 \leq p_T^{assoc} < 10$ GeV/c.

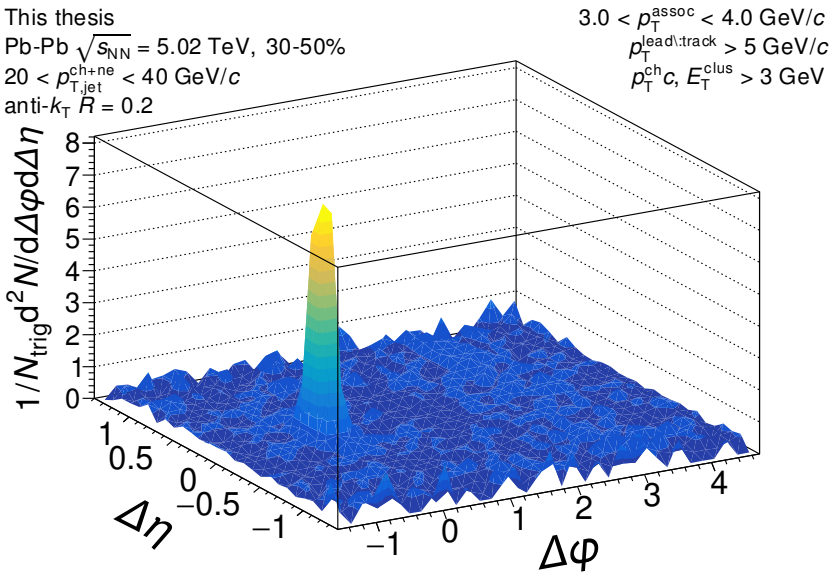

Figure D.83: The signal correlation corrected by pair acceptance. The correlations are measured for mid-plane orientation for $20 < p_{T,jet}^{ch+ne} < 40$ GeV/c jets with $3.0 < p_T^{assoc} < 4.0$ GeV/c in 30–50% Pb–Pb collisions at $\sqrt{s_{NN}} = 5.02$ TeV.

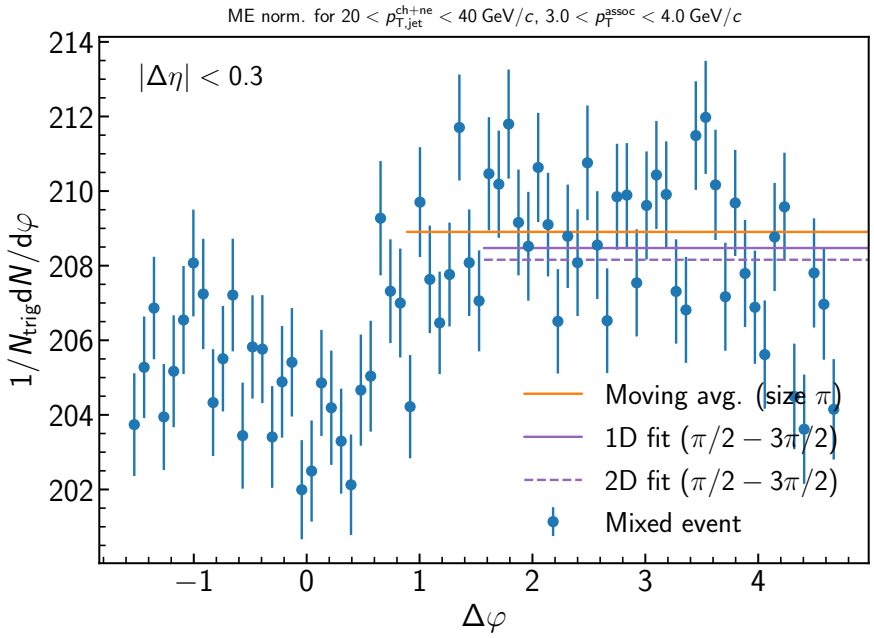

Figure D.84: Determination of the normalization of the mixed event for the inclusive event plane orientation in 30–50% Pb–Pb collisions at $\sqrt{s_{\mathrm{NN}}} = 5.02$ TeV. Here the mixed event is projected over the plateau range in $\Delta\eta$ onto to the $\Delta\varphi$ axis. The moving average is evaluated over the entire $\Delta\varphi$ range using a window of π, while the fit range is fixed from $\pi/2 < \Delta\varphi < 3\pi/2$. Since the mixed events are merged above 2 GeV/c, the normalization factor is also the same for all correlations within $3.0 < p_{\mathrm{T}}^{\mathrm{assoc}} < 4.0$ GeV/c. A variety of normalization methods were evaluated, with further details described in the text.

D.1.22 $20 < p_{\mathrm{T,jet}}^{\mathrm{ch+ne}} < 40\ \mathrm{GeV}/c$, $4.0 < p_{\mathrm{T}}^{\mathrm{assoc}} < 5.0\ \mathrm{GeV}/c$, Mid-plane orientation

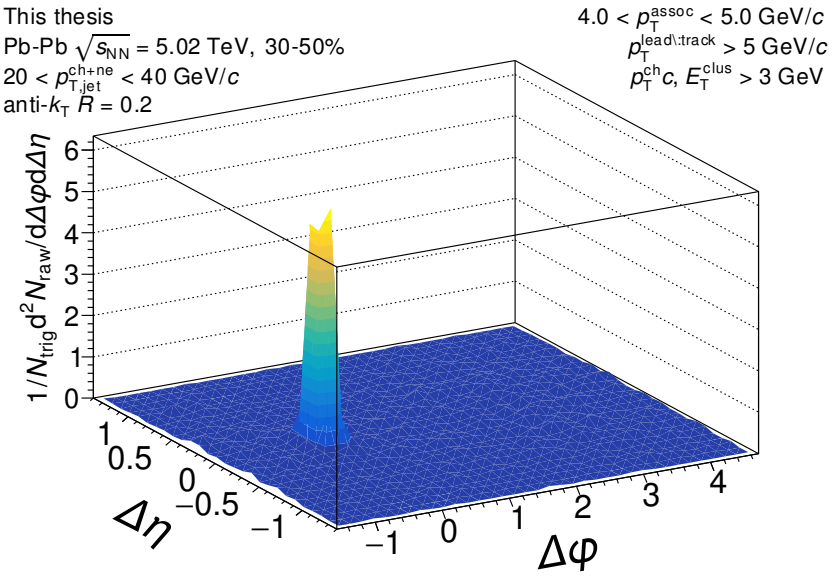

Figure D.85: The measured correlation function with the the efficiency correction $\epsilon(p_{\mathrm{T}}, \eta)$ applied, but before acceptance correction via the mixed events. The correlation is measured for mid-plane orientation for $20 < p_{\mathrm{T,jet}}^{\mathrm{ch+ne}} < 40\ \mathrm{GeV}/c$ jets with $4.0 < p_{\mathrm{T}}^{\mathrm{assoc}} < 5.0\ \mathrm{GeV}/c$ in 30–50% Pb–Pb collisions at $\sqrt{s_{\mathrm{NN}}} = 5.02$ TeV.

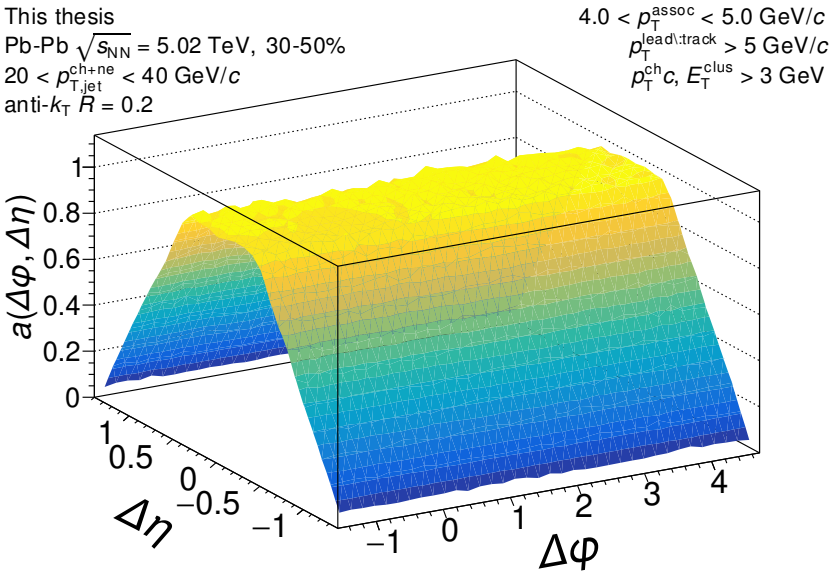

Figure D.86: The mixed event pair acceptance correction with the efficiency correction $\epsilon(p_{\mathrm{T}}, \eta)$ applied. The correlations are measured for mid-plane orientation for $20 < p_{\mathrm{T,jet}}^{\mathrm{ch+ne}} < 40\,\mathrm{GeV}/c$ jets with $4.0 < p_{\mathrm{T}}^{\mathrm{assoc}} < 5.0\,\mathrm{GeV}/c$ in 30–50% Pb–Pb collisions at $\sqrt{s_{\mathrm{NN}}} = 5.02\,\mathrm{TeV}$. They have already been normalized such that it they are unity at maximum efficiency. Above 2 GeV/c, the mixed events are merged together to increase statistics, so it is the same for all for correlations within $2.0 \leq p_{\mathrm{T}}^{\mathrm{assoc}} < 10\,\mathrm{GeV}/c$.

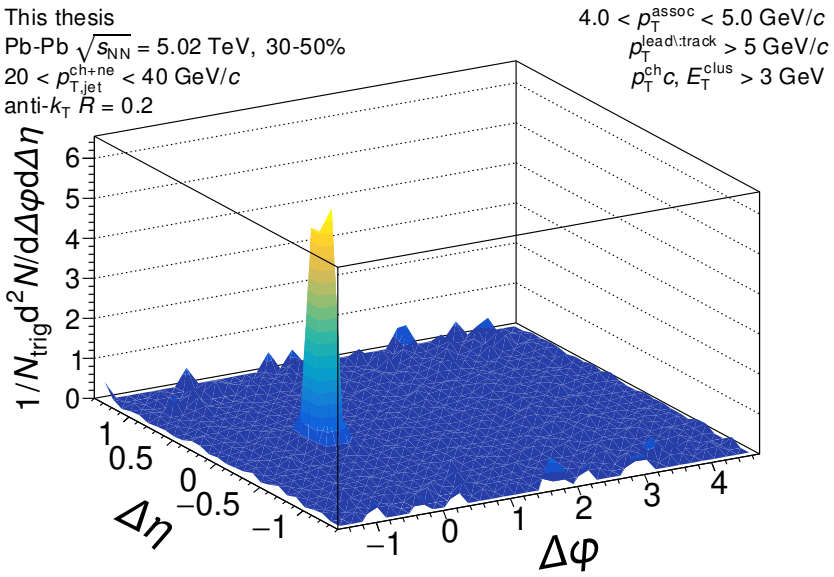

Figure D.87: The signal correlation corrected by pair acceptance. The correlations are measured for mid-plane orientation for $20 < p_{\mathrm{T,jet}}^{\mathrm{ch+ne}} < 40\,\mathrm{GeV}/c$ jets with $4.0 < p_{\mathrm{T}}^{\mathrm{assoc}} < 5.0\,\mathrm{GeV}/c$ in 30–50% Pb–Pb collisions at $\sqrt{s_{\mathrm{NN}}} = 5.02\,\mathrm{TeV}$.

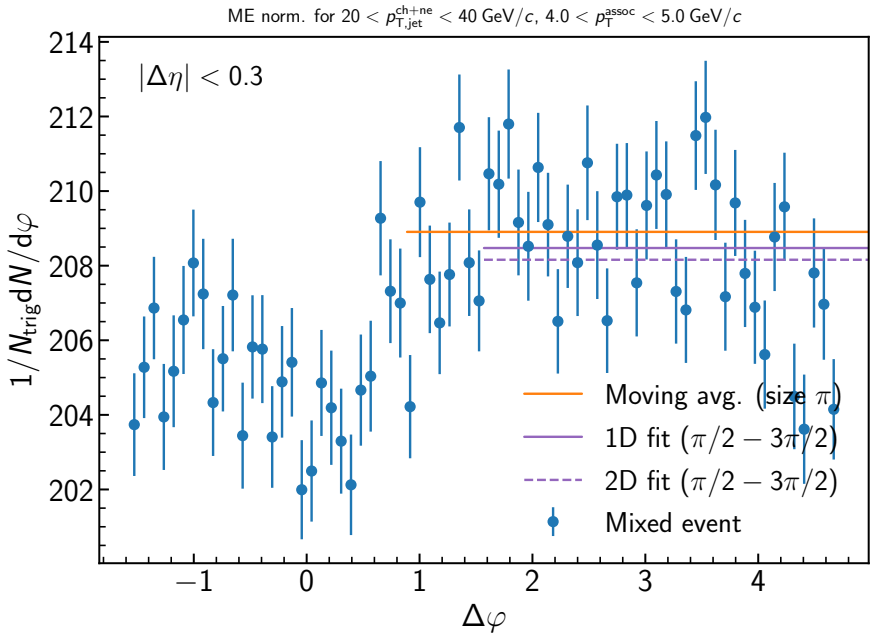

Figure D.88: Determination of the normalization of the mixed event for the inclusive event plane orientation in 30–50% Pb–Pb collisions at $\sqrt{s_{\mathrm{NN}}} = 5.02$ TeV. Here the mixed event is projected over the plateau range in $\Delta\eta$ onto to the $\Delta\varphi$ axis. The moving average is evaluated over the entire $\Delta\varphi$ range using a window of π, while the fit range is fixed from $\pi/2 < \Delta\varphi < 3\pi/2$. Since the mixed events are merged above 2 GeV/c, the normalization factor is also the same for all correlations within $4.0 < p_{\mathrm{T}}^{\mathrm{assoc}} < 5.0$ GeV/c. A variety of normalization methods were evaluated, with further details described in the text.

D.1.23 $20 < p_{\mathrm{T,jet}}^{\mathrm{ch+ne}} < 40\ \mathrm{GeV}/c$, $5.0 < p_{\mathrm{T}}^{\mathrm{assoc}} < 6.0\ \mathrm{GeV}/c$, Mid-plane orientation

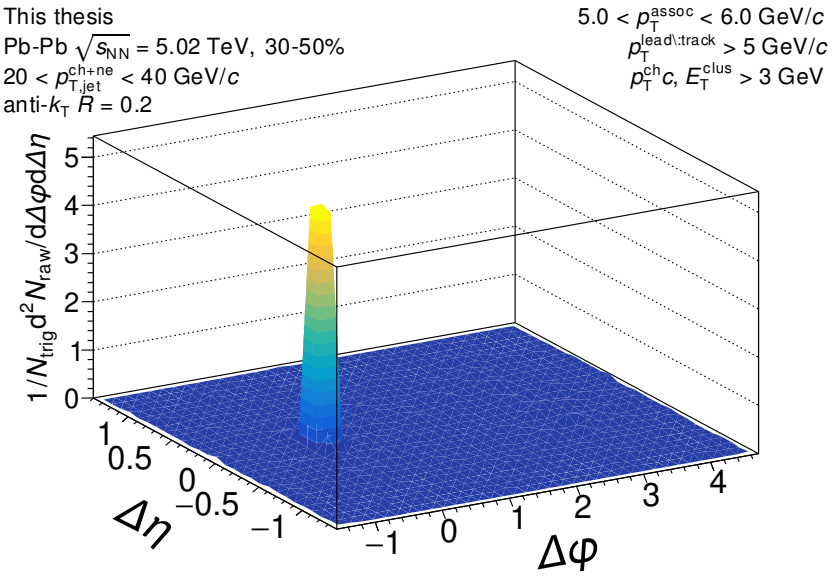

Figure D.89: The measured correlation function with the the efficiency correction $\epsilon(p_{\mathrm{T}}, \eta)$ applied, but before acceptance correction via the mixed events. The correlation is measured for mid-plane orientation for $20 < p_{\mathrm{T,jet}}^{\mathrm{ch+ne}} < 40\ \mathrm{GeV}/c$ jets with $5.0 < p_{\mathrm{T}}^{\mathrm{assoc}} < 6.0\ \mathrm{GeV}/c$ in 30–50% Pb–Pb collisions at $\sqrt{s_{\mathrm{NN}}} = 5.02$ TeV.

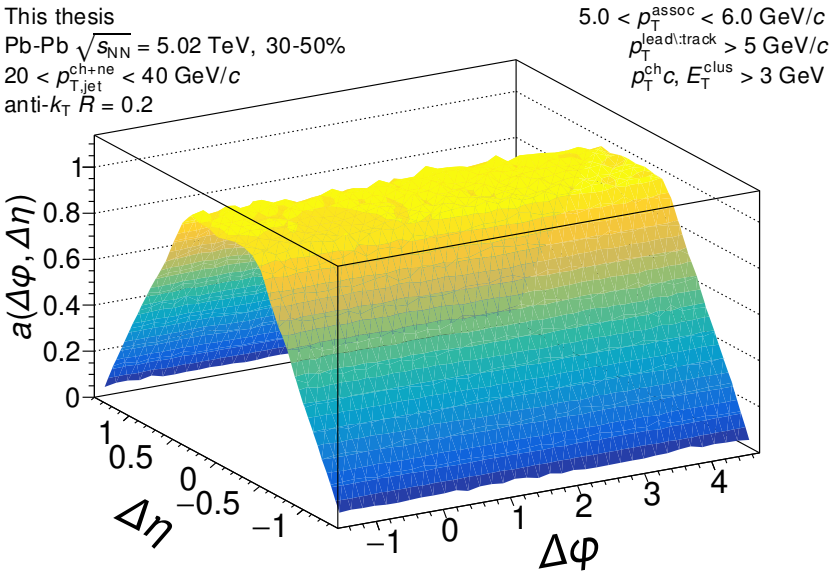

Figure D.90: The mixed event pair acceptance correction with the efficiency correction $\epsilon(p_T, \eta)$ applied. The correlations are measured for mid-plane orientation for $20 < p_{T,jet}^{ch+ne} < 40$ GeV/c jets with $5.0 < p_T^{assoc} < 6.0$ GeV/c in 30–50% Pb–Pb collisions at $\sqrt{s_{NN}} = 5.02$ TeV. They have already been normalized such that it they are unity at maximum efficiency. Above 2 GeV/c, the mixed events are merged together to increase statistics, so it is the same for all for correlations within $2.0 \leq p_T^{assoc} < 10$ GeV/c.

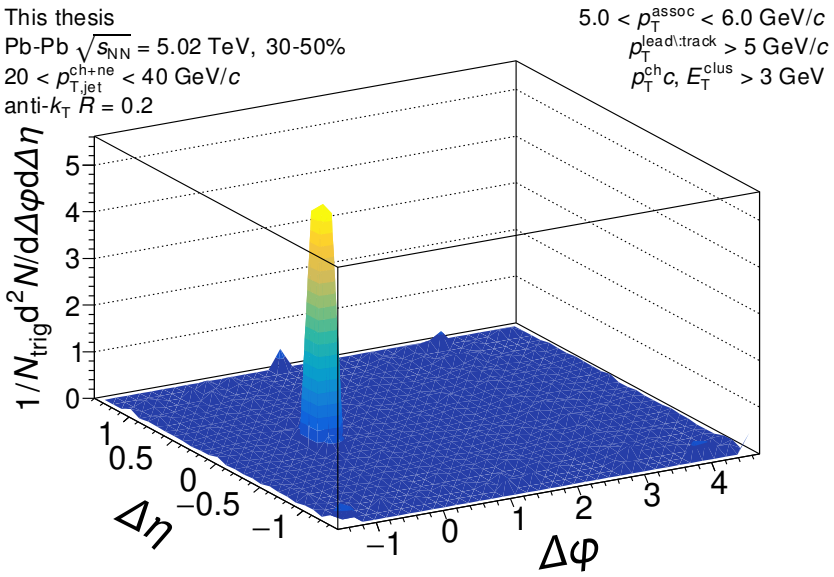

Figure D.91: The signal correlation corrected by pair acceptance. The correlations are measured for mid-plane orientation for $20 < p_{T,jet}^{ch+ne} < 40$ GeV/c jets with $5.0 < p_T^{assoc} < 6.0$ GeV/c in 30–50% Pb–Pb collisions at $\sqrt{s_{NN}} = 5.02$ TeV.

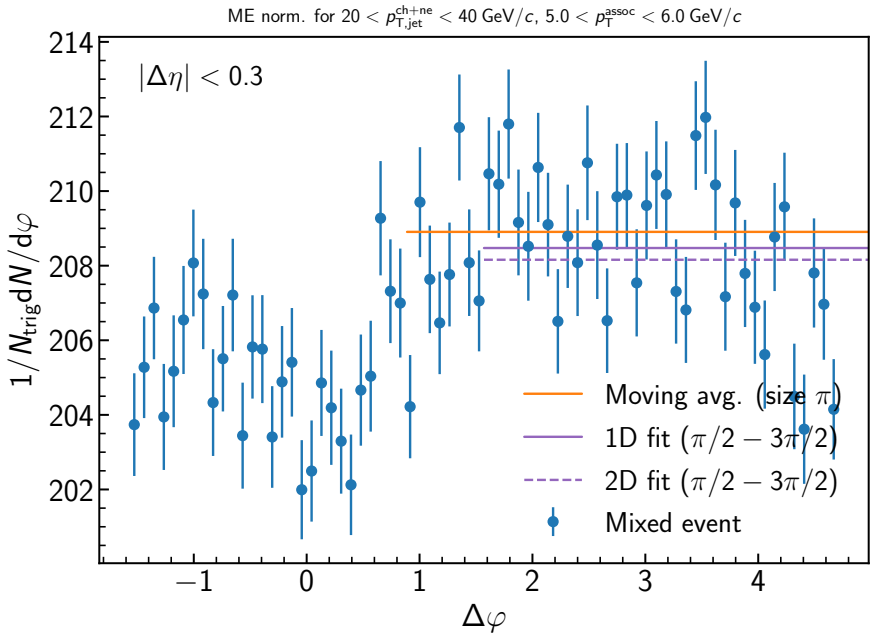

Figure D.92: Determination of the normalization of the mixed event for the inclusive event plane orientation in 30–50% Pb–Pb collisions at $\sqrt{s_{\mathrm{NN}}} = 5.02$ TeV. Here the mixed event is projected over the plateau range in $\Delta\eta$ onto to the $\Delta\varphi$ axis. The moving average is evaluated over the entire $\Delta\varphi$ range using a window of π, while the fit range is fixed from $\pi/2 < \Delta\varphi < 3\pi/2$. Since the mixed events are merged above 2 GeV/c, the normalization factor is also the same for all correlations within $5.0 < p_{\mathrm{T}}^{\mathrm{assoc}} < 6.0$ GeV/c. A variety of normalization methods were evaluated, with further details described in the text.

D.1.24 $20 < p_{\mathrm{T,jet}}^{\mathrm{ch+ne}} < 40\ \mathrm{GeV}/c$, $6.0 < p_{\mathrm{T}}^{\mathrm{assoc}} < 10.0\ \mathrm{GeV}/c$, Mid-plane orientation

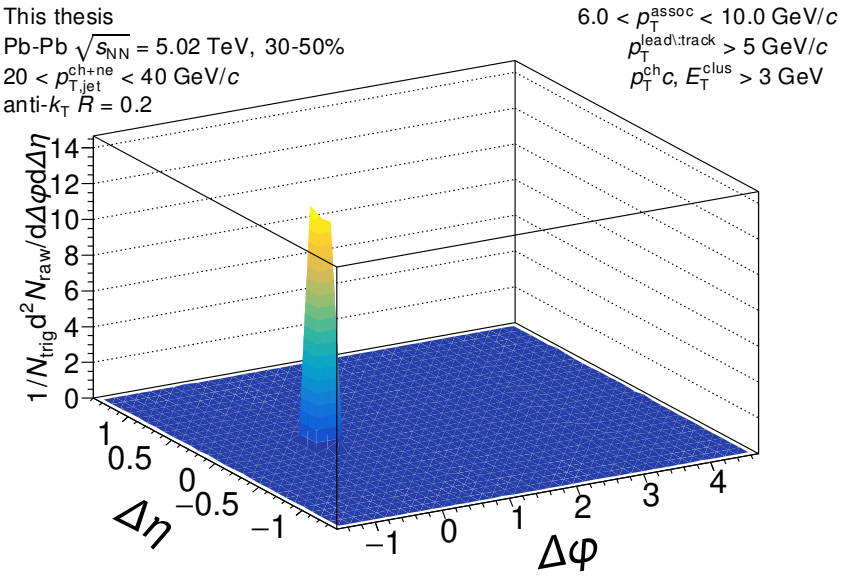

Figure D.93: The measured correlation function with the the efficiency correction $\epsilon(p_{\mathrm{T}}, \eta)$ applied, but before acceptance correction via the mixed events. The correlation is measured for mid-plane orientation for $20 < p_{\mathrm{T,jet}}^{\mathrm{ch+ne}} < 40\ \mathrm{GeV}/c$ jets with $6.0 < p_{\mathrm{T}}^{\mathrm{assoc}} < 10.0\ \mathrm{GeV}/c$ in 30–50% Pb–Pb collisions at $\sqrt{s_{\mathrm{NN}}} = 5.02\ \mathrm{TeV}$.

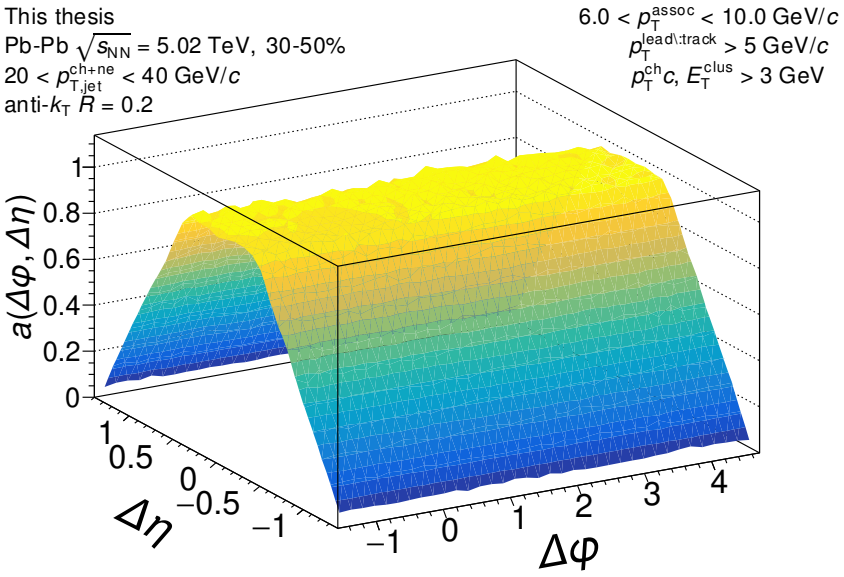

Figure D.94: The mixed event pair acceptance correction with the efficiency correction $\epsilon(p_{\mathrm{T}}, \eta)$ applied. The correlations are measured for mid-plane orientation for $20 < p_{\mathrm{T,jet}}^{\mathrm{ch+ne}} < 40\,\mathrm{GeV}/c$ jets with $6.0 < p_{\mathrm{T}}^{\mathrm{assoc}} < 10.0\,\mathrm{GeV}/c$ in 30–50% Pb–Pb collisions at $\sqrt{s_{\mathrm{NN}}} = 5.02\,\mathrm{TeV}$. They have already been normalized such that it they are unity at maximum efficiency. Above 2 GeV/c, the mixed events are merged together to increase statistics, so it is the same for all for correlations within $2.0 \leq p_{\mathrm{T}}^{\mathrm{assoc}} < 10$ GeV/c.

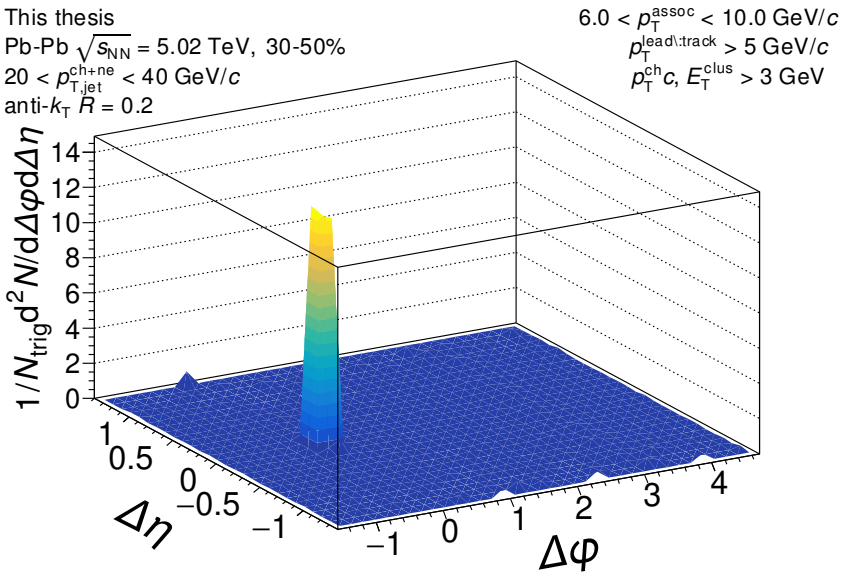

Figure D.95: The signal correlation corrected by pair acceptance. The correlations are measured for mid-plane orientation for $20 < p_{\mathrm{T,jet}}^{\mathrm{ch+ne}} < 40\,\mathrm{GeV}/c$ jets with $6.0 < p_{\mathrm{T}}^{\mathrm{assoc}} < 10.0\,\mathrm{GeV}/c$ in 30–50% Pb–Pb collisions at $\sqrt{s_{\mathrm{NN}}} = 5.02\,\mathrm{TeV}$.

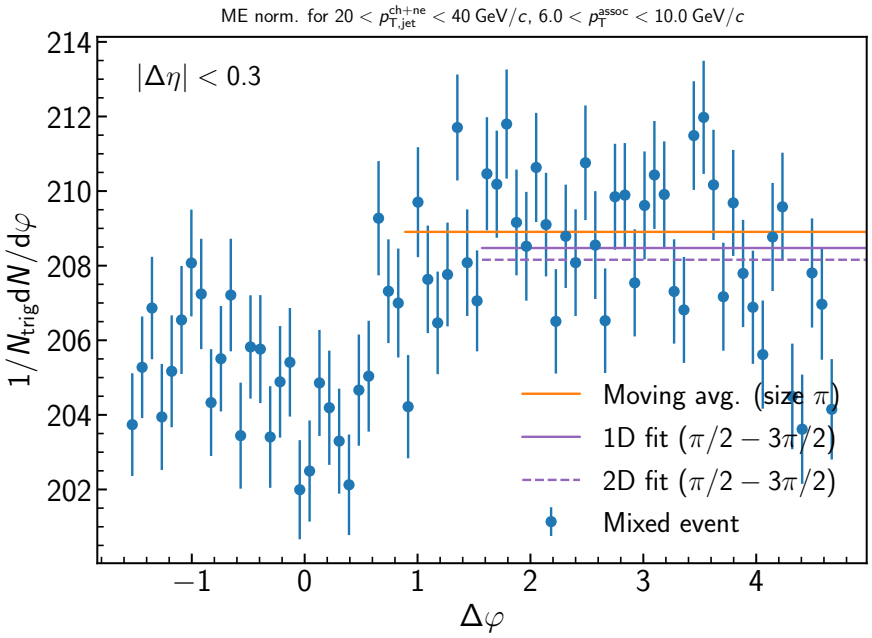

Figure D.96: Determination of the normalization of the mixed event for the inclusive event plane orientation in 30–50% Pb–Pb collisions at $\sqrt{s_{\mathrm{NN}}} = 5.02$ TeV. Here the mixed event is projected over the plateau range in $\Delta\eta$ onto to the $\Delta\varphi$ axis. The moving average is evaluated over the entire $\Delta\varphi$ range using a window of π, while the fit range is fixed from $\pi/2 < \Delta\varphi < 3\pi/2$. Since the mixed events are merged above 2 GeV/c, the normalization factor is also the same for all correlations within $6.0 < p_{\mathrm{T}}^{\mathrm{assoc}} < 10.0$ GeV/c. A variety of normalization methods were evaluated, with further details described in the text.

D.1.25 $20 < p_{\mathrm{T,jet}}^{\mathrm{ch+ne}} < 40\ \mathrm{GeV}/c$, $0.5 < p_{\mathrm{T}}^{\mathrm{assoc}} < 1.0\ \mathrm{GeV}/c$, Out-of-plane orientation

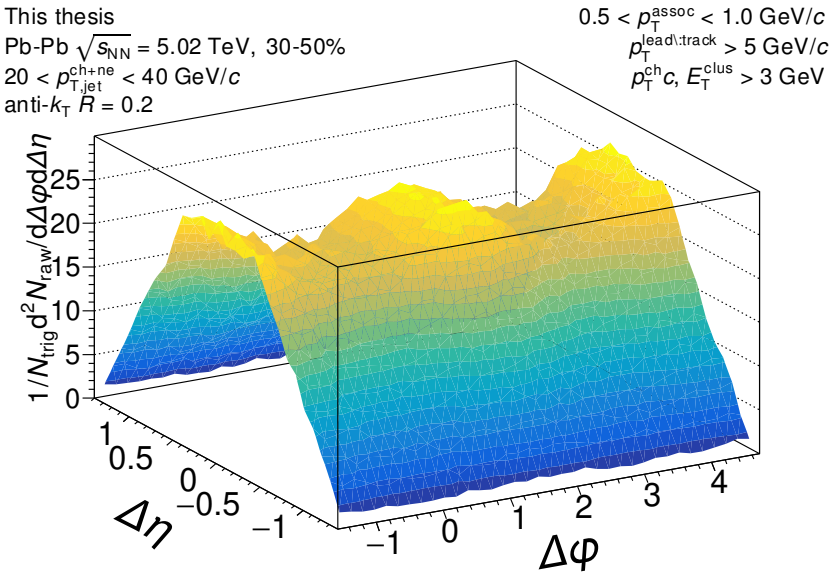

Figure D.97: The measured correlation function with the the efficiency correction $\epsilon(p_{\mathrm{T}}, \eta)$ applied, but before acceptance correction via the mixed events. The correlation is measured for out-of-plane orientation for $20 < p_{\mathrm{T,jet}}^{\mathrm{ch+ne}} < 40\ \mathrm{GeV}/c$ jets with $0.5 < p_{\mathrm{T}}^{\mathrm{assoc}} < 1.0\ \mathrm{GeV}/c$ in 30–50% Pb–Pb collisions at $\sqrt{s_{\mathrm{NN}}} = 5.02$ TeV.

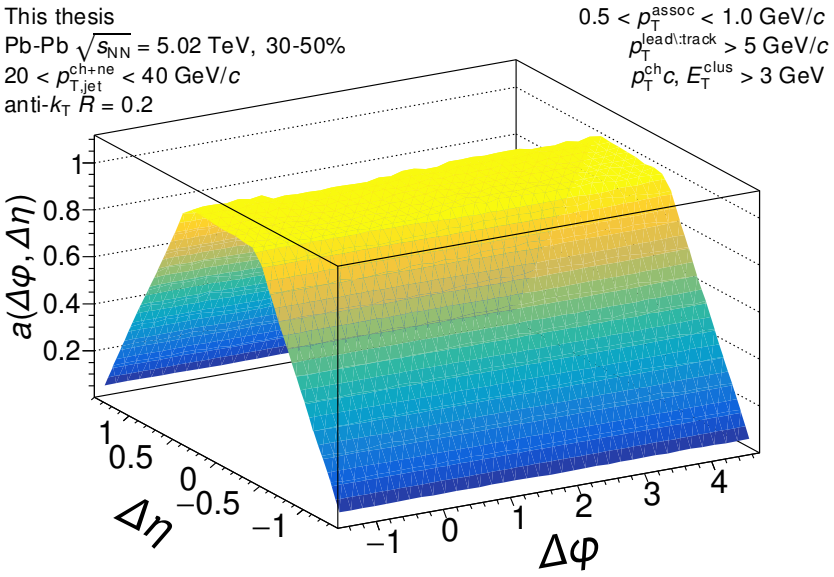

Figure D.98: The mixed event pair acceptance correction with the efficiency correction $\epsilon(p_{\mathrm{T}}, \eta)$ applied. The correlations are measured for out-of-plane orientation for $20 < p_{\mathrm{T,jet}}^{\mathrm{ch+ne}} < 40$ GeV/c jets with $0.5 < p_{\mathrm{T}}^{\mathrm{assoc}} < 1.0$ GeV/c in 30–50% Pb–Pb collisions at $\sqrt{s_{\mathrm{NN}}} = 5.02$ TeV. They have already been normalized such that it they are unity at maximum efficiency. Above 2 GeV/c, the mixed events are merged together to increase statistics, so it is the same for all for correlations within $2.0 \leq p_{\mathrm{T}}^{\mathrm{assoc}} < 10$ GeV/c.

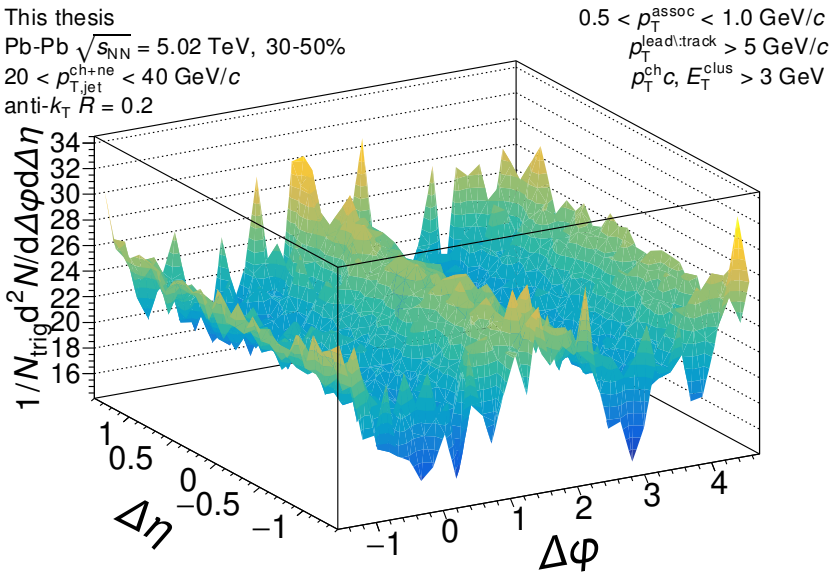

Figure D.99: The signal correlation corrected by pair acceptance. The correlations are measured for out-of-plane orientation for $20 < p_{\mathrm{T,jet}}^{\mathrm{ch+ne}} < 40$ GeV/c jets with $0.5 < p_{\mathrm{T}}^{\mathrm{assoc}} < 1.0$ GeV/c in 30–50% Pb–Pb collisions at $\sqrt{s_{\mathrm{NN}}} = 5.02$ TeV.

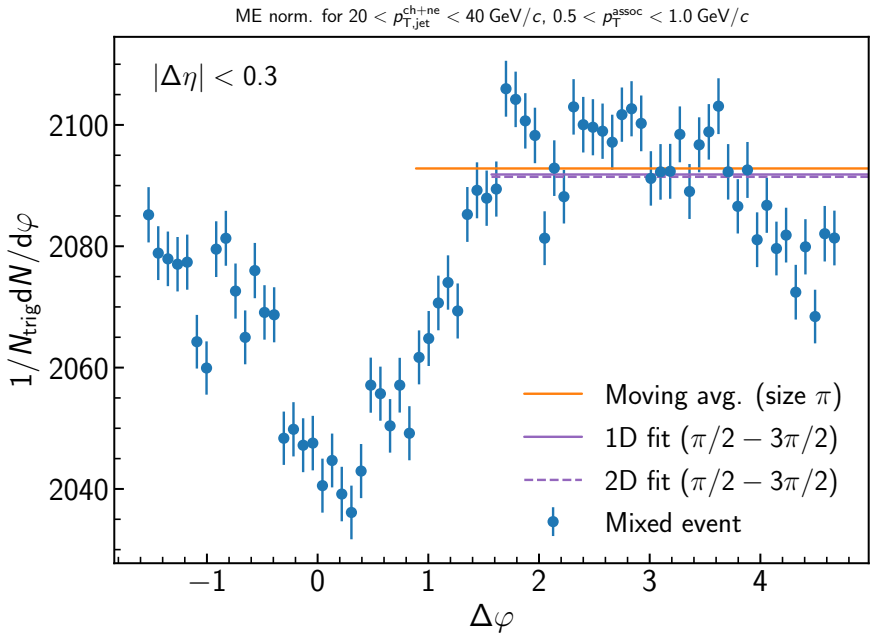

Figure D.100: Determination of the normalization of the mixed event for the inclusive event plane orientation in 30–50% Pb–Pb collisions at $\sqrt{s_{\mathrm{NN}}} = 5.02$ TeV. Here the mixed event is projected over the plateau range in $\Delta\eta$ onto to the $\Delta\varphi$ axis. The moving average is evaluated over the entire $\Delta\varphi$ range using a window of π, while the fit range is fixed from $\pi/2 < \Delta\varphi < 3\pi/2$. Since the mixed events are merged above 2 GeV/c, the normalization factor is also the same for all correlations within $0.5 < p_{\mathrm{T}}^{\mathrm{assoc}} < 1.0$ GeV/c. A variety of normalization methods were evaluated, with further details described in the text.

D.1.26 $20 < p_{\mathrm{T,jet}}^{\mathrm{ch+ne}} < 40\ \mathrm{GeV}/c$, $1.0 < p_{\mathrm{T}}^{\mathrm{assoc}} < 1.5\ \mathrm{GeV}/c$, Out-of-plane orientation

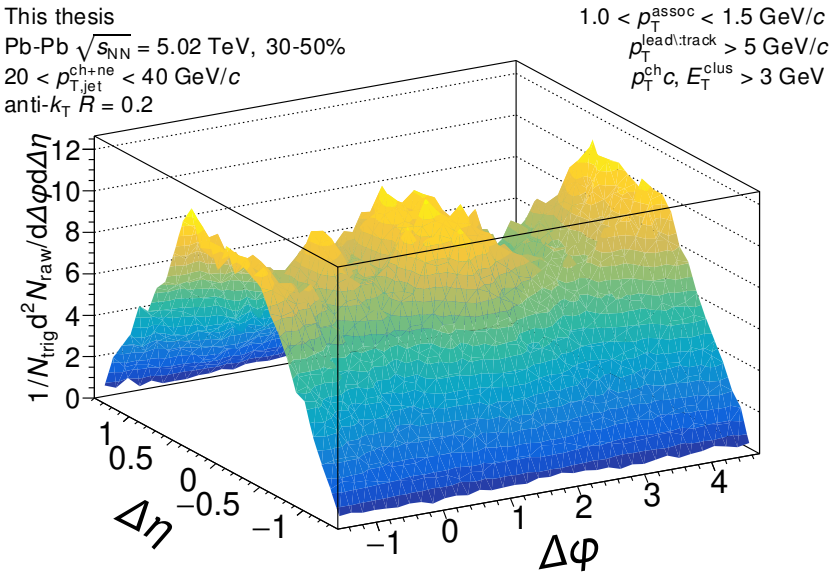

Figure D.101: The measured correlation function with the the efficiency correction $\epsilon(p_{\mathrm{T}}, \eta)$ applied, but before acceptance correction via the mixed events. The correlation is measured for out-of-plane orientation for $20 < p_{\mathrm{T,jet}}^{\mathrm{ch+ne}} < 40\ \mathrm{GeV}/c$ jets with $1.0 < p_{\mathrm{T}}^{\mathrm{assoc}} < 1.5\ \mathrm{GeV}/c$ in 30–50% Pb–Pb collisions at $\sqrt{s_{\mathrm{NN}}} = 5.02$ TeV.

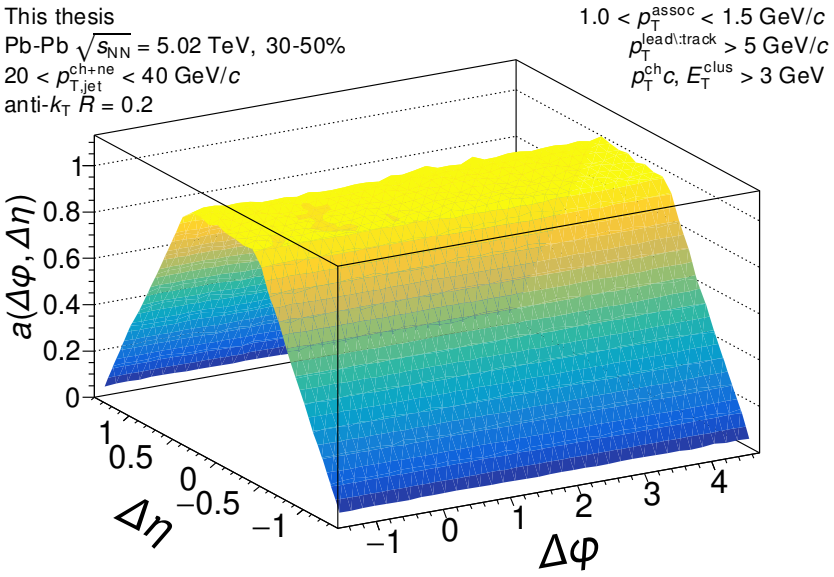

Figure D.102: The mixed event pair acceptance correction with the efficiency correction $\epsilon(p_{\mathrm{T}}, \eta)$ applied. The correlations are measured for out-of-plane orientation for $20 < p_{\mathrm{T,jet}}^{\mathrm{ch+ne}} < 40$ GeV/c jets with $1.0 < p_{\mathrm{T}}^{\mathrm{assoc}} < 1.5$ GeV/c in 30–50% Pb–Pb collisions at $\sqrt{s_{\mathrm{NN}}} = 5.02$ TeV. They have already been normalized such that it they are unity at maximum efficiency. Above 2 GeV/c, the mixed events are merged together to increase statistics, so it is the same for all for correlations within $2.0 \leq p_{\mathrm{T}}^{\mathrm{assoc}} < 10$ GeV/c.

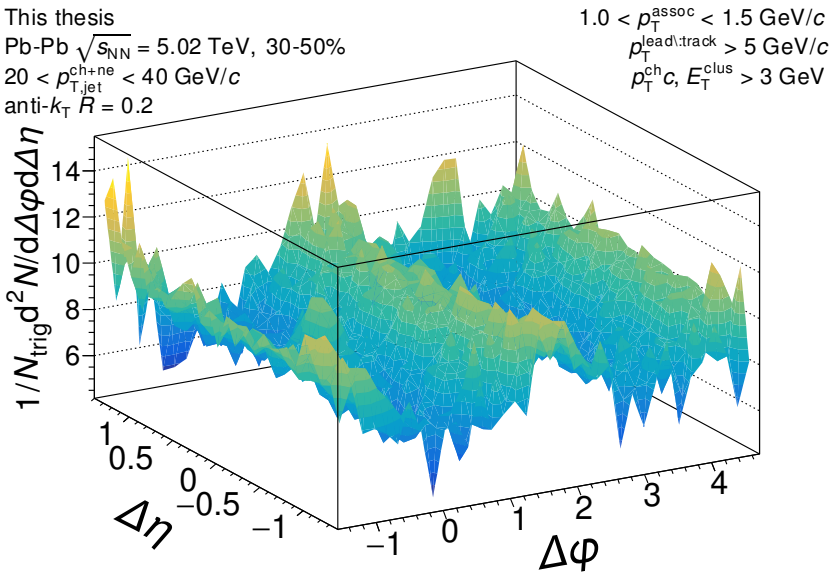

Figure D.103: The signal correlation corrected by pair acceptance. The correlations are measured for out-of-plane orientation for $20 < p_{\mathrm{T,jet}}^{\mathrm{ch+ne}} < 40$ GeV/c jets with $1.0 < p_{\mathrm{T}}^{\mathrm{assoc}} < 1.5$ GeV/c in 30–50% Pb–Pb collisions at $\sqrt{s_{\mathrm{NN}}} = 5.02$ TeV.

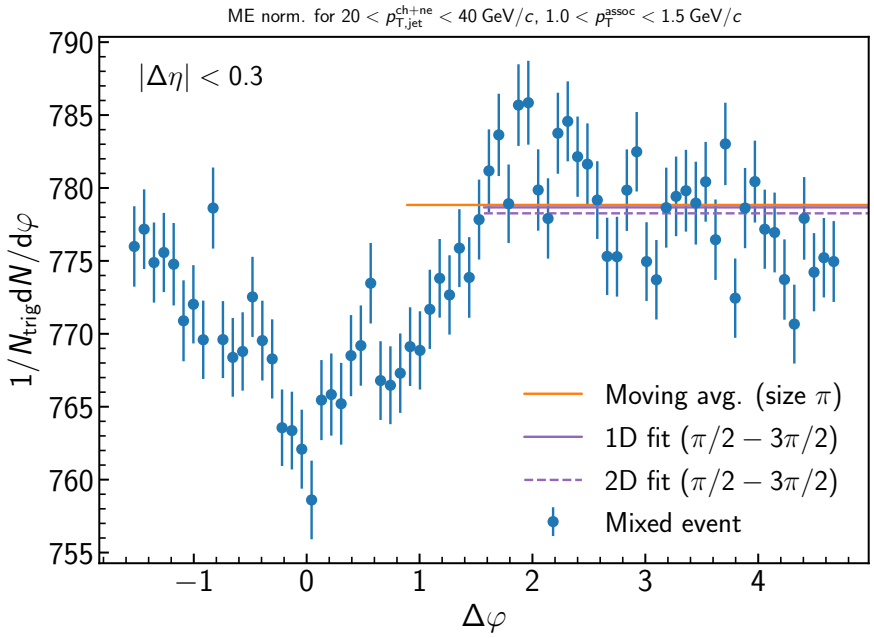

Figure D.104: Determination of the normalization of the mixed event for the inclusive event plane orientation in 30–50% Pb–Pb collisions at $\sqrt{s_{\mathrm{NN}}} = 5.02$ TeV. Here the mixed event is projected over the plateau range in $\Delta\eta$ onto to the $\Delta\varphi$ axis. The moving average is evaluated over the entire $\Delta\varphi$ range using a window of π, while the fit range is fixed from $\pi/2 < \Delta\varphi < 3\pi/2$. Since the mixed events are merged above 2 GeV/c, the normalization factor is also the same for all correlations within $1.0 < p_{\mathrm{T}}^{\mathrm{assoc}} < 1.5$ GeV/c. A variety of normalization methods were evaluated, with further details described in the text.

D.1.27 $20 < p_{\mathrm{T,jet}}^{\mathrm{ch+ne}} < 40\ \mathrm{GeV}/c$, $1.5 < p_{\mathrm{T}}^{\mathrm{assoc}} < 2.0\ \mathrm{GeV}/c$, Out-of-plane orientation

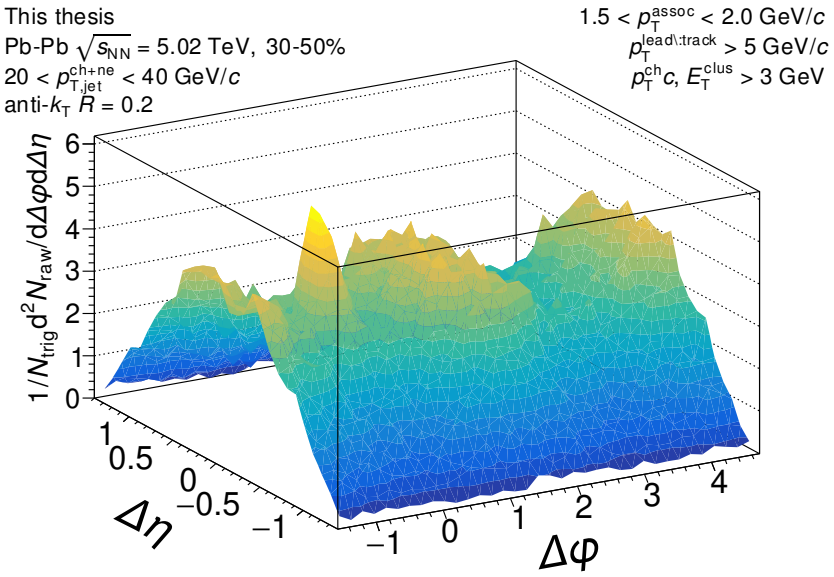

Figure D.105: The measured correlation function with the the efficiency correction $\epsilon(p_{\mathrm{T}}, \eta)$ applied, but before acceptance correction via the mixed events. The correlation is measured for out-of-plane orientation for $20 < p_{\mathrm{T,jet}}^{\mathrm{ch+ne}} < 40\ \mathrm{GeV}/c$ jets with $1.5 < p_{\mathrm{T}}^{\mathrm{assoc}} < 2.0\ \mathrm{GeV}/c$ in 30–50% Pb–Pb collisions at $\sqrt{s_{\mathrm{NN}}} = 5.02$ TeV.

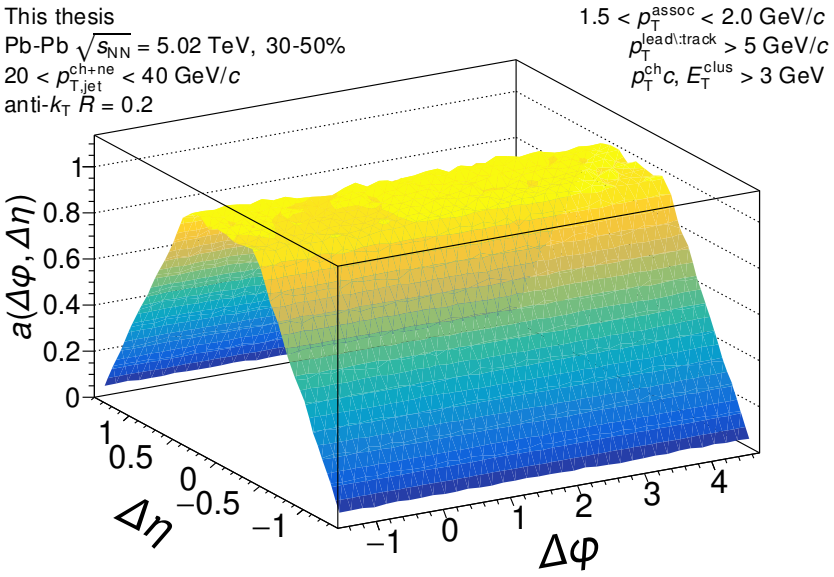

Figure D.106: The mixed event pair acceptance correction with the efficiency correction $\epsilon(p_{\mathrm{T}}, \eta)$ applied. The correlations are measured for out-of-plane orientation for $20 < p_{\mathrm{T,jet}}^{\mathrm{ch+ne}} < 40$ GeV/c jets with $1.5 < p_{\mathrm{T}}^{\mathrm{assoc}} < 2.0$ GeV/c in 30–50% Pb–Pb collisions at $\sqrt{s_{\mathrm{NN}}} = 5.02$ TeV. They have already been normalized such that it they are unity at maximum efficiency. Above 2 GeV/c, the mixed events are merged together to increase statistics, so it is the same for all for correlations within $2.0 \leq p_{\mathrm{T}}^{\mathrm{assoc}} < 10$ GeV/c.

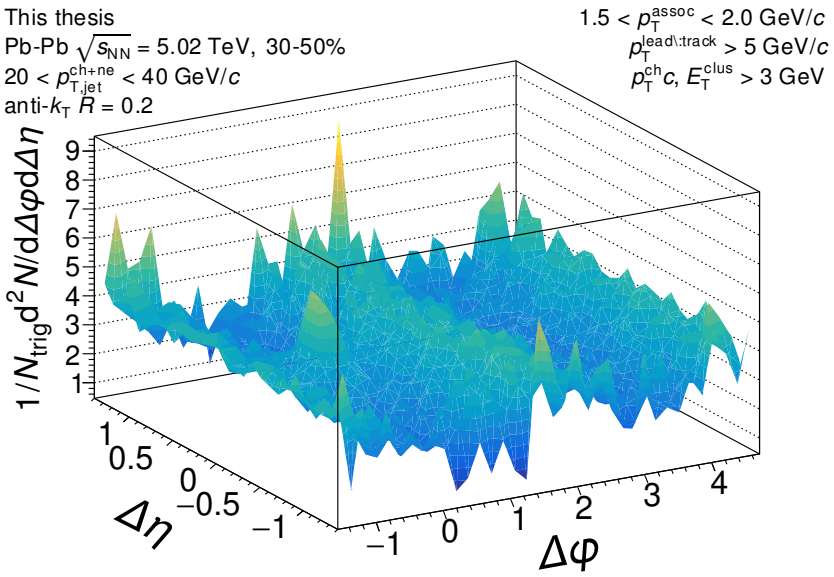

Figure D.107: The signal correlation corrected by pair acceptance. The correlations are measured for out-of-plane orientation for $20 < p_{\mathrm{T,jet}}^{\mathrm{ch+ne}} < 40$ GeV/c jets with $1.5 < p_{\mathrm{T}}^{\mathrm{assoc}} < 2.0$ GeV/c in 30–50% Pb–Pb collisions at $\sqrt{s_{\mathrm{NN}}} = 5.02$ TeV.

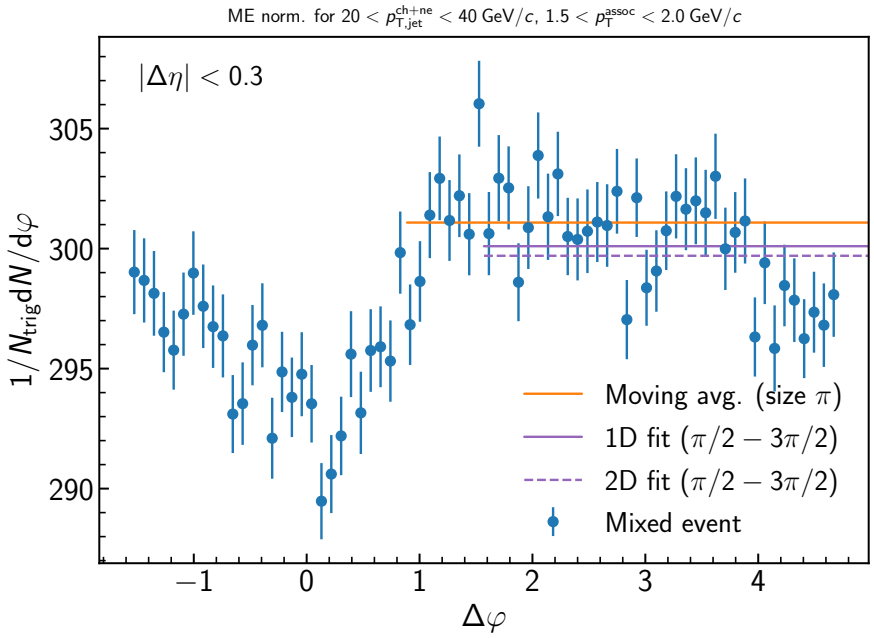

Figure D.108: Determination of the normalization of the mixed event for the inclusive event plane orientation in 30–50% Pb–Pb collisions at $\sqrt{s_{\mathrm{NN}}} = 5.02$ TeV. Here the mixed event is projected over the plateau range in $\Delta\eta$ onto to the $\Delta\varphi$ axis. The moving average is evaluated over the entire $\Delta\varphi$ range using a window of π, while the fit range is fixed from $\pi/2 < \Delta\varphi < 3\pi/2$. Since the mixed events are merged above 2 GeV/c, the normalization factor is also the same for all correlations within $1.5 < p_{\mathrm{T}}^{\mathrm{assoc}} < 2.0$ GeV/c. A variety of normalization methods were evaluated, with further details described in the text.

D.1.28 $20 < p_{\mathrm{T,jet}}^{\mathrm{ch+ne}} < 40\ \mathrm{GeV}/c$, $2.0 < p_{\mathrm{T}}^{\mathrm{assoc}} < 3.0\ \mathrm{GeV}/c$, Out-of-plane orientation

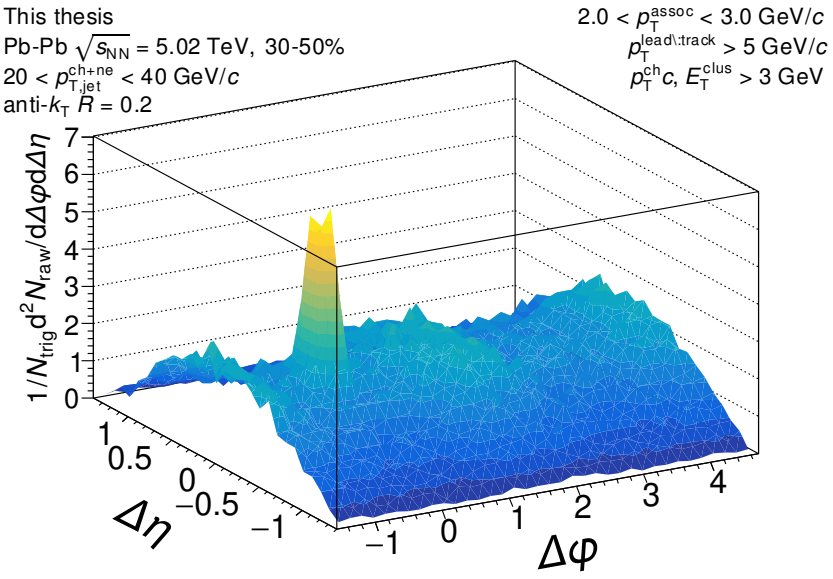

Figure D.109: The measured correlation function with the the efficiency correction $\epsilon(p_{\mathrm{T}}, \eta)$ applied, but before acceptance correction via the mixed events. The correlation is measured for out-of-plane orientation for $20 < p_{\mathrm{T,jet}}^{\mathrm{ch+ne}} < 40\ \mathrm{GeV}/c$ jets with $2.0 < p_{\mathrm{T}}^{\mathrm{assoc}} < 3.0\ \mathrm{GeV}/c$ in 30–50% Pb–Pb collisions at $\sqrt{s_{\mathrm{NN}}} = 5.02$ TeV.

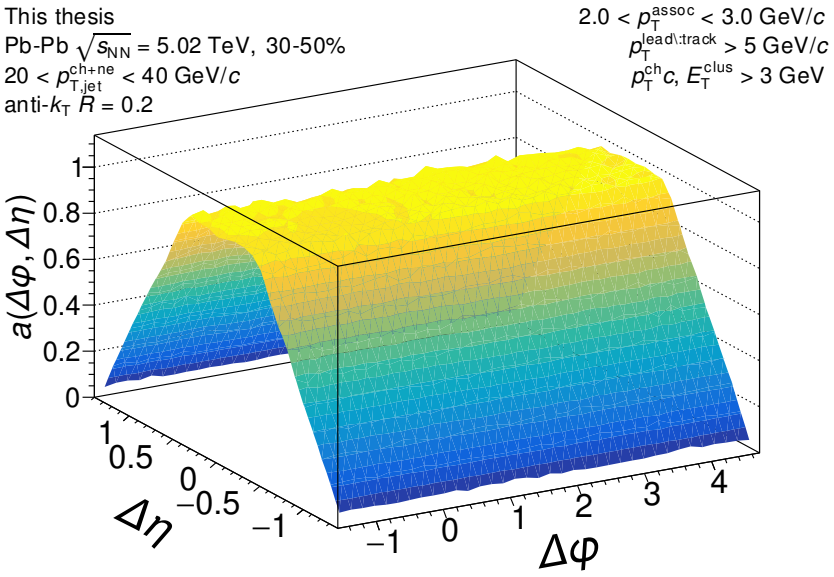

Figure D.110: The mixed event pair acceptance correction with the efficiency correction $\epsilon(p_{\mathrm{T}}, \eta)$ applied. The correlations are measured for out-of-plane orientation for $20 < p_{\mathrm{T,jet}}^{\mathrm{ch+ne}} < 40$ GeV/c jets with $2.0 < p_{\mathrm{T}}^{\mathrm{assoc}} < 3.0$ GeV/c in 30–50% Pb–Pb collisions at $\sqrt{s_{\mathrm{NN}}} = 5.02$ TeV. They have already been normalized such that it they are unity at maximum efficiency. Above 2 GeV/c, the mixed events are merged together to increase statistics, so it is the same for all for correlations within $2.0 \leq p_{\mathrm{T}}^{\mathrm{assoc}} < 10$ GeV/c.

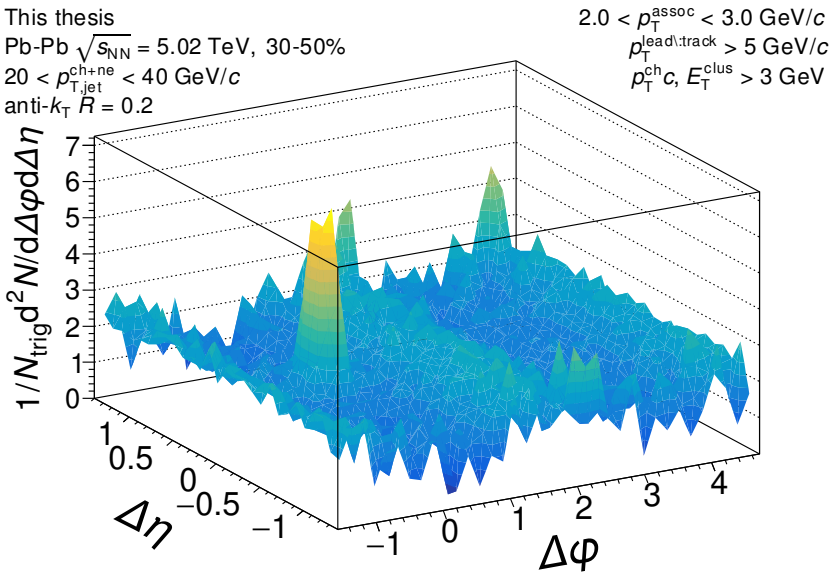

Figure D.111: The signal correlation corrected by pair acceptance. The correlations are measured for out-of-plane orientation for $20 < p_{\mathrm{T,jet}}^{\mathrm{ch+ne}} < 40$ GeV/c jets with $2.0 < p_{\mathrm{T}}^{\mathrm{assoc}} < 3.0$ GeV/c in 30–50% Pb–Pb collisions at $\sqrt{s_{\mathrm{NN}}} = 5.02$ TeV.

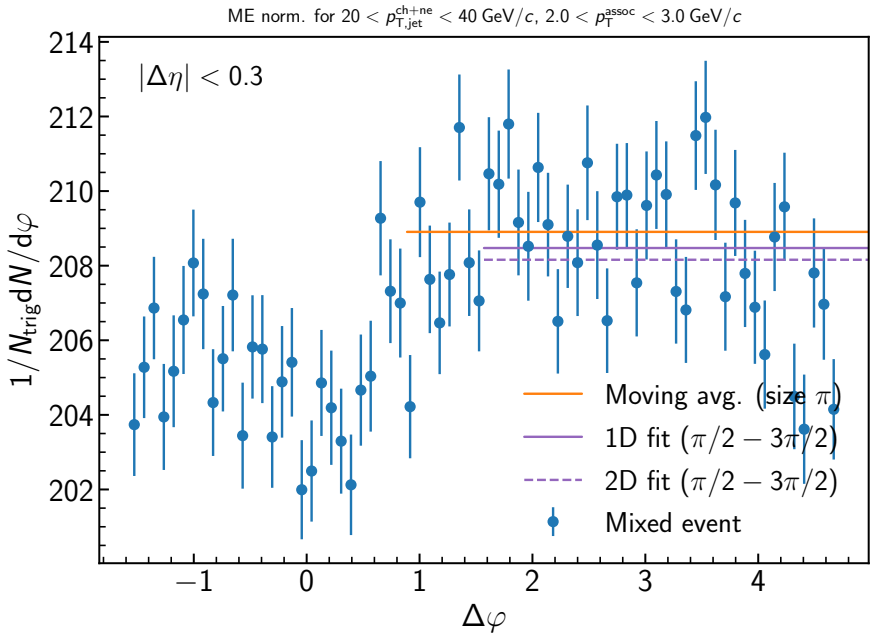

Figure D.112: Determination of the normalization of the mixed event for the inclusive event plane orientation in 30–50% Pb–Pb collisions at $\sqrt{s_{\mathrm{NN}}} = 5.02$ TeV. Here the mixed event is projected over the plateau range in $\Delta\eta$ onto to the $\Delta\varphi$ axis. The moving average is evaluated over the entire $\Delta\varphi$ range using a window of π, while the fit range is fixed from $\pi/2 < \Delta\varphi < 3\pi/2$. Since the mixed events are merged above 2 GeV/c, the normalization factor is also the same for all correlations within $2.0 < p_{\mathrm{T}}^{\mathrm{assoc}} < 3.0$ GeV/c. A variety of normalization methods were evaluated, with further details described in the text.

D.1.29 $20 < p_{\mathrm{T,jet}}^{\mathrm{ch+ne}} < 40\ \mathrm{GeV}/c$, $3.0 < p_{\mathrm{T}}^{\mathrm{assoc}} < 4.0\ \mathrm{GeV}/c$, Out-of-plane orientation

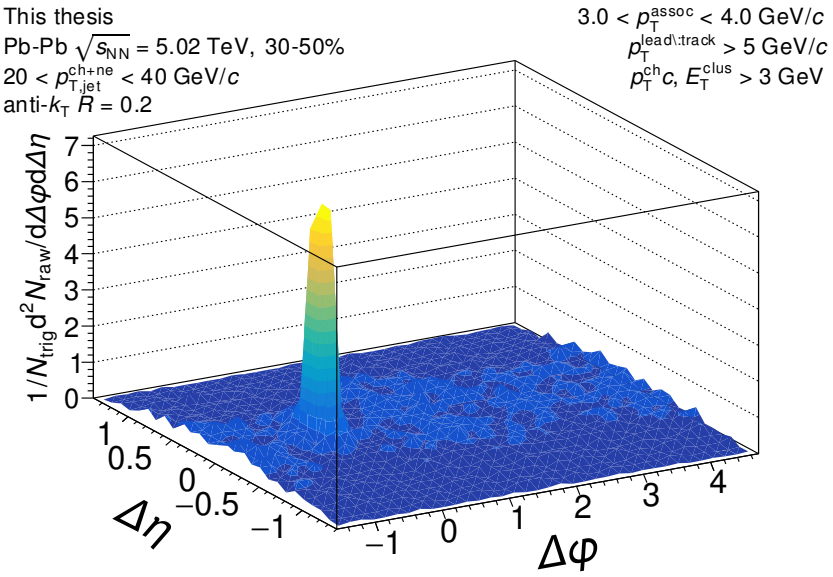

Figure D.113: The measured correlation function with the the efficiency correction $\epsilon(p_{\mathrm{T}}, \eta)$ applied, but before acceptance correction via the mixed events. The correlation is measured for out-of-plane orientation for $20 < p_{\mathrm{T,jet}}^{\mathrm{ch+ne}} < 40\ \mathrm{GeV}/c$ jets with $3.0 < p_{\mathrm{T}}^{\mathrm{assoc}} < 4.0\ \mathrm{GeV}/c$ in 30–50% Pb–Pb collisions at $\sqrt{s_{\mathrm{NN}}} = 5.02$ TeV.

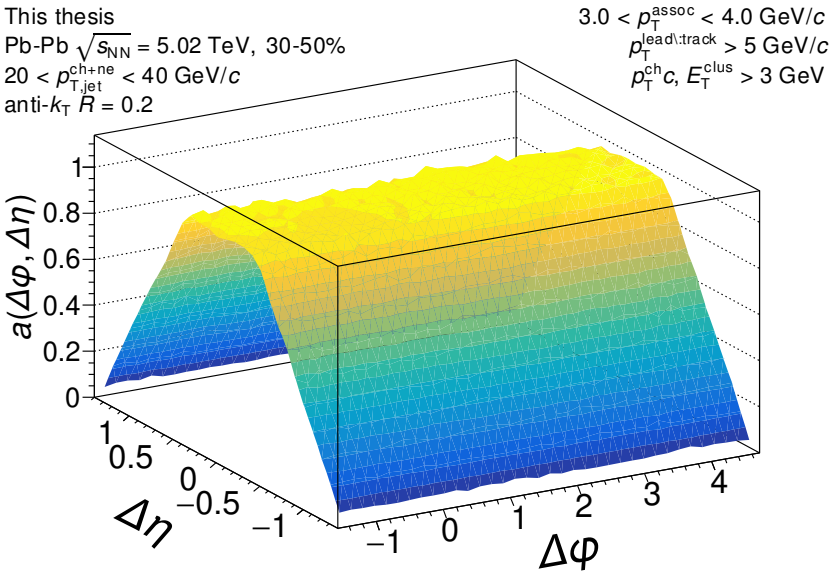

Figure D.114: The mixed event pair acceptance correction with the efficiency correction $\epsilon(p_{\mathrm{T}}, \eta)$ applied. The correlations are measured for out-of-plane orientation for $20 < p_{\mathrm{T,jet}}^{\mathrm{ch+ne}} < 40$ GeV/c jets with $3.0 < p_{\mathrm{T}}^{\mathrm{assoc}} < 4.0$ GeV/c in 30–50% Pb–Pb collisions at $\sqrt{s_{\mathrm{NN}}} = 5.02$ TeV. They have already been normalized such that it they are unity at maximum efficiency. Above 2 GeV/c, the mixed events are merged together to increase statistics, so it is the same for all for correlations within $2.0 \leq p_{\mathrm{T}}^{\mathrm{assoc}} < 10$ GeV/c.

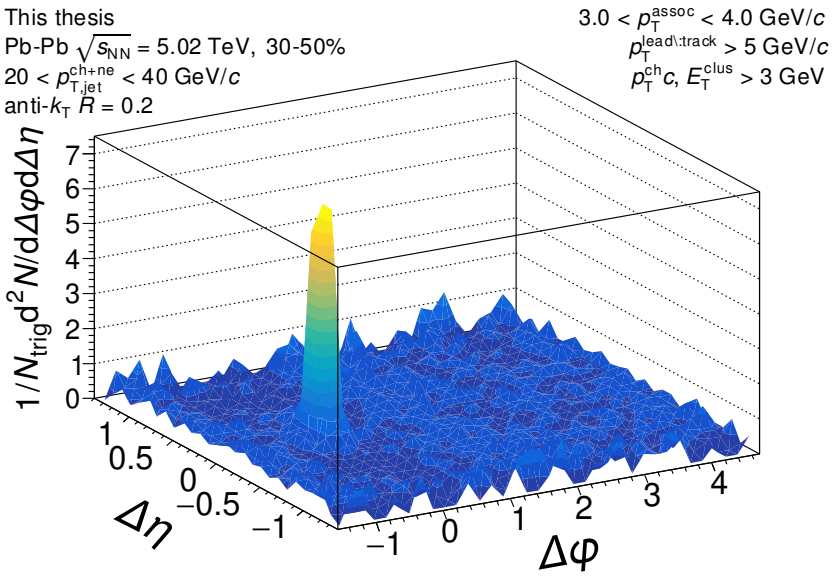

Figure D.115: The signal correlation corrected by pair acceptance. The correlations are measured for out-of-plane orientation for $20 < p_{\mathrm{T,jet}}^{\mathrm{ch+ne}} < 40$ GeV/c jets with $3.0 < p_{\mathrm{T}}^{\mathrm{assoc}} < 4.0$ GeV/c in 30–50% Pb–Pb collisions at $\sqrt{s_{\mathrm{NN}}} = 5.02$ TeV.

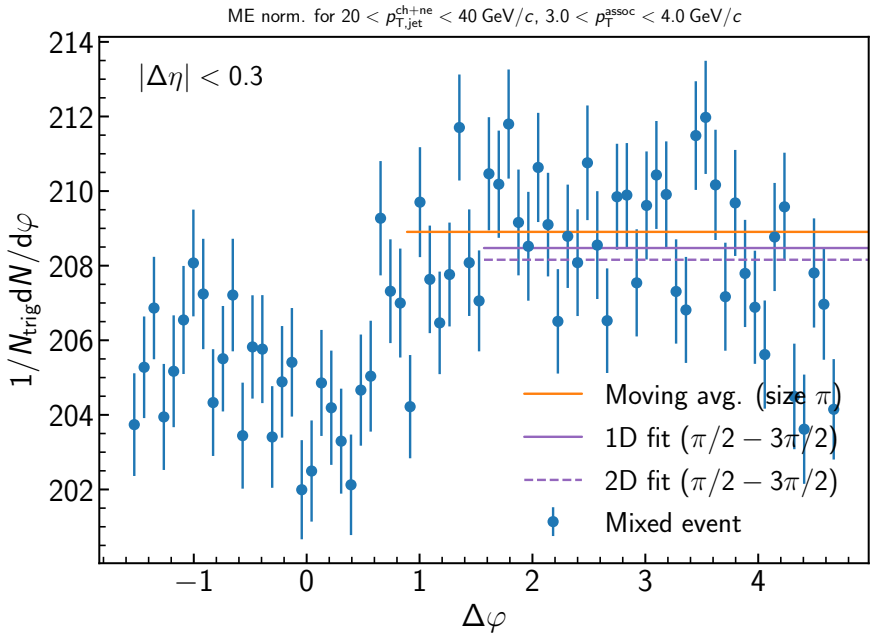

Figure D.116: Determination of the normalization of the mixed event for the inclusive event plane orientation in 30–50% Pb–Pb collisions at $\sqrt{s_{\mathrm{NN}}} = 5.02$ TeV. Here the mixed event is projected over the plateau range in $\Delta\eta$ onto to the $\Delta\varphi$ axis. The moving average is evaluated over the entire $\Delta\varphi$ range using a window of π, while the fit range is fixed from $\pi/2 < \Delta\varphi < 3\pi/2$. Since the mixed events are merged above 2 GeV/c, the normalization factor is also the same for all correlations within $3.0 < p_{\mathrm{T}}^{\mathrm{assoc}} < 4.0$ GeV/c. A variety of normalization methods were evaluated, with further details described in the text.

D.1.30 $20 < p_{\mathrm{T,jet}}^{\mathrm{ch+ne}} < 40\ \mathrm{GeV}/c$, $4.0 < p_{\mathrm{T}}^{\mathrm{assoc}} < 5.0\ \mathrm{GeV}/c$, Out-of-plane orientation

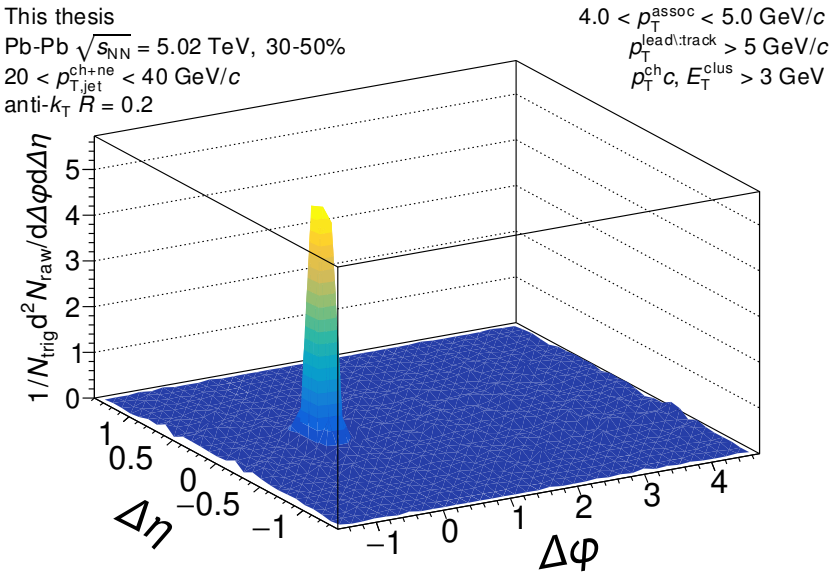

Figure D.117: The measured correlation function with the the efficiency correction $\epsilon(p_{\mathrm{T}}, \eta)$ applied, but before acceptance correction via the mixed events. The correlation is measured for out-of-plane orientation for $20 < p_{\mathrm{T,jet}}^{\mathrm{ch+ne}} < 40\ \mathrm{GeV}/c$ jets with $4.0 < p_{\mathrm{T}}^{\mathrm{assoc}} < 5.0\ \mathrm{GeV}/c$ in 30–50% Pb–Pb collisions at $\sqrt{s_{\mathrm{NN}}} = 5.02$ TeV.

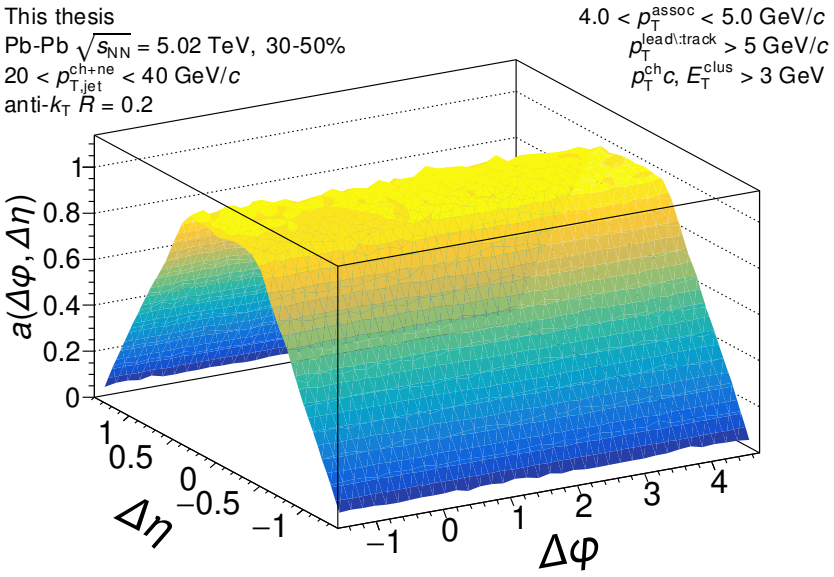

Figure D.118: The mixed event pair acceptance correction with the efficiency correction $\epsilon(p_{\mathrm{T}}, \eta)$ applied. The correlations are measured for out-of-plane orientation for $20 < p_{\mathrm{T,jet}}^{\mathrm{ch+ne}} < 40$ GeV/c jets with $4.0 < p_{\mathrm{T}}^{\mathrm{assoc}} < 5.0$ GeV/c in 30–50% Pb–Pb collisions at $\sqrt{s_{\mathrm{NN}}} = 5.02$ TeV. They have already been normalized such that it they are unity at maximum efficiency. Above 2 GeV/c, the mixed events are merged together to increase statistics, so it is the same for all for correlations within $2.0 \leq p_{\mathrm{T}}^{\mathrm{assoc}} < 10$ GeV/c.

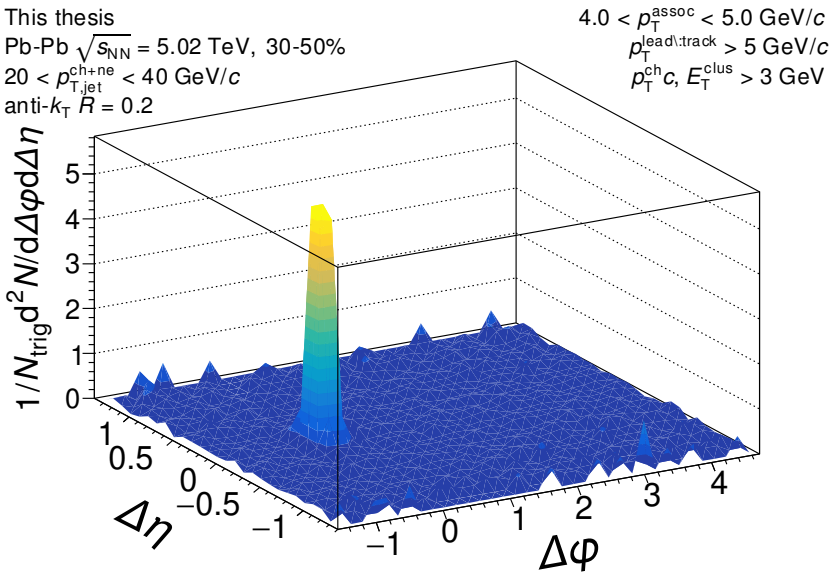

Figure D.119: The signal correlation corrected by pair acceptance. The correlations are measured for out-of-plane orientation for $20 < p_{\mathrm{T,jet}}^{\mathrm{ch+ne}} < 40$ GeV/c jets with $4.0 < p_{\mathrm{T}}^{\mathrm{assoc}} < 5.0$ GeV/c in 30–50% Pb–Pb collisions at $\sqrt{s_{\mathrm{NN}}} = 5.02$ TeV.

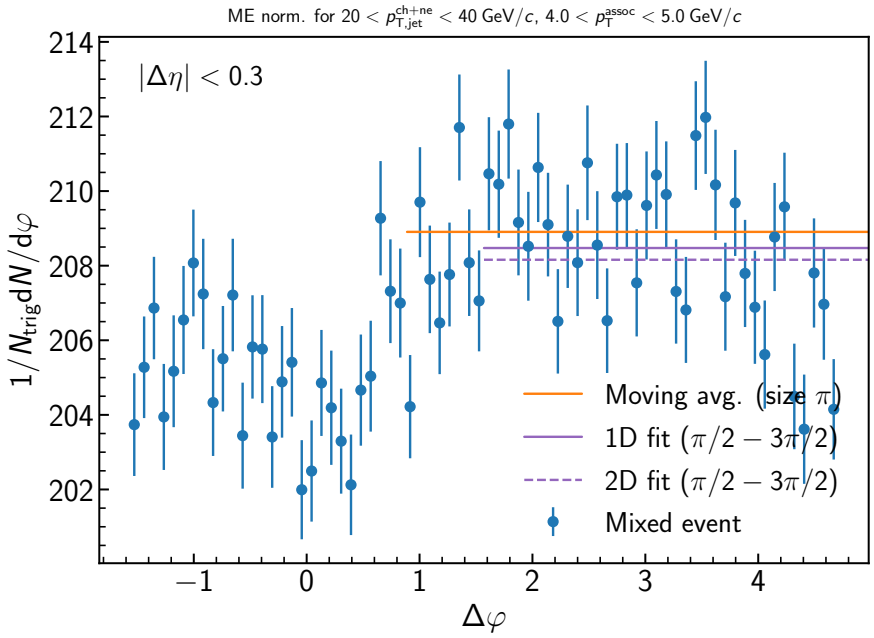

Figure D.120: Determination of the normalization of the mixed event for the inclusive event plane orientation in 30–50% Pb–Pb collisions at $\sqrt{s_{\mathrm{NN}}} = 5.02$ TeV. Here the mixed event is projected over the plateau range in $\Delta\eta$ onto to the $\Delta\varphi$ axis. The moving average is evaluated over the entire $\Delta\varphi$ range using a window of π, while the fit range is fixed from $\pi/2 < \Delta\varphi < 3\pi/2$. Since the mixed events are merged above 2 GeV/c, the normalization factor is also the same for all correlations within $4.0 < p_{\mathrm{T}}^{\mathrm{assoc}} < 5.0$ GeV/c. A variety of normalization methods were evaluated, with further details described in the text.

D.1.31 $20 < p_{\mathrm{T,jet}}^{\mathrm{ch+ne}} < 40\ \mathrm{GeV}/c$, $5.0 < p_{\mathrm{T}}^{\mathrm{assoc}} < 6.0\ \mathrm{GeV}/c$, Out-of-plane orientation

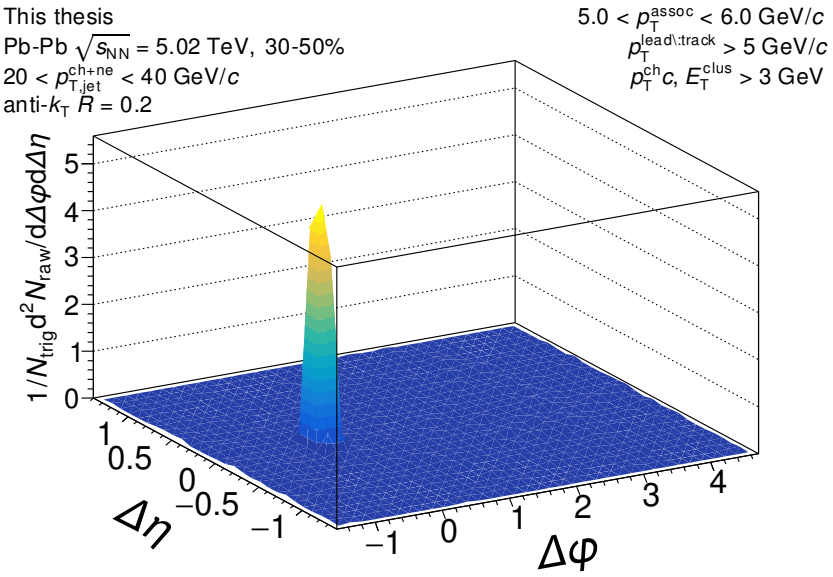

Figure D.121: The measured correlation function with the the efficiency correction $\epsilon(p_{\mathrm{T}}, \eta)$ applied, but before acceptance correction via the mixed events. The correlation is measured for out-of-plane orientation for $20 < p_{\mathrm{T,jet}}^{\mathrm{ch+ne}} < 40\ \mathrm{GeV}/c$ jets with $5.0 < p_{\mathrm{T}}^{\mathrm{assoc}} < 6.0\ \mathrm{GeV}/c$ in 30–50% Pb–Pb collisions at $\sqrt{s_{\mathrm{NN}}} = 5.02$ TeV.

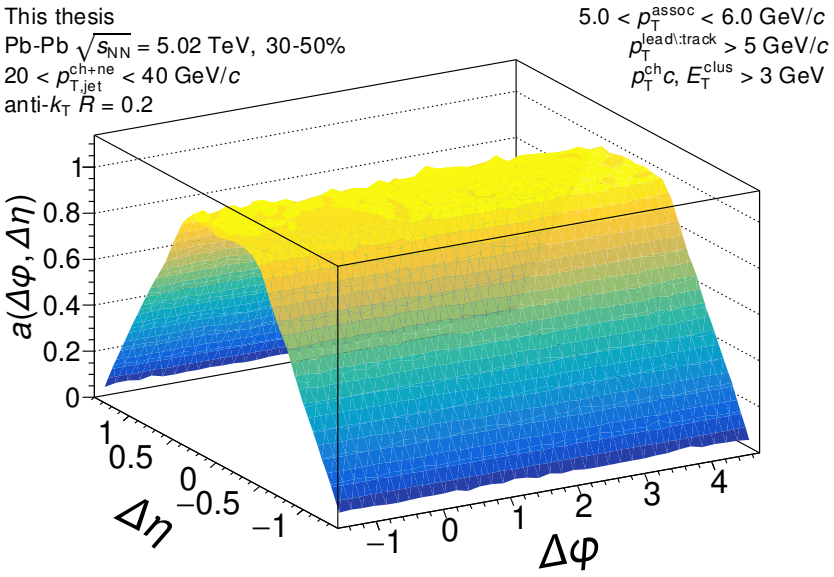

Figure D.122: The mixed event pair acceptance correction with the efficiency correction $\epsilon(p_{\mathrm{T}}, \eta)$ applied. The correlations are measured for out-of-plane orientation for $20 < p_{\mathrm{T,jet}}^{\mathrm{ch+ne}} < 40$ GeV/c jets with $5.0 < p_{\mathrm{T}}^{\mathrm{assoc}} < 6.0$ GeV/c in 30–50% Pb–Pb collisions at $\sqrt{s_{\mathrm{NN}}} = 5.02$ TeV. They have already been normalized such that it they are unity at maximum efficiency. Above 2 GeV/c, the mixed events are merged together to increase statistics, so it is the same for all for correlations within $2.0 \leq p_{\mathrm{T}}^{\mathrm{assoc}} < 10$ GeV/c.

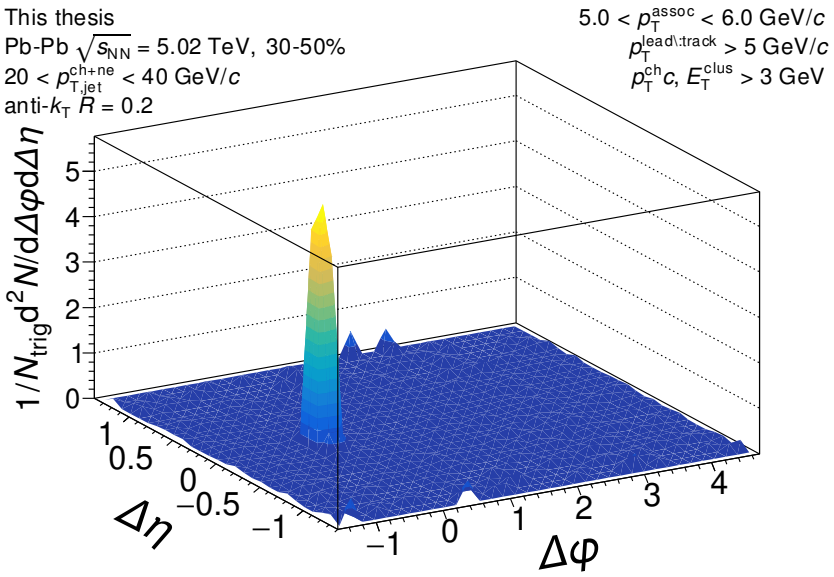

Figure D.123: The signal correlation corrected by pair acceptance. The correlations are measured for out-of-plane orientation for $20 < p_{\mathrm{T,jet}}^{\mathrm{ch+ne}} < 40$ GeV/c jets with $5.0 < p_{\mathrm{T}}^{\mathrm{assoc}} < 6.0$ GeV/c in 30–50% Pb–Pb collisions at $\sqrt{s_{\mathrm{NN}}} = 5.02$ TeV.

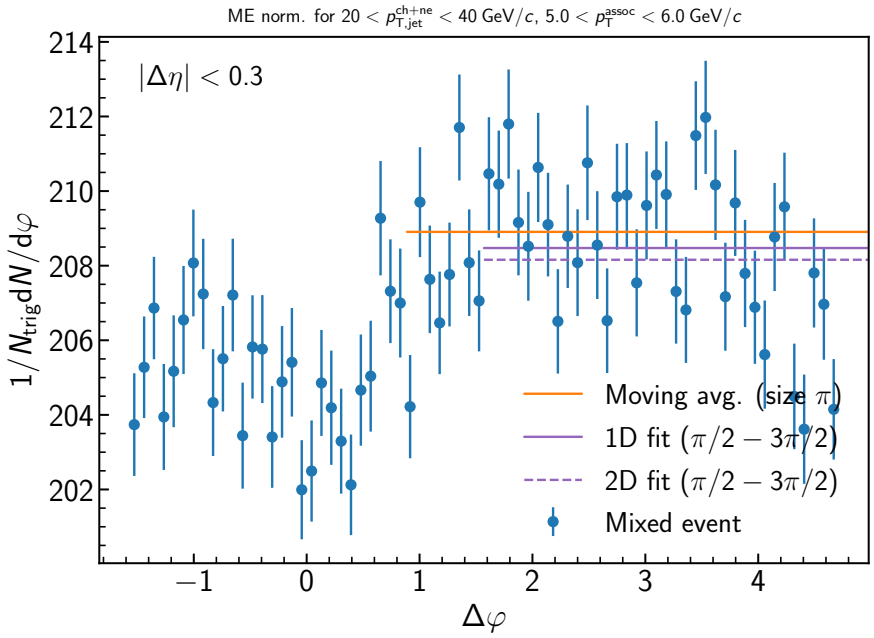

Figure D.124: Determination of the normalization of the mixed event for the inclusive event plane orientation in 30–50% Pb–Pb collisions at $\sqrt{s_{\mathrm{NN}}} = 5.02$ TeV. Here the mixed event is projected over the plateau range in $\Delta\eta$ onto to the $\Delta\varphi$ axis. The moving average is evaluated over the entire $\Delta\varphi$ range using a window of π, while the fit range is fixed from $\pi/2 < \Delta\varphi < 3\pi/2$. Since the mixed events are merged above 2 GeV/c, the normalization factor is also the same for all correlations within $5.0 < p_{\mathrm{T}}^{\mathrm{assoc}} < 6.0$ GeV/c. A variety of normalization methods were evaluated, with further details described in the text.

D.1.32 $20 < p_{\mathrm{T,jet}}^{\mathrm{ch+ne}} < 40$ GeV/c, $6.0 < p_{\mathrm{T}}^{\mathrm{assoc}} < 10.0$ GeV/c, Out-of-plane orientation

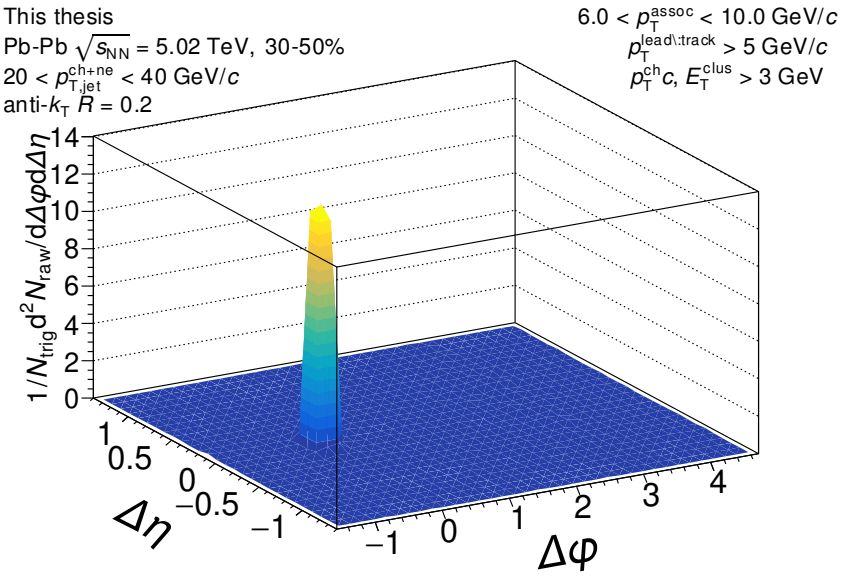

Figure D.125: The measured correlation function with the the efficiency correction $\epsilon(p_{\mathrm{T}}, \eta)$ applied, but before acceptance correction via the mixed events. The correlation is measured for out-of-plane orientation for $20 < p_{\mathrm{T,jet}}^{\mathrm{ch+ne}} < 40$ GeV/c jets with $6.0 < p_{\mathrm{T}}^{\mathrm{assoc}} < 10.0$ GeV/c in 30–50% Pb–Pb collisions at $\sqrt{s_{\mathrm{NN}}} = 5.02$ TeV.

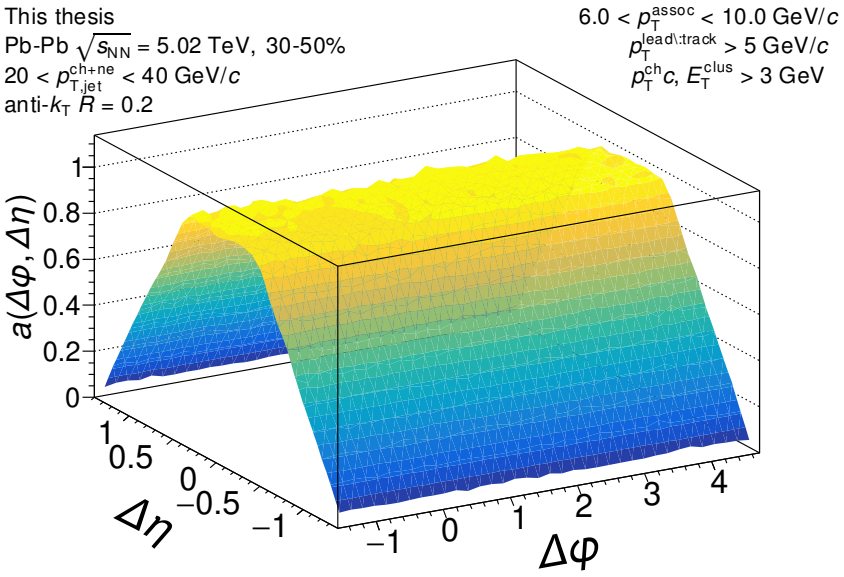

Figure D.126: The mixed event pair acceptance correction with the efficiency correction $\epsilon(p_{\mathrm{T}}, \eta)$ applied. The correlations are measured for out-of-plane orientation for $20 < p_{\mathrm{T,jet}}^{\mathrm{ch+ne}} < 40\,\mathrm{GeV}/c$ jets with $6.0 < p_{\mathrm{T}}^{\mathrm{assoc}} < 10.0\,\mathrm{GeV}/c$ in 30–50% Pb–Pb collisions at $\sqrt{s_{\mathrm{NN}}} = 5.02\,\mathrm{TeV}$. They have already been normalized such that it they are unity at maximum efficiency. Above 2 GeV/c, the mixed events are merged together to increase statistics, so it is the same for all for correlations within $2.0 \leq p_{\mathrm{T}}^{\mathrm{assoc}} < 10$ GeV/c.

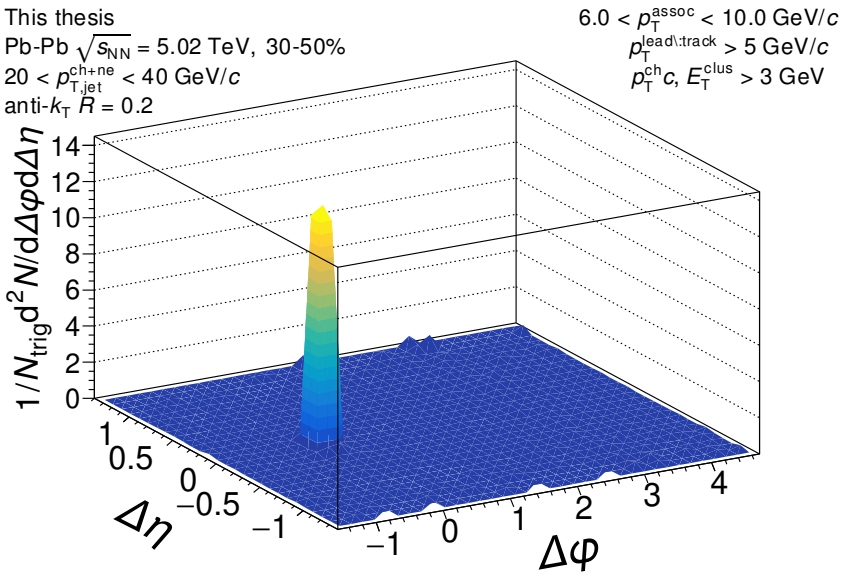

Figure D.127: The signal correlation corrected by pair acceptance. The correlations are measured for out-of-plane orientation for $20 < p_{\mathrm{T,jet}}^{\mathrm{ch+ne}} < 40\,\mathrm{GeV}/c$ jets with $6.0 < p_{\mathrm{T}}^{\mathrm{assoc}} < 10.0\,\mathrm{GeV}/c$ in 30–50% Pb–Pb collisions at $\sqrt{s_{\mathrm{NN}}} = 5.02\,\mathrm{TeV}$.

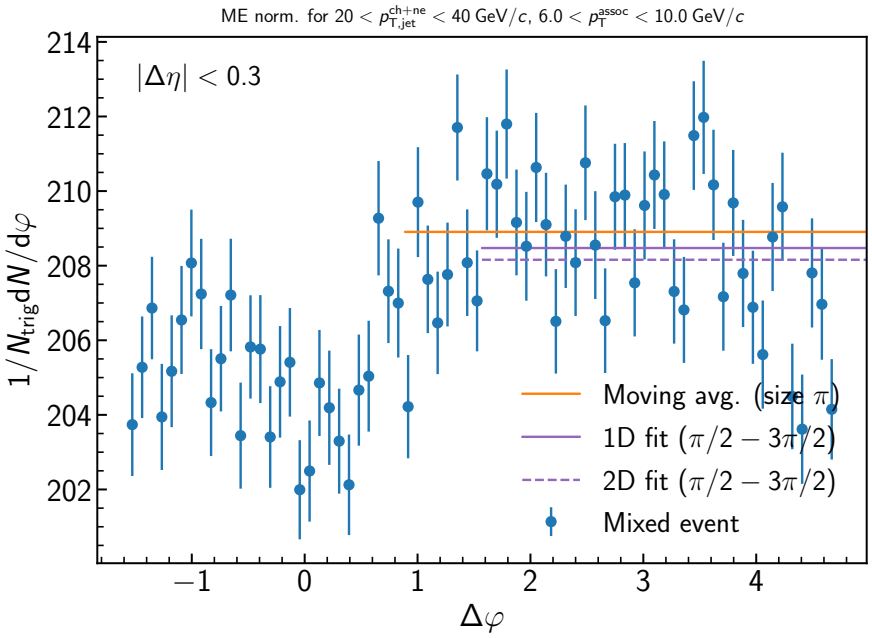

Figure D.128: Determination of the normalization of the mixed event for the inclusive event plane orientation in 30–50% Pb–Pb collisions at $\sqrt{s_{\mathrm{NN}}} = 5.02$ TeV. Here the mixed event is projected over the plateau range in $\Delta\eta$ onto to the $\Delta\varphi$ axis. The moving average is evaluated over the entire $\Delta\varphi$ range using a window of π, while the fit range is fixed from $\pi/2 < \Delta\varphi < 3\pi/2$. Since the mixed events are merged above 2 GeV/c, the normalization factor is also the same for all correlations within $6.0 < p_{\mathrm{T}}^{\mathrm{assoc}} < 10.0$ GeV/c. A variety of normalization methods were evaluated, with further details described in the text.

D.1.33 Reaction Plane Fit

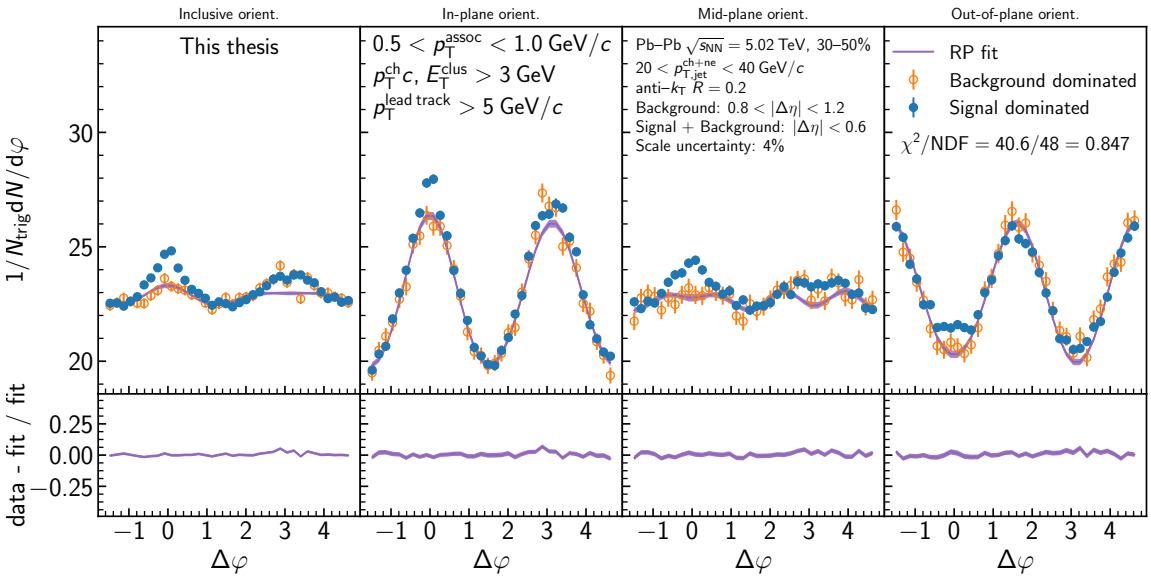

Figure D.129: The Reaction Plane Fit of jet-hadron correlations measured for $20 < p_{\mathrm{T,jet}}^{\mathrm{ch+ne}} < 40$ GeV/c and $0.5 < p_{\mathrm{T}}^{\mathrm{assoc}} < 1.0$ GeV/c in 30–50% collisions. The signal dominated data are shown in blue, the background dominated in orange, and the fit in purple. The upper panels show the signal and background dominated correlations measured in each event plane orientation. The lower panels show the fit residuals.

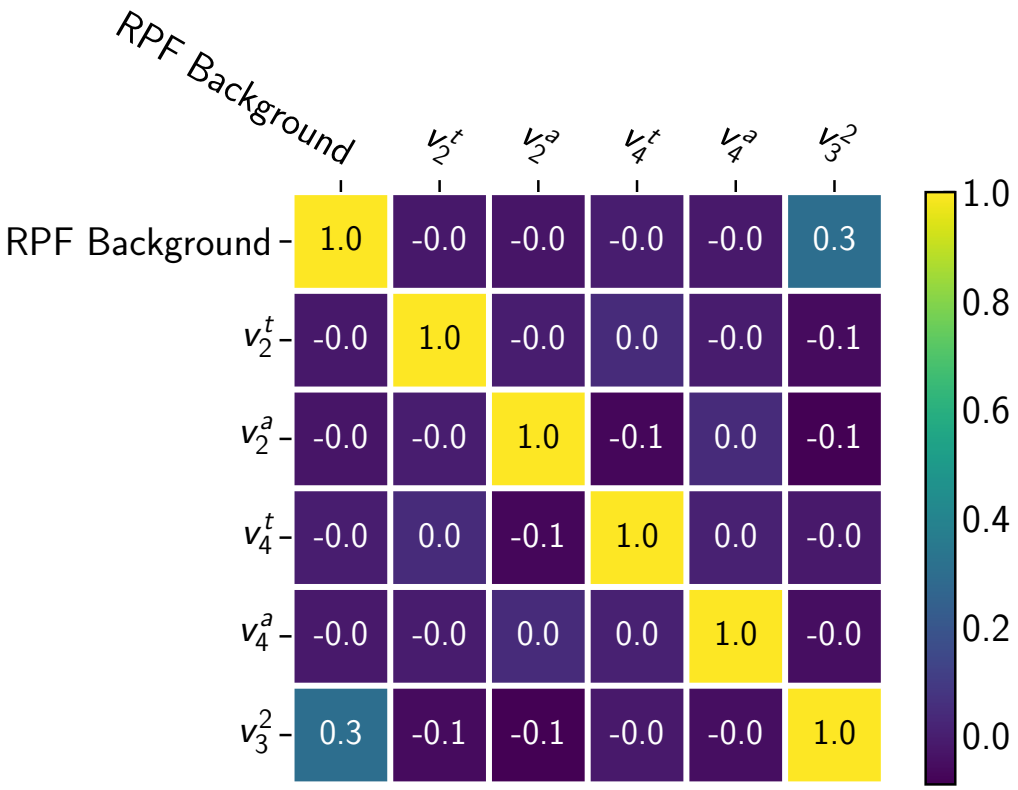

Figure D.130: Correlation matrix for the Reaction Plane Fit of jet-hadron correlations measured for $20 < p_{\mathrm{T,jet}}^{\mathrm{ch+ne}} < 40$ GeV/c and $0.5 < p_{\mathrm{T}}^{\mathrm{assoc}} < 1.0$ GeV/c in 30–50% collisions.

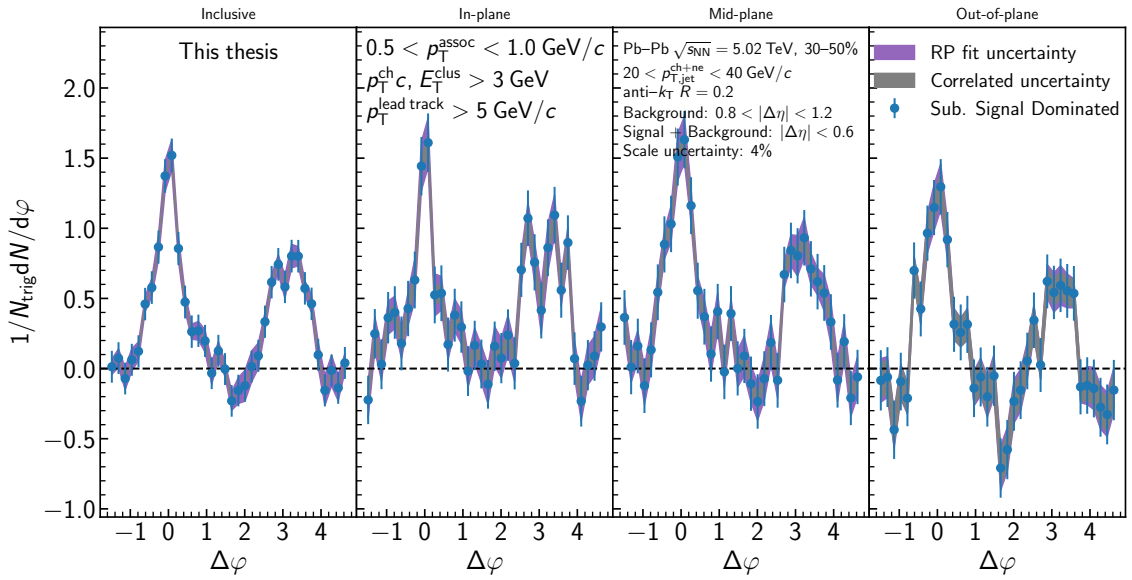

Figure D.131: The Reaction Plane Fit subtracted jet-hadron correlations measured for $20 < p_{\mathrm{T,jet}}^{\mathrm{ch+ne}} < 40\,\mathrm{GeV}/c$ and $0.5 < p_{\mathrm{T}}^{\mathrm{assoc}} < 1.0\,\mathrm{GeV}/c$ in 30–50% collisions. The subtracted data are shown in blue for each event plane orientation, with the fit uncertainty in purple and the correlated uncertainty in gray.

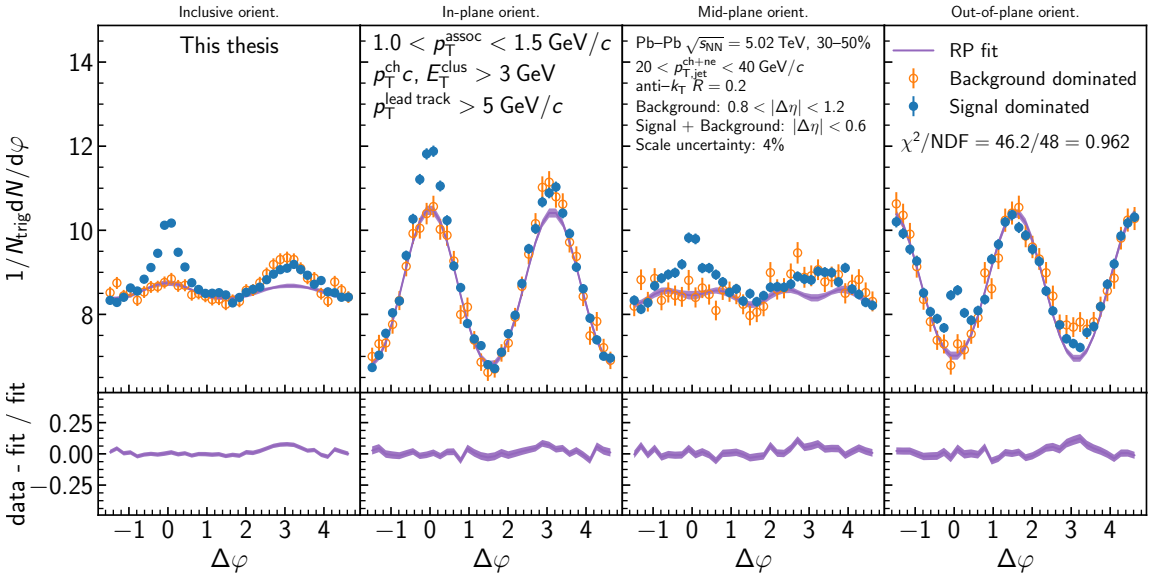

Figure D.132: The Reaction Plane Fit of jet-hadron correlations measured for $20 < p_{\mathrm{T,jet}}^{\mathrm{ch+ne}} < 40\,\mathrm{GeV}/c$ and $1.0 < p_{\mathrm{T}}^{\mathrm{assoc}} < 1.5\,\mathrm{GeV}/c$ in 30–50% collisions. The signal dominated data are shown in blue, the background dominated in orange, and the fit in purple. The upper panels show the signal and background dominated correlations measured in each event plane orientation. The lower panels show the fit residuals.

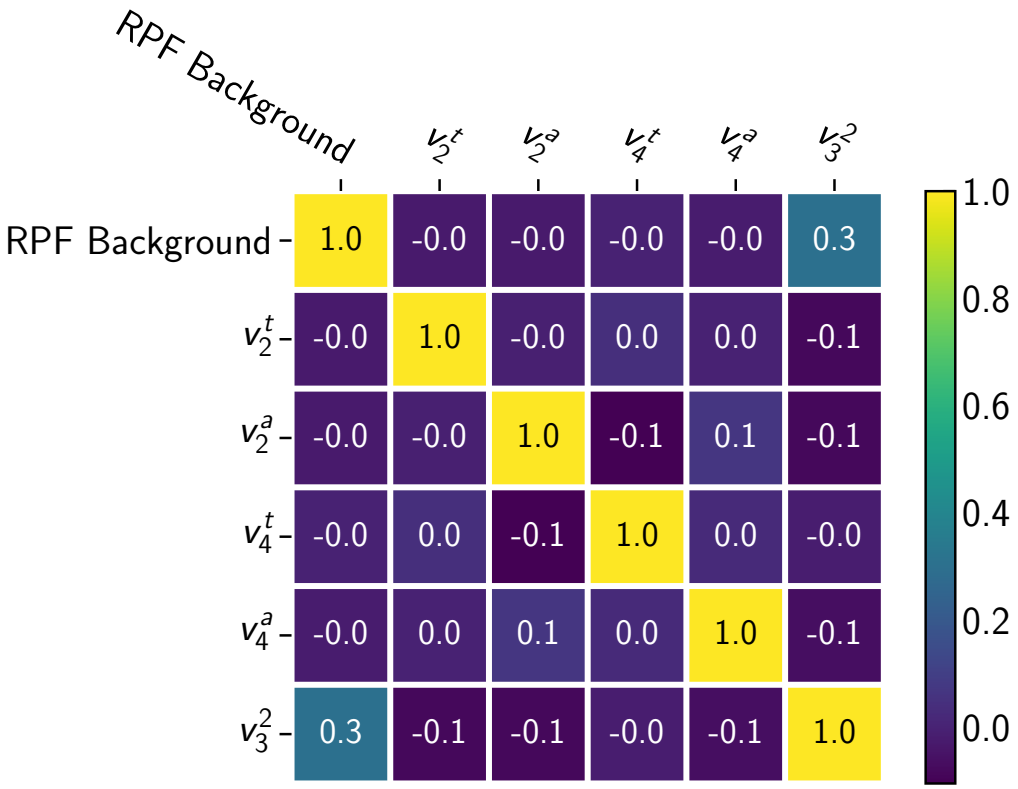

Figure D.133: Correlation matrix for the Reaction Plane Fit of jet-hadron correlations measured for $20 < p_{\mathrm{T,jet}}^{\mathrm{ch+ne}} < 40$ GeV/c and $1.0 < p_{\mathrm{T}}^{\mathrm{assoc}} < 1.5$ GeV/c in 30–50% collisions.

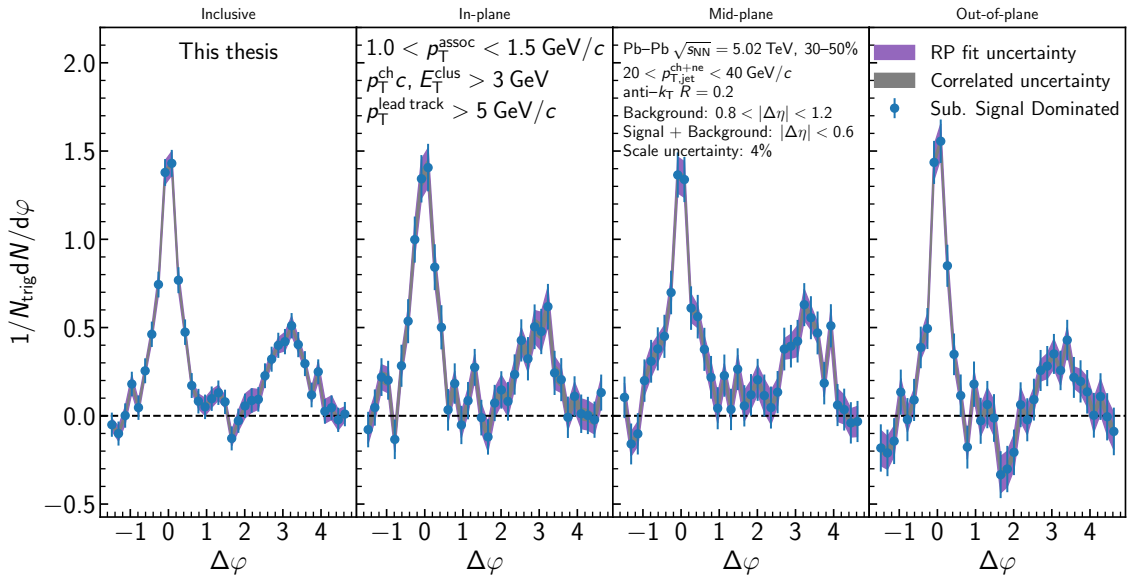

Figure D.134: The Reaction Plane Fit subtracted jet-hadron correlations measured for $20 < p_{\mathrm{T,jet}}^{\mathrm{ch+ne}} < 40\,\mathrm{GeV}/c$ and $1.0 < p_{\mathrm{T}}^{\mathrm{assoc}} < 1.5\,\mathrm{GeV}/c$ in 30–50% collisions. The subtracted data are shown in blue for each event plane orientation, with the fit uncertainty in purple and the correlated uncertainty in gray.

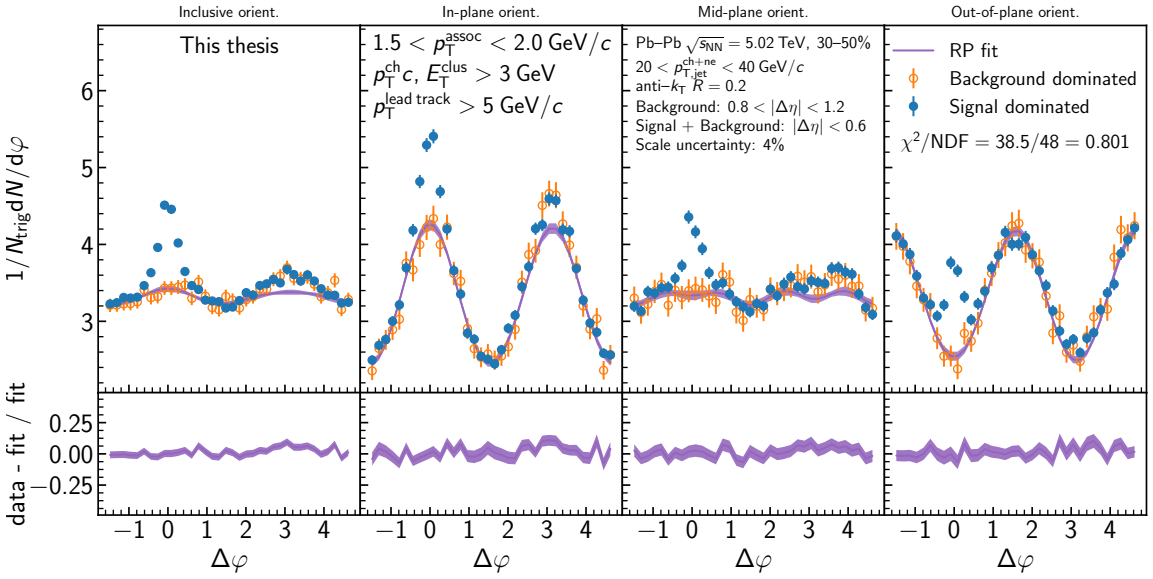

Figure D.135: The Reaction Plane Fit of jet-hadron correlations measured for $20 < p_{\mathrm{T,jet}}^{\mathrm{ch+ne}} < 40\,\mathrm{GeV}/c$ and $1.5 < p_{\mathrm{T}}^{\mathrm{assoc}} < 2.0\,\mathrm{GeV}/c$ in 30–50% collisions. The signal dominated data are shown in blue, the background dominated in orange, and the fit in purple. The upper panels show the signal and background dominated correlations measured in each event plane orientation. The lower panels show the fit residuals.

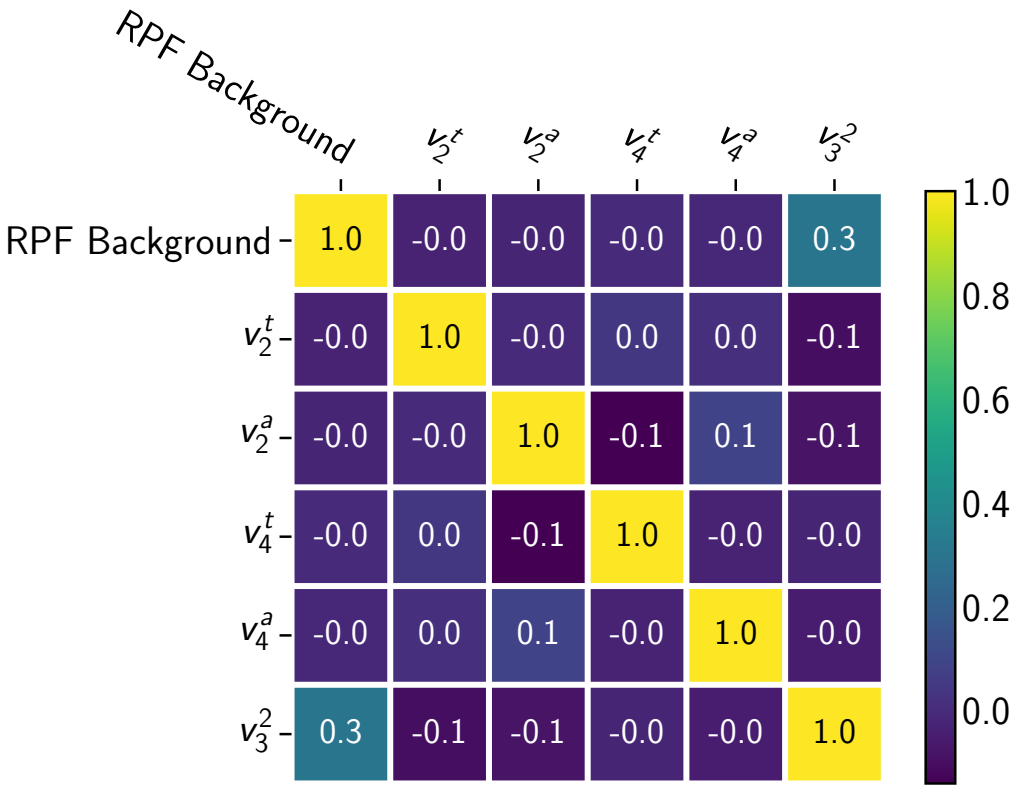

Figure D.136: Correlation matrix for the Reaction Plane Fit of jet-hadron correlations measured for $20 < p_{\mathrm{T,jet}}^{\mathrm{ch+ne}} < 40$ GeV/c and $1.5 < p_{\mathrm{T}}^{\mathrm{assoc}} < 2.0$ GeV/c in 30–50% collisions.

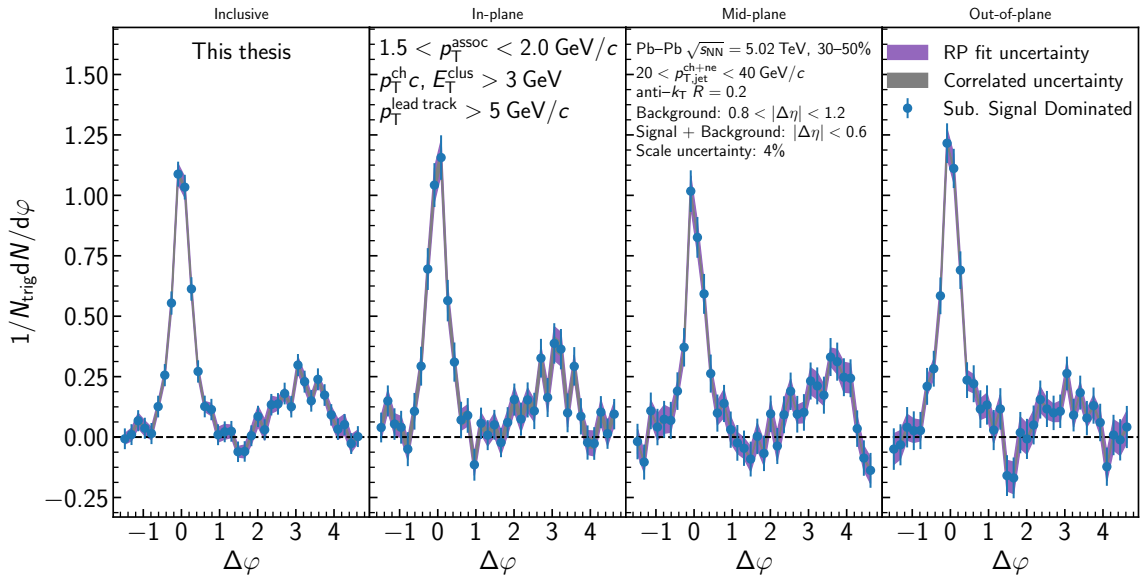

Figure D.137: The Reaction Plane Fit subtracted jet-hadron correlations measured for $20 < p_{\mathrm{T,jet}}^{\mathrm{ch+ne}} < 40\,\mathrm{GeV}/c$ and $1.5 < p_{\mathrm{T}}^{\mathrm{assoc}} < 2.0\,\mathrm{GeV}/c$ in 30–50% collisions. The subtracted data are shown in blue for each event plane orientation, with the fit uncertainty in purple and the correlated uncertainty in gray.

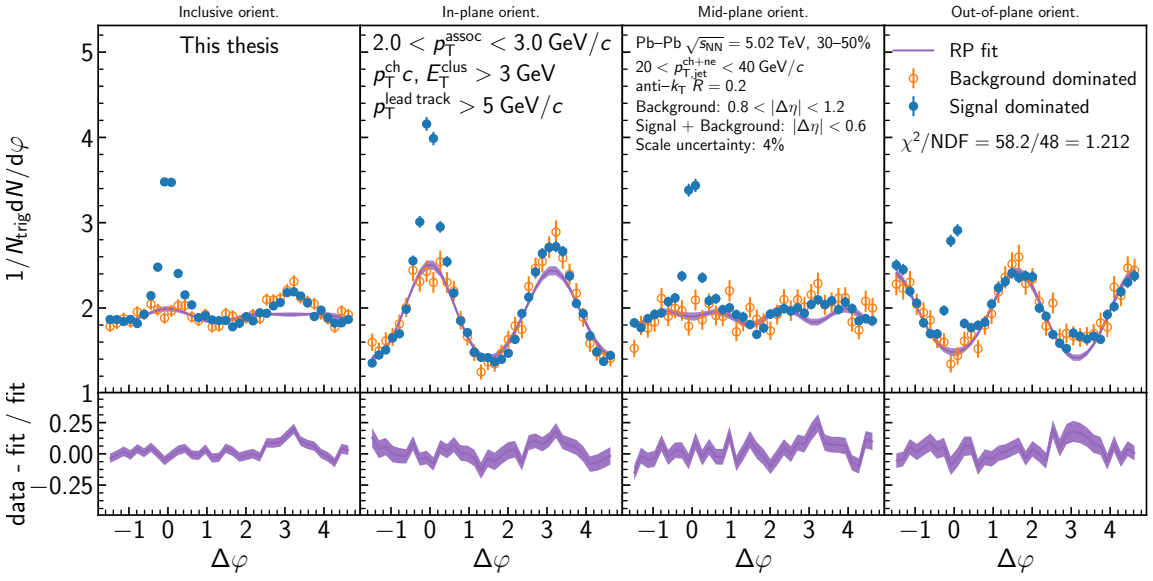

Figure D.138: The Reaction Plane Fit of jet-hadron correlations measured for $20 < p_{\mathrm{T,jet}}^{\mathrm{ch+ne}} < 40\,\mathrm{GeV}/c$ and $2.0 < p_{\mathrm{T}}^{\mathrm{assoc}} < 3.0\,\mathrm{GeV}/c$ in 30–50% collisions. The signal dominated data are shown in blue, the background dominated in orange, and the fit in purple. The upper panels show the signal and background dominated correlations measured in each event plane orientation. The lower panels show the fit residuals.

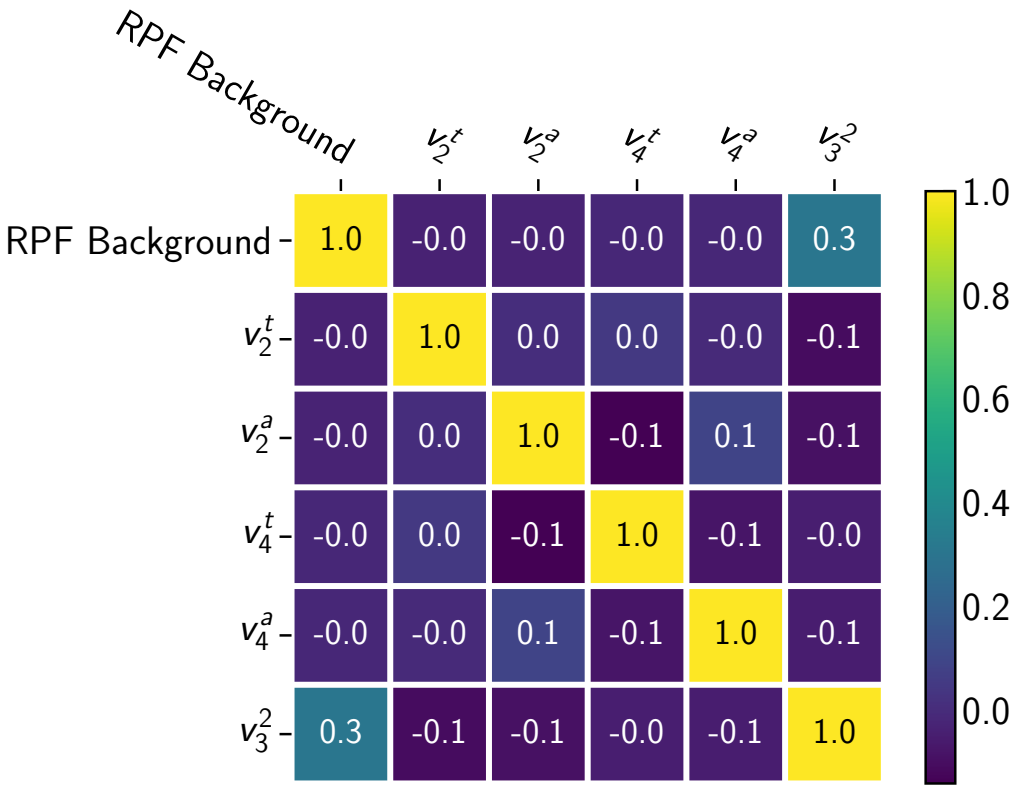

Figure D.139: Correlation matrix for the Reaction Plane Fit of jet-hadron correlations measured for $20 < p_{\mathrm{T,jet}}^{\mathrm{ch+ne}} < 40$ GeV/c and $2.0 < p_{\mathrm{T}}^{\mathrm{assoc}} < 3.0$ GeV/c in 30–50% collisions.

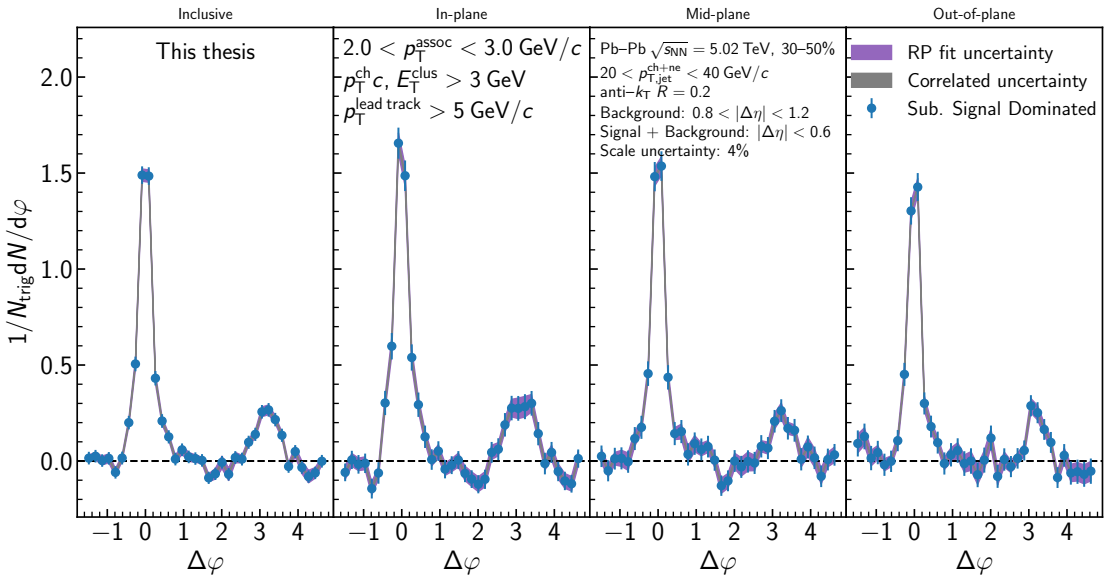

Figure D.140: The Reaction Plane Fit subtracted jet-hadron correlations measured for $20 < p_{\mathrm{T,jet}}^{\mathrm{ch+ne}} < 40\,\mathrm{GeV}/c$ and $2.0 < p_{\mathrm{T}}^{\mathrm{assoc}} < 3.0\,\mathrm{GeV}/c$ in 30–50% collisions. The subtracted data are shown in blue for each event plane orientation, with the fit uncertainty in purple and the correlated uncertainty in gray.

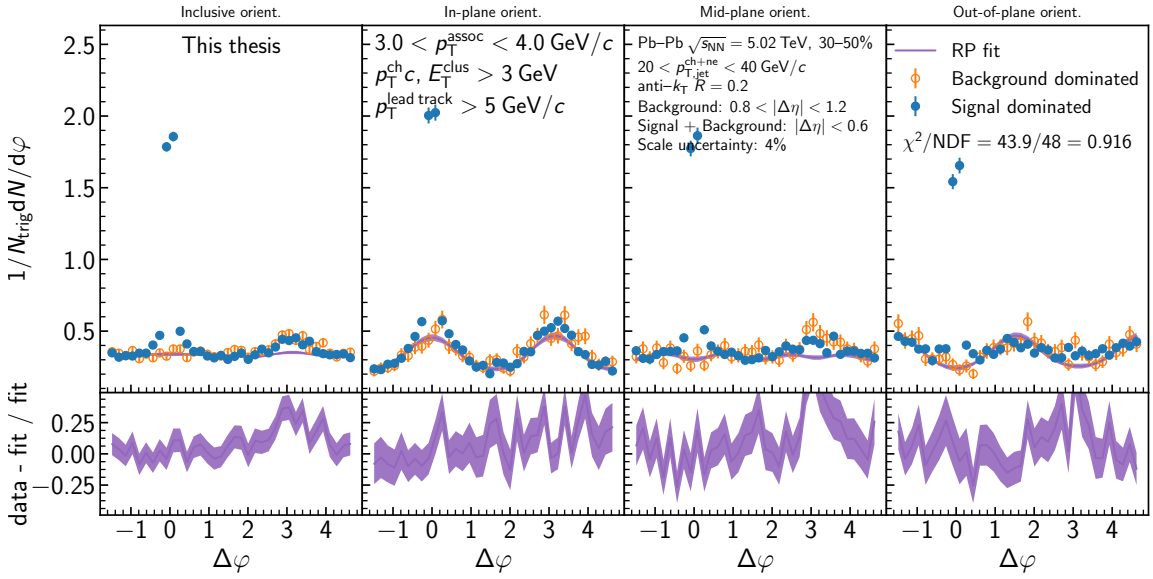

Figure D.141: The Reaction Plane Fit of jet-hadron correlations measured for $20 < p_{\mathrm{T,jet}}^{\mathrm{ch+ne}} < 40\,\mathrm{GeV}/c$ and $3.0 < p_{\mathrm{T}}^{\mathrm{assoc}} < 4.0\,\mathrm{GeV}/c$ in 30–50% collisions. The signal dominated data are shown in blue, the background dominated in orange, and the fit in purple. The upper panels show the signal and background dominated correlations measured in each event plane orientation. The lower panels show the fit residuals.

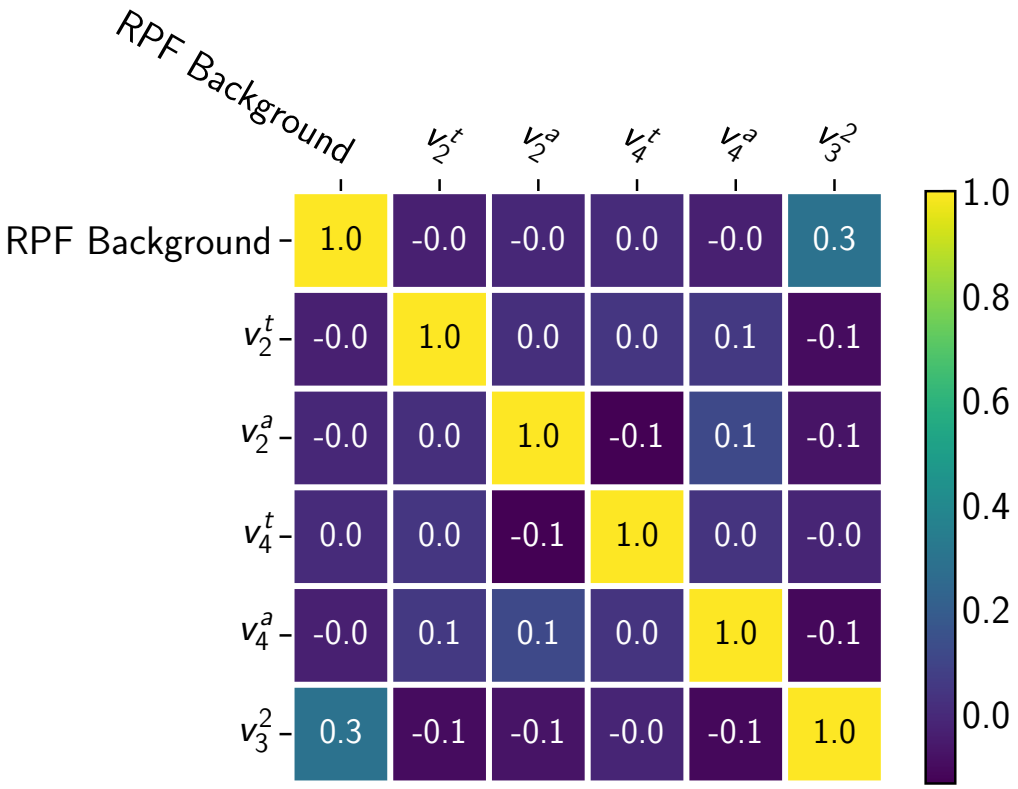

Figure D.142: Correlation matrix for the Reaction Plane Fit of jet-hadron correlations measured for $20 < p_{\mathrm{T,jet}}^{\mathrm{ch+ne}} < 40$ GeV/c and $3.0 < p_{\mathrm{T}}^{\mathrm{assoc}} < 4.0$ GeV/c in 30–50% collisions.

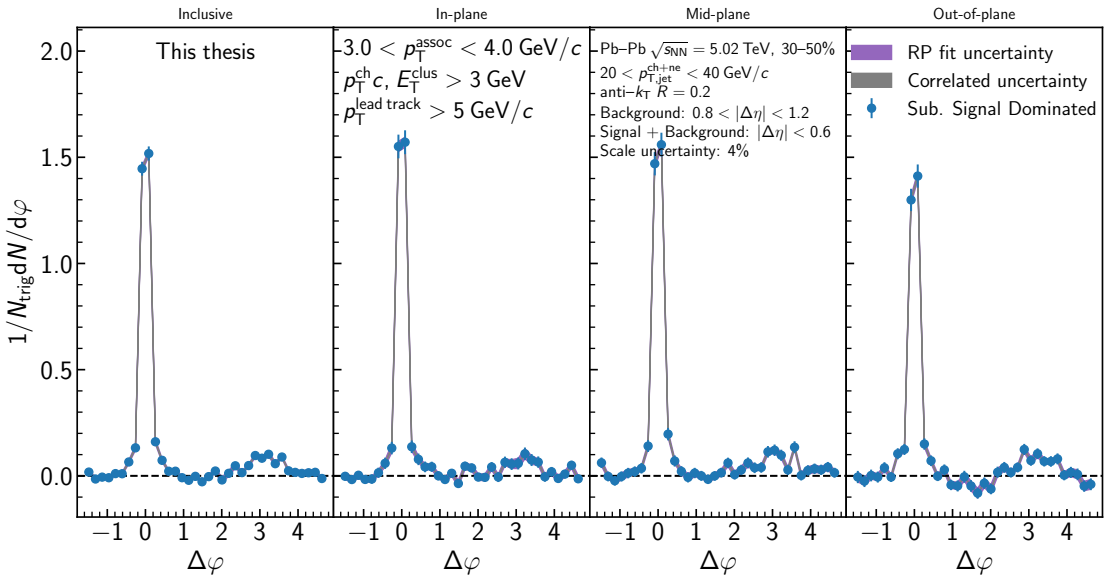

Figure D.143: The Reaction Plane Fit subtracted jet-hadron correlations measured for $20 < p_{\mathrm{T,jet}}^{\mathrm{ch+ne}} < 40\,\mathrm{GeV}/c$ and $3.0 < p_{\mathrm{T}}^{\mathrm{assoc}} < 4.0\,\mathrm{GeV}/c$ in 30–50% collisions. The subtracted data are shown in blue for each event plane orientation, with the fit uncertainty in purple and the correlated uncertainty in gray.

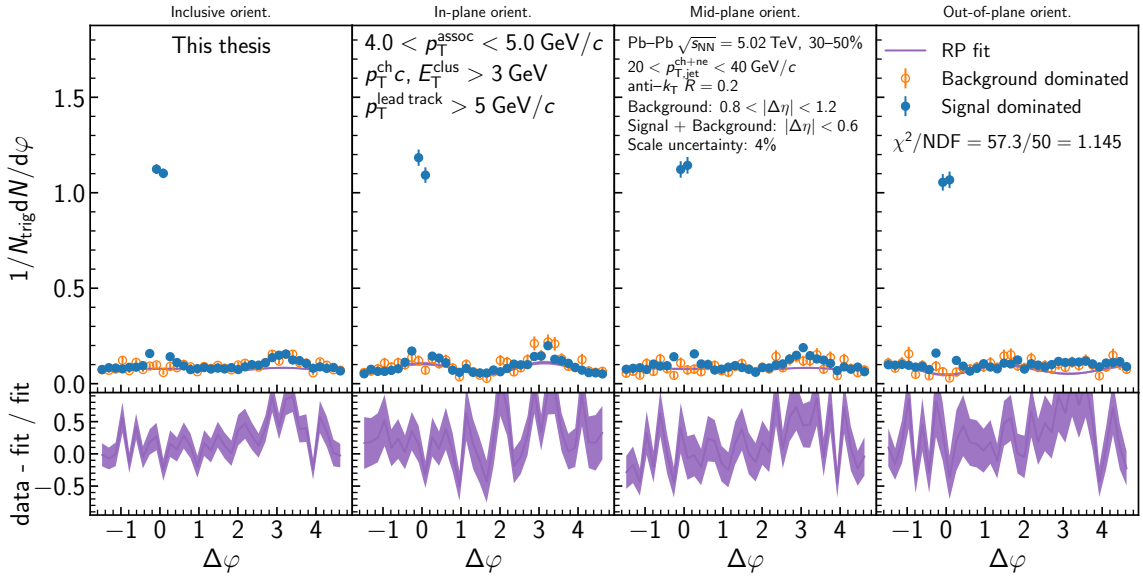

Figure D.144: The Reaction Plane Fit of jet-hadron correlations measured for $20 < p_{\mathrm{T,jet}}^{\mathrm{ch+ne}} < 40\,\mathrm{GeV}/c$ and $4.0 < p_{\mathrm{T}}^{\mathrm{assoc}} < 5.0\,\mathrm{GeV}/c$ in 30–50% collisions. The signal dominated data are shown in blue, the background dominated in orange, and the fit in purple. The upper panels show the signal and background dominated correlations measured in each event plane orientation. The lower panels show the fit residuals.

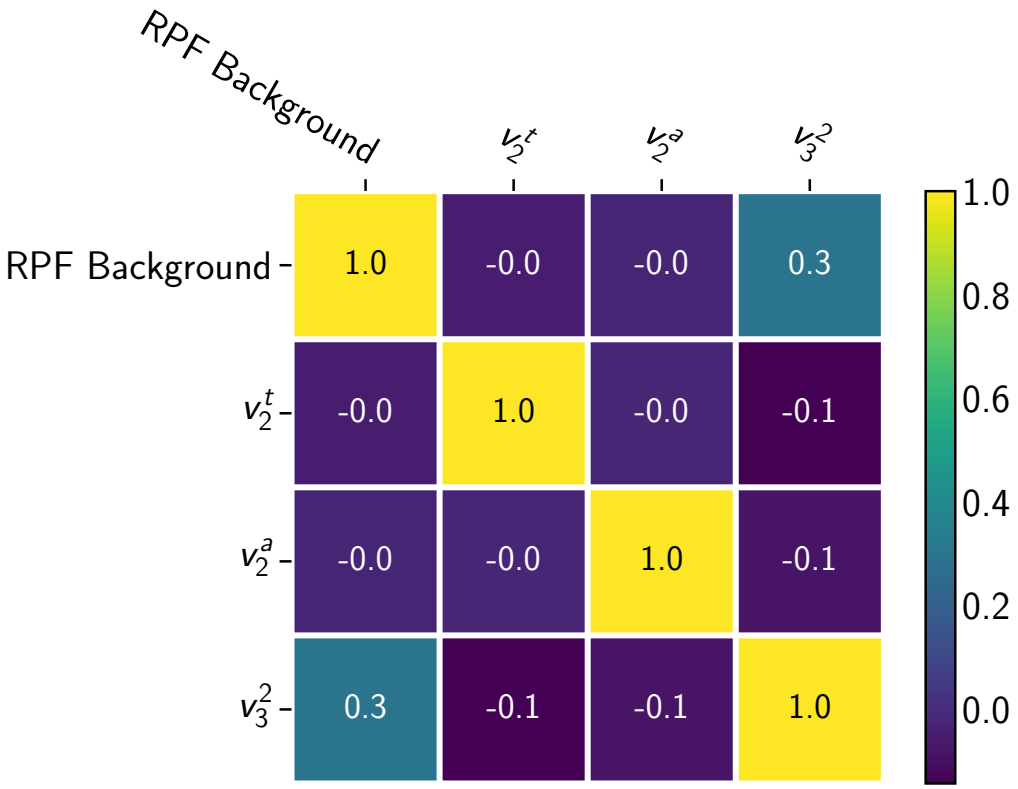

Figure D.145: Correlation matrix for the Reaction Plane Fit of jet-hadron correlations measured for $20 < p_{\mathrm{T,jet}}^{\mathrm{ch+ne}} < 40$ GeV/c and $4.0 < p_{\mathrm{T}}^{\mathrm{assoc}} < 5.0$ GeV/c in 30–50% collisions.

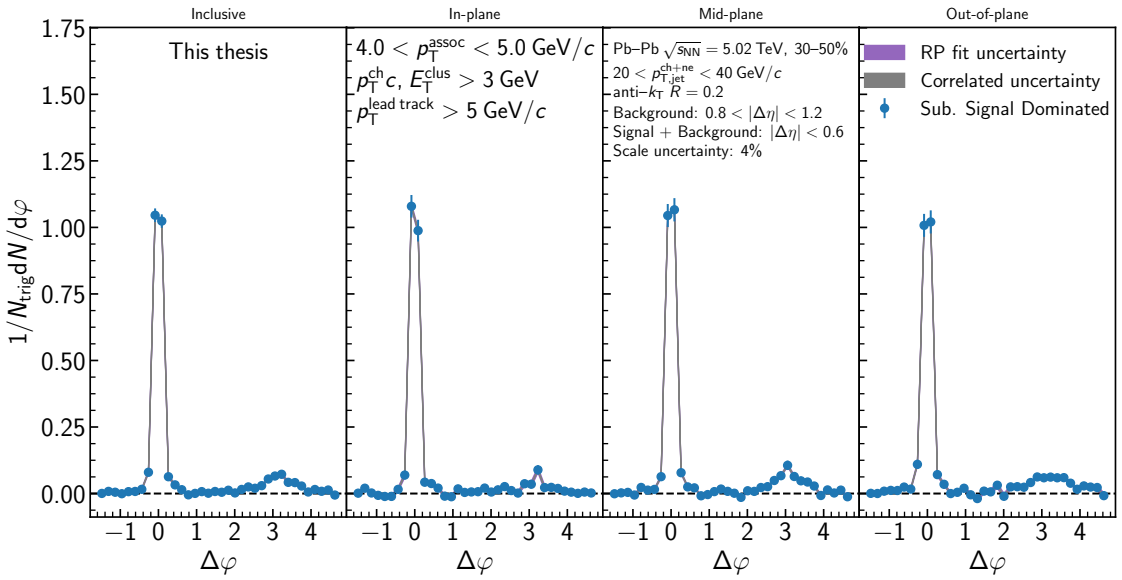

Figure D.146: The Reaction Plane Fit subtracted jet-hadron correlations measured for $20 < p_{\mathrm{T,jet}}^{\mathrm{ch+ne}} < 40\,\mathrm{GeV}/c$ and $4.0 < p_{\mathrm{T}}^{\mathrm{assoc}} < 5.0\,\mathrm{GeV}/c$ in 30–50% collisions. The subtracted data are shown in blue for each event plane orientation, with the fit uncertainty in purple and the correlated uncertainty in gray.

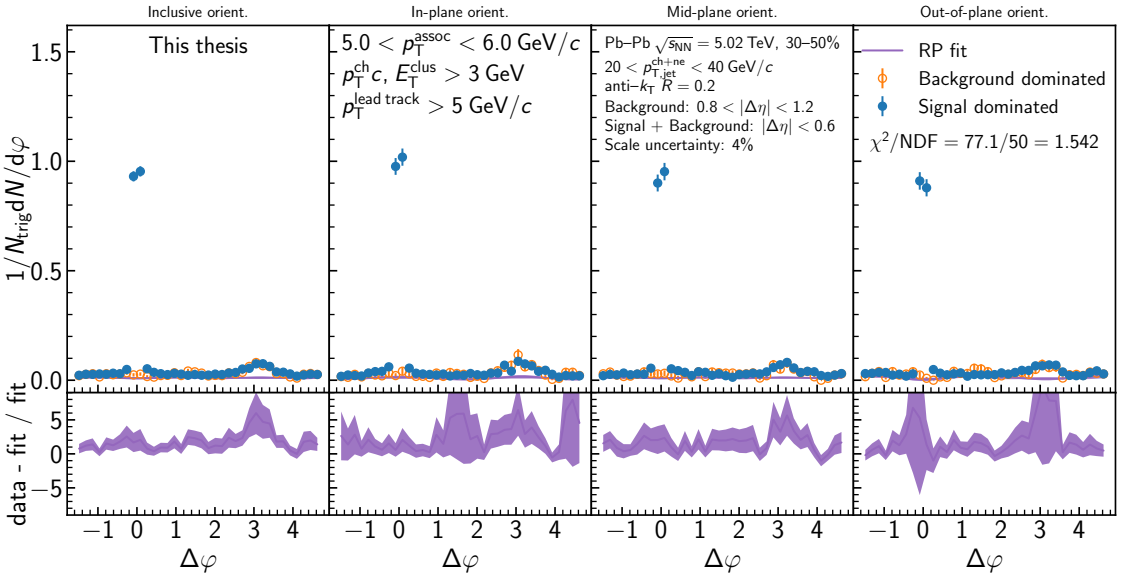

Figure D.147: The Reaction Plane Fit of jet-hadron correlations measured for $20 < p_{\mathrm{T,jet}}^{\mathrm{ch+ne}} < 40\,\mathrm{GeV}/c$ and $5.0 < p_{\mathrm{T}}^{\mathrm{assoc}} < 6.0\,\mathrm{GeV}/c$ in 30–50% collisions. The signal dominated data are shown in blue, the background dominated in orange, and the fit in purple. The upper panels show the signal and background dominated correlations measured in each event plane orientation. The lower panels show the fit residuals.

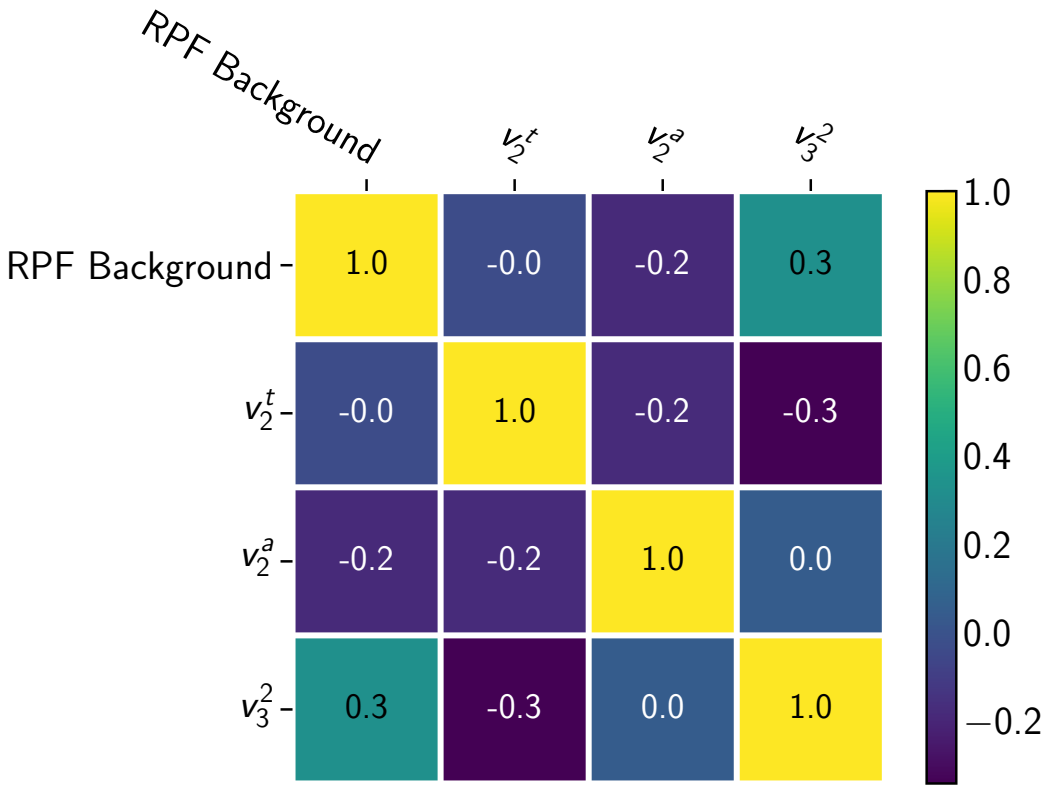

Figure D.148: Correlation matrix for the Reaction Plane Fit of jet-hadron correlations measured for $20 < p_{\mathrm{T,jet}}^{\mathrm{ch+ne}} < 40$ GeV/c and $5.0 < p_{\mathrm{T}}^{\mathrm{assoc}} < 6.0$ GeV/c in 30–50% collisions.

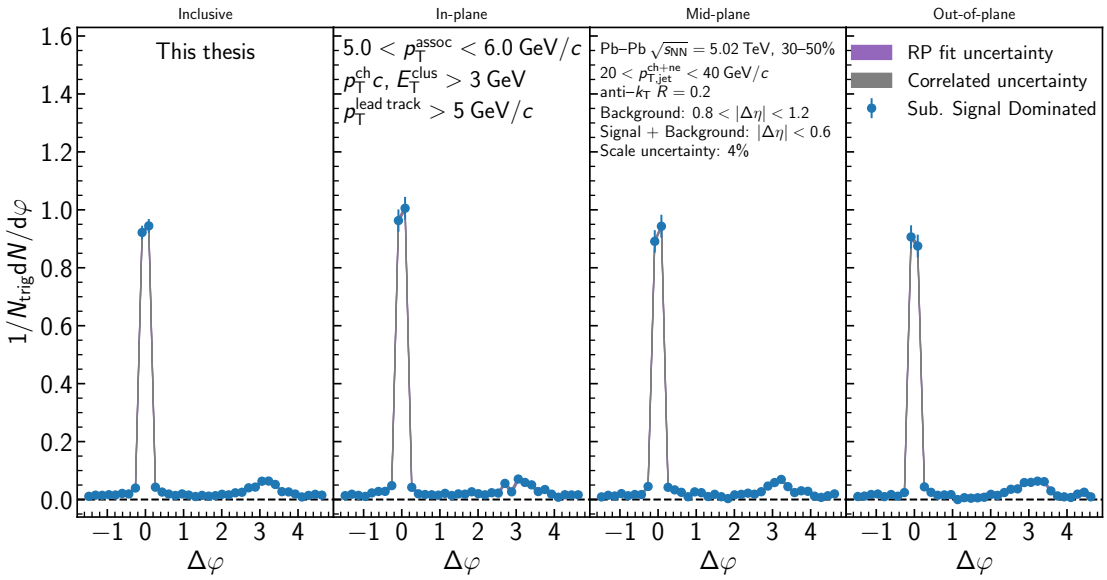

Figure D.149: The Reaction Plane Fit subtracted jet-hadron correlations measured for $20 < p_{\mathrm{T,jet}}^{\mathrm{ch+ne}} < 40\,\mathrm{GeV}/c$ and $5.0 < p_{\mathrm{T}}^{\mathrm{assoc}} < 6.0\,\mathrm{GeV}/c$ in 30–50% collisions. The subtracted data are shown in blue for each event plane orientation, with the fit uncertainty in purple and the correlated uncertainty in gray.

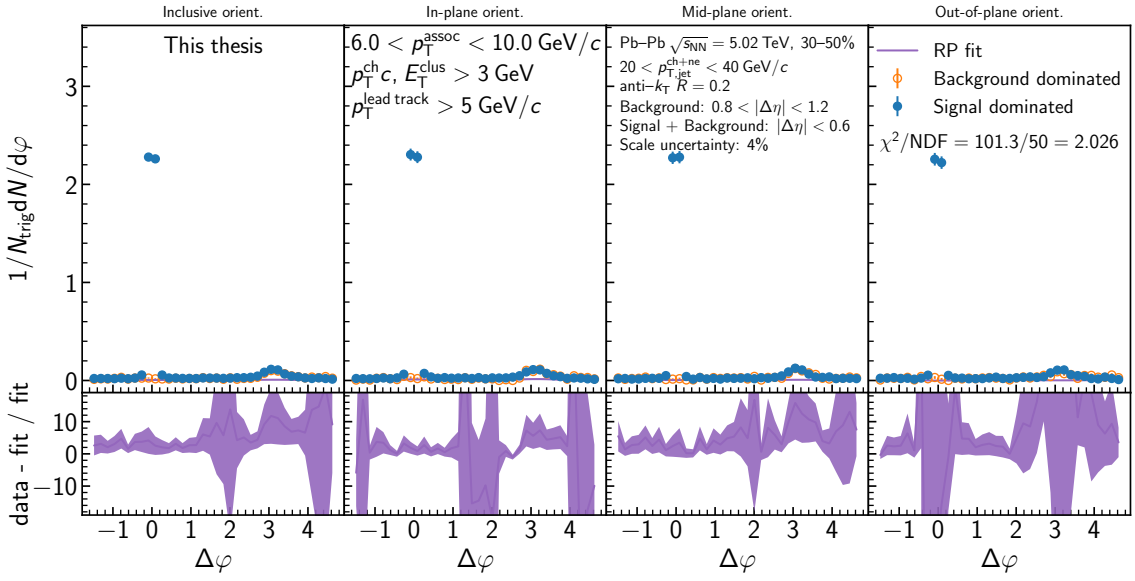

Figure D.150: The Reaction Plane Fit of jet-hadron correlations measured for $20 < p_{\mathrm{T,jet}}^{\mathrm{ch+ne}} < 40\,\mathrm{GeV}/c$ and $6.0 < p_{\mathrm{T}}^{\mathrm{assoc}} < 10.0\,\mathrm{GeV}/c$ in 30–50% collisions. The signal dominated data are shown in blue, the background dominated in orange, and the fit in purple. The upper panels show the signal and background dominated correlations measured in each event plane orientation. The lower panels show the fit residuals.

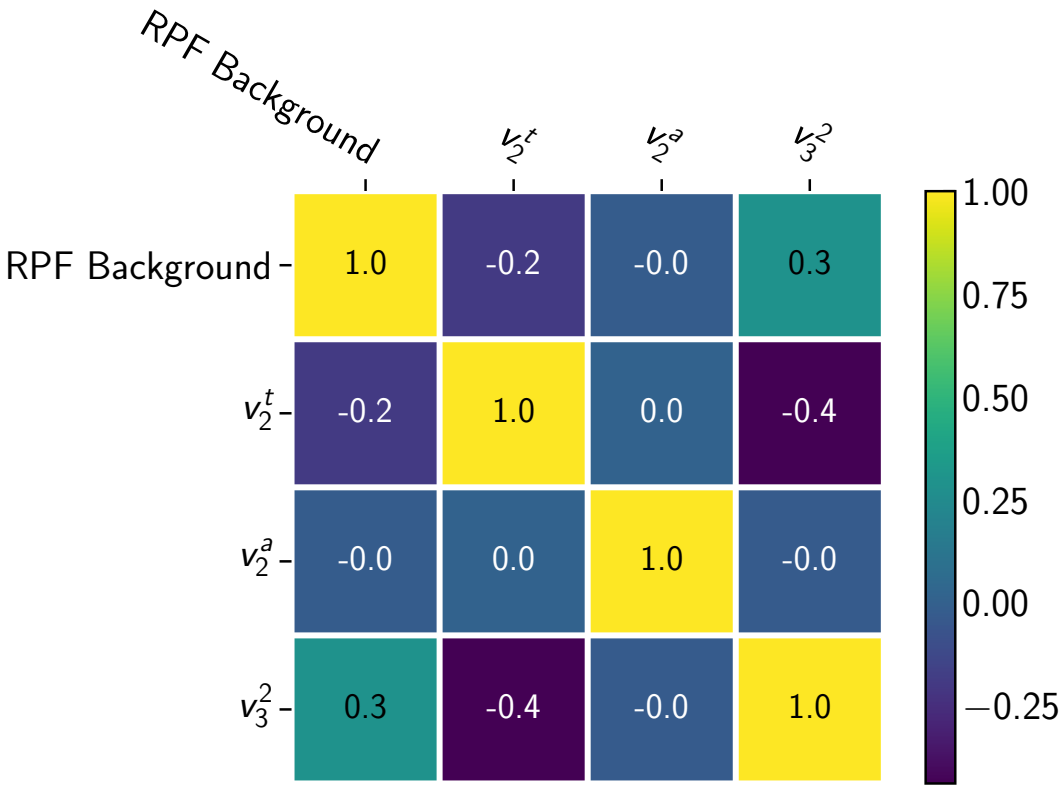

Figure D.151: Correlation matrix for the Reaction Plane Fit of jet-hadron correlations measured for $20 < p_{\mathrm{T,jet}}^{\mathrm{ch+ne}} < 40$ GeV/c and $6.0 < p_{\mathrm{T}}^{\mathrm{assoc}} < 10.0$ GeV/c in 30–50% collisions.

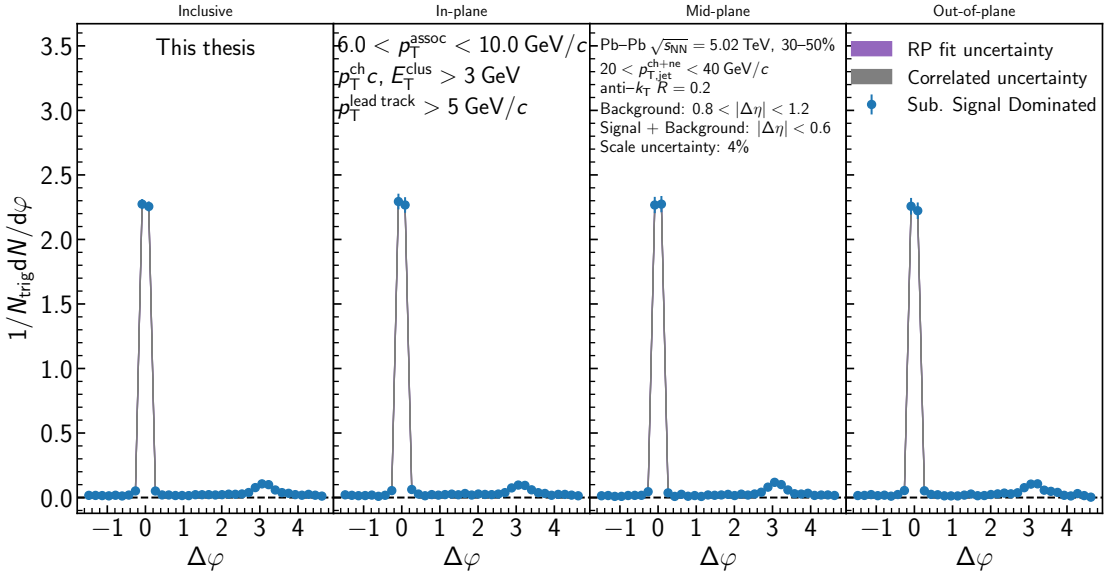

Figure D.152: The Reaction Plane Fit subtracted jet-hadron correlations measured for $20 < p_{\mathrm{T,jet}}^{\mathrm{ch+ne}} < 40$ GeV/c and $6.0 < p_{\mathrm{T}}^{\mathrm{assoc}} < 10.0$ GeV/c in 30–50% collisions. The subtracted data are shown in blue for each event plane orientation, with the fit uncertainty in purple and the correlated uncertainty in gray.

D.2 0–10% Central Pb–Pb Collisions

D.2.1 $20 < p_{\mathrm{T,jet}}^{\mathrm{ch+ne}} < 40\,\mathrm{GeV}/c$, $1.0 < p_{\mathrm{T}}^{\mathrm{assoc}} < 1.5\,\mathrm{GeV}/c$, Inclusive orientation

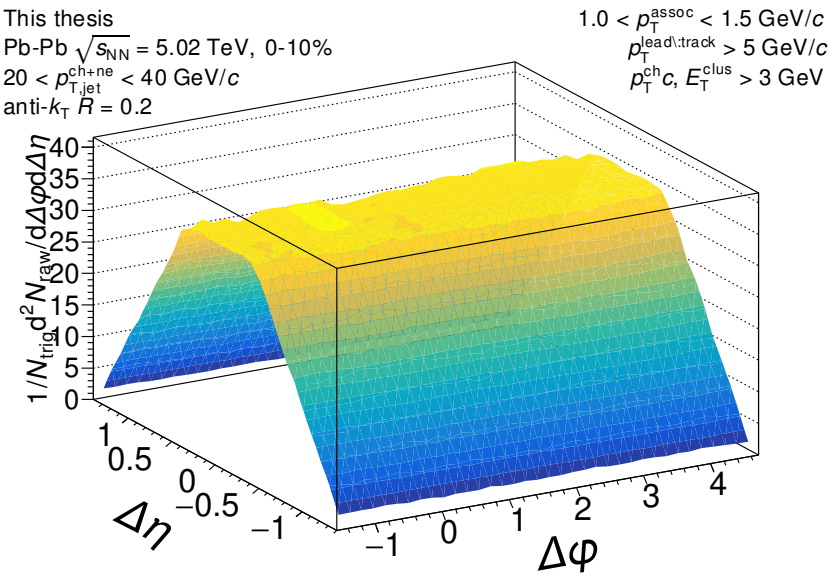

Figure D.153: The measured correlation function with the the efficiency correction $\epsilon(p_{\mathrm{T}}, \eta)$ applied, but before acceptance correction via the mixed events. The correlation is measured for inclusive orientation for $20 < p_{\mathrm{T,jet}}^{\mathrm{ch+ne}} < 40\mathrm{GeV}/c$ jets with $1.0 < p_{\mathrm{T}}^{\mathrm{assoc}} < 1.5\,\mathrm{GeV}/c$ in 0–10% Pb–Pb collisions at $\sqrt{s_{\mathrm{NN}}} = 5.02$ TeV.

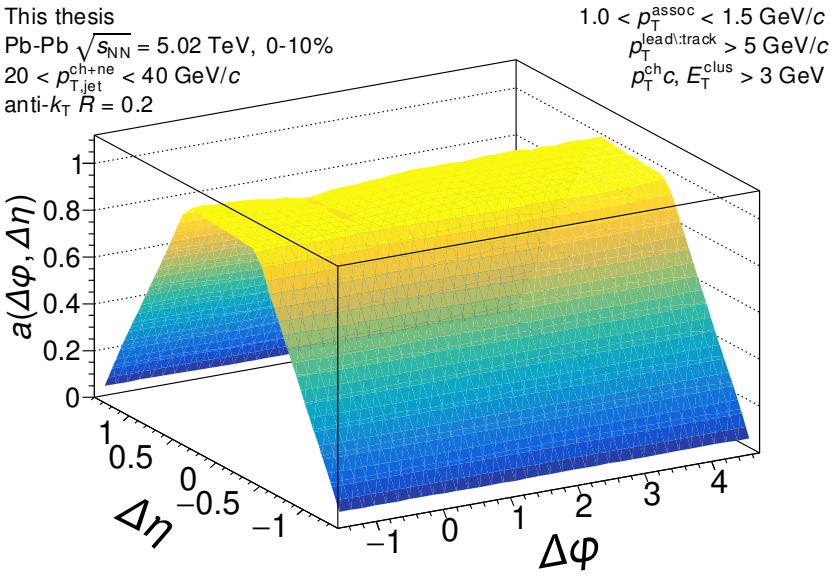

Figure D.154: The mixed event pair acceptance correction with the efficiency correction $\epsilon(p_{\mathrm{T}}, \eta)$ applied. The correlations are measured for inclusive orientation for $20 < p_{\mathrm{T,jet}}^{\mathrm{ch+ne}} < 40\ \mathrm{GeV}/c$ jets with $1.0 < p_{\mathrm{T}}^{\mathrm{assoc}} < 1.5\ \mathrm{GeV}/c$ in 0–10% Pb–Pb collisions at $\sqrt{s_{\mathrm{NN}}} = 5.02\ \mathrm{TeV}$. They have already been normalized such that it they are unity at maximum efficiency. Above 2 GeV/c, the mixed events are merged together to increase statistics, so it is the same for all for correlations within $2.0 \leq p_{\mathrm{T}}^{\mathrm{assoc}} < 10\ \mathrm{GeV}/c$.

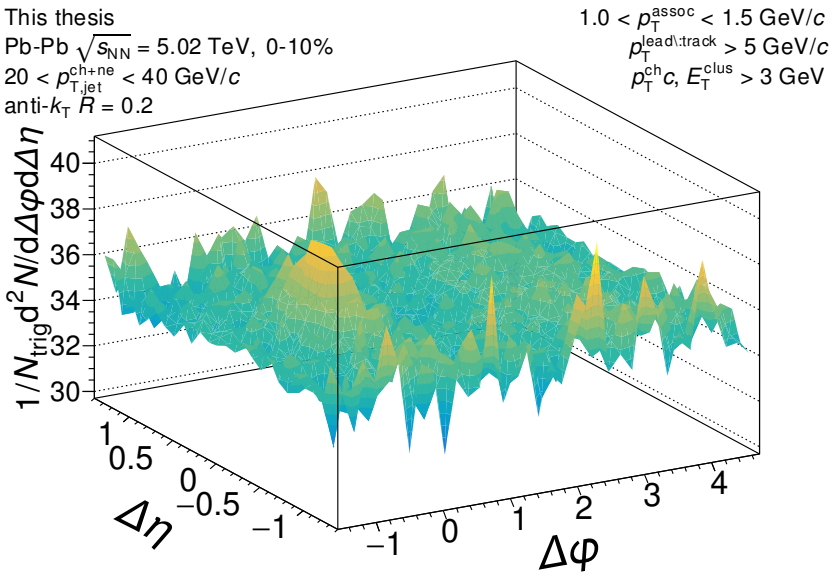

Figure D.155: The signal correlation corrected by pair acceptance. The correlations are measured for inclusive orientation for $20 < p_{\mathrm{T,jet}}^{\mathrm{ch+ne}} < 40\ \mathrm{GeV}/c$ jets with $1.0 < p_{\mathrm{T}}^{\mathrm{assoc}} < 1.5\ \mathrm{GeV}/c$ in 0–10% Pb–Pb collisions at $\sqrt{s_{\mathrm{NN}}} = 5.02\ \mathrm{TeV}$.

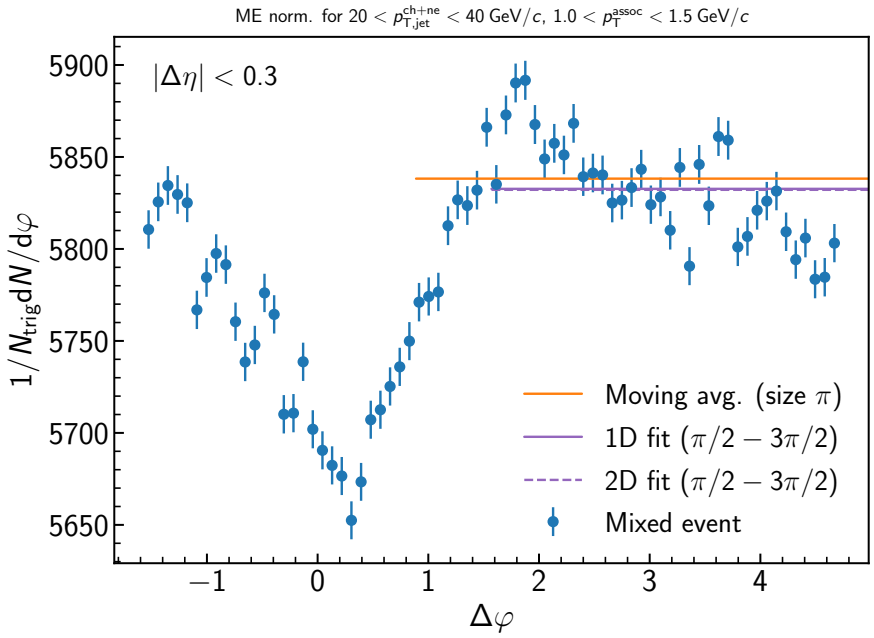

Figure D.156: Determination of the normalization of the mixed event for the inclusive event plane orientation in 0–10% Pb–Pb collisions at $\sqrt{s_{\mathrm{NN}}} = 5.02$ TeV. Here the mixed event is projected over the plateau range in $\Delta\eta$ onto to the $\Delta\varphi$ axis. The moving average is evaluated over the entire $\Delta\varphi$ range using a window of π, while the fit range is fixed from $\pi/2 < \Delta\varphi < 3\pi/2$. Since the mixed events are merged above 2 GeV/c, the normalization factor is also the same for all correlations within $1.0 < p_{\mathrm{T}}^{\mathrm{assoc}} < 1.5$ GeV/c. A variety of normalization methods were evaluated, with further details described in the text.

D.2.2 $20 < p_{\mathrm{T,jet}}^{\mathrm{ch+ne}} < 40\,\mathrm{GeV}/c$, $1.5 < p_{\mathrm{T}}^{\mathrm{assoc}} < 2.0\,\mathrm{GeV}/c$, Inclusive orientation

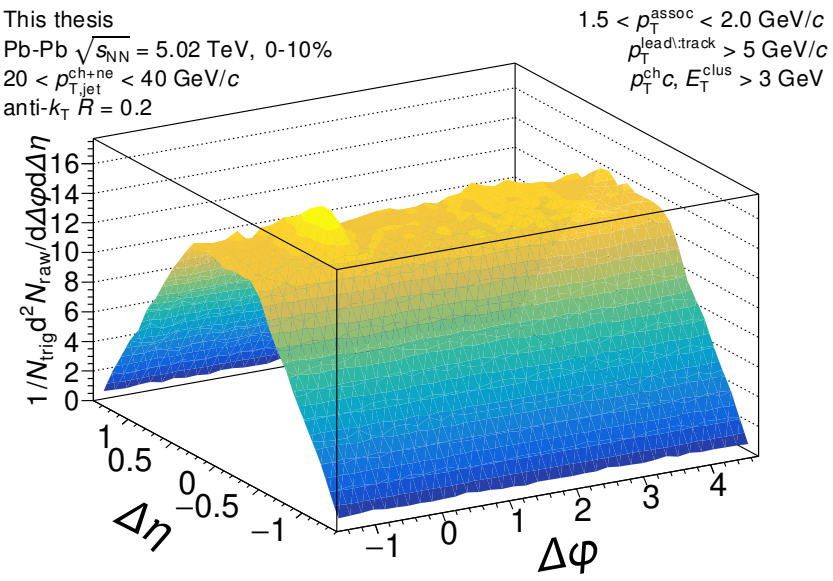

Figure D.157: The measured correlation function with the the efficiency correction $\epsilon(p_{\mathrm{T}}, \eta)$ applied, but before acceptance correction via the mixed events. The correlation is measured for inclusive orientation for $20 < p_{\mathrm{T,jet}}^{\mathrm{ch+ne}} < 40\mathrm{GeV}/c$ jets with $1.5 < p_{\mathrm{T}}^{\mathrm{assoc}} < 2.0\,\mathrm{GeV}/c$ in 0–10% Pb–Pb collisions at $\sqrt{s_{\mathrm{NN}}} = 5.02$ TeV.

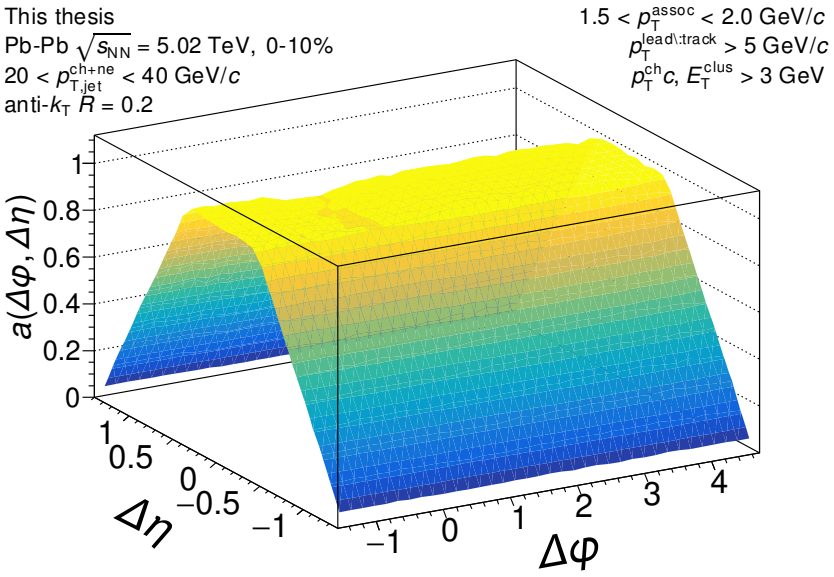

Figure D.158: The mixed event pair acceptance correction with the efficiency correction $\epsilon(p_{\mathrm{T}}, \eta)$ applied. The correlations are measured for inclusive orientation for $20 < p_{\mathrm{T,jet}}^{\mathrm{ch+ne}} < 40\,\mathrm{GeV}/c$ jets with $1.5 < p_{\mathrm{T}}^{\mathrm{assoc}} < 2.0\,\mathrm{GeV}/c$ in 0–10% Pb–Pb collisions at $\sqrt{s_{\mathrm{NN}}} = 5.02\,\mathrm{TeV}$. They have already been normalized such that it they are unity at maximum efficiency. Above 2 GeV/c, the mixed events are merged together to increase statistics, so it is the same for all for correlations within $2.0 \leq p_{\mathrm{T}}^{\mathrm{assoc}} < 10\,\mathrm{GeV}/c$.

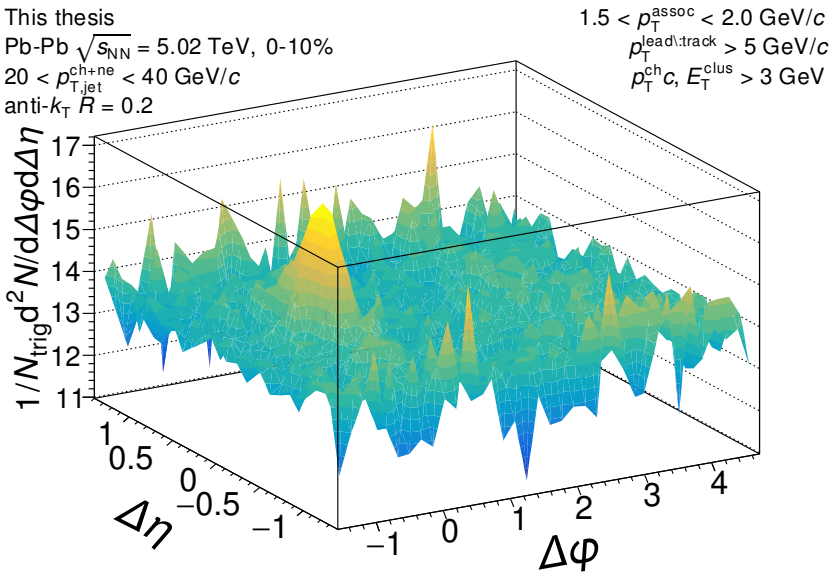

Figure D.159: The signal correlation corrected by pair acceptance. The correlations are measured for inclusive orientation for $20 < p_{\mathrm{T,jet}}^{\mathrm{ch+ne}} < 40\,\mathrm{GeV}/c$ jets with $1.5 < p_{\mathrm{T}}^{\mathrm{assoc}} < 2.0\,\mathrm{GeV}/c$ in 0–10% Pb–Pb collisions at $\sqrt{s_{\mathrm{NN}}} = 5.02\,\mathrm{TeV}$.

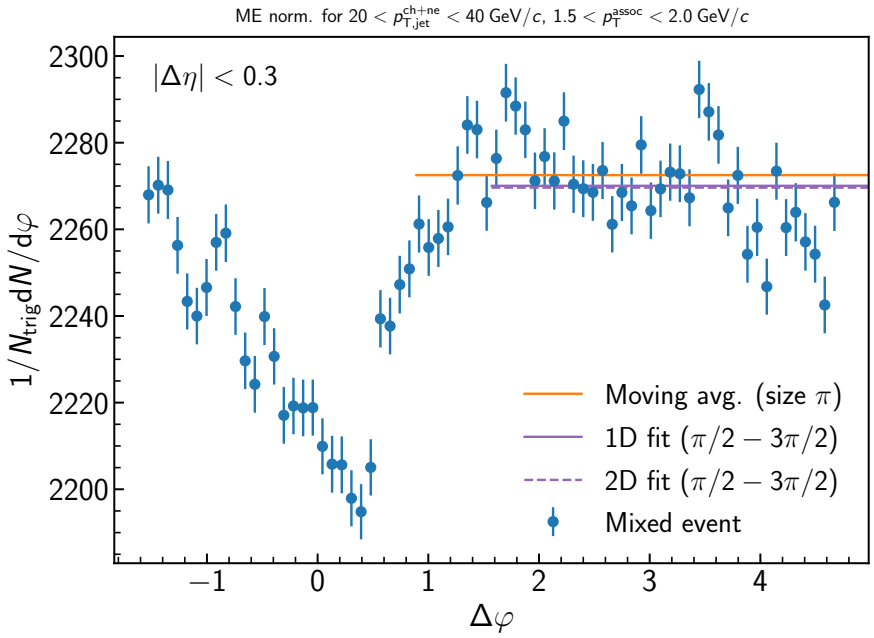

Figure D.160: Determination of the normalization of the mixed event for the inclusive event plane orientation in 0–10% Pb–Pb collisions at $\sqrt{s_{\mathrm{NN}}} = 5.02$ TeV. Here the mixed event is projected over the plateau range in $\Delta\eta$ onto to the $\Delta\varphi$ axis. The moving average is evaluated over the entire $\Delta\varphi$ range using a window of π, while the fit range is fixed from $\pi/2 < \Delta\varphi < 3\pi/2$. Since the mixed events are merged above 2 GeV/c, the normalization factor is also the same for all correlations within $1.5 < p_{\mathrm{T}}^{\mathrm{assoc}} < 2.0$ GeV/c. A variety of normalization methods were evaluated, with further details described in the text.

D.2.3 $20 < p_{\mathrm{T,jet}}^{\mathrm{ch+ne}} < 40\,\mathrm{GeV}/c$, $2.0 < p_{\mathrm{T}}^{\mathrm{assoc}} < 3.0\,\mathrm{GeV}/c$, Inclusive orientation

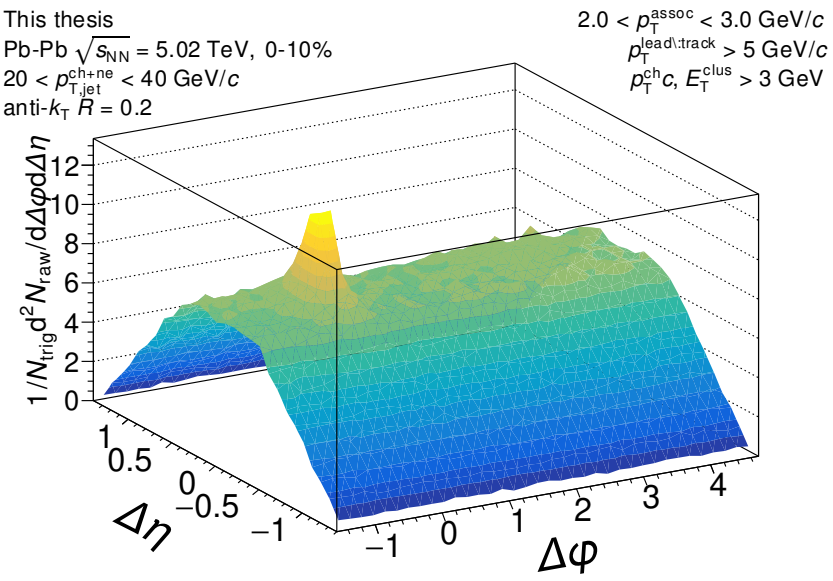

Figure D.161: The measured correlation function with the the efficiency correction $\epsilon(p_{\mathrm{T}}, \eta)$ applied, but before acceptance correction via the mixed events. The correlation is measured for inclusive orientation for $20 < p_{\mathrm{T,jet}}^{\mathrm{ch+ne}} < 40\mathrm{GeV}/c$ jets with $2.0 < p_{\mathrm{T}}^{\mathrm{assoc}} < 3.0\,\mathrm{GeV}/c$ in 0–10% Pb–Pb collisions at $\sqrt{s_{\mathrm{NN}}} = 5.02$ TeV.

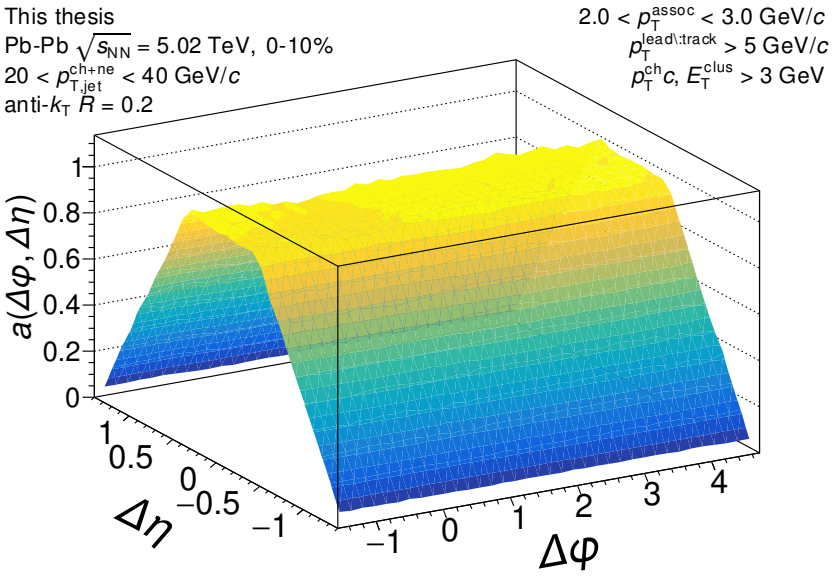

Figure D.162: The mixed event pair acceptance correction with the efficiency correction $\epsilon(p_{\mathrm{T}}, \eta)$ applied. The correlations are measured for inclusive orientation for $20 < p_{\mathrm{T,jet}}^{\mathrm{ch+ne}} < 40\ \mathrm{GeV}/c$ jets with $2.0 < p_{\mathrm{T}}^{\mathrm{assoc}} < 3.0\ \mathrm{GeV}/c$ in 0–10% Pb–Pb collisions at $\sqrt{s_{\mathrm{NN}}} = 5.02\ \mathrm{TeV}$. They have already been normalized such that it they are unity at maximum efficiency. Above 2 GeV/c, the mixed events are merged together to increase statistics, so it is the same for all for correlations within $2.0 \leq p_{\mathrm{T}}^{\mathrm{assoc}} < 10\ \mathrm{GeV}/c$.

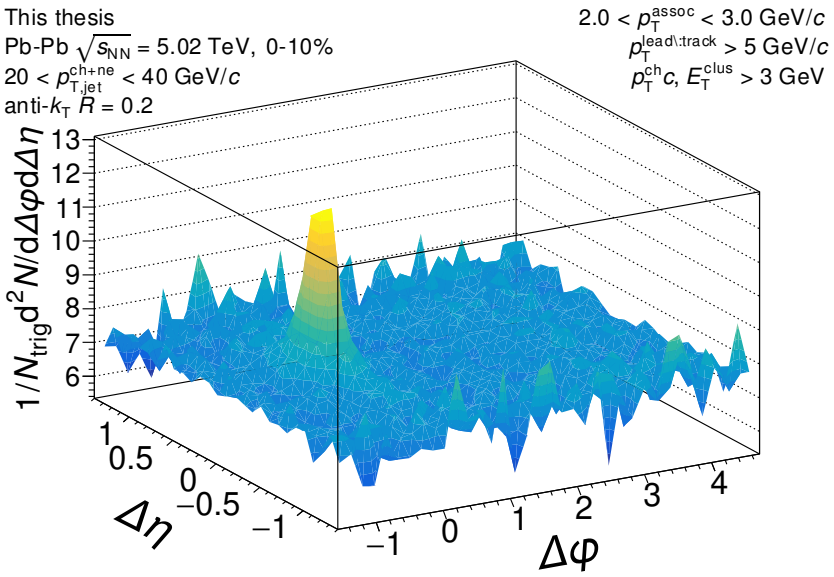

Figure D.163: The signal correlation corrected by pair acceptance. The correlations are measured for inclusive orientation for $20 < p_{\mathrm{T,jet}}^{\mathrm{ch+ne}} < 40\ \mathrm{GeV}/c$ jets with $2.0 < p_{\mathrm{T}}^{\mathrm{assoc}} < 3.0\ \mathrm{GeV}/c$ in 0–10% Pb–Pb collisions at $\sqrt{s_{\mathrm{NN}}} = 5.02\ \mathrm{TeV}$.

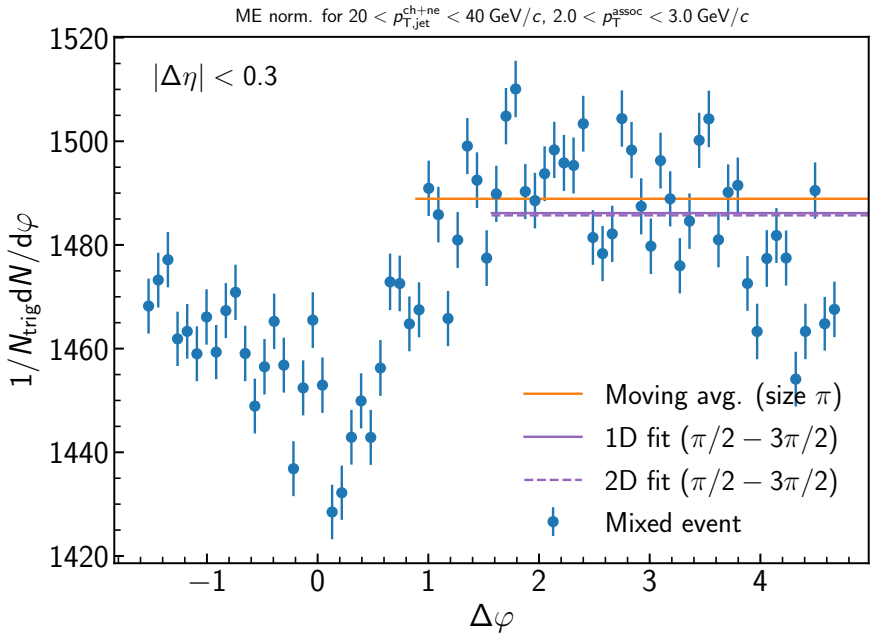

Figure D.164: Determination of the normalization of the mixed event for the inclusive event plane orientation in 0–10% Pb–Pb collisions at $\sqrt{s_{\mathrm{NN}}} = 5.02$ TeV. Here the mixed event is projected over the plateau range in $\Delta\eta$ onto to the $\Delta\varphi$ axis. The moving average is evaluated over the entire $\Delta\varphi$ range using a window of π, while the fit range is fixed from $\pi/2 < \Delta\varphi < 3\pi/2$. Since the mixed events are merged above 2 GeV/c, the normalization factor is also the same for all correlations within $2.0 < p_{\mathrm{T}}^{\mathrm{assoc}} < 3.0$ GeV/c. A variety of normalization methods were evaluated, with further details described in the text.

D.2.4 $20 < p_{\mathrm{T,jet}}^{\mathrm{ch+ne}} < 40\,\mathrm{GeV}/c$, $3.0 < p_{\mathrm{T}}^{\mathrm{assoc}} < 4.0\,\mathrm{GeV}/c$, Inclusive orientation

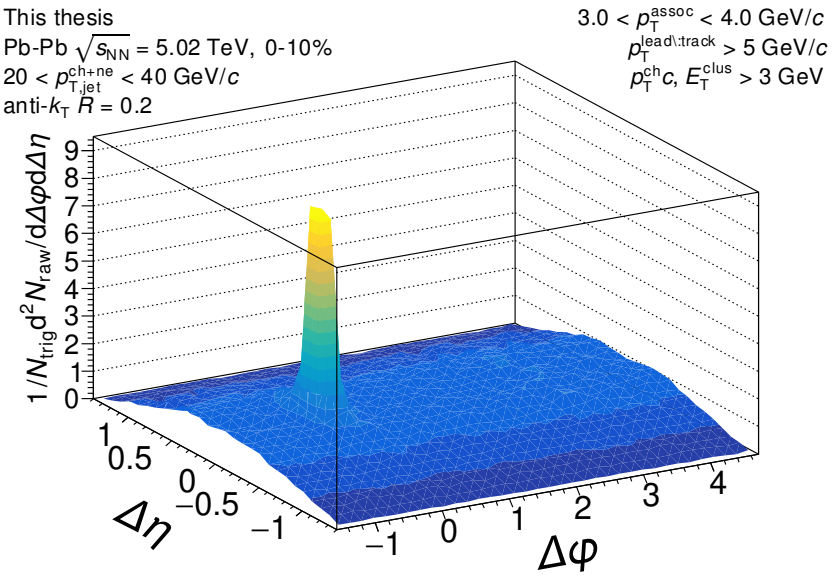

Figure D.165: The measured correlation function with the the efficiency correction $\epsilon(p_{\mathrm{T}}, \eta)$ applied, but before acceptance correction via the mixed events. The correlation is measured for inclusive orientation for $20 < p_{\mathrm{T,jet}}^{\mathrm{ch+ne}} < 40\mathrm{GeV}/c$ jets with $3.0 < p_{\mathrm{T}}^{\mathrm{assoc}} < 4.0\,\mathrm{GeV}/c$ in 0–10% Pb–Pb collisions at $\sqrt{s_{\mathrm{NN}}} = 5.02$ TeV.

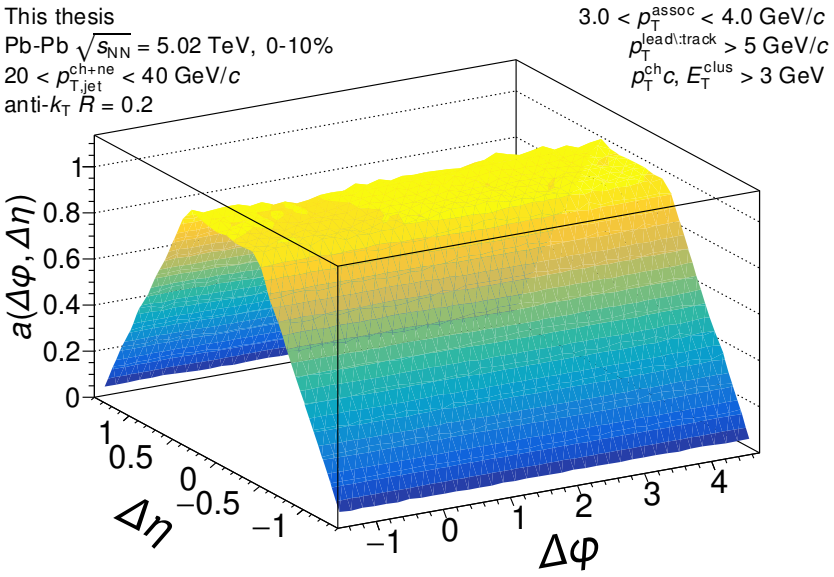

Figure D.166: The mixed event pair acceptance correction with the efficiency correction $\epsilon(p_T, \eta)$ applied. The correlations are measured for inclusive orientation for $20 < p_{T,jet}^{ch+ne} < 40$ GeV/c jets with $3.0 < p_T^{assoc} < 4.0$ GeV/c in 0–10% Pb–Pb collisions at $\sqrt{s_{NN}} = 5.02$ TeV. They have already been normalized such that it they are unity at maximum efficiency. Above 2 GeV/c, the mixed events are merged together to increase statistics, so it is the same for all for correlations within $2.0 \leq p_T^{assoc} < 10$ GeV/c.

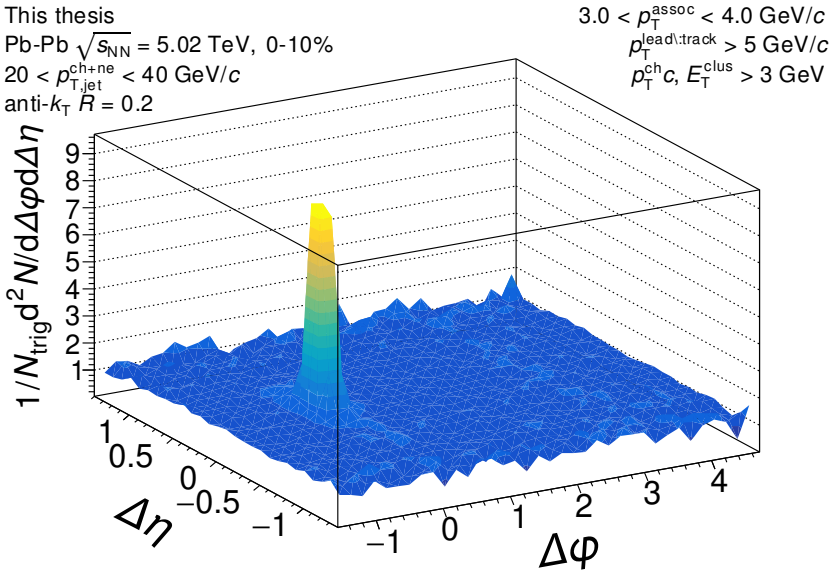

Figure D.167: The signal correlation corrected by pair acceptance. The correlations are measured for inclusive orientation for $20 < p_{T,jet}^{ch+ne} < 40$ GeV/c jets with $3.0 < p_T^{assoc} < 4.0$ GeV/c in 0–10% Pb–Pb collisions at $\sqrt{s_{NN}} = 5.02$ TeV.

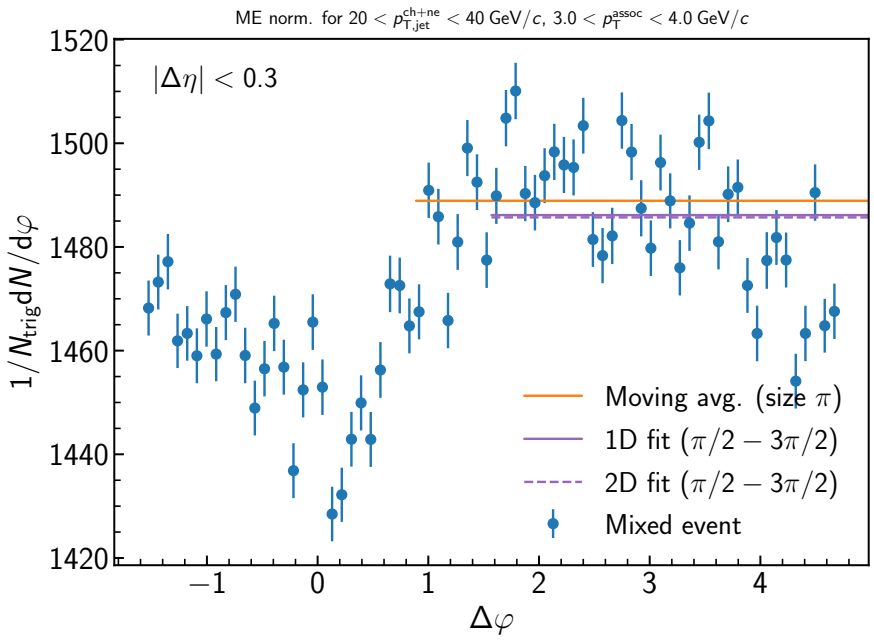

Figure D.168: Determination of the normalization of the mixed event for the inclusive event plane orientation in 0–10% Pb–Pb collisions at $\sqrt{s_{\mathrm{NN}}} = 5.02$ TeV. Here the mixed event is projected over the plateau range in $\Delta\eta$ onto to the $\Delta\varphi$ axis. The moving average is evaluated over the entire $\Delta\varphi$ range using a window of π, while the fit range is fixed from $\pi/2 < \Delta\varphi < 3\pi/2$. Since the mixed events are merged above 2 GeV/c, the normalization factor is also the same for all correlations within $3.0 < p_{\mathrm{T}}^{\mathrm{assoc}} < 4.0$ GeV/c. A variety of normalization methods were evaluated, with further details described in the text.

D.2.5 $20 < p_{\mathrm{T,jet}}^{\mathrm{ch+ne}} < 40\,\mathrm{GeV}/c$, $4.0 < p_{\mathrm{T}}^{\mathrm{assoc}} < 5.0\,\mathrm{GeV}/c$, Inclusive orientation

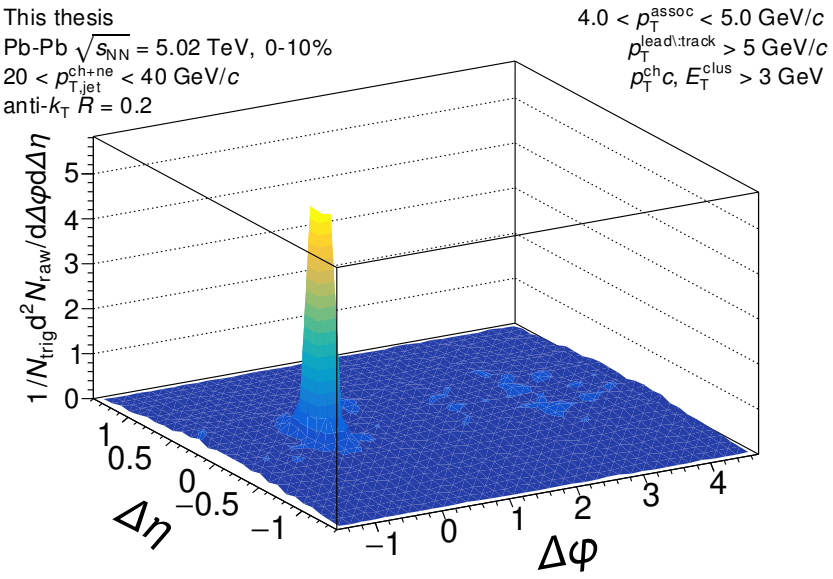

Figure D.169: The measured correlation function with the the efficiency correction $\epsilon(p_{\mathrm{T}}, \eta)$ applied, but before acceptance correction via the mixed events. The correlation is measured for inclusive orientation for $20 < p_{\mathrm{T,jet}}^{\mathrm{ch+ne}} < 40\mathrm{GeV}/c$ jets with $4.0 < p_{\mathrm{T}}^{\mathrm{assoc}} < 5.0\,\mathrm{GeV}/c$ in 0–10% Pb–Pb collisions at $\sqrt{s_{\mathrm{NN}}} = 5.02$ TeV.

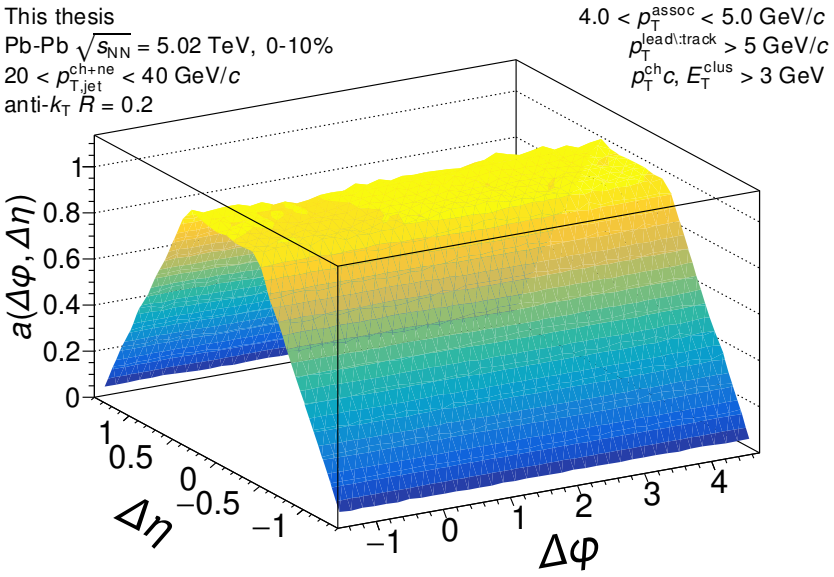

Figure D.170: The mixed event pair acceptance correction with the efficiency correction $\epsilon(p_{\mathrm{T}}, \eta)$ applied. The correlations are measured for inclusive orientation for $20 < p_{\mathrm{T,jet}}^{\mathrm{ch+ne}} < 40\ \mathrm{GeV}/c$ jets with $4.0 < p_{\mathrm{T}}^{\mathrm{assoc}} < 5.0\ \mathrm{GeV}/c$ in 0–10% Pb–Pb collisions at $\sqrt{s_{\mathrm{NN}}} = 5.02\ \mathrm{TeV}$. They have already been normalized such that it they are unity at maximum efficiency. Above 2 GeV/c, the mixed events are merged together to increase statistics, so it is the same for all for correlations within $2.0 \leq p_{\mathrm{T}}^{\mathrm{assoc}} < 10\ \mathrm{GeV}/c$.

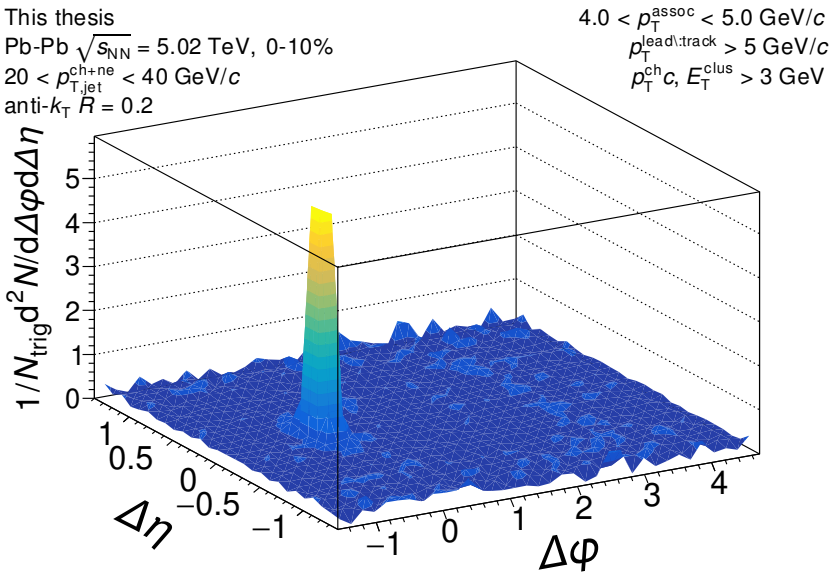

Figure D.171: The signal correlation corrected by pair acceptance. The correlations are measured for inclusive orientation for $20 < p_{\mathrm{T,jet}}^{\mathrm{ch+ne}} < 40\ \mathrm{GeV}/c$ jets with $4.0 < p_{\mathrm{T}}^{\mathrm{assoc}} < 5.0\ \mathrm{GeV}/c$ in 0–10% Pb–Pb collisions at $\sqrt{s_{\mathrm{NN}}} = 5.02\ \mathrm{TeV}$.

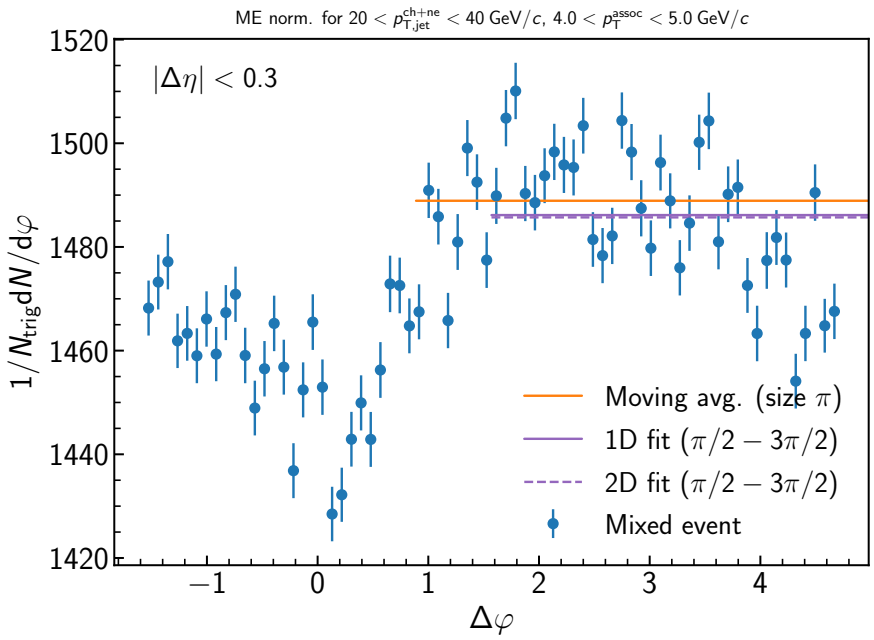

Figure D.172: Determination of the normalization of the mixed event for the inclusive event plane orientation in 0–10% Pb–Pb collisions at $\sqrt{s_{\mathrm{NN}}} = 5.02$ TeV. Here the mixed event is projected over the plateau range in $\Delta\eta$ onto to the $\Delta\varphi$ axis. The moving average is evaluated over the entire $\Delta\varphi$ range using a window of π, while the fit range is fixed from $\pi/2 < \Delta\varphi < 3\pi/2$. Since the mixed events are merged above 2 GeV/c, the normalization factor is also the same for all correlations within $4.0 < p_{\mathrm{T}}^{\mathrm{assoc}} < 5.0$ GeV/c. A variety of normalization methods were evaluated, with further details described in the text.

D.2.6 $20 < p_{\mathrm{T,jet}}^{\mathrm{ch+ne}} < 40\,\mathrm{GeV}/c$, $5.0 < p_{\mathrm{T}}^{\mathrm{assoc}} < 6.0\,\mathrm{GeV}/c$, Inclusive orientation

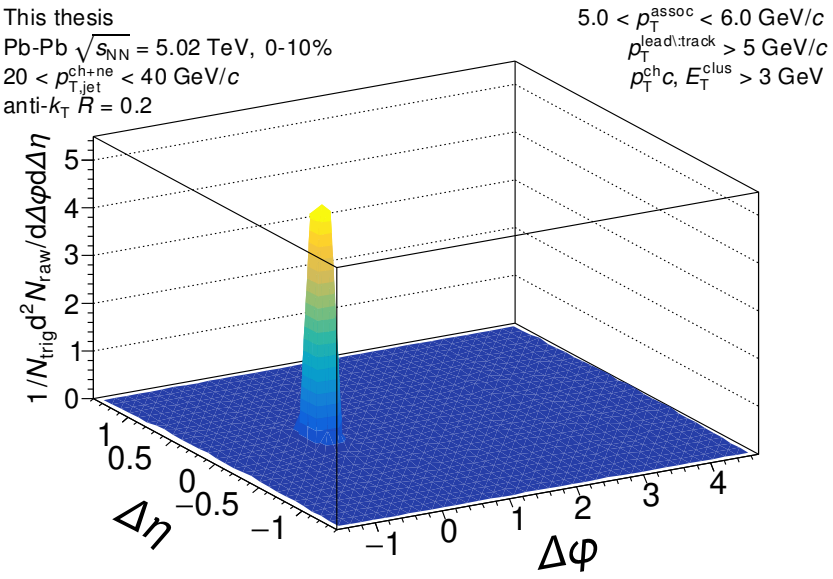

Figure D.173: The measured correlation function with the the efficiency correction $\epsilon(p_{\mathrm{T}}, \eta)$ applied, but before acceptance correction via the mixed events. The correlation is measured for inclusive orientation for $20 < p_{\mathrm{T,jet}}^{\mathrm{ch+ne}} < 40\mathrm{GeV}/c$ jets with $5.0 < p_{\mathrm{T}}^{\mathrm{assoc}} < 6.0\,\mathrm{GeV}/c$ in 0–10% Pb–Pb collisions at $\sqrt{s_{\mathrm{NN}}} = 5.02$ TeV.

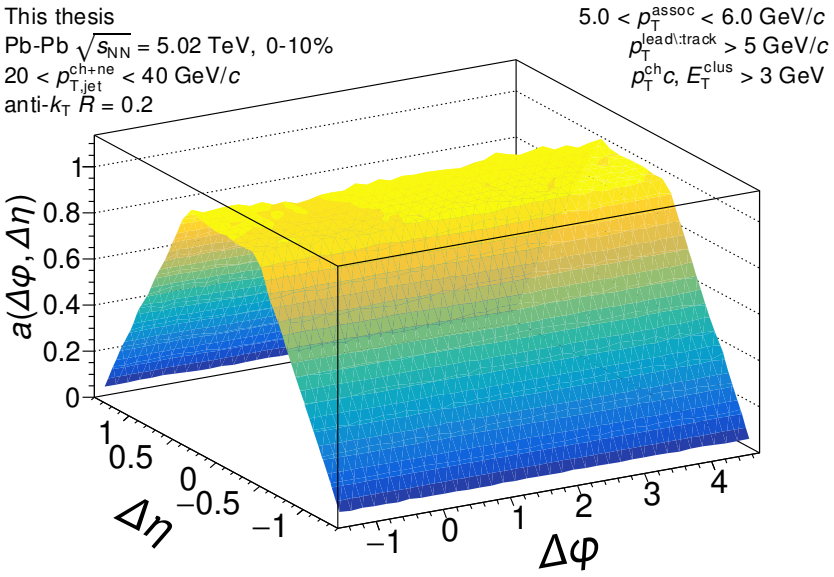

Figure D.174: The mixed event pair acceptance correction with the efficiency correction $\epsilon(p_{\mathrm{T}}, \eta)$ applied. The correlations are measured for inclusive orientation for $20 < p_{\mathrm{T,jet}}^{\mathrm{ch+ne}} < 40\ \mathrm{GeV}/c$ jets with $5.0 < p_{\mathrm{T}}^{\mathrm{assoc}} < 6.0\ \mathrm{GeV}/c$ in 0–10% Pb–Pb collisions at $\sqrt{s_{\mathrm{NN}}} = 5.02\ \mathrm{TeV}$. They have already been normalized such that it they are unity at maximum efficiency. Above 2 GeV/c, the mixed events are merged together to increase statistics, so it is the same for all for correlations within $2.0 \leq p_{\mathrm{T}}^{\mathrm{assoc}} < 10\ \mathrm{GeV}/c$.

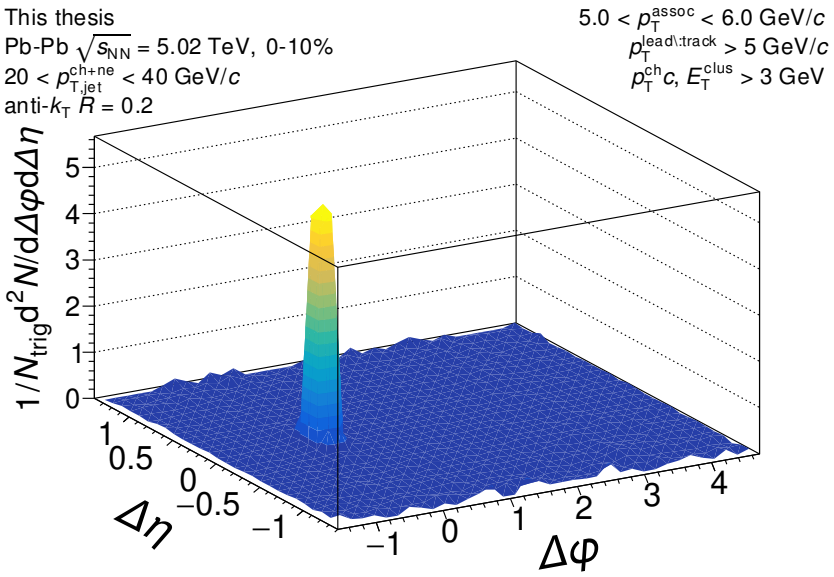

Figure D.175: The signal correlation corrected by pair acceptance. The correlations are measured for inclusive orientation for $20 < p_{\mathrm{T,jet}}^{\mathrm{ch+ne}} < 40\ \mathrm{GeV}/c$ jets with $5.0 < p_{\mathrm{T}}^{\mathrm{assoc}} < 6.0\ \mathrm{GeV}/c$ in 0–10% Pb–Pb collisions at $\sqrt{s_{\mathrm{NN}}} = 5.02\ \mathrm{TeV}$.

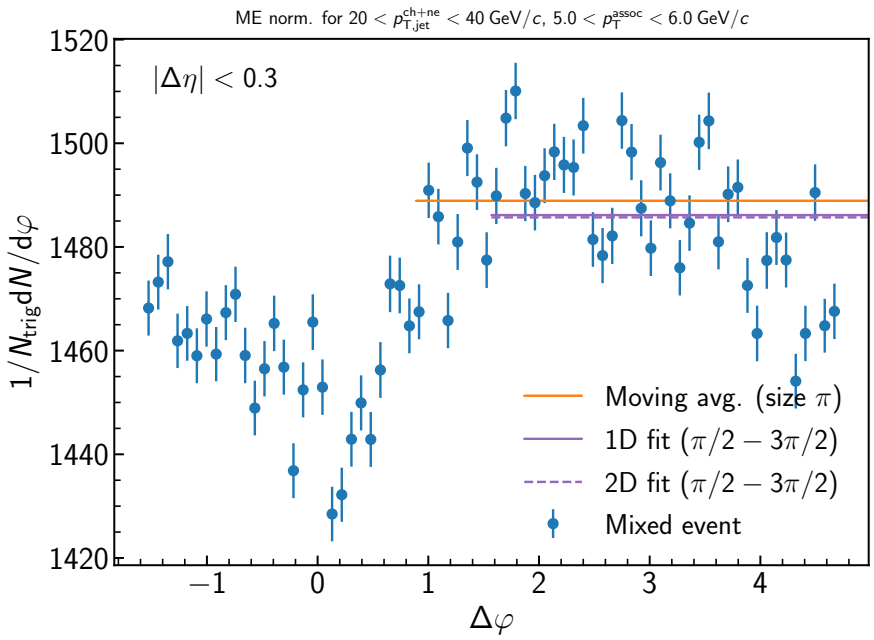

Figure D.176: Determination of the normalization of the mixed event for the inclusive event plane orientation in 0–10% Pb–Pb collisions at $\sqrt{s_{\mathrm{NN}}} = 5.02$ TeV. Here the mixed event is projected over the plateau range in $\Delta\eta$ onto to the $\Delta\varphi$ axis. The moving average is evaluated over the entire $\Delta\varphi$ range using a window of π, while the fit range is fixed from $\pi/2 < \Delta\varphi < 3\pi/2$. Since the mixed events are merged above 2 GeV/c, the normalization factor is also the same for all correlations within $5.0 < p_{\mathrm{T}}^{\mathrm{assoc}} < 6.0$ GeV/c. A variety of normalization methods were evaluated, with further details described in the text.

D.2.7 $20 < p_{\mathrm{T,jet}}^{\mathrm{ch+ne}} < 40\mathrm{GeV}/c$, $6.0 < p_{\mathrm{T}}^{\mathrm{assoc}} < 10.0\mathrm{GeV}/c$, Inclusive orientation

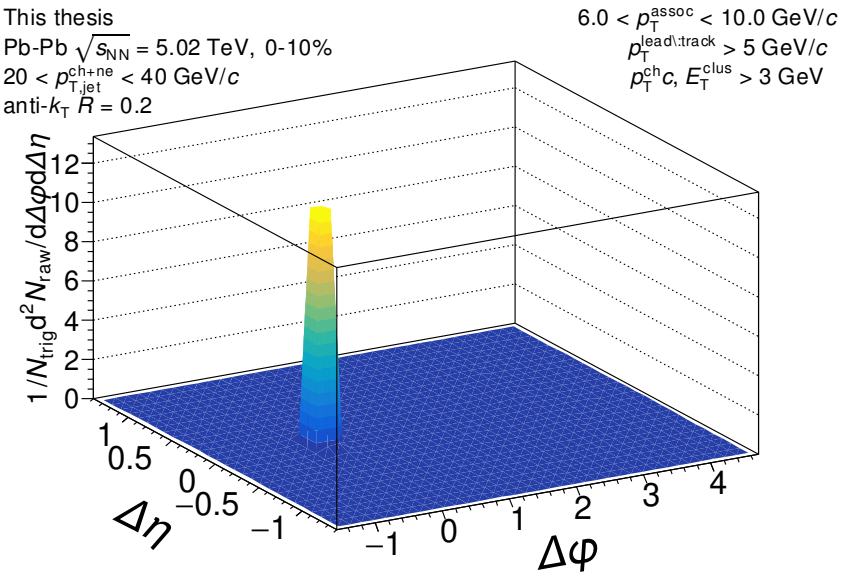

Figure D.177: The measured correlation function with the the efficiency correction $\epsilon(p_{\mathrm{T}}, \eta)$ applied, but before acceptance correction via the mixed events. The correlation is measured for inclusive orientation for $20 < p_{\mathrm{T,jet}}^{\mathrm{ch+ne}} < 40\mathrm{GeV}/c$ jets with $6.0 < p_{\mathrm{T}}^{\mathrm{assoc}} < 10.0\,\mathrm{GeV}/c$ in 0–10% Pb–Pb collisions at $\sqrt{s_{\mathrm{NN}}} = 5.02$ TeV.

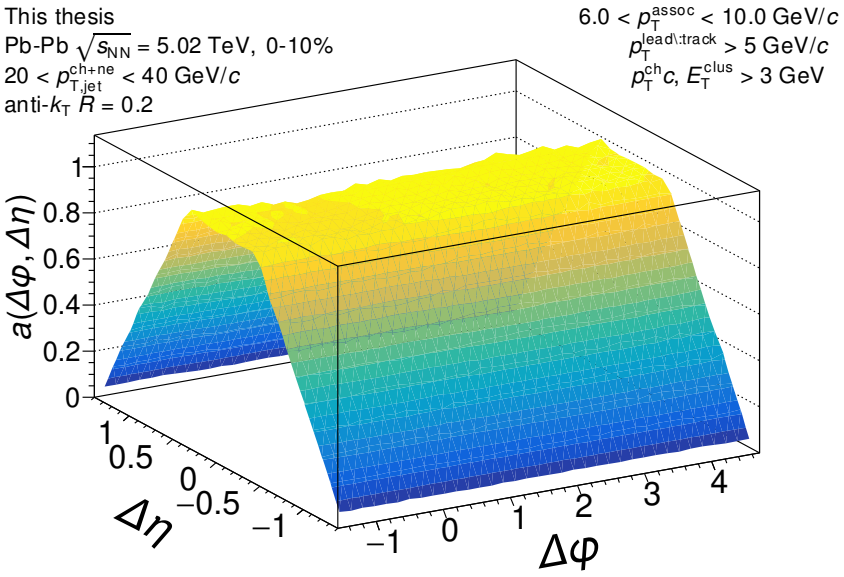

Figure D.178: The mixed event pair acceptance correction with the efficiency correction $\epsilon(p_{\mathrm{T}}, \eta)$ applied. The correlations are measured for inclusive orientation for $20 < p_{\mathrm{T,jet}}^{\mathrm{ch+ne}} < 40\,\mathrm{GeV}/c$ jets with $6.0 < p_{\mathrm{T}}^{\mathrm{assoc}} < 10.0\,\mathrm{GeV}/c$ in 0–10% Pb–Pb collisions at $\sqrt{s_{\mathrm{NN}}} = 5.02\,\mathrm{TeV}$. They have already been normalized such that it they are unity at maximum efficiency. Above 2 GeV/c, the mixed events are merged together to increase statistics, so it is the same for all for correlations within $2.0 \leq p_{\mathrm{T}}^{\mathrm{assoc}} < 10$ GeV/c.

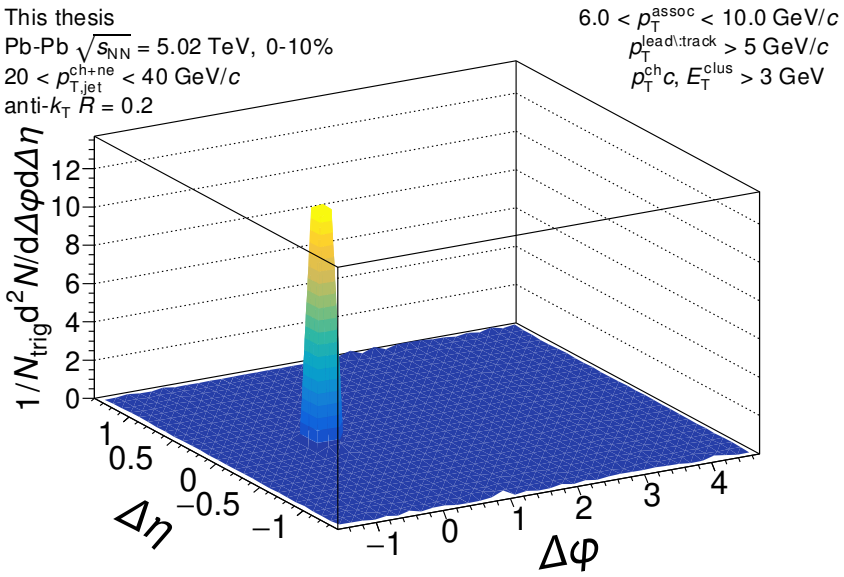

Figure D.179: The signal correlation corrected by pair acceptance. The correlations are measured for inclusive orientation for $20 < p_{\mathrm{T,jet}}^{\mathrm{ch+ne}} < 40\,\mathrm{GeV}/c$ jets with $6.0 < p_{\mathrm{T}}^{\mathrm{assoc}} < 10.0\,\mathrm{GeV}/c$ in 0–10% Pb–Pb collisions at $\sqrt{s_{\mathrm{NN}}} = 5.02\,\mathrm{TeV}$.

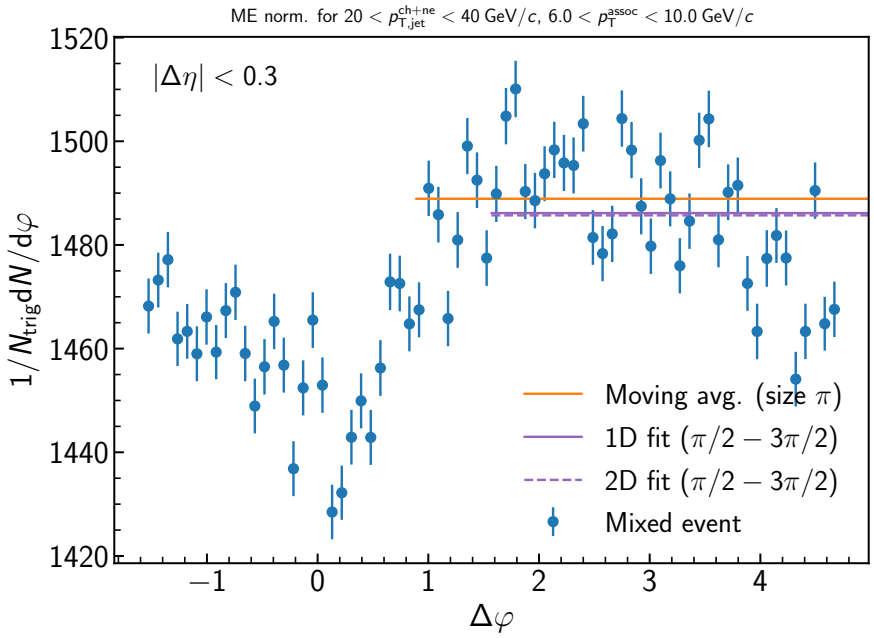

Figure D.180: Determination of the normalization of the mixed event for the inclusive event plane orientation in 0–10% Pb–Pb collisions at $\sqrt{s_{\mathrm{NN}}} = 5.02$ TeV. Here the mixed event is projected over the plateau range in $\Delta\eta$ onto to the $\Delta\varphi$ axis. The moving average is evaluated over the entire $\Delta\varphi$ range using a window of π, while the fit range is fixed from $\pi/2 < \Delta\varphi < 3\pi/2$. Since the mixed events are merged above 2 GeV/c, the normalization factor is also the same for all correlations within $6.0 < p_{\mathrm{T}}^{\mathrm{assoc}} < 10.0$ GeV/c. A variety of normalization methods were evaluated, with further details described in the text.

D.2.8 $20 < p_{\mathrm{T,jet}}^{\mathrm{ch+ne}} < 40\ \mathrm{GeV}/c$, $1.0 < p_{\mathrm{T}}^{\mathrm{assoc}} < 1.5\ \mathrm{GeV}/c$, In-plane orientation

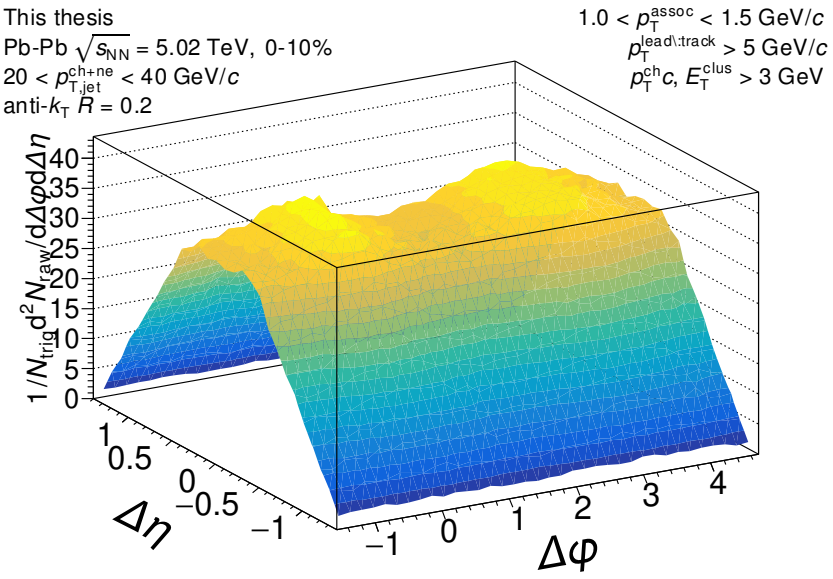

Figure D.181: The measured correlation function with the the efficiency correction $\epsilon(p_{\mathrm{T}}, \eta)$ applied, but before acceptance correction via the mixed events. The correlation is measured for in-plane orientation for $20 < p_{\mathrm{T,jet}}^{\mathrm{ch+ne}} < 40\mathrm{GeV}/c$ jets with $1.0 < p_{\mathrm{T}}^{\mathrm{assoc}} < 1.5\ \mathrm{GeV}/c$ in 0–10% Pb–Pb collisions at $\sqrt{s_{\mathrm{NN}}} = 5.02$ TeV.

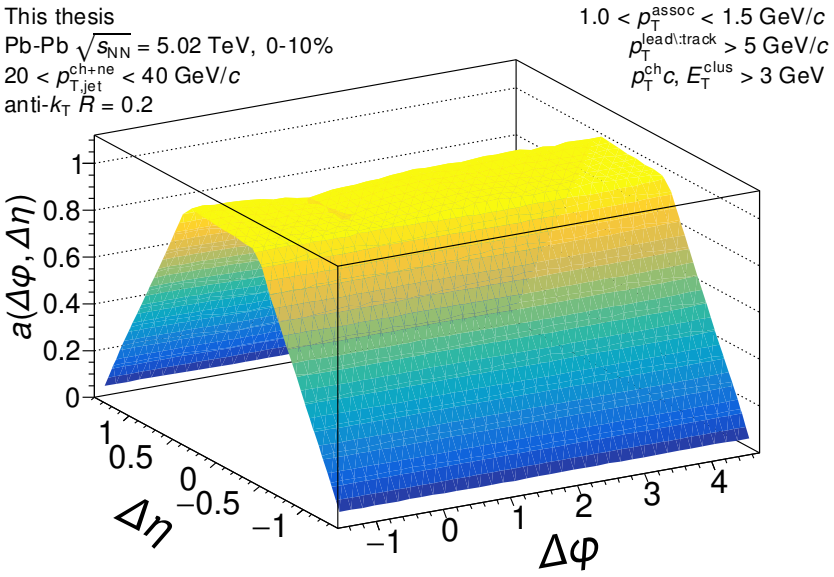

Figure D.182: The mixed event pair acceptance correction with the efficiency correction $\epsilon(p_T, \eta)$ applied. The correlations are measured for in-plane orientation for $20 < p_{T,jet}^{ch+ne} < 40$ GeV/c jets with $1.0 < p_T^{assoc} < 1.5$ GeV/c in 0–10% Pb–Pb collisions at $\sqrt{s_{NN}} = 5.02$ TeV. They have already been normalized such that it they are unity at maximum efficiency. Above 2 GeV/c, the mixed events are merged together to increase statistics, so it is the same for all for correlations within $2.0 \leq p_T^{assoc} < 10$ GeV/c.

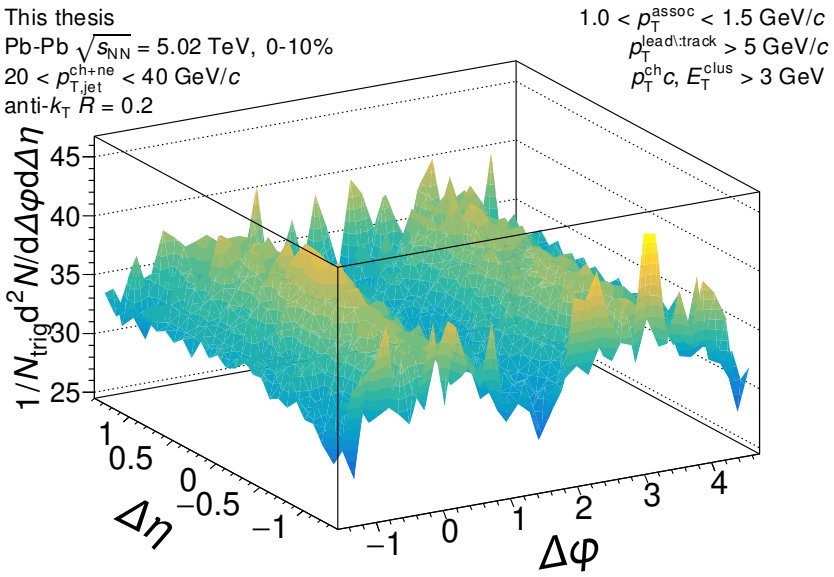

Figure D.183: The signal correlation corrected by pair acceptance. The correlations are measured for in-plane orientation for $20 < p_{T,jet}^{ch+ne} < 40$ GeV/c jets with $1.0 < p_T^{assoc} < 1.5$ GeV/c in 0–10% Pb–Pb collisions at $\sqrt{s_{NN}} = 5.02$ TeV.

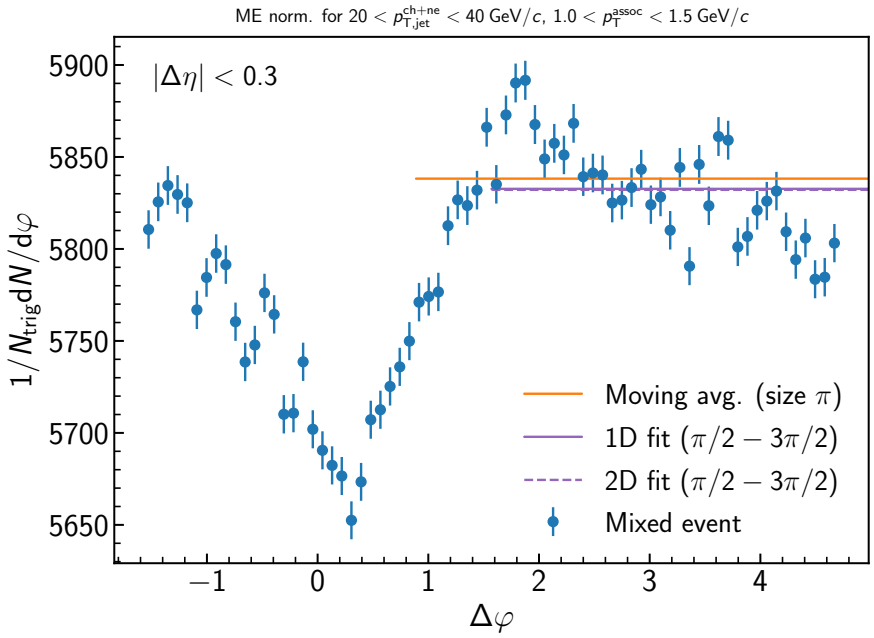

Figure D.184: Determination of the normalization of the mixed event for the inclusive event plane orientation in 0–10% Pb–Pb collisions at $\sqrt{s_{\mathrm{NN}}} = 5.02$ TeV. Here the mixed event is projected over the plateau range in $\Delta\eta$ onto to the $\Delta\varphi$ axis. The moving average is evaluated over the entire $\Delta\varphi$ range using a window of π, while the fit range is fixed from $\pi/2 < \Delta\varphi < 3\pi/2$. Since the mixed events are merged above 2 GeV/c, the normalization factor is also the same for all correlations within $1.0 < p_{\mathrm{T}}^{\mathrm{assoc}} < 1.5$ GeV/c. A variety of normalization methods were evaluated, with further details described in the text.

D.2.9 $20 < p_{\mathrm{T,jet}}^{\mathrm{ch+ne}} < 40\ \mathrm{GeV}/c$, $1.5 < p_{\mathrm{T}}^{\mathrm{assoc}} < 2.0\ \mathrm{GeV}/c$, In-plane orientation

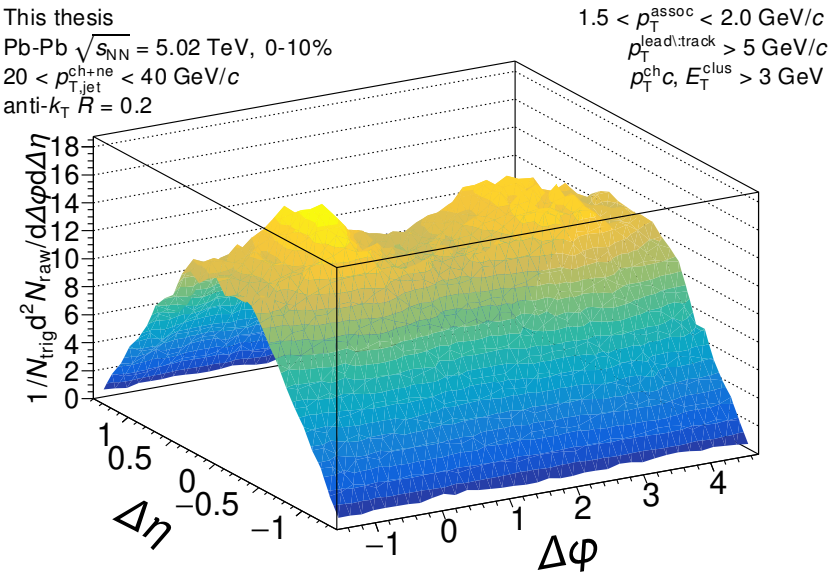

Figure D.185: The measured correlation function with the the efficiency correction $\epsilon(p_{\mathrm{T}}, \eta)$ applied, but before acceptance correction via the mixed events. The correlation is measured for in-plane orientation for $20 < p_{\mathrm{T,jet}}^{\mathrm{ch+ne}} < 40\,\mathrm{GeV}/c$ jets with $1.5 < p_{\mathrm{T}}^{\mathrm{assoc}} < 2.0\ \mathrm{GeV}/c$ in 0–10% Pb–Pb collisions at $\sqrt{s_{\mathrm{NN}}} = 5.02$ TeV.

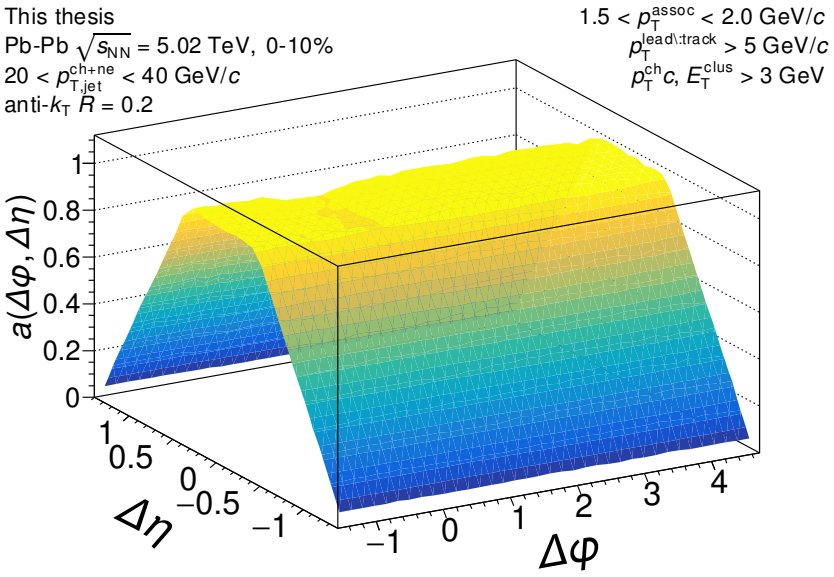

Figure D.186: The mixed event pair acceptance correction with the efficiency correction $\epsilon(p_{\mathrm{T}}, \eta)$ applied. The correlations are measured for in-plane orientation for $20 < p_{\mathrm{T,jet}}^{\mathrm{ch+ne}} < 40\,\mathrm{GeV}/c$ jets with $1.5 < p_{\mathrm{T}}^{\mathrm{assoc}} < 2.0\,\mathrm{GeV}/c$ in 0–10% Pb–Pb collisions at $\sqrt{s_{\mathrm{NN}}} = 5.02\,\mathrm{TeV}$. They have already been normalized such that it they are unity at maximum efficiency. Above 2 GeV/c, the mixed events are merged together to increase statistics, so it is the same for all for correlations within $2.0 \leq p_{\mathrm{T}}^{\mathrm{assoc}} < 10\,\mathrm{GeV}/c$.

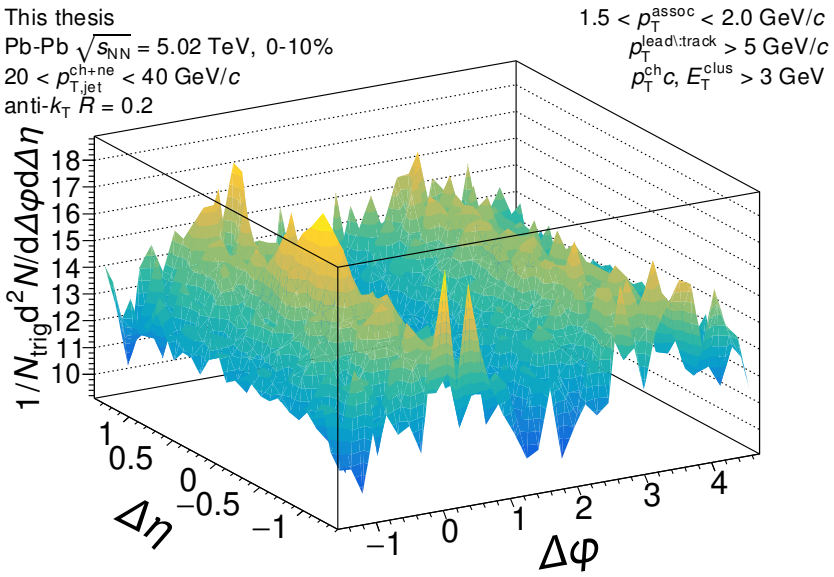

Figure D.187: The signal correlation corrected by pair acceptance. The correlations are measured for in-plane orientation for $20 < p_{\mathrm{T,jet}}^{\mathrm{ch+ne}} < 40\,\mathrm{GeV}/c$ jets with $1.5 < p_{\mathrm{T}}^{\mathrm{assoc}} < 2.0\,\mathrm{GeV}/c$ in 0–10% Pb–Pb collisions at $\sqrt{s_{\mathrm{NN}}} = 5.02\,\mathrm{TeV}$.

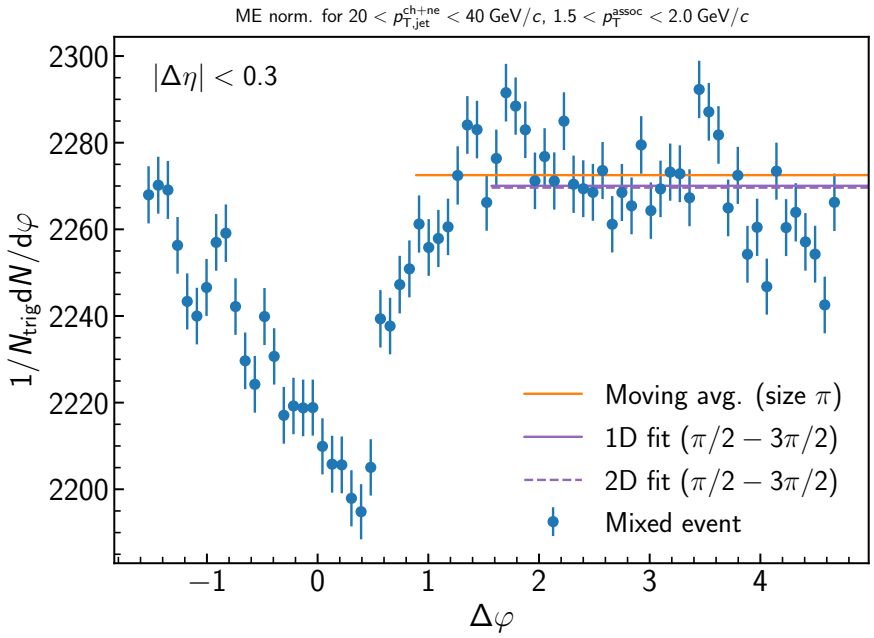

Figure D.188: Determination of the normalization of the mixed event for the inclusive event plane orientation in 0–10% Pb–Pb collisions at $\sqrt{s_{\mathrm{NN}}} = 5.02$ TeV. Here the mixed event is projected over the plateau range in $\Delta\eta$ onto to the $\Delta\varphi$ axis. The moving average is evaluated over the entire $\Delta\varphi$ range using a window of π, while the fit range is fixed from $\pi/2 < \Delta\varphi < 3\pi/2$. Since the mixed events are merged above 2 GeV/c, the normalization factor is also the same for all correlations within $1.5 < p_{\mathrm{T}}^{\mathrm{assoc}} < 2.0$ GeV/c. A variety of normalization methods were evaluated, with further details described in the text.

D.2.10 $20 < p_{\mathrm{T,jet}}^{\mathrm{ch+ne}} < 40\,\mathrm{GeV}/c$, $2.0 < p_{\mathrm{T}}^{\mathrm{assoc}} < 3.0\,\mathrm{GeV}/c$, In-plane orientation

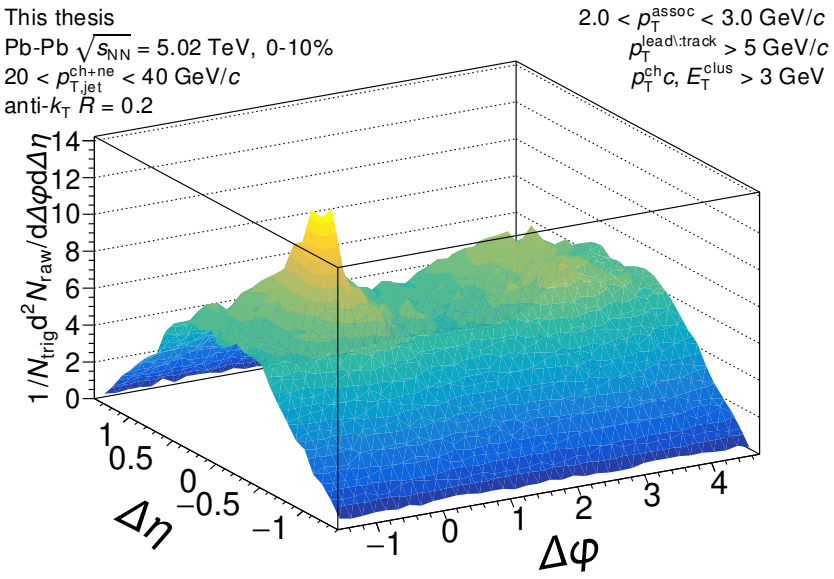

Figure D.189: The measured correlation function with the the efficiency correction $\epsilon(p_{\mathrm{T}}, \eta)$ applied, but before acceptance correction via the mixed events. The correlation is measured for in-plane orientation for $20 < p_{\mathrm{T,jet}}^{\mathrm{ch+ne}} < 40\,\mathrm{GeV}/c$ jets with $2.0 < p_{\mathrm{T}}^{\mathrm{assoc}} < 3.0\,\mathrm{GeV}/c$ in 0–10% Pb–Pb collisions at $\sqrt{s_{\mathrm{NN}}} = 5.02$ TeV.

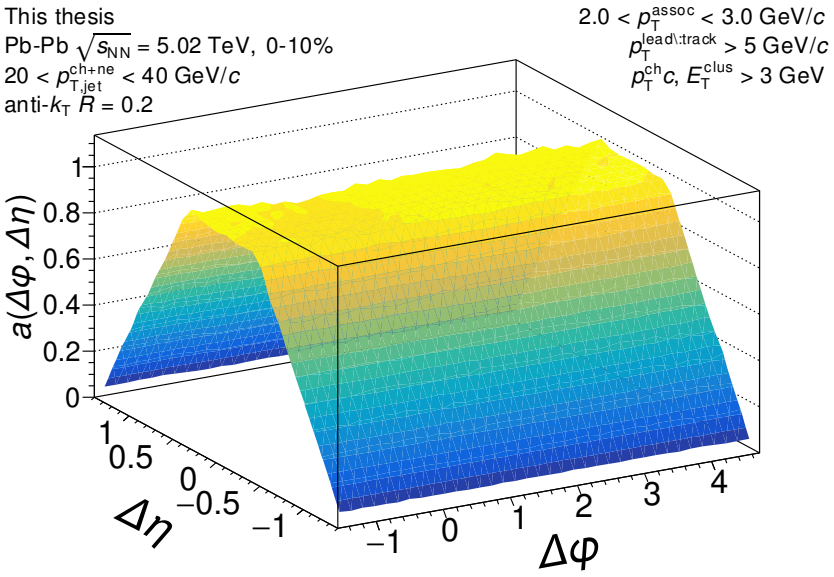

Figure D.190: The mixed event pair acceptance correction with the efficiency correction $\epsilon(p_{\mathrm{T}}, \eta)$ applied. The correlations are measured for in-plane orientation for $20 < p_{\mathrm{T,jet}}^{\mathrm{ch+ne}} < 40\,\mathrm{GeV}/c$ jets with $2.0 < p_{\mathrm{T}}^{\mathrm{assoc}} < 3.0\,\mathrm{GeV}/c$ in 0–10% Pb–Pb collisions at $\sqrt{s_{\mathrm{NN}}} = 5.02\,\mathrm{TeV}$. They have already been normalized such that it they are unity at maximum efficiency. Above 2 GeV/c, the mixed events are merged together to increase statistics, so it is the same for all for correlations within $2.0 \leq p_{\mathrm{T}}^{\mathrm{assoc}} < 10\,\mathrm{GeV}/c$.

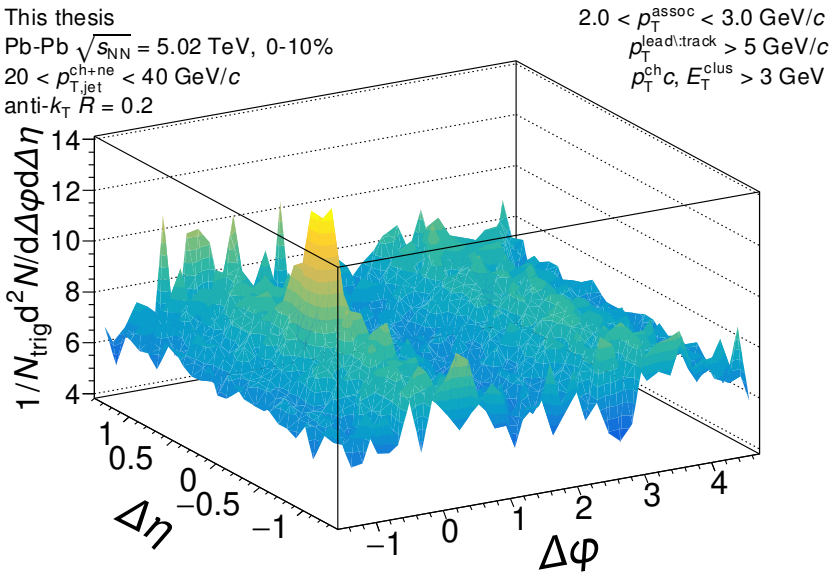

Figure D.191: The signal correlation corrected by pair acceptance. The correlations are measured for in-plane orientation for $20 < p_{\mathrm{T,jet}}^{\mathrm{ch+ne}} < 40\,\mathrm{GeV}/c$ jets with $2.0 < p_{\mathrm{T}}^{\mathrm{assoc}} < 3.0\,\mathrm{GeV}/c$ in 0–10% Pb–Pb collisions at $\sqrt{s_{\mathrm{NN}}} = 5.02\,\mathrm{TeV}$.

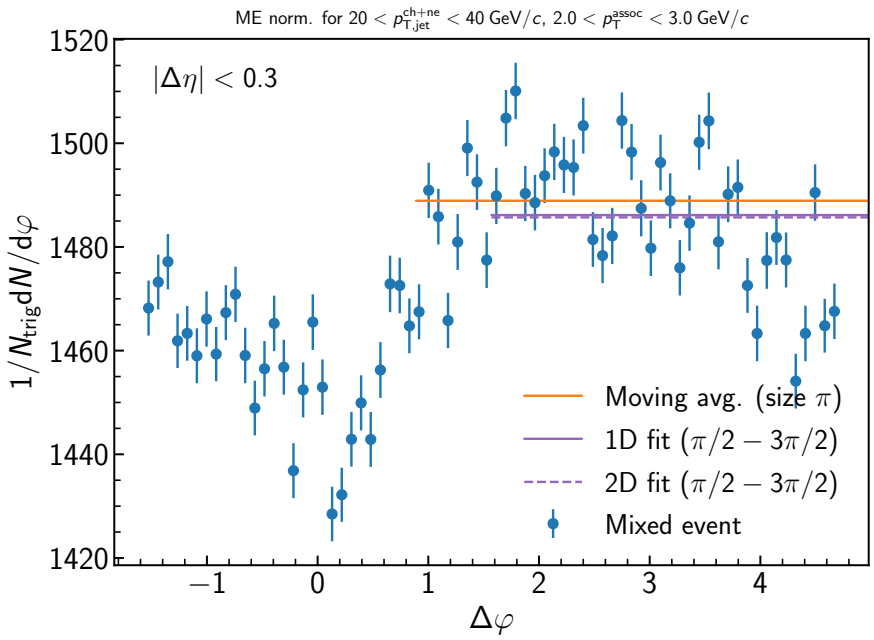

Figure D.192: Determination of the normalization of the mixed event for the inclusive event plane orientation in 0–10% Pb–Pb collisions at $\sqrt{s_{\mathrm{NN}}} = 5.02$ TeV. Here the mixed event is projected over the plateau range in $\Delta\eta$ onto to the $\Delta\varphi$ axis. The moving average is evaluated over the entire $\Delta\varphi$ range using a window of π, while the fit range is fixed from $\pi/2 < \Delta\varphi < 3\pi/2$. Since the mixed events are merged above 2 GeV/c, the normalization factor is also the same for all correlations within $2.0 < p_{\mathrm{T}}^{\mathrm{assoc}} < 3.0$ GeV/c. A variety of normalization methods were evaluated, with further details described in the text.

D.2.11 $20 < p_{\mathrm{T,jet}}^{\mathrm{ch+ne}} < 40\,\mathrm{GeV}/c$, $3.0 < p_{\mathrm{T}}^{\mathrm{assoc}} < 4.0\,\mathrm{GeV}/c$, In-plane orientation

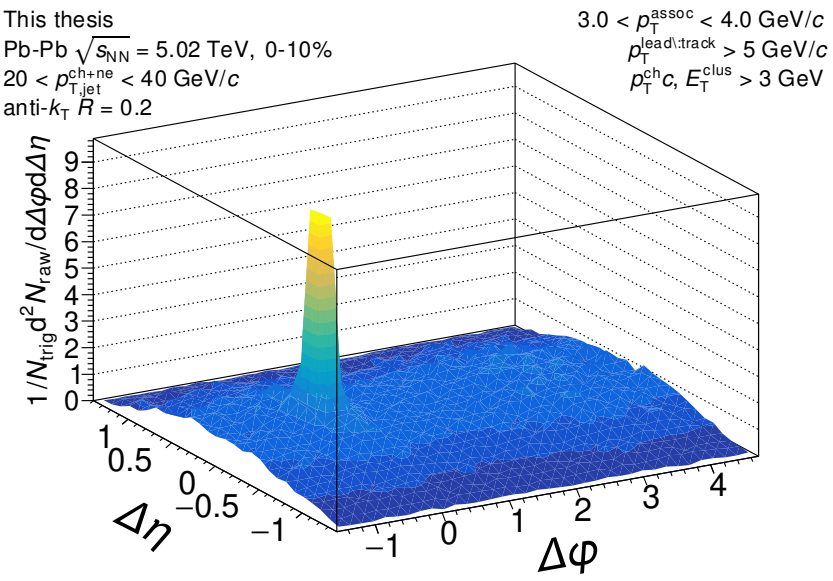

Figure D.193: The measured correlation function with the the efficiency correction $\epsilon(p_{\mathrm{T}}, \eta)$ applied, but before acceptance correction via the mixed events. The correlation is measured for in-plane orientation for $20 < p_{\mathrm{T,jet}}^{\mathrm{ch+ne}} < 40\,\mathrm{GeV}/c$ jets with $3.0 < p_{\mathrm{T}}^{\mathrm{assoc}} < 4.0\,\mathrm{GeV}/c$ in 0–10% Pb–Pb collisions at $\sqrt{s_{\mathrm{NN}}} = 5.02$ TeV.

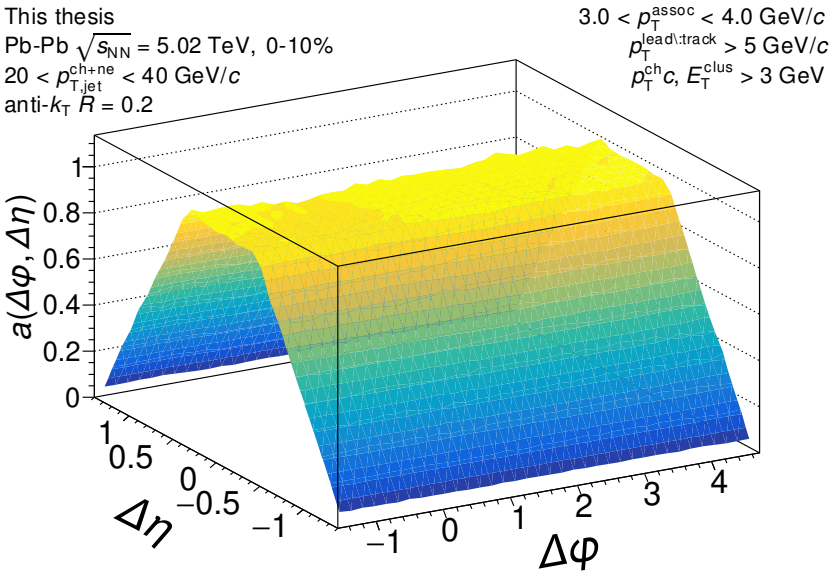

Figure D.194: The mixed event pair acceptance correction with the efficiency correction $\epsilon(p_T, \eta)$ applied. The correlations are measured for in-plane orientation for $20 < p_{T,jet}^{ch+ne} < 40$ GeV/c jets with $3.0 < p_T^{assoc} < 4.0$ GeV/c in 0–10% Pb–Pb collisions at $\sqrt{s_{NN}} = 5.02$ TeV. They have already been normalized such that it they are unity at maximum efficiency. Above 2 GeV/c, the mixed events are merged together to increase statistics, so it is the same for all for correlations within $2.0 \leq p_T^{assoc} < 10$ GeV/c.

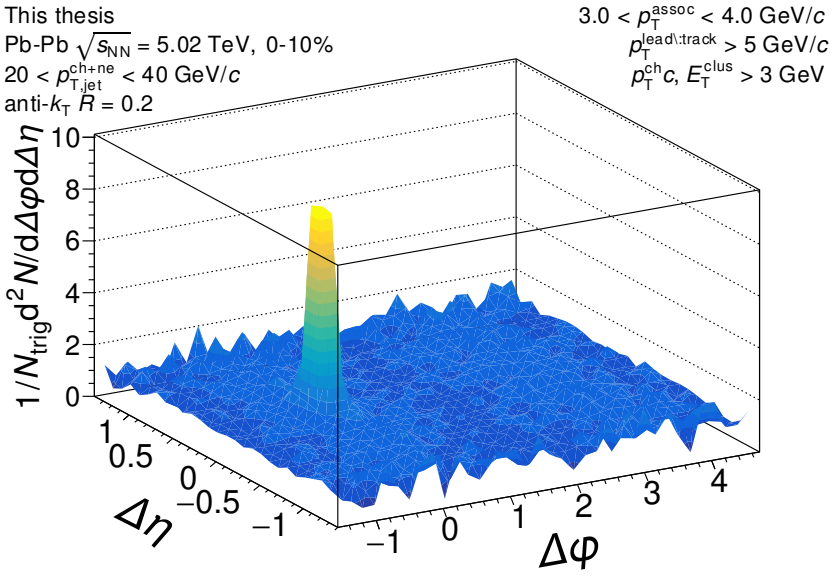

Figure D.195: The signal correlation corrected by pair acceptance. The correlations are measured for in-plane orientation for $20 < p_{T,jet}^{ch+ne} < 40$ GeV/c jets with $3.0 < p_T^{assoc} < 4.0$ GeV/c in 0–10% Pb–Pb collisions at $\sqrt{s_{NN}} = 5.02$ TeV.

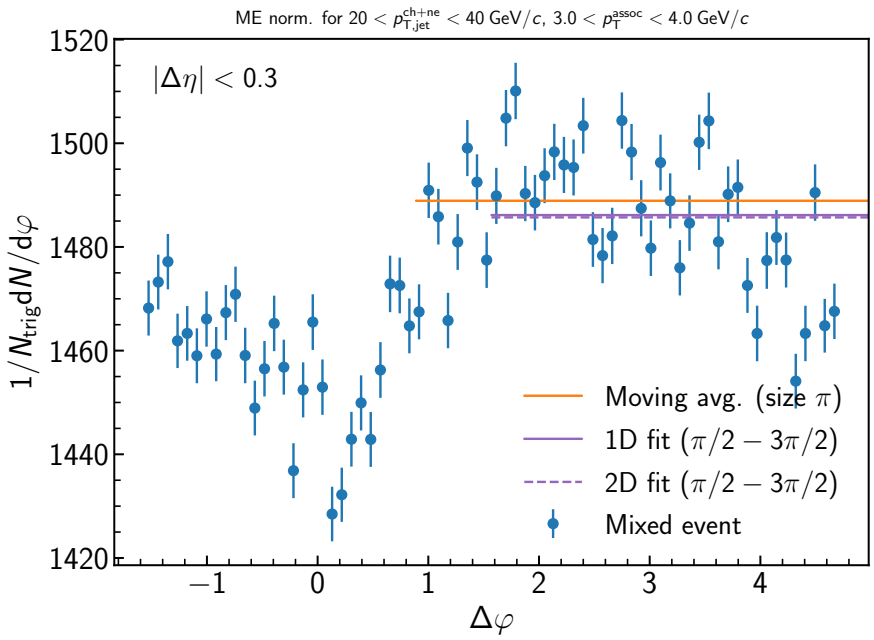

Figure D.196: Determination of the normalization of the mixed event for the inclusive event plane orientation in 0–10% Pb–Pb collisions at $\sqrt{s_{\mathrm{NN}}} = 5.02$ TeV. Here the mixed event is projected over the plateau range in $\Delta\eta$ onto to the $\Delta\varphi$ axis. The moving average is evaluated over the entire $\Delta\varphi$ range using a window of π, while the fit range is fixed from $\pi/2 < \Delta\varphi < 3\pi/2$. Since the mixed events are merged above 2 GeV/c, the normalization factor is also the same for all correlations within $3.0 < p_{\mathrm{T}}^{\mathrm{assoc}} < 4.0$ GeV/c. A variety of normalization methods were evaluated, with further details described in the text.

D.2.12 $20 < p_{\mathrm{T,jet}}^{\mathrm{ch+ne}} < 40\,\mathrm{GeV}/c$, $4.0 < p_{\mathrm{T}}^{\mathrm{assoc}} < 5.0\,\mathrm{GeV}/c$, In-plane orientation

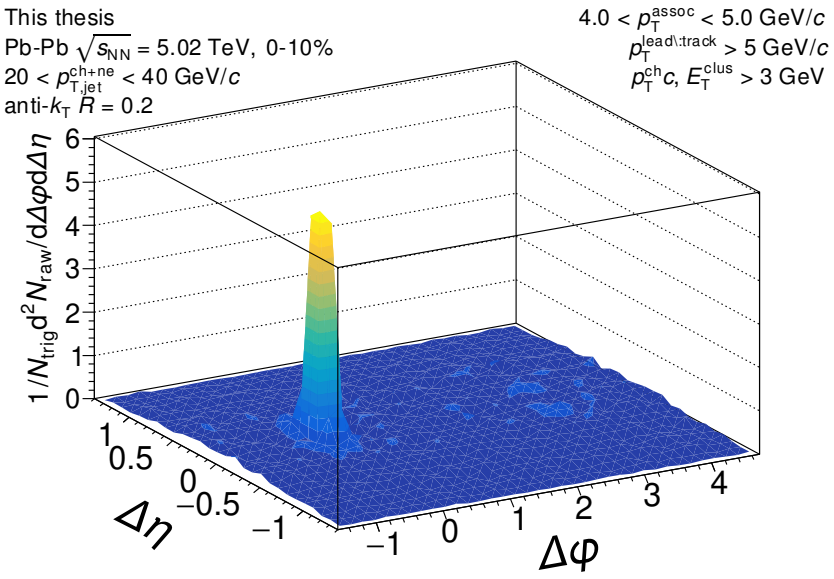

Figure D.197: The measured correlation function with the the efficiency correction $\epsilon(p_{\mathrm{T}}, \eta)$ applied, but before acceptance correction via the mixed events. The correlation is measured for in-plane orientation for $20 < p_{\mathrm{T,jet}}^{\mathrm{ch+ne}} < 40\,\mathrm{GeV}/c$ jets with $4.0 < p_{\mathrm{T}}^{\mathrm{assoc}} < 5.0\,\mathrm{GeV}/c$ in 0–10% Pb–Pb collisions at $\sqrt{s_{\mathrm{NN}}} = 5.02$ TeV.

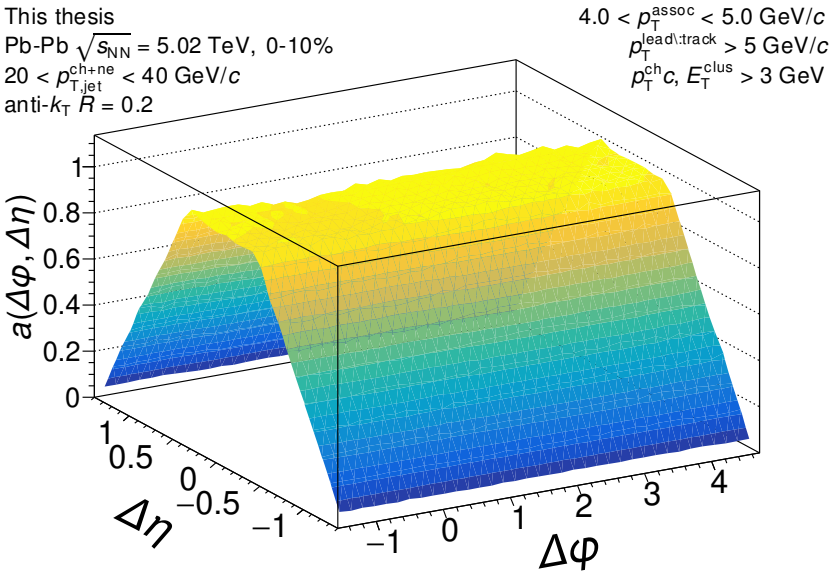

Figure D.198: The mixed event pair acceptance correction with the efficiency correction $\epsilon(p_T, \eta)$ applied. The correlations are measured for in-plane orientation for $20 < p_{T,jet}^{ch+ne} < 40$ GeV/c jets with $4.0 < p_T^{assoc} < 5.0$ GeV/c in 0–10% Pb–Pb collisions at $\sqrt{s_{NN}} = 5.02$ TeV. They have already been normalized such that it they are unity at maximum efficiency. Above 2 GeV/c, the mixed events are merged together to increase statistics, so it is the same for all for correlations within $2.0 \leq p_T^{assoc} < 10$ GeV/c.

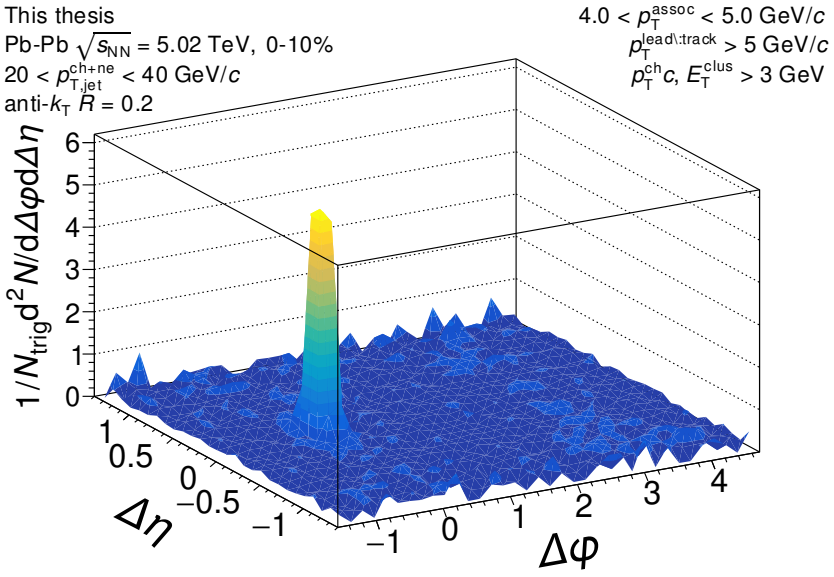

Figure D.199: The signal correlation corrected by pair acceptance. The correlations are measured for in-plane orientation for $20 < p_{T,jet}^{ch+ne} < 40$ GeV/c jets with $4.0 < p_T^{assoc} < 5.0$ GeV/c in 0–10% Pb–Pb collisions at $\sqrt{s_{NN}} = 5.02$ TeV.

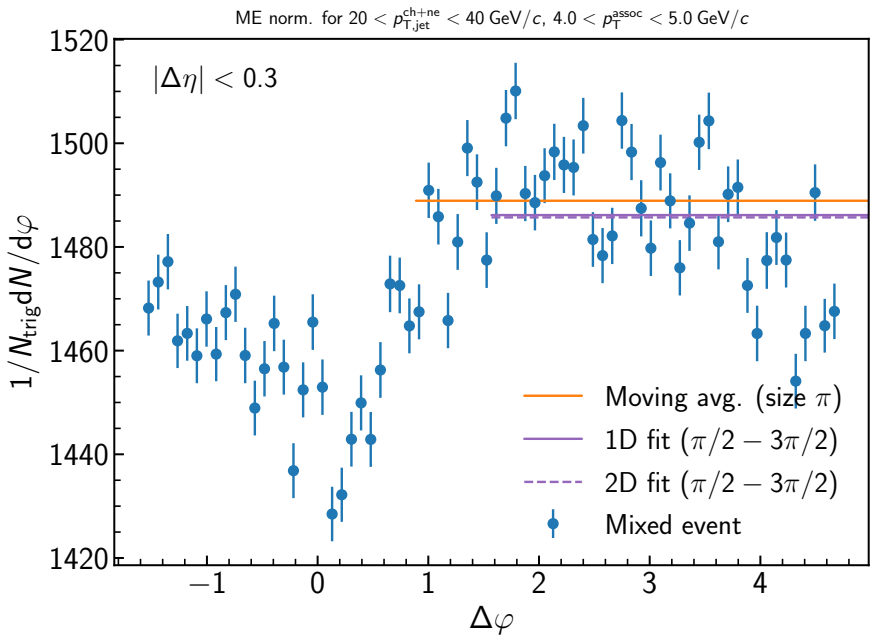

Figure D.200: Determination of the normalization of the mixed event for the inclusive event plane orientation in 0–10% Pb–Pb collisions at $\sqrt{s_{\mathrm{NN}}} = 5.02$ TeV. Here the mixed event is projected over the plateau range in $\Delta\eta$ onto to the $\Delta\varphi$ axis. The moving average is evaluated over the entire $\Delta\varphi$ range using a window of π, while the fit range is fixed from $\pi/2 < \Delta\varphi < 3\pi/2$. Since the mixed events are merged above 2 GeV/c, the normalization factor is also the same for all correlations within $4.0 < p_{\mathrm{T}}^{\mathrm{assoc}} < 5.0$ GeV/c. A variety of normalization methods were evaluated, with further details described in the text.

D.2.13 $20 < p_{\mathrm{T,jet}}^{\mathrm{ch+ne}} < 40\,\mathrm{GeV}/c$, $5.0 < p_{\mathrm{T}}^{\mathrm{assoc}} < 6.0\,\mathrm{GeV}/c$, In-plane orientation

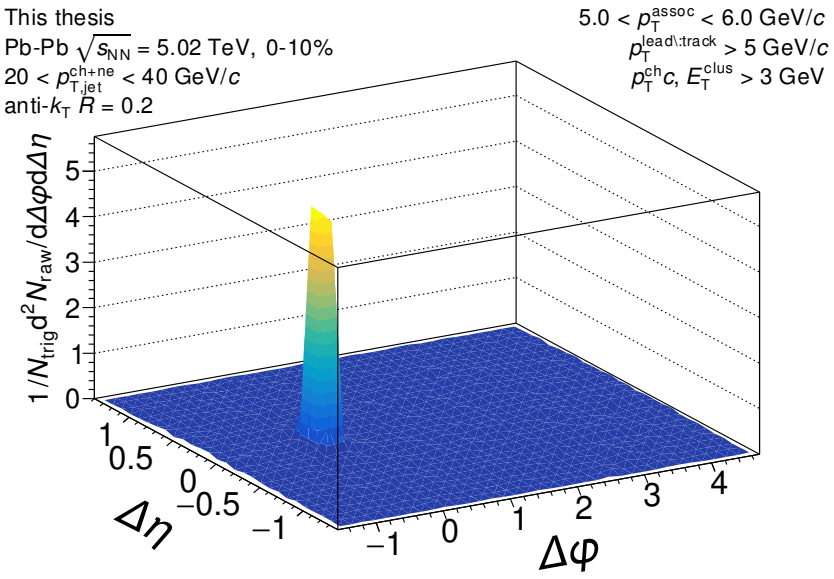

Figure D.201: The measured correlation function with the the efficiency correction $\epsilon(p_{\mathrm{T}}, \eta)$ applied, but before acceptance correction via the mixed events. The correlation is measured for in-plane orientation for $20 < p_{\mathrm{T,jet}}^{\mathrm{ch+ne}} < 40\,\mathrm{GeV}/c$ jets with $5.0 < p_{\mathrm{T}}^{\mathrm{assoc}} < 6.0\,\mathrm{GeV}/c$ in 0–10% Pb–Pb collisions at $\sqrt{s_{\mathrm{NN}}} = 5.02$ TeV.

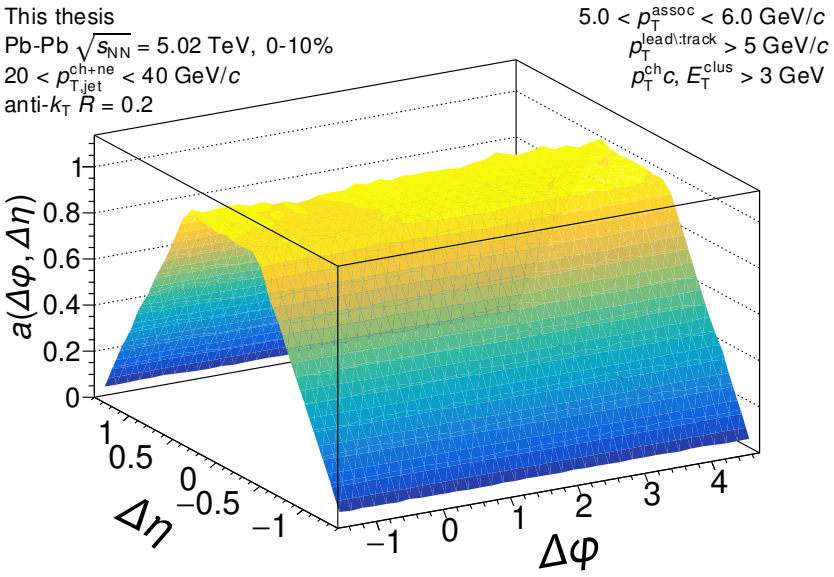

Figure D.202: The mixed event pair acceptance correction with the efficiency correction $\epsilon(p_{\mathrm{T}}, \eta)$ applied. The correlations are measured for in-plane orientation for $20 < p_{\mathrm{T,jet}}^{\mathrm{ch+ne}} < 40\,\mathrm{GeV}/c$ jets with $5.0 < p_{\mathrm{T}}^{\mathrm{assoc}} < 6.0\,\mathrm{GeV}/c$ in 0–10% Pb–Pb collisions at $\sqrt{s_{\mathrm{NN}}} = 5.02\,\mathrm{TeV}$. They have already been normalized such that it they are unity at maximum efficiency. Above 2 GeV/c, the mixed events are merged together to increase statistics, so it is the same for all for correlations within $2.0 \leq p_{\mathrm{T}}^{\mathrm{assoc}} < 10\,\mathrm{GeV}/c$.

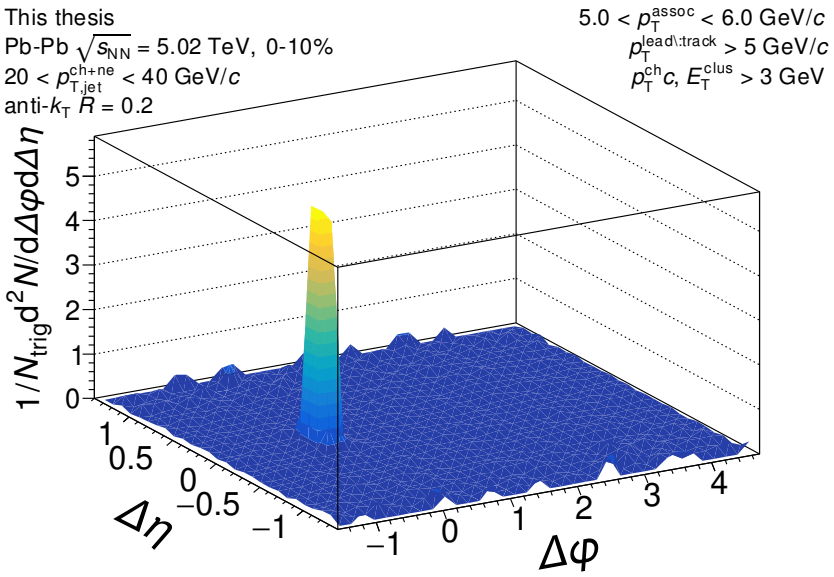

Figure D.203: The signal correlation corrected by pair acceptance. The correlations are measured for in-plane orientation for $20 < p_{\mathrm{T,jet}}^{\mathrm{ch+ne}} < 40\,\mathrm{GeV}/c$ jets with $5.0 < p_{\mathrm{T}}^{\mathrm{assoc}} < 6.0\,\mathrm{GeV}/c$ in 0–10% Pb–Pb collisions at $\sqrt{s_{\mathrm{NN}}} = 5.02\,\mathrm{TeV}$.

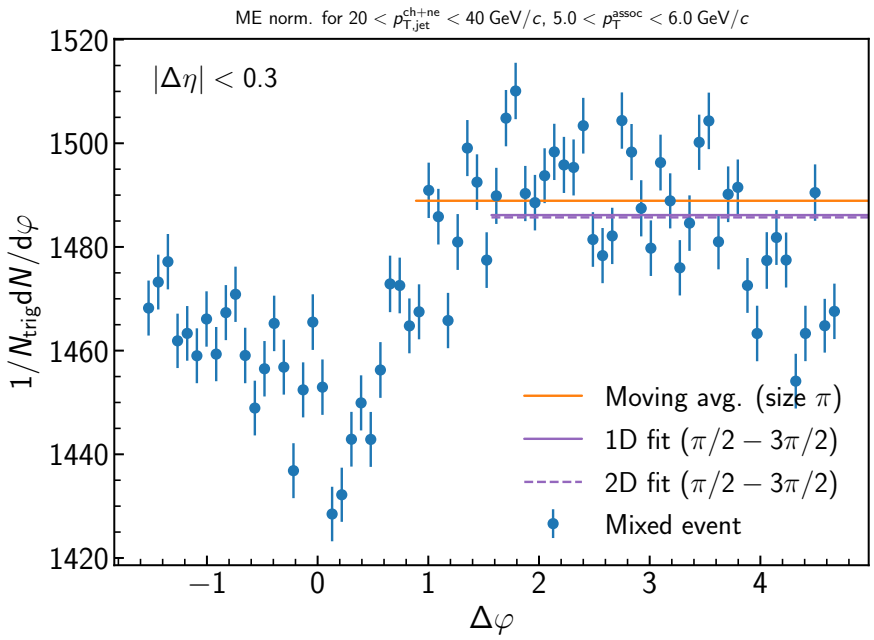

Figure D.204: Determination of the normalization of the mixed event for the inclusive event plane orientation in 0–10% Pb–Pb collisions at $\sqrt{s_{\mathrm{NN}}} = 5.02$ TeV. Here the mixed event is projected over the plateau range in $\Delta\eta$ onto to the $\Delta\varphi$ axis. The moving average is evaluated over the entire $\Delta\varphi$ range using a window of π, while the fit range is fixed from $\pi/2 < \Delta\varphi < 3\pi/2$. Since the mixed events are merged above 2 GeV/c, the normalization factor is also the same for all correlations within $5.0 < p_{\mathrm{T}}^{\mathrm{assoc}} < 6.0$ GeV/c. A variety of normalization methods were evaluated, with further details described in the text.

D.2.14 $20 < p_{\mathrm{T,jet}}^{\mathrm{ch+ne}} < 40$ GeV/c, $6.0 < p_{\mathrm{T}}^{\mathrm{assoc}} < 10.0$ GeV/c, In-plane orientation

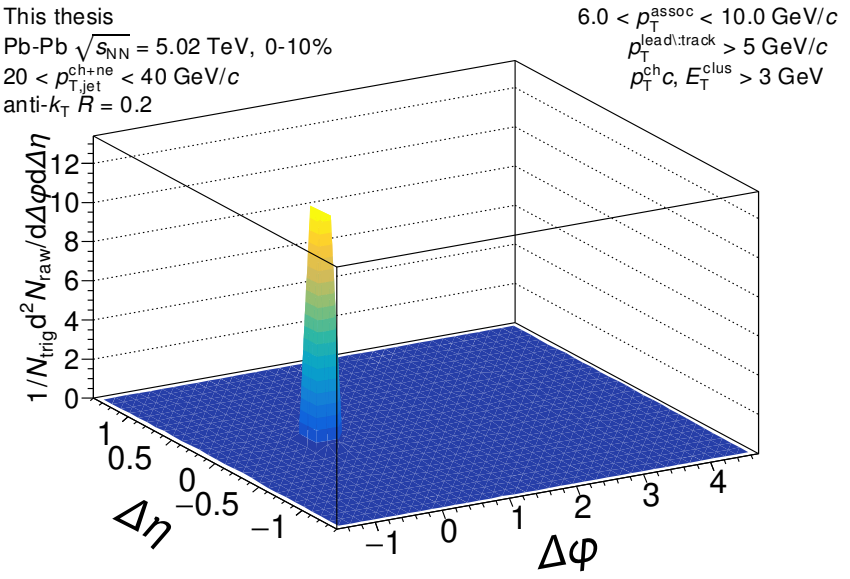

Figure D.205: The measured correlation function with the the efficiency correction $\epsilon(p_{\mathrm{T}}, \eta)$ applied, but before acceptance correction via the mixed events. The correlation is measured for in-plane orientation for $20 < p_{\mathrm{T,jet}}^{\mathrm{ch+ne}} < 40\,\mathrm{GeV}/c$ jets with $6.0 < p_{\mathrm{T}}^{\mathrm{assoc}} < 10.0\,\mathrm{GeV}/c$ in 0–10% Pb–Pb collisions at $\sqrt{s_{\mathrm{NN}}} = 5.02$ TeV.

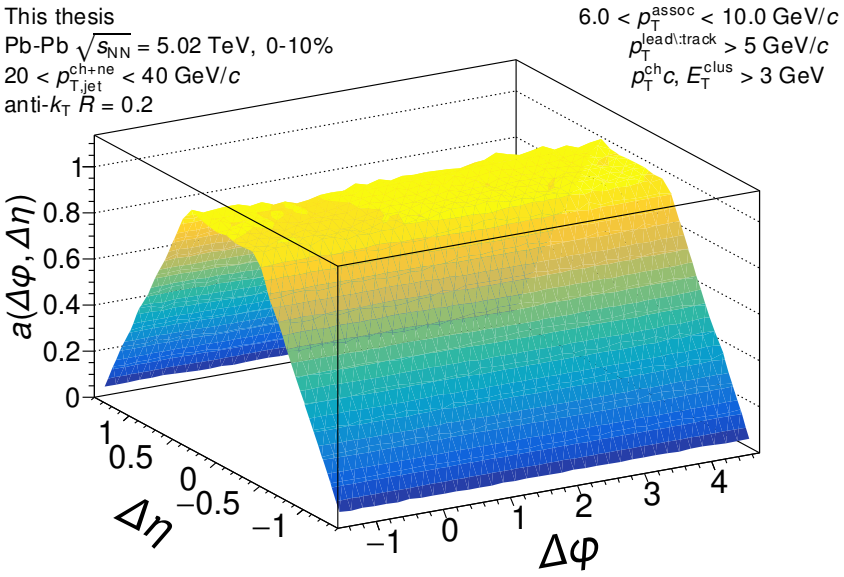

Figure D.206: The mixed event pair acceptance correction with the efficiency correction $\epsilon(p_{\mathrm{T}}, \eta)$ applied. The correlations are measured for in-plane orientation for $20 < p_{\mathrm{T,jet}}^{\mathrm{ch+ne}} < 40\,\mathrm{GeV}/c$ jets with $6.0 < p_{\mathrm{T}}^{\mathrm{assoc}} < 10.0\,\mathrm{GeV}/c$ in 0–10% Pb–Pb collisions at $\sqrt{s_{\mathrm{NN}}} = 5.02\,\mathrm{TeV}$. They have already been normalized such that it they are unity at maximum efficiency. Above 2 GeV/c, the mixed events are merged together to increase statistics, so it is the same for all for correlations within $2.0 \leq p_{\mathrm{T}}^{\mathrm{assoc}} < 10\,\mathrm{GeV}/c$.

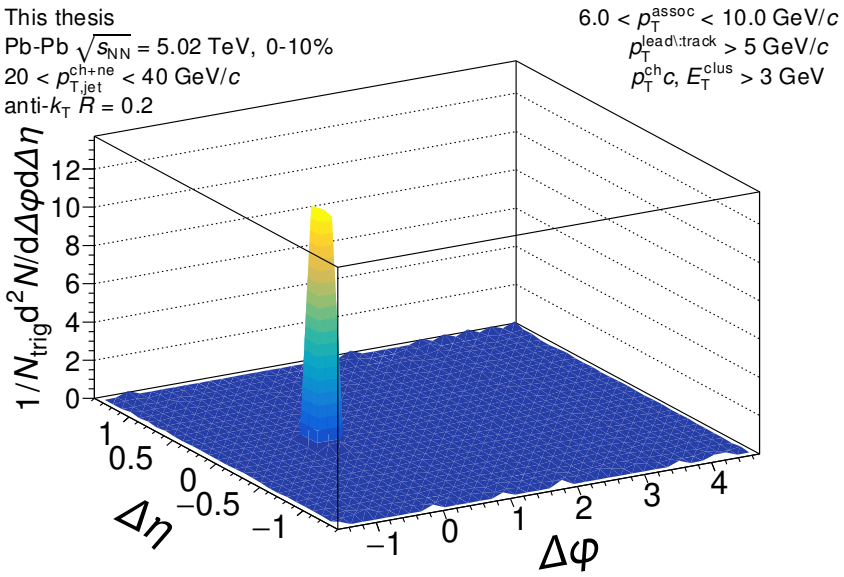

Figure D.207: The signal correlation corrected by pair acceptance. The correlations are measured for in-plane orientation for $20 < p_{\mathrm{T,jet}}^{\mathrm{ch+ne}} < 40\,\mathrm{GeV}/c$ jets with $6.0 < p_{\mathrm{T}}^{\mathrm{assoc}} < 10.0\,\mathrm{GeV}/c$ in 0–10% Pb–Pb collisions at $\sqrt{s_{\mathrm{NN}}} = 5.02\,\mathrm{TeV}$.

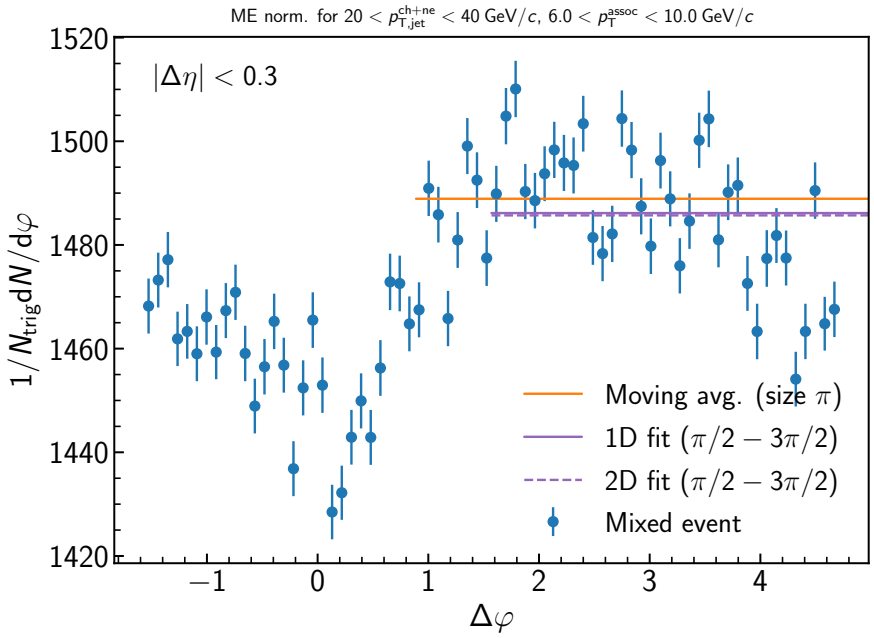

Figure D.208: Determination of the normalization of the mixed event for the inclusive event plane orientation in 0–10% Pb–Pb collisions at $\sqrt{s_{\mathrm{NN}}} = 5.02$ TeV. Here the mixed event is projected over the plateau range in $\Delta\eta$ onto to the $\Delta\varphi$ axis. The moving average is evaluated over the entire $\Delta\varphi$ range using a window of π, while the fit range is fixed from $\pi/2 < \Delta\varphi < 3\pi/2$. Since the mixed events are merged above 2 GeV/c, the normalization factor is also the same for all correlations within $6.0 < p_{\mathrm{T}}^{\mathrm{assoc}} < 10.0$ GeV/c. A variety of normalization methods were evaluated, with further details described in the text.

D.2.15 $20 < p_{\mathrm{T,jet}}^{\mathrm{ch+ne}} < 40\ \mathrm{GeV}/c$, $1.0 < p_{\mathrm{T}}^{\mathrm{assoc}} < 1.5\ \mathrm{GeV}/c$, Mid-plane orientation

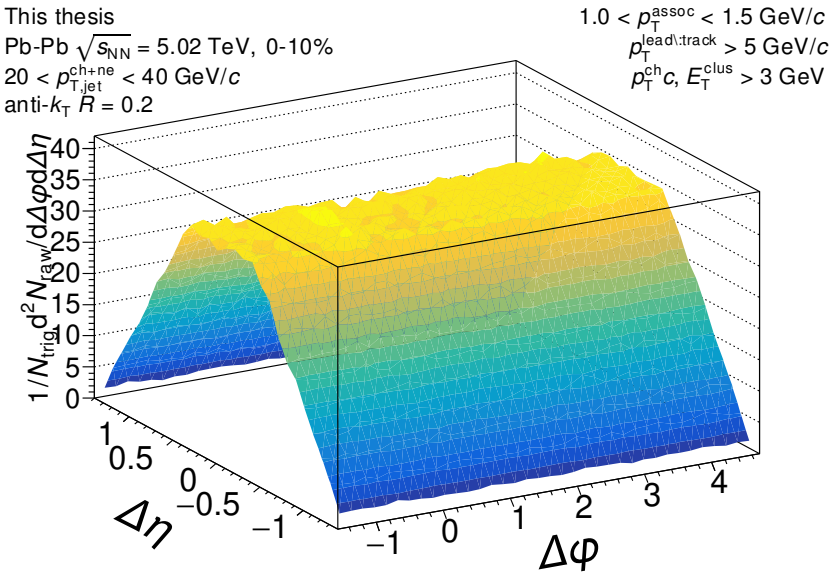

Figure D.209: The measured correlation function with the the efficiency correction $\epsilon(p_{\mathrm{T}}, \eta)$ applied, but before acceptance correction via the mixed events. The correlation is measured for mid-plane orientation for $20 < p_{\mathrm{T,jet}}^{\mathrm{ch+ne}} < 40\ \mathrm{GeV}/c$ jets with $1.0 < p_{\mathrm{T}}^{\mathrm{assoc}} < 1.5\ \mathrm{GeV}/c$ in 0–10% Pb–Pb collisions at $\sqrt{s_{\mathrm{NN}}} = 5.02$ TeV.

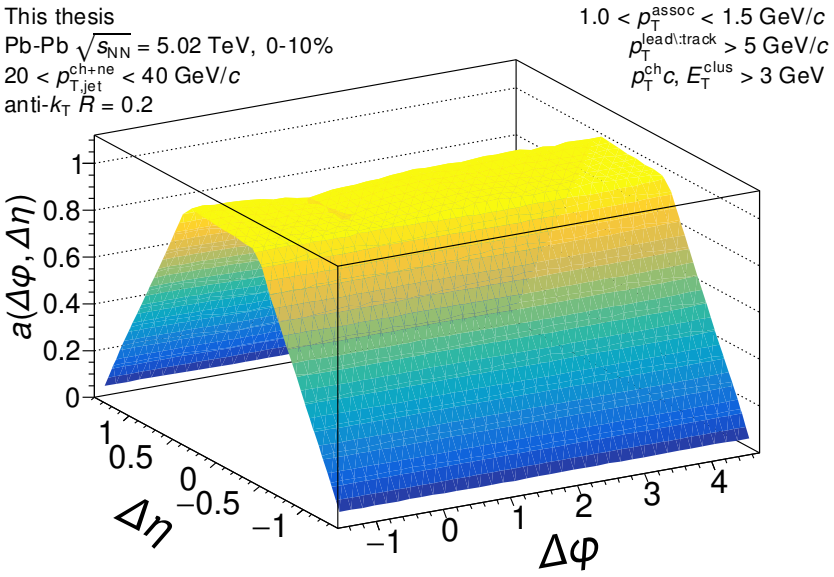

Figure D.210: The mixed event pair acceptance correction with the efficiency correction $\epsilon(p_T, \eta)$ applied. The correlations are measured for mid-plane orientation for $20 < p_{T,jet}^{ch+ne} < 40$ GeV/c jets with $1.0 < p_T^{assoc} < 1.5$ GeV/c in 0–10% Pb–Pb collisions at $\sqrt{s_{NN}} = 5.02$ TeV. They have already been normalized such that it they are unity at maximum efficiency. Above 2 GeV/c, the mixed events are merged together to increase statistics, so it is the same for all for correlations within $2.0 \leq p_T^{assoc} < 10$ GeV/c.

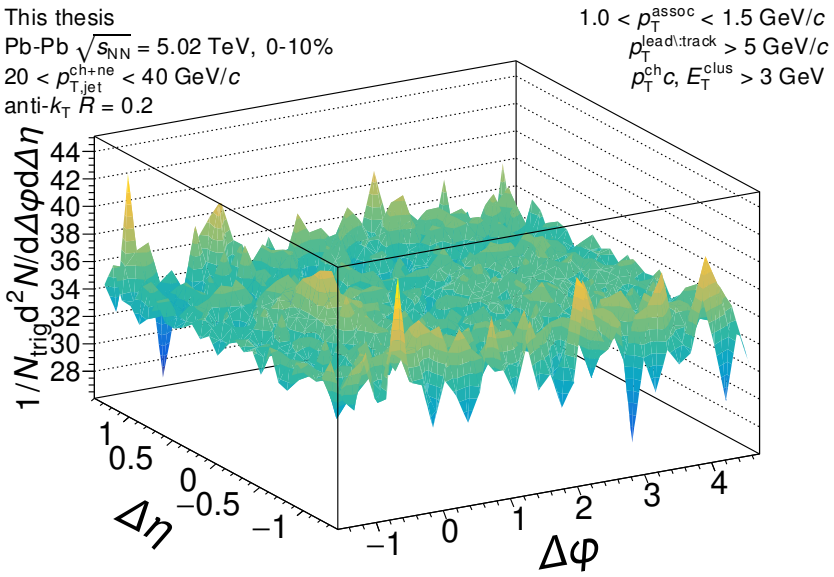

Figure D.211: The signal correlation corrected by pair acceptance. The correlations are measured for mid-plane orientation for $20 < p_{T,jet}^{ch+ne} < 40$ GeV/c jets with $1.0 < p_T^{assoc} < 1.5$ GeV/c in 0–10% Pb–Pb collisions at $\sqrt{s_{NN}} = 5.02$ TeV.

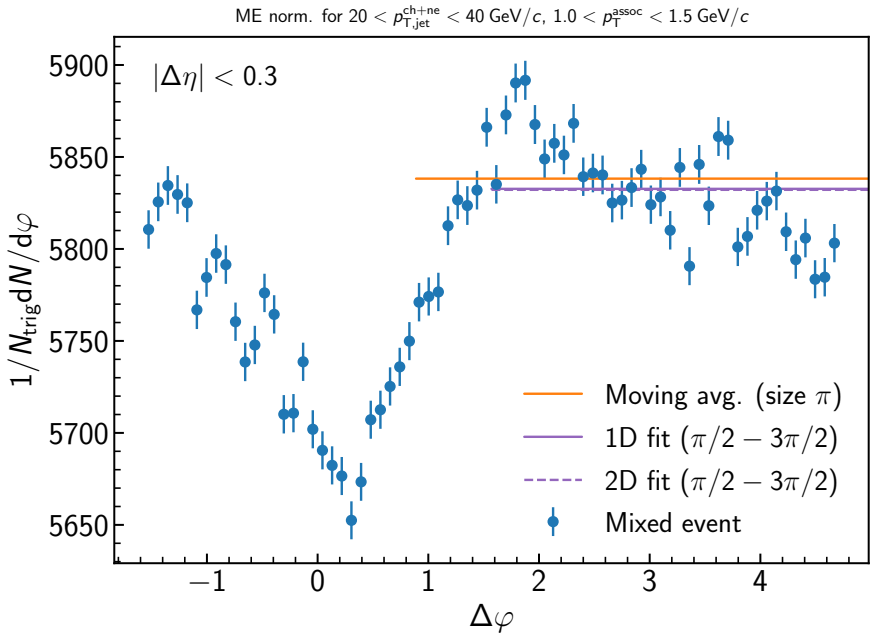

Figure D.212: Determination of the normalization of the mixed event for the inclusive event plane orientation in 0–10% Pb–Pb collisions at $\sqrt{s_{\mathrm{NN}}} = 5.02$ TeV. Here the mixed event is projected over the plateau range in $\Delta\eta$ onto to the $\Delta\varphi$ axis. The moving average is evaluated over the entire $\Delta\varphi$ range using a window of π, while the fit range is fixed from $\pi/2 < \Delta\varphi < 3\pi/2$. Since the mixed events are merged above 2 GeV/c, the normalization factor is also the same for all correlations within $1.0 < p_{\mathrm{T}}^{\mathrm{assoc}} < 1.5$ GeV/c. A variety of normalization methods were evaluated, with further details described in the text.

D.2.16 $20 < p_{\mathrm{T,jet}}^{\mathrm{ch+ne}} < 40$ GeV/c, $1.5 < p_{\mathrm{T}}^{\mathrm{assoc}} < 2.0$ GeV/c, Mid-plane orientation

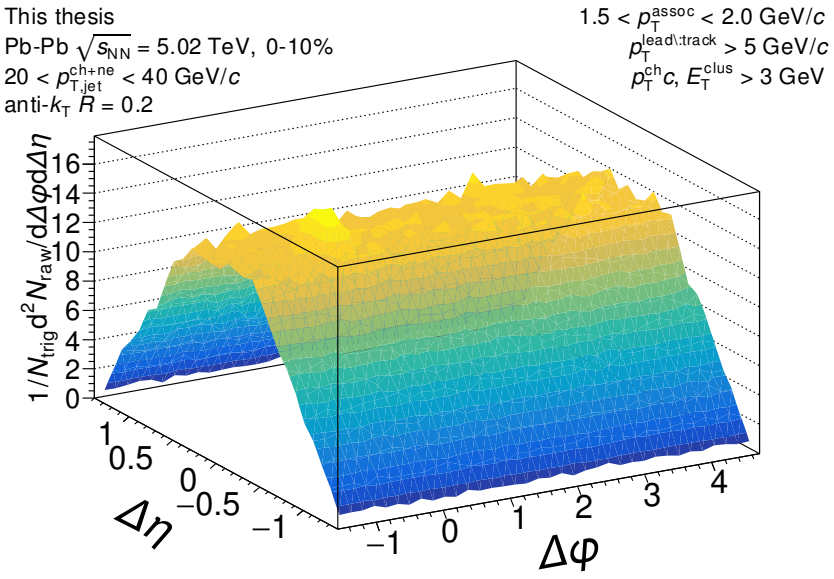

Figure D.213: The measured correlation function with the the efficiency correction $\epsilon(p_{\mathrm{T}}, \eta)$ applied, but before acceptance correction via the mixed events. The correlation is measured for mid-plane orientation for $20 < p_{\mathrm{T,jet}}^{\mathrm{ch+ne}} < 40$ GeV/c jets with $1.5 < p_{\mathrm{T}}^{\mathrm{assoc}} < 2.0$ GeV/c in 0–10% Pb–Pb collisions at $\sqrt{s_{\mathrm{NN}}} = 5.02$ TeV.

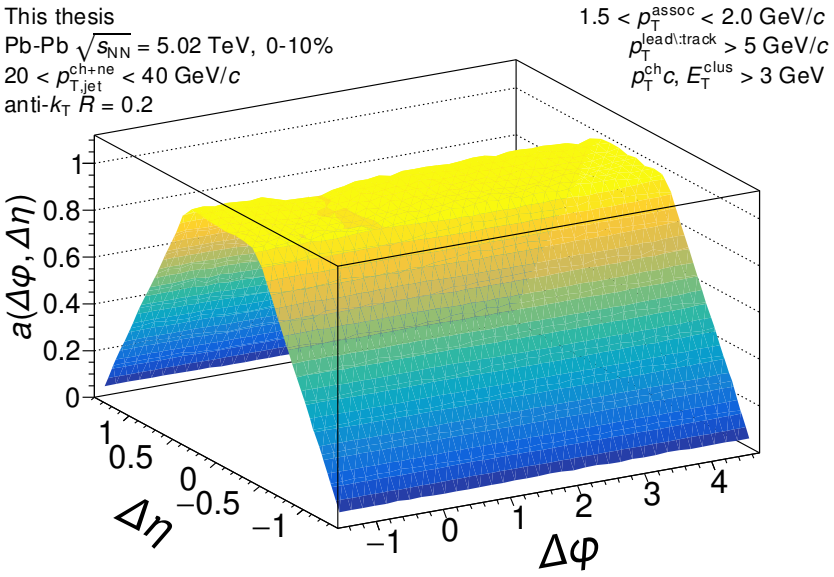

Figure D.214: The mixed event pair acceptance correction with the efficiency correction $\epsilon(p_{\mathrm{T}}, \eta)$ applied. The correlations are measured for mid-plane orientation for $20 < p_{\mathrm{T,jet}}^{\mathrm{ch+ne}} < 40\ \mathrm{GeV}/c$ jets with $1.5 < p_{\mathrm{T}}^{\mathrm{assoc}} < 2.0\ \mathrm{GeV}/c$ in 0–10% Pb–Pb collisions at $\sqrt{s_{\mathrm{NN}}} = 5.02\ \mathrm{TeV}$. They have already been normalized such that it they are unity at maximum efficiency. Above 2 GeV/c, the mixed events are merged together to increase statistics, so it is the same for all for correlations within $2.0 \leq p_{\mathrm{T}}^{\mathrm{assoc}} < 10\ \mathrm{GeV}/c$.

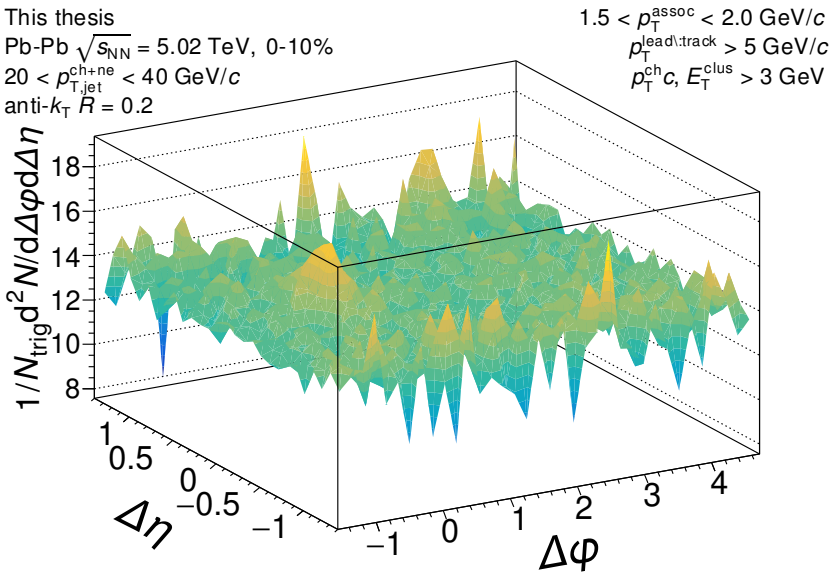

Figure D.215: The signal correlation corrected by pair acceptance. The correlations are measured for mid-plane orientation for $20 < p_{\mathrm{T,jet}}^{\mathrm{ch+ne}} < 40\ \mathrm{GeV}/c$ jets with $1.5 < p_{\mathrm{T}}^{\mathrm{assoc}} < 2.0\ \mathrm{GeV}/c$ in 0–10% Pb–Pb collisions at $\sqrt{s_{\mathrm{NN}}} = 5.02\ \mathrm{TeV}$.

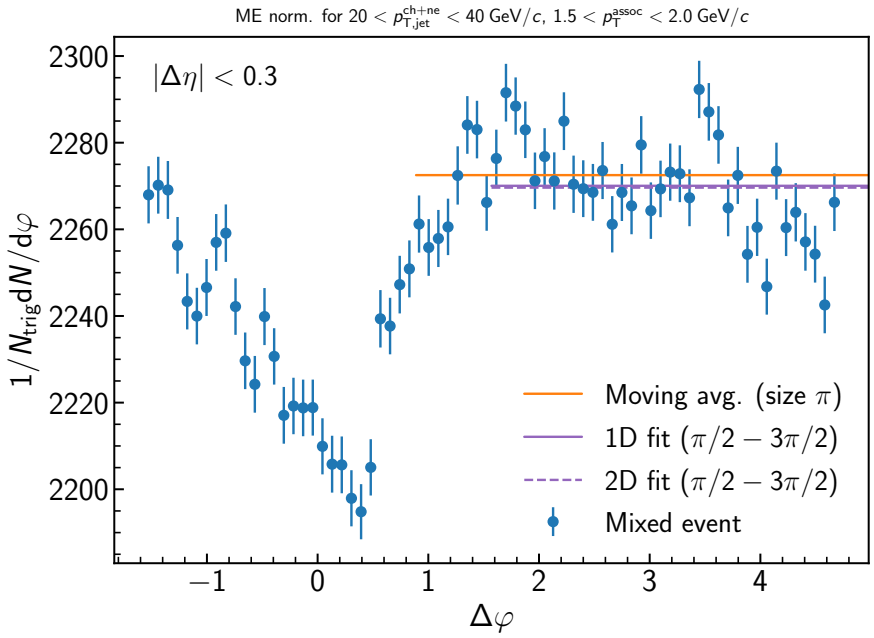

Figure D.216: Determination of the normalization of the mixed event for the inclusive event plane orientation in 0–10% Pb–Pb collisions at $\sqrt{s_{\mathrm{NN}}} = 5.02$ TeV. Here the mixed event is projected over the plateau range in $\Delta\eta$ onto to the $\Delta\varphi$ axis. The moving average is evaluated over the entire $\Delta\varphi$ range using a window of π, while the fit range is fixed from $\pi/2 < \Delta\varphi < 3\pi/2$. Since the mixed events are merged above 2 GeV/c, the normalization factor is also the same for all correlations within $1.5 < p_{\mathrm{T}}^{\mathrm{assoc}} < 2.0$ GeV/c. A variety of normalization methods were evaluated, with further details described in the text.

D.2.17 $20 < p_{\mathrm{T,jet}}^{\mathrm{ch+ne}} < 40$ GeV/c, $2.0 < p_{\mathrm{T}}^{\mathrm{assoc}} < 3.0$ GeV/c, Mid-plane orientation

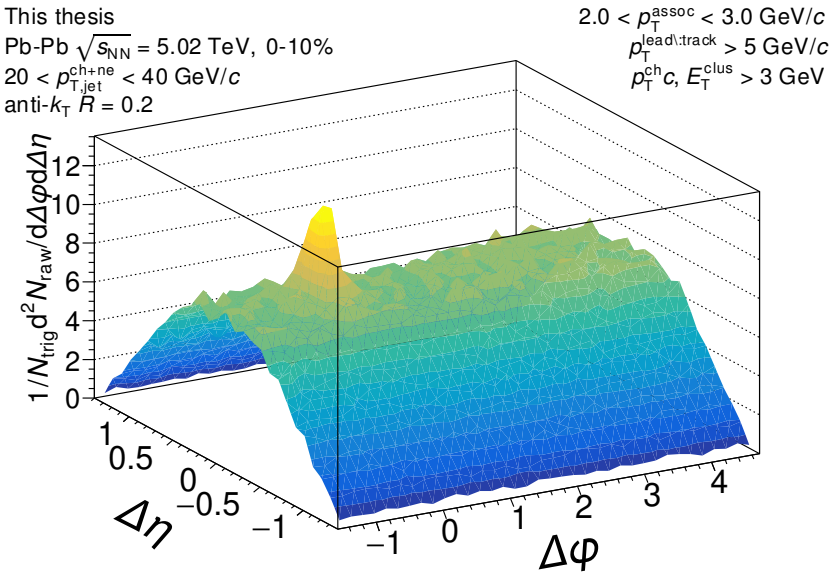

Figure D.217: The measured correlation function with the the efficiency correction $\epsilon(p_{\mathrm{T}}, \eta)$ applied, but before acceptance correction via the mixed events. The correlation is measured for mid-plane orientation for $20 < p_{\mathrm{T,jet}}^{\mathrm{ch+ne}} < 40$ GeV/c jets with $2.0 < p_{\mathrm{T}}^{\mathrm{assoc}} < 3.0$ GeV/c in 0–10% Pb–Pb collisions at $\sqrt{s_{\mathrm{NN}}} = 5.02$ TeV.

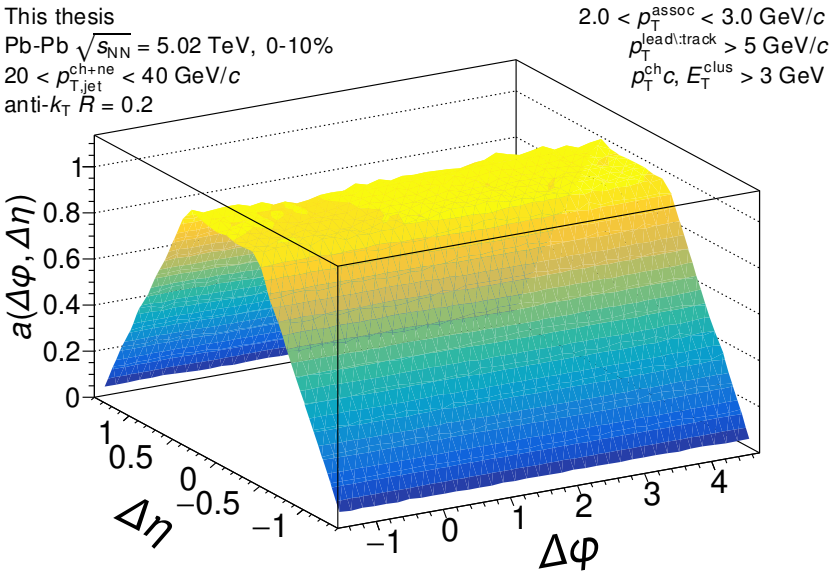

Figure D.218: The mixed event pair acceptance correction with the efficiency correction $\epsilon(p_{\mathrm{T}}, \eta)$ applied. The correlations are measured for mid-plane orientation for $20 < p_{\mathrm{T,jet}}^{\mathrm{ch+ne}} < 40\,\mathrm{GeV}/c$ jets with $2.0 < p_{\mathrm{T}}^{\mathrm{assoc}} < 3.0\,\mathrm{GeV}/c$ in 0–10% Pb–Pb collisions at $\sqrt{s_{\mathrm{NN}}} = 5.02\,\mathrm{TeV}$. They have already been normalized such that it they are unity at maximum efficiency. Above 2 GeV/c, the mixed events are merged together to increase statistics, so it is the same for all for correlations within $2.0 \leq p_{\mathrm{T}}^{\mathrm{assoc}} < 10\,\mathrm{GeV}/c$.

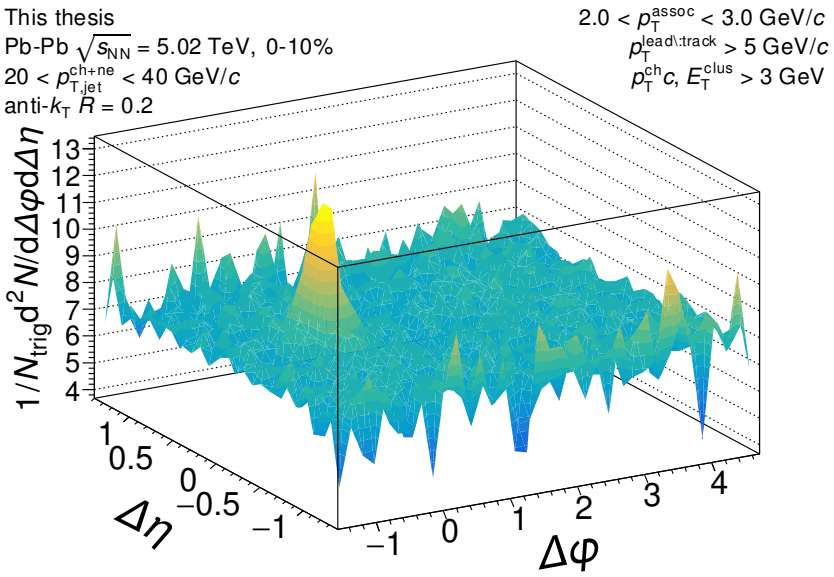

Figure D.219: The signal correlation corrected by pair acceptance. The correlations are measured for mid-plane orientation for $20 < p_{\mathrm{T,jet}}^{\mathrm{ch+ne}} < 40\,\mathrm{GeV}/c$ jets with $2.0 < p_{\mathrm{T}}^{\mathrm{assoc}} < 3.0\,\mathrm{GeV}/c$ in 0–10% Pb–Pb collisions at $\sqrt{s_{\mathrm{NN}}} = 5.02\,\mathrm{TeV}$.

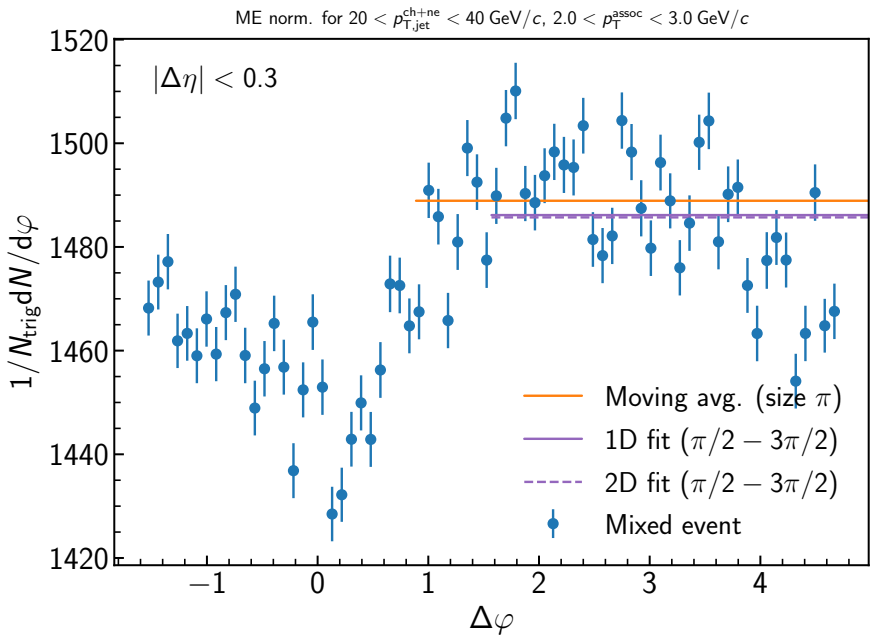

Figure D.220: Determination of the normalization of the mixed event for the inclusive event plane orientation in 0–10% Pb–Pb collisions at $\sqrt{s_{\mathrm{NN}}} = 5.02$ TeV. Here the mixed event is projected over the plateau range in $\Delta\eta$ onto to the $\Delta\varphi$ axis. The moving average is evaluated over the entire $\Delta\varphi$ range using a window of π, while the fit range is fixed from $\pi/2 < \Delta\varphi < 3\pi/2$. Since the mixed events are merged above 2 GeV/c, the normalization factor is also the same for all correlations within $2.0 < p_{\mathrm{T}}^{\mathrm{assoc}} < 3.0$ GeV/c. A variety of normalization methods were evaluated, with further details described in the text.

D.2.18 $20 < p_{\mathrm{T,jet}}^{\mathrm{ch+ne}} < 40$ GeV/c, $3.0 < p_{\mathrm{T}}^{\mathrm{assoc}} < 4.0$ GeV/c, Mid-plane orientation

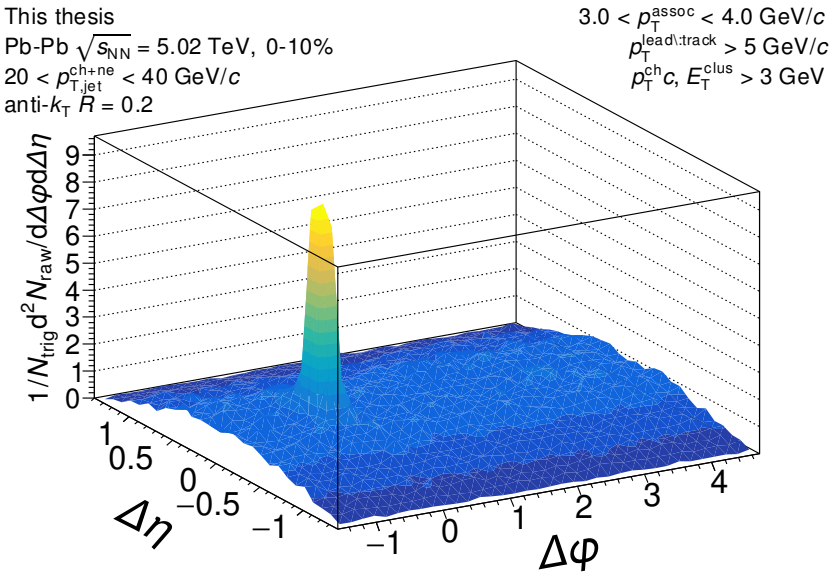

Figure D.221: The measured correlation function with the the efficiency correction $\epsilon(p_{\mathrm{T}}, \eta)$ applied, but before acceptance correction via the mixed events. The correlation is measured for mid-plane orientation for $20 < p_{\mathrm{T,jet}}^{\mathrm{ch+ne}} < 40$ GeV/c jets with $3.0 < p_{\mathrm{T}}^{\mathrm{assoc}} < 4.0$ GeV/c in 0–10% Pb–Pb collisions at $\sqrt{s_{\mathrm{NN}}} = 5.02$ TeV.

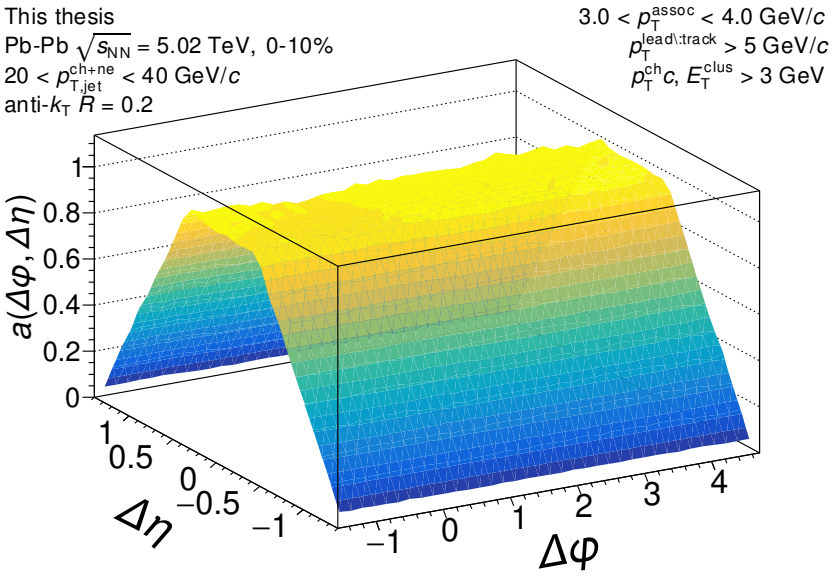

Figure D.222: The mixed event pair acceptance correction with the efficiency correction $\epsilon(p_T, \eta)$ applied. The correlations are measured for mid-plane orientation for $20 < p_{T,jet}^{ch+ne} < 40$ GeV/c jets with $3.0 < p_T^{assoc} < 4.0$ GeV/c in 0–10% Pb–Pb collisions at $\sqrt{s_{NN}} = 5.02$ TeV. They have already been normalized such that it they are unity at maximum efficiency. Above 2 GeV/c, the mixed events are merged together to increase statistics, so it is the same for all for correlations within $2.0 \leq p_T^{assoc} < 10$ GeV/c.

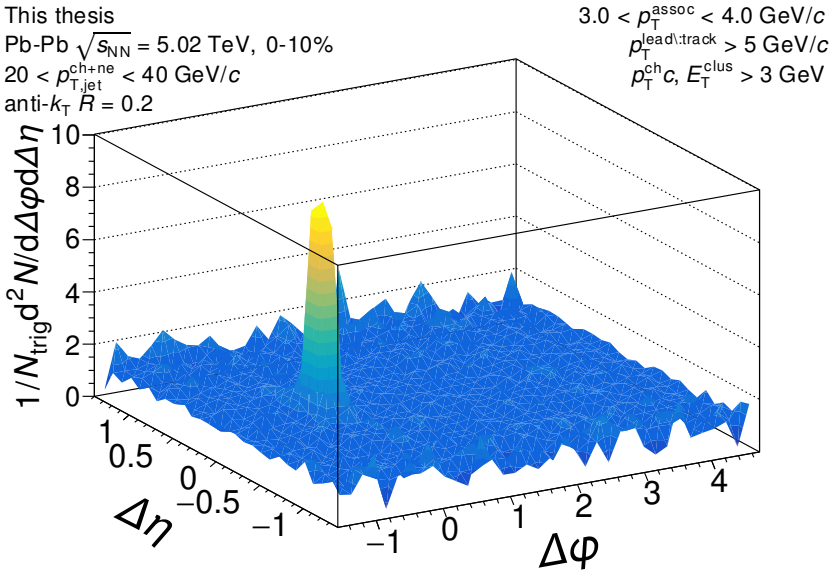

Figure D.223: The signal correlation corrected by pair acceptance. The correlations are measured for mid-plane orientation for $20 < p_{T,jet}^{ch+ne} < 40$ GeV/c jets with $3.0 < p_T^{assoc} < 4.0$ GeV/c in 0–10% Pb–Pb collisions at $\sqrt{s_{NN}} = 5.02$ TeV.

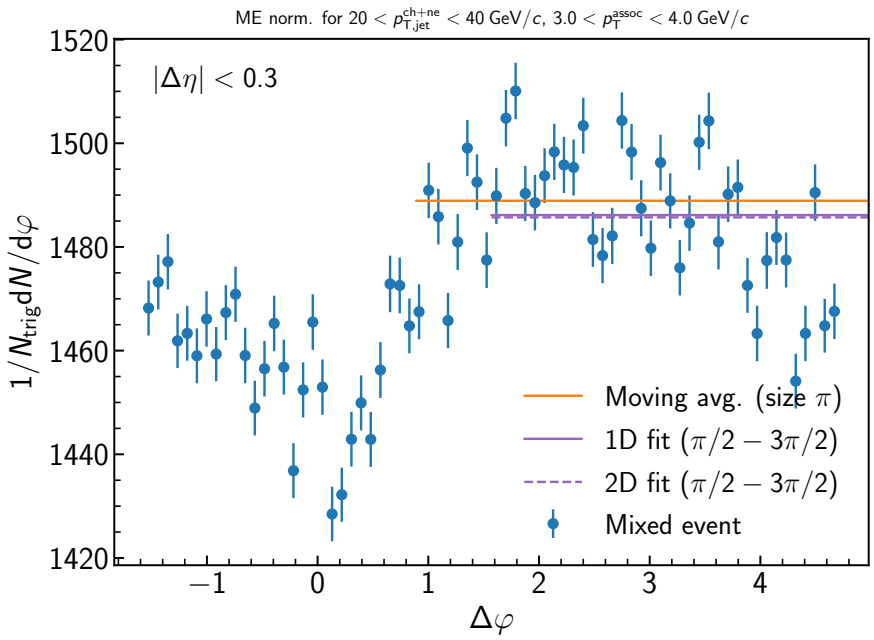

Figure D.224: Determination of the normalization of the mixed event for the inclusive event plane orientation in 0–10% Pb–Pb collisions at $\sqrt{s_{\mathrm{NN}}} = 5.02\,\mathrm{TeV}$. Here the mixed event is projected over the plateau range in $\Delta\eta$ onto to the $\Delta\varphi$ axis. The moving average is evaluated over the entire $\Delta\varphi$ range using a window of π, while the fit range is fixed from $\pi/2 < \Delta\varphi < 3\pi/2$. Since the mixed events are merged above 2 GeV/c, the normalization factor is also the same for all correlations within $3.0 < p_{\mathrm{T}}^{\mathrm{assoc}} < 4.0\,\mathrm{GeV}/c$. A variety of normalization methods were evaluated, with further details described in the text.

D.2.19 $20 < p_{\mathrm{T,jet}}^{\mathrm{ch+ne}} < 40\ \mathrm{GeV}/c$, $4.0 < p_{\mathrm{T}}^{\mathrm{assoc}} < 5.0\ \mathrm{GeV}/c$, Mid-plane orientation

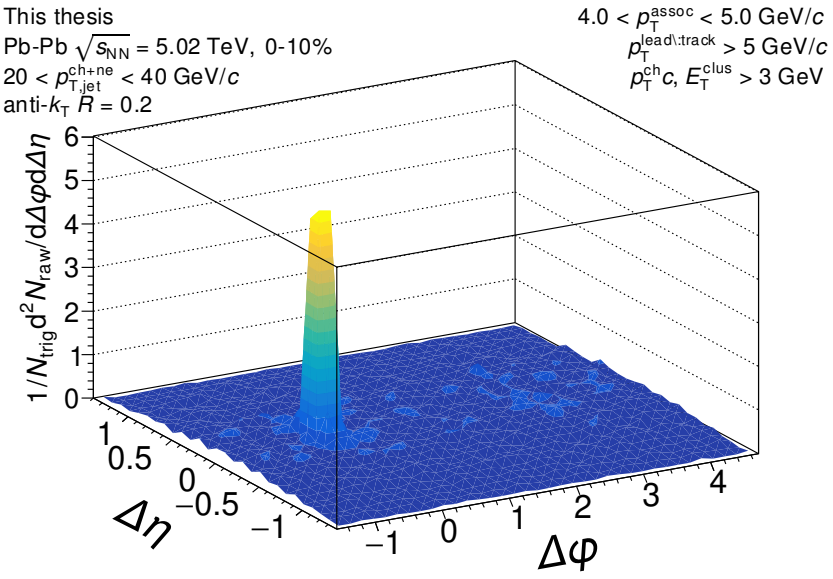

Figure D.225: The measured correlation function with the the efficiency correction $\epsilon(p_{\mathrm{T}}, \eta)$ applied, but before acceptance correction via the mixed events. The correlation is measured for mid-plane orientation for $20 < p_{\mathrm{T,jet}}^{\mathrm{ch+ne}} < 40\ \mathrm{GeV}/c$ jets with $4.0 < p_{\mathrm{T}}^{\mathrm{assoc}} < 5.0\ \mathrm{GeV}/c$ in 0–10% Pb–Pb collisions at $\sqrt{s_{\mathrm{NN}}} = 5.02$ TeV.

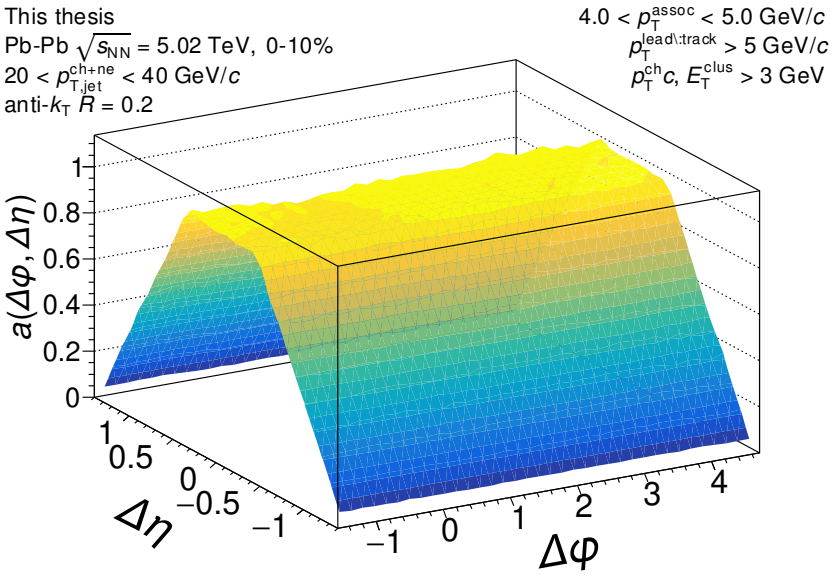

Figure D.226: The mixed event pair acceptance correction with the efficiency correction $\epsilon(p_T, \eta)$ applied. The correlations are measured for mid-plane orientation for $20 < p_{T,jet}^{ch+ne} < 40$ GeV/c jets with $4.0 < p_T^{assoc} < 5.0$ GeV/c in 0–10% Pb–Pb collisions at $\sqrt{s_{NN}} = 5.02$ TeV. They have already been normalized such that it they are unity at maximum efficiency. Above 2 GeV/c, the mixed events are merged together to increase statistics, so it is the same for all for correlations within $2.0 \leq p_T^{assoc} < 10$ GeV/c.

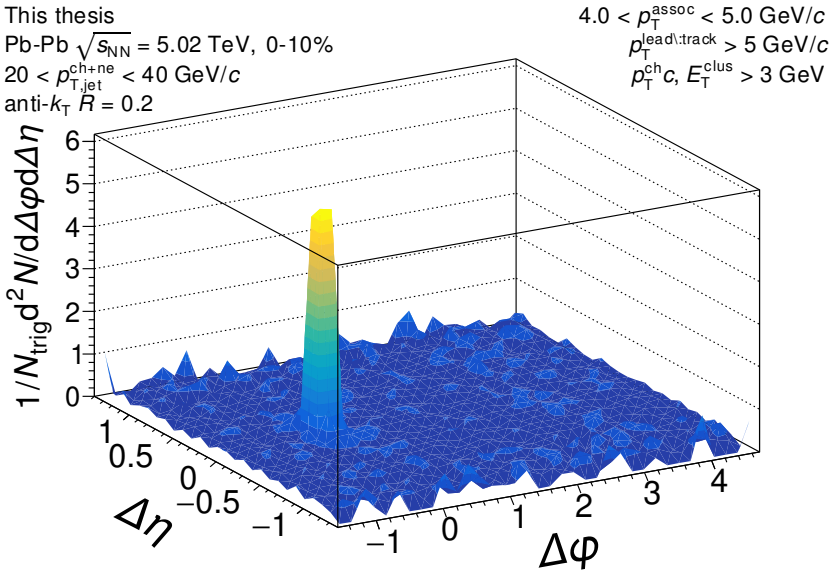

Figure D.227: The signal correlation corrected by pair acceptance. The correlations are measured for mid-plane orientation for $20 < p_{T,jet}^{ch+ne} < 40$ GeV/c jets with $4.0 < p_T^{assoc} < 5.0$ GeV/c in 0–10% Pb–Pb collisions at $\sqrt{s_{NN}} = 5.02$ TeV.

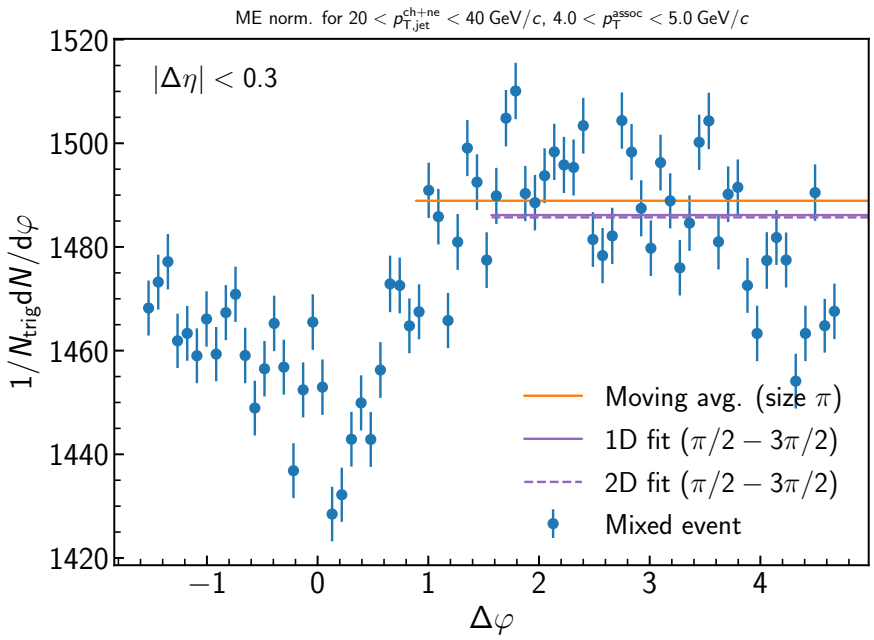

Figure D.228: Determination of the normalization of the mixed event for the inclusive event plane orientation in 0–10% Pb–Pb collisions at $\sqrt{s_{\mathrm{NN}}} = 5.02$ TeV. Here the mixed event is projected over the plateau range in $\Delta\eta$ onto to the $\Delta\varphi$ axis. The moving average is evaluated over the entire $\Delta\varphi$ range using a window of π, while the fit range is fixed from $\pi/2 < \Delta\varphi < 3\pi/2$. Since the mixed events are merged above 2 GeV/c, the normalization factor is also the same for all correlations within $4.0 < p_{\mathrm{T}}^{\mathrm{assoc}} < 5.0$ GeV/c. A variety of normalization methods were evaluated, with further details described in the text.

D.2.20 $20 < p_{\mathrm{T,jet}}^{\mathrm{ch+ne}} < 40$ GeV/c, $5.0 < p_{\mathrm{T}}^{\mathrm{assoc}} < 6.0$ GeV/c, Mid-plane orientation

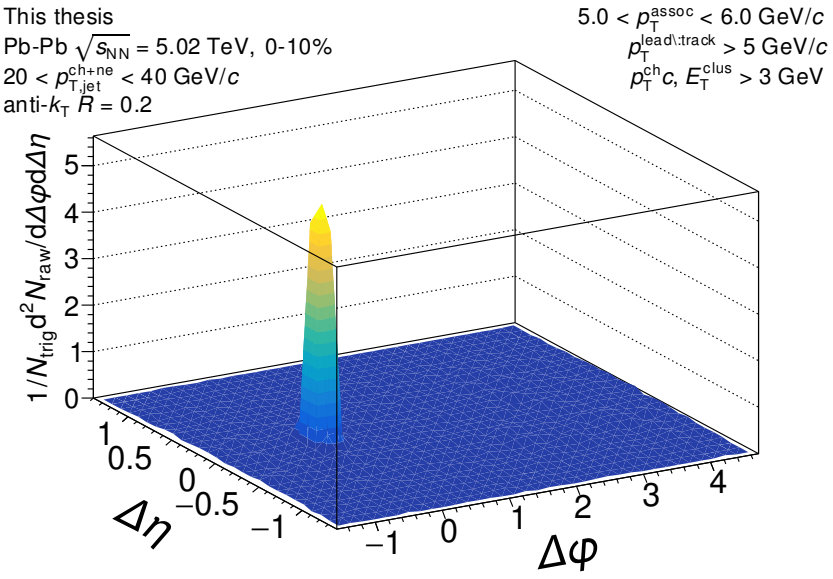

Figure D.229: The measured correlation function with the the efficiency correction $\epsilon(p_{\mathrm{T}}, \eta)$ applied, but before acceptance correction via the mixed events. The correlation is measured for mid-plane orientation for $20 < p_{\mathrm{T,jet}}^{\mathrm{ch+ne}} < 40$ GeV/c jets with $5.0 < p_{\mathrm{T}}^{\mathrm{assoc}} < 6.0$ GeV/c in 0–10% Pb–Pb collisions at $\sqrt{s_{\mathrm{NN}}} = 5.02$ TeV.

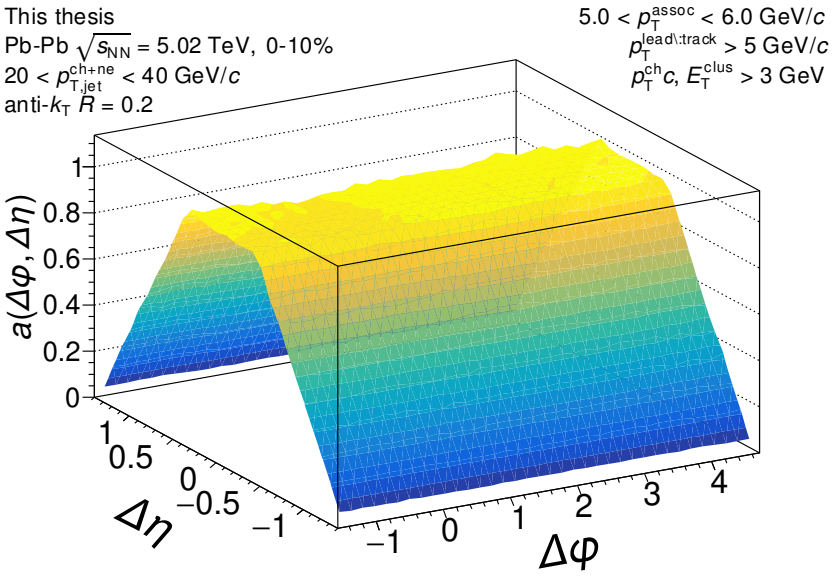

Figure D.230: The mixed event pair acceptance correction with the efficiency correction $\epsilon(p_T, \eta)$ applied. The correlations are measured for mid-plane orientation for $20 < p_{T,jet}^{ch+ne} < 40$ GeV/c jets with $5.0 < p_T^{assoc} < 6.0$ GeV/c in 0–10% Pb–Pb collisions at $\sqrt{s_{NN}} = 5.02$ TeV. They have already been normalized such that it they are unity at maximum efficiency. Above 2 GeV/c, the mixed events are merged together to increase statistics, so it is the same for all for correlations within $2.0 \leq p_T^{assoc} < 10$ GeV/c.

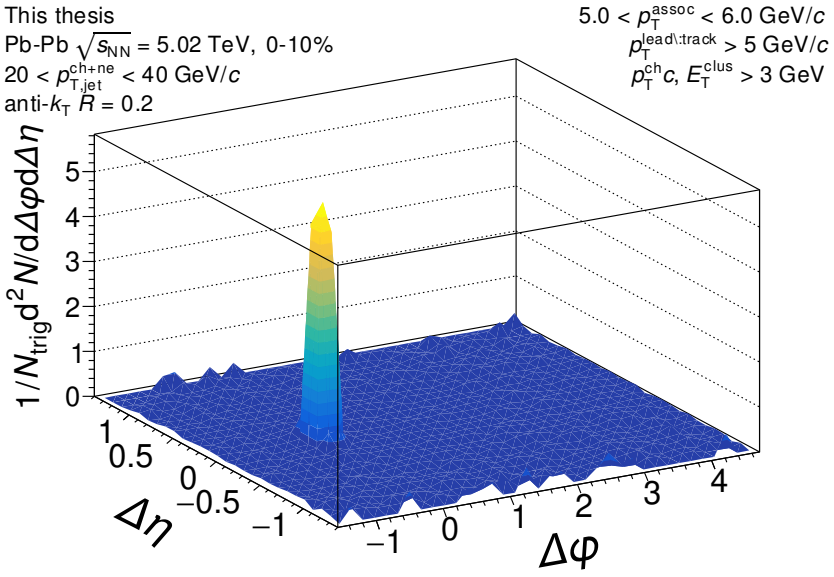

Figure D.231: The signal correlation corrected by pair acceptance. The correlations are measured for mid-plane orientation for $20 < p_{T,jet}^{ch+ne} < 40$ GeV/c jets with $5.0 < p_T^{assoc} < 6.0$ GeV/c in 0–10% Pb–Pb collisions at $\sqrt{s_{NN}} = 5.02$ TeV.

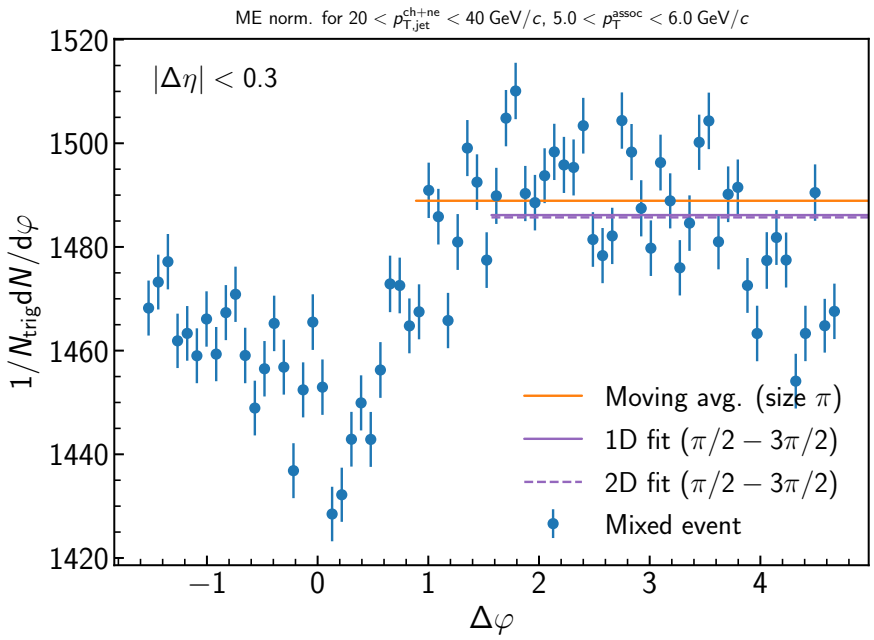

Figure D.232: Determination of the normalization of the mixed event for the inclusive event plane orientation in 0–10% Pb–Pb collisions at $\sqrt{s_{\mathrm{NN}}} = 5.02$ TeV. Here the mixed event is projected over the plateau range in $\Delta\eta$ onto to the $\Delta\varphi$ axis. The moving average is evaluated over the entire $\Delta\varphi$ range using a window of π, while the fit range is fixed from $\pi/2 < \Delta\varphi < 3\pi/2$. Since the mixed events are merged above 2 GeV/c, the normalization factor is also the same for all correlations within $5.0 < p_{\mathrm{T}}^{\mathrm{assoc}} < 6.0$ GeV/c. A variety of normalization methods were evaluated, with further details described in the text.

D.2.21 $20 < p_{\mathrm{T,jet}}^{\mathrm{ch+ne}} < 40\ \mathrm{GeV}/c$, $6.0 < p_{\mathrm{T}}^{\mathrm{assoc}} < 10.0\ \mathrm{GeV}/c$, Mid-plane orientation

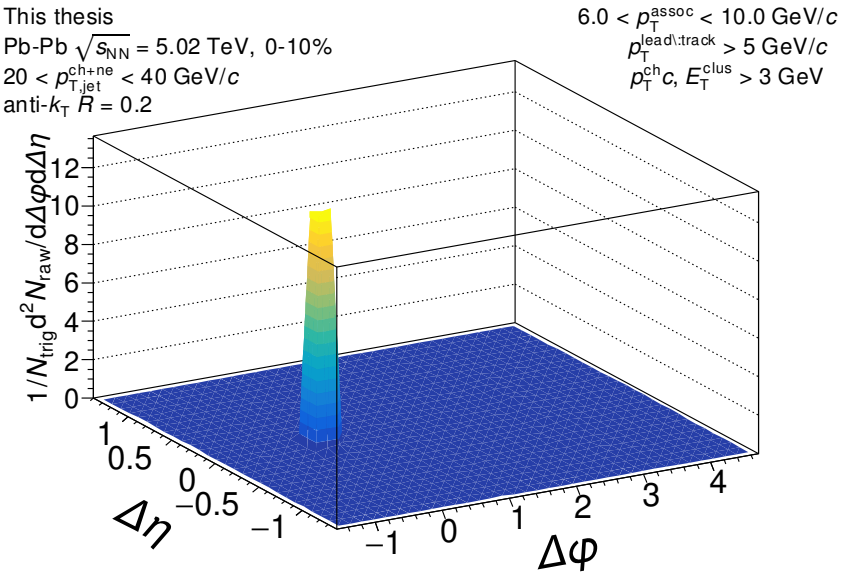

Figure D.233: The measured correlation function with the the efficiency correction $\epsilon(p_{\mathrm{T}}, \eta)$ applied, but before acceptance correction via the mixed events. The correlation is measured for mid-plane orientation for $20 < p_{\mathrm{T,jet}}^{\mathrm{ch+ne}} < 40\ \mathrm{GeV}/c$ jets with $6.0 < p_{\mathrm{T}}^{\mathrm{assoc}} < 10.0\ \mathrm{GeV}/c$ in 0–10% Pb–Pb collisions at $\sqrt{s_{\mathrm{NN}}} = 5.02$ TeV.

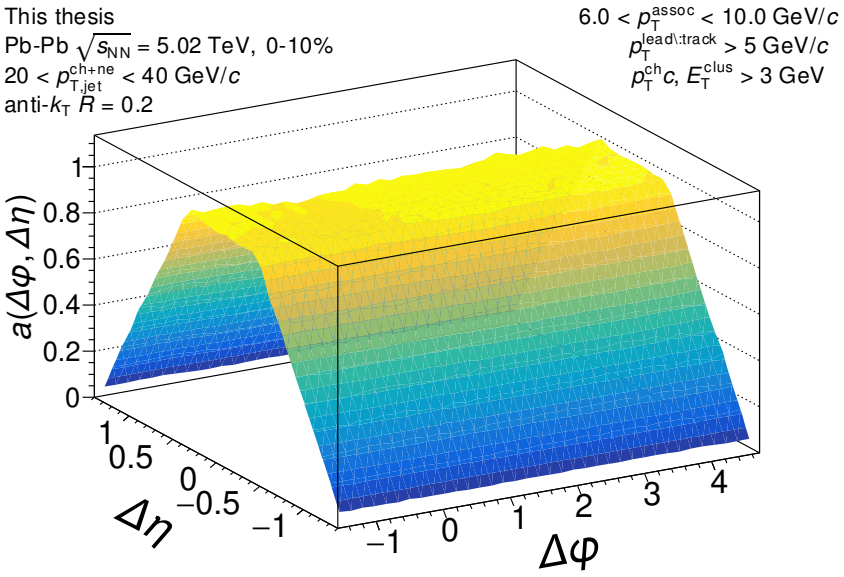

Figure D.234: The mixed event pair acceptance correction with the efficiency correction $\epsilon(p_{\mathrm{T}}, \eta)$ applied. The correlations are measured for mid-plane orientation for $20 < p_{\mathrm{T,jet}}^{\mathrm{ch+ne}} < 40\ \mathrm{GeV}/c$ jets with $6.0 < p_{\mathrm{T}}^{\mathrm{assoc}} < 10.0\ \mathrm{GeV}/c$ in 0–10% Pb–Pb collisions at $\sqrt{s_{\mathrm{NN}}} = 5.02\ \mathrm{TeV}$. They have already been normalized such that it they are unity at maximum efficiency. Above 2 GeV/c, the mixed events are merged together to increase statistics, so it is the same for all for correlations within $2.0 \leq p_{\mathrm{T}}^{\mathrm{assoc}} < 10\ \mathrm{GeV}/c$.

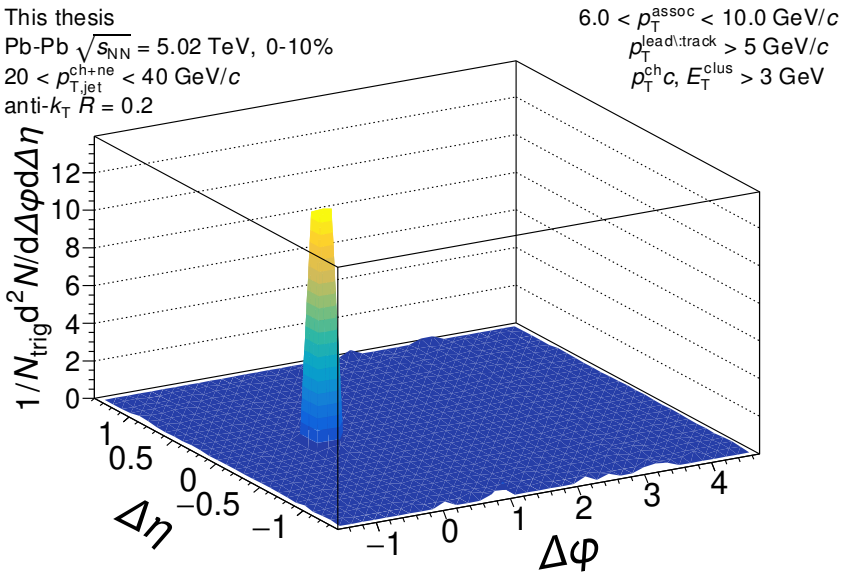

Figure D.235: The signal correlation corrected by pair acceptance. The correlations are measured for mid-plane orientation for $20 < p_{\mathrm{T,jet}}^{\mathrm{ch+ne}} < 40\ \mathrm{GeV}/c$ jets with $6.0 < p_{\mathrm{T}}^{\mathrm{assoc}} < 10.0\ \mathrm{GeV}/c$ in 0–10% Pb–Pb collisions at $\sqrt{s_{\mathrm{NN}}} = 5.02\ \mathrm{TeV}$.

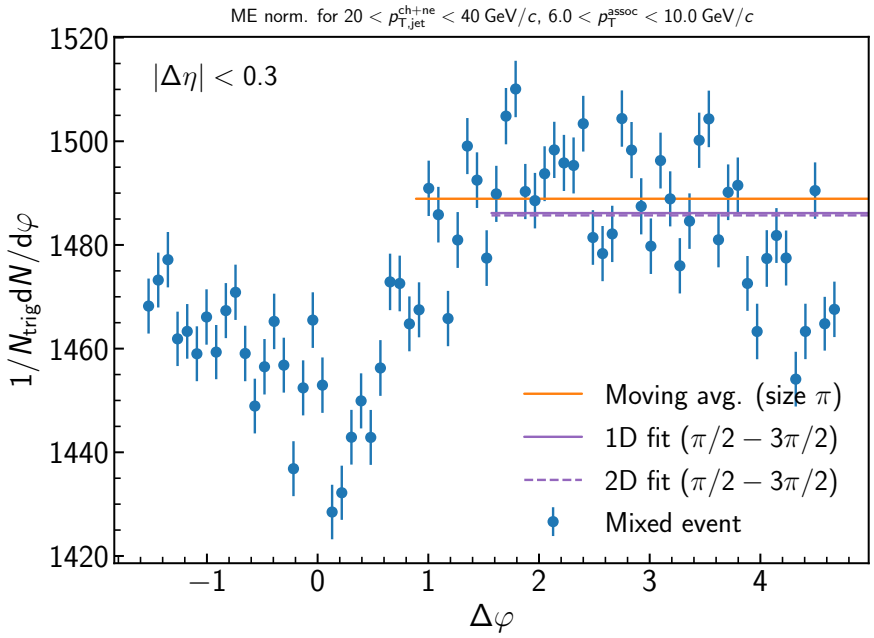

Figure D.236: Determination of the normalization of the mixed event for the inclusive event plane orientation in 0–10% Pb–Pb collisions at $\sqrt{s_{\mathrm{NN}}} = 5.02$ TeV. Here the mixed event is projected over the plateau range in $\Delta\eta$ onto to the $\Delta\varphi$ axis. The moving average is evaluated over the entire $\Delta\varphi$ range using a window of π, while the fit range is fixed from $\pi/2 < \Delta\varphi < 3\pi/2$. Since the mixed events are merged above 2 GeV/c, the normalization factor is also the same for all correlations within $6.0 < p_{\mathrm{T}}^{\mathrm{assoc}} < 10.0$ GeV/c. A variety of normalization methods were evaluated, with further details described in the text.

D.2.22 $20 < p_{\mathrm{T,jet}}^{\mathrm{ch+ne}} < 40\ \mathrm{GeV}/c$, $1.0 < p_{\mathrm{T}}^{\mathrm{assoc}} < 1.5\ \mathrm{GeV}/c$, Out-of-plane orientation

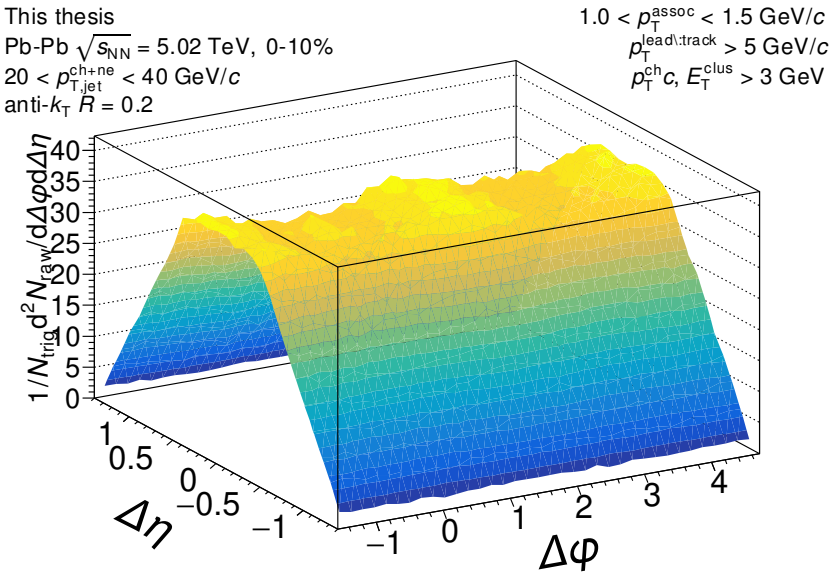

Figure D.237: The measured correlation function with the the efficiency correction $\epsilon(p_{\mathrm{T}}, \eta)$ applied, but before acceptance correction via the mixed events. The correlation is measured for out-of-plane orientation for $20 < p_{\mathrm{T,jet}}^{\mathrm{ch+ne}} < 40\ \mathrm{GeV}/c$ jets with $1.0 < p_{\mathrm{T}}^{\mathrm{assoc}} < 1.5\ \mathrm{GeV}/c$ in 0–10% Pb–Pb collisions at $\sqrt{s_{\mathrm{NN}}} = 5.02$ TeV.

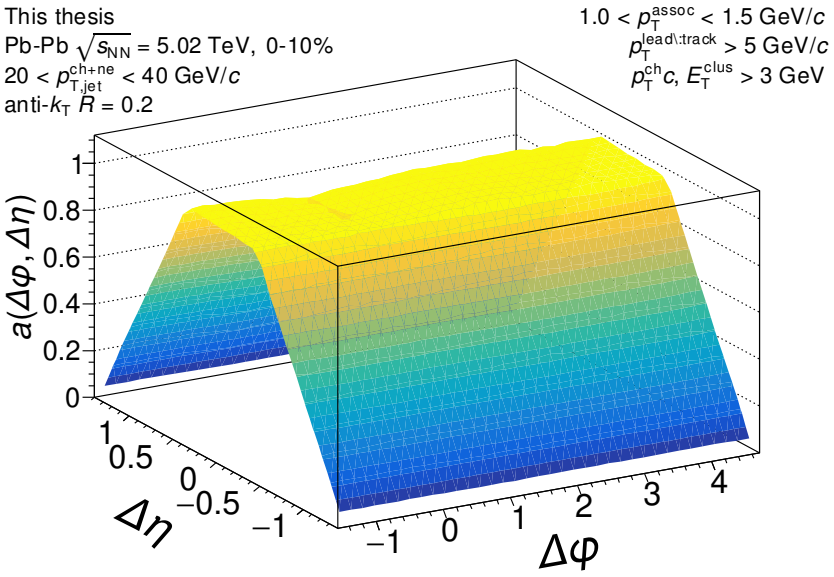

Figure D.238: The mixed event pair acceptance correction with the efficiency correction $\epsilon(p_{\mathrm{T}}, \eta)$ applied. The correlations are measured for out-of-plane orientation for $20 < p_{\mathrm{T,jet}}^{\mathrm{ch+ne}} < 40$ GeV/c jets with $1.0 < p_{\mathrm{T}}^{\mathrm{assoc}} < 1.5$ GeV/c in 0–10% Pb–Pb collisions at $\sqrt{s_{\mathrm{NN}}} = 5.02$ TeV. They have already been normalized such that it they are unity at maximum efficiency. Above 2 GeV/c, the mixed events are merged together to increase statistics, so it is the same for all for correlations within $2.0 \leq p_{\mathrm{T}}^{\mathrm{assoc}} < 10$ GeV/c.

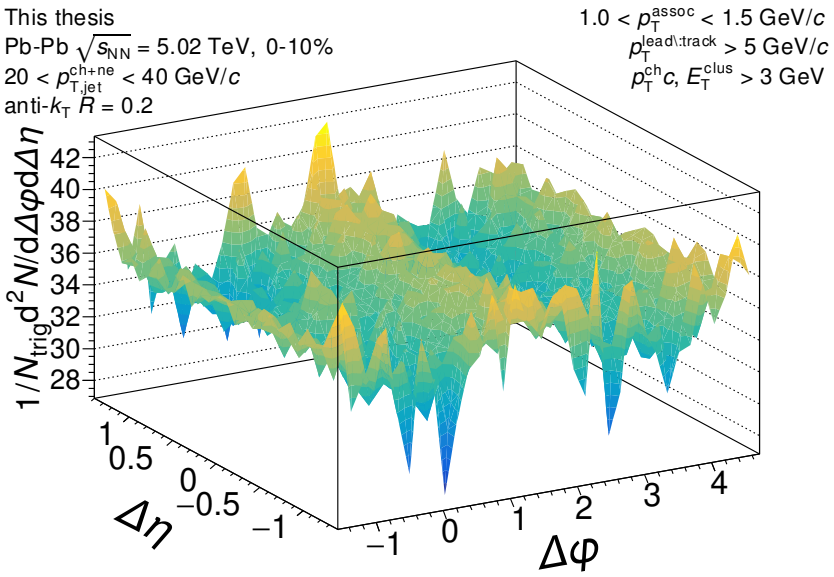

Figure D.239: The signal correlation corrected by pair acceptance. The correlations are measured for out-of-plane orientation for $20 < p_{\mathrm{T,jet}}^{\mathrm{ch+ne}} < 40$ GeV/c jets with $1.0 < p_{\mathrm{T}}^{\mathrm{assoc}} < 1.5$ GeV/c in 0–10% Pb–Pb collisions at $\sqrt{s_{\mathrm{NN}}} = 5.02$ TeV.

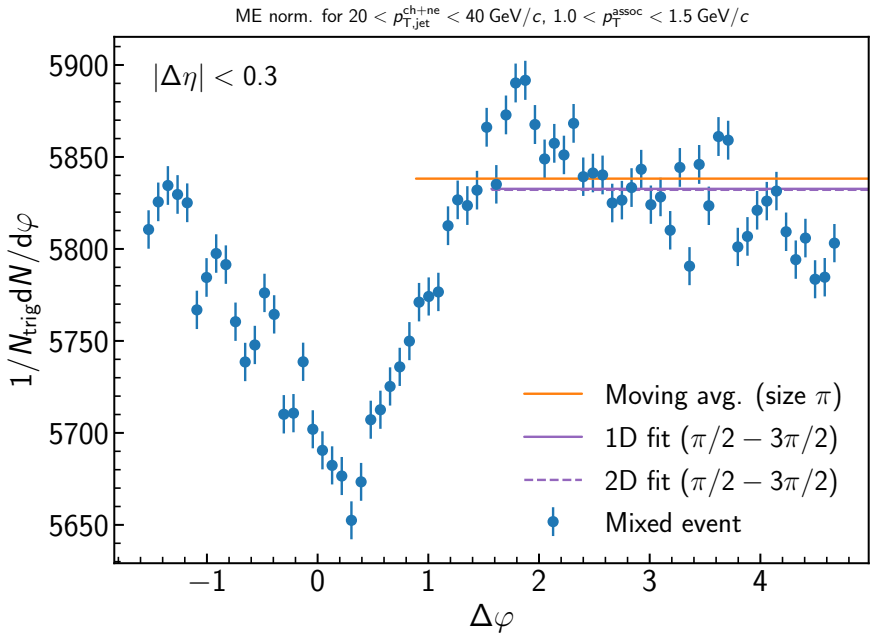

Figure D.240: Determination of the normalization of the mixed event for the inclusive event plane orientation in 0–10% Pb–Pb collisions at $\sqrt{s_{\mathrm{NN}}} = 5.02$ TeV. Here the mixed event is projected over the plateau range in $\Delta\eta$ onto to the $\Delta\varphi$ axis. The moving average is evaluated over the entire $\Delta\varphi$ range using a window of π, while the fit range is fixed from $\pi/2 < \Delta\varphi < 3\pi/2$. Since the mixed events are merged above 2 GeV/c, the normalization factor is also the same for all correlations within $1.0 < p_{\mathrm{T}}^{\mathrm{assoc}} < 1.5$ GeV/c. A variety of normalization methods were evaluated, with further details described in the text.

D.2.23 $20 < p_{\mathrm{T,jet}}^{\mathrm{ch+ne}} < 40\ \mathrm{GeV}/c$, $1.5 < p_{\mathrm{T}}^{\mathrm{assoc}} < 2.0\ \mathrm{GeV}/c$, Out-of-plane orientation

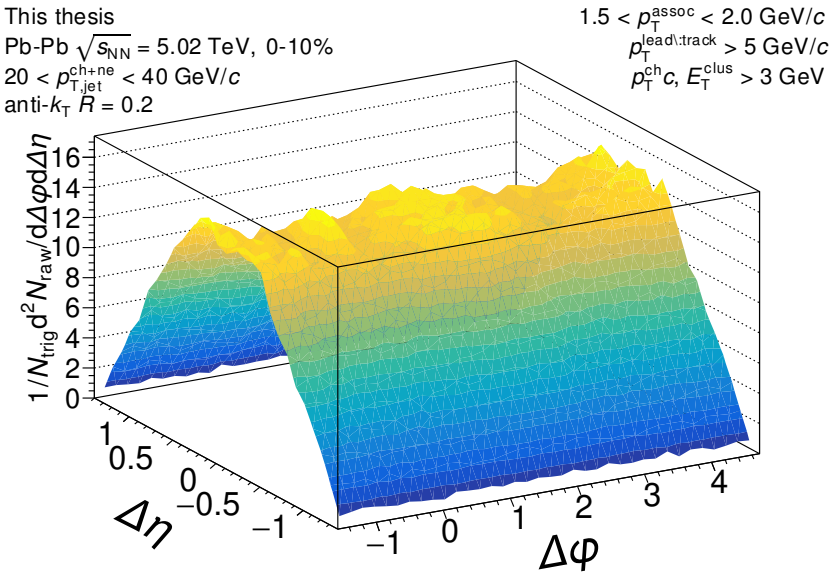

Figure D.241: The measured correlation function with the the efficiency correction $\epsilon(p_{\mathrm{T}}, \eta)$ applied, but before acceptance correction via the mixed events. The correlation is measured for out-of-plane orientation for $20 < p_{\mathrm{T,jet}}^{\mathrm{ch+ne}} < 40\ \mathrm{GeV}/c$ jets with $1.5 < p_{\mathrm{T}}^{\mathrm{assoc}} < 2.0\ \mathrm{GeV}/c$ in 0–10% Pb–Pb collisions at $\sqrt{s_{\mathrm{NN}}} = 5.02$ TeV.

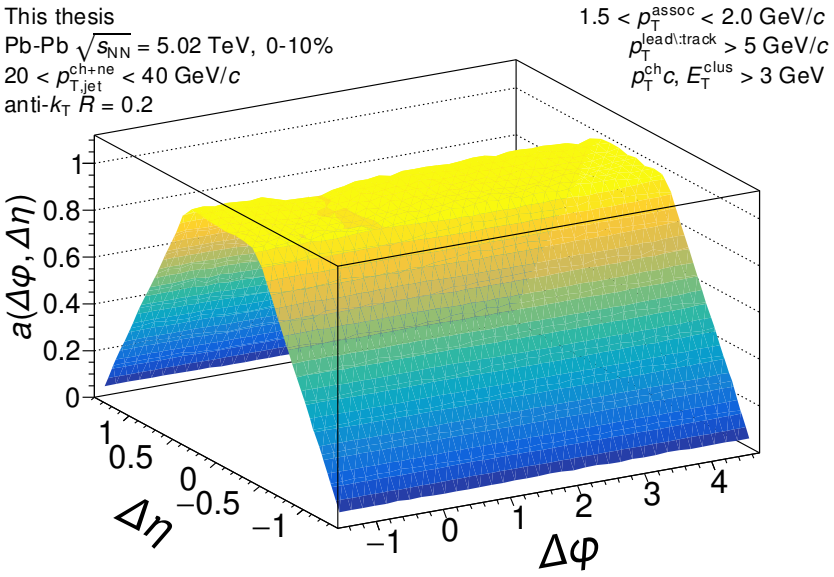

Figure D.242: The mixed event pair acceptance correction with the efficiency correction $\epsilon(p_{\mathrm{T}}, \eta)$ applied. The correlations are measured for out-of-plane orientation for $20 < p_{\mathrm{T,jet}}^{\mathrm{ch+ne}} < 40\,\mathrm{GeV}/c$ jets with $1.5 < p_{\mathrm{T}}^{\mathrm{assoc}} < 2.0\,\mathrm{GeV}/c$ in 0–10% Pb–Pb collisions at $\sqrt{s_{\mathrm{NN}}} = 5.02\,\mathrm{TeV}$. They have already been normalized such that it they are unity at maximum efficiency. Above 2 GeV/c, the mixed events are merged together to increase statistics, so it is the same for all for correlations within $2.0 \leq p_{\mathrm{T}}^{\mathrm{assoc}} < 10\,\mathrm{GeV}/c$.

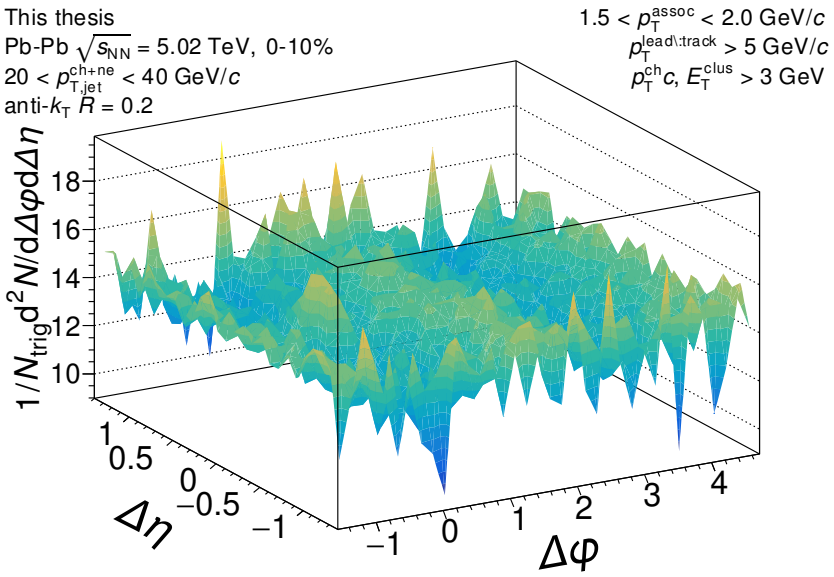

Figure D.243: The signal correlation corrected by pair acceptance. The correlations are measured for out-of-plane orientation for $20 < p_{\mathrm{T,jet}}^{\mathrm{ch+ne}} < 40\,\mathrm{GeV}/c$ jets with $1.5 < p_{\mathrm{T}}^{\mathrm{assoc}} < 2.0\,\mathrm{GeV}/c$ in 0–10% Pb–Pb collisions at $\sqrt{s_{\mathrm{NN}}} = 5.02\,\mathrm{TeV}$.

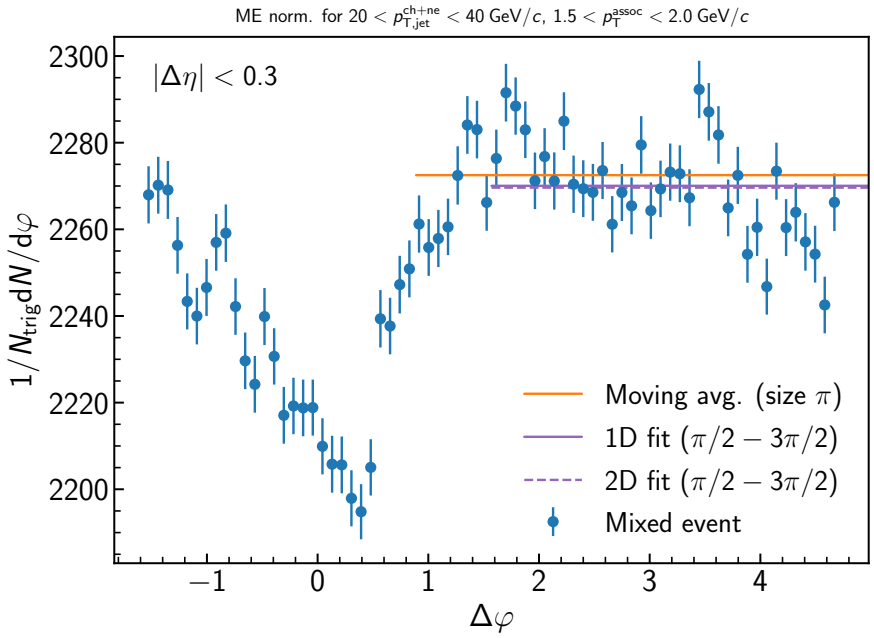

Figure D.244: Determination of the normalization of the mixed event for the inclusive event plane orientation in 0–10% Pb–Pb collisions at $\sqrt{s_{\mathrm{NN}}} = 5.02$ TeV. Here the mixed event is projected over the plateau range in $\Delta\eta$ onto to the $\Delta\varphi$ axis. The moving average is evaluated over the entire $\Delta\varphi$ range using a window of π, while the fit range is fixed from $\pi/2 < \Delta\varphi < 3\pi/2$. Since the mixed events are merged above 2 GeV/c, the normalization factor is also the same for all correlations within $1.5 < p_{\mathrm{T}}^{\mathrm{assoc}} < 2.0$ GeV/c. A variety of normalization methods were evaluated, with further details described in the text.

D.2.24 $20 < p_{\mathrm{T,jet}}^{\mathrm{ch+ne}} < 40\ \mathrm{GeV}/c$, $2.0 < p_{\mathrm{T}}^{\mathrm{assoc}} < 3.0\ \mathrm{GeV}/c$, Out-of-plane orientation

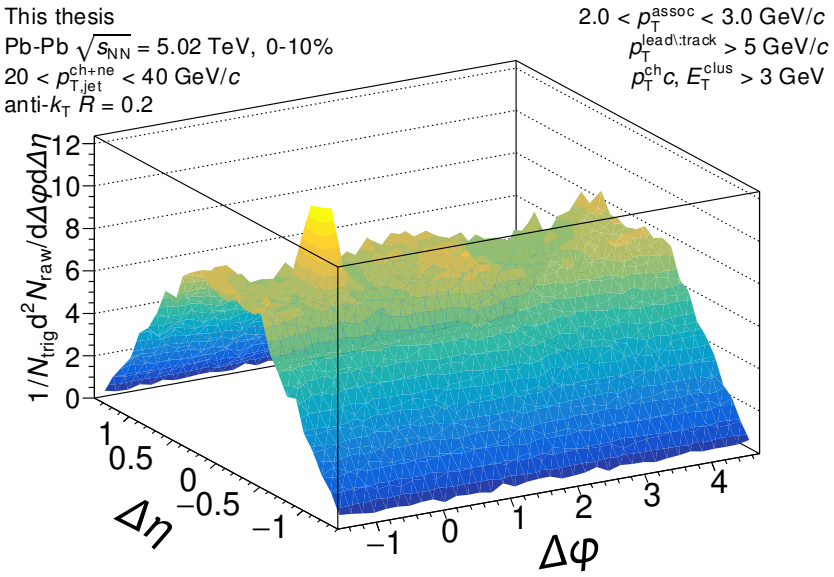

Figure D.245: The measured correlation function with the the efficiency correction $\epsilon(p_{\mathrm{T}}, \eta)$ applied, but before acceptance correction via the mixed events. The correlation is measured for out-of-plane orientation for $20 < p_{\mathrm{T,jet}}^{\mathrm{ch+ne}} < 40\ \mathrm{GeV}/c$ jets with $2.0 < p_{\mathrm{T}}^{\mathrm{assoc}} < 3.0\ \mathrm{GeV}/c$ in 0–10% Pb–Pb collisions at $\sqrt{s_{\mathrm{NN}}} = 5.02$ TeV.

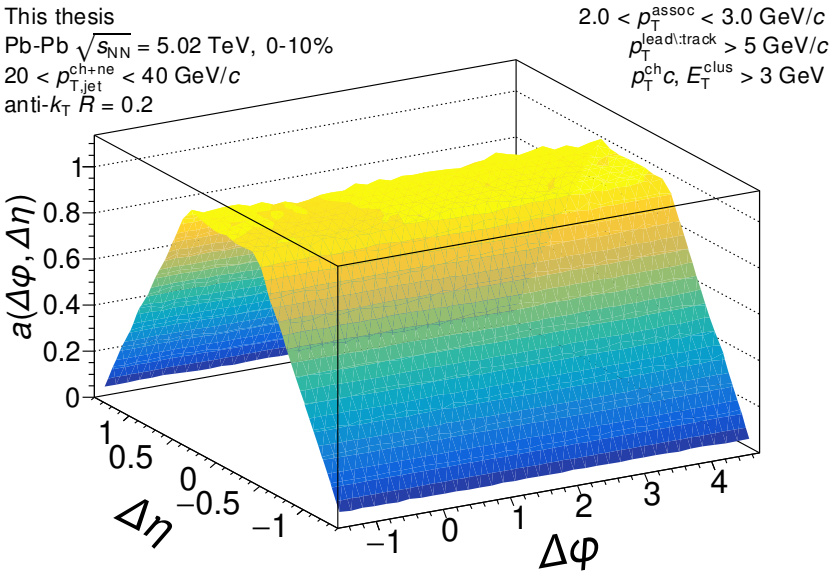

Figure D.246: The mixed event pair acceptance correction with the efficiency correction $\epsilon(p_{\mathrm{T}}, \eta)$ applied. The correlations are measured for out-of-plane orientation for $20 < p_{\mathrm{T,jet}}^{\mathrm{ch+ne}} < 40\,\mathrm{GeV}/c$ jets with $2.0 < p_{\mathrm{T}}^{\mathrm{assoc}} < 3.0\,\mathrm{GeV}/c$ in 0–10% Pb–Pb collisions at $\sqrt{s_{\mathrm{NN}}} = 5.02\,\mathrm{TeV}$. They have already been normalized such that it they are unity at maximum efficiency. Above 2 GeV/c, the mixed events are merged together to increase statistics, so it is the same for all for correlations within $2.0 \leq p_{\mathrm{T}}^{\mathrm{assoc}} < 10\,\mathrm{GeV}/c$.

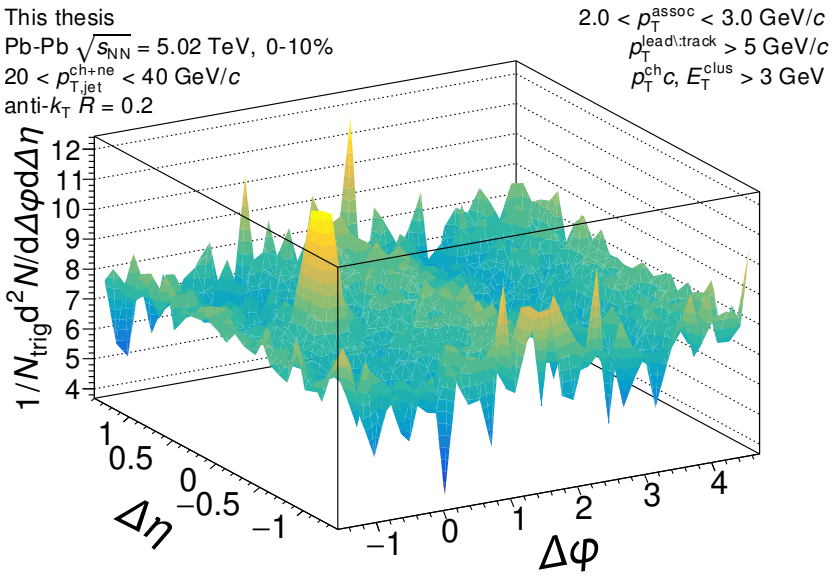

Figure D.247: The signal correlation corrected by pair acceptance. The correlations are measured for out-of-plane orientation for $20 < p_{\mathrm{T,jet}}^{\mathrm{ch+ne}} < 40\,\mathrm{GeV}/c$ jets with $2.0 < p_{\mathrm{T}}^{\mathrm{assoc}} < 3.0\,\mathrm{GeV}/c$ in 0–10% Pb–Pb collisions at $\sqrt{s_{\mathrm{NN}}} = 5.02\,\mathrm{TeV}$.

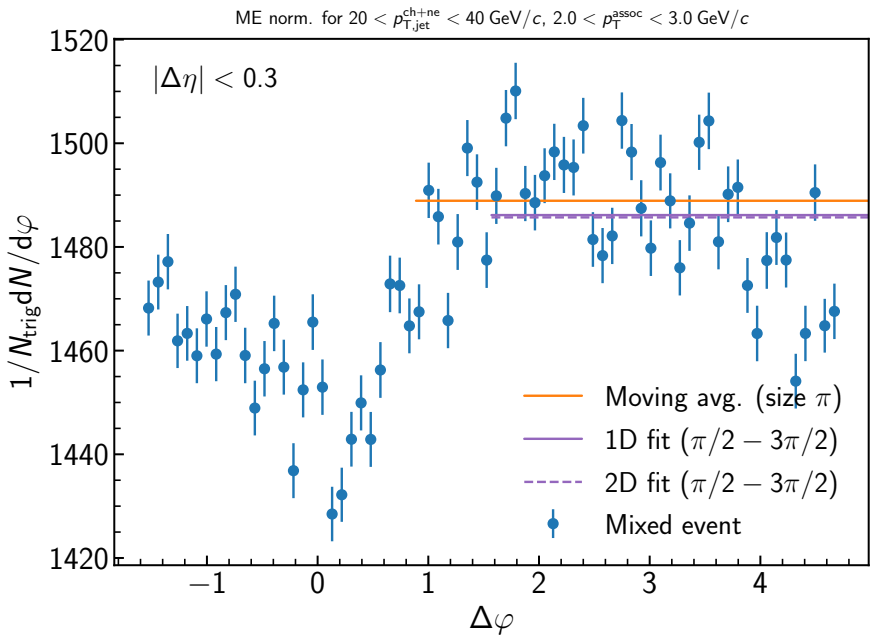

Figure D.248: Determination of the normalization of the mixed event for the inclusive event plane orientation in 0–10% Pb–Pb collisions at $\sqrt{s_{\mathrm{NN}}} = 5.02$ TeV. Here the mixed event is projected over the plateau range in $\Delta\eta$ onto to the $\Delta\varphi$ axis. The moving average is evaluated over the entire $\Delta\varphi$ range using a window of π, while the fit range is fixed from $\pi/2 < \Delta\varphi < 3\pi/2$. Since the mixed events are merged above 2 GeV/c, the normalization factor is also the same for all correlations within $2.0 < p_{\mathrm{T}}^{\mathrm{assoc}} < 3.0$ GeV/c. A variety of normalization methods were evaluated, with further details described in the text.

D.2.25 $20 < p_{\mathrm{T,jet}}^{\mathrm{ch+ne}} < 40\ \mathrm{GeV}/c$, $3.0 < p_{\mathrm{T}}^{\mathrm{assoc}} < 4.0\ \mathrm{GeV}/c$, Out-of-plane orientation

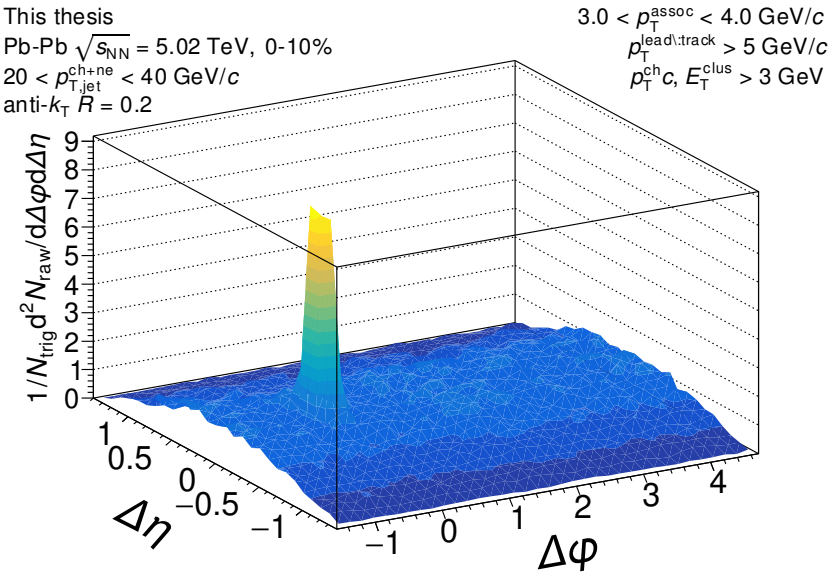

Figure D.249: The measured correlation function with the the efficiency correction $\epsilon(p_{\mathrm{T}}, \eta)$ applied, but before acceptance correction via the mixed events. The correlation is measured for out-of-plane orientation for $20 < p_{\mathrm{T,jet}}^{\mathrm{ch+ne}} < 40\ \mathrm{GeV}/c$ jets with $3.0 < p_{\mathrm{T}}^{\mathrm{assoc}} < 4.0\ \mathrm{GeV}/c$ in 0–10% Pb–Pb collisions at $\sqrt{s_{\mathrm{NN}}} = 5.02$ TeV.

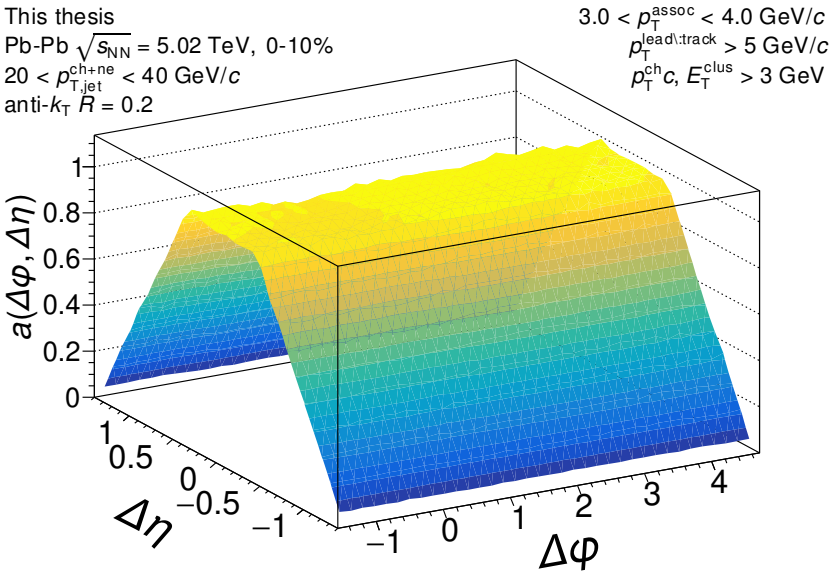

Figure D.250: The mixed event pair acceptance correction with the efficiency correction $\epsilon(p_T, \eta)$ applied. The correlations are measured for out-of-plane orientation for $20 < p_{T,jet}^{ch+ne} < 40$ GeV/c jets with $3.0 < p_T^{assoc} < 4.0$ GeV/c in 0–10% Pb–Pb collisions at $\sqrt{s_{NN}} = 5.02$ TeV. They have already been normalized such that it they are unity at maximum efficiency. Above 2 GeV/c, the mixed events are merged together to increase statistics, so it is the same for all for correlations within $2.0 \leq p_T^{assoc} < 10$ GeV/c.

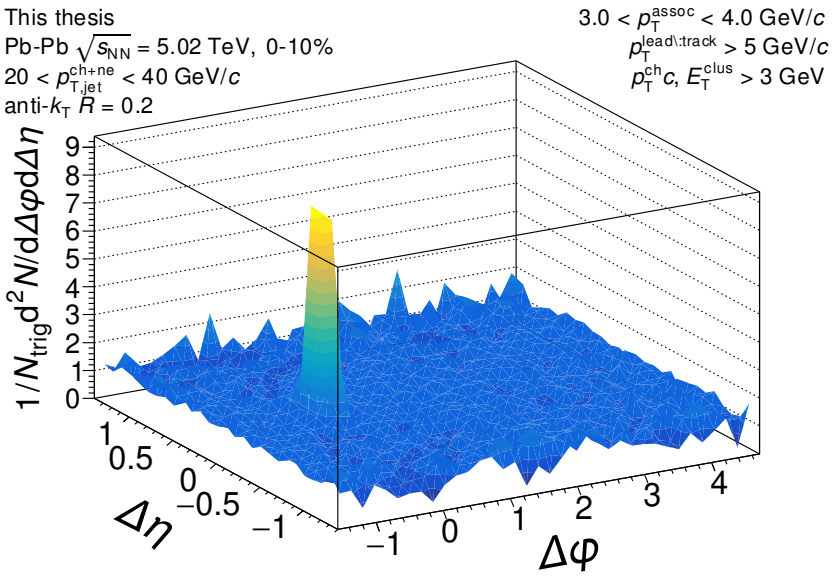

Figure D.251: The signal correlation corrected by pair acceptance. The correlations are measured for out-of-plane orientation for $20 < p_{T,jet}^{ch+ne} < 40$ GeV/c jets with $3.0 < p_T^{assoc} < 4.0$ GeV/c in 0–10% Pb–Pb collisions at $\sqrt{s_{NN}} = 5.02$ TeV.

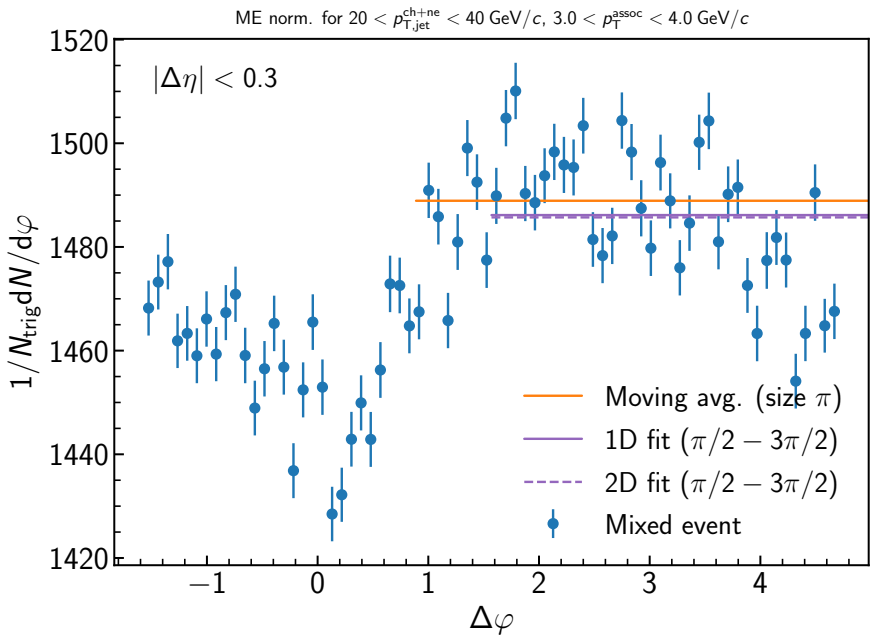

Figure D.252: Determination of the normalization of the mixed event for the inclusive event plane orientation in 0–10% Pb–Pb collisions at $\sqrt{s_{\mathrm{NN}}} = 5.02$ TeV. Here the mixed event is projected over the plateau range in $\Delta\eta$ onto to the $\Delta\varphi$ axis. The moving average is evaluated over the entire $\Delta\varphi$ range using a window of π, while the fit range is fixed from $\pi/2 < \Delta\varphi < 3\pi/2$. Since the mixed events are merged above 2 GeV/c, the normalization factor is also the same for all correlations within $3.0 < p_{\mathrm{T}}^{\mathrm{assoc}} < 4.0$ GeV/c. A variety of normalization methods were evaluated, with further details described in the text.

D.2.26 $20 < p_{\mathrm{T,jet}}^{\mathrm{ch+ne}} < 40\ \mathrm{GeV}/c$, $4.0 < p_{\mathrm{T}}^{\mathrm{assoc}} < 5.0\ \mathrm{GeV}/c$, Out-of-plane orientation

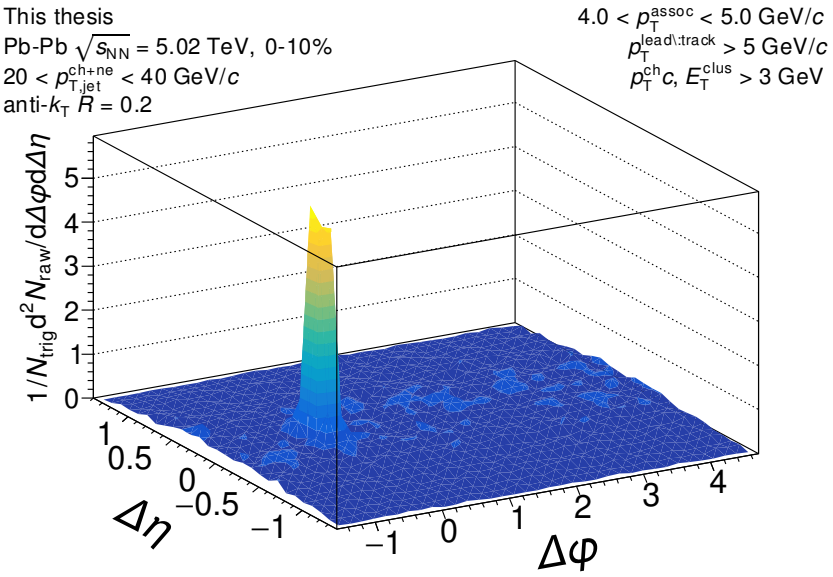

Figure D.253: The measured correlation function with the the efficiency correction $\epsilon(p_{\mathrm{T}}, \eta)$ applied, but before acceptance correction via the mixed events. The correlation is measured for out-of-plane orientation for $20 < p_{\mathrm{T,jet}}^{\mathrm{ch+ne}} < 40\ \mathrm{GeV}/c$ jets with $4.0 < p_{\mathrm{T}}^{\mathrm{assoc}} < 5.0\ \mathrm{GeV}/c$ in 0–10% Pb–Pb collisions at $\sqrt{s_{\mathrm{NN}}} = 5.02$ TeV.

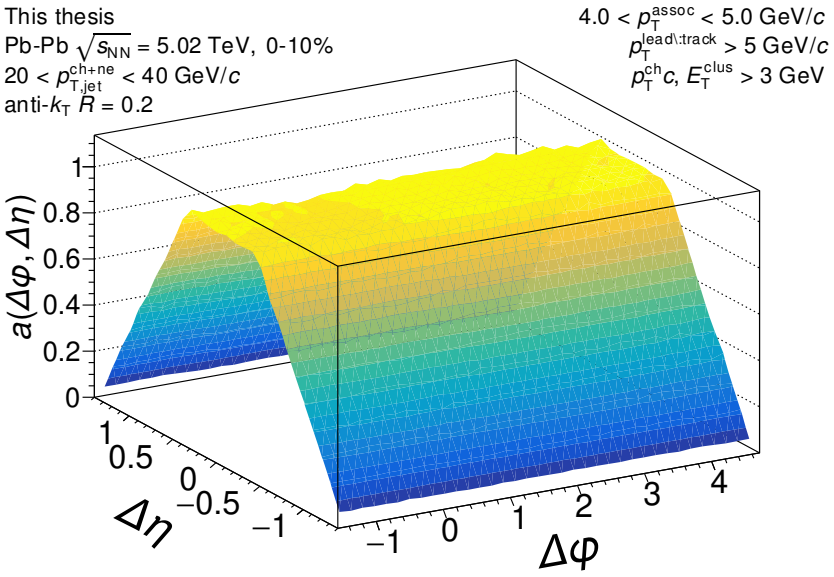

Figure D.254: The mixed event pair acceptance correction with the efficiency correction $\epsilon(p_{\mathrm{T}}, \eta)$ applied. The correlations are measured for out-of-plane orientation for $20 < p_{\mathrm{T,jet}}^{\mathrm{ch+ne}} < 40\,\mathrm{GeV}/c$ jets with $4.0 < p_{\mathrm{T}}^{\mathrm{assoc}} < 5.0\,\mathrm{GeV}/c$ in 0–10% Pb–Pb collisions at $\sqrt{s_{\mathrm{NN}}} = 5.02\,\mathrm{TeV}$. They have already been normalized such that it they are unity at maximum efficiency. Above 2 GeV/c, the mixed events are merged together to increase statistics, so it is the same for all for correlations within $2.0 \leq p_{\mathrm{T}}^{\mathrm{assoc}} < 10\,\mathrm{GeV}/c$.

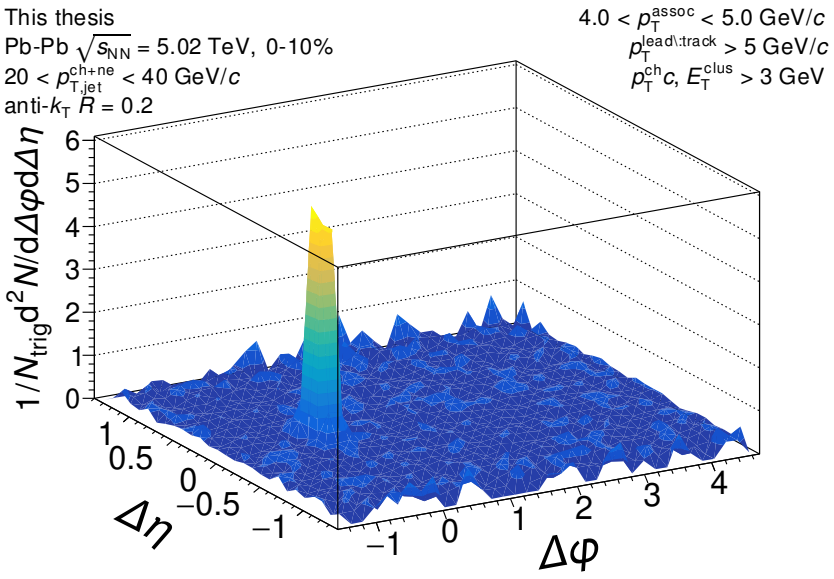

Figure D.255: The signal correlation corrected by pair acceptance. The correlations are measured for out-of-plane orientation for $20 < p_{\mathrm{T,jet}}^{\mathrm{ch+ne}} < 40\,\mathrm{GeV}/c$ jets with $4.0 < p_{\mathrm{T}}^{\mathrm{assoc}} < 5.0\,\mathrm{GeV}/c$ in 0–10% Pb–Pb collisions at $\sqrt{s_{\mathrm{NN}}} = 5.02\,\mathrm{TeV}$.

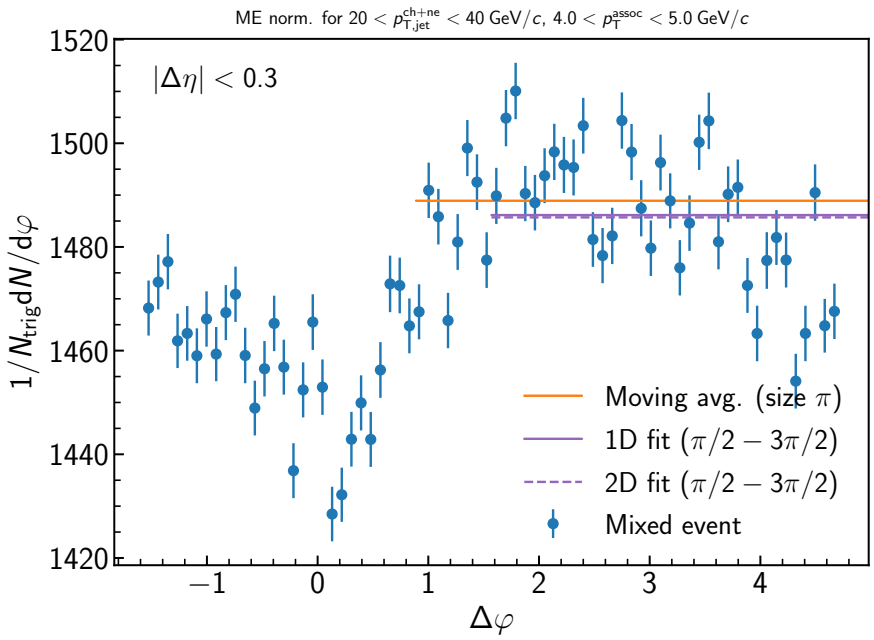

Figure D.256: Determination of the normalization of the mixed event for the inclusive event plane orientation in 0–10% Pb–Pb collisions at $\sqrt{s_{\mathrm{NN}}} = 5.02$ TeV. Here the mixed event is projected over the plateau range in $\Delta\eta$ onto to the $\Delta\varphi$ axis. The moving average is evaluated over the entire $\Delta\varphi$ range using a window of π, while the fit range is fixed from $\pi/2 < \Delta\varphi < 3\pi/2$. Since the mixed events are merged above 2 GeV/c, the normalization factor is also the same for all correlations within $4.0 < p_{\mathrm{T}}^{\mathrm{assoc}} < 5.0$ GeV/c. A variety of normalization methods were evaluated, with further details described in the text.

D.2.27 $20 < p_{\mathrm{T,jet}}^{\mathrm{ch+ne}} < 40\ \mathrm{GeV}/c$, $5.0 < p_{\mathrm{T}}^{\mathrm{assoc}} < 6.0\ \mathrm{GeV}/c$, Out-of-plane orientation

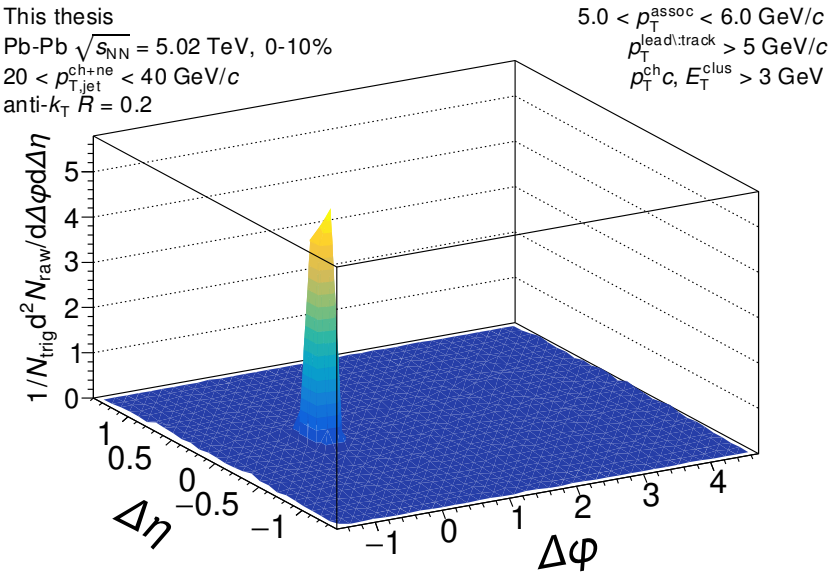

Figure D.257: The measured correlation function with the the efficiency correction $\epsilon(p_{\mathrm{T}}, \eta)$ applied, but before acceptance correction via the mixed events. The correlation is measured for out-of-plane orientation for $20 < p_{\mathrm{T,jet}}^{\mathrm{ch+ne}} < 40\ \mathrm{GeV}/c$ jets with $5.0 < p_{\mathrm{T}}^{\mathrm{assoc}} < 6.0\ \mathrm{GeV}/c$ in 0–10% Pb–Pb collisions at $\sqrt{s_{\mathrm{NN}}} = 5.02$ TeV.

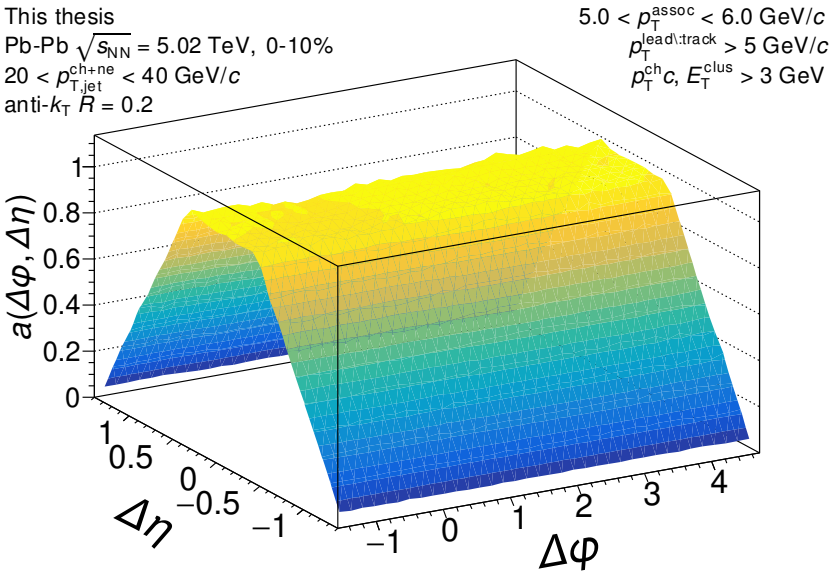

Figure D.258: The mixed event pair acceptance correction with the efficiency correction $\epsilon(p_{\mathrm{T}}, \eta)$ applied. The correlations are measured for out-of-plane orientation for $20 < p_{\mathrm{T,jet}}^{\mathrm{ch+ne}} < 40\,\mathrm{GeV}/c$ jets with $5.0 < p_{\mathrm{T}}^{\mathrm{assoc}} < 6.0\,\mathrm{GeV}/c$ in 0–10% Pb–Pb collisions at $\sqrt{s_{\mathrm{NN}}} = 5.02\,\mathrm{TeV}$. They have already been normalized such that it they are unity at maximum efficiency. Above 2 GeV/c, the mixed events are merged together to increase statistics, so it is the same for all for correlations within $2.0 \leq p_{\mathrm{T}}^{\mathrm{assoc}} < 10\,\mathrm{GeV}/c$.

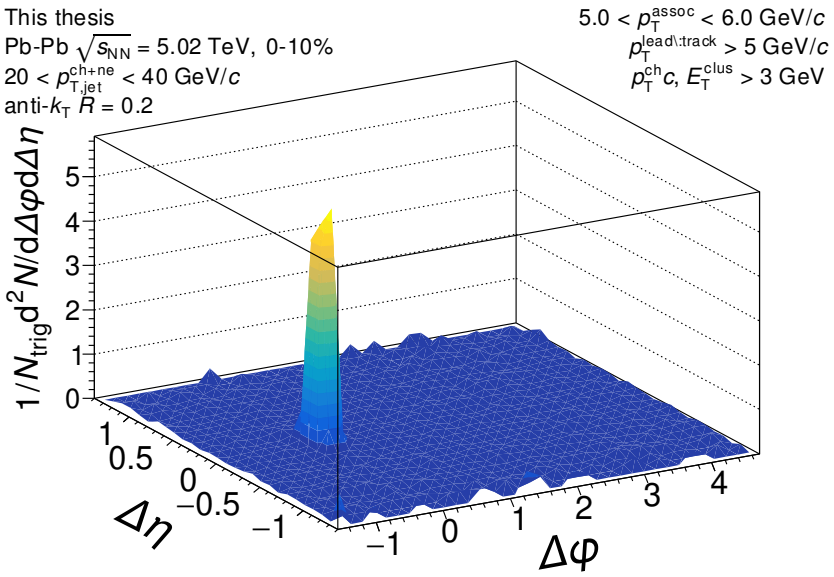

Figure D.259: The signal correlation corrected by pair acceptance. The correlations are measured for out-of-plane orientation for $20 < p_{\mathrm{T,jet}}^{\mathrm{ch+ne}} < 40\,\mathrm{GeV}/c$ jets with $5.0 < p_{\mathrm{T}}^{\mathrm{assoc}} < 6.0\,\mathrm{GeV}/c$ in 0–10% Pb–Pb collisions at $\sqrt{s_{\mathrm{NN}}} = 5.02\,\mathrm{TeV}$.

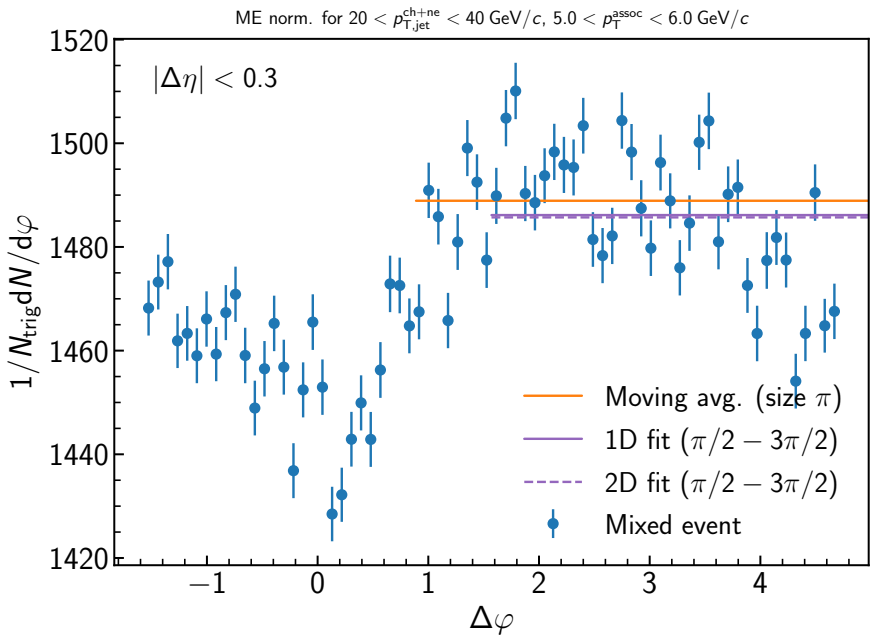

Figure D.260: Determination of the normalization of the mixed event for the inclusive event plane orientation in 0–10% Pb–Pb collisions at $\sqrt{s_{\mathrm{NN}}} = 5.02$ TeV. Here the mixed event is projected over the plateau range in $\Delta\eta$ onto to the $\Delta\varphi$ axis. The moving average is evaluated over the entire $\Delta\varphi$ range using a window of π, while the fit range is fixed from $\pi/2 < \Delta\varphi < 3\pi/2$. Since the mixed events are merged above 2 GeV/c, the normalization factor is also the same for all correlations within $5.0 < p_{\mathrm{T}}^{\mathrm{assoc}} < 6.0$ GeV/c. A variety of normalization methods were evaluated, with further details described in the text.

D.2.28 $20 < p_{\mathrm{T,jet}}^{\mathrm{ch+ne}} < 40$ GeV/c, $6.0 < p_{\mathrm{T}}^{\mathrm{assoc}} < 10.0$ GeV/c, Out-of-plane orientation

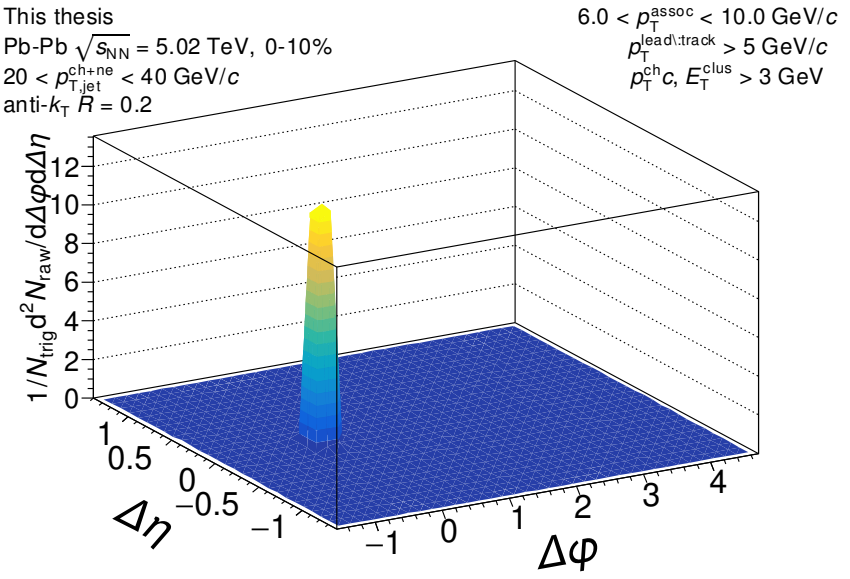

Figure D.261: The measured correlation function with the the efficiency correction $\epsilon(p_{\mathrm{T}}, \eta)$ applied, but before acceptance correction via the mixed events. The correlation is measured for out-of-plane orientation for $20 < p_{\mathrm{T,jet}}^{\mathrm{ch+ne}} < 40$ GeV/c jets with $6.0 < p_{\mathrm{T}}^{\mathrm{assoc}} < 10.0$ GeV/c in 0–10% Pb–Pb collisions at $\sqrt{s_{\mathrm{NN}}} = 5.02$ TeV.

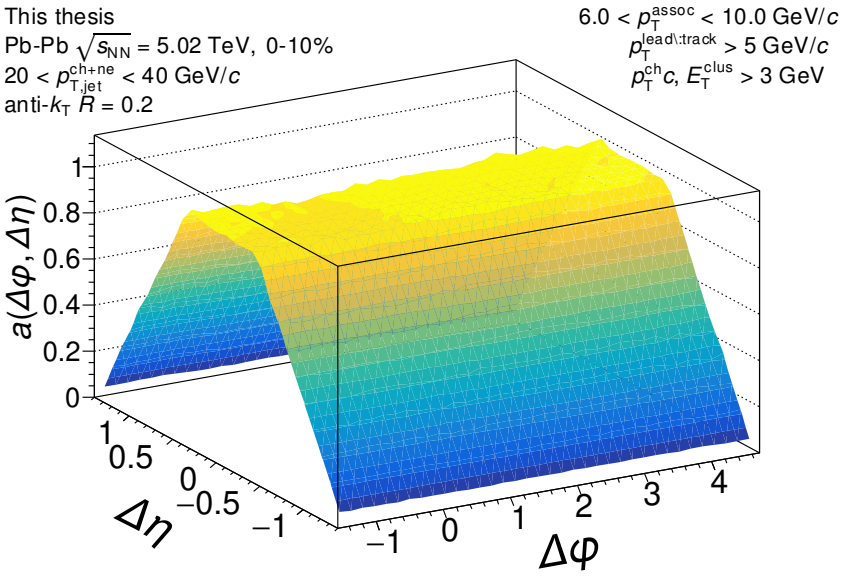

Figure D.262: The mixed event pair acceptance correction with the efficiency correction $\epsilon(p_{\mathrm{T}}, \eta)$ applied. The correlations are measured for out-of-plane orientation for $20 < p_{\mathrm{T,jet}}^{\mathrm{ch+ne}} < 40\,\mathrm{GeV}/c$ jets with $6.0 < p_{\mathrm{T}}^{\mathrm{assoc}} < 10.0\,\mathrm{GeV}/c$ in 0–10% Pb–Pb collisions at $\sqrt{s_{\mathrm{NN}}} = 5.02\,\mathrm{TeV}$. They have already been normalized such that it they are unity at maximum efficiency. Above 2 GeV/c, the mixed events are merged together to increase statistics, so it is the same for all for correlations within $2.0 \leq p_{\mathrm{T}}^{\mathrm{assoc}} < 10$ GeV/c.

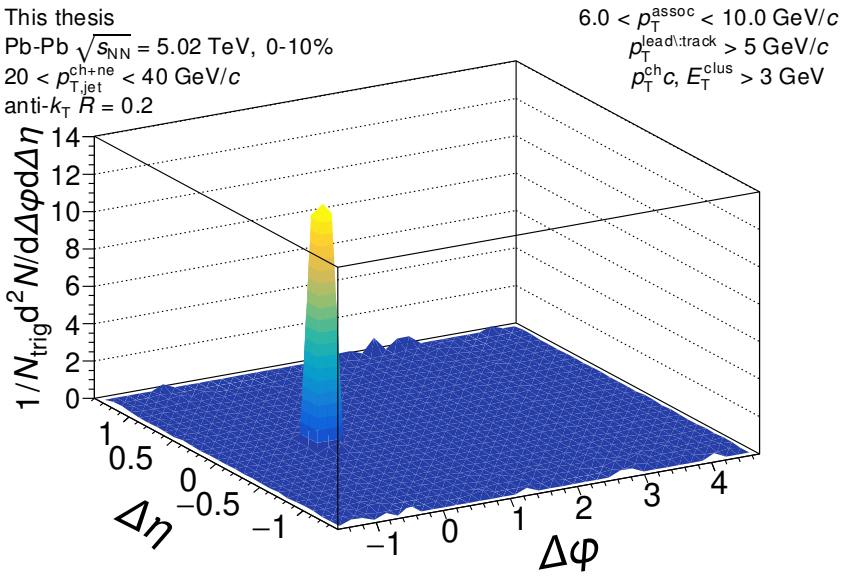

Figure D.263: The signal correlation corrected by pair acceptance. The correlations are measured for out-of-plane orientation for $20 < p_{\mathrm{T,jet}}^{\mathrm{ch+ne}} < 40\,\mathrm{GeV}/c$ jets with $6.0 < p_{\mathrm{T}}^{\mathrm{assoc}} < 10.0\,\mathrm{GeV}/c$ in 0–10% Pb–Pb collisions at $\sqrt{s_{\mathrm{NN}}} = 5.02\,\mathrm{TeV}$.

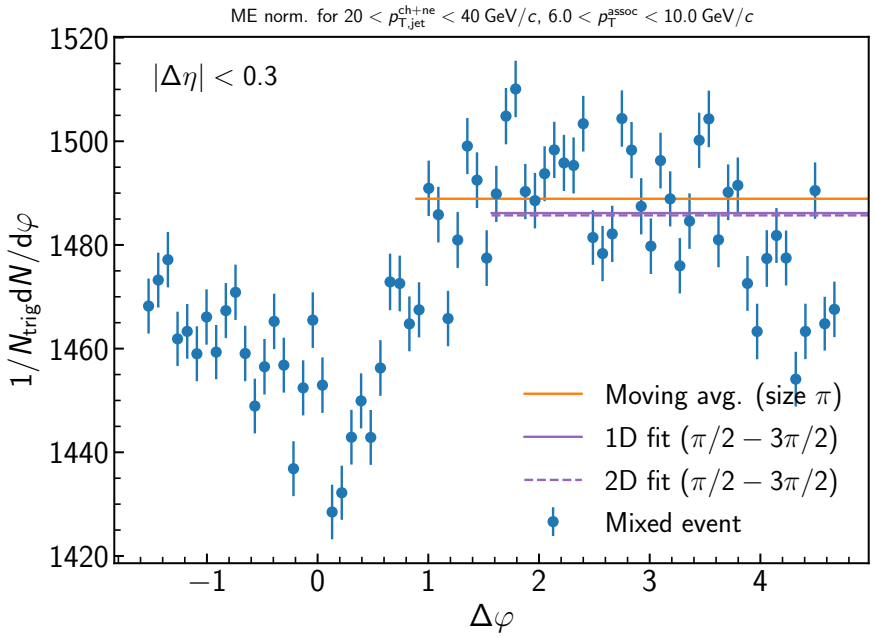

Figure D.264: Determination of the normalization of the mixed event for the inclusive event plane orientation in 0–10% Pb–Pb collisions at $\sqrt{s_{\mathrm{NN}}} = 5.02$ TeV. Here the mixed event is projected over the plateau range in $\Delta\eta$ onto to the $\Delta\varphi$ axis. The moving average is evaluated over the entire $\Delta\varphi$ range using a window of π, while the fit range is fixed from $\pi/2 < \Delta\varphi < 3\pi/2$. Since the mixed events are merged above 2 GeV/c, the normalization factor is also the same for all correlations within $6.0 < p_{\mathrm{T}}^{\mathrm{assoc}} < 10.0$ GeV/c. A variety of normalization methods were evaluated, with further details described in the text.

D.2.29 Reaction Plane Fit

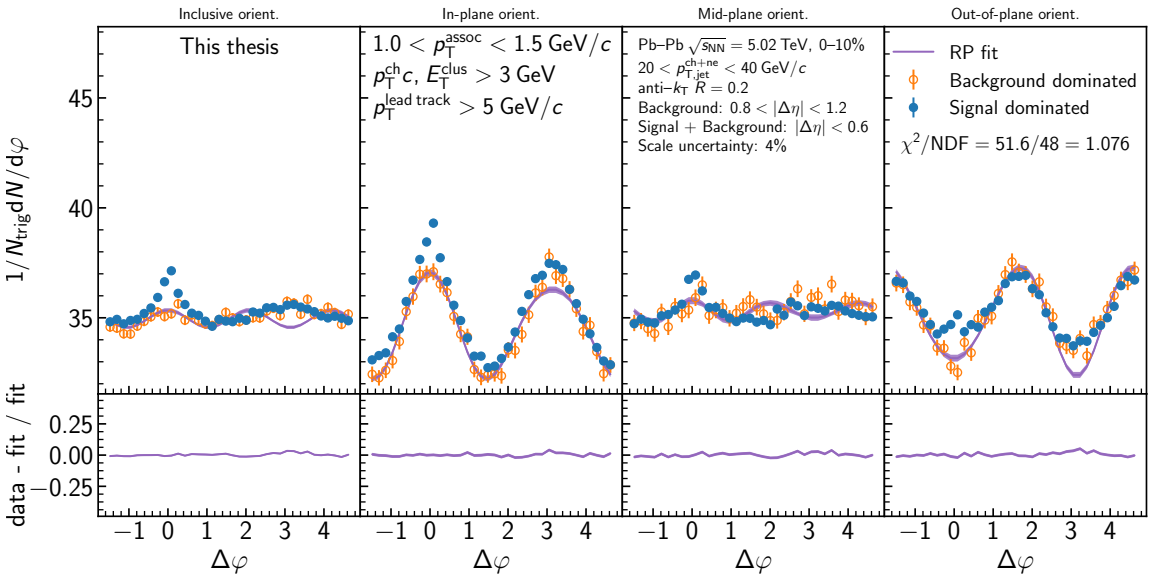

Figure D.265: The Reaction Plane Fit of jet-hadron correlations measured for $20 < p_{\mathrm{T,jet}}^{\mathrm{ch+ne}} < 40$ GeV/c and $1.0 < p_{\mathrm{T}}^{\mathrm{assoc}} < 1.5$ GeV/c in 0–10% collisions. The signal dominated data are shown in blue, the background dominated in orange, and the fit in purple. The upper panels show the signal and background dominated correlations measured in each event plane orientation. The lower panels show the fit residuals.

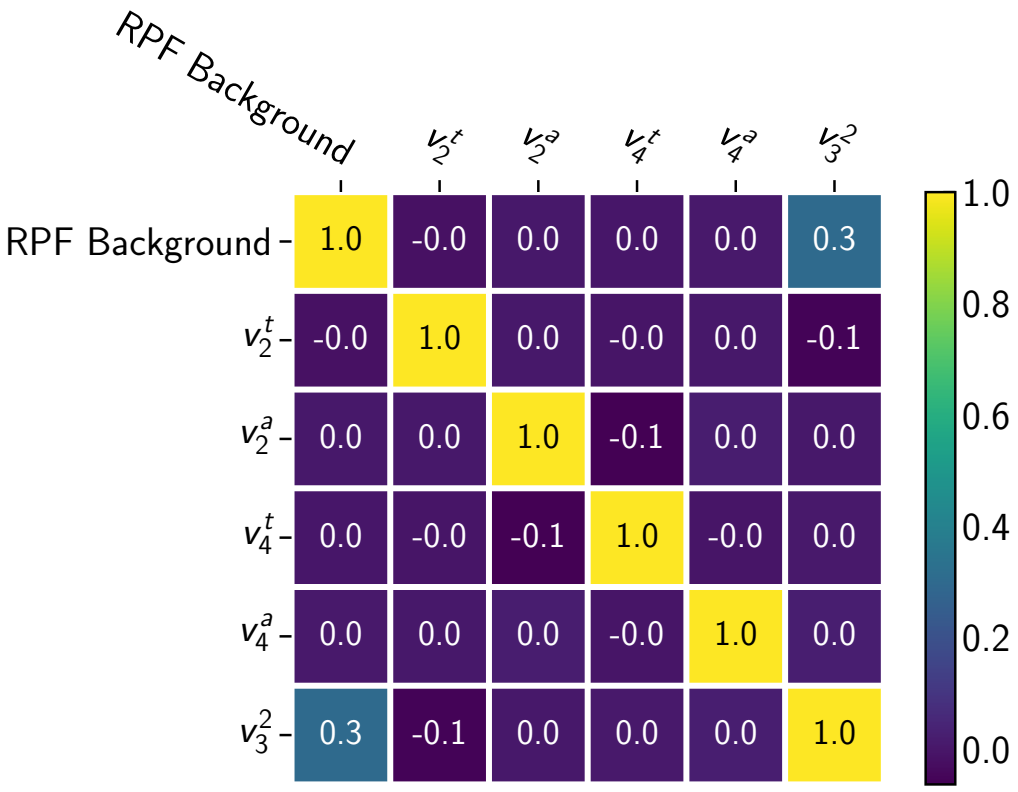

Figure D.266: Correlation matrix for the Reaction Plane Fit of jet-hadron correlations measured for $20 < p_{\mathrm{T,jet}}^{\mathrm{ch+ne}} < 40\,\mathrm{GeV}/c$ and $1.0 < p_{\mathrm{T}}^{\mathrm{assoc}} < 1.5\,\mathrm{GeV}/c$ in 0–10% collisions.

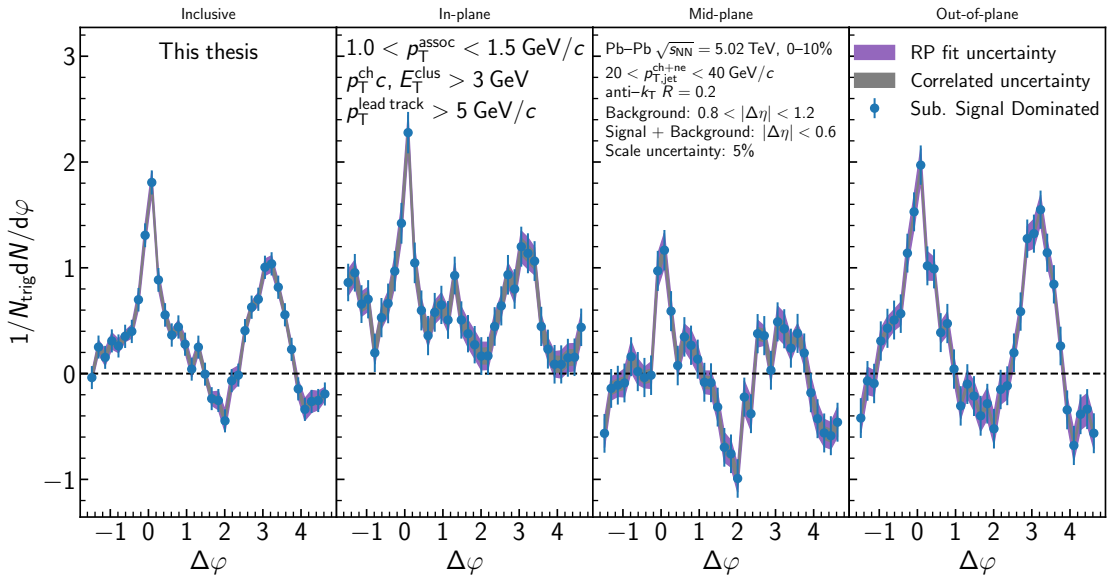

Figure D.267: The Reaction Plane Fit subtracted jet-hadron correlations measured for $20 < p_{\mathrm{T,jet}}^{\mathrm{ch+ne}} < 40\ \mathrm{GeV}/c$ and $1.0 < p_{\mathrm{T}}^{\mathrm{assoc}} < 1.5\ \mathrm{GeV}/c$ in 0–10% collisions. The subtracted data are shown in blue for each event plane orientation, with the fit uncertainty in purple and the correlated uncertainty in gray.

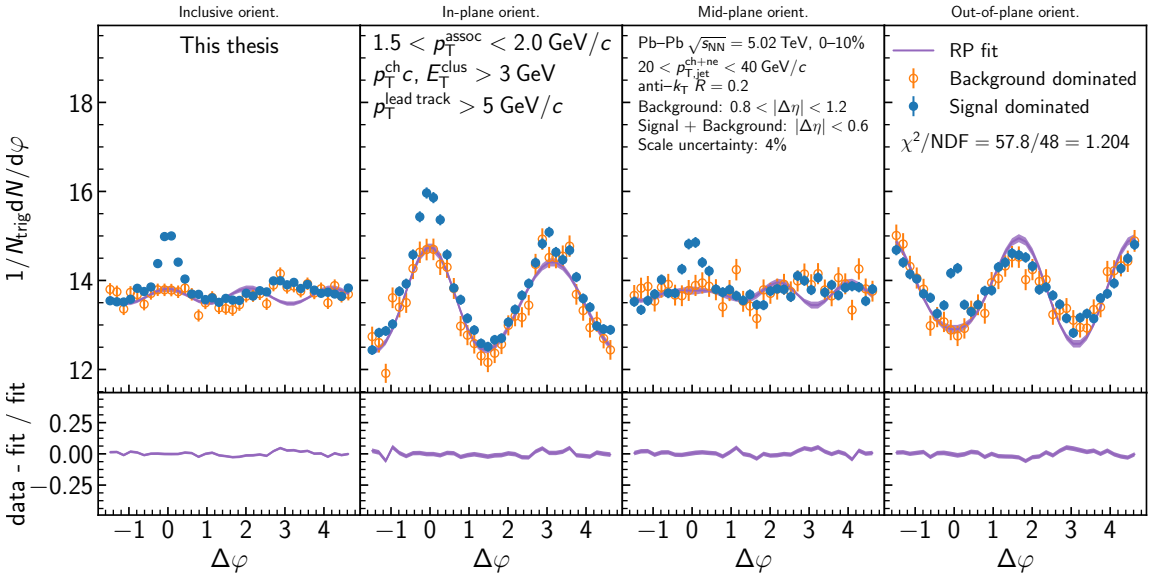

Figure D.268: The Reaction Plane Fit of jet-hadron correlations measured for $20 < p_{\mathrm{T,jet}}^{\mathrm{ch+ne}} < 40\ \mathrm{GeV}/c$ and $1.5 < p_{\mathrm{T}}^{\mathrm{assoc}} < 2.0\ \mathrm{GeV}/c$ in 0–10% collisions. The signal dominated data are shown in blue, the background dominated in orange, and the fit in purple. The upper panels show the signal and background dominated correlations measured in each event plane orientation. The lower panels show the fit residuals.

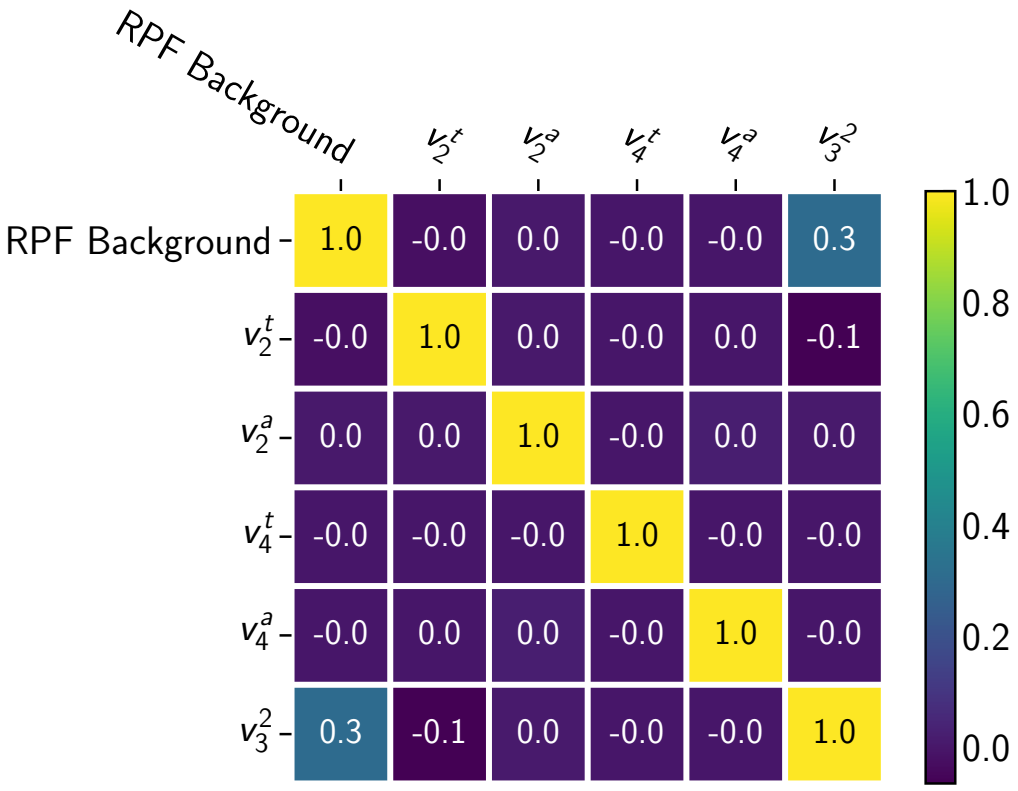

Figure D.269: Correlation matrix for the Reaction Plane Fit of jet-hadron correlations measured for $20 < p_{\mathrm{T,jet}}^{\mathrm{ch+ne}} < 40\,\mathrm{GeV}/c$ and $1.5 < p_{\mathrm{T}}^{\mathrm{assoc}} < 2.0\,\mathrm{GeV}/c$ in 0–10% collisions.

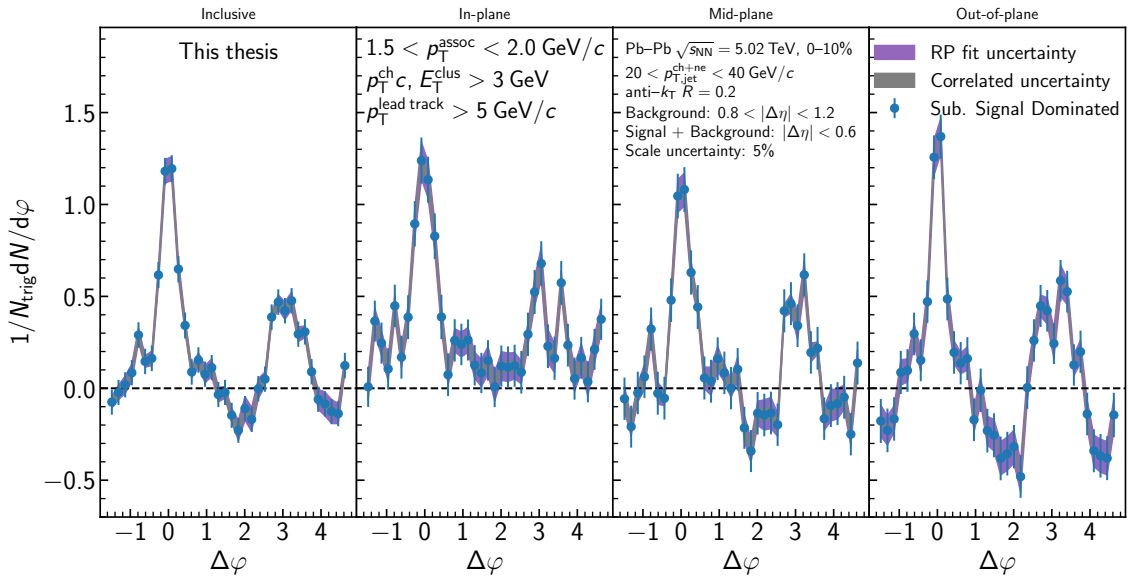

Figure D.270: The Reaction Plane Fit subtracted jet-hadron correlations measured for $20 < p_{\mathrm{T,jet}}^{\mathrm{ch+ne}} < 40\,\mathrm{GeV}/c$ and $1.5 < p_{\mathrm{T}}^{\mathrm{assoc}} < 2.0\,\mathrm{GeV}/c$ in 0–10% collisions. The subtracted data are shown in blue for each event plane orientation, with the fit uncertainty in purple and the correlated uncertainty in gray.

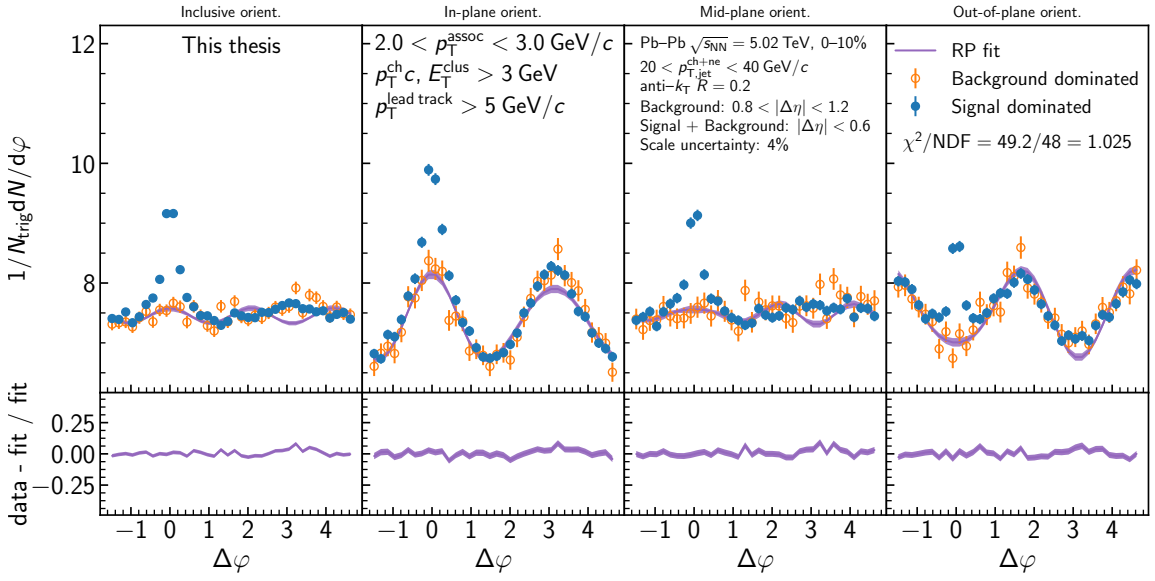

Figure D.271: The Reaction Plane Fit of jet-hadron correlations measured for $20 < p_{\mathrm{T,jet}}^{\mathrm{ch+ne}} < 40\,\mathrm{GeV}/c$ and $2.0 < p_{\mathrm{T}}^{\mathrm{assoc}} < 3.0\,\mathrm{GeV}/c$ in 0–10% collisions. The signal dominated data are shown in blue, the background dominated in orange, and the fit in purple. The upper panels show the signal and background dominated correlations measured in each event plane orientation. The lower panels show the fit residuals.

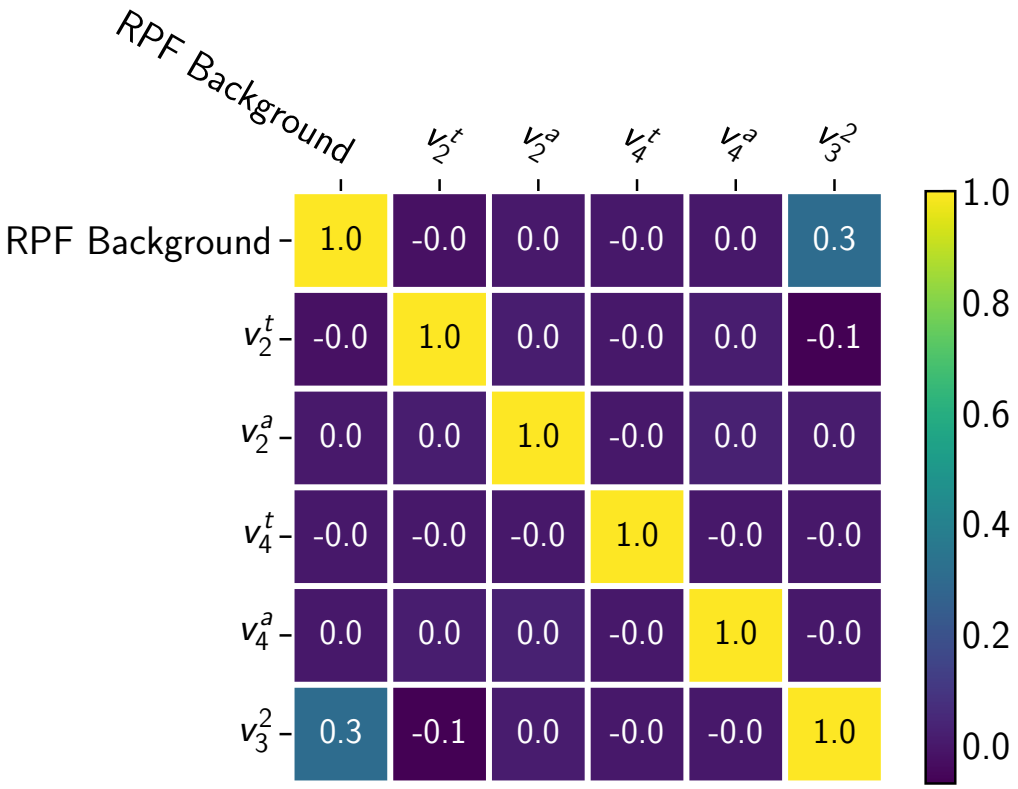

Figure D.272: Correlation matrix for the Reaction Plane Fit of jet-hadron correlations measured for $20 < p_{\mathrm{T,jet}}^{\mathrm{ch+ne}} < 40\,\mathrm{GeV}/c$ and $2.0 < p_{\mathrm{T}}^{\mathrm{assoc}} < 3.0\,\mathrm{GeV}/c$ in 0–10% collisions.

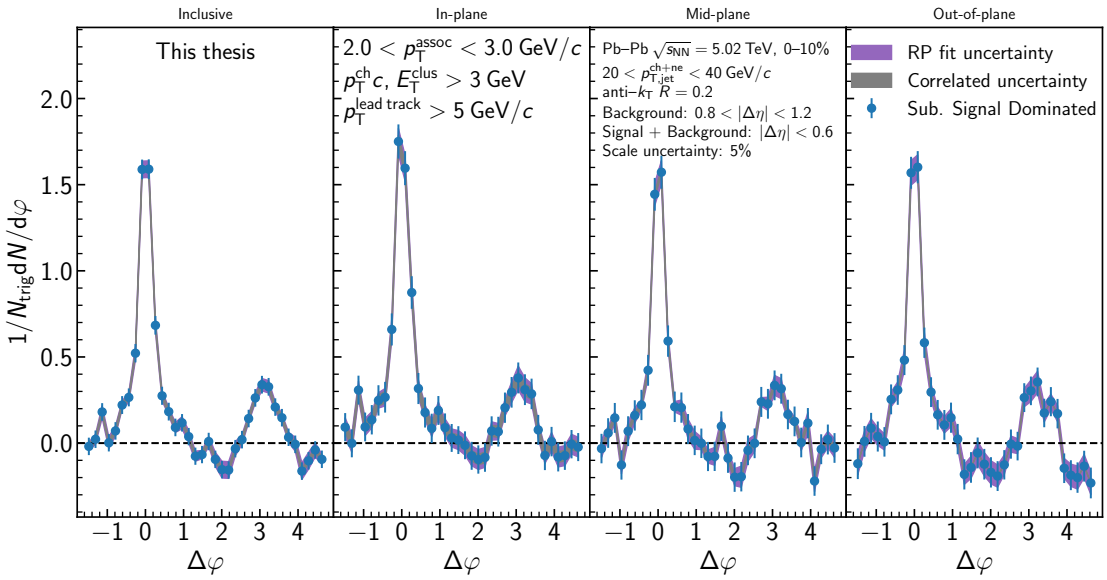

Figure D.273: The Reaction Plane Fit subtracted jet-hadron correlations measured for $20 < p_{\mathrm{T,jet}}^{\mathrm{ch+ne}} < 40\,\mathrm{GeV}/c$ and $2.0 < p_{\mathrm{T}}^{\mathrm{assoc}} < 3.0\,\mathrm{GeV}/c$ in 0–10% collisions. The subtracted data are shown in blue for each event plane orientation, with the fit uncertainty in purple and the correlated uncertainty in gray.

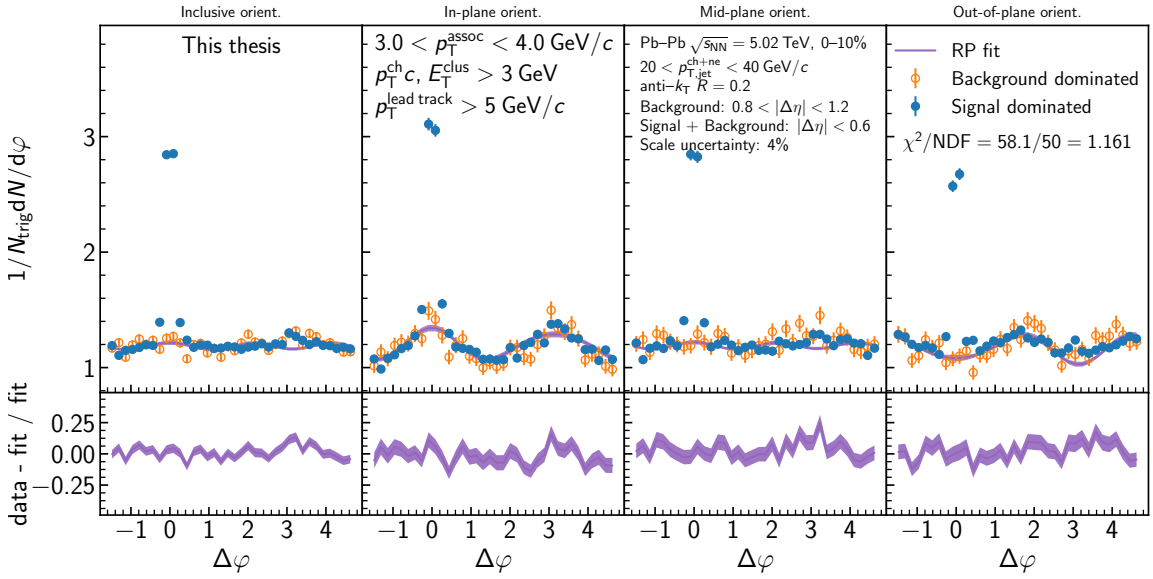

Figure D.274: The Reaction Plane Fit of jet-hadron correlations measured for $20 < p_{\mathrm{T,jet}}^{\mathrm{ch+ne}} < 40\,\mathrm{GeV}/c$ and $3.0 < p_{\mathrm{T}}^{\mathrm{assoc}} < 4.0\,\mathrm{GeV}/c$ in 0–10% collisions. The signal dominated data are shown in blue, the background dominated in orange, and the fit in purple. The upper panels show the signal and background dominated correlations measured in each event plane orientation. The lower panels show the fit residuals.

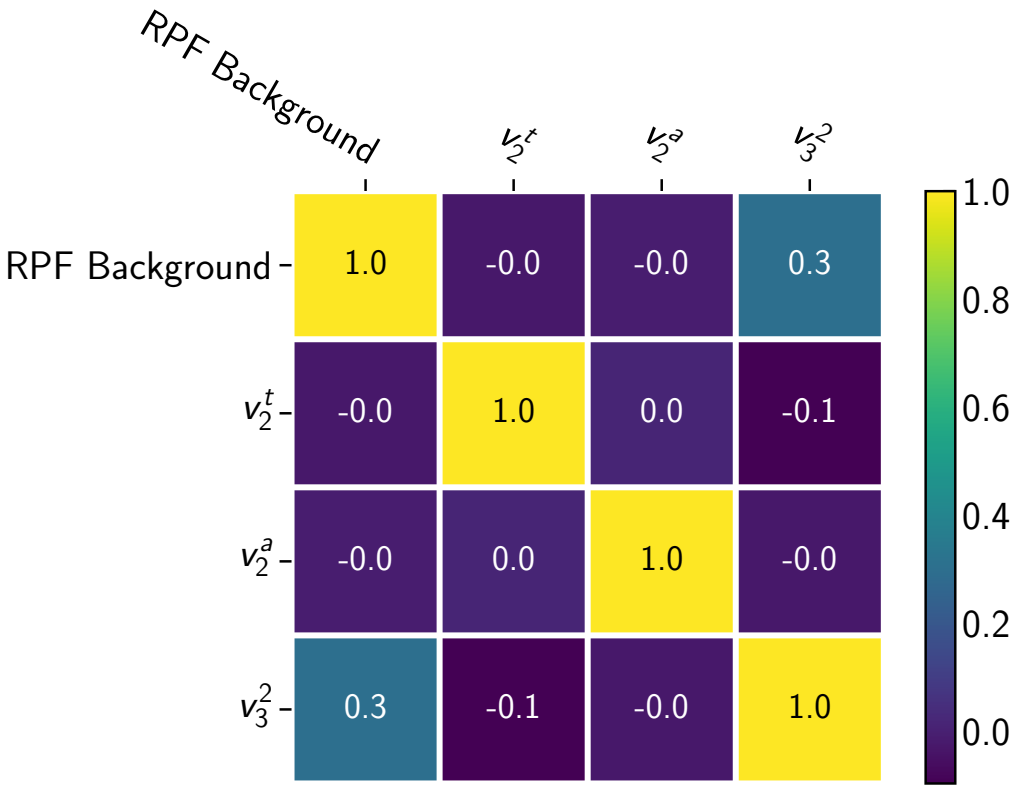

Figure D.275: Correlation matrix for the Reaction Plane Fit of jet-hadron correlations measured for $20 < p_{\mathrm{T,jet}}^{\mathrm{ch+ne}} < 40\,\mathrm{GeV}/c$ and $3.0 < p_{\mathrm{T}}^{\mathrm{assoc}} < 4.0\,\mathrm{GeV}/c$ in 0–10% collisions.

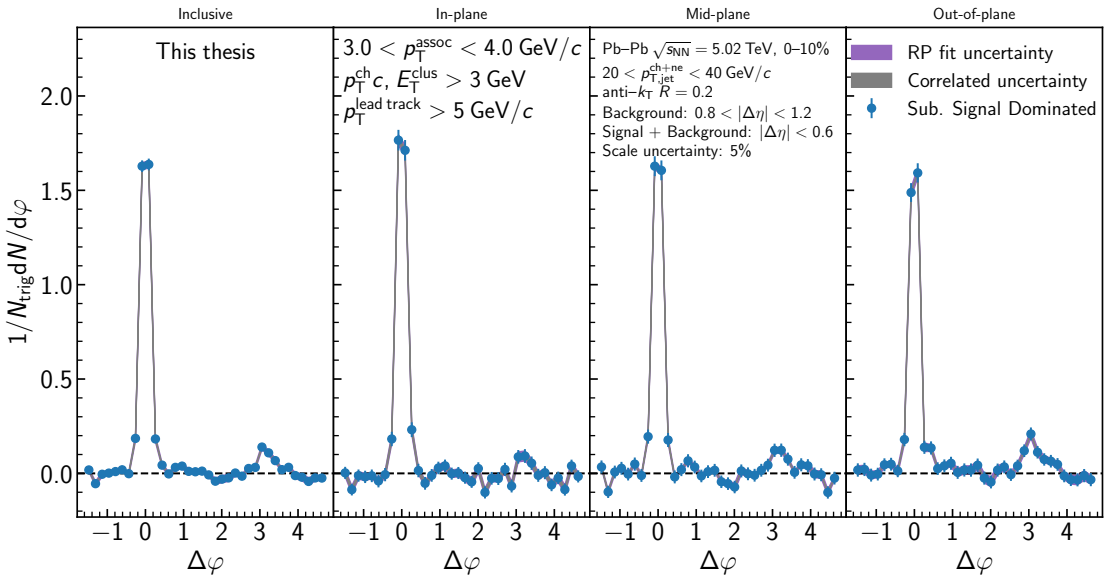

Figure D.276: The Reaction Plane Fit subtracted jet-hadron correlations measured for $20 < p_{\mathrm{T,jet}}^{\mathrm{ch+ne}} < 40\,\mathrm{GeV}/c$ and $3.0 < p_{\mathrm{T}}^{\mathrm{assoc}} < 4.0\,\mathrm{GeV}/c$ in 0–10% collisions. The subtracted data are shown in blue for each event plane orientation, with the fit uncertainty in purple and the correlated uncertainty in gray.

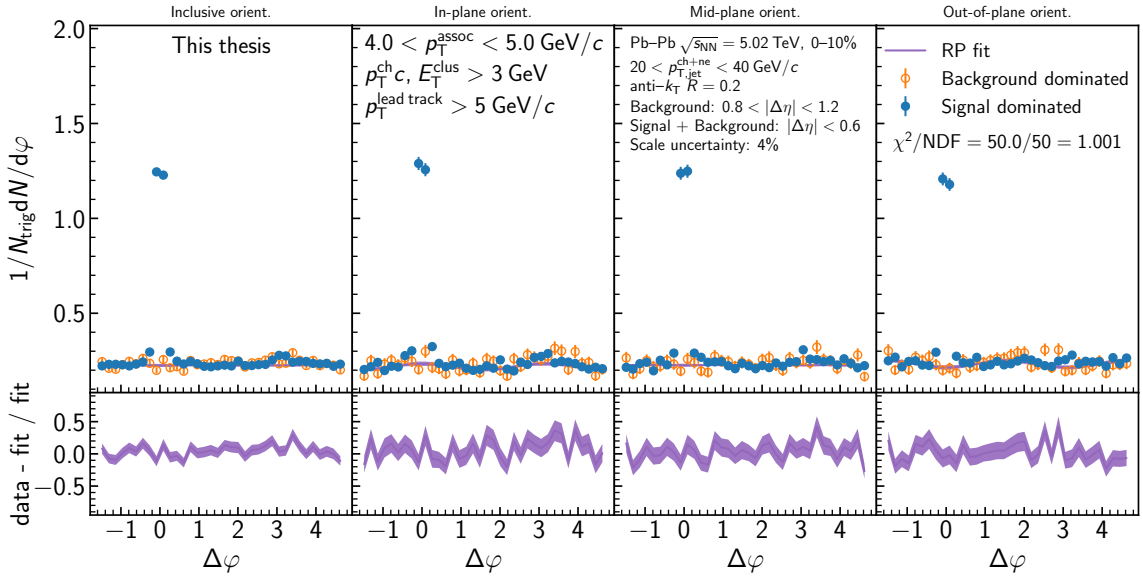

Figure D.277: The Reaction Plane Fit of jet-hadron correlations measured for $20 < p_{\mathrm{T,jet}}^{\mathrm{ch+ne}} < 40\,\mathrm{GeV}/c$ and $4.0 < p_{\mathrm{T}}^{\mathrm{assoc}} < 5.0\,\mathrm{GeV}/c$ in 0–10% collisions. The signal dominated data are shown in blue, the background dominated in orange, and the fit in purple. The upper panels show the signal and background dominated correlations measured in each event plane orientation. The lower panels show the fit residuals.

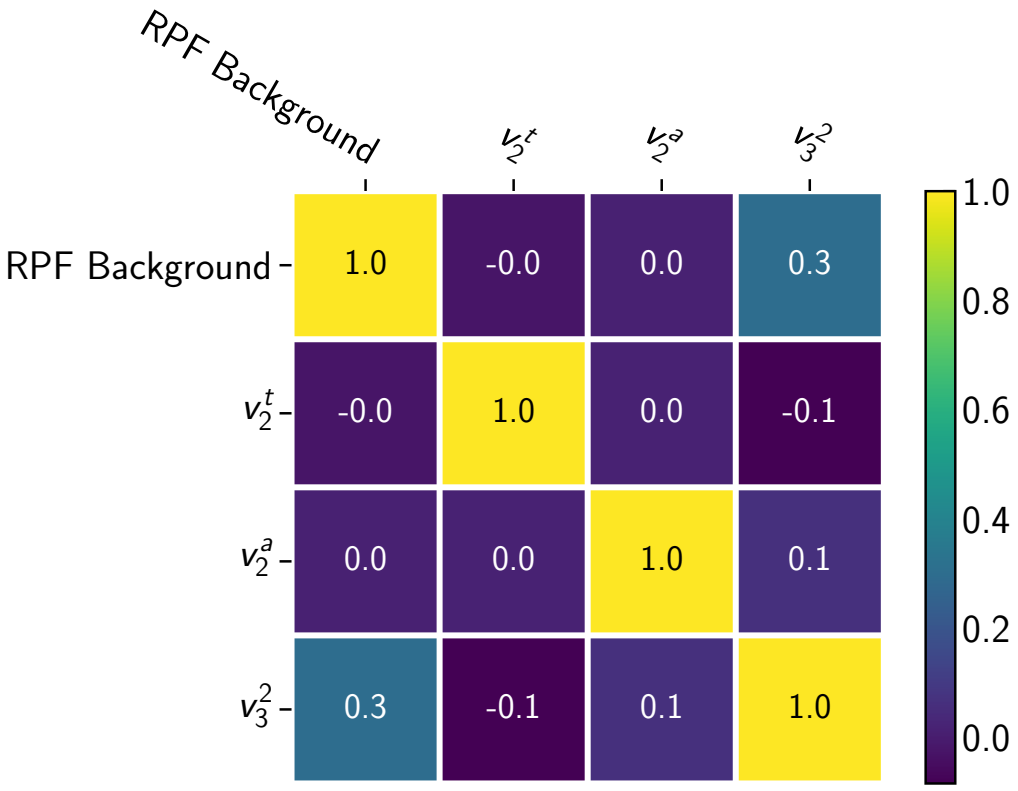

Figure D.278: Correlation matrix for the Reaction Plane Fit of jet-hadron correlations measured for $20 < p_{\mathrm{T,jet}}^{\mathrm{ch+ne}} < 40\,\mathrm{GeV}/c$ and $4.0 < p_{\mathrm{T}}^{\mathrm{assoc}} < 5.0\,\mathrm{GeV}/c$ in 0–10% collisions.

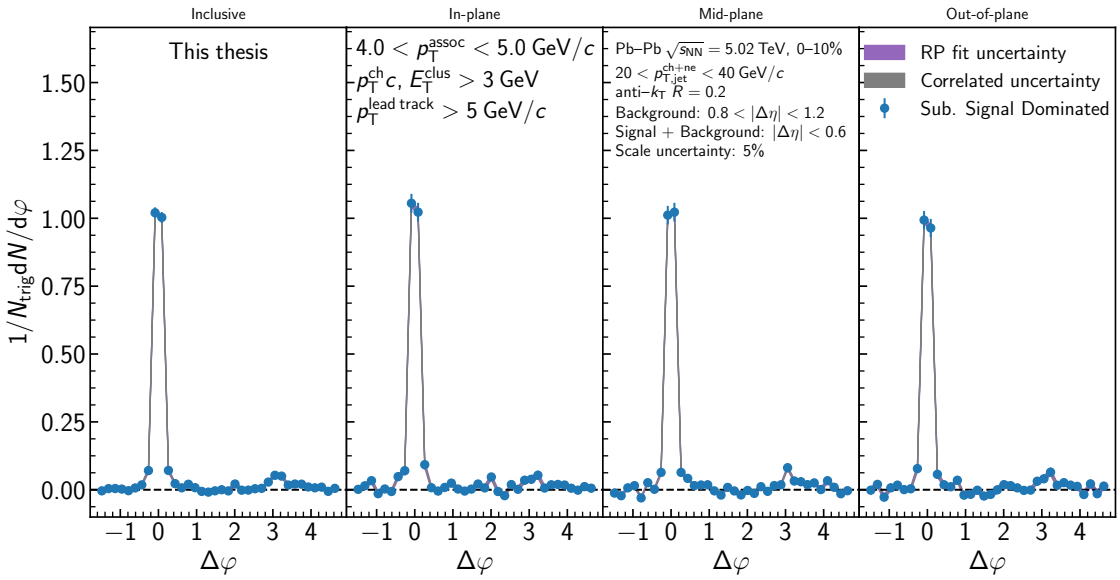

Figure D.279: The Reaction Plane Fit subtracted jet-hadron correlations measured for $20 < p_{\mathrm{T,jet}}^{\mathrm{ch+ne}} < 40\,\mathrm{GeV}/c$ and $4.0 < p_{\mathrm{T}}^{\mathrm{assoc}} < 5.0\,\mathrm{GeV}/c$ in 0–10% collisions. The subtracted data are shown in blue for each event plane orientation, with the fit uncertainty in purple and the correlated uncertainty in gray.

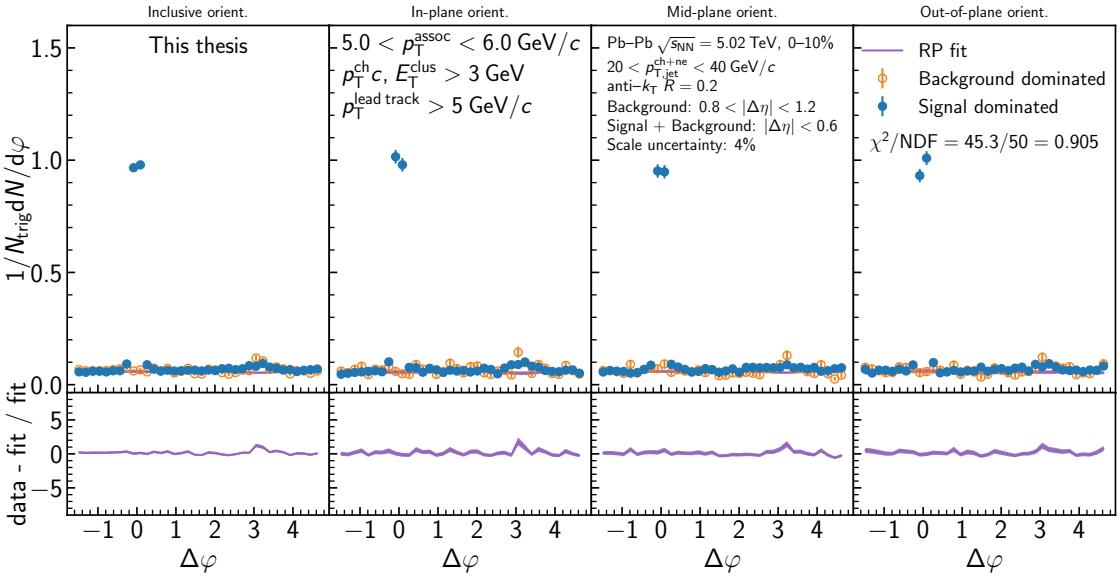

Figure D.280: The Reaction Plane Fit of jet-hadron correlations measured for $20 < p_{\mathrm{T,jet}}^{\mathrm{ch+ne}} < 40\,\mathrm{GeV}/c$ and $5.0 < p_{\mathrm{T}}^{\mathrm{assoc}} < 6.0\,\mathrm{GeV}/c$ in 0–10% collisions. The signal dominated data are shown in blue, the background dominated in orange, and the fit in purple. The upper panels show the signal and background dominated correlations measured in each event plane orientation. The lower panels show the fit residuals.

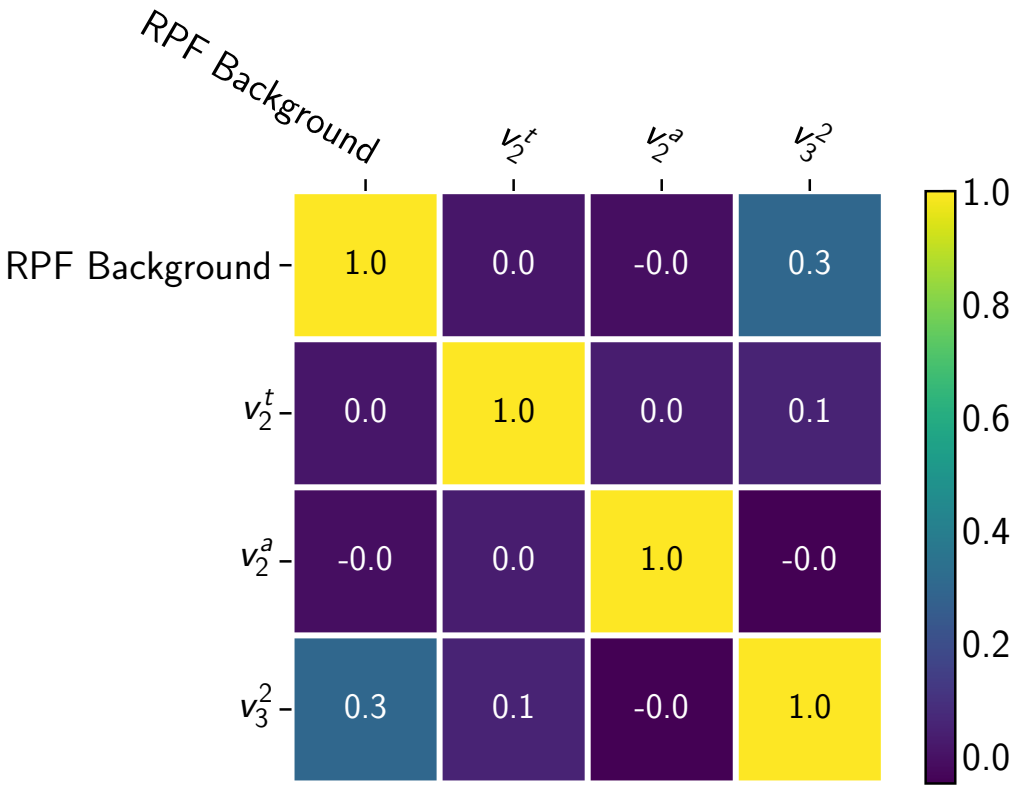

Figure D.281: Correlation matrix for the Reaction Plane Fit of jet-hadron correlations measured for $20 < p_{\mathrm{T,jet}}^{\mathrm{ch+ne}} < 40\,\mathrm{GeV}/c$ and $5.0 < p_{\mathrm{T}}^{\mathrm{assoc}} < 6.0\,\mathrm{GeV}/c$ in 0–10% collisions.

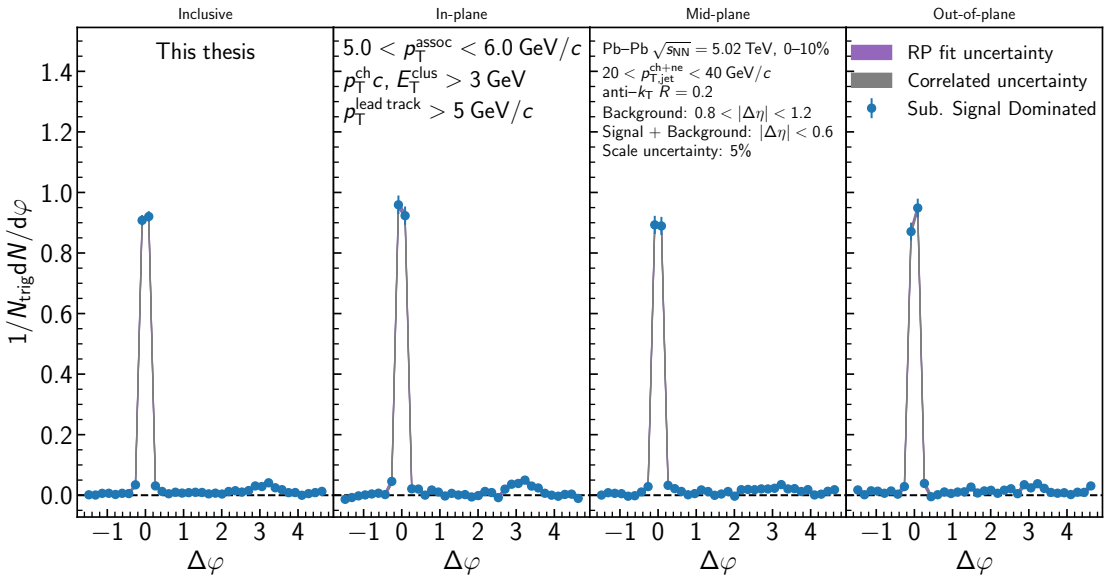

Figure D.282: The Reaction Plane Fit subtracted jet-hadron correlations measured for $20 < p_{\mathrm{T,jet}}^{\mathrm{ch+ne}} < 40\,\mathrm{GeV}/c$ and $5.0 < p_{\mathrm{T}}^{\mathrm{assoc}} < 6.0\,\mathrm{GeV}/c$ in 0–10% collisions. The subtracted data are shown in blue for each event plane orientation, with the fit uncertainty in purple and the correlated uncertainty in gray.

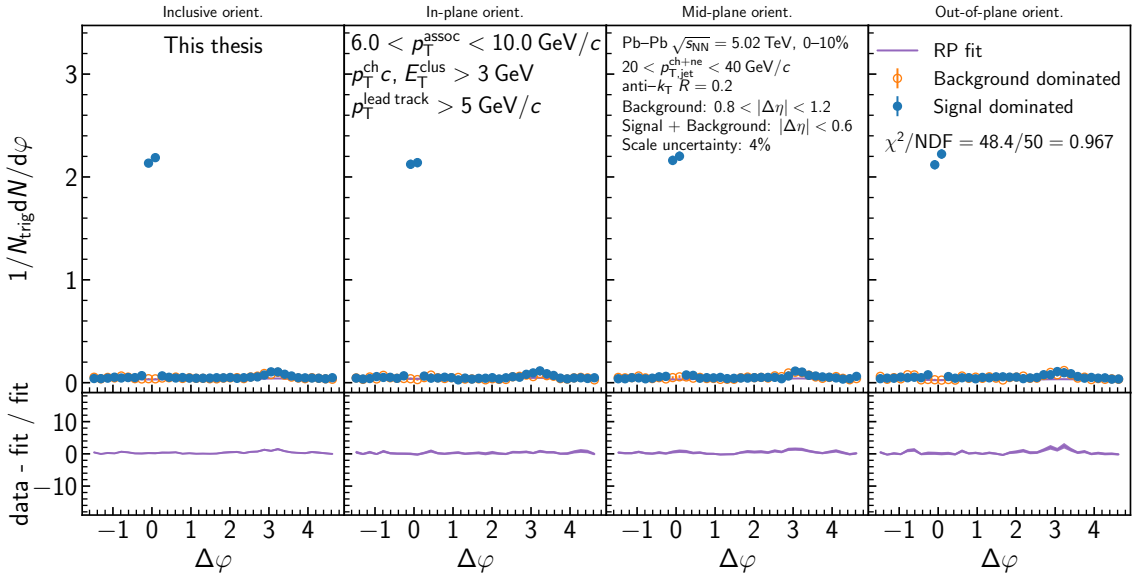

Figure D.283: The Reaction Plane Fit of jet-hadron correlations measured for $20 < p_{\mathrm{T,jet}}^{\mathrm{ch+ne}} < 40\,\mathrm{GeV}/c$ and $6.0 < p_{\mathrm{T}}^{\mathrm{assoc}} < 10.0\,\mathrm{GeV}/c$ in 0–10% collisions. The signal dominated data are shown in blue, the background dominated in orange, and the fit in purple. The upper panels show the signal and background dominated correlations measured in each event plane orientation. The lower panels show the fit residuals.

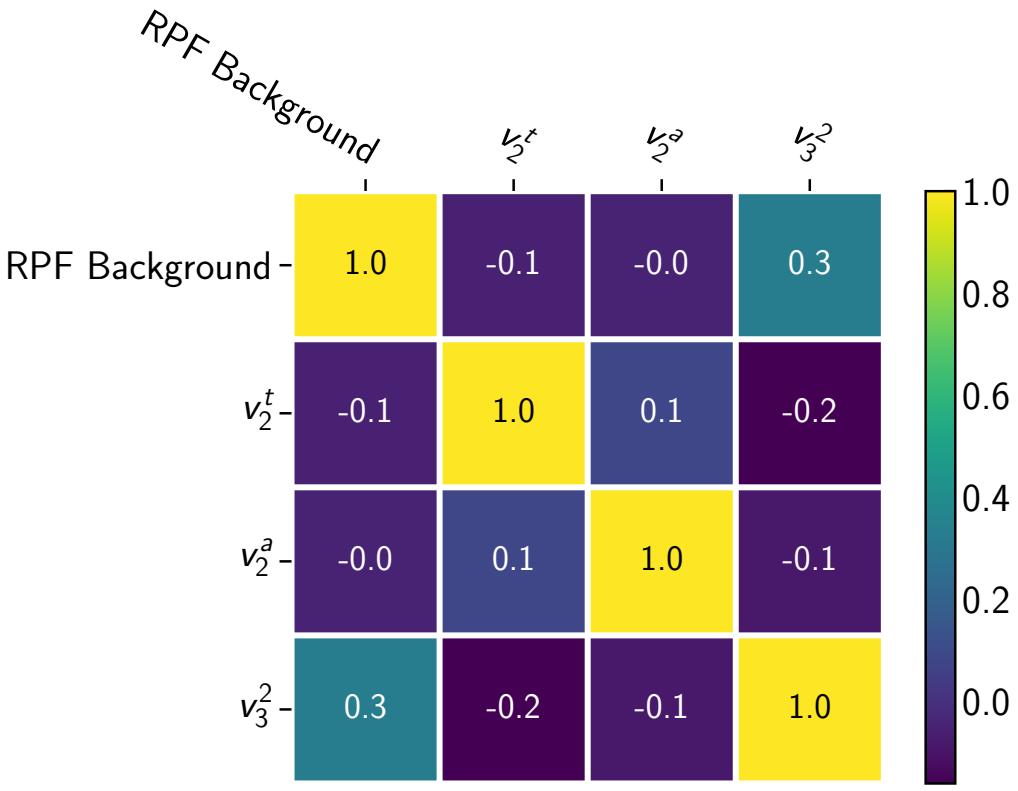

Figure D.284: Correlation matrix for the Reaction Plane Fit of jet-hadron correlations measured for $20 < p_{\mathrm{T,jet}}^{\mathrm{ch+ne}} < 40$ GeV/c and $6.0 < p_{\mathrm{T}}^{\mathrm{assoc}} < 10.0$ GeV/c in 0–10% collisions.

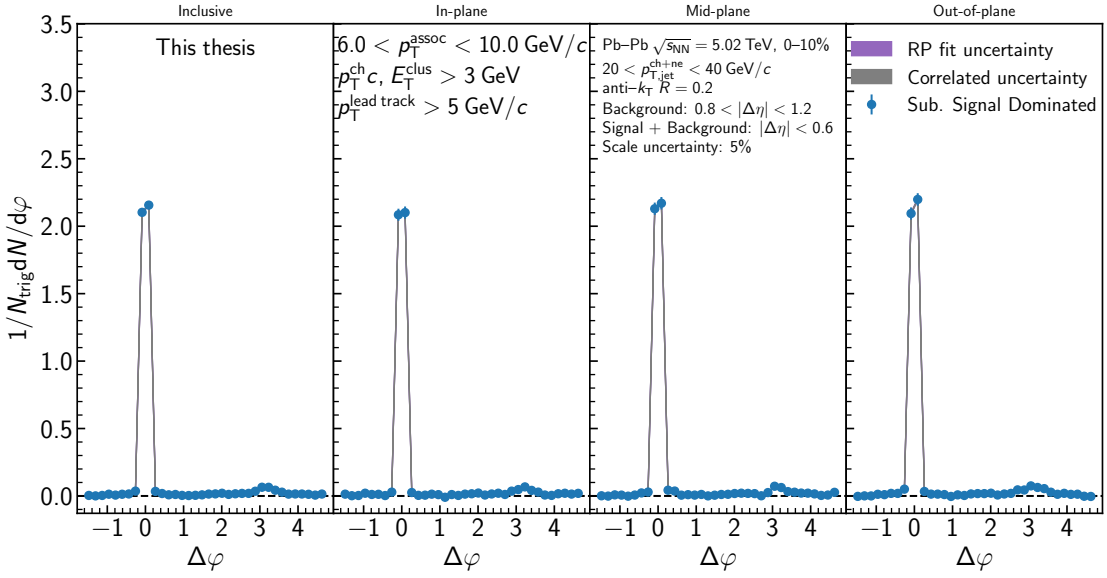

Figure D.285: The Reaction Plane Fit subtracted jet-hadron correlations measured for $20 < p_{\mathrm{T,jet}}^{\mathrm{ch+ne}} < 40\,\mathrm{GeV}/c$ and $6.0 < p_{\mathrm{T}}^{\mathrm{assoc}} < 10.0\,\mathrm{GeV}/c$ in 0–10% collisions. The subtracted data are shown in blue for each event plane orientation, with the fit uncertainty in purple and the correlated uncertainty in gray.

References

[1] C.N. Yang, R.L. Mills, Conservation of isotopic spin and isotopic gauge invariance, Phys. Rev. 96 (1954) 191–195. doi:10.1103/PhysRev.96.191.

[2] S. Bethke, The 2009 World Average of alpha(s), Eur. Phys. J. C64 (2009) 689–703. doi:10.1140/epjc/s10052-009-1173-1.

[3] J.C. Collins, D.E. Soper, G.F. Sterman, Factorization of Hard Processes in QCD, Adv. Ser. Direct. High Energy Phys. 5 (1989) 1–91. doi:10.1142/9789814503266_0001.

[4] G. Altarelli, G. Parisi, Asymptotic Freedom in Parton Language, Nucl. Phys. B126 (1977) 298–318. doi:10.1016/0550-3213(77)90384-4.

[5] Y.L. Dokshitzer, Calculation of the Structure Functions for Deep Inelastic Scattering and e+ e- Annihilation by Perturbation Theory in Quantum Chromodynamics., Sov. Phys. JETP. 46 (1977) 641–653.

[6] V.N. Gribov, L.N. Lipatov, Deep inelastic ep scattering in perturbation theory, Sov. J. Nucl. Phys. 15 (1972) 438–450.

[7] Ball, Richard D. *et al.*, Parton distributions from high-precision collider data, Eur. Phys. J. C77 (2017) 663. doi:10.1140/epjc/s10052-017-5199-5.

[8] T. Sjostrand, S. Mrenna, P.Z. Skands, PYTHIA 6.4 Physics and Manual, JHEP. 05 (2006) 026. doi:10.1088/1126-6708/2006/05/026.

[9] T. Sjostrand, S. Mrenna, P.Z. Skands, A Brief Introduction to PYTHIA 8.1, Comput. Phys. Commun. 178 (2008) 852–867. doi:10.1016/j.cpc.2008.01.036.

[10] QCD phase diagram, (n.d.). http://theorie.ikp.physik.tu-darmstadt.de/~tripolt/conferences/Tripolt_QCD_Phase_Diagram_2012.pdf.

[11] P. Steinbrecher, The QCD crossover at zero and non-zero baryon densities from Lattice QCD, Nucl. Phys. A982 (2019) 847–850. doi:10.1016/j.nuclphysa.2018.08.025.

[12] HotQCD Collaboration, Bazavov, A. *et al.*, Equation of state in (2+1)-flavor QCD, Phys. Rev. D90 (2014) 094503. doi:10.1103/PhysRevD.90.094503.

[13] PHENIX Collaboration, Adare, A. *et al.*, Centrality dependence of low-momentum direct-photon production in Au+Au collisions at $\sqrt{s_{NN}} = 200$ GeV, Phys. Rev. C91 (2015) 064904. doi:10.1103/PhysRevC.91.064904.

[14] ALICE Collaboration, Adam, Jaroslav *et al.*, Direct photon production in Pb-Pb collisions at $\sqrt{s_{\rm NN}} = 2.76$ TeV, Phys. Lett. B754 (2016) 235–248. doi:10.1016/j.physletb.2016.01.020.

[15] G. Policastro, D.T. Son, A.O. Starinets, The Shear viscosity of strongly coupled N=4 supersymmetric Yang-Mills plasma, Phys. Rev. Lett. 87 (2001) 081601. doi:10.1103/PhysRevLett.87.081601.

[16] P. Kovtun, D.T. Son, A.O. Starinets, Holography and hydrodynamics: Diffusion on stretched horizons, JHEP. 10 (2003) 064. doi:10.1088/1126-6708/2003/10/064.

[17] S. McDonald, C. Shen, F. Fillion-Gourdeau, S. Jeon, C. Gale, Hydrodynamic predictions for Pb+Pb collisions at 5.02 TeV, Phys. Rev. C95 (2017) 064913.

doi:10.1103/PhysRevC.95.064913.

[18] STAR Collaboration, Adamczyk, L. *et al.*, Global Λ hyperon polarization in nuclear collisions: evidence for the most vortical fluid, Nature. 548 (2017) 62–65. doi:10.1038/nature23004.

[19] B. Schenke, S. Jeon, C. Gale, Higher flow harmonics from (3+1)D event-by-event viscous hydrodynamics, Phys. Rev. C85 (2012) 024901. doi:10.1103/PhysRevC.85.024901.

[20] Chun Shen, Stages of a heavy ion collision, (n.d.). https://u.osu.edu/vishnu/2014/08/06/sketch-of-relativistic-heavy-ion-collisions/.

[21] R.J. Glauber, Lecture on theoretical physics, Ed. W.E. Brittin, L.G. Dunham, 1:315. New York: Interscience. (1959).

[22] R.J. Glauber, G. Matthiae, High-energy scattering of protons by nuclei, Nucl. Phys. B21 (1970) 135–157. doi:10.1016/0550-3213(70)90511-0.

[23] M.L. Miller, K. Reygers, S.J. Sanders, P. Steinberg, Glauber modeling in high energy nuclear collisions, Ann. Rev. Nucl. Part. Sci. 57 (2007) 205–243. doi:10.1146/annurev.nucl.57.090506.123020.

[24] ALICE Collaboration, Centrality determination of Pb-Pb collisions at $\sqrt{s_{NN}} = 2.76$ TeV with ALICE, Phys. Rev. C88 (2013) 044909. doi:10.1103/PhysRevC.88.044909.

[25] M. Cacciari, G.P. Salam, G. Soyez, The anti-k_t jet clustering algorithm, JHEP. 04 (2008) 063. doi:10.1088/1126-6708/2008/04/063.

[26] M. Cacciari, G.P. Salam, G. Soyez, FastJet User Manual, Eur. Phys. J. C72 (2012) 1896. doi:10.1140/epjc/s10052-012-1896-2.

[27] M. Cacciari, G.P. Salam, G. Soyez, The Catchment Area of Jets, JHEP. 04 (2008) 005. doi:10.1088/1126-6708/2008/04/005.

[28] H. Song, Y. Zhou, K. Gajdosova, Collective flow and hydrodynamics in large and small systems at the LHC, Nucl. Sci. Tech. 28 (2017) 99. doi:10.1007/s41365-017-0245-4.

[29] S. Voloshin, Y. Zhang, Flow study in relativistic nuclear collisions by Fourier expansion of Azimuthal particle distributions, Z. Phys. C70 (1996) 665–672. doi:10.1007/s002880050141.

[30] M. Rybar, Jets in pp and pbpb collisions at lhc, (2010). https://dspace.cuni.cz/bitstream/handle/20.500.11956/30607/DPTX_2007_1_11320_0_236034_0_48414.pdf?sequence=1&isAllowed=y.

[31] STAR Collaboration, Adler, C. *et al.*, Disappearance of back-to-back high p_T hadron correlations in central Au+Au collisions at $\sqrt{s_{NN}}$ = 200-GeV, Phys. Rev. Lett. 90 (2003) 082302. doi:10.1103/PhysRevLett.90.082302.

[32] STAR Collaboration, Adams, J. *et al.*, Evidence from d + Au measurements for final state suppression of high p(T) hadrons in Au+Au collisions at RHIC, Phys. Rev. Lett. 91 (2003) 072304. doi:10.1103/PhysRevLett.91.072304.

[33] STAR Collaboration, Adams, John *et al.*, Experimental and theoretical challenges in the search for the quark gluon plasma: The STAR Collaboration's critical assessment of the evidence from RHIC collisions, Nucl. Phys. A757 (2005) 102–183. doi:10.1016/j.nuclphysa.2005.03.085.

[34] M. Miller, Measurement of jets and jet quenching at rhic, PhD thesis, Yale University, 2004. http://star.physics.yale.edu/Theses/Thesis/_Miller.pdf.

[35] ALICE Collaboration, Acharya, Shreyasi *et al.*, Measurements of inclusive jet spectra in pp and central Pb-Pb collisions at $\sqrt{s_{\mathrm{NN}}} = 5.02$ TeV, (2019). http://arxiv.org/abs/1909.09718.

[36] ATLAS Collaboration, Aaboud, Morad *et al.*, Measurement of the nuclear modification factor for inclusive jets in Pb+Pb collisions at $\sqrt{s_{\mathrm{NN}}} = 5.02$ TeV with the ATLAS detector, Phys. Lett. B790 (2019) 108–128. doi:10.1016/j.physletb.2018.10.076.

[37] CMS Collaboration, Khachatryan, Vardan *et al.*, Measurement of transverse momentum relative to dijet systems in PbPb and pp collisions at $\sqrt{s_{\mathrm{NN}}} = 2.76$ TeV, JHEP. 01 (2016) 006. doi:10.1007/JHEP01(2016)006.

[38] CMS Collaboration, Chatrchyan, Serguei *et al.*, Measurement of Jet Fragmentation in PbPb and pp Collisions at $\sqrt{s_{NN}} = 2.76$ TeV, Phys. Rev. C90 (2014) 024908. doi:10.1103/PhysRevC.90.024908.

[39] ATLAS Collaboration, Aaboud, Morad *et al.*, Measurement of jet fragmentation in Pb+Pb and *pp* collisions at $\sqrt{s_{NN}} = 5.02$ TeV with the ATLAS detector, Phys. Rev. C98 (2018) 024908. doi:10.1103/PhysRevC.98.024908.

[40] D. d'Enterria, Jet quenching, Landolt-Bornstein. 23 (2010) 471. doi:10.1007/978-3-642-01539-7_16.

[41] JETSCAPE Collaboration, Putschke, J. H. *et al.*, The JETSCAPE framework, (2019). http://arxiv.org/abs/1903.07706.

[42] K. Zapp, G. Ingelman, J. Rathsman, J. Stachel, U.A. Wiedemann, A Monte Carlo Model for 'Jet Quenching', Eur. Phys. J. C60 (2009) 617–632. doi:10.1140/epjc/s10052-009-0941-2.

[43] K.C. Zapp, F. Krauss, U.A. Wiedemann, A perturbative framework for jet

quenching, JHEP. 03 (2013) 080. doi:10.1007/JHEP03(2013)080.

[44] STAR Collaboration, Jet-Hadron Correlations in $\sqrt{s_{\rm NN}}$ = 200 GeV p+p and Central Au+Au Collisions, Physical Review Letters. 15 (2013) 1–7. doi:10.1103/PhysRevLett.112.122301.

[45] CMS Collaboration, Khachatryan, Vardan *et al.*, Correlations between jets and charged particles in PbPb and pp collisions at $\sqrt{s_{\rm NN}}$ = 2.76 TeV, JHEP. 02 (2016) 156. doi:10.1007/JHEP02(2016)156.

[46] O.S. Bruning, P. Collier, P. Lebrun, S. Myers, R. Ostojic, J. Poole, P. Proudlock, LHC Design Report Vol.1: The LHC Main Ring, (2004).

[47] O. Buning, P. Collier, P. Lebrun, S. Myers, R. Ostojic, J. Poole, P. Proudlock, LHC Design Report. 2. The LHC infrastructure and general services, (2004).

[48] M. Benedikt, P. Collier, V. Mertens, J. Poole, K. Schindl, LHC Design Report. 3. The LHC injector chain, (2004).

[49] LHC Machine, The CERN large hadron collider: accelerator and experiments, J. Instrum. 3 (2008).

[50] ALICE Collaboration, Aamodt, K. *et al.*, The ALICE experiment at the CERN LHC, JINST. 3 (2008) S08002. doi:10.1088/1748-0221/3/08/S08002.

[51] ATLAS Collaboration, Aad, G. *et al.*, The ATLAS Experiment at the CERN Large Hadron Collider, JINST. 3 (2008) S08003. doi:10.1088/1748-0221/3/08/S08003.

[52] CMS Collaboration, Chatrchyan, S. *et al.*, The CMS Experiment at the CERN LHC, JINST. 3 (2008) S08004. doi:10.1088/1748-0221/3/08/S08004.

[53] LHCb Collaboration, Alves, Jr., A. Augusto *et al.*, The LHCb Detector at the

LHC, JINST. 3 (2008) S08005. doi:10.1088/1748-0221/3/08/S08005.

[54] ATLAS Collaboration, Aad, Georges *et al.*, Observation of a new particle in the search for the Standard Model Higgs boson with the ATLAS detector at the LHC, Phys. Lett. B716 (2012) 1–29. doi:10.1016/j.physletb.2012.08.020.

[55] CMS Collaboration, Chatrchyan, Serguei *et al.*, Observation of a New Boson at a Mass of 125 GeV with the CMS Experiment at the LHC, Phys. Lett. B716 (2012) 30–61. doi:10.1016/j.physletb.2012.08.021.

[56] M. Schaumann, others, First Xenon-Xenon Collisions in the LHC, in: Proceedings, 9th International Particle Accelerator Conference (IPAC 2018): Vancouver, BC Canada, April 29-May 4, 2018, 2018: p. MOPMF039. doi:10.18429/JACoW-IPAC2018-MOPMF039.

[57] Service graphique, CERN, Overall view of the LHC. Vue d'ensemble du LHC, (2014). https://cds.cern.ch/record/1708849.

[58] C. Lefèvre, The CERN accelerator complex. Complexe des accélérateurs du CERN, (2008). https://cds.cern.ch/record/1260465.

[59] ALICE Collaboration, Enhanced production of multi-strange hadrons in high-multiplicity proton-proton collisions, Nature Phys. 13 (2017) 535–539. doi:10.1038/nphys4111.

[60] ALICE Collaboration, Precision measurement of the mass difference between light nuclei and anti-nuclei, Nature Phys. 11 (2015) 811–814. doi:10.1038/nphys3432.

[61] ALICE Collaboration, Acharya, Shreyasi *et al.*, J/ψ elliptic flow in Pb-Pb collisions at $\sqrt{s_{\rm NN}}$ = 5.02 TeV, Phys. Rev. Lett. 119 (2017) 242301. doi:10.1103/PhysRevLett.119.242301.

[62] R. Fruhwirth, Application of Kalman filtering to track and vertex fitting, Nucl. Instrum. Meth. A262 (1987) 444–450. doi:10.1016/0168-9002(87)90887-4.

[63] ALICE Collaboration, Performance of the ALICE Experiment at the CERN LHC, Int. J. Mod. Phys. A29 (2014).

[64] ALICE Collaboration, Dellacasa, G. *et al.*, ALICE: Technical design report of the time projection chamber, (2000).

[65] ALICE Collaboration, ALICE electromagnetic calorimeter technical design report, CERN-ALICE-TDR-014, CERN-LHCC-2008-014 (2015). http://inspirehep.net/record/794183.

[66] J. Mazer, Jet-hadron correlations relative to the event plane in Pb–Pb collisions at the LHC in ALICE, 2017. https://cds.cern.ch/record/2257086.

[67] N. Sharma, J. Mazer, M. Stuart, C. Nattrass, Background subtraction methods for precision measurements of di-hadron and jet-hadron correlations in heavy ion collisions, Phys. Rev. C. 93 (2016) 044915. doi:10.1103/PhysRevC.93.044915.

[68] ALICE Collaboration, Anomalous evolution of the near-side jet peak shape in Pb-Pb collisions at $\sqrt{s_{\mathrm{NN}}} = 2.76$ TeV, Phys. Rev. Lett. 119 (2017) 102301. doi:10.1103/PhysRevLett.119.102301.

[69] X.-N. Wang, M. Gyulassy, HIJING: A Monte Carlo model for multiple jet production in p p, p A and A A collisions, Phys. Rev. D44 (1991) 3501–3516. doi:10.1103/PhysRevD.44.3501.

[70] M. Gyulassy, X.-N. Wang, HIJING 1.0: A Monte Carlo program for parton and particle production in high-energy hadronic and nuclear collisions, Comput. Phys. Commun. 83 (1994) 307. doi:10.1016/0010-4655(94)90057-4.

[71] M. Cacciari, G.P. Salam, Dispelling the N^3 myth for the k_t jet-finder, Phys. Lett. B641 (2006) 57–61. doi:10.1016/j.physletb.2006.08.037.

[72] ALICE Collaboration, Abelev, Betty *et al.*, Measurement of Event Background Fluctuations for Charged Particle Jet Reconstruction in Pb-Pb collisions at $\sqrt{s_{NN}} =$ 2.76 TeV, JHEP. 03 (2012) 053. doi:10.1007/JHEP03(2012)053.

[73] A.M. Poskanzer, S.A. Voloshin, Methods for analyzing anisotropic flow in relativistic nuclear collisions, Phys. Rev. C58 (1998) 1671–1678. doi:10.1103/PhysRevC.58.1671.

[74] I. Selyuzhenkov, S. Voloshin, Effects of non-uniform acceptance in anisotropic flow measurement, Phys. Rev. C77 (2008) 034904. doi:10.1103/PhysRevC.77.034904.

[75] J. Onderwaater, lIya Selyuzhenkov, V. Gonzalez, Flow Vector Corrections framework [software], (2016). https://github.com/FlowCorrections/FlowVectorCorrections.

[76] P. Skands, S. Carrazza, J. Rojo, Tuning PYTHIA 8.1: the Monash 2013 Tune, Eur. Phys. J. C74 (2014) 3024. doi:10.1140/epjc/s10052-014-3024-y.

[77] R. Brun, F. Bruyant, F. Carminati, S. Giani, M. Maire, A. McPherson, G. Patrick, L. Urban, GEANT Detector Description and Simulation Tool, (1994). doi:10.17181/CERN.MUHF.DMJ1.

[78] ALICE Collaboration, Adam, Jaroslav *et al.*, Anisotropic flow of charged particles in Pb-Pb collisions at $\sqrt{s_{\rm NN}} = 5.02$ TeV, Phys. Rev. Lett. 116 (2016) 132302. doi:10.1103/PhysRevLett.116.132302.

[79] ALICE Collaboration, Aamodt, K. *et al.*, Elliptic flow of charged particles in Pb-Pb collisions at 2.76 TeV, Phys. Rev. Lett. 105 (2010) 252302. doi:10.1103/PhysRevLett.105.252302.

[80] STAR Collaboration, Adams, J. *et al.*, Azimuthal anisotropy in Au+Au collisions at $\sqrt{s_{\rm NN}}$ = 200 GeV, Phys. Rev. C72 (2005) 014904. doi:10.1103/PhysRevC.72.014904.

[81] CMS Collaboration, Chatrchyan, Serguei *et al.*, Azimuthal anisotropy of charged particles at high transverse momenta in PbPb collisions at $\sqrt{s_{NN}} = 2.76$ TeV, Phys. Rev. Lett. 109 (2012) 022301. doi:10.1103/PhysRevLett.109.022301.

[82] ATLAS Collaboration, Aad, Georges *et al.*, Measurement of flow harmonics with multi-particle cumulants in Pb+Pb collisions at $\sqrt{s_{\rm NN}} = 2.76$ TeV with the ATLAS detector, Eur. Phys. J. C74 (2014) 3157. doi:10.1140/epjc/s10052-014-3157-z.

[83] ATLAS Collaboration, Aaboud, Morad *et al.*, Measurement of the azimuthal anisotropy of charged particles produced in $\sqrt{s_{\rm NN}} = 5.02$ TeV Pb+Pb collisions with the ATLAS detector, Eur. Phys. J. C78 (2018) 997. doi:10.1140/epjc/s10052-018-6468-7.

[84] ALICE Collaboration, Azimuthal anisotropy of charged jet production in $\sqrt{s_{\rm NN}}$ = 2.76 TeV Pb-Pb collisions, (2015). doi:10.1016/j.physletb.2015.12.047.

[85] ATLAS Collaboration, Measurement of the Azimuthal Angle Dependence of Inclusive Jet Yields in Pb+Pb Collisions at $\sqrt{s_{NN}}$=2.76 TeV with the ATLAS Detector, Phys. Rev. Lett. 111 (2013) 152301. doi:10.1103/PhysRevLett.111.152301.

[86] C. Nattrass, T. Todoroki, Event plane dependence of the flow modulated background in dihadron and jet-hadron correlations in heavy ion collisions, Phys. Rev. C. 97 (2018) 054911. doi:10.1103/PhysRevC.97.054911.

[87] J. Bielcikova, S. Esumi, K. Filimonov, S. Voloshin, J.P. Wurm, Elliptic flow contribution to two particle correlations at different orientations to the reaction plane, Phys. Rev. C69 (2004) 021901. doi:10.1103/PhysRevC.69.021901.

[88] F. James, M. Roos, Minuit – a system for function minimization and analysis of

the parameter errors and correlations, Computer Physics Communications. 10 (1975) 343–367. doi:10.1016/0010-4655(75)90039-9.

[89] F. James, M. Winkler, MINUIT User's Guide, (2004). http://seal.web.cern.ch/seal/documents/minuit/mnusersguide.pdf.

[90] iminuit team, Iminuit – a python interface to minuit, (n.d.).

[91] C. Nattrass, N. Sharma, J. Mazer, M. Stuart, A. Bejnood, Disappearance of the Mach Cone in heavy ion collisions, Phys. Rev. C94 (2016) 011901. doi:10.1103/PhysRevC.94.011901.

[92] ALICE preliminary results, Measurement of charged jet spectra in collisions at $\sqrt{s_{\rm NN}}$ = 5.02 TeV with ALICE at LHC (update including high interaction Pb-Pb runs), (n.d.). https://alice-figure.web.cern.ch/node/9760.

[93] R. Field, R.C. Group, PYTHIA tune A, HERWIG, and JIMMY in Run 2 at CDF, (2005). http://arxiv.org/abs/hep-ph/0510198.

[94] Alver, B. *et al.*, Importance of correlations and fluctuations on the initial source eccentricity in high-energy nucleus-nucleus collisions, Phys. Rev. C. 77 (2008) 014906. doi:10.1103/PhysRevC.77.014906.

[95] C. Loizides, J. Kamin, D. d'Enterria, Improved monte carlo glauber predictions at present and future nuclear colliders, Phys. Rev. C. 97 (2018) 054910. doi:10.1103/PhysRevC.97.054910.

[96] ALICE Collaboration, Centrality determination in heavy ion collisions, (n.d.). http://cds.cern.ch/record/2636623.

[97] K. Lapidus, Private communication, (2018).

[98] M. Oliver, Private communication, (2019).

[99] P.Z. Skands, Tuning Monte Carlo Generators: The Perugia Tunes, Phys. Rev. D82 (2010) 074018. doi:10.1103/PhysRevD.82.074018.

[100] S. Oh, Private communication, (2019).

[101] J. Noronha-Hostler, B. Betz, J. Noronha, M. Gyulassy, Event-by-event hydrodynamics + jet energy loss: A solution to the $R_{AA} \otimes v_2$ puzzle, Phys. Rev. Lett. 116 (2016) 252301. doi:10.1103/PhysRevLett.116.252301.

[102] J. Noronha-Hostler, Solving the $R_{AA} \otimes v_2$ puzzle, J. Phys. Conf. Ser. 736 (2016) 012019. doi:10.1088/1742-6596/736/1/012019.

[103] R. Ehlers, J. Mulligan, Alice Overwatch: Online Monitoring and Data Quality Assurance Using HLT Data, EPJ Web Conf. 214 (2019) 01038. doi:10.1051/epjconf/201921401038.

[104] B. von Haller, A. Telesca, S. Chapeland, F. Carena, W. Carena, V.C. Barroso, F. Costa, E. Denes, R. Divià, U. Fuchs, G. Simonetti, C. Soós, P.V. Vyvre, for the ALICE Collaboration, The alice data quality monitoring system, Journal of Physics: Conference Series. 331 (2011) 022030. http://stacks.iop.org/1742-6596/331/i=2/a=022030.

[105] ALICE Collaboration, Acharya, Shreyasi *et al.*, Real-time data processing in the ALICE High Level Trigger at the LHC, Comput. Phys. Commun. 242 (2019) 25–48. doi:10.1016/j.cpc.2019.04.011.

[106] M. Krzewicki, V. Lindenstruth, for the ALICE Collaboration, ALICE HLT Run 2 performance overview, Journal of Physics: Conference Series. 898 (2017) 032056. http://stacks.iop.org/1742-6596/898/i=3/a=032056.

[107] P. Buncic, M. Krzewicki, P. Vande Vyvre, Technical Design Report for the Upgrade of the Online-Offline Computing System, 2015. https://cds.cern.ch/record/2011297.

[108] R. Ehlers, J. Mulligan, ALICE Overwatch [software] v1.0, (2018). doi:10.5281/zenodo.1309376.

[109] ZeroMQ Project, ZeroMQ [software, v 4.2.5, (2018). http://zeromq.org/intro:get-the-software.

[110] ISO/IEC 14882:2011 Information technology — Programming languages — C++, International Organization for Standardization, 2011.

[111] Python project, Python [software], v. 3.7.4, (2019). https://www.python.org/downloads/release/python-374/.

[112] R. Brun, F. Rademakers, ROOT: An object oriented data analysis framework, Nucl. Instrum. Meth. A389 (1997) 81–86. doi:10.1016/S0168-9002(97)00048-X.

[113] ROOT project, ROOT [software], v 6.10/08, (2018). https://root.cern.ch/content/release-61008.

[114] Pallets Project, Flask [software], v 1.0.2, (2018). https://github.com/pallets/flask/releases/tag/1.0.2.

[115] Polymer Project, Polymer [software] v1.0, (2018). https://www.polymer-project.org/1.0/start/.

[116] B. Bellenot, S. Linev, JavaScript root, Journal of Physics: Conference Series. 664 (2015) 062033. http://stacks.iop.org/1742-6596/664/i=6/a=062033.

[117] B. Bellenot, S. Linev, JavaScript ROOT [software], v. 5.5.0, (2018). https:

//github.com/root-project/jsroot/releases/tag/5.5.0.

[118] R. Ehlers, Reaction Plane Fit [software] v3.1, (2018). doi:10.5281/zenodo.1599239.

[119] S. van der Walt, S.C. Colbert, G. Varoquaux, The numpy array: A structure for efficient numerical computation, Computing in Science Engineering. 13 (2011) 22–30. doi:10.1109/MCSE.2011.37.

[120] E. Jones, T. Oliphant, P. Peterson, others, SciPy: Open source scientific tools for Python, (n.d.). http://www.scipy.org/.

[121] J.D. Hunter, Matplotlib: A 2D graphics environment, Computing in Science & Engineering. 9 (2007) 90–95. doi:10.1109/MCSE.2007.55.

[122] P.A. Brodtkorb, Numdifftools [software], v0.9.39, (2014). https://github.com/pbrod/numdifftools.

[123] R.D. Cousins, Generalization of chisquare goodness-of-fit testfor binned data using saturated models, withApplication to histograms, (2013). http://www.physics.ucla.edu/~cousins/stats/cousins_saturated.pdf.

[124] R.D. Cousins, On goodness-of-fit tests, (2016). http://cousins.web.cern.ch/cousins/ongoodness6march2016.pdf.

[125] S. Baker, R.D. Cousins, Clarification of the Use of Chi Square and Likelihood Functions in Fits to Histograms, Nucl. Instrum. Meth. 221 (1984) 437–442. doi:10.1016/0167-5087(84)90016-4.

[126] R. Ehlers, J. Mulligan, ALICE EMCal Corrections Framework, (2016). http://alidoc.cern.ch/AliPhysics/master/READMEemcCorrections.html.

[127] R. Ehlers, ALICE EMCal Embedding Framework, (2017). http://alidoc.cern.ch

/AliPhysics/master/READMEemcEmbedding.html.

[128] Upgrade of the ALICE Time Projection Chamber, 2013. https://cds.cern.ch/record/1622286.

[129] F. Sauli, GEM: A new concept for electron amplification in gas detectors, Nucl. Instrum. Meth. A386 (1997) 531–534. doi:10.1016/S0168-9002(96)01172-2.

[130] Y. Giomataris, P. Rebourgeard, J.P. Robert, G. Charpak, MICROMEGAS: A High granularity position sensitive gaseous detector for high particle flux environments, Nucl. Instrum. Meth. A376 (1996) 29–35. doi:10.1016/0168-9002(96)00175-1.

[131] S. Aiola, R.J. Ehlers, S. Gu, J.W. Harris, R. Majka, J.D. Mulligan, M. Oliver, J. Schambach, N. Smirnov, Combination of two Gas Electron Multipliers and a Micromegas as gain elements for a time projection chamber, Nucl. Instrum. Meth. A834 (2016) 149–157. doi:10.1016/j.nima.2016.08.007.

[132] Addendum to the Technical Design Report for the Upgrade of the ALICE Time Projection Chamber, 2015. https://cds.cern.ch/record/1984329.